Dissertation

Submitted to the

Combined Faculty of Mathematics, Engineering and Natural Sciences

of the

Ruperto-Carola-University of Heidelberg, Germany

for the degree of

Doctor of Natural Sciences (Dr. rer. nat.)

Put forward by

David Maximilian Immig

born in Preetz, Germany

Oral examination: 27.01.2026

Straggling in Underdepleted Ultra-Thin Silicon HV-CMOS Sensors

A hitchhiker's guide to the energy response calibration of a pixel detector to understand energy deposition and charge collection via drift and diffusion in HV-MAPS

Referees:

Prof. Dr. André Schöning

Prof. Dr. Ulrich Uwer

Abstract

The pursuit of increasingly rare processes with higher precision in modern high-energy particle physics experiments drives the development of silicon pixel detectors offering excellent spatial and timing resolution, radiation hardness, and minimal material budget. However, a lower material budget necessitates thinner detectors, which provide less active volume for energy deposition, thereby reducing the signal-to-noise ratio.

A promising approach is represented by HV-MAPS (**H**igh-**V**oltage **M**onolithic **A**ctive **P**ixel **S**ensor). These monolithic pixel sensors integrate the active pixel matrix and readout electronics on a single die, allowing the silicon sensors to be thinned down to 50 µm. The sensor studied in this work is the MuPix10, a full-reticle prototype of about $2 \times 2\,\mathrm{cm}^2$, developed for the *Mu3e* experiment. Each pixel features a large fill factor electrode design of a deep *n*-well embedded in a low to medium resistivity *p*-substrate.

HV-MAPS are generally biased from the top through guard-ring structures, and cannot be operated beyond full depletion. However, variations in substrate resistivity and manufacturing tolerances lead to varying depletion depths across sensors, mandating a better understanding of charge collection in under-depleted operation.

To investigate the corresponding charge collection spectrum, a dedicated testbeam campaign was performed using $350\,\mathrm{MeV\,c^{-1}}$ pions. This is done for different sensor thicknesses, ranging from 50 µm to 100 µm, as well as substrate resistivities and reverse bias voltages. By measuring the hit efficiency as function of the applied detection threshold, the integrated charge spectrum is reconstructed. To unfold the impact of detector effects on these measurements, a dedicated calibration procedure was developed based on charge injection to the pixel electronics and Fe-55 source measurements for absolute charge calibration.

The charge spectrum is modeled by a convolution of a Landau distribution with a normal distribution to account for energy deposition fluctuations and detector effects, respectively. This approach has been evaluated using simulated charge deposition spectra and has proven to be valid even for thin silicon sensors. By applying theoretical predictions for the scale and the most probable energy loss for incident particles of known kinematics, the effective charge deposition thickness can be extracted.

The measured charge collection exceeds expectations based solely on the depleted region, indicating that the non-depleted volume significantly contributes to the charge collection in under-depleted operation. Even for low bias voltages, where charge losses due to charge sharing are expected, the observed charge collection exceeds the depleted thickness expectation. Comparing an almost fully depleted 50 µm sensor with a 100 µm sensor at −20 V shows a 40 % higher most probable charge collection, corresponding to an excess effective deposition thickness of about 12 µm. The relative excess observed under equivalent bias conditions increases with the sensor thickness, implying that the size of the non-depleted region governs the overall charge collection behavior in this thickness range. This suggests that even in thicker sensors, a notable fraction of the non-depleted region participates in charge collection.

Kurzreferat

Die Suche nach immer selteneren Zerfallskanälen in modernen Hochenergiephysikexperimenten treibt die Entwicklung hochpräziser Silizium-Pixeldetektoren voran, die eine exzellente räumliche und zeitliche Auflösung, hohe Strahlungstoleranz sowie ein minimales Materialbudget bieten. Ein geringeres Materialbudget erfordert jedoch dünnere Detektoren, die weniger aktives Volumen für den Energieübertrag einfallender Teilchen bieten und dadurch das Signal-Rausch-Verhältnis verringern können.

Ein vielversprechender Ansatz, diese Anforderungen zu erfüllen, sind hochspannungsbetriebene monolithische aktive Pixelsensoren (HV-MAPS). Diese integrieren die aktive Pixelmatrix und die Ausleseelektronik auf einem einzigen Chip, wodurch die Siliziumsensoren auf 50 µm gedünnt werden können. In dieser Arbeit wurde der MuPix10 untersucht, ein Prototyp mit einer aktiven Fläche von etwa $2 \times 2\,\mathrm{cm}^2$, der für das Mu3e-Experiment entwickelt wurde. Die Pixel basieren auf einem Elektroden-Design mit großem Füllfaktor und bestehen aus tiefen n-Wannen, die in einem p-Substrat mit niedriger bis mittlerer Resistivität eingebettet sind.

Die Hochspannung für HV-MAPS wird üblicherweise von der Oberseite über sogenannte Guard-Ring-Strukturen angelegt, wodurch ein Betrieb über die vollständige Verarmung des Substrats hinaus nicht möglich ist. Variationen in den Substratresistivitäten und Toleranzen in der Herstellung führen jedoch zu unterschiedlichen Verarmungstiefen bei den Sensoren, sodass ein besseres Verständnis der Ladungssammlung im unterverarmten Betrieb erforderlich ist.

Zur Untersuchung des Spektrums der zur Ladungssammlung beitragenden Elektronen wurde eine Teststrahlkampagne mit positiv geladenen Pionen bei $350\,\mathrm{MeV\,c^{-1}}$ durchgeführt. Dabei kamen verschiedene Sensordicken im Bereich von 50 µm bis 100 µm sowie unterschiedliche Substratresistivitäten und Hochspannungen zum Einsatz. Durch die Messung der Teilchendetektionseffizienz in Abhängigkeit von der Detektionsschwelle wird das integrierte Ladungsspektrum erfasst. Um den Einfluss von Detektoreffekten auf diese Messungen zu berücksichtigen, wurde ein Kalibrierungsverfahren entwickelt, das auf Ladungsinjektion in die Pixelelektronik und Messungen mit einer Fe-55-Quelle zur absoluten Ladungskalibrierung basiert.

Das Ladungsspektrum selbst wird durch eine Faltung einer Landau-Verteilung mit einer Normalverteilung modelliert, um Schwankungen im Energieübertrag zwischen Teilchen und Detektor sowie Rauscheffekte zu berücksichtigen. Dieser Ansatz wurde anhand simulierter Ladungsablagespektren evaluiert und hat sich auch für dünne Siliziumsensoren als valide erwiesen. Unter Verwendung theoretischer Vorhersagen zur Parametrisierung der Landau-Verteilung für Teilchen mit bekannter Kinematik kann dadurch die effektive Sensordicke für die Ladungssammlung rekonstruiert werden.

Die gemessene gesammelte Ladungsmenge übertrifft den erwarteten Wert eines Modells, das ausschließlich auf dem verarmten Volumen basiert. Dies deutet darauf hin, dass Diffusion im nicht verarmten Volumen wesentlich zur Ladungssammlung beiträgt. Selbst bei niedrigen Hochspannungen, bei denen es vermehrt zu Ladungsaufteilung zwischen benachbarten Pixeln kommen kann, übersteigt die beobachtete Ladungssammlung die Erwartungen hinsichtlich der verarmten Dicke. Der Vergleich eines nahezu vollständig verarmten 50 µm-Sensors mit einem 100 µm-Sensor bei $-20\,\mathrm{V}$ zeigt etwa 40 % mehr gesammelte Ladung, was einer relativen Zunahme der effektiven Dicke um rund 12 µm entspricht. Die unter gleichen Hochspannungsbedingungen beobachtete relative Zunahme nimmt mit der absoluten Sensordicke zu, was darauf hinweist, dass die Größe des nicht verarmten Bereichs das gesamte Ladungssammelverhalten in diesem Dickenbereich bestimmt. Daraus folgt, dass auch bei dickeren Sensoren ein beträchtlicher Teil des nicht verarmten Volumens aktiv zur Ladungssammlung beitragen kann.

Contents

Preface

Doctoral research involves numerous tasks and responsibilities, many of which do not appear in the final thesis. This document represents the culmination of years of experience in detector development, with a special focus on silicon pixel sensors. With thorough dedication, this work aims to provide a useful resource for researchers exploring pixel detector technology, although some shortcomings may remain.

> "I also am only a human being, and the one without mistakes may throw the first criticism."

The work presented here addresses a selection of the activities carried out during the PhD, with a focus on in-depth studies of energy straggling in ultra-thin, underdepleted pixel sensors. Alongside the primary research, extensive commissioning and characterization efforts were undertaken for multiple sensors and chips supporting sensor R&D on ATLASPix3, MuPix10, Run2020 & Run2021 (including TelePix1), and MuPix11 (cf. *Publications*). These efforts included coordinating testbeam campaigns at DESY and PSI, as well as guiding several bachelor and master theses related to these projects: MuPix8 [1], ATLASPix3 [2, 3], MuPix10 [4, 5, 6, 7], and Run2020/21 [8]. Further contributions encompassed maintenance and development of the DAQ and the analysis software for these projects. Collaboration with numerous colleagues within the joint HV-MAPS R&D efforts of *Mu3e*, LHCb, and DESY formed a vital part of the research activities.

To support the research presented in this thesis, several software frameworks and tools were developed. The `PCDF` framework [9] — based on `ROOT` — handles probability density and cumulative distribution functions alongside statistical tools, serving as the basis for all model fitting and statistical analysis presented. The `SILICA` [10] calculator addresses physics computations for silicon pixel detectors, particularly energy loss models, incorporating different incident particles and absorber materials. `Scurve` [11] enables parallelized preprocessing, fitting, filtering, and analysis of S-curve data from charge injection and radioactive sources like Fe-55. `PiCa` [12] facilitates the determination and calibration of pixel sensor responses, while `CISE` [13] provides comprehensive pixel sensor hit efficiency handling and analysis across multiple dimensions, including threshold calibration and efficiency curve fitting based on energy loss models. These tools are intended to support not only the work presented in this thesis but also future research in pixel detector development, though they are not yet publicly available at the time of writing this thesis.

Introduction

"The year is 2012. The last missing piece of the Standard Model of particle physics, the Higgs boson, is discovered at CERN, completing a century-long quest to uncover the building blocks of everything. Well, not entirely... Several frontiers still resist explanation by the Standard Model: dark matter and energy, baryon asymmetry, the neutrino hierarchy, and more. Life is anything but simple for particle physicists seeking to resolve these remaining uncertainties."[1]

These unsolved problems in particle physics drive the search for ever more precise and sensitive experiments, demanding cutting-edge detector technology. As a consequence, advanced detector technologies are pursuit to achieve unprecedented levels of performance in terms of granularity, radiation tolerance, rate capability, spatial, momentum and time resolution, while minimizing the material budget.

A particularly critical parameter is the material budget of tracking detectors. Lower material budgets improve tracking resolution in low-momentum regimes, as multiple Coulomb scattering effects grow with the amount of material traversed. However, this often comes at the expense of smaller detection signals, as charge carrier deposition scales with the traversed thickness of a sensor. To compensate for this effect, advanced semiconductor technologies are being explored to enhance the charge collection efficiency of ever thinner sensors.

One such development is driven by the requirements of the *Mu3e* experiment, a project at the high-intensity frontier to study the charged lepton flavor violating decay of a muon into three electrons ($\mu^+ \to e^+ e^- e^+$). For this purpose, muons are stopped in a hollow Mylar® target and decay at rest, necessitating an ultra-low material budget detector to precisely track the low-momentum $\left(\lesssim 53\,\mathrm{MeV\,c^{-1}}\right)$ decay products.

To meet its demands, a novel silicon pixel detector based on the HV-MAPS (**H**igh-**V**oltage **M**onolithic **A**ctive **P**ixel **S**ensor) technology has been developed. An HV-MAPS features fully monolithic integration of sensing and readout electronics, and operates at high voltages, enabling rapid charge collection by drift in a depleted sensor volume. Currently deployed HV-MAPS are thinned to 50 µm without additional backside processing, such as doping implantation and/or metallization, thereby enabling backside biasing for full or over-depletion, while relying solely on the guard-ring structure for high-voltage application from the front side.

To study the charge collection performance of thin HV-MAPS under various depletion conditions, a comprehensive measurement campaign was conducted using the MuPix10 chip — a full reticle size prototype developed for the *Mu3e* experiment. Here, the charge deposition spectrum is probed via the hit detection efficiency as a function of the detection threshold. The detection threshold represents the energy limit a deposited charge must exceed to be registered as a hit. By varying the detection threshold and measuring the corresponding hit efficiency, the integral of the underlying charge deposition spectrum is reconstructed. Adjusting the depletion voltage enables analysis under various depletion scenarios, including evaluation of charge contributions from non-depleted regions. These contributions are expected to scale with the excess thickness beyond the depletion depth, which can be isolated by comparing sensors of different thicknesses at equivalent depletion voltages.

Since extracting the underlying charge deposition statistics from the hit efficiency measurement is not standard procedure and non-linearities in the energy response of the MuPix10 sensor are expected, a dedicated energy calibration procedure is developed and applied to convert the electronic threshold settings to an energy (detection) threshold. This calibration provides further insight into HV-MAPS operating principles and sensor performance regarding gain, noise, and energy resolution, while supplying reference data for future developments and simulations.

[1] The reader may notice the homage to the Asterix and Obelix comics.

Furthermore, all tools developed as byproducts of this thesis will aid future HV-MAPS characterization campaigns, establishing a basis for standardized testing and comparison of different sensor designs and technologies.

This thesis unfolds in three interconnected parts, beginning with the fundamentals of charged particles and photons interactions with matter (Chapter 1), a detailed introduction to the working principles of silicon pixel detectors (Chapter 2), and the MuPix10 sensor itself (Chapter 3).

To understand the physics underlying the measurement campaign presented here, Chapter 4 provides comprehensive insight into energy deposition fluctuations (straggling) and charge collection mechanisms in silicon detectors, while Chapter 5 describes the experimental setup and conditions, highlighting the need for the energy calibration procedure detailed in Chapter 6.

The thesis culminates in the presentation and discussion of the results. The calibration campaign and its implications for detector response are detailed in Chapter 7, enabling charge collection studies based on calibrated hit efficiency data in Chapter 8. Corresponding charge deposition models are validated, yielding the effective charge collection depth of the MuPix10 as a quantitative measure of sensor performance under various depletion scenarios. The thesis concludes with an epilogue summarizing the findings and discussing potential optimizations and applications of the developed methods to enhance future HV-MAPS characterization campaigns.

1. Particle Interaction with Matter

This chapter presents the fundamental principles governing the interaction of charged particle and photon with matter. A distinction is made between electrons, positrons and heavier charged particles. Since this work focuses on silicon pixel sensors, example calculations are based on relevant materials — such as Si (**si**licon) or Al (**al**uminium) — and typical particle configurations, namely particle type and velocity (see kinematic relations in Section A.1.2).

1.1 Charged Particle Interaction with Matter

A charged particle with speed $v = \beta c$ (c is the speed of light) traversing a medium interacts with its shell electrons, resulting in single collisions with kinetic energy transfer $\mathcal{T}$. Here, the corresponding differential cross section $\left(\frac{\mathrm{d}\sigma}{\mathrm{d}\mathcal{T}}\right)$ depends on the type of incident particle. A distinction is made here between electrons, positrons and heavier particles.

To characterize the collisions, one can use *statistical moments* of the differential cross section, obtained by integrating its energy-transfer dependence weighted by $\mathcal{T}$ to the j-th power, from the minimal ($\mathcal{T}_{min}$) to the maximal ($\mathcal{T}_{max}$) energy transfer in a single collision [14, p. 575, eq. 34.3]:

$$\mathcal{M}_j(\beta) = \underbrace{\rho \cdot N_A \frac{Z}{A}}_{n_e \text{ (electron density)}} \cdot \Delta x \int_{\mathcal{T}_{min}}^{\mathcal{T}_{max}} T^j \frac{\mathrm{d}\sigma(\mathcal{T} \mid \beta)}{\mathrm{d}\mathcal{T}} \mathrm{d}\mathcal{T}, \tag{1.1}$$

where the pre-factor n_e accounts for the number of target electrons in the traversed material thickness Δx. It is determined from the Avogadro constant N_A, the material density ρ, and the atomic-number-to-mass-number ratio Z/A of the medium. Here, the zeroth moment $\mathcal{M}_0$ corresponds to the mean number of collisions[1], which is Poisson-distributed [16, p. 206]:

$$\mathrm{PDF}_{\text{poisson}}(n \mid \mathcal{M}_0) = \frac{\mathcal{M}_0^n}{n!} \mathrm{e}^{-\mathcal{M}_0}, \quad \mathcal{M}_0 \in (0, \infty),\ n \in \mathbb{N}_0. \tag{1.2}$$

The first moment $\mathcal{M}_1$ describes the mean energy loss in Δx, whereas $(\mathcal{M}_2 - \mathcal{M}_1)^2$ represents the variance.
The maximal kinetic energy transfer[2] of the incident particle originates from the kinematic of a head-on (central) collision of the incident particle and the shell electron and depends on the incident particle's mass (M) and β, respectively, the Lorentz factor $\gamma = 1/\sqrt{1-\beta^2}$ [14, p. 576, eq. 34.4]:

$$\mathcal{T}_{max} = \frac{2 m_e c^2 \beta^2 \gamma^2}{1 + 2\gamma m_e / M + (m_e/M)^2}, \tag{1.3}$$

with m_e being the electron mass.
The maximal energy transfer can be approximated for different cases [17, p. 28, eq. 3.21] [14, p. 576]:

$$\mathcal{T}_{max} \approx \begin{cases} 2 m_e c^2 \beta^2 \gamma^2 & \text{for } \gamma m_e \ll M \\ M c^2 \beta^2 \gamma & \text{for } 2\gamma m_e \gg M \\ \gamma M c^2 = E & \text{for } \gamma \to \infty \\ m_e c^2 (\gamma - 1) = E - m_e c^2 & \text{for } M = m_e \text{ (positron)} \\ m_e c^2 (\gamma - 1)/2 = (E - m_e c^2)/2 & \text{for } M = m_e \text{ (electron)} \end{cases} \tag{1.4}$$

[1] In silicon $\mathcal{M}_0/\Delta x$ is about $\mathcal{O}(4\,\mu\mathrm{m}^{-1})$ for $\beta\gamma \gtrsim 3$ [15, p. 25, tab. 2.2]. The minimum is reached at $\beta\gamma \sim 18$.
[2] $\mathcal{T}_{max}$ can be derived assuming elastic collisions with "quasi" free electrons as shown in [17, p. 38].

The minimal energy transfer from the incident particle to an electron of the medium is given by [17, p. 29]:

$$\mathcal{T}_{min} = \frac{I^2}{2m_e c^2 \beta^2}, \tag{1.5}$$

where I is the mean excitation energy of the medium, which can be expressed as the logarithmic average according to [18, p. 26, eq. 51]:

$$\ln(I) = \sum_k f_k \cdot \ln(I_k) \rightarrow I = \prod_k I_k^{f_k}. \tag{1.6}$$

where I_k is the excitation energy and f_k is the corresponding oscillator strength of the k-th shell electron (cf. Section A.6.1). I is typically extracted from measurement data (cf. [19]), as its computation is non-trivial. The values for I, ρ, Z/A used in this thesis can be found in Table A.17.

Plot 1.1 illustrates examples for $\mathcal{T}_{max}$ and $\mathcal{T}_{min}$ for different charged particles in **si**licon as a function of their momenta.

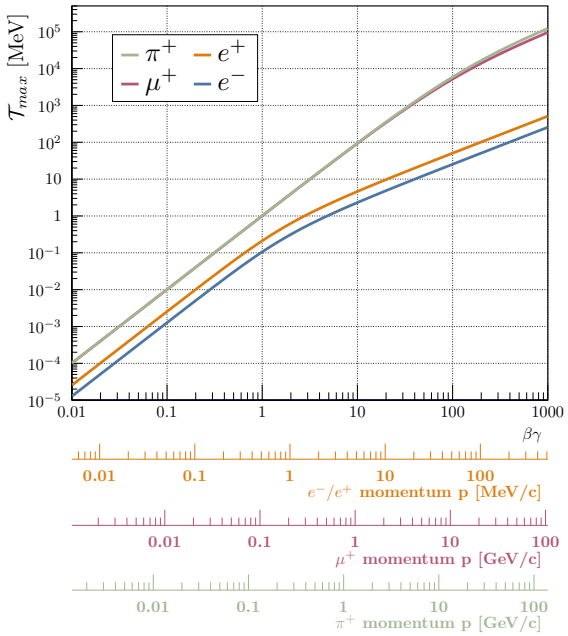

(a) Calculation of $\mathcal{T}_{max}$ as a function of $\beta\gamma$ based on Equation 1.4.

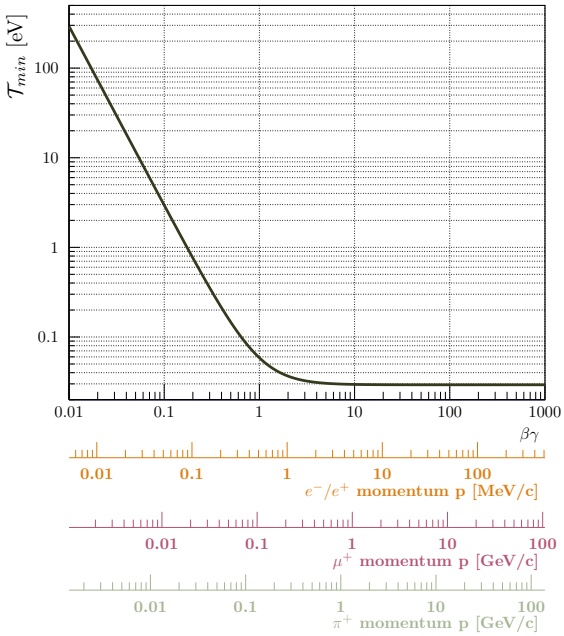

(b) Calculation of $\mathcal{T}_{min}$ in Si (**si**licon) as a function of $\beta\gamma$ based on Equation 1.5.

Plot 1.1: Calculations of $\mathcal{T}_{max}$ and $\mathcal{T}_{min}$ for electron (e^-), positron (e^+), antimuon (μ^+) and pion-plus (π^+) in **si**licon. Corresponding data presented in Tables A.16 and A.17.

1.1.1 Bethe-Bloch Formula for "Heavy" Charged Particles

The energy loss of a point-like charged particle with mass $M \gg m_e$ (essentially excluding electron and positron) is described in detail by [20, 21, 22, 23] and follows what is generally referred to as the Bethe-Bloch formula. Its measure is the mean energy loss per unit length[3] which can be derived from Equation 1.1[4]. A common form [5] for a charged particle with speed β and charge z traversing a medium of density ρ with atomic number Z and mass number A is provided by [14, p. 576, eq. 34.5] and is accurate[6] for $(0.1 \lesssim)\ \beta\gamma\ (\lesssim 1000)$, with both limits being Z-dependent:

$$-\left\langle \frac{\mathrm{d}E}{\mathrm{d}x} \right\rangle = \underbrace{\frac{K}{2}\rho\frac{Z}{A}\frac{z^2}{\beta^2}}_{\xi(\Delta x,\beta)/\Delta x\ [\mathrm{MeV\,cm^{-1}}]} \left[\ln\left(\frac{2m_e c^2\beta^2\gamma^2\mathcal{T}_{max}}{I^2}\right) - 2\beta^2 - \delta(\beta\gamma)\right] \tag{1.7}$$

where I is defined by Equation 1.6 and K being a constant given by [17, p.30]:

$$K = 4\pi N_A r_e^2 m_e c^2 \approx 0.307\,075\,\mathrm{MeV\,cm^2\,mol^{-1}} \tag{1.8}$$

Here, N_A is the Avogadro constant, r_e the classical electron radius and m_e the electron mass.
For further simplification, $\xi(\Delta x, \beta)$ is introduced, which is the pre-factor (of the bracket-term) of the Bethe-Bloch formula times Δx, being a reoccurring factor in the following equations:

$$\xi(\Delta x, \beta) = \frac{K}{2}\rho\frac{Z}{A}\frac{z^2}{\beta^2}\cdot\Delta x \overset{\mathrm{Si}}{\approx} 17.825\,\mathrm{eV\,\mu m^{-1}}\cdot\frac{\Delta x}{\beta^2} \tag{1.9}$$

Since low particle momenta p correspond to a longer effective interaction time with the medium, the energy loss is influenced by the time-scaling momentum transfer, which is described by the $1/\beta^2$-term. Around a $\beta\gamma$ of 2 to 4, the energy loss reaches its minimum; an incident particle with this energy is in general referred to as MIP (**M**inimum **I**onizing **P**article). At higher momenta, the logarithmic term dominates, where the γ^2 factor within the logarithm "accounts for the relativistic growth of the electric field extension perpendicular to the direction of the moving charge"[17, p. 29]. However, this extension of the electric field is "limited by the screening effect of nearby atoms as a consequence of the polarisation of the medium"[17, p. 33]. This density effect is parametrized by [14, p. 577, eq. 34.7]:

$$\delta(\beta\gamma) = \begin{cases} 2\zeta\cdot\ln(10) - \bar{C}_D & \text{for } \zeta \geq \zeta_1 \\ 2\zeta\cdot\ln(10) - \bar{C}_D + a(\zeta_1 - \zeta)^k & \text{for } \zeta_0 \leq \zeta \leq \zeta_1 \\ \delta_0\cdot 10^{2(\zeta-\zeta_0)} & \text{for } \zeta < \zeta_0 \text{ (semi-/conductor)} \\ 0 & \text{for } \zeta < \zeta_0 \text{ (insulator)} \end{cases} \tag{1.10}$$

$$\delta(\beta\gamma) \xrightarrow{\beta\to 1,\gamma\to\infty} 2\ln\left(\frac{\hbar\omega_p}{I}\right) + 2\ln(\beta\gamma) - 1 \tag{1.11}$$

with a, k, ζ_1, ζ_0 and δ_0 being material depended constants (cf. [24, 25, 26]). In addition, the following parameterization are to be used $\zeta = log_{10}(\beta\gamma)$ and $\bar{C}_D = 1 - 2\ln(\hbar\omega_p/I)$ (see [17, p. 33])[7], where $\hbar\omega_p$ is the plasma energy and I the mean excitation energy of the medium. Literature values are listed in Table A.17.

The basic form of the Bethe-Bloch formula provides an adequate description of energy loss in a thick absorber but is no longer sufficient when considering energy deposition. Especially in thinner absorbers in combination with high momentum incident particles, the mean energy loss is significantly affected by single "hard" collisions, whereby the energy is transferred to so-called δ-electrons (see Section 1.1.3). These δ-electrons can leave the medium before losing all its energy, resulting in a significant energy loss fluctuation. Therefore, a "restricted energy loss" form of Equation 1.7 is defined, which introduces the cut-off energy $\mathcal{T}_{cut}$ ($< \mathcal{T}_{max}$) and leads to the form given by [14, p. 579, eq. 34.11]:

[3] Contrary to some convention, this work does not use an implicit density weighted length ($x \not\to \rho x$), also called column-density.
[4] A derivation of the base form, assuming Mott cross section, is presented in [17, p. 26-29].
[5] "For incident spin 1/2 particles, $(T_{max}/E)^2/4$ is included in the square brackets. Although this correction is within the uncertainties in the total stopping power, its inclusion avoids a systematic bias" [14].
[6] At small $\beta \lesssim 0.1$ a shell correction term relevant C/Z arises in the bracket term of Bethe-Bloch. For further simplification this term is neglected.
[7] The following applies for the specified source: $-C_D = \bar{C}_D$.

$$-\left\langle \frac{\mathrm{d}E}{\mathrm{d}x} \right\rangle = \frac{\xi(\Delta x, \beta)}{\Delta x} \left[\ln\left(\frac{2m_e c^2 \beta^2 \gamma^2 \mathcal{T}_{cut}}{I^2} \right) - \beta^2 \cdot \left(1 + \frac{\mathcal{T}_{cut}}{\mathcal{T}_{max}} \right) - \delta(\beta\gamma) \right] \tag{1.12}$$

An illustration of the Bethe-Bloch formula in silicon with and without $\mathcal{T}_{cut}$ is presented in Plot 1.2a.

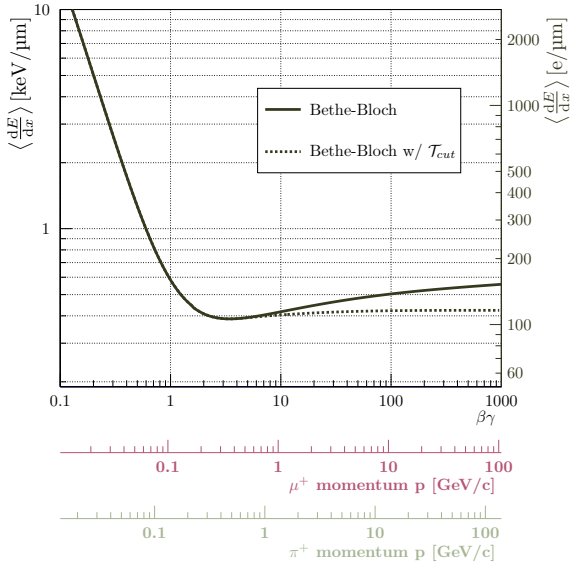

(a) Calculation of Bethe-Bloch in silicon with Equation 1.7.

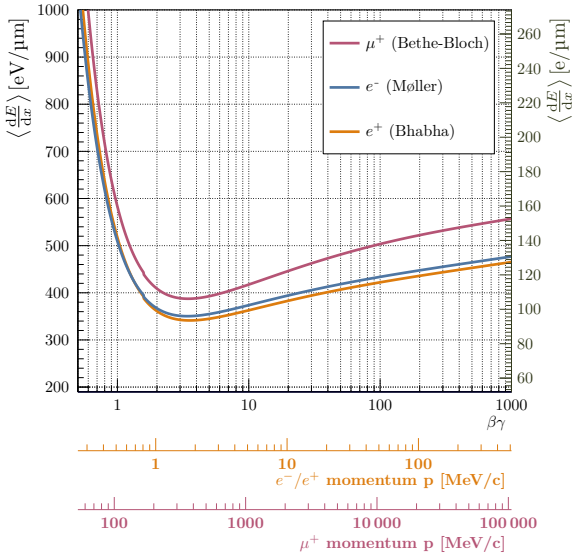

(b) Calculation of Berger-Seltzer formula for electrons and positrons in silicon with Equation 1.13 and Equation 1.14.

Plot 1.2: Calculations of Bethe-Bloch and Berger-Seltzer formula in silicon. The point of discontinuity at $\beta\gamma \approx 1.6$ is due to the case distinction in $\delta(\beta\gamma)$ at $\zeta_0 = log_{10}(\beta\gamma) = 0.2015$ for silicon. Corresponding data presented in Tables A.16 and A.17.

1.1.2 Berger-Seltzer Formula for Electrons & Positrons

The nature of the energy loss for electrons and positrons differs from that of other charged particles, due to their identity in relation to the electron in the ionized medium. Notably, a positron can transfer its entire energy to the medium via annihilation, whereas an electron can transfer at most half of its energy. This limitation arises from the indistinguishability of the incident electron and the shell electron; in such cases, the "scattered" electron is defined as the one with smaller energy (see Equation 1.3). Their interactions are discussed in detail by Berger and Seltzer in [27, 28], and the corresponding mean energy losses for electrons and positrons are illustrated in Plot 1.2b.

Møller: Electrons

For an incoming electron, the interaction is described by the Møller cross section. Taking into account the first moment of the cross section in Equation 1.1 yields the form given by [14, p. 581, eq. 34.23][8]:

$$-\left\langle \frac{\mathrm{d}E}{\mathrm{d}x} \right\rangle = \frac{\xi(\Delta x, \beta)}{\Delta x} \left[\ln\left(\frac{m_e c^2 \beta^2 \gamma^2 \mathcal{T}_{max}}{I^2} \right) + (1 - \beta^2) - \frac{2\gamma - 1}{\gamma^2} \ln(2) + \frac{1}{8} \left(\frac{\gamma - 1}{\gamma} \right)^2 - \delta(\beta\gamma) \right] \tag{1.13}$$

where $\xi(\Delta x, \beta)$ being defined by Equation 1.9 and $\delta(\beta\gamma)$ is the density correction defined by Equation 1.10. Compared to Equation 1.7, the logarithm term differs both in the value of $\mathcal{T}_{max}$ used and by the absence of a factor of 2. The indistinguishability of the incident electron and shell electrons is reflected in the factor $1/2$ in $\mathcal{T}_{max}$ given in Equation 1.4, where the electron with lower kinetic energy after the collision is defined as the "scattered" electron.

Bhabha: Positrons

For an incoming positron, the interaction is described by the Bhabha cross section. Considering the first moment of the cross section in Equation 1.1 yields the form given by [14, p. 581, eq. 34.24][8] :

$$-\left\langle \frac{\mathrm{d}E}{\mathrm{d}x} \right\rangle = \frac{\xi(\Delta x, \beta)}{\Delta x} \left[\ln\left(\frac{m_e c^2 \beta^2 \gamma^2 \mathcal{T}_{max}}{2I^2} \right) + 2\ln(2) - \frac{\beta^2}{12}\left(23 + \frac{14}{\gamma+1} + \frac{10}{(\gamma+1)^2} + \frac{4}{(\gamma+1)^3} \right) - \delta(\beta\gamma) \right] \tag{1.14}$$

where $\xi(\Delta x, \beta)$ being defined by Equation 1.9 and $\delta(\beta\gamma)$ is the density correction defined by Equation 1.10. Compared to Equation 1.7, the logarithmic term differs both in the value of $\mathcal{T}_{max}$ used and by the presence of a factor of $1/2$ instead of a factor of 2. Because the incident particle is the antiparticle of the shell electron, the maximum transferable energy $\mathcal{T}_{max}$ in Equation 1.4 equals its entire kinetic energy in a central collision.

1.1.3 Delta Electrons

The maximum energy transfer (see Equation 1.3) occurs in a central collision between the incident particle and an atomic electron. As this scenario is approached, the probability increases that an atomic electron will be ejected from the atom, resulting in the "production" of a so-called δ-electron (or knock-on electron). The number of δ-electrons[9] with energies between $\mathcal{T}_{min}$ and $\mathcal{T}_{max}$ created in a medium of thickness Δx is given by [17, p. 39, eq. 3.47]:

$$N_{\delta e^-} = \xi(\Delta x, \beta) \cdot \left[\frac{1}{\mathcal{T}_{min}} - \frac{1}{\mathcal{T}_{max}} \right] \tag{1.15}$$

where $\xi(\Delta x, \beta)$ (Equation 1.9) incorporates material properties and kinematic factors.
The δ-electron emission angle $\vartheta_{\delta e^-}$ is kinematically related to its kinetic energy $\mathcal{T}$ by [30, p. 8, eq. 7]:

$$\vartheta_{\delta e^-}(\mathcal{T}) = \arctan\left(\frac{1}{\gamma} \sqrt{\frac{\mathcal{T}_{max}}{\mathcal{T}} - 1} \right) \tag{1.16}$$

where γ is the Lorentz factor of the incident particle. High-energetic δ-electrons ($\mathcal{T} \to \mathcal{T}_{max}$) are emitted close to the forward direction ($\vartheta_{\delta e^-} \to 0$) and, particularly in thin materials, may escape before depositing all their energy, thus contributing only partially to the measurable spectrum in a medium. In contrast, low-energetic δ-electrons can emerge at large angles, producing elongated ionization clusters and thereby broadening the distribution of local energy depositions.

Since Equation 1.15 diverges for $\mathcal{T}_{min}$ approaching zero, the lower limit should be chosen to correspond to the threshold for a "true" δ-electron, i.e. one that escapes the medium or travels a significant distance before losing all its energy.

A practical estimate can be made from the CSDA (**C**ontinuous **S**lowing **D**own **A**pproximation) range in **si**licon, for which a 100 keV electron has a mean path length shorter than 100 µm [31] (cf. Section A.1.1) For example, for a π^+ with a momentum of 350 MeV/c, Equation 1.15 yields a probability of about 0.02 % µm^{-1} for producing a δ-electron with a kinetic energy between 100 keV and $\mathcal{T}_{max}$ (≈ 6.3 MeV) in **si**licon.

1.1.4 Bremsstrahlung

The energy loss of charged particles in a medium is governed not only by ionization losses but also by radiation losses, which become significant at high energies. When an incident particle interacts with the Coulomb field of a nucleus in the medium, a photon can be emitted - a process known as bremsstrahlung. For heavier particles (see Section 1.1.1), the energy loss is dominated by ionization, and radiative effects only become relevant for values of $\beta\gamma \gtrsim 1000$. However, for electrons and positrons (see Section 1.1.2), radiation losses become important at much lower energies, due to their comparable small rest mass (m_e).

[8] Take note that the form of Equation 1.13 and Equation 1.14 includes the material density ρ.
[9] The approximation of number of "produced" δ-electrons is tightly coupled with the mean number of $\mathcal{M}_0$ (cf. [29, sec. 4.5, eq. 23]).

The energy at which the loss due to bremsstrahlung equals the loss due to ionization is called the critical energy[10] $E_{critical}$. For solids and liquids, it can be approximated by [17, p. 63, eq. 3.94]:

$$E_{critical} \approx \frac{610\,\text{MeV}}{Z+1.24} \overset{\text{Si}}{\approx} \begin{cases} 40.19\,\text{MeV} & \text{for electrons} \\ 39.05\,\text{MeV} & \text{for positrons} \end{cases} \quad [32] \tag{1.17}$$

The characteristic energy loss due to bremsstrahlung is given by [17, p. 61, eq. 3.86 & 3.87]:

$$\frac{\mathrm{d}E}{\mathrm{d}x} = -\frac{E}{X_0} \rightarrow E(x) = E_0 e^{-\frac{x}{X_0}} \tag{1.18}$$

Here, X_0 is the radiation length of the medium, defined as the mean distance over which a high-energy electron's energy is reduced to $1/e$ (about 37 %) of its initial value due to bremsstrahlung. The radiation length characterizes the probability of photon emission and is a crucial material parameter for the electromagnetic interaction. For most elements (except Helium), the radiation length can be approximated by [33, p. 291, eq. 27.24]:

$$X_0\,[cm] \approx \frac{A}{[\text{g mol}^{-1}]} \cdot \frac{[\text{g cm}^{-3}]}{\rho} \cdot \frac{716.408}{\left[Z(Z+1)\cdot \ln\left(\frac{287}{\sqrt{Z}}\right)\right]} \tag{1.19}$$

For compounds or mixtures, the total radiation length is determined by the sum of the density-weighted contributions from each component [17, p. 61, eq. 3.91]:

$$\frac{1}{X_0} = \sum_i \frac{\rho_i}{\rho} \frac{1}{X_{0,i}} \tag{1.20}$$

where ρ is the density of the compound, and ρ_i, $X_{0,i}$ are the density and radiation length of the i-th component, respectively.

1.1.5 Multiple Coulomb Scattering

For sufficiently thick absorbers, the scattering and displacement distribution of a charged particle is well described by a normal distribution, as predicted by the central limit theorem and formalized in Molière theory [34]. The incident charged particle undergoes frequent small-angle Coulomb scattering on the nuclei of the medium, with additional contributions from strong interactions in the case of hadronic projectiles.

The RMS width of the angular distribution is given by the so-called "Highland formula" [35], which describes the inner 98 % of the distribution[11]. Its most recent form is expressed as [36, p. 10, eq. 12]:

$$\vartheta_{RMS} = \frac{13.6\,\text{MeV}}{\beta cp} z \sqrt{\frac{\Delta x}{X_0}} \left[1 + 0.038 \cdot \ln\left(\frac{\Delta x}{X_0}\frac{z^2}{\beta^2}\right)\right] \tag{1.21}$$

where X_0 is the radiation length of the medium. This width is predominantly determined by the relative radiation length $\Delta x/X_0$, which depends on the medium, and the velocity and momentum properties of the incident particle, set by β and p respectively. For compounds and mixtures, ϑ_{RMS} cannot be simply added in quadrature for each component. Instead, the corresponding radiation length should be determined using Equation 1.20. More detailed information can be found in standard references such as [14, p. 580-581] and [17, p. 65-70].

[10] The critical energy for muons in silicon is 582 GeV [32].
[11] "Less frequent 'hard' scatters produce non-Gaussian tails" [14, p. 580].

1.2 Photon Interaction with Matter

The most important processes of photon interaction with matter are the photoelectric effect, the Compton effect and pair production. In the context of studying silicon sensors the first two are most relevant in laboratory settings, particularly due to fluorescence and radioactive decay. Pair production becomes significant only for high-energy photons. The dominant region of each process depends on the atomic number Z of the medium and the energy of the incident photon (E_γ). An overview is provided in Figure 1.1 and Table 1.1. Additionally, Thomson scattering (elastic scattering off free charges at low energies) and Rayleigh scattering (coherent scattering without shell excitation or ionization) can become relevant at low photon energies, but are neglected in the context of this work. A brief discussion of the processes follows.

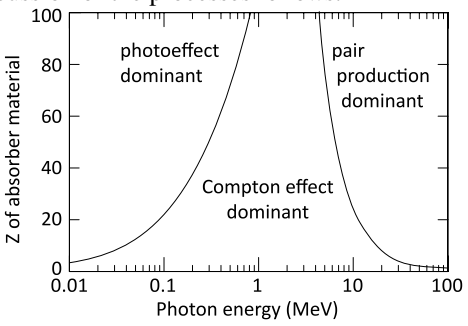

Figure 1.1: Dominant regions of photon absorption processes as function of the photon energy and Z of the medium. Taken from [17, p. 86, fig. 3.49].

Process	Z	E_γ
photoeffect	Z^4 to Z^5	E_γ^k, $k \lesssim 3.5$
$E_\gamma \to \infty$	Z^5	E_γ^k, $k \to 1$
compton effect	Z	E_γ^{-1}
pair production	Z^2	$\sim$ const

Table 1.1: Dominant photon interaction processes as functions of the Z and the energy of the incident photon. Taken from [17, p. 85].

Photons passing through a material are either absorbed or scattered, with the probability proportional to the thickness of the absorber. The "survival" probability — and thus the absorption probability — follows an exponential power law [17, p. 71, eq. 3.111] for the number of photons:

$$N_{\text{survival}}(\Delta x \mid N_0, \lambda_a) = N_0 \cdot \mathrm{e}^{-\frac{\Delta x}{\lambda_a}} \longrightarrow N_{\text{absorption}}(\Delta x \mid N_0, \lambda_a) = N_0 \cdot \left(1 - \mathrm{e}^{-\frac{\Delta x}{\lambda_a}}\right) \tag{1.22}$$

Here, λ_a is the absorption length of the medium, which can be obtained from X-ray databases such as "Henke" [37] and NIST [38]. The absorption length is defined as the distance at which the number of photons is reduced to a factor $1/e$. Plot 1.3 shows typical values of λ_a for materials commonly used in a silicon sensor, as well as the fraction of absorbed photons in pure silicon for various thicknesses Δx.

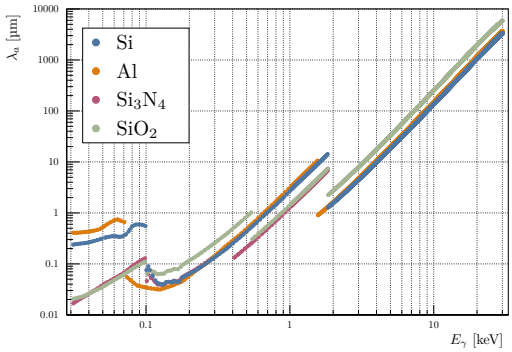

(a) Attenuation length for **si**licon, **al**uminium, SiO_2 (**si**licon **d**ioxide) and Si_3N_4 (**si**licon **n**itride) for photons with energies of 0.03 keV to 30 keV.

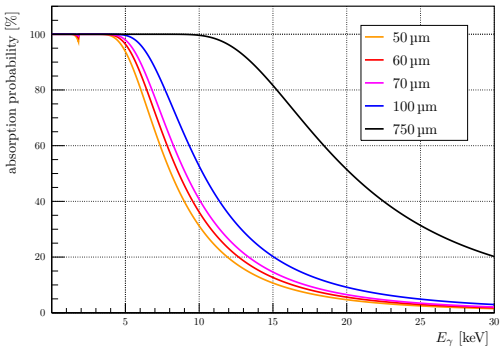

(b) Absorption probability for **si**licon with a Δx of 50 µm to 750 µm and photon energies of 0.03 keV to 30 keV. Calculation based on Equation 1.22.

Plot 1.3: Characteristics of photon absorption in various materials. Data taken from [37].

1.2.1 Photo Effect

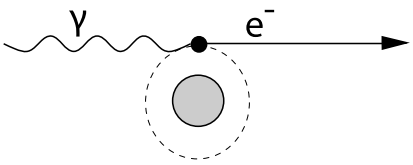

(a) Diagram of the photoelectric effect. Taken from [17, p. 70, fig. 3.34a].

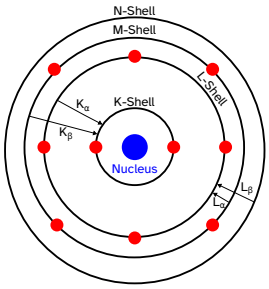

(b) Sketch of the shell transition naming terminology.

Figure 1.2: Photoelectric effect and shell transition naming scheme.

The photoelectric effect (or photoeffect) describes the interaction in which an incident photon transfers all its energy to a shell electron of an atom. If the photon's energy exceeds the binding energy of a shell-electron, the atom emits the electron, which is then referred to as photoelectron. Values for the shell binding energies of silicon can be found in Table A.13. The excess energy is imparted to the emitted electron as kinetic energy, while the recoil energy transferred to the atom is typically negligible.

The vacancy created in the inner shell is subsequently filled by an electron of an outer shell. This transition is accompanied by the re-emission of either a characteristic photon or an Auger electron, both of which have discrete energies. These characteristic energy lines are named according to the shell transition (K, L, M etc.). When the total energy deposited by these processes is detected, it appears as the photopeak in the measured spectrum.

1.2.2 Compton Effect

When an incident photon undergoes elastic scattering with a "quasi-free" electron, the process is known as Compton scattering. In contrast to the photoelectric effect, only part of the photons's energy is transferred to the shell electron, which is then ejected from the atom. The remaining energy is retained by the scattered photon, whose direction and energy change as a result of the interaction. The kinematics of the Compton scattering are determined by the conservation of energy and momentum as illustrated in Figure 1.3a. The kinetic energy $\mathcal{T}$ of the recoil electron is given by:

$$\mathcal{T} = E_\gamma - E'_\gamma \tag{1.23}$$

where E_γ and E'_γ are the energies of the incident and scattered photon, respectively. The energy of the scattered photon can be expressed as function of the scattering angle θ_γ [17, p. 79, eq. 3.125]:

$$E'_\gamma(\theta_\gamma \mid E_\gamma) = \frac{E_\gamma}{1 + \frac{E_\gamma}{m_e c^2}(1 - \cos\theta_\gamma)} \tag{1.24}$$

where m_e is the electron mass and c is the speed of light.

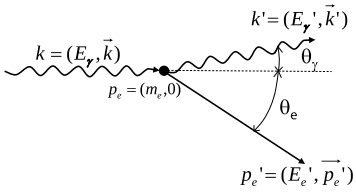

(a) Kinematics of the Compton effect. Taken from [17, p. 79, fig. 3.42].

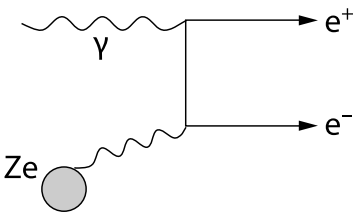

(b) Diagram of the pair production process. Taken from [17, p. 83, fig. 3.46b].

Figure 1.3: Diagrams of the Compton effect and pair production.

1.2.3 Pair Production

If the incident photon has an energy exceeding the energy threshold $E_\gamma \approx 2m_e c^2$, it can convert in the Coulomb field of a charged particle (predominantly the nucleus) into an electron-positron pair. This process, known as pair production, is illustrated in Figure 1.3b. The energy of the incident photon is distributed among the rest mass energies of the electron and positron, their kinetic energies, and the recoil energy of the nucleus (which is typically negligible). The threshold energy of this process is thus set by the combined rest mass energy of the electron and positron.

The cross section for pair production is commonly expressed in terms of the radiation length X_0, allowing the absorption length of this process to be written as [17, p. 84, eq. 3.143]:

$$\lambda_{\alpha,\text{pair-production}} = \frac{9}{7} \cdot X_0 \tag{1.25}$$

2. Semiconductor Pixel Detectors

Semiconductor detectors, and in particular silicon pixel detectors, are a cornerstone of modern particle physics experiments. They provide exceptional spatial, temporal, and momentum resolution, even under high rates and after harsh radiation conditions.

This chapter presents the fundamental principles of semiconductors, with a strong emphasis on silicon as the material of choice for advanced detector systems. It discusses silicon's primary application as a particle detector and reviews the major state-of-the-art technologies in the field.

2.1 Semiconductor Basics

In principle materials can be classified into three major categories based on their electrical conductivity: conductors, semiconductors and insulators. Figure 2.1 illustrates the basic principle used to differentiation between these three types of materials, which is based on their energy band structure. In conductors, the conduction and valence band overlap, allowing electrons and holes — missing electrons in the valence band, which behave like positive charges — to move freely, which results in a high conductivity.

In semiconductors, the conduction and valence band are separated by an energy difference known as the band gap (indicated by E_g), which is relatively small. This allows, electrons in the valence band to be excited, either thermally or through external stimuli (e.g. ionization or photons), into the conduction band, thereby enabling limited conductivity. Semiconductors can be further subdivided into elemental semiconductors, such as silicon or germanium, and compound semiconductors, such as gallium arsenide or cadmium telluride. These materials constitute the most commonly used semiconductor materials in particle physics detectors[1].

In insulators, the band gap is sufficiently large that thermal excitation alone is not enough to elevate electrons into the conduction band. As a result, electrons remain bound in the valence band an cannot move freely, leading to a very low — effectively negligible — electrical conductivity.
A more detailed discussion of the energy band structure and its implications for the electrical properties of semiconductors is provided in the following sections.

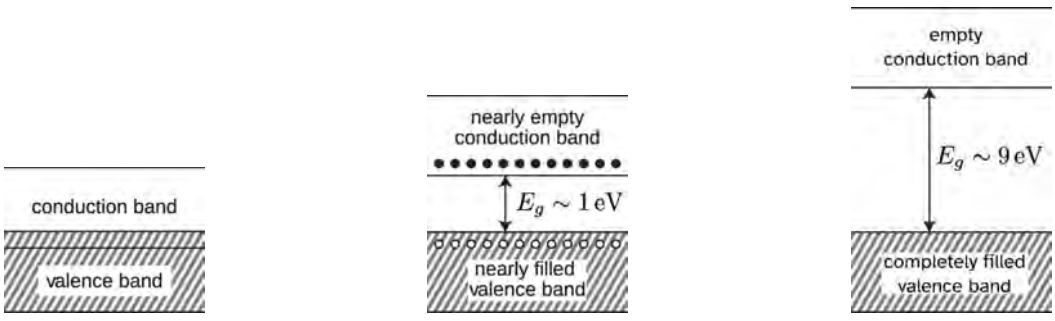

(a) Conductor. *(b)* Semiconductor. *(c)* Insulator.

Figure 2.1: Schematic energy-band structure of insulators, semiconductors and conductors with E_g indicating the band gap. Adapted from [17, p. 263, fig. 8.7].

[1] The production of wafers for detector fabrication is typically carried out using either the *CZ* (*Czochralski*) or the *FZ* (*Float-Zone*) method. The *CZ* method is more widely used due to its lower production cost and ability to produce larger wafers, whereas the *FZ* method — used mainly for silicon — is preferred when superior crystal purity is required, such as for high-resistivity wafers.

2.1.1 Crystal lattice & Energy Bands

Crystalline solids are predominantly used as semiconductors in electronics and detectors. Their constituent atoms are arranged in a regular repeating pattern, known as the crystal lattice.
Silicon, for example, crystallizes in a diamond (face-centred cubic) lattice structure[2], where each atom forms four covalent bonds with its nearest neighbors in a tetrahedral arrangement.
This periodic atomic structure causes the discrete energy levels of individual atoms to split and merge into continuous energy bands. The highest occupied energy band at absolute zero (0 K) is referred to as the valence band (E_V), while the lowest unoccupied band is called the conduction band (E_C). The energy difference between them, the band gap E_g, is a key parameter determining a semiconductor's electrical properties (see Section 2.1).

Semiconductors can be further classified as direct and indirect semiconductors depending on the relative position of the conduction band minimum and the valence band maximum in the (*crystal momentum*) space ($\vec{k}$-space). In an indirect semiconductor like silicon, these extrema occur at different *crystal momentum* values, as shown in Figure 2.2a. Consequently, an electron transition between them requires an additional momentum transfer — typically by a phonon — resulting in lattice heating and a temperature increase (see Section 2.2.1). In contrast, a direct semiconductor (Figure 2.2b) has the conduction band minimum and valence band maximum aligned in $\vec{k}$-space, allowing for the generation of electron-hole pairs purely through excitation without the need of transferring kinetic energy to the lattice.

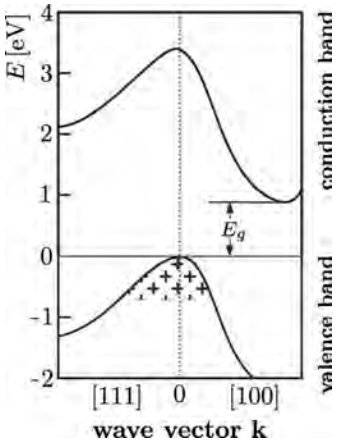

(a) Band structure of an indirect band gap semiconductor like silicon.

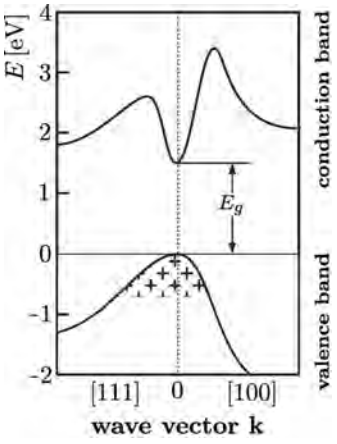

(b) Band structure of an direct band gap semiconductor like gallium arsenide.

Figure 2.2: Schematic the indirect and direct band gap structure of a semiconductor. Adapted from [17, p. 265, fig. 8.8].

2.1.2 Intrinsic Semiconductor and Charge Carriers

A semiconductor is called intrinsic if it contains no external dopants or impurities (see Section 2.1.3). In such a material, electrons can be thermally excited from the valence band into the conduction band, leaving behind a hole. These free charge carriers — electrons in the conduction band and holes in the valence band — can move freely in their respective bands, but are bound in the opposite band.

To derive the charge carrier concentration in thermal equilibrium, one must consider both the density of energy states $Z(E) \propto \sqrt{E}$ available for electrons and holes, and their occupation probability $f(E)$. For particles with spin-1/2, such as electrons and holes, this occupation is given by the Fermi-Dirac distribution [17, p. 267, eq. 8.9 & 8.10]:

$$f_{n,p}(E \mid E_f, T) = \left[\mathrm{e}^{\frac{\Delta E_{n,p}}{k_B T}} + 1 \right]^{-1} \quad \text{with} \quad \begin{cases} \Delta E_n = E - E_f & \text{for electrons} \\ \Delta E_p = E_f - E & \text{for holes} \end{cases} \tag{2.1}$$

[2] The orientation of the crystal structure is described by Miller indices, which define crystal planes. In silicon, the $\langle 100 \rangle$ orientation corresponds to a plane parallel to the y-z plane and is the standard cutting orientation of a silicon ingot in current production.

Here, k_B is the Boltzmann constant, T is the absolute temperature and E_f the intrinsic Fermi level, which can be interpreted as the chemical potential of electrons. At non-zero temperatures ($T > 0\,\mathrm{K}$), E_f lies near the middle of the band gap. At 0 K, E_f marks the highest occupied energy level for electrons.

By integrating the respective carrier densities over their band energy ranges, the density number of electron (n) and holes (p) can be expressed by [17, p.268-269, eq. 8.14-8.16]:

$$\begin{aligned} n &= \underbrace{2 \cdot \left(\frac{m_n^* k_B T}{2\pi\hbar^2} \right)^{\frac{3}{2}}}_{N_C \overset{300\,\mathrm{K}}{\approx} 3.05\times10^{19}\,\mathrm{cm}^{-3}} \mathrm{e}^{-\frac{E_C - E_f}{k_B T}} \quad \text{with} \quad m_n^* = 1.14 \cdot m_e \\ p &= \underbrace{2 \cdot \left(\frac{m_p^* k_B T}{2\pi\hbar^2} \right)^{\frac{3}{2}}}_{N_V \overset{300\,\mathrm{K}}{\approx} 2.55\times10^{19}\,\mathrm{cm}^{-3}} \mathrm{e}^{-\frac{E_f - E_V}{k_B T}} \quad \text{with} \quad m_p^* = 1.01 \cdot m_e \end{aligned} \tag{2.2}$$

Here, $\hbar$ is the reduced Planck constant, m_n^* and m_p^* are the effective masses of the electrons and holes, respectively. The pre-factors define the effective density states in the conduction N_C and valence N_V band, respectively. At thermal equilibrium, generation and recombination of charge carriers are balanced, leading to equal electron and hole densities in their respective bands.

The intrinsic carrier concentration n_i is constant and is defined by the product of the two carrier densities as [17, p. 269, eq 8.17-8.20]:

$$n_i^2 = n \cdot p \overset{(E_C - E_V = E_g)}{=} N_C \cdot N_V \cdot \mathrm{e}^{-\frac{E_g}{k_B T}} \xrightarrow{300\,\mathrm{K}, Si} n_i \approx 1.01 \times 10^{10}\,\mathrm{cm}^{-3} \tag{2.3}$$

The temperature dependence of band gap can be described empirically by the Varshni equation [39, p.149, eq. 1]:

$$E_g(T) = E_{g,0} - \frac{\eta T^2}{T + \theta_D} \tag{2.4}$$

where $E_{g,0}$ is the band gap at 0 K, and η and θ_D are material-specific constants. This equation shows that the band gap decreases with increasing temperature, a critical factor influencing the leakage current in silicon detectors, as discussed in Section 2.3.3.

2.1.3 Doping

The conductivity of a semiconductor can be significantly increased by introducing impurities in the form of foreign atoms — a process known as doping. By selecting the appropriate dopant type, the electrical behavior of the material can be tailored as desired.

In silicon, a tetravalent semiconductor, foreign atoms such as pentavalent phosphorus or trivalent boron can be incorporated into the crystal lattice. In n-type doping, the pentavalent element — known as donor — contributes an excess electron (see Figure 2.3a), which occupies an energy level just below the conduction-band edge (E_C). This electron can be thermally excited into the conduction band, becoming a free charge carrier — the majority carrier in an n-type material — while the donor atom remains as a fixed positive ion in the lattice. In contrast, p-type doping involves a trivalent element — an acceptor — that has one fewer valence electron than silicon (see Figure 2.3b). This deficit creates an energy level just above the valence-band edge (E_V) that can capture an electron from the valence band, leaving a mobile hole as the majority carrier. In both cases, the resulting carrier imbalance shifts the Fermi level from the intrinsic position (E_f) to a new value (E_F): upward toward E_C in n-type material, and downward toward E_V in p-type material.

The doped material remains electrically neutral overall, as the doping process introduces electrically neutral atoms into the lattice. However, the concentration of the majority charge carrier increases, while the concentration of the minority charge carrier decreases, according to the mass-action law (Equation 2.3).

In a uniformly doped semiconductor, the donor and acceptor impurities are evenly distributed throughout the material, and the net charge density remains zero ($n - p = \mathcal{N}_D - \mathcal{N}_A$), a condition known as space charge neutrality.

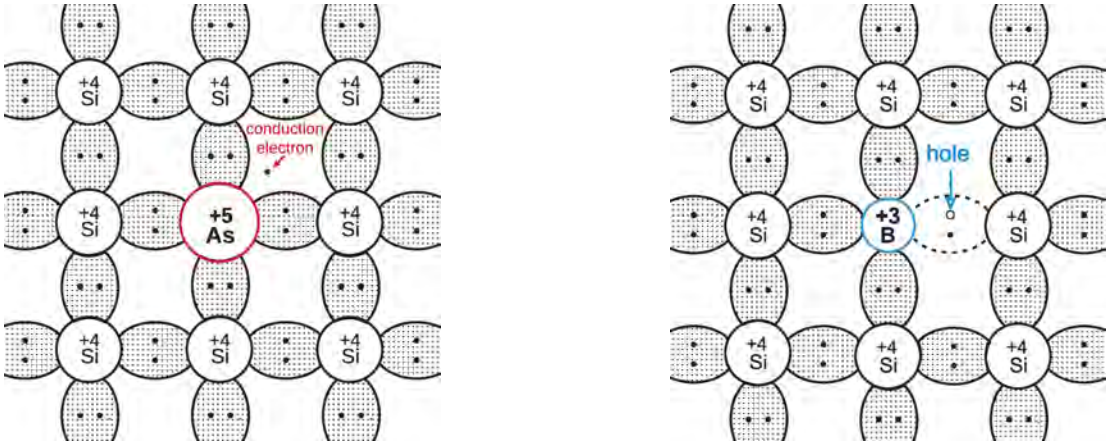

(a) Schematic of n-doping in silicon using arsen.

(b) Schematic of p-doping in silicon using boron.

Figure 2.3: Schematics of n-doping & p-doping in silicon. Taken from [17, p. 271, fig. 8.12].

The relationship between carrier concentrations and doping levels, assuming dominant doping and full ionization, are given by [17, p. 271-272, eq. 8.27 & 8.28]:

$$\begin{aligned} n \approx \mathcal{N}_D = N_C \cdot \mathrm{e}^{-\frac{E_C - E_F}{k_B T}} &= n_i \cdot \mathrm{e}^{\frac{E_F - E_f}{k_B T}} \\ p \approx \mathcal{N}_A = N_V \cdot \mathrm{e}^{-\frac{E_F - E_V}{k_B T}} &= n_i \cdot \mathrm{e}^{\frac{E_f - E_F}{k_B T}} \end{aligned} \tag{2.5}$$

Here, the concentration of donor and acceptor atoms is denoted by $\mathcal{N}_D$ and $\mathcal{N}_A$, respectively.
For simplicity, it is often assumed that a material is exclusively n-doped or p-doped, an assumption that holds for most practical applications. In reality, however, both types of dopants may be present. In such cases, the total doping concentration is given by $\mathcal{N} = \mathcal{N}_D + \mathcal{N}_A$, and the level of E_F can shift outside the band gap.

It should be noted that selective doping inevitably entails the introduction of additional foreign atoms or defects alongside the intended dopant, so the doping is never perfectly pure. These impurities may give rise to localized energy levels within the band gap, enhancing charge-generation and recombination processes, and thereby increasing the leakage current of a semiconductor detector (see Section 2.3.3).

2.2 Silicon as a Semiconductor

Silicon is the most widely used semiconductor material today, both in industry and in particle physics applications. The following sections present the most relevant properties of silicon with a focus placed on key concepts, essential for operational understanding, such as electron-hole pair creation, mobility, and charge carrier lifetime. A brief overview of the resistivity of silicon as a function of doping concentrations is also included.

The basic properties of silicon as a semiconductor are summarized in Table 2.1[3][4]. Additionally, standard literature values relevant to detector applications — such as stopping powers for silicon and related materials — are compiled in Table A.17. Evaluated shell binding energies of silicon atoms are provided in Table A.13.

Property	Symbol	**Value**	**Unit**	**Reference**
Band gap (indirect)	E_g	~ 1.12 at 300 K	eV	[42, p. 1847, tab. 1]
Pair creation energy	$\mathcal{W}_{pair}$	3.65 ± 0.009 (3.73 ± 0.09)		[43]‡ ([44]‡‡)
Fano Factor	$\mathcal{F}$	0.129 ± 0.001 (0.118 ± 0.004)	—	
Relative permittivity	$\varepsilon_{\mathrm{Si}}$	11.7 ± 0.2 (11.6 ± 0.05)		[45]† ([46]††)
Thermal conductivity	-	1.48	W m^{-1} K^{-1}	[17, p. 261, tab. 8.2]
Electron mobility	μ_e	1450	cm^2 V^{-1} s^{-1}	
Hole mobility	μ_h	500		

Table 2.1: Properties of silicon. †: Stated for 465 kHz (measured at 0.5 kHz to 30 × 10^3 kHz) with (>1 × 10^{10} Ω cm) nearly pure silicon. ††: Measured at 26.5 GHz to 40 GHz for silicon of 2 kΩ cm and 50 kΩ cm. ‡: Pair creation energy and Fano factor measured with Fe-55 X-rays at 185 K. ‡‡: Pair creation energy and Fano factor measured with 5.9 keV X-rays in the temperature range of 80 K to 270 K, resulting in a gradient of the pair creation energy of (−0.0131 ± 0.0004) % K^{-1}.

2.2.1 Electron-Hole Pair Creation

To create an electron-hole pair in silicon through interaction with an incident particle (either a photon or a charged particle) in silicon, the transferred energy must exceed the so-called pair creation energy, W_{pair}, which is the energy required to raise an electron from the valence band to the conduction band.

One might naively assume that this energy corresponds to the band gap energy, E_g, see Section 2.1.1. However, not all of the kinetic energy transferred to the electron goes into generating electron-hole pairs. A significant fraction is lost to other processes, most notably phonon excitation and the formation of plasma states, with phonon excitation — which transfers heat to the crystal lattice — being the dominant mechanism (cf. [47]).

An empirical approximation often used to estimate the pair creation energy is $W_{pair} \sim 3{\cdot}E_g$, as suggested in [48, p. 2]. It is important to note that E_g is temperature dependent (see Equation 2.4), and as a result, W_{pair} is also influenced. A more sophisticated model for W_{pair}, which accounts for the temperature dependence of the band gap, is provided in [48, p. 2, eq.1]. Here, W_{pair} decreases with increasing temperature.
In general, for transferred energy $\mathcal{T}_{dep.}$, the mean number of electron-hole pairs $\langle n \rangle$ created, is given by:

$$\mathcal{W}_{pair} = \frac{\mathcal{T}_{dep.}}{\langle n \rangle} \tag{2.6}$$

Since the electron-hole pair creation is a statistical process, the actual number of pairs created fluctuates around the mean. This fluctuation is described by the Fano factor, $\mathcal{F}$, which quantifies the variance ($\langle (n - \langle n \rangle)^2 \rangle$) of n relative to a Poisson process. It is defined as [49, p.27, eq. 3]:

$$\mathcal{F} = \frac{\langle (n - \langle n \rangle)^2 \rangle}{\langle n \rangle} \tag{2.7}$$

[3] Take Note: A frequency dependence on the measurement of the relative permittivity is observed as presented in [40, p. 6, fig. 5].
[4] It is expected that an increase of the impurity concentration (resistivity) affects the relative permittivity of silicon. Significant deviations to be expected for resistivities below 0.01 Ω cm [41, p. 244, fig. 4], which corresponds to doping concentrations of $> 1 \times 10^{17}$ cm^{-3}.

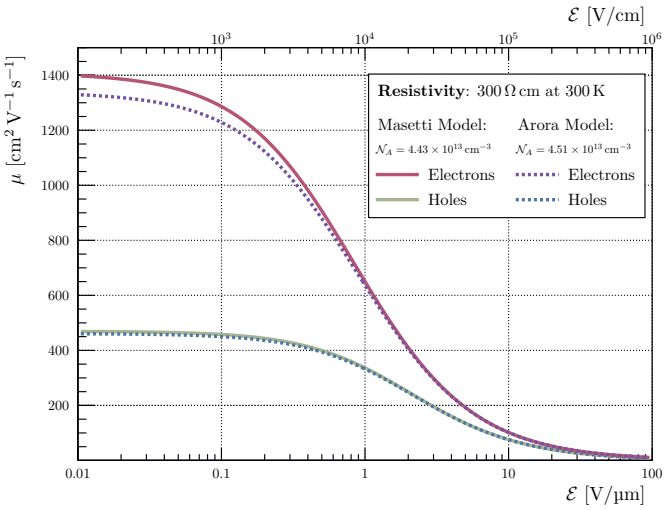

Plot 2.1: Effect of electric field on carrier mobility in silicon. Calculated values based on Equation 2.8 in combination with the Arora- and Masetti-Models for the charge carrier mobilities (cf. Section A.2).

It is important to emphasize that the number of electron-hole pairs measured in a detector does not depend solely on the number initially created by the incident particle. Charge collection inefficiencies due to recombination or trapping can reduce the detected charge, while impact ionization in strong electric fields can increase it. In the latter case, charge carriers are accelerated by the electric field, gaining enough energy to liberate additional electric-hole pairs along their path.

2.2.2 Mobility of Electrons & Holes

Mobility quantifies the ease with which charge carriers traverse a semiconductor lattice. Because it governs both drift (see Section 4.2.1) and diffusion (see Section 4.2.2), mobility is a key parameter in device physics. Standard values for both charge carrier mobilities in intrinsic silicon are provided in Table 2.1, yet mobility is not fixed. It varies with the lattice temperature T, the doping concentration $\mathcal{N}$, and the local electric field strength $\mathcal{E}$ (cf. A.2 for a survey of models).

A widely adopted model for describing carrier mobilities in silicon as function of the applied electric field $\mathcal{E}$ was introduced by Jacoboni & Canali [50, p. 87, eq. 9][5]. This model can be further extended to account for the dependence of the mobility on both temperature and doping concentration. This generalization is commonly known as the Caughey-Thomas parameterization[6][51, p. 2193, eq. 3] and is given by:

$$\mu_{e/h}(\mathcal{E},\mathcal{N},T) = \frac{\mu_{e/h}(\mathcal{N},T)}{\left[1+\left(\frac{\mu_{e/h}(\mathcal{N},T)\cdot\mathcal{E}}{\nu_{m,e/h}}\right)^{c_{e/h}}\right]^{1/c_{e/h}}} \tag{2.8}$$

where $\mu_{e/h}(\mathcal{N},T)$ denotes the zero-$\mathcal{E}$-field mobility (see common models presented in Section A.2), $\nu_{m,e/h}$ the saturation velocity, and $c_{e/h}$ an empirical curvature exponent, listed in Table 2.2.

At constant temperature and low electric field, carrier mobility remains essentially invariant, but its magnitude decreases as elastic collisions — scattering off lattice phonons and crystal defects — become more frequent. As temperature rises *acoustic-phonon* scattering intensifies, further reducing the mobility [52, p.28ff]. Conversely, at high electric fields the dominant scattering mechanism shifts to *optical phonons*, causing the mobility to decrease as it approaches saturation (see Plot 2.1).

[5] Originally derived for ⟨111⟩ silicon lattice orientation, nowadays also commonly used for ⟨100⟩ oriented silicon wafers.
[6] Used by Synopsys Sentaurus TCAD, with $\mu_{e/h}(\mathcal{N},T)$ being described by the Masetti-Model (see Section A.2.2).

Parameter	e: **Electron**	h: **Hole**
$\nu_{m,i}$ [cm s^{-1}]	$1.53 \cdot 10^{9} \cdot T^{-0.87}$	$1.62 \cdot 10^{8} \cdot T^{-0.52}$
c_i	$2.57 \cdot 10^{-2} \cdot T^{0.66}$	$0.46 \cdot T^{0.17}$

Table 2.2: Parameters for Caughey-Thomas parameterization of the Jacoboni-Canali Model. Values taken from [50, p. 87, tab. 5].

2.2.3 Charge Carrier Lifetime

The lifetime of charge carriers in the bulk of silicon is determined primarily by two recombination processes: SRH (Shockley-Read-Hall) recombination and Auger recombination. The total bulk carrier lifetime, τ_{bulk}, is given by the sum of the inverse individual lifetimes for each process[7]:

$$\frac{1}{\tau_{bulk}} = \frac{1}{\tau_{SRH}} + \frac{1}{\tau_{Auger}} \tag{2.9}$$

SRH, or trap-assisted recombination [53, 54], is mediated by defect states in the lattice and is described as a function of the total doping concentration ($\mathcal{N} = \mathcal{N}_D + \mathcal{N}_A$). The carrier lifetime due to SRH recombination in its basic form [55, p. 742, eq. 1] can be extended to also include the temperature dependence. A commonly used form is given by [56, p. 1594, eq. 56][8]:

$$\tau_{SRH}(\mathcal{N}, T) = \underbrace{\frac{\tau_{0,e/h}}{1 + \frac{\mathcal{N}}{\mathcal{N}_{d0,e/h}}}}_{\tau_{SRH,e/h}(\mathcal{N})} \cdot T_n^{-3/2} \quad \text{with} \quad T_n = \frac{T}{300\,\text{K}} \tag{2.10}$$

where $\tau_{0,e/h}$ is the carrier lifetime at 300 K in pure silicon for electrons and holes, respectively. $\mathcal{N}_{d0,e/h}$ is the doping concentration where the lifetime halved and T_n is the normalized temperature.
Values for electrons and holes are given in Table 2.3[9].

Parameter	e: **Electron**	h: **Hole**	
$\tau_{0,i}$ [µs]	10	3	400
$\mathcal{N}_{d0,i}$ [cm^{-3}]	$1.0 \cdot 10^{16}$		$7.1 \cdot 10^{15}$
Reference	[57, p. 497, tab. 86]		[55, p. 742]

Table 2.3: Parameters for the Shockley-Read-Hall lifetime according to values reported in both [55, p. 742] and the Synopsys Sentaurus TCAD software manual [57, p. 497, tab. 86]. See also [59].

At high doping concentrations ($\gtrsim \mathcal{O}(1 \times 10^{18}\,\text{cm}^{-3})$), Auger recombination [60, 61] dominates. Here, the recombination of an electron and hole result in the excess energy being transferred to another charge carrier — either an electron (e-e-h process) or a hole (e-h-h process). The Auger lifetime for minority carriers in highly doped silicon is:

$$\tau_{Auger} = \frac{1}{(C_n + C_p) \cdot \mathcal{N}^2} = \frac{1}{C_{Auger} \cdot \mathcal{N}^2} \tag{2.11}$$

where C_n is the coefficient associated to the "e-e-h process", and C_p is the coefficient associated to the "e-h-h process". $C_{Auger} = 3.8 \times 10^{-31}\,\text{cm}^6/\text{s}$ is the ambipolar Auger coefficient. Reference value can are given in [62].

[7] The lifetime due to radiative combination, which is referred to as band-to-band recombination, is significantly greater in silicon than in the other processes presented. This effect can therefore be neglected and is not included in the equation.
[8] Take note of the negative sign in the exponent of T_n, as the ratio is inversely defined relative to the original source.
[9] Be aware that there is a significant deviation for the values of holes between [55, p. 742] and the Synopsys Sentaurus TCAD software manual [57, p. 497, tab. 86]. In addition, any surface effects [58] are not taken into account.

2.2.4 Substrate Resistivity

Although the doping concentration is the primary parameter influencing almost all electrical characteristics of silicon as a semiconductor, the bulk resistivity[10] (ϱ) is typically specified by the wafer manufacturer[11]. Resistivity is inversely proportional to the material's electrical conductivity, and is given by:

$$\varrho = \frac{1}{q \cdot (\mu_e \cdot \mathcal{N}_D + \mu_h \cdot \mathcal{N}_A)} \tag{2.12}$$

where q donates the elementary charge, μ_e and μ_h represent the electron and hole mobilities, and $\mathcal{N}_D$ and $\mathcal{N}_A$ donate the donor and acceptor doping concentrations, respectively. In case of a p-type substrate, assuming full ionization ($\mathcal{N}_D \approx 0$), the expression simplifies to:

$$\varrho_{substrate} = \frac{1}{q \cdot \mu_h \cdot \mathcal{N}_A} \tag{2.13}$$

This relation shows that, for a "pure" p-type substrate, the resistivity depends only on the hole mobility μ_h and the acceptor doping concentration $\mathcal{N}_A$. It is important to note that the resistivity is temperature dependent due to the temperature dependence of the carrier mobility. For simplicity and consistency, values at 300 K, as listed in Table 2.1, are used throughout this work (if not stated otherwise) to convert between resistivity and doping concentration.

Plot 2.2a illustrates the relationship between substrate resistivity and acceptor doping concentration at a fixed temperature of 300 K. In this case, no significant deviations are observed between the different mobility models. In contrast, Plot 2.2b shows that, for a fixed doping concentration, resistivity exhibits a strong temperature dependence, highlighting the impact of the temperature-dependent carrier mobility.

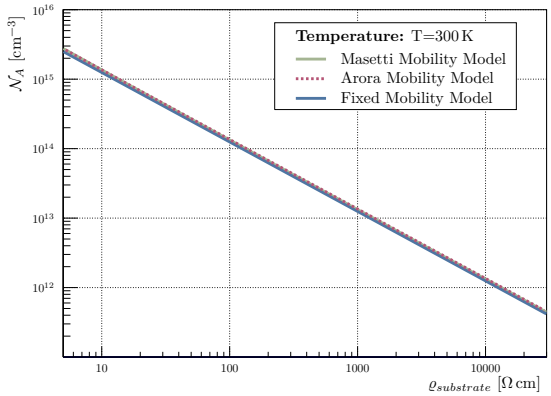

(a) $\mathcal{N}_A$ as function of the substrate resistivity $\varrho_{substrate}$ at 300 K.

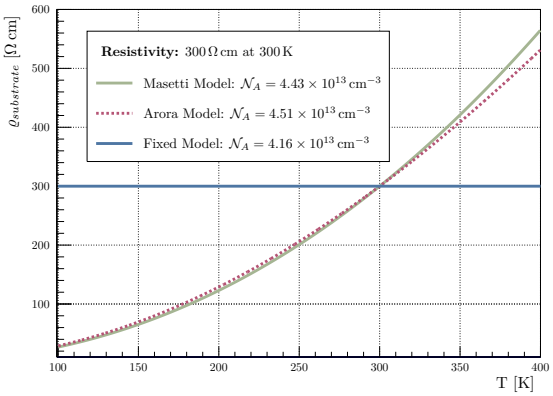

(b) Resistivity $\varrho_{substrate}$ as function of the temperature T for $\varrho_{substrate}$ = 300 Ω cm at 300 K.

Plot 2.2: Resistivity relations in p-substrate silicon using fixed carrier mobility and the Arora- and Masetti-Models (see Section A.2).

[10] Not to be confused with the sheet resistance, which is a measure for the resistance of a thin layer of material.
[11] A common method to measure the resistivity of a silicon wafer is the four-point probe method, which is described exemplary in [63].

2.3 The pn-Junction of a Silicon Detector

In the previous section, the basic properties of (doped) semiconductors were introduced — knowledge essential for understanding the *pn*-junction. In the context of silicon as a particle detector material, the *pn*-junction functions as a *diode* and serves as the main active detection volume for incident particles, making it crucial for the operation of depleted silicon detectors.

A *pn*-junction is formed when *p*-doped and *n*-doped regions of silicon are brought into contact. The concentration gradient between these regions establishes a diffusion current of charge carriers across the junction. The majority charge carriers in the *p*-doped part (holes) diffuse into the *n*-doped region, while the majority charge carriers in the *n*-doped part (electrons), diffuse into the *p*-doped region. Recombination of these carriers near the junction boundary depletes the region of mobile charge, leaving behind ionized atoms, and thereby introducing a space charge density.

The uncompensated charges on the *p*-side and *n*-side create an electric field across the depletion region, which induces a drift current that opposes the diffusion current. An equilibrium is established in which the space-charge density is given by:

$$\rho_{SC} = \begin{cases} -e \cdot \mathcal{N}_A & \text{for } -x_p < x < 0 \\ +e \cdot \mathcal{N}_D & \text{for } 0 < x < x_n \end{cases} \tag{2.14}$$

where e is elementary charge magnitude of the electron. To maintain charge neutrality, the condition $\mathcal{N}_A \cdot x_p = \mathcal{N}_D \cdot x_n$ holds.
Applying Maxwell's equations, the electric field $\mathcal{E}$ in the depletion region can be expressed as:

$$\mathcal{E}(x) = \begin{cases} -\frac{e \cdot \mathcal{N}_A}{\varepsilon_{\text{Si}} \varepsilon_0}(x + x_p) & \text{for } -x_p < x < 0 \\ \frac{e \cdot \mathcal{N}_D}{\varepsilon_{\text{Si}} \varepsilon_0}(x - x_n) & \text{for } 0 < x < x_n \end{cases} \tag{2.15}$$

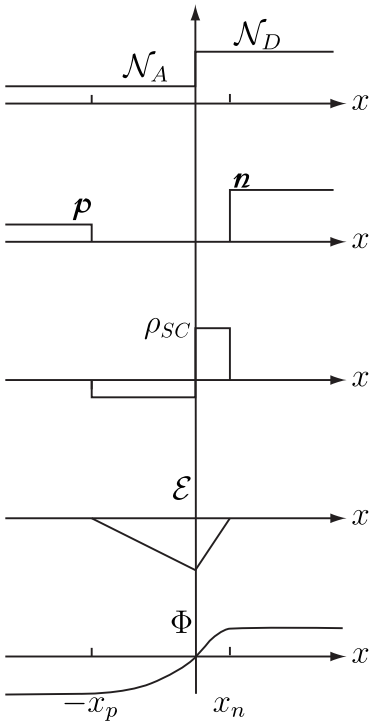

Figure 2.4: Schematic of doping concentrations ($\mathcal{N}_A$ & $\mathcal{N}_D$), charge carrier densities (*n* & *p*), space charge density (ρ_{SC}), electric field ($\mathcal{E}$) and potential (Φ) in a *pn*-junction. Adapted from [17, p. 276, fig. 8.17].

where ε_0 is the vacuum permittivity and ε_{Si} is the relative permittivity of silicon. The electric field reaches its maximum at the junction ($x = 0$).
By integrating the electric field, the potential difference across the depletion region is:

$$\Phi(x) = \begin{cases} \Phi(x_p) + \frac{e \cdot \mathcal{N}_A}{2\varepsilon_{\text{Si}} \varepsilon_0}(x + x_p)^2 & \text{for } -x_p < x < 0 \\ \Phi(x_n) - \frac{e \cdot \mathcal{N}_D}{2\varepsilon_{\text{Si}} \varepsilon_0}(x - x_n)^2 & \text{for } 0 < x < x_n \end{cases} \tag{2.16}$$

where $\Phi(x_p)$ and $\Phi(x_n)$ represent the potentials at the *p*-side and *n*-side boundaries, respectively.
A schematic illustration of these mechanism is provided in Figure 2.4.

2.3.1 Depletion Region

The potential difference described in Equation 2.16 defines the so-called built-in voltage U_{bi}. It is given by [17, p.277, eq. 8.37]:

$$U_{bi} = \Phi(x_n) - \Phi(x_p) = \frac{k_B T}{e} \ln\left(\frac{\mathcal{N}_A \mathcal{N}_D}{n_i^2}\right) \overset{Si}{\approx} 0.4\,\text{V to } 0.8\,\text{V} \quad (2.17)$$

This built-in voltage parametrizes the depletion depth w of the *pn*-junction, defined as the total distance from the junction to the edge of the depletion region where the electric field becomes zero. By integrating the electric field with appropriate boundary conditions and setting the result equal to U_{bi}, yields [17, p. 277, eq. 8.38]:

$$U_{bi} = \frac{e}{2\varepsilon_{\text{Si}}\varepsilon_0}\left(\mathcal{N}_A \cdot x_p^2 + \mathcal{N}_D \cdot x_n^2\right) \quad (2.18)$$

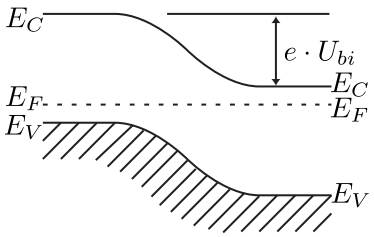

Figure 2.5: Schematic energy band levels in a *pn*-junction. Adapted from [17, p. 280, fig. 8.18].

Following from this, the total depletion width is given by:

$$w = x_p + x_n = \sqrt{\frac{2\varepsilon_{\text{Si}}\varepsilon_0}{e}\frac{(\mathcal{N}_A + \mathcal{N}_D)}{\mathcal{N}_A \cdot \mathcal{N}_D} U_{bi}} \quad (2.19)$$

In case of $\mathcal{N}_D \gg \mathcal{N}_A$ (typically for *p*-doped silicon detectors)[12], the approximation $x_p \gg x_n$ holds, and the depletion region extends almost entirely into the lightly doped *p*-region. Thus, the depletion width simplifies to:

$$w \approx x_p \approx \sqrt{\frac{2\varepsilon_{\text{Si}}\varepsilon_0}{e}\frac{1}{\mathcal{N}_A} U_{bi}} \quad (2.20)$$

This approximation is valid for strongly asymmetric doping concentrations.

2.3.2 External Bias

Applying an external bias voltage U to a *pn*-junction drives the system out of thermal equilibrium. Depending on the polarity of the applied bias voltage, one distinguishes between forward ($U > 0$, positive on *p*-doped side relative to *n*-doped side) and reverse bias ($U < 0$, opposite polarity). The applied bias shifts the conduction band (E_C) and valence band (E_V) by an energy $e \cdot U$ (see Figure 2.6).

- In forward bias, the effective potential barrier is reduced by $e \cdot U$, which narrows the depletion region. As a result, electrons diffuse from the *n*-doped side to the *p*-doped side, while holes move in the opposite direction. The electric field (and hence the drift current) decreases, whereas the diffusion current increases.
- In reverse bias, the effective potential barrier increases by $e \cdot U$, widening the depletion region. The drift current increases, due to the stronger electric field, while the diffusion current is decreases, resulting in a small net reverse leakage current.

The depletion width under reverse bias can be calculated using a modified version of Equation 2.20. For a *p*-type substrate, the depletion width simplifies to:

$$w(U) \approx \sqrt{\frac{2\varepsilon_{\text{Si}}\varepsilon_0}{e}\frac{1}{\mathcal{N}_A}(U_{bi} - U)} \quad (2.21)$$

If the acceptor concentration is expressed in terms of the substrate resistivity (see Equation 2.13), the depletion width can be approximated by:

$$w(U) \approx \sqrt{2\varepsilon_{\text{Si}}\varepsilon_0\mu_h\varrho_{substrate}(U_{bi} + |U|)} \quad \rightarrow \quad w(U)\,[\mu\text{m}] \approx 0.32186 \cdot \sqrt{\frac{\varrho_{substrate}}{[\Omega\,\text{cm}]}\frac{(U_{bi} + |U|)}{[\text{V}]}} \quad (2.22)$$

This formula shows that the depletion depth depends primarily on the substrate resistivity $\varrho_{substrate}$, assuming the doping concentration on the *n*-doped side is sufficiently high such that its contribution to the depletion depth is negligible.

The approximation holds under typical conditions at room temperature (300 K). For a fixed doping concentration, the depletion depth is, to first order, insensitive to temperature[13]. However, introducing the resistivity via Equation 2.13 necessitates a carrier mobility model; since mobility varies with temperature, it affects the corresponding $\varrho_{substrate}$, although this dependence ultimately cancels out in the depletion-depth calculation. For consistency, the silicon parameters listed in Table 2.1 are treated as fixed when evaluating Equation 2.22 throughout this thesis, unless explicitly noted otherwise.

(a) Forward bias. *(b)* Reverse bias.

Figure 2.6: Schematic energy band level shift by external bias in a *pn*-junction. Adapted from [17, p. 280, fig. 8.18].

2.3.3 Leakage Current & Temperature Influence

The idealized model of a *pn*-junction assumes that no charge generation occurs in the depleted volume. In this case, the resulting current-voltage (IV) characteristic is governed solely by carriers originating from the neutral regions, where no space charge is present. The current is driven by the diffusion of minority charge carriers and displays an exponential dependence on the applied forward voltage (U), described by the Shockley equation [64, p. 454, eq. 3.11]:

$$\mathcal{I} = \mathcal{I}_S \left(\mathrm{e}^{\frac{e \cdot U}{k_B T}} - 1 \right) \tag{2.23}$$

where ($\mathcal{I}_S$) is the reverse saturation current.

In reality, the current in reverse bias is dominated by thermally generated electron-hole pairs in the depletion volume, a process that is strongly affected by defect states introduced by impurities or damage within the crystal structure (see Section 2.1.3). These defects can introduce intermediate energy levels in the band gap that enhance charge generation through the mechanism commonly referred to as trap-assisted tunneling [65]. The resulting reverse current is referred to as leakage current, and is given by [17, p.284, eq. 8.61]:

$$\mathcal{I}_{\text{leakage}} = e A_{\text{electrode}} \cdot w(U) \cdot \frac{n_i}{\tau_g} \tag{2.24}$$

In this expression, $A_{\text{electrode}}$ is the area of the junction (electrode area), $w(U)$ is the depletion depth under applied voltage U (see Equation 2.21), n_i is the intrinsic carrier concentration , and τ_g is the generation lifetime of electron-hole pairs in the depletion region.

The leakage current is thus directly proportional to the depletion volume, $A_{\text{electrode}} \cdot w(U)$. Since both the intrinsic carrier concentration ($n_i \propto T^{3/2} \mathrm{e}^{-\frac{E_g}{2k_B T}}$, see Equation 2.3) and the generation lifetime ($\tau_g \propto T^{-1/2}$, cf. [66, p.33]) — which quantifies the average time period it takes to re-create an electron-hole-pair by thermal excitation — are temperature-dependent, the leakage current also varies with the temperature.

[12] The actual doping concentration of the n-well is not known, but is expected to be in the range of 1×10^{16} cm^{-3} to 1×10^{20} cm^{-3}.

[13] The doping concentration is assumed to not change, the temperature dependence of the resistivity is governed by the temperature dependence of the mobility.

Combining these two relations, the temperature dependence of the leakage current can be approximated by [67, p.2, eq. 2.4]:

$$\mathcal{I}_{\text{leakage}} \sim T^2 \mathrm{e}^{-\frac{E_a}{2k_B T}} \tag{2.25}$$

where E_a is the effective activation energy. For silicon, this parameter[14] is typically approximated to be 1.21 eV (more details in [67]).

Additional factors beyond the temperature dependence described above can significantly influence the leakage current. Mechanisms such as Frenkel defect, vacancies, and radiation-induced lattice damage introduce extra generation-recombination centers, resulting in increased leakage current. While these contributions are not explored in the present work, they are thoroughly discussed in standard semiconductor device literature such as [17, p. 341ff.].

[14] $E_a = 1.21$ eV should not be confused with the band gap energy E_g, which is about 1.12 eV for silicon at 300 K.

2.4 Pixel Sensor Technologies

Silicon pixel detectors are a key technology in modern particle physics experiments, where they are used for achieving precise spatial, temporal and momentum resolution. Owing to their high granularity, these detectors are primarily used close to the interaction point as vertex and tracking detectors.

In the following sections, the most commonly used silicon pixel detector technologies are introduced. These can be broadly categorized into three main groups: Hybrid detectors, **M**onolithic **A**ctive **P**ixel **S**ensor and **D**epleted **M**onolithic **A**ctive **P**ixel **S**ensor. Many other technologies exist — such as CCD (**C**harge-**C**oupled **D**evice), DEPFET (**De**pleted **P**-channel **F**ield-**E**ffect **T**ransistor) and SOI-MAPS (**S**ilicon-**O**n-**I**nsulator **M**onolithic **A**ctive **P**ixel **S**ensor) — but these are not discussed further in this thesis.

2.4.1 Hybrid Pixel Detectors

A hybrid pixel detector, as the name suggest, features a modular design in which the detector is separated into two main components: a (passive) silicon diode sensor for charge collection, and one or more readout **A**pplication-**S**pecific **I**ntegrated **C**ircuit for signal processing, as illustrated in Figure 2.7b. This modular concept enables the "independent" development of the sensor and the readout ASIC, offering design flexibility at the cost of increases assembly complexity and higher material budget due to the bump bonding process.

While the readout ASIC is typically developed using available CMOS technology, the sensor can be flexibly adapted to various requirements, such as enhanced radiation hardness, or sensor material modifications, for optimized response of x-ray or particle detection. The pixels are usually DC-coupled to their corresponding readout cell via bump bonds (see Figure 2.7a), enabling fast and low-loss transmission of the current signal.

The **si**licon sensor is typically backside-biased by applying a high-voltage potential. This is achieved through a backside surface treatment that includes a high-dose doping implantation followed by a metalization, allowing the detector to operation at — and beyond — its full depletion voltage.

Today, hybrid pixel detectors are used in several fields. In medical imaging, chips from the Medipix family [68] are widely deployed, while in high-energy physics, they are employed in experiments such as LHCb (using VeloPix [69]) and in the ATLAS and CMS detectors, both of which use custom variants of the RD53 chip [70].

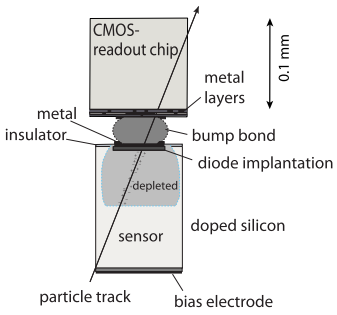

(a) Layout of a single pixel cell bump-bonded to a readout cell.

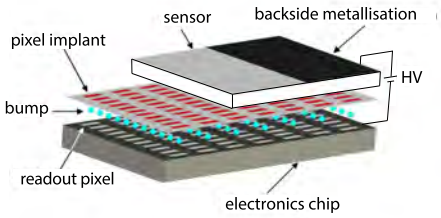

(b) Layout of a hybrid pixel sensor matrix.

Figure 2.7: Schematic of a hybrid pixel detector. The pixel cell is bump-bonded to a readout cell, which is connected to the readout electronics. Taken from [17, p. 315, fig. 8.53].

2.4.2 Monolithic Active Pixel Sensors

In contrast to hybrid pixel detectors, **M**onolithic **A**ctive **P**ixel **S**ensor integrate both the readout ASIC and the sensing volume within a single **si**licon die, hence the term monolithic. The term active refers to the integration of pixel-level electronics, which are embedded in shallow wells outside the charge collection region.

A low-resistivity substrates is used as the base wafer, topped with an epitaxial layer that serves as the charge collection medium. A schematic of the **M**onolithic **A**ctive **P**ixel **S**ensor principle is shown in Figure 2.8a. The electronics are fabricated using a standard CMOS process. The collection electrode is typically realized as a small n-doped implant, which creates only a limited depletion region around it. As a result, charge collection is primarily governed by diffusion, with minimal contribution from drift. This leads to charge loss and relatively slow charge collection times, typically $\mathcal{O}(100\,\text{ns})$.

Because the low-resistivity substrate does not participate in the charge collection, the sensors can be thinned to 50 µm to 100 µm, significantly reducing the total material budget compared to hybrid pixel detectors.

MAPS have been deployed in several particle physics experiments, such as the STAR experiment [71] at RHIC and the ALICE experiment at CERN, which uses the ALPIDE sensor [72]. Additionally, MIMOSA-26 sensors [73] are employed at test beam facilities, including the EUDET telescopes at CERN, DESY and SLAC, as well as at ELSA at the University of Bonn.

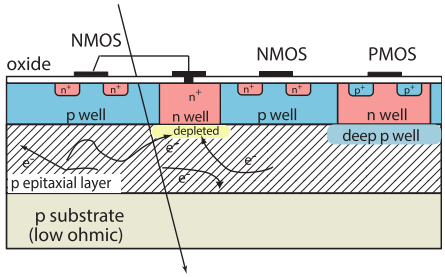

(a) Schematic of a **M**onolithic **A**ctive **P**ixel **S**ensor. Taken from [17, p. 334, fig. 8.72].

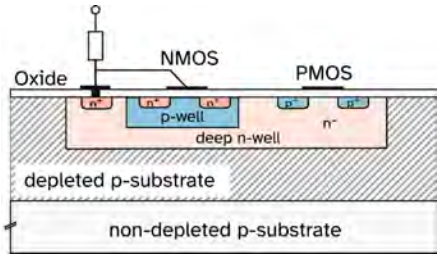

(b) Schematic of **D**epleted **M**onolithic **A**ctive **P**ixel **S**ensor using the example of the HV-MAPS. Adapted from [74, p. 358, fig. 8.75].

Figure 2.8: Schematics of MAPS and DMAPS.

2.4.3 Depleted Monolithic Active Pixel Sensor

The **D**epleted **M**onolithic **A**ctive **P**ixel **S**ensor is an advancement of the MAPS technology (see Section 2.4.2) that incorporates fast charge collection via drift within an electric field. In DMAPS, charge carriers are collected through drift in the depletion zone of a high-resistivity substrate, typically ranging from $\mathcal{O}(20\,\Omega\,\text{cm}$ to $20 \times 10^3\,\Omega\,\text{cm})$, as opposed to relying predominantly on diffusion.

This approach enables rapid and efficient charge collection on the order of nanoseconds, even with larger pixel pitches. The resulting improvement in timing resolution allows DMAPS to cope with higher particle rates. The detection diode is formed by a *n*-well implant in a *p*-substrate and is reverse biased. The bias voltage can be applied either directly to the backside of the sensor — similar to hybrid pixel detectors (see Section 2.4.1) — or via a top-side *guard-ring*. Depending on the application's performance requirements, high-resistivity substrates and/or high-voltage biasing are used to achieve a depletion depths of $\mathcal{O}(10\,\mu\text{m})$ to $\mathcal{O}(100\,\mu\text{m})$.

The charge collection electrode can be connected to the CMOS electronics via capacitive (AC (**A**lternating **C**urrent)) or resistive (DC (**D**irect **C**urrent)) coupling. AC coupling involves placing a capacitor between the electrode and electronics, which helps suppress leakage currents and reduces noise, but also acts as an additional shaping element that can delay the signal. This makes it important to fine-tune the input capacitance so the signal bandwidth matches the detector's response time. In contrast, DC coupling provides a direct electrical connection that enables immediate charge transfer without signal delays, which is advantageous in high-rate environments because it shortens dead time. However, it requires tighter control of leakage currents, as excessive leakage can increase noise.

There are two principle designs for the charge collection electrode. The small fill-factor design (see Figure 2.9a) yields lower capacitance and noise, but requires a deep *p*-well to shield the CMOS electronics near the collection electrode. The large fill-factor design (see Figure 2.9b), in contrast, integrates the CMOS electronics directly within the *n*-well, providing geometrically shorter drift paths for charge collection. Although this design can improve the charge collection efficiency, it results in increased capacitance and hereby higher noise.

The selection of electrode design is driven by application-specific needs, including noise performance, timing resolution, and radiation hardness. In this thesis, focus is placed on the large fill-factor electrode design, as implemented in **H**igh-**V**oltage **M**onolithic **A**ctive **P**ixel **S**ensor.

High-Voltage Monolithic Active Pixel Sensor

HV-MAPS (**H**igh-**V**oltage **M**onolithic **A**ctive **P**ixel **S**ensor) were the first DMAPS development, invented by Ivan Perić [75], and specialized on a large fill-factor electrode design. They are primarily manufactured in a 180 nm HV-

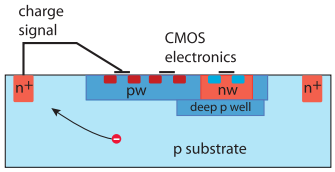

(a) Schematic of a small fill-factor collection electrode design.

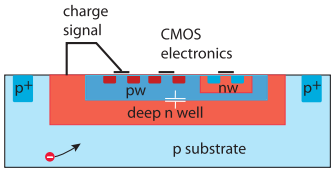

(b) Schematic of a large fill-factor collection electrode design.

Figure 2.9: Schematics of different fill-factor electrode designs for DMAPS sensors. Taken from [17, p. 280, fig. 8.18].

CMOS process[15] and have been developed for several particle physics applications, including the *Mu3e* experiment (see Section 3.1). The development timeline of HV-MAPS is illustrated in Figure 2.10.

HV-MAPS integrate in-pixel electronics for signal amplification, shaping, and discrimination. These components are embedded in a deep n-well, which — together with the surrounding p-type substrate — forms the charge collection diode. Notably, the MuPix series omits in-pixel signal discrimination, instead relying on up to two comparators per channel in the periphery (see Section 3.5).

Applying a sufficiently high reverse bias voltage to the substrate extends the depletion zone to approximately $\mathcal{O}(30\,\mu\text{m})$, depending on the substrate resistivity (see Section 2.3.2). Electron-hole pairs generated by ionizing radiation are separated by the electric field and drift towards the n-well within a few nanoseconds, inducing an influence signal on the readout circuitry.

This thesis focusses on the MuPix10 sensor (see Chapter 3), although many of the concepts discussed are also relevant to the other HV-MAPS series and to silicon pixel detectors with similar architecture.

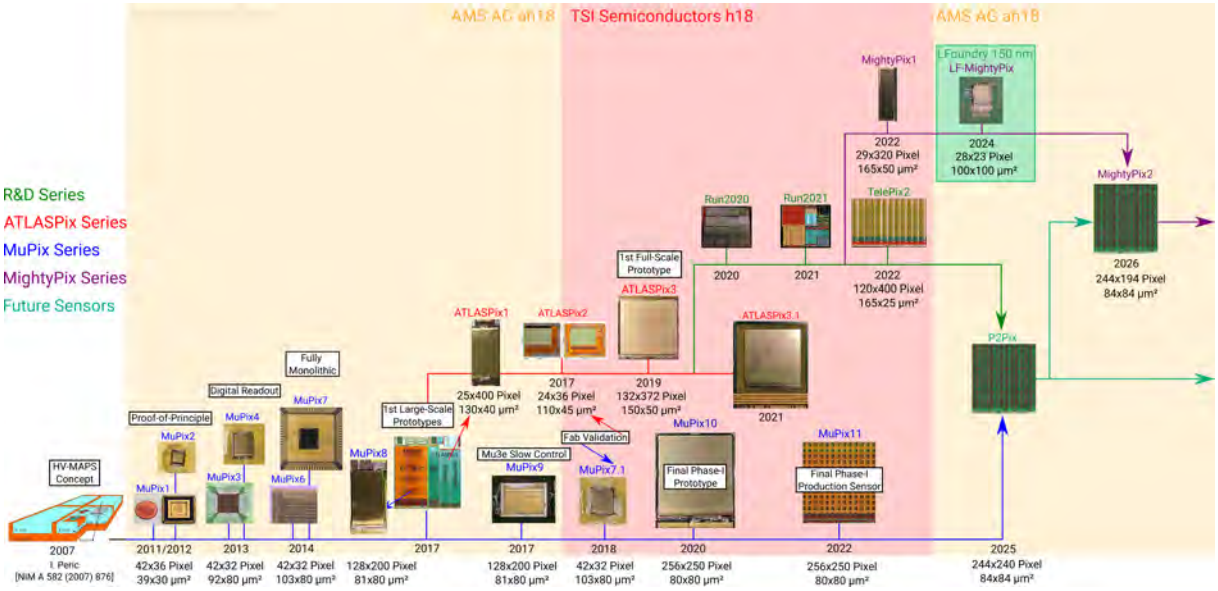

Figure 2.10: Roadmap of the HV-MAPS development.

[15] Current primary manufacturing is handled by ams OSRAM, with interim production managed by TSI Semiconductors, which was acquired in 2023 by BOSCH and subsequently renamed Robert Bosch Semiconductor LLC.

3. MuPix10

MuPix10 is the final prototype of the MuPix series (see Section 2.4.3), designed for the *Mu3e* experiment, and is simultaneously the first full-scale sensor of its series. It serves as testbed for the *Mu3e* experiment's tracking detector requirements (see Section 3.1.2), and as the last prototype in which to implement any final changes before the production of the MuPix11 sensors. In the following sections, a brief introduction to *Mu3e* and the planned pixel-based tracking detector is given, followed by a more detailed description of MuPix10 and its components. Most concepts presented are not exclusive to MuPix10, but are also transferable to other HV-MAPS.

3.1 The Mu3e Experiment

The history of cLFV (**c**harged **L**epton **F**lavor **V**iolation) dates back to the early 1940s, with the main decay channels under investigation being $\mu \to e\gamma$, $\mu \to 3e$ and $\mu N \to eN$. A comprehensive overview is provided in Figure 3.1a.

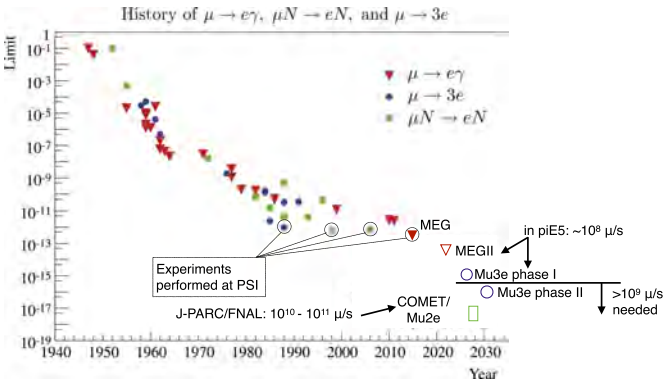

(a) History pf BR-limits of the three "golden" cLFV-channels. Non-filled symbols indicate projected measurements. Taken from [76, p. 7, fig. 1] (adaption from [77]).

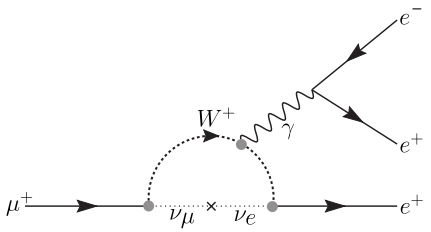

(b) Standard Model feynman diagram of $\mu^+ \to e^+ e^- e^+$ with neutrino oscillation.

Figure 3.1: History of cLFV searches and the Feynman diagram of the *Mu3e* decay channel.

The *Mu3e* experiment [78] is designed to search for the cLFV decay $\mu^+ \to e^+ e^- e^+$ (see Figure 3.1b), a process that is heavily suppressed in the Standard Model of particle physics — including neutrino oscillation — with an expected BR (**B**ranching **R**atio) $< \mathcal{O}(10^{-54})$ [78, p. 2]. While lepton flavor violation is established in the neutral sector (via neutrino oscillation), it has not yet been observed for charged leptons. The *SINDRUM* collaboration set the current limit on this **B**ranching **R**atio at BR by $< 10^{-12}$ (90 % C.L.) in 1988 [79].

The *Mu3e* experiment will utilize a high-intensity μ^+-beam provided by PSI (**P**aul-**S**cherrer **I**nstitute) (cf. Section 5.2), where the muons are stopped in a thin Mylar target, resulting in a clean event topology. For a valid *Mu3e* signal decay, the total momentum of the final-state particles has to cancel out ($|\vec{p}_{tot}| = |\sum \vec{p}_i| = 0$), and the invariant mass has to be equal to the (anti-)muon mass ($M_{inv.} = |\sum p_i| = \sum E_i = M_\mu$) [78, p. 2, eq. 1.1 & 1.2].

The dominant background is the *Michel decay* ($\mu^+ \to e^+ \bar{\nu}_\mu \nu_e$), which is characteristic with a single observable decay product, the positron, and missing energy from the two neutrinos. However, in combination with Bhabha scattering ($e^+ e^- \to e^+ e^-$) (see Section 1.1.2), the *Michel decay* can mimic the *Mu3e* signal, constituting an accidental background. Radiative muon decays with internal conversion $\mu^+ \to \bar{\nu}_\mu \nu_e (e^+ \to e^- e^+)$ also contribute to the background, necessitating precise momentum resolution to identify the missing energy carried by the neutrinos.

To achieve the desired sensitivity — up to $\mathcal{O}(10^{-16})$ in phase-II [78] — the experiment requires a μ^+-beam of 10^8 μ^+/s to 10^9 μ^+/s (phase-I to phase-II). This demands a detector system with excellent momentum, spatial and timing resolution, as well as high hit rate capability. The following sections present the *Mu3e* detector concept designed to meet these challenges.

3.1.1 The Detector Concept

The concept of the *Mu3e* detector [78] is illustrated in Figure 3.2. An μ^+-beam with a momentum of 28 MeV c^{-1} is directed onto a hollow double-cone-shaped 70 µm Mylar, where the muons are stopped and decay at rest. The trajectories of the decay positrons (and electrons) are bent by the magnetic field of a 1 T solenoid magnet, which is aligned along the beam axis. The decay products are detected by a cylindrical detector system surrounding the interaction point at the center of the solenoid.

The interaction region is enclosed by a double layer of HV-MAPS (inner layers) for precise vertex reconstruction, supported by a scintillating fibre detector that provides high-resolution timing information. Two additional layers of HV-MAPS (outer layers) are positioned further out to enhance tracking of the decay products. Up- and down-stream of the inner barrel, further double-layered stations of HV-MAPS are installed to reconstruct higher-momentum decay particles and improve the overall momentum resolution. Finally, the high-momentum decay products are stopped and timed in a layer of scintillating tiles below the up- and down-stream stations.

Because the decay products are kinematically limited to a maximum momentum of about half of the muon mass, multiple Coulomb scattering (see Section 1.1.5) is a key factor in the detector design. This is especially important for the silicon pixel detector modules, where minimizing material is essential to reduce scattering effects.

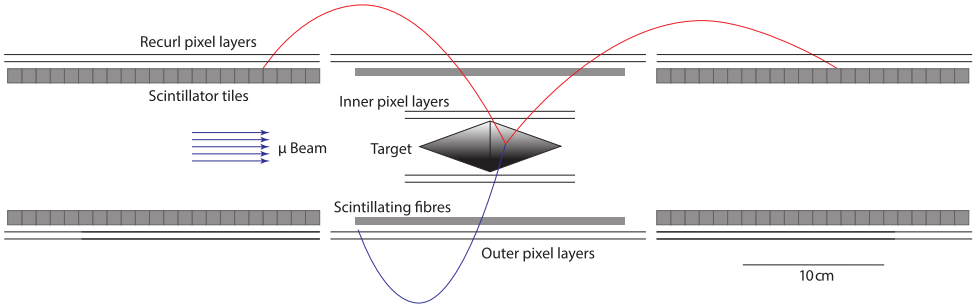

Figure 3.2: Schematic view of the *Mu3e* detector phase I concept cut along the beam axis. Taken from [78, p. 6, fig. 2.6].

3.1.2 The Pixel Tracking Detector

The pixel-based tracking detector is designed to meet stringent requirements for occupancy, material budget, and power consumption, while delivering excellent spatial and time resolution with high efficiencies and low noise rates (see Table 3.1).

The inner layers (see Section 3.1.1) are optimized for precise vertex reconstruction and are therefore placed as close as possible to the interaction point. Each inner layer ist structured as a ladder, consisting of six sensors, each approximately 21 mm×23 mm in size. The sensors are glued and SpTa-bonded to a HDI (**H**igh-**D**ensity **I**nterconnect)-flex (see Figure 3.3b), which provides all electrical connections, including supply voltages, communication signals and high-speed differential readout lines.

The outer layers follow the same design principles, but are extended to 18 sensors per ladder (see Figure 3.3a). To minimize the material budget contribution by the HDI-flex, the layer stack is kept as thin as possible. A significant area of the flex is to dedicated to routing of the necessary supply voltage levels (GND, VDD & HV) to ensure minimal losses.

Due to the high-rate environment, each inner layer sensor requires three high-speed readout links, while each outer layer sensor operates with a single link, managed by a link multiplexer. The remaining communication lines — such as clocks, synchronization reset, and slow control signals (all differential) — are shared in bus-like configuration. Therefore, each sensor is assigned an “unique” 4 bit hardwired address for communication.

	Requirement	**MuPix10**
pixel pitch [µm^2]	80×80	80×80
active area [mm^2]	$\approx 20 \times 20$	20.48×20
sensor size [mm^2]	$\leq 21 \times 23$	20.66×23.18
sensor thickness [µm]	50 (70)†	50, 60, 70 & 100
LVDS links	$3 + 1$ (mux)	$3 + 1$ (mux)
maximum bandwidth [gigabits]	3×1.25	3×1.25
RMS of spatial resolution [µm]	≤ 30	$\leq 30^\ddagger$
power consumption [mW cm^{-2}]	≤ 350	≤ 350
time resolution per pixel [ns]	≤ 20	$(6 \pm 1)^{\ddagger\ddagger}$
hit efficiency	$\geq 99\%$	$\geq 99\%$
noise rate [Hz pixel^{-1}]	≤ 20	$\leq 2^{\dagger\dagger}$

Table 3.1: Pixel detector requirements [78, p.23, tab. 8.1] and MuPix10 parameters [80, p. 41, tab, 3.6]. †: Recent simulation study indicated that 70 µm is sufficient. ‡: Intrinsically fulfilled by the pixel pitch, $80\,\mu m/\sqrt{12} \approx 23.1\,\mu m$. ‡‡: Measured with a 100 µm MuPix10 sensor.††: The mean noise rate per pixel.

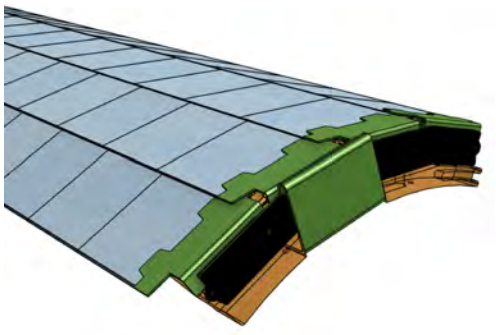

(a) Schematic of an outer layer pixel module containing four ladders of 18 sensors each. Taken from [78, p. 16, fig. 7.8].

(b) Layer stack of a HDI-flex consisting of alternating layers of aluminium, polyimide and glue.Taken from [78, p. 17, fig. 7.11].

Figure 3.3: Schematic view of a Mu3e pixel module and its HDI-flex produced by *LTU Enterprise*.

3.2 The MuPix10 Chip

MuPix10 is fabricated in the 180 nm HV-CMOS-process by TSI Semiconductors, qualified for operation up to 120 V. The use of this technology allows deep n-well structures to form the pixel diode's active detection volume while integrating CMOS electronics in the same substrate (see Figure 3.4a).

The sensor die measures approximately 21 mm×23 mm, and is divided vertically into three sub-matrices (A: columns 0-83; B: columns 84-169; C: columns 170-255), each served by a dedicated readout link (see Figure 3.4b, cf. Section 3.6.2). Most pixels share a common design, except for the uppermost 24 columns, where an alternative timestamp logic mode is used that does not provide Time-over-Threshold information.

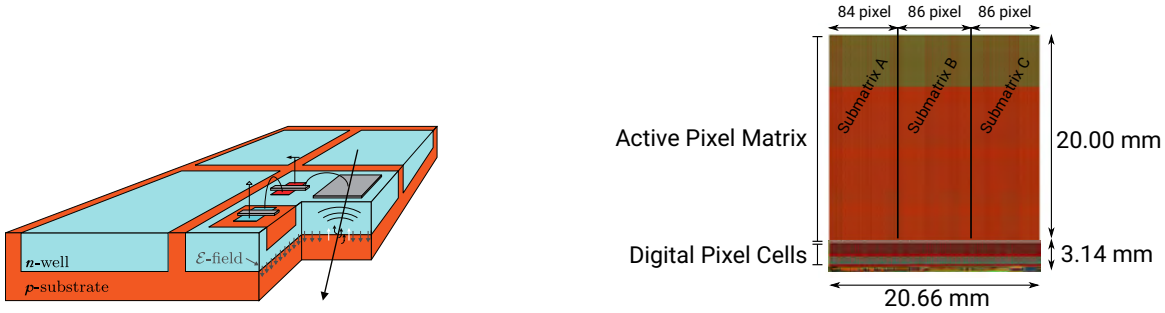

(a) Sketch of the HV-MAPS presenting 4 pixels. Adapted from [75, p. 877, fig.2].

(b) Dimensions of the MuPix10 die. The pixel matrix is subdivided in three matrices, each with and individual data link. Taken from [80, p.38, fig. 3.12].

Figure 3.4: Sketch of the HV-MAPS technology and the MuPix10 chip.

The basic readout architecture is illustrated in Figure 3.5 and is introduced in more detail in the following sections. In brief, the sensor diode serves as the charge-collection volume, with its signal processed by the active in-pixel electronics. Unlike other HV-MAPS developments (cf. Section 2.4.3), the MuPix series integrates only a Charge Sensitive Amplifier and line driver within the in-pixel electronics (see Section 3.3). The resulting signal pulses are digitized in peripheral cells (see Section 3.5) using one — or optionally two — comparators to suppress time walk.

Each sub-matrix has a dedicated FSM (Finite State Machine) that encodes the hit data in 8 bit/10 bit format and transmits it via a dedicated LVDS data link (see Section 3.6). Additionally, the data from all three links can be merged into a fourth, multiplexed data link, which is managed by its own FSM.

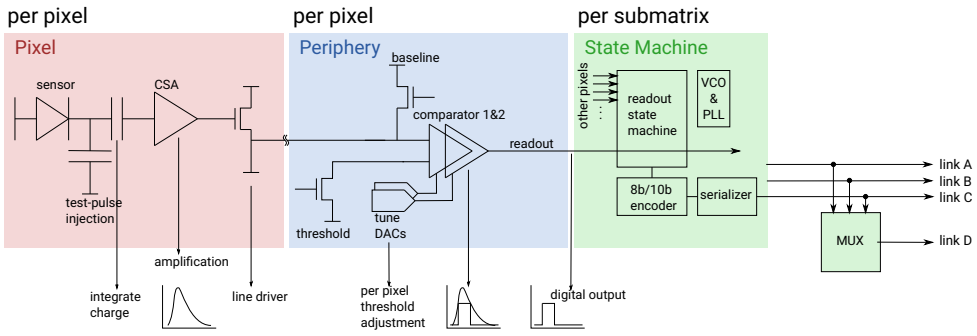

Figure 3.5: Sketch of the MuPix10 readout architecture. Taken from [80, p. 29, fig. 3.13] (based on [81, p. 39, fig. 5.1]).

3.2.1 Sensor Layout & Cross-sectional View

The key parameters of the MuPix10 sensor are summarized in Table 3.1. The sensor is surrounded by a chip *guard-ring*, which encloses both the pixel matrix and the periphery to provide electrical isolation and protect against edge effects from the cutting edge.

The pixel matrix consists of 256 × 250 symmetrical pixels, each measuring 80 µm×80 µm (see Figure 3.6b). The 80 µm dimensions is defined as the distance from the center between two pixel *guard-ring* on one side of a pixel

to the center of the opposite side. The pixel pitch, which is the distance between the centers of two neighboring pixels, thus amounts to the same. Notably, the distance between *n*-well edge and the pixel *guard-ring* is 9.5 µm on each side. Although the *n*-well is typically depicted as box-like, its edges are likely rounded in reality, resulting in a more cuboid shape.

Both pixel *guard-ring* as well as the periphery *guard-ring* are electrically shorted to the chip *guard-ring*, which is connected to the HV supply. Most pixels are expected to behave similarly in terms of the depletion zone growth. However, edge pixel (see Figure 3.6c and Figure 3.6d), having one neighboring pixels less (and corner pixels having only two neighboring pixels), may exhibit different depletion behavior. Due to this asymmetry, the depletion zone can extend beyond the pixel border, allowing charge collection via drift from outside the pixel. This can reduce the spatial resolution of the outer pixels. Additionally, because the distance between the outer pixel *guard-ring* and chip *guard-ring* varies, differences in the charge collection are expected between left (pixel column address 0), right edge (pixel column address 255), respectively, and pixels at the top (pixel row address 249) as well as bottom edge pixels (pixel row address 0).
As in the pixel matrix, the periphery electronics — which houses the digital cells, FSMs and further components — are embedded in a deep *n*-well.
The periphery measures 2.436 mm×20.509 mm, with the same 9.5 µm distance between the *n*-well and *guard-ring* being as in the pixels. This means the periphery also develops a depletion zone that can extend beyond its "physical" borders.

(a) MuPix10 cross-sectional view of a single pixel (not up to scale). In red the pixel *guard-ring* is shown. Optional layers such as glue and PCB are indicated.

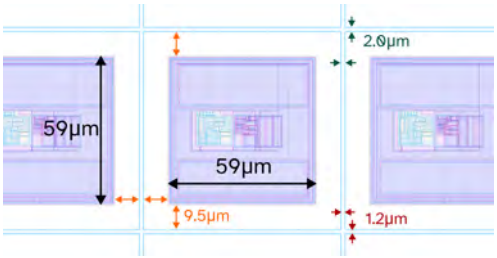

(b) Indexed cutout of the MuPix10 showing the symmetrical design of an individual pixel. Shown are the *n*-well dimensions, the distance to the pixel *guard-ring* (orange), and the inner (green) and outer (red) width of two neighboring pixel *guard-rings*.

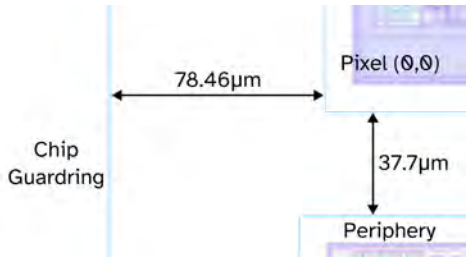

(c) Indexed cutout of the MuPix10 layout showing the region around pixel (0,0). Indicated are the distances from the pixel *guard-ring* to the chip *guard-ring* and the *guard-ring* of the periphery.

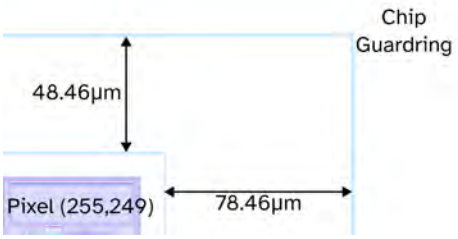

(d) Indexed cutout of the MuPix10 layout showing the region around pixel (255,249). Indicated are the distances from the pixel *guard-ring* to the chip *guard-ring* on both sides, the top and right.

Figure 3.6: Indexed cutouts of the of the MuPix10 layout.

The cross-sectional view (see Figure 3.6a) shows that the sensor consists not only of a silicon substrate for charge collection and electronics, but also of multiple layers for routing and protection. Seven metal layers made of **al**uminium alloys are used for signal routing and the power grid, separated by SiO_2 (**si**licon **di**oxide) for isolation. A thin Si_3N_4 (**si**licon **n**itride) layer on top serves as passivation to protect the metal layers from oxidation and contamination.

These additional layers contribute a total thickness of about 15 µm to 18 µm[1], which has to be subtracted from the total sensor thickness to estimate the remaining silicon available for charge collection.

3.2.2 Pixel Diode & Capacitance

The capacitance of the MuPix10 pixel diode can be approximated, to first order, by modeling it as a parallel plate capacitor with the electrode area A and the depletion width $w(U)$ (see Section 2.3.2):

$$C_d = \frac{\varepsilon_0 \cdot \varepsilon_{\mathrm{Si}} \cdot A}{w(U)} \approx \begin{cases} A \cdot \sqrt{\frac{\varepsilon_0 \cdot \varepsilon_{\mathrm{Si}} \cdot e \cdot \mathcal{N}_A}{2 \cdot (U_{bi} + |U|)}} & U < U_{depl.} \\ \frac{\varepsilon_0 \cdot \varepsilon_{\mathrm{Si}} \cdot A}{d} & U \geq U_{depl.} \end{cases} \longrightarrow \quad C_d\,[\mathrm{fF}] \approx \frac{0.32186 \cdot \frac{A}{[\mu\mathrm{m}^2]}}{\sqrt{\frac{\varrho_{substrate}}{[\Omega\,\mathrm{cm}]} \cdot \frac{(U_{bi} + |U|)}{[\mathrm{V}]}}} \tag{3.1}$$

In reality, the total capacitance is not solely determined by the depletion region. Parasitic capacitances to the metal layers and inter-pixel capacitances (see Figure 3.7a and Figure 3.7b) also contribute significantly. For low bias voltages or low substrate resistivities, the parallel plate approximation becomes less accurate and offers only limited insight. A more detailed discussion of inter-pixel and parasitic capacitances effects can be found in [82].

It is important to note that the HV is applied via the *p guard-ring* (both chip *guard-ring* and pixel *guard-ring* are electrically shorted), rather than from a backside contact. Additionally, the *n*-well potential is not floating; its is set by the bias circuit to approximately the analog supply voltage (≈*vdda*). As a result, the diode experience an external bias even when no HV is applied.

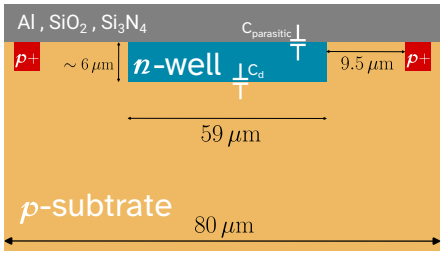

(a) Cross section of a MuPix10 pixel diode. The diode capacitance C_d and the parasitic coupling to the metal layers ($C_{parasitic}$) are indicated.

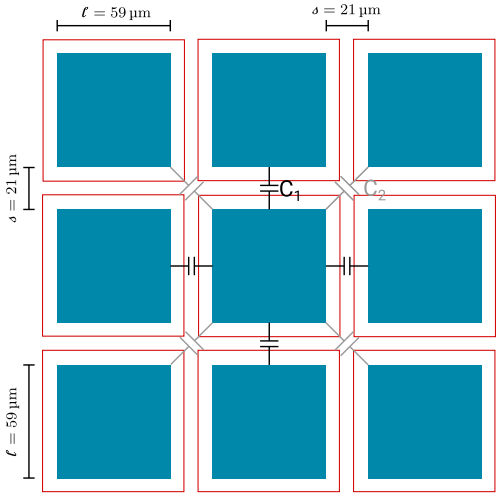

(b) 3 × 3 pixel array to sketch inter-pixel capacitance. It is differentiated between coupling capacitances direct neighbors and diagonal neighbors.

Figure 3.7: Pixel capacitance of the MuPix10. The *p guard-ring* is indicated in red and the *n*-well in blue.

[1] The exact numbers are known, but cannot be published due to the confidentiality of the process (Non-Disclosure Agreement).

3.2.3 Thinning Process

Thinning a die of about 2 cm×2 cm to a thickness as low as 50 µm is not a standard process in the semiconductor industry. Currently, HV-MAPS are thinned in a **D**icing **b**efore **G**rinding process, as offered by OPTIM **W**afer **S**ervice [83]. A notable observation is a sharp increase in the leakage current, which is associated with the depletion region extending to the backside of the sensor (see Plot 3.1). In contrast to back-biased sensors such as hybrid detectors (see Section 2.4.1), HV-MAPS do not undergo any additional backside treatment.

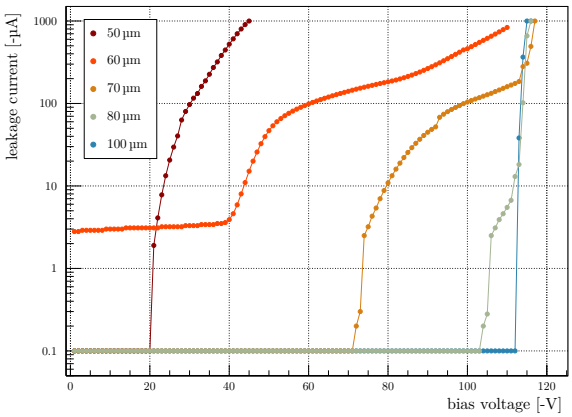

Plot 3.1: IV-curves of 50 µm to 100 µm thinned MuPix10 sensors (w/o *plasma* etching). Data taken with a *Keithley 2611B SourceMeter*® [84] by Dohun Kim. Adapted from [85] (presented in [86, fig. 8]).

This increase in leakage current has been reported by [87] to result from damage caused to the ground backside during the thinning process (see Figure 3.9). **A**tomic **F**orce **M**icroscopy measurements on 50 µm thinned MuPix10 (see Figure 3.2) reveal significant backside surface roughness[2]. The roughness, and the associated leakage current, can be mitigated by an additional *plasma etching* step applied after grinding, which removes the final micrometers of backside material.

As shown in [89], this step significantly improves the leakage current behavior; however, it does not guarantee operation at voltages above full depletion, which is expected to require further backside doping and metalization steps. Additionally, *plasma etching* relieves stress in the wafer, resulting in less bending of the thinned sensors. This is particularly important for sensors thinner 70 µm, as it facilitates subsequent production steps for sensor module assembly.

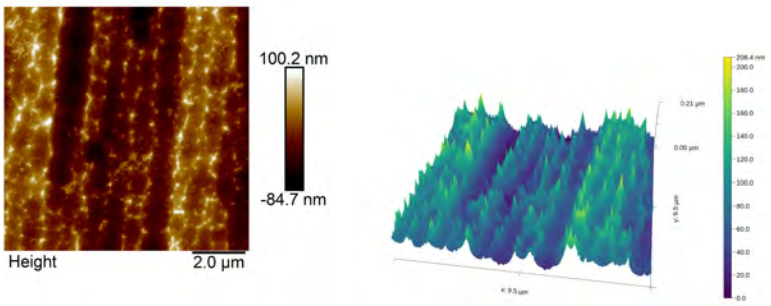

Plot 3.2: Thinning process effect: 2D and 3D AFM images of a small cutout of the backside of a 50 µm thinned MuPix10. AFM images taken from [85] (also presented in [86, fig. 9]).

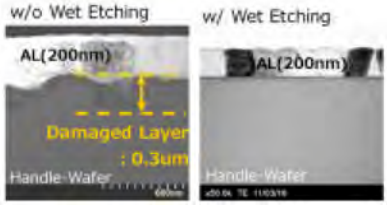

Figure 3.9: TEM image of a backside w/o (left) and with (right) wet etching treatment. Taken from [87, fig. 5].

[2] A similar effect is observed by [88, p. 131, fig. 6.5] and mitigated by an additional backside etching process.

3.3 Analog Pixel Cell

The analog pixel cell of the MuPix10 has its active electronics component embedded in the n-well of the pixel diode. An overview of the in-pixel electronics is shown in Figure 3.10a, which illustrates the CSA (Charge Sensitive Amplifier), the signal line driver and the *Injection* circuitry.

The CSA is the central component of the analog pixel cell, amplifying the charge collected by the pixel diode and converting it to a voltage signal (see Section 3.3.1 for a detailed view). Since the CSA is not intended to drive a large output capacitances, its output is connected to a NMOS source follower, which provides near-unity gain and is capable of driving the output capacitance of the signal line to the periphery. Additionally, the lowermost pixel row features a so-called *AmpOut*, which is the analog CSA output driven by its own source follower.

The charge *Injection* circuit is designed to mimic different input charges to the amplifier by a "externally" charging a capacitance in the pixel. Upon release, the stored charge is injected directly into the deep n-well of the pixel diode, bypassing the normal charge collection process in the p-substrate. This provides an excellent means to test the CSA response independently (to first order) of the charge collection efficiency. For more details on the in-pixel injection, see Section 6.3.

The analog pixel cell requires three externally supplied voltage levels; *vdda*, *vssa* and *gnda*. The *vssa* level can be generated on-chip via a linear series regulator (see Section 3.7.1), while other internally used voltage levels are generated on-chip using DACs. An overview of the analog pixel cell parameters is provided in Table A.9.

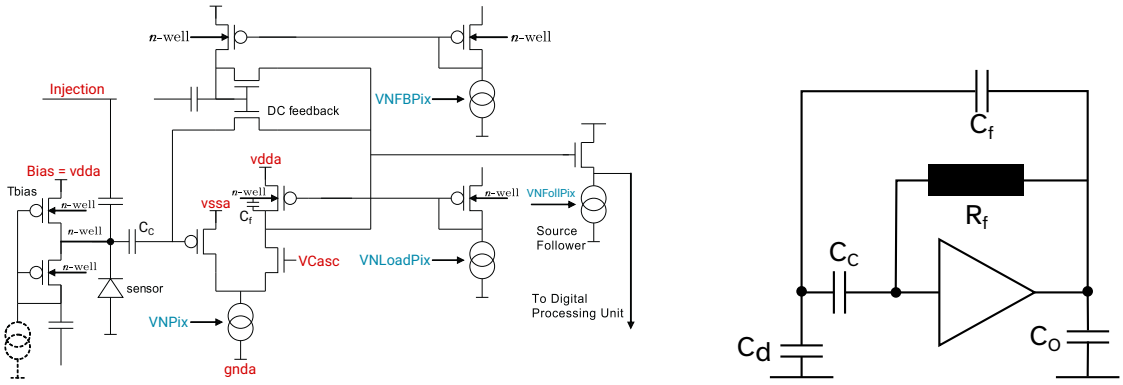

(a) Schematic of the in-pixel electronics of the MuPix10. Red indicated levels are supplied externally and blue indicates important DAC controlled levels. Adapted from [80, p.30, fig. 3.14].

(b) Simplified schematic of the CSA with feedback. Adapted from [90, p. 2493, fig. 3].

Figure 3.10: Schematic views of the in-pixel analog electronics of the MuPix10.

3.3.1 Charge Sensitive Amplifier

The Charge Sensitive Amplifier in MuPix10 is implemented as a folded-cascode gain stage with a PMOS input transistor. This configuration is referred to as a PMOS-amplifier, following the convention of naming by the input transistor type[3].

In a simplified schematic (see Figure 3.10b), the feedback network consists of a "resistive feedback" (R_f), which provides a constant current, and a capacitive feedback (C_f), realized by the drain contact of the PMOS cascode transistor. The constant current feedback results in a linear falling edge of the output signal for signals larger than the thermal voltage $U_T = \frac{k_B T}{q}$. For smaller signals, the feedback resistance becomes proportional to U_T over the feedback current, introducing a non-linearity in the output signal. Both the resistive and capacitive feedback can be adjusted via the DAC *VNFBPix* and *VPLoadPix*, respectively, allowing for tuning of the CSA gain.

The linear amplification range of the CSA is limited; for large input charges, the feedback current saturates and the output voltage may exceed the supply rails, resulting in a saturation of the amplification. While the amplitude is thus confined to the dynamic range of the CSA output, the pulse length is not limited, causing the output pulse shape from a "triangular" to a more "trapezoidal" form.

[3] Other HV-MAPS do not use a so-called PMOS-amplifier, but its NMOS or CMOS version which often only refers to a change of the input transistor.

A detailed discussion of the CSA design can be found in [90]. It provides an approximation for the rise and fall times of the output signal:

$$\tau_{\text{rise}} \approx \frac{C_O \cdot C_d}{C_f \cdot g_m} \quad \text{and} \quad \tau_{\text{fall}} \approx R_f \frac{C_f \cdot C_C}{C_d + C_f + C_C} \tag{3.2}$$

where C_d is the detector capacitance (see Section 3.2.2), C_O is the output capacitance, $C_f \approx 1.6\,\text{fF}$ [90, p. 2493, tab. 2] is the feedback capacitance, g_m is the transconductance and C_C the input stage capacitance of the CSA. This allows the pulse shape in the linear regime of the amplifier (neglected eventual undershoots) to be approximated by a $CR - RC$-shaper, as given in [91, p. 135, eq. 4.3]:

$$U_{\text{pulse}}(t) \approx \frac{Q_{dep}(t)}{C_f} \cdot \frac{\tau_{\text{fall}}}{\tau_{\text{fall}} - \tau_{\text{rise}}} \left[\mathrm{e}^{-\frac{t}{\tau_{\text{fall}}}} - \mathrm{e}^{-\frac{t}{\tau_{\text{rise}}}} \right] \tag{3.3}$$

where $Q_{dep}(t)$ is the charge collected by the pixel diode at time t.

3.4 Routing of Point-to-Point Connections

The signal line routing in MuPix10, which connects each analog pixel cell to its corresponding digital partner cell, is designed with particular attention to crosstalk (Section 3.4.1) identification and suppression. The routing utilizes two metal layers — metal 4 and metal 5 (Figure 3.11) — to accommodate 250 signal lines per pixel column within the 80 µm pixel column pitch. On these two metal layers, signal lines are routed directly above one another, allowing a maximum individual line length of approximately 20 mm in MuPix10.

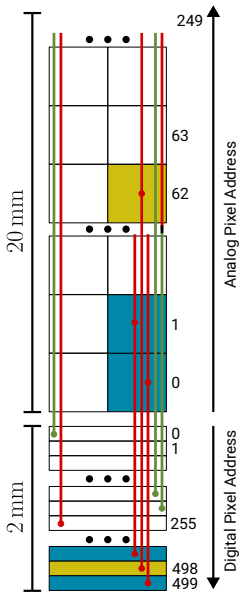

(a) Routing scheme of the MuPix10 of the double column structure.

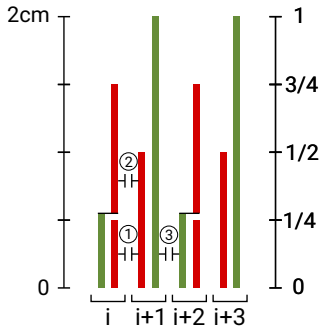

(b) Top view of the signal line routing scheme of the MuPix10.

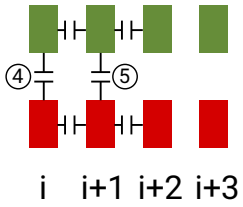

(c) Cross section of the signal line routing scheme of the MuPix10.

Figure 3.11: Schematics of the signal line routing scheme of the MuPix10. The circled numbers indicate the different capacitive coupling domains indicated for cross talk (Section 3.4.1). Metal4 and Metal5 are the two metal layers used for routing the signal lines. Adapted from [92, p. 8, fig. 9a].

For connections to the periphery, an even-odd column pair shares a set of 500 periphery cells (Figure 3.11a), with each digital partner cell spanning the width of two pixels ("double column" structure). Because crosstalk probability increases with the adjacent length of two signal lines, the routing is optimized so that the maximum neighboring length is limited to one-quarter of the maximal line length — about 5 mm for MuPix10. This limit is based on measurements from MuPix8 [93, p. 119, fig.10.9ff], where the critical parallel length for significant crosstalk at a 50 mV threshold is about 4.8 mm [80, p. 89].
The routing scheme for even and odd columns, detailed in Table 3.2, results in a spatial offset of neighboring lines by a sector in the row address, producing a characteristic crosstalk pattern. Further details on the MuPix10 routing scheme are given in [80, p. 89ff].

Sector	Pixel Row Address Range	
	Odd Pixel Column	Even Pixel Column
1	0-59	0-61
2	60-118	62-124
3	119-184	125-186
4	185-249	187-249

Table 3.2: Pixel row address ranges of the 4 sectors of line routing, split for even and odd pixel column addresses. Taken from [80, p. 99, tab. 5.3]

3.4.1 Signal Line Crosstalk

The basic principle behind line crosstalk is that a time-varying voltage across a capacitance induces a current, given by $\mathcal{I} = C \cdot \frac{dU}{dt}$. Neighboring signal lines form a capacitive coupling, as illustrated in Figure 3.11, which can be modeled as a chain of capacitances along the adjacent length of the transmission lines. When a signal pulse propagates along one line, it induces a current in the neighboring lines via this parasitic capacitance (Figure 3.12a).

The component of induced current that flows in the same direction as the primary signal superimposes and forms a smaller, delayed crosstalk pulse — referred to as "far-end" or "forward crosstalk" [80, p. 83]. The component flowing in the opposite direction — "near-end" or "reverse crosstalk" [80, p. 83] — is not relevant in this context, as it does not appear at the readout end and thus cannot be misidentified as a hit.

The magnitude of the crosstalk pulse depends on the amplitude of the primary signal — more precisely the rate at which its voltage rises — and on the parasitic capacitance, which scales with the adjacent length of the signal lines. If large enough, the induced pulse can exceed the detection threshold and be registered as a false hit, as shown in Figure 3.12b.

With the optimized MuPix10 routing (see Section 3.4), the probability of cross talk pulses exceeding the detection threshold is reduced to about 1 % to 10 % (nominally 2 %) [80]. In addition, the fixed "neighbor-offset pattern" (Plot 3.3), together with the fact that crosstalk pulses are typically short and of low amplitude — and therefore have small ToT values — enables efficient identification and removal of residual false hits during data processing. Further information on the signal line crosstalk and its suppression in MuPix10 can be found in [80, p. 78ff].

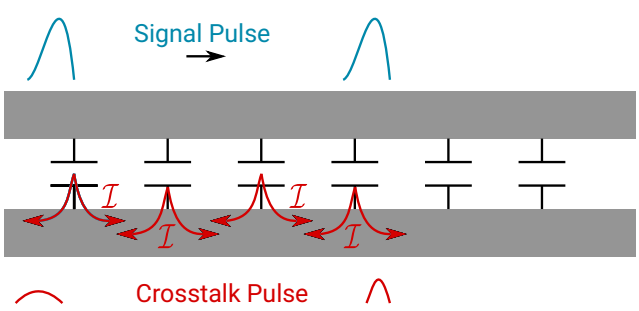

(a) Current injection model. Adapted from [80, p. 83, fig. 5.9].

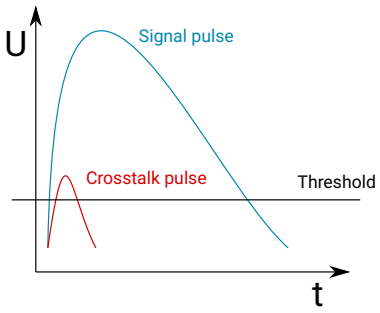

(b) Crosstalk pulse induction in MuPix signal lines. Adapted from [80, p. 77, fig. 5.2].

Figure 3.12: Signal line crosstalk of MuPix10.

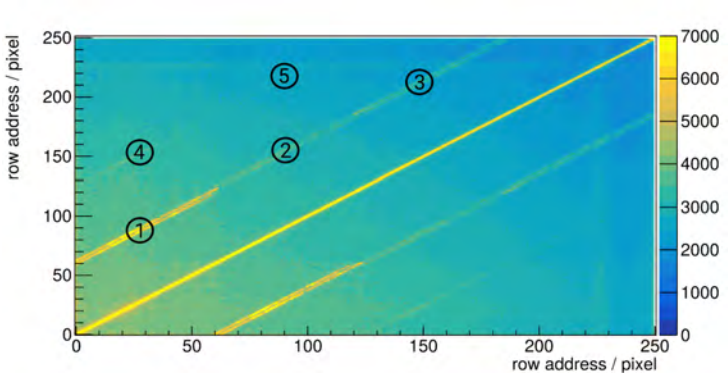

Plot 3.3: Crosstalk in pixel row address self correlation of MuPix10. Off-diagonal elements are enhanced by setting a lower maximum value on the z-axis. Encircled numbers indicate the different capacitive couplings for cross talk according to Figure 3.11. Taken from [92, p. 8, fig. 9b].

3.5 Digital Peripheral Cell

Each analog pixel cell has its own dedicated digital peripheral cell, whose simplified schematic is shown in Figure 3.13. Its main function is to digitize the analog signal transmitted from the pixel cell in the matrix. The signal pulse is filtered by an additional high-pass filter, governed by the *digital* baseline, which couples the analog signal capacitively to the comparators. The baseline can be adjusted using the voltage DAC *BLDig*, whereas the filter characteristics are controlled by *BLResDig*.

The user can select between two operational modes, which determine whether the digitization is performed by one comparator or by two comparators, as set by the DAC *En2thres*. In single-comparator mode, the ToA (**T**ime-**o**f-**A**rrival), the ToT (**T**ime-**o**ver-**T**hreshold) timestamp and hit flag are all generated by *Comp1*, which compares the analog level to the threshold *ThLow*. The 2-comparator mode is designed to mitigate time walk effects: *Comp1* is responsible for the ToA, while *Comp2* (with threshold *ThHigh*) handles the ToT and hit flag. This configuration allows *ThLow* to be set in a noise regime that is less sensitive to time walk, while *ThHigh* can be set higher to suppress fake hits.

If a pixel exhibits a high fake rate due to noise, the comparator threshold can be individually adjusted using a 3 bit tuning DAC, whose absolute range is set by the global defined DAC *VPDAC*. If this adjustment is insufficient, an additional masking bit can be set for each pixel, which prevents its readout by raising the digital cell baseline to the upper digital supply voltage level *VDDD*.

For testing purposes, a so-called *HitBus* feature is implemented as a logical OR for each double column, providing a combined output from all comparators in the double column, with each output driven by its own dedicated driver.

An overview of the DACs in the digital cell is provided in Table A.10. The following sections introduce the timestamp sampling, time walk and the readout delay.

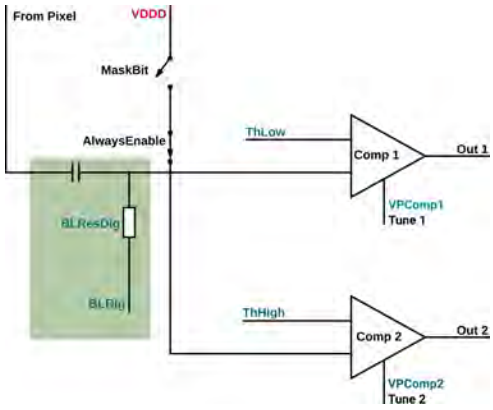

Figure 3.13: Sketch of the digital peripheral cell of the MuPix10. The cell is responsible for the digitization of the analog signal and readout of the pixel hits. Red indicated levels are supplied externally and blue indicates important DAC controlled levels. Adapted from [94, p. 45, fig. 7.4].

3.5.1 Time-of-Arrival & Time-over-Threshold

The logic signal from the comparator is latched by an edge detector, which raises the hit flag for the readout logic. At this moment, the ToA (**T**ime-**o**f-**A**rrival) is sampled — this is the timestamp corresponding to when the rising edge of the analog signal crosses the threshold. The ToA is represented by an 11 bit value, where each LSB (**L**east **S**ignificant **B**it) corresponds to one clock cycle of the externally supplied reference clock (see Section 3.6), which for MuPix10 is typically set to 125 MHz (8 ns per clock cycle).

When the analog signal falls back below the threshold, a second timestamp, *TS2*, is sampled using a 5 bit counter (also in LSB (**L**east **S**ignificant **B**it) units). The ToT can then be calculated as the difference of these two timestamps, representing the duration which the analog signal remains above the threshold (see Figure 3.14) — a measure correlated with the input charge:

$$ToT = TS2 - ToA \tag{3.4}$$

Since the pulse length depends on both the amplifier settings and the input charge, the speed of the timestamp counters can be adjusted using clock dividers (*ckdivend1/2*), which slow down the sampling by a factor of $(1 + ckdivend)$. Typically, the ToA counter runs without division (*ckdivend1* = 0x0), while the ToT counter uses a clock divider of 0xF, resulting in a bin width of 128 ns and a total range of 4096 ns.[4]

Sampling the ToT is particularly important because it provides a measure of the input charge, and thus the energy deposited in the sensor. Since larger pulses cross the threshold earlier than smaller ones, time walk (Plot 3.4) affects the accuracy of the ToA measurement. By sampling the ToT and ToA, and correcting the ToA based on the ToT value, this effect can be mitigated. Accurate ToT sampling is essential, especially in high-rate environments, where delays in the pixel hit readout can occur (see Section 3.5.2).

To further reduce sampling errors and lower power consumption, all timestamp counters are as *Gray encoded* counters. This minimizes the risk of bit errors during sampling transitions and helps optimize the overall power efficiency of the timestamp logic.

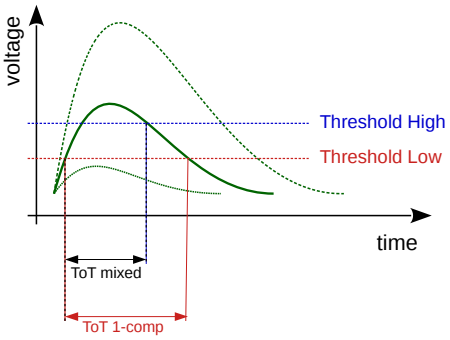

Figure 3.14: Analog pulse digitization by the two comparators to sample ToA and *TS2* to determine the ToT in the MuPix10. Taken from [80, p. 31, fig. 3.17].

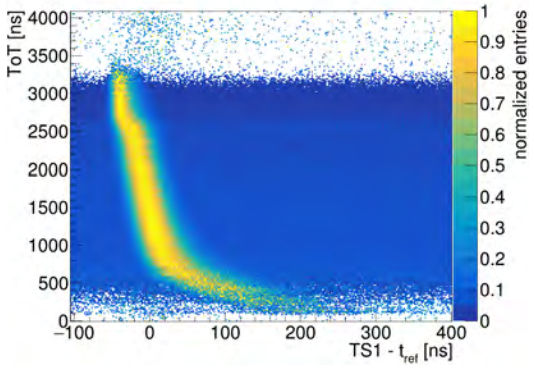

Plot 3.4: Exemplary time walk plot for MuPix10, with *TS1* being the ToA and t_{ref} the timestamp of the reference system. Taken from [80, p. 39, fig. 3.26a].

3.5.2 Readout Delay

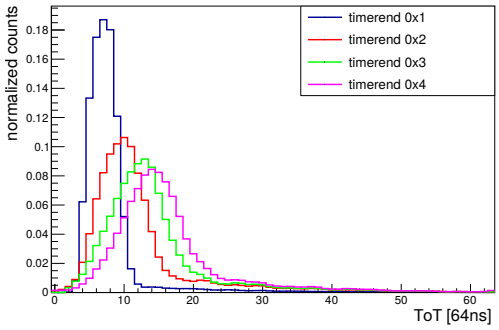

(a) ToT spectra of MuPix8 for Fe-55 depending on the speed of the FSM controlled via *timerend*. Taken from [94, p. 81, fig. 9.3].

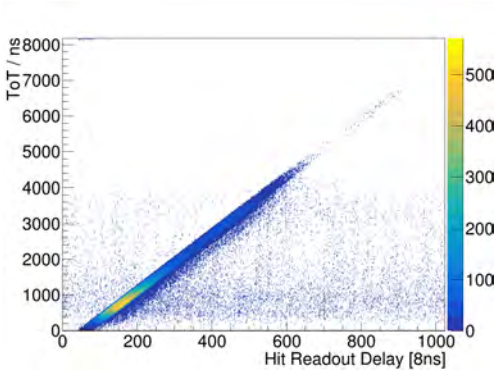

(b) An example of the hit readout delay versus the ToT for ATLASPix3.

Plot 3.5: Examples for the problems of ToT sampling and readout delay in HV-MAPS.

Initial problems with accurate ToT sampling were reported in [94], where the ToT spectra of MuPix8 were measured for Fe-55 as function of the FSM speed (see Section 3.6). In this case, hits were read out before the ToT were

[4] Simplified: To calculate the ToT the ToA is trimmed to the same range as the ToT to handle timestamp lapsing effects.

correctly sampled, as shown in Plot 3.5a. To address this, the readout logic in ATLASPix3 was designed to delay hit readout until the ToT had been sampled. While this ensures correct ToT sampling, it introduces a variable delay in the readout process, as shown in Plot 3.5b. This delay can be corrected at low particle fluxes; however, at higher occupancies, the column drain readout speed becomes insufficient to maintain the correct data chronology.

One possible mitigation is to shorten the analog pulse length by increasing the feedback resistance of the amplifier (see Section 3.3.1). However, this approach can result in signal loss, particularly for low-energy deposits, leading to potential inefficiency and therefore not a viable solution.

In MuPix10, this issue is resolved by introducing a constant delay of the hit readout. This is achieved with a new delay logic, illustrated in Figure 3.15b, which is based on a capacitor charging circuit. When a hit is registered, a current source charges a capacitor, and the increasing voltage is compared to a threshold by a discriminating element. The hit is read out when the threshold is crossed, resulting in a constant delay (to first order). If the analog pulse is longer than the constant delay, the ToT is sampled at the crossing time of the delay circuitry, as shown in Figure 3.15a.

The strength of the current source, and thus the delay, can be adjusted using two DACs (primarily *VPTimerDel*). Plot 3.6 presents the ToT spectra for different delay configurations controlled by *VPTimerDel* for a MuPix10 sensor. The cut-off of larger ToT values in the spectra are not a concern, since time walk is dominated by small, short pulses, which are sampled correctly.

Note that in the rare case where a second hit occurs in the same pixel during the delay period, not only is the second hit not registered, but it also modifies the measured value of the ToT for the first hit. This occurs because the corresponding timestamp (*TS2*) is not write-protected when the second hit arrives, allowing it to be overwritten at the last falling edge threshold crossing within the delay period. Therefore, the delay circuitry settings should be optimized in accordance with the expected particle hit rate, in order to minimize distortions in the ToT measurement and to reduce efficiency losses in hit detection.

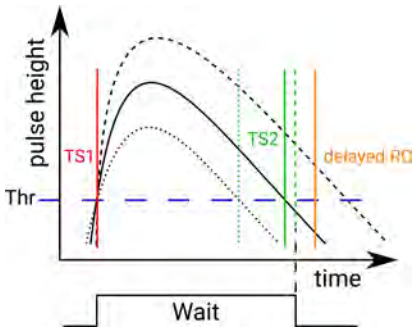

(a) Sketch of constant withholding of the pixel hit readout, after hit recognition. Taken from [92, p. 6, fig. 7a].

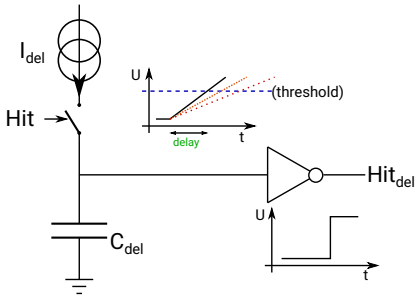

(b) Schematic of the delay circuit logic (reset circuit not shown). Taken from [92, p. 6, fig. 7b].

Figure 3.15: Readout delay logic of MuPix10.

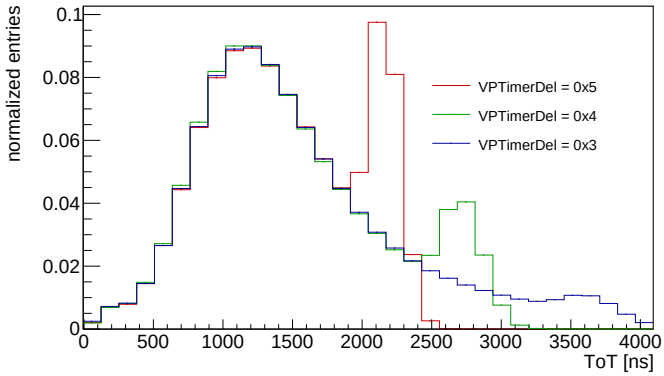

Plot 3.6: ToT spectra for 3 different delay configurations controlled by the DAC *VPTimerDel*. Second peak in spectra correspond to the "delay peak". Taken from [92, p. 7, fig. 8].

3.6 Communication Interface

The communication interfaces of the MuPix10 chip are divided into two main parts: the slow control interface and the readout interface. The slow control interface is responsible for configuring the chip and its pixels, while the readout interface transmits hit data from the chip to the readout system. Both interfaces are essential for the operation of MuPix10 and are briefly introduced in the following sections.

3.6.1 Slow Control

The configuration interface of MuPix10 is based on six parallel linear shift registers, as depicted in Figure 3.16a. Of these, three are dedicated to the global chip configuration, which includes the bias block, steering of the analogue circuits, voltage DACs for baselines and thresholds, and configuration of the digital domain (such as clock control, FSM and readout data links). One register is reserved for the test infrastructure, enabling features such as *Injection*, *HitBus* and *AmpOut* of the pixels. The remaining two registers define the pixel RAM (**R**andom **A**ccess **M**emory). Each pixel contains a 7 bit RAM, divided into 3 bit threshold trimming for each comparator and 1 bit for masking.

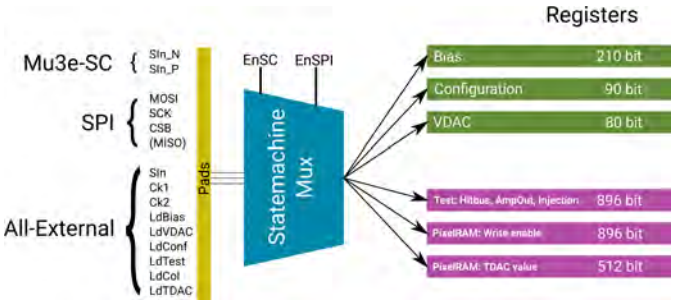

(a) The MuPix10 parallel register structure. Adapted from [80, p. 62, fig. 4.16].

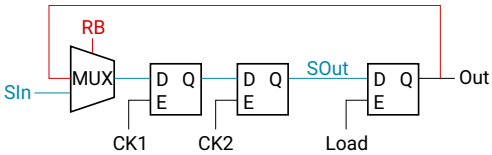

(b) Register cell with 2 gated latches. Shift register path marked in blue and the read back path in red. Adapted from [80, p. 48, fig. 4.2a].

Figure 3.16: The MuPix10 configuration registers interface.

The linear shift registers are custom-designed with a serial-in-parallel-out architecture and are connected to a storage interface. Each register cell consists of a chain of two gated latches, controlled by two independent clock inputs (*ck1* & *ck2*), and a third gated latch that serves as the configurable memory, activated by a *load* signal. Additionally, a read back (*RB*) function is implemented via a 2-to-1 multiplexer, allowing selection between the shift register input and the stored memory value output. This structure forms the basic building block of the configuration interface, as illustrated in Figure 3.16b.

MuPix10 supports three different configuration interfaces, all based on the same register structure. Two interfaces are single-ended: the SPI (**S**erial **P**eripheral **I**nterface) and the so-called *all-external* interface. The third is a custom-designed differential LVDS (**L**ow **V**oltage **D**ifferential **S**ignaling) interface, which is used for the Mu3e slow control [80]. During commissioning, a bug was discovered in the configuration register [80, p. 65 ff., sec. 4.4.4]: the register do not permanently store loaded values unless the *load* signal remains continuously active. This workaround is not feasible for the *all-external* and the Mu3e slow control interfaces, which are designed to apply the load signal only briefly. Only the SPI interface can circumvent this issue, as it allows flexible control of the load signal.

However, this results in a significant limitation on the configuration speed of the MuPix10 chip. Not only being a single-ended nature of the SPI interface cap the speed, but the protocol also introduces substantial overhead in data transmission. Although all registers can be written to in parallel, each bit must to be written multiple times, since for each register, the individual *ck1*, *ck2* and *load* signals must be sent and toggled.

3.6.2 Readout

The readout architecture of MuPix10 assigns each of the three sub-matrices (cf. Section 3.2) its own FSM (**F**inite **S**tate **M**achine) and dedicated data output link, enabling parallel hit processing and increasing overall throughput. In addition, MuPix10 features a fourth output link, which can either mirror one of the sub-matrix data links or output a combined data stream from all three sub-matrices. For simplicity, the multiplexed output is not discussed here, as it operates analogously.

When a hit is registered in a digital periphery cell (see Section 3.5), its signal is sent to an End of Column cell shared by all 500 digital cells of the corresponding "double column" (cf. Section 3.4). A priority encoder reads out hits starting from the lowest digital pixel address and proceeding to higher addresses. Since this encoding scheme does not preserve the chronological order of hits, the correct timing sequence must be reconstructed offline during data analysis. The hit data collected in the EoC cell is then transmitted to the serializing logic, described in detail in [95].

The readout structure is shown exemplarily for one sub-matrix — from FSM to the data output link — in Figure 3.17. The clock generation tree is shared among all FSMs and cannot be adjusted individually. It includes a Phase-Locked Loop that synchronizes the clocks required for the FSMs and the timestamp counters to the external reference clock (nominally $f_{ref} = 125\,\text{MHz}$). The speed of each FSM is determined by the reference clock f_{ref} and the value of the *timerend* parameter, which is set via a DAC:

$$f_{FSM} = \frac{f_{ref}}{2 \cdot (1 + \text{timerend})} \tag{3.5}$$

The nominal FSM transition speed would be set to a frequency of 62.5 MHz, with a 32 bit data word sampled on every second state. A differential current mode logic serializer encodes the data into 8 bit/10 bit format, which is zero-suppressed transmitted via a 1.25 Gbit s^{-1} Low Voltage Differential Signaling link. This configuration theoretically supports a hit data rate of up to 30 MHz per sub-matrix, for a total maximum of 90 MHz across the entire chip. Unfortunately, MuPix10 cannot be operated at full speed due to a timing issue in the digital logic. When the FSM is configured for maximum speed (*timerend* = 0x0), the chip produces incorrect hit addresses. To guarantee correct operation[5] and reliable data output, MuPix10 is therefore run at a reduced FSM speed, using *timerend* = 0x1.

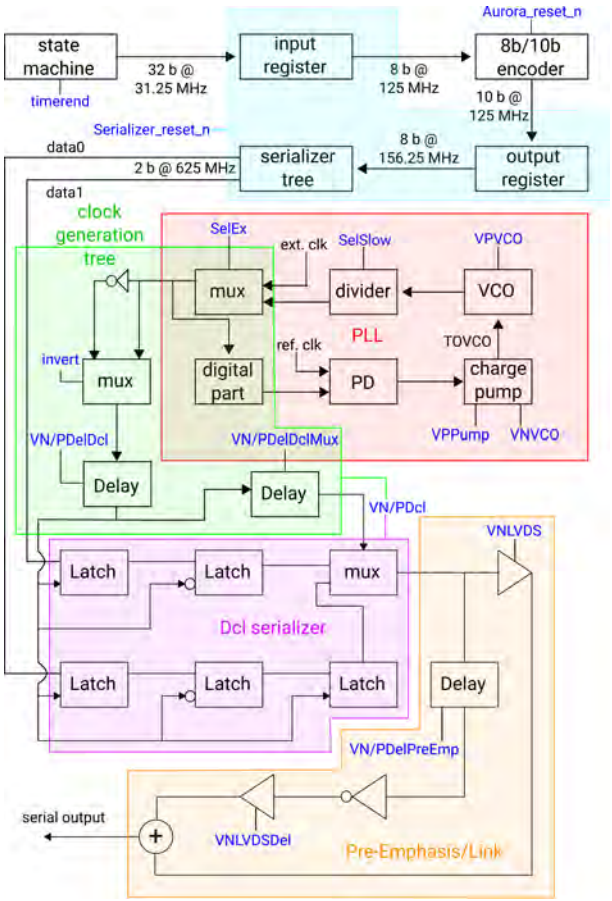

Figure 3.17: Schematic of the Readout scheme. Taken from [96, p. 48, fig. 7.6] (adapted from [95] & [97])

[5] This problem is solved for MuPix11, which operates at full FSM speed.

3.7 Sensor Biasing

To operate the MuPix10 sensor, one high voltage (in reverse bias mode) and several low voltage levels are required. The high voltage is used to reverse bias the sensor diode, while the low voltage supplies power both the digital and analog domains of the sensor. In total, five distinct low voltage levels are present: two for the digital (*gndd*) and analog (*gnda*) grounds, one for the digital suply (*vddd*), one for the analog supply (*vdda*), and one adjustable voltage level for the amplifier (*vssa*). The latter is typically generated on-chip via a linear series regulator (see Section 3.7.1), routed out of the sensor, and then fed back in. The high voltage level is supplied relative to the *n*-well bias, which is approximately at *vdda* level.

To further reduce the number of required supply voltages, the digital and analog grounds (*gndd* & *gnda*) are electrically shorted, as are the digital and analog supply voltages (*vddd* & *vdda*). These shorted levels are referred to as GND and VDD, respectively. This simplification is possible because the chip operates at the same supply voltage levels in both the digital and the analog domains, with an on-chip voltage of about 1.8 V. Due to voltage drops across cables and on-chip resistances in the powering network, the externally supplied voltage is always set higher than the actual on-chip voltages (see Section 3.7.2).
In the following, a brief introduction to the sensor powering scheme and strategy is given.

3.7.1 VSSA Regulator

The *vssa* regulator on the MuPix10 is implemented as a linear series regulator (see Figure 3.18). It employs a differential amplifier to adjust its output level relative to the *gnda* level. An on-chip DAC, called *vss_ref*, controls the reference level of the regulator and can be adjusted from 0 V to 1.4 V. Although the regulator can be configured to various voltage levels, it essentially acts acts as a self-adjusting voltage divider, enabling the use of a single low voltage supply for sensor operation.

Plot 3.7 illustrates the regulator's functionality, showing the output voltage as a function of *vss_ref*. At voltages below approximately 0.6 V, the amplifier supply is insufficient, resulting in a constantly "low" supply current. The point at which current begins to rise marks the "turn-on" threshold of the amplifier, occurring at around 0.6 V. The current increase plateaus at about 1 V, which defines the lower boundary of the nominal working range for the CSA. The regulator's upper output limit is reached at approximately 1.4 V, with the nominal working point being around 1.2 V for high-gain operation and about 1.0 V for low-gain settings (see Section 5.1.1).

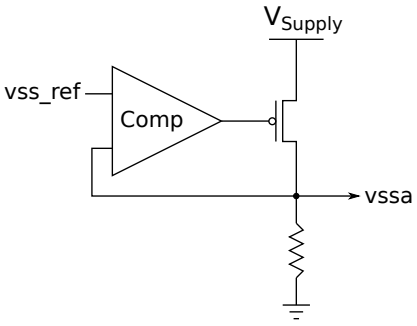

Figure 3.18: Functional sketch of the linear series regulator for *vssa*, controlled via the reference level *vss_ref*. Taken from [92].

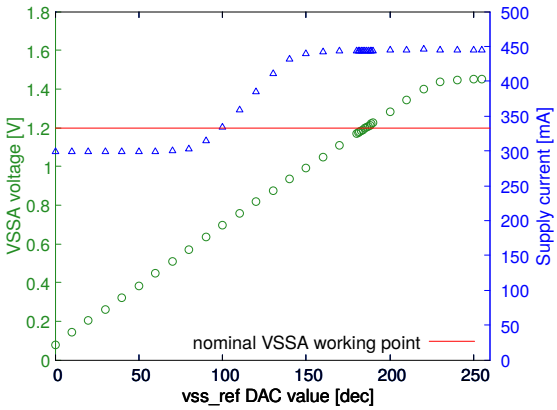

Plot 3.7: *vssa* voltage (circle) and supply current (triangle) plotted for a scan of the regulator reference voltage (vss_ref). Taken from [92].

3.7.2 Voltage Drops & Test Points

It has been observed that the combination of the number of bond pads allocated for the sensor powering and a non-optimal power grid layout (see Figure 3.19a) leads to non-negligible voltage drops in the low voltage supplies of the MuPix10 sensor. This issue is easily traceable thanks to a feature of the MuPix10 sensor known as *TestOut* (see Figure 3.19b). A DAC-configurable multiplexer allows selection of various test points, including the voltage

levels of the digital and analog domains at two different positions on the sensor. Each selected test point is routed through the multiplexer to a dedicated bond pad, which can then be probed with a multimeter or an oscilloscope for debugging purposes.

The magnitude of the voltage drop (see Figure 3.19c) depends on the sensor's power consumption, which varies with different operating settings. Significant voltage drops must be compensated by increasing the supply voltage. For the settings used in the context of this thesis (see Section 5.1.1), the voltage drops are optimized for the analog domain, as it is the dominant power consumer of the sensor. Measured value are listed in Table A.12.

Because the voltage drop is not uniform between high and low levels, and since the analog and digital supply voltages are electrically connected (see Section 3.7), a voltage offset occurs between *vdda* and *vddd*, with *vddd* typically being higher. As all on-chip DACs use *vdda* as their reference, the *vddd* settings are adjusted accordingly.

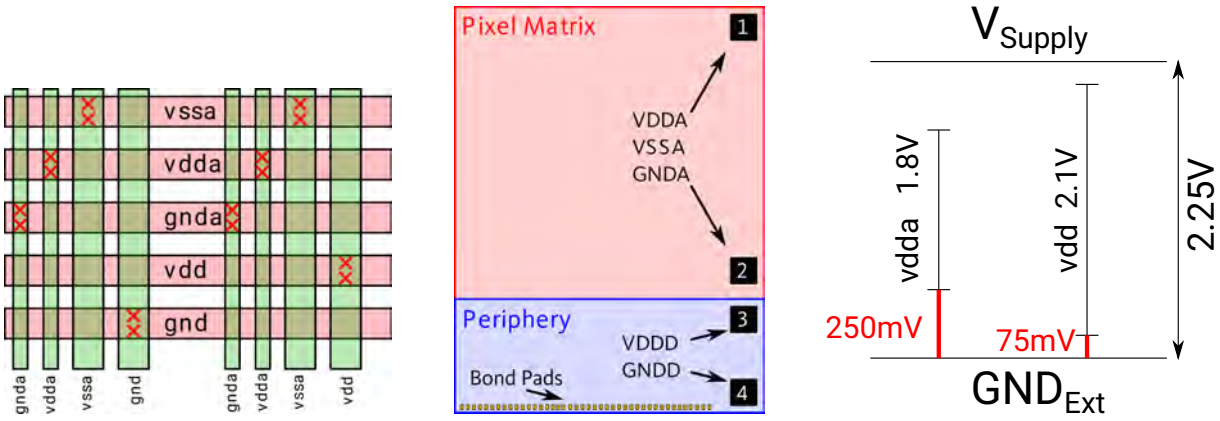

(a) Sketch of the MuPix10 power distribution network. The red crosses mark the connection from the lines coming from the bond bads to the power grid.

(b) Sketch of the MuPix10 *TestOut* points.

(c) Sketch of voltage drops observed in MuPix10.

Figure 3.19: The MuPix10 power distribution network and the observed voltage drops.

4. From Particle to Measurement

In Chapter 1, a general introduction to particle interactions with matter was provided. While the measures presented for the energy loss of charged particles are adequate to explain the basic concepts, they are insufficient to describe the actual *energy deposition spectrum* in silicon sensors. This is particularly true for thin absorbers, where the mean value is an unsuitable descriptor due to the underlying PDF (Probability Density Function) being highly skewed[1], and the most probable energy loss value (mode) is more representative of the typical energy loss in these materials.

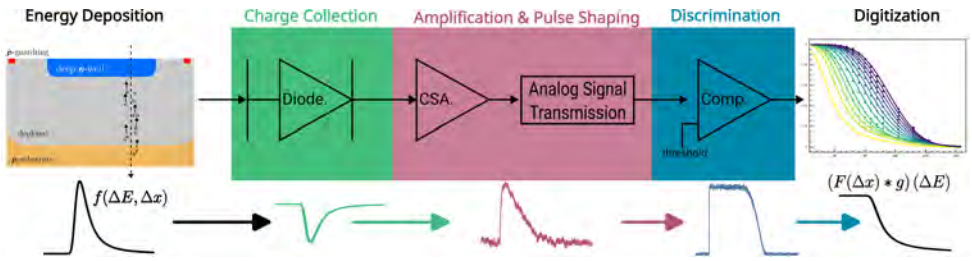

Figure 4.1: Sketch of the charge processing flow in the MuPix10 detector. Charge deposition $f(\Delta E, \Delta x)$ and collection in the sensor diode (green) are followed by amplification in the in-pixel CSA (red), transfer to the digital cell, and discrimination at a defined threshold (blue). Scanning the threshold yields the integrated deposition statistic convoluted with all detector effects.

First, it is important to distinguish between the *energy loss spectrum* and the *energy deposition spectrum*. Not all energy loss events contribute to the *energy deposition spectrum* of a detector. In thin absorbers, for example, δ-electrons (cf. Section 1.1.3) and bremsstrahlung (cf. Section 1.1.4) contribute to *energy loss spectrum*; however, since both can escape the detector without depositing charge, they have little impact on the *energy deposition spectrum*. For δ-electrons, this effect is especially pronounced in the high-energy tail of the distribution, where the escape of these particles without full absorption can lead to increased statistical fluctuations. The underlying energy deposition PDFs forms the basis for modeling the charge collection.

Starting from the *energy deposition spectrum*, the complete charge processing chain — illustrated in Figure 4.1 — consists of the following steps: The deposited charge in the detection volume of the sensor is collected by the electrodes. Already at this stage, the initial charge spectrum is influenced by noise, arising from thermal excitation of charge carriers in the silicon-lattice, and charge collection inefficiencies, such as charge sharing between neighboring pixels. Following the charge collection process, the signal undergoes amplification by the CSA (cf. Section 3.3.1) and transmission to the digital partner cell (cf. Section 3.5). The limited dynamic range of the CSA introduces a non-linearity between the deposited charge and the measured charge, while the transfer to the digital cell imposes additional shaping of the signal (as incorporated in the CSA model). Furthermore, potential signal losses can occur due to AC coupling of the signal pulse, which may cause crosstalk between signal lines (cf. Section 3.4.1). Finally, the signal is compared to a threshold by a discriminator, which introduces an additional smearing of the *charge collection spectrum*, arising from the dispersion of the applied threshold (in relation to its baseline).

All noise and smearing contributions are assumed to combine into the measured *charge collection spectrum* in a Gaussian manner. According to the associative property[2] of convolution ($*$):

[1] The difference between the average and most probable energy loss is discussed in more detail by [98, 99].
[2] This can be shown with "Fubini's theorem", which states that a double integral can be calculated using iterated integrals in any order.

$$f * (g * h) = (f * g) * h \tag{4.1}$$

each new source of dispersion in the initial *energy deposition spectrum* can be combined with existing smearing effects through convolution. When two independent variables, both following normal distributions, are convolved, the result is also a normal distribution with the variance equal to the sum of the individual variances [100, p. 4, eq. 26 & 27]:

$$\sigma_{f*g}^2 = \sigma_f^2 + \sigma_g^2 \tag{4.2}$$

In this work, the *charge collection spectrum* is not measured directly (e.g. ToT spectrum), but rather through the CCE (**C**harge **C**ollection **E**fficiency), an integration over the underlying PDF — the (complementary) Cumulative Distribution Function. This is achieved by performing a threshold scan: varying the charge detection threshold and measuring the number of events exceeding the threshold as a ratio of the total number of events. Such scans are typically performed during testbeam campaigns, where the detector is exposed to a known particle flux and the CCE is measured as a function of the threshold for tracked particles.

To quantitatively relate the measured detector response under varying charge detection thresholds to the underlying physical processes, it is useful to invoke the integration-convolution identity, which connects integrals of convolutions with convolutions of integrals, expressed as:

$$\int_t^\infty (f * g)(t')\,\mathrm{d}t' = (F * g)(t) = (f * G)(t) \quad \text{for} \quad F(t) = \int_t^\infty f(t')\,\mathrm{d}t', \quad G(t) = \int_t^\infty g(t')\,\mathrm{d}t' \tag{4.3}$$

As in the case of CDFs, this identity means that the integral of the convolution of two functions equals the convolution of the first function with the integral of the second function, or vice versa[3].

All the previous steps combined demonstrate that the measured *charge collection spectrum* is different from the initial *energy deposition spectrum* within the detector, which itself differs from the *energy loss spectrum* in the material. In the following, a detailed introduction to the *energy deposition spectrum* and its impact on the *charge collection spectrum* is provided. This will be followed by a general introduction to the collection and transport of charge in **si**licon detectors, and their dispersion mechanisms.

4.1 Energy Deposition and Fluctuation for Charged Particles

When a charged particle traverses a medium, the energy loss (even for identical particles under equivalent conditions) is not uniform. Significant statistical fluctuations arise from the random atomic interactions between the particle and the medium. As a result, after passing through the medium, the particles emerge with a range of energies, forming a *distribution of energy losses*. The shape of this distribution is determined primarily by the number of collisions and the relevant cross sections of the particle with the medium.

The probability that a charged particle loses energy between E and $E + \mathrm{d}E$ in a single collision is given by the corresponding normalized differential cross section[4] (see Figure 4.2a) [15, p. 28]:

$$f^{(1)}(E) = \frac{\omega(E)}{\mathcal{M}_0'} \quad \textit{with} \quad \omega(E) = n_e \cdot \frac{\mathrm{d}\sigma}{\mathrm{d}\mathcal{T}} \tag{4.4}$$

where n_e is the electron density, and $\mathcal{M}_0' = \mathcal{M}_0/\Delta x$ is the mean number of collisions per unit path length[5] (cf. Equation 1.1). The probability distribution of the total energy loss ΔE after n independent collisions is given by the n-fold convolution of the single-collision probability (see Figure 4.2b) [15, p. 28]:

$$f^{(n)}(\Delta E) = \underbrace{(f^{(1)} * f^{(1)} * \ldots * f^{(1)})}_{\text{n times}}(\Delta E) = \int f^{(n-1)}(\Delta E - E) \cdot f^{(1)}(E)\,\mathrm{d}E \tag{4.5}$$

In this formulation, the initial energy-loss distribution is assumed to be a Dirac delta function, $f^{(0)}(E) = \delta(E)$, implying that all particles start with the same initial energy.

[3] This follows from the associative property of convolution (cf. Equation 4.1). Likewise, the differentiation-convolution identity states that the derivative of a convolution equals the convolution of either function with the derivative of the other.

[4] For consistency with the cited sources, energy (E) and kinetic energy ($\mathcal{T}$) are used synonymously, as they differ only by the rest mass.

[5] When comparing the zeroth moment from [15, p. 6, eq. 2.1], as used in [15, p. 28], with Equation 1.1, note that the former is normalized to unit length.

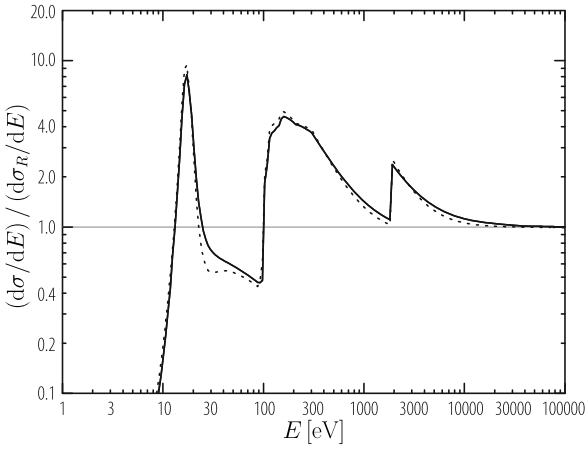

(a) Differential cross section $\mathrm{d}\sigma/\mathrm{d}E$, normalized by the *Rutherford cross section* $\mathrm{d}\sigma_R/\mathrm{d}E$, for particles with $\beta\gamma$ = 4 in silicon, as function of the energy loss E in a single collision. The solid line is obtained from the *Bethe-Fano method* ([101, p. 675, fig. 9], cf. [15, p. 16ff]), and the dashed line from the *Fermi Virtual-Photon (FVP) method* (cf. [15, p.18ff]). Adapted from [15, p. 19, fig. 2.6].

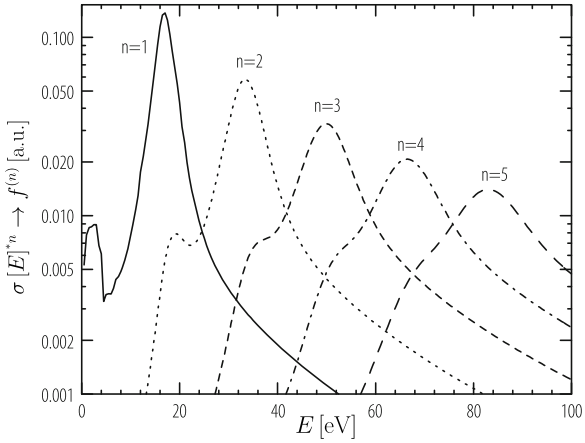

(b) Distributions $f^{(n)}$ of the energy loss in n collisions in silicon. The plasmon peak shifts in each spectrum by $n \cdot 17\,\mathrm{eV}$, whereas the lower structure appearing at $2 + (n-1) \cdot 17\,\mathrm{eV}$ diminishes with increasing n. For $n = 6$ (not shown) the plasmon peak merges with the L-shell energy loss at 100 eV. Adapted from [15, p. 29, fig. 2.10].

Figure 4.2: Differential cross section and n-fold probability distribution of energy loss in silicon.

The PDF for a particle to lose the total energy ΔE in traversing a thickness Δx is then given by the straggling function [15, p. 28, eq. 2.35]:

$$f(\Delta E \mid \Delta x) = \sum_{n=0}^{\infty} \mathrm{PDF}_{\mathrm{poisson}}(n \mid \mathcal{M}_0) \cdot f^{(n)}(\Delta E) \tag{4.6}$$

where $\mathrm{PDF}_{\mathrm{poisson}}(n \mid \Delta x)$ is the Poisson distribution (see Equation 1.2) of n collisions given an average $\mathcal{M}_0$.

The unknown straggling function denoted by $f(\Delta E \mid \Delta x)$ is the probability density to lose energy ΔE in a medium of given thickness Δx, and must fulfill the normalization condition [17, p. 41, eq. 3.52]:

$$1 = \int_{\Delta E_{min}}^{\Delta E_{max}} f(\Delta E \mid \Delta x)\,\mathrm{d}\Delta E \tag{4.7}$$

Several methods can be applied to evaluate $f(\Delta E \mid \Delta x)$, including direct numerical integrations, integral (Laplace) transforms (cf. [15, p. 31 ff., sec. 2.5.3]) or stochastic methods.

Originally, the PDF was derived from the kinetic (Boltzmann-like) transport equation by Landau [102, p. 417, eq. 1] (derivation from Equation 4.6 presented in Section A.3.1):

$$\frac{\partial f(\Delta E \mid \Delta x)}{\partial \Delta x} = \int_0^{\Delta E_{max}} \omega(E)\,[f(\Delta E - E \mid \Delta x) - f(\Delta E \mid \Delta x)]\,\mathrm{d}E \tag{4.8}$$

where $\omega(E)$ is the cross section for a collision (cf. Equation 4.4) over an energy interval up to ΔE_{max}. The left-hand side gives the evolution with respect to thickness Δx of the probability density for having lost energy ΔE. The right-hand side accounts for the gain and loss of probability density in this interval due to collisions with energy transfer E: particles can enter the ΔE interval (by suffering a collision with energy loss E) and can also leave it by losing more energy in subsequent collisions.

From the solution of Equation 4.8, one obtains the most probable energy loss (for $M > m_e$)[6] for a particle traversing thickness Δx [101, p. 695, eq. E1, 14, p. 570, eq. 34.13]:

$$\Delta E_{\mathrm{MPV}} = \xi \cdot \left[\ln\left(\frac{2m_e c^2 \beta^2 \gamma^2 \xi}{I^2}\right) + j - \beta^2 - \delta(\beta\gamma)\right] \quad \xrightarrow{\beta\gamma \gtrsim 100} \quad \xi \cdot \left[\ln\left(\frac{2m_e c^2 \xi}{(\hbar w_p)^2}\right) + j\right] \tag{4.9}$$

[6] For most cases Equation 4.9 is sufficient to use to determine ΔE_{MPV}. The influence due to the change in cross section for electrons and positrons is briefly discussed in Section 4.1.4 (cf. [103, 104] and erratum [105]).

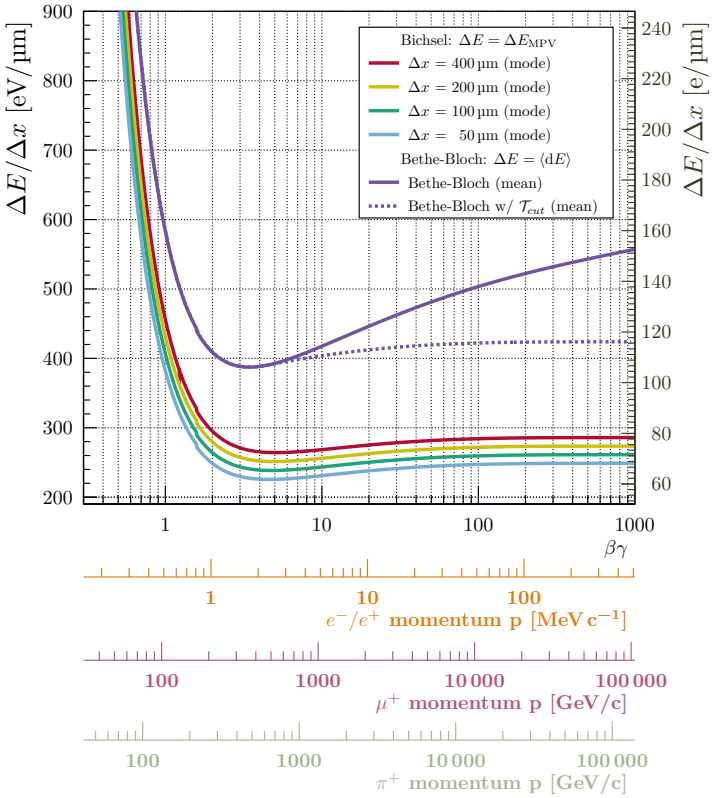

Plot 4.1: Most probable energy loss ΔE_{MPV} normalized by the absorber thickness Δx as function of $\beta\gamma$ in silicon for differing absorber thicknesses. Calculations based on Equation 4.9 with values taken from Tables A.16 and A.17.

where $\xi(\Delta x, \beta)$ is defined by Equation 1.9, I is the mean excitation energy, $\delta(\beta\gamma)$ is the density correction defined in Equation 1.10, and $j = 0.200$ is a constant[7] [101, p. 695]. In the high energy limit ($\beta\gamma \gtrsim 100$), the expressions simplifies according to Equation 1.10 and the plasma energy $\hbar\omega_p$ of the medium becomes relevant. The course of ΔE_{MPV}, illustrated in Plot 4.1, demonstrates the typical behavior of a charged particle traversing matter as described by Bethe-Bloch in Section 1.1.1; however, it does not rise as steeply at high energy, saturating due to the cut-off limit of $\xi(\Delta x, \beta)$ — which is proportional to $\Delta x/\beta^2$ — similar to the Bethe-Bloch formula with a cut-off scale Equation 1.12.
The peak position (mode) described by ΔE_{MPV} is determined by frequent *soft collisions* ($\Delta E \ll \xi(\Delta x, \beta)$) and *intermediate collisions* ($\Delta E \sim \xi(\Delta x, \beta)$), whereas *hard collisions* ($\Delta E \gg \xi(\Delta x, \beta)$) are rare and do not contribute significantly to the mode. Therefore, the maximal energy transfer $\mathcal{T}_{max}$ is of insignificant consideration for the most probable value. The expected form takes on a Gaussian like shape around the ΔE_{MPV} caused by the *soft collisions* with a long tail towards higher energy losses due to *hard collisions*. However, both contributions are dominantly influenced by the *intermediate collisions*, overall governing the shape. The form is directly influenced by the number of possible collisions which directly scales with the thickness Δx. For many collisions, the distribution approaches a Gaussian shape, while for few collisions, it becomes more and more skewed. [103, p. 40ff]

Consequently, various approaches exist for the energy loss PDF, each valid in different parameter regimes. Vavilov characterized their domains of applicability by introducing the dimensionless parameter κ, a measure for the ratio of the mean energy loss to the maximum possible energy loss[8] (see Equation 1.3):

$$\kappa = \frac{\xi(\Delta x, \beta)}{\mathcal{T}_{max}} \tag{4.10}$$

[7] The value for j changed over time as reported in [101, p. 695] (cf. [106, p. 165, eq. 4], [107, p. 194, eq. 24], or [108, p. 698, eq. 45]). However, the value of Equation 4.9 is not sensitive to it.
[8] Note Equation 4.10 is not the ratio of the mean energy loss over the maximum possible energy loss itself.

where $\mathcal{T}_{max}$ is the maximum energy loss in a single collision (see Equation 1.3). The regimes in which the respective model is applicable are not sharply defined and overlap at the boundaries, but can be approximated as follows [109, p.750ff]:

$\boldsymbol{\kappa \gg 1}$:	$f(\Delta E \mid \Delta x)$ takes on a symmetric shape, which can be expressed by a Gaussian distribution with variance $\sigma^2 = \xi \cdot \mathcal{T}_{max}\left(1 - \frac{\beta^2}{2}\right)$ [17, p.45, eq. 3.61].
$\boldsymbol{0.01 \lesssim \kappa \lesssim 1}$:	$f(\Delta E \mid \Delta x)$ is increasingly asymmetric with decreasing κ and is best to be described by the Vavilov distribution (see Section 4.1.3)
$\boldsymbol{\kappa \lesssim 0.01}$:	$f(\Delta E \mid \Delta x)$ is highly asymmetric and takes on the form of the Landau distribution (see Section 4.1.1)

The choice of the respective model is therefore determined by the value of κ. Exemplary calculations for κ shown in Plot 4.2, illustrate the transition between the Landau and Vavilov regimes for different particles in silicon.

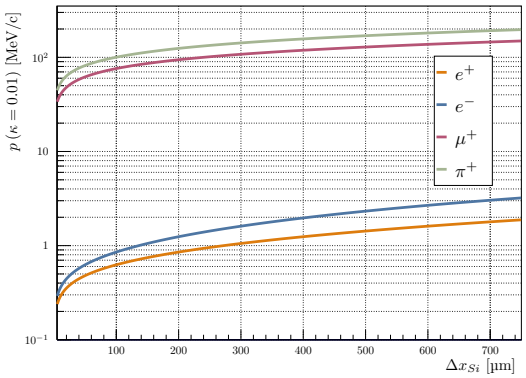

(a) Calculation of p for κ = 0.01 (transition from Landau to Vavilov) as function of Δx in silicon.

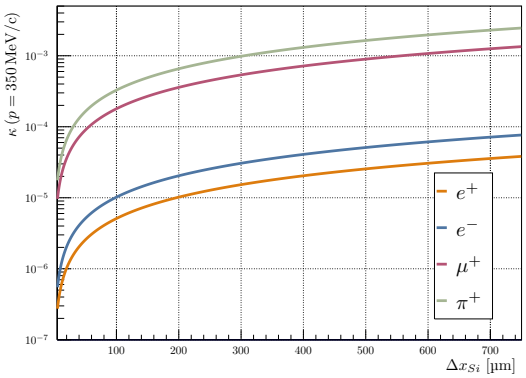

(b) Calculation of κ at p=350 MeV c^{-1} as function of Δx in silicon.

Plot 4.2: Calculation of the transition points between the Landau and Vavilov distributions for p and κ as a function of the Δx in silicon for electrons, positrons, anti-muons, and pion-plus. Calculations based on Equation 4.10 with values taken from Tables A.16 and A.17.

4.1.1 Landau's Free Electron Approach

In order to derive the *straggling function* $f(\Delta E \mid \Delta x)$ from Equation 4.8, Landau made several assumptions that facilitate the derivation but come with important implications (cf. [108, 110]).

First, the absorber is assumed to be thin, i.e., its thickness Δx is much less than the characteristic range R of the particle ($R \gg \Delta x$). In such a thin target, the incident particle typically undergoes on average only one *hard collision* with an atomic electron, making the ionization losses small compared to the particle's initial energy. Consequently, the decrease of the incident particle's velocity can be neglected, and $\omega(E)$ becomes independent of the initial energy of the particle.

Second, in analyzing these *hard collisions* — interactions that transfer energies far greater than the atomic binding energies — Landau assumed that the atomic electrons can be treated as *quasi-free*. In this regime, binding effects are negligible and the electrons behave effectively as free particles. This allows the use of the classical "Thomson formula" for Rutherford's differential cross section in a Coulomb field [108, p. 687], expressed as $\omega(E) = \frac{\xi}{\Delta x} \cdot \frac{1}{\mathcal{T}^2}$.

Finally, two additional conditions are imposed to simplify the derivation: (1) the differential cross section $\omega(E)$ is zero for energy transfers E exceeding the particle's initial energy, and (2) the energy transfers distribution $f(\Delta E \mid \Delta x)$ vanishes for negative energy transfers ($\Delta E < 0$). These conditions permit the upper limit of the integral in Equation 4.8 to be extended to infinity, a step that facilitates the use of the Laplace transformation for

solving the equation analytically. Additionally, a non-zero minimum energy transfer — corresponding roughly to the atomic electron binding energy (cf. Section A.6) — is introduced to exclude unrealistically low energy transfers. The solution of Equation 4.8 in its original form is given by Landau [102, p. 420-423, eq. 12 & eq. 24]:

$$f_L(\Delta E \mid \Delta x) = \frac{\phi_L(\lambda_L)}{\xi} \quad \text{with} \quad \phi_L(\lambda_L) = \frac{1}{\pi}\int_0^\infty \mathrm{e}^{-u\cdot\ln(u)-\lambda_L\cdot u}\cdot\sin(\pi u)\,\mathrm{d}u \tag{4.11}$$

where $\xi(\Delta x, \beta)$ serves as normalization factor, $\phi(\lambda_L)$ is the real form of the Landau distribution, $u = \xi(\Delta x, \beta)\cdot p$, and λ_L is a dimensionless parameter (often referred to as *Landau-parameterization*) given by:

$$\lambda_L = \frac{\Delta E - \Delta E_{\text{MPV}}}{\xi} - 0.222782... \tag{4.12}$$

The thickness Δx enters the distribution only indirectly, via the most probable energy loss ΔE_{MPV} and $\xi(\Delta x, \beta)$, which are defined by Equation 4.9 and Equation 1.9, respectively.

The Landau distribution is highly skewed, exhibiting a long tail toward higher energy losses (see Plot 4.3a), a direct consequence of its underlying assumptions, which allow for energy transfers up to an *unphysical* infinite limit with non-zero probability. Therefore, its mean, variance, and all higher moments of the distribution are undefined (cf. [111, 292.ff]). The mode of the distribution shifts with increasing thickness Δx in a "$x\cdot(a\cdot\ln(x)+b)$"-like manner, whereas the width scales approximately linear with Δx (see Plot 4.3b, cf. Equation 4.9). When normalized by Δx, the mode still shifts towards higher values, reflecting the logarithmic dependence of ΔE_{MPV} on $\xi(\Delta x, \beta)$. An approximation for the FWHM of the Landau distribution is given by [17, p. 42]:

$$W_L \approx 4.018\cdot\xi \tag{4.13}$$

These properties may imply that the Landau distribution does not strictly satisfy Equation 4.7; however, it has been shown by [112] that it is indeed a valid PDF, and thus can be parameterized as:

$$\text{PDF}_{Landau}(\Delta E \mid \Delta E_{\text{MPV}}, \xi) = \frac{\phi_L(\lambda_L)}{\xi(\Delta x, \beta)} = \frac{\phi_L(\Delta E \mid \Delta E_{\text{MPV}}, \xi)}{\xi(\Delta x, \beta)} \tag{4.14}$$

Accordingly, the corresponding (complementary) CDF is given by the upper and lower tail integrations of the PDF from the respective infinite limit to the energy loss ΔE. More information on the Landau distribution, its properties, and its applications can be found in Section A.3.2.

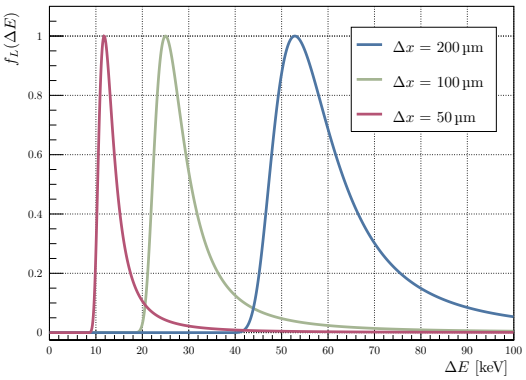

(a) The Landau distribution normalized to 1 for different Δx as function of the energy loss ΔE.

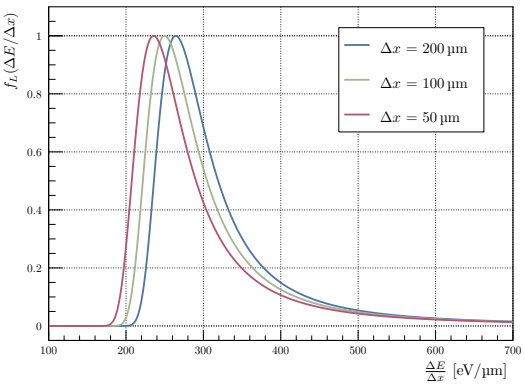

(b) The Landau distribution normalized to 1 for different Δx as function of the $\Delta E/\Delta x$. It shows that the width of the "pure" Landau distribution is independent of the Δx and does not describe the straggling behavior in thin materials (cf. Section 4.1.4).

Plot 4.3: Calculated Landau distributions in silicon for a π^+ with a momentum of 350 MeV c^{-1}. Calculation based on Equation 4.14 taken Equation 4.9 and Equation 1.9 to determine the ΔE_{MPV} and $\xi(\Delta x, \beta)$, respectively. Corresponding data presented in Tables A.16 and A.17.

4.1.2 Moyal's Approximation of the Landau Distribution

Landau's distribution, introduced in Section 4.1.1, may be a correct theoretical approach for energy loss fluctuations, but it lacks a closed-form expression suitable for practical applications. Employing a model with an analytical solution would eliminate the need for numerical integrations or approximation methods, which are often computationally expensive.

Moyal proposed an approximation of the Landau distribution [113], which is also a *heavy-tailed* distribution, though with a tail that falls off more steeply and is therefore less *fat-tailed* than Landau's distribution (see Plot 4.4a). To obtain a closed-form expression, Moyal applied mathematical approximations — most notably the saddle-point method — to simplify the integral equations in Landau's original implicit formulation. This procedure yielded an explicit probability density function, known as the Moyal distribution, which effectively approximates the Landau distribution while being more analytically manageable. According to Moyal's statement: "Surprisingly, no appreciable departure is found from Landau's distribution for $[\mathcal{M}_0] \geq$20;..." [113, p. 269].
The Moyal distribution[9] introduced in [113, p. 271, eq. 5.8], can be generalized to the form [114, p. 91-93]:

$$\text{PDF}_{\text{Moyal}}(E \mid \Delta E_{\text{MPV}}, \xi) = \frac{1}{\sqrt{2\pi}\xi} \cdot \mathrm{e}^{-\frac{1}{2}\left[\frac{E-\Delta E_{\text{MPV}}}{\xi} + \mathrm{e}^{-\frac{E-\Delta E_{\text{MPV}}}{\xi}}\right]} \tag{4.15}$$

where ΔE_{MPV} is the most probable energy loss and $\xi(\Delta x, \beta)$ is the scale parameter of the Moyal distribution. From this the FWHM of the distribution can simply be calculated as:

$$W_M \approx 3.591 \cdot \xi \tag{4.16}$$

which directly shows that the expected form of the Moyal distribution is more narrow than the Landau distribution (cf. Equation 4.13).

In contrast to the Landau distribution, the Moyal distribution also offers a closed form of the (complementary) CDF, which is given by [114, p. 93]:

$$\text{CDF\_C}_{\text{Moyal}}(E \mid \Delta E_{\text{MPV}}, \xi) = \int_x^{\infty} \text{PDF}_{\text{Moyal}}(E' \mid \Delta E_{\text{MPV}}, \xi)\, \mathrm{d}E' = 1 - \text{Q}_{\text{upper}}\left(\frac{1}{2}, \frac{\mathrm{e}^{-\frac{E-\Delta E_{\text{MPV}}}{\xi}}}{2}\right) \tag{4.17}$$

where Q_{upper} is the regularized upper incomplete gamma functions (see Equation A.18).

The presented Moyal distribution may be an useful approximation in cases where the computational cost is of higher concern, then the resolution, which is affected by rare large energy transfer outlier events causing the fatter tail of the Landau distribution.
For more general information on the Moyal distribution, its properties and usage, see Section A.3.3.

4.1.3 Electron Spin and Limits by Vavilov

The Vavilov distribution is regarded as the generalization of the Landau distribution (cf. Section 4.1.1). In contrast to Landau's model, the Vavilov distribution is valid for a wider range of parameters and is not restricted to *thin absorber* approximation. The modification introduced relative to the Landau distribution includes the consideration of the electron's spin and the maximum energy loss in a single collision, denoted by $\mathcal{T}_{max}$ (see Equation 1.3), which is infinite for the Landau formulation. The electron's spin is incorporated into the cross section by substituting the Rutherford cross section for the Mott cross section, yielding $\omega(E) = \frac{\xi}{\Delta x}\frac{1}{\mathcal{T}^2}\left[1 - \beta^2\frac{\mathcal{T}}{\mathcal{T}_{max}}\right]$ (cf. [17, p. 28, eq. 3.17]).
The Vavilov distribution is defined in [109, p.750, eq. 8] and can be expressed in terms of the Landau parameterization (see Equation 4.12) [115, p. 216, eq. 1.2ff][10]:

$$\begin{aligned} \phi_V(\lambda_L \mid \kappa, \beta^2) &= \frac{1}{2\pi i}\int_{c-i\infty}^{c+i\infty} \mathrm{e}^{\kappa(1+\beta^2\cdot\gamma_{\text{EM}})} \cdot \mathrm{e}^{\psi(s)} \cdot \mathrm{e}^{\lambda_L \cdot s}\, \mathrm{d}s \\ \text{with} \quad \psi(s) &= s \cdot \ln(\kappa) + \left(s + \beta^2\kappa\right) \cdot \left[\int_0^1 \frac{1 - \mathrm{e}^{-\frac{s\cdot t}{\kappa}}}{t} dt - \gamma_{\text{EM}}\right] - \kappa \cdot \mathrm{e}^{-\frac{s}{\kappa}} \end{aligned} \tag{4.18}$$

[9] Landau also employed the saddle-point method to derive an implicit form, but he did not pursue a full analytical expression suitable for practical applications (see [102, p. 423, eq. 23]).
[10] "s" in Equation 4.18 is the complex integration variable used in the inverse Laplace transform that defines the Vavilov distribution.

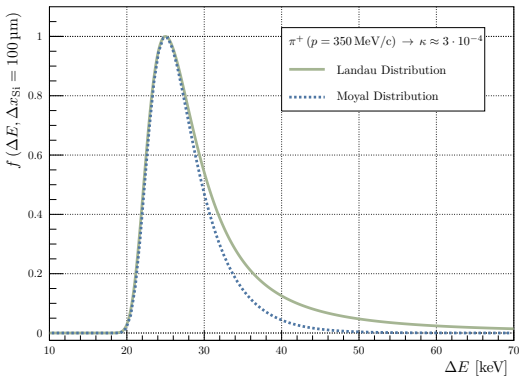

(a) Comparison of the Moyal and Landau distributions.

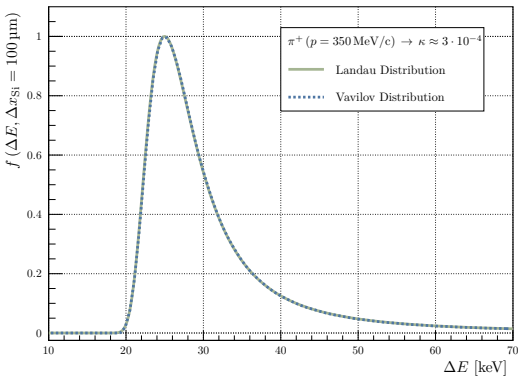

(b) Comparison of the Vavilov and Landau distributions.

Plot 4.4: Comparison of the shape of *straggling functions* for the same input of a π^+ with a momentum of 350 MeV c^{-1} traversing 100 µm silicon (which corresponds to a κ value of approximately 0.0003). The functions $f(\Delta E)$ are normalized to one. Calculation based on Equations 4.14, 4.15 and 4.19 taken Equation 4.9 and Equation 1.9 to determine the ΔE_{MPV} and $\xi(\Delta x, \beta)$, respectively. Corresponding data presented in Tables A.16 and A.17.

where γ_{EM} is the Euler-Mascheroni constant, κ is the dimensionless parameter defined in Equation 4.10, and β is the relative velocity of the incident particle.
To relate this formal definition to a usable probability density function for the energy loss ΔE, the parametrization of Equation 4.11 for Vavilov's model is expressed in the following way:

$$\mathrm{PDF}_{\mathrm{Vavilov}}(\Delta E \mid \Delta E_{\mathrm{MPV}}, \xi(\Delta x, \beta)) = \frac{\phi_V(\lambda_L \mid \kappa, \beta^2)}{\xi(\Delta x, \beta)} = \frac{\phi_V(\Delta E \mid \Delta E_{\mathrm{MPV}}, \xi(\Delta x, \beta))}{\xi(\Delta x, \beta)} \tag{4.19}$$

As detailed in Section 4.1, the Vavilov distribution provides an appropriate model for energy loss across a broad range of materials and conditions, converging to the Landau or Gaussian distribution under specific limiting cases[11]. For further details on the Vavilov distribution, its properties, and applications, see Section A.3.4.

4.1.4 Straggling Function Modifications

Generally, a *straggling function* is defined as the solution to Equation 4.8 that specifies the probability distribution of energy losses of a particle in a medium. Various effects can arise that can influence the shape of the assumed distribution and thus the applied model, which are discussed in the following.

Straggling for Electrons and Positrons

As it may have been noticed the introduced distributions in Sections 4.1.1 to 4.1.3 all consider the case of an incident particle, which is neither an electron nor a positron, as can be deducted from the respective use of cross section.

In the case of electrons and positrons, the cross section is not given by the Rutherford or Mott cross section, but rather by the Møller (for electrons) or Bhabha (for positrons) cross section (cf. Section 1.1.2). These special cases have been studied in [103] and [104, 105][12], whereby the latter employs a more advanced cross section model.

Although [104, 105] offers a more sophisticated (but also more complex and computationally expensive) model, the simpler approach of [103] is sufficient to get an insight into the modification for electrons ($-$) and positrons ($+$) probability (normalized to unity) of an energy loss in range $\mathrm{d}\Delta E$, which can be expressed by [103, p. 41, eq. 12]:

$$f^{\pm}(\Delta E \mid \Delta x)\,\mathrm{d}\Delta E = \mathrm{e}^{-\alpha^+ \cdot \left[\lambda_L^{\pm} + \ln(\alpha^+)\right]} \cdot \phi(\lambda_L^{\pm})\,\mathrm{d}\Delta\lambda_L^{\pm} \tag{4.20}$$

[11] `ROOT` offers two implementations of the Vavilov distribution — `ROOT::Math::VavilovAccurate` and `ROOT::Math::VavilovFast` — which are valid within the ranges 10 (12) $\geq \kappa \geq$ 0.001 (0.01), respectively.
[12] Be aware that [103] uses incorrect values to determine the energy loss, which have been correct for by [104, 105].

where $\phi(\lambda_L^{\pm})$ is the landau distribution given by Equation 4.11, and $\lambda_L^{\pm}$ is a reparameterization of the Landau variable λ_L (see Equation 4.12) for electrons and positrons, respectively. Here, ΔE_{MPV} is modified by introducing a correction term [104, p. 1637, eq. 44][13]:

$$\Delta E_{\text{MPV}} \quad \xrightarrow{e^-/e^+} \quad \Delta E_{\text{MPV}}^{\pm} = \Delta E_{\text{MPV}} - \xi(\Delta x, \beta)\left(\nu \cdot \alpha^{\pm}\right) \tag{4.21}$$

As a consequence, also the FWHM of the distribution is affected, which can be expressed as [104, p. 1637, eq. 45]:

$$W_L \quad \xrightarrow{e^-/e^+} \quad W_L^{\pm} \approx \underbrace{W_L}_{\approx 4.02 \cdot \xi} - \mu \cdot \alpha^{\pm} \cdot \xi(\Delta x, \beta) \tag{4.22}$$

The correction terms $\alpha^{\pm}$ are defined for electrons and positrons [104, p. 1637, eq. 46][14] (cf. erratum [105]), respectively, and are complimented by the parameters $\nu = (2.34 \pm 0.08)$ and $\mu = (6.62 \pm 0.09)$ [104, p. 1638, eq. 47], which are defined as:

$$\alpha^{+} = \kappa \cdot \beta^2 \left[2 - \frac{1}{(\gamma+1)^2}\right], \quad \alpha^{-} = \frac{\kappa}{2} \cdot \frac{2\gamma - 1}{\gamma^2} \tag{4.23}$$

Be aware, that both ν and μ are taken from fit values and "[...] are approximately constant over a broad range of parameter values of interest [...]" [104, p. 1638].

Since in most applications the parameter κ is small, the correction terms can be considered negligible. Especially, the effect in the ΔE_{MPV} is an order of magnitude smaller than for the FWHM, and thus one has to take care of these deviations only in the case of "thick" silicon pixel sensors at low energies. Consequently, deviations of the *straggling functions* derived from Møller and Bhabha scattering, as compared to the Rutherford approach used by Landau, are generally not of major concern. It is, however, important to note that the deviation for Bhabha scattering is larger than that for Møller scattering.

Channeled Energy Loss in Silicon Crystals

In general, it is assumed that energy loss occurs in an amorphous medium, where angular dependence is not a major concern. However, in crystalline materials, the stopping power depends on the incident angle of particles relative to the crystalline axis (cf. Section 2.1.1), thus affecting the energy loss distribution. This phenomenon is known as the *channeling effect*, which involves small-angle scattering governed by the crystal's channels.

Measurements and simulations reported by several authors [116, 117, 118, 119, 120][15] suggest that the energy loss for particles aligned with the silicon crystal orientation influences the overall energy loss, the most probable value, the shape, and thus the FWHM of the distribution.

For positively charged particles, a strong reduction and narrowing of the energy loss distribution is observed. These particles are repelled by the atomic nuclei and are channeled through spaces between atomic planes or axes, resulting in less frequent scattering. Conversely, negatively charged particles are attracted to the atomic nuclei, passing through regions of higher electron density and experiencing more frequent scattering, leading to increased energy loss and a broader distribution.

For completeness, this effect is discussed here but is not considered in the modeling of the *straggling functions*, since precise alignment of the sensor with the beam axis is not expected. Moreover, the effect may be damped by defects and imperfections in the crystal structure, which is further disrupted by the manufacturing process of the upper layers of a silicon sensor — including doped regions, metalization, oxide layers, and passivation (cf. Section 3.2.1). Nevertheless, the effect should not be entirely disregarded, as a small fraction of incident particles may enter a channel and influence part of the energy-loss distribution.
For more general information on the *channeling effect*, academic literature such as [121, p. 93 ff., ch. 8] or [122, p. 549 ff., ch. 11] can be consulted.

[13] Note that the parameter $\xi(\Delta x, \beta)$ in [104, p. 1633, eq. 4] is, in contrast to Equation 1.9, normalized by the kinetic energy $\mathcal{T}$ of the incident particle to be unitless.
[14] Note the adjustment of $\xi(\Delta x, \beta)$ with respect to [104, p. 1637, eq. 46] in Equation 4.23. The $\xi(\Delta x, \beta)$ is defined as a dimensionless factor in [104, p. 1637, eq. 46] and is replaced by κ in Equation 4.23. Consider the difference in treatment between electrons and positrons in $\mathcal{T}_{max}$, where a factor of $1/2$ is introduced for electrons.
[15] Many more sources study the effect of channeling in silicon crystals, and the listed references only represent a small selection.

Resonance Excitation Effects of Bound Shell Electrons

Measurements of the energy loss distribution in thin materials reported significant deviations in the FWHM compared to theoretical predictions [123, 124]. These deviations cannot be explained by electronic noise or imperfect resolution, and thus have to arise from physical effects.

It is assumed that this is caused by "resonance excitation" of the shell electrons (cf. Figure 4.3a), an effect not considered in the cross sections employed so far. In collisions where the projectile energy is much higher than the electron binding energy, the electrons can be approximated as quasi-free (as assumed by Landau, Moyal, and Vavilov). However, this approximation breaks down for distant interactions involving low energy transfers. In such cases, the discrete energy structure of bound electrons becomes more evident, and the electrons must be treated as bound with respect to their binding energies (cf. Section A.6.1).

To address this, *Blunck and Leisegang* [125] (cf. [126]), as well as *Shulek et al.* [127] (in [128]), each introduced an equivalent correction term[16]. The corresponding form is proposed by [127, eq. 8] (cf. [101, p. 695 ff., eq. F1, H2])[17] to be:

$$\delta_2^{\mathrm{S}} = \frac{8}{3} \cdot \xi \cdot \sum_k I_k \cdot f_k \cdot \ln\left(\frac{E_M}{I_k}\right) \tag{4.24}$$

where I_k is the excitation energy and f_k is the oscillator strength of the k-th shell electron (cf. Section 1.1). The summation is performed over all shells satisfying the condition $I_k < E_M$, which, for silicon, is generally valid in most high-energy particle applications. The value of E_M is defined by *Shulek et al.* as $2m_e c^2\beta^2$; however, as Bichsel points out: "It is not obvious whether the value [of E_M] [...] should be replaced by [$E_M = 2m_e c^2\beta^2$] or by [Equation 1.3]."[101, p. 696]

This correction modifies the *straggling function* by convolving the Landau-Vavilov (or Moyal) distribution with a normal distribution of variance δ_2^{S}, as stated in [101, p. 695, eq. F1]:

$$f(\Delta E \mid \Delta x, \delta_2^{\mathrm{S}}) = \frac{1}{\sqrt{2\pi\delta_2^{\mathrm{S}}}} \cdot \int_{-\infty}^{\infty} f_{LVM}(\Delta E - E \mid \Delta x) \cdot \mathrm{e}^{-\frac{E^2}{2\delta_2^{\mathrm{S}}}}\,\mathrm{d}E = (f_{LVM}(\Delta x) * \mathrm{PDF}_{\mathrm{normal}}(\delta_2^{\mathrm{S}}))(\Delta E) \tag{4.25}$$

where f_{LVM} is the Landau-Vavilov or Moyal distribution (see Sections 4.1.1 to 4.1.3).

The convolution broadens the energy loss distribution and shifts its peak towards higher energy loss — an effect that becomes more pronounced for low-energy particles. Since detector resolution effects (such as noise) are generally modeled by an additional Gaussian broadening (cf. Section 4.1), the total variance in Equation 4.25 can be expressed as the sum of the individual variances (the resulting σ is the RSS (**R**oot **S**um **S**quare)):

$$\sigma_{\mathrm{RSS}}^2 = \sigma_{\mathrm{detector}}^2 + \delta_2^{\mathrm{S}} \tag{4.26}$$

Further details regarding δ_2^{S} and calculation methods are discussed in Section A.3.5.

Energy Loss Broadening in Thin Silicon

The approach of *Shulek et al.* (see Equation 4.25) was tested by *Hancock et al.* [130] using 300 µm silicon detectors and later applied in more recent measurements by *Meroli et al.* [131][18].
Hancock et al.[19] observed that Equation 4.25 provides a reasonable model [130], although deviations appear in the tail region, which are attributed to escaping delta-electrons (cf. Section 1.1.3).

However, Bichsel's more detailed evaluation [132, 133] (cf. [134]) demonstrated that values derived from Equation 4.24 tend to overestimate fluctuations and fail for thin silicon sensors (e.g. 20 µm, see [133, p. 176, fig. 12], cf. [101, p. 696, app. G]). According to Bichsel:

> "Values of [δ_2^{S}] calculated with this approach may give a function with a width [W_{FWHM}] close to the correct one, but the function [Equation 4.25] still rise too slowly below [ΔE_{MPV}] and drop too fast [...]" [101, p. 696, A.G]

[16] The quantity K_r^2 in [125] is equal to Equation 4.24 from [127, eq. 8].[101, p.696]
[17] Take note that the convention for $\xi(\Delta x, \beta)$ differs from the one used in [101, p. 696, eq. H2] and has to be adjusted for the normalization preferred to specify the energy loss (normalized to Δx or not).
[18] Note that the expression for Equation 4.24, as given in [131, p. 3, eq. 2.10], differs not only in the normalization by Δx, but also in that the factor I in front of the logarithmic term within the summation is given as I, rather than indexed as I_k, which would be more appropriate.
[19] It should be noted that Bichsel criticized the calculated values of δ_2^{S}, as derived by *Hancock et al.*, as incorrect [101, p. 697, Appendix H].

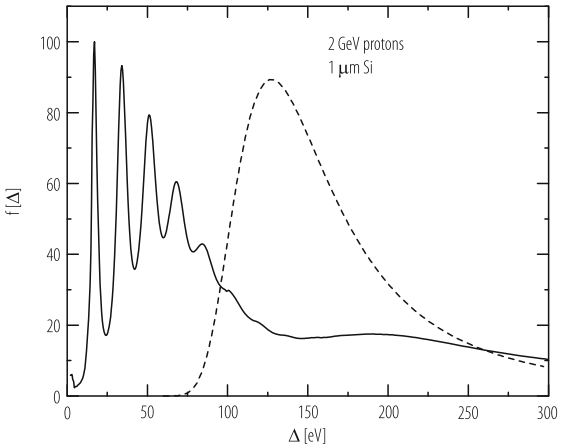

(a) Straggling in 1 µm of Si ($\mathcal{M}_0 = 4$) for particles with $\beta\gamma = 2.1$, compared to the Landau function (dashed line). The Bethe mean energy loss is $\langle \Delta E \rangle = 400$ eV. Taken from [15, p. 35, fig. 2.12]. Original from [29, p. 158, fig. 2].

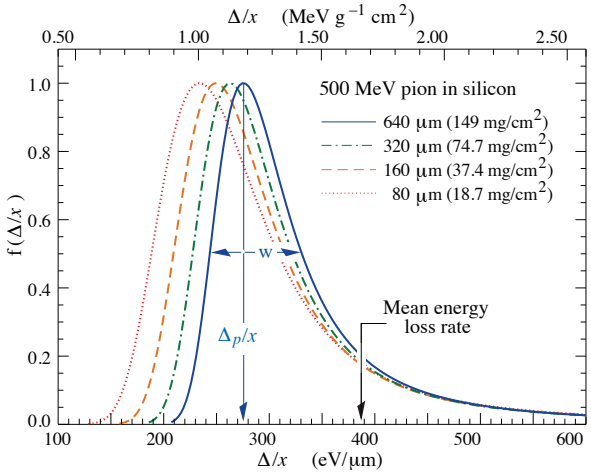

(b) Normalized (to unity) *straggling functions* in thin silicon for 500 MeV pions with w denoting the FWHM. Taken from [14, p. 580, fig. 34.8].

Figure 4.3: Straggling in thin silicon (cf. [129] for measurements in aluminium).

Furthermore:

> "This approach would break down for absorbers thinner than 10 µm, where the structure of the single collision spectrum would be important [...]" [101, p. 696, A.G]

When attempting the convolution method with calculated values of δ_2^{S} (cf. Section A.3.5), one may observe that as Δx decreases, the associated sigma related to δ_2^{S} becomes disproportionately large, causing the convolution function $f(\Delta E \mid \Delta x, \delta_2^{\mathrm{S}})$ to yield non-physical values with non-zero probability for $\Delta E \leq 0$. To which should be added that Bichsel pointed out:

> "[N]o method [is] available to obtain the proper value of [δ_2^{S}] (except by use of the convolution method, and then find [δ_2^{S}] by trial and error)" [133, p. 178, sec. 5].

Figure 4.3b illustrates the relative broadening compared to Landau function (see Plot 4.3b) of the *straggling functions* for thin silicon sensors. This form is achieved via the so-called *convolution method*[20] of Equation 4.6 (cf. [101, p. 679ff]), which incorporates the different cross section of the atomic sub-shells into the model — an effect which becomes more significant as Δx decreases.

In the context of this thesis, a more agnostic treatment is adopted; it recognizes the effect arising from excitation of bound electrons but does not directly incorporate calculations of δ_2^{S}. However, the convolution approach is still employed to account for detector effects treated in this manner. For this reason, the corresponding sigma of Equation 4.26 is defined as a free parameter and is compared with measured noise and corresponding excess arising from δ_2^{S}.

[20] Not to be confused with the convolution method of Equation 4.25, which is used to incorporate the δ_2^{S} into the Landau-Vavilov distribution.

4.2 Charge Collection & Transport in a Silicon Pixel Sensor

Subsequently to the deposition of energy by a charged particle in a silicon pixel sensor (see Section 4.1), and creation of electron-hole pairs (see Section 2.2.1), one of two dominating processes take place: either the charge carriers are separated by the electric field in the depleted volume, or they diffuse within the non-depleted volume. Both processes are described in more detail in the following sections.

Although the motion of charge carriers is governed by these mechanisms, signal formation results from an instantaneous current induced on the electrodes by the motion of the charges relative to the electrodes — not from the collection of the charges themselves. In principle, charges do not need to be collected to generate a signal; a charge can recombine or be lost through other processes, as long as it induces a signal before its motion ceases.

This fundamental concept is described by the Shockley-Ramo theorem [135, 136], which states that the current induced on an electrode is proportional to the velocity of the charge carriers and the geometrical configuration of the electrodes. A pixel sensor can therefore be regarded as an electrometer that measures the charges induced on the "collection" electrode by the motion of charge carriers. The instantaneous current induced by a single charge is given by:

$$i_{S,i}(t) = -\frac{\mathrm{d}Q}{\mathrm{d}t} = q \cdot \vec{\nu}_D(t) \cdot \vec{\mathcal{E}}_{w,i}(t) = q \cdot \vec{\nu}_D(t) \cdot \vec{\nabla}\phi_{w,i}(\vec{r}(t)) \tag{4.27}$$

where q is the charge of the carrier, $\vec{\nu}_D = \frac{\mathrm{d}\vec{r}}{\mathrm{d}t}$ the drift velocity[21] of the carrier, and $\vec{\mathcal{E}}_w$ the *weighting field*[22] associated with the i-th electrode. The weighting field (unit: 1/length) is defined as the gradient of the *weighting potential* $\phi_{w,i}(\vec{r}(t)) = \frac{\partial\phi_i(\vec{r}(t))}{U_i}$, a dimensionless hypothetical electrostatic potential.

To determine the *weighting potential*, the electrode of interest is set to unit potential (U_i = 1 V), while all other electrodes are grounded ($U_{j\neq i}$ = 0 V). Most importantly, all "real" charges within the sensor volume — including mobile charge carriers, space charge regions, and ionization-created charges — are removed. This ensures that the *weighting potential* is solely determined by the geometry of the electrodes. The *weighting potential* is the solution to the Laplace[23] equation ($\nabla^2\phi_{w,i} = 0$) and is independent of the applied bias or internal electric fields. Thereby, it provides no information on how carriers move in the sensor volume, but it is a purely geometrical sensitivity map of the induced current to the motion of charge carriers.

The charge induced on an electrode by a moving charge can be obtained by integrating the induced current over time:

$$Q_{S,i}(t) = \int_{t_0}^{t} i_{S,i}(t')\,\mathrm{d}t' = q\left[\phi_{w,i}(\vec{r}(t)) - \phi_{w,i}(\vec{r}(t_0))\right] \tag{4.28}$$

where t_0 is the time of charge deposition. The total charge induced on the electrode is then given by the sum of all charges induced by all charge carriers.

In an ideal insulator — such as vacuum or a dielectric — or a fully depleted semiconductor, the *weighting potential* is static and time-independent. This applies as long as free charge carriers are absent and newly created charges do not significantly affect the existing electric field[24].

In contrast, in a conductive medium or in a partially depleted semiconductor, mobile charge carriers can flow and respond dynamically to disturbances from the motion of charge carriers, which are generated by the passage of charged particles. In this case, the *weighting potential* becomes time-dependent, and the formulation to describe the induced current requires to incorporate the material conductivity.

One particularly relevant case for silicon detectors is that of a partially depleted substrate[25], where part of the sensor remains non-depleted and thus conductive. In a p-type substrate, holes created within the depletion region drift toward the backplane. As they approach the boundary to the non-depleted volume, they decelerate, causing a long tail in the induced current. Meanwhile, electrons drift towards the n-well electrode, accelerating and then stopping in its vicinity.

[21] Take note that $\vec{\nu}_{Drift}$ and $\vec{\mathcal{E}}_w$ are not necessarily parallel, as the *weighting field* can be a superposition with a magnetic field or be affected by other electrodes.

[22] Do not confuse the weighting field with the electric field in the sensor, which is defined by the applied voltage and the geometry of the sensor. The weighting field is solely a function of the geometry of the electrodes and their respective potential configuration.

[23] In case of a space charge region, the Poisson equation ($\nabla^2\phi_{w,i} = -\frac{\phi_{SC}}{\varepsilon}$) has to be solved instead.

[24] This is the case in the typical case of charge deposition, which is subject to change if a particle is stopped in the sensor volume, which is not considered here.

[25] It is assumed that an abrupt boundary between depleted and non-depleted volume is given.

If it is assumed that charge carriers generated in the non-depleted volume recombine before diffusing into the depleted volume, then it is typically assumed that they do not contribute to the induced charge. However, the electric field associated with the signal charge still induces a time-dependent response in the conductive region. This leads to an exponentially decaying component in the induced signal current, with the decay constant given by the *relaxation time* times a geometric factor [137, p. 457, eq. 29]:

$$\tau = \underbrace{\frac{\varepsilon_0 \varepsilon_r}{\sigma_{substrate}}}_{\text{relaxation time}} \cdot \frac{d}{w(U)} \overset{\text{Si}}{\approx} 0.001\,036\,\text{ns} \cdot \frac{\varrho_{substrate}}{[\Omega\,\text{cm}]} \cdot \frac{d}{[\mu\text{m}]} \cdot \frac{[\mu\text{m}]}{w(U)} \tag{4.29}$$

where ε_0 is the vacuum permittivity, ε_r the relative permittivity, $\varrho_{substrate}$ the substrate resistivity, $w(U)$ the depletion depth (see Equation 2.22), and d the total sensor thickness.

In the limit of an ideal conductor ($\varrho_{substrate} \to 0$), any electric field induced by generated charge carriers in the non-depleted layer (conductive) is immediately neutralized due to electrostatic screening of mobile charges, and the induced signal solely depends on the depleted layer. Conversely, if the substrate becomes an ideal insulator ($\varrho_{substrate} \to \infty$), no mobile charge carriers are present, weighting potential is again static, and the induced current is determined by the weighting potential of the entire sensor volume. In this limit, the time constant τ becomes so large that it exceeds the charge collection time, rendering any possible time dependence in the weighting field irrelevant for signal formation (cf. [138]). In the intermediate case of finite conductivity, the time constant τ can become comparable to or shorter than the characteristic charge collection time. In this regime, the assumption of a static weighting field no longer holds, and a time-dependent weighting field must be considered to accurately describe signal formation. More details and exemplary cases for single electron-hole pairs and an uniform charge deposition along a particle trajectory are presented in [137, 139].

In pixel detectors, where the electrode size is comparable to or smaller than the sensor thickness, the weighting potential is near unity in the vicinity of the electrode and drops steeply towards zero elsewhere. Here, the magnitude of the weighting potential decreases as the ratio of electrode size to sensor thickness decreases (see Figure 4.4). This configuration gives rise to the so-called *small pixel effect* [140, p. 61], with two important implications:

1. The majority of the current is induced during the final segment of the charge carrier's drift path as it approaches the proximity of the electrode and the weighting field is the strongest.

2. The contribution of minority charge carriers (e.g. holes in a p-doped substrate) drifting to the opposite direction toward the backplane is small or negligible.

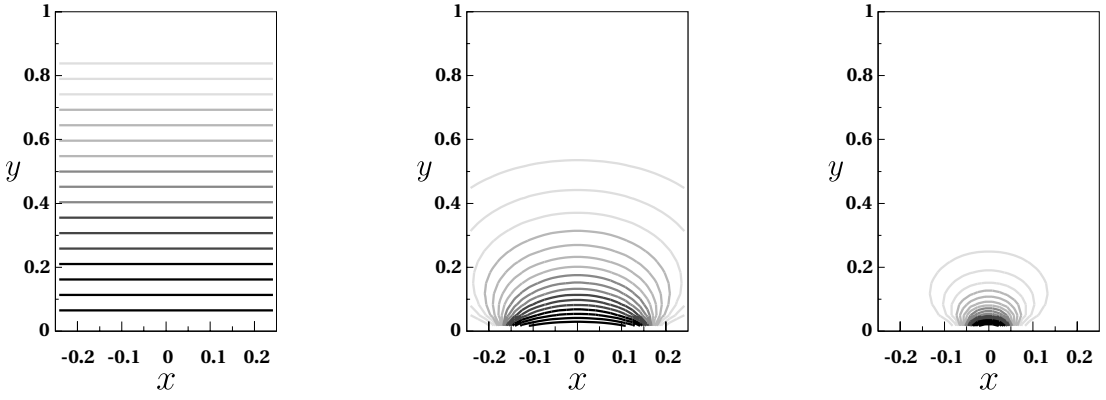

(a) Two infinite parallel plates.

(b) An electrode with a size of $1/3$ of the sensor thickness.

(c) An electrode with a size of $1/10$ of the sensor thickness.

Figure 4.4: Plot of weighting potentials for various collecting electrode configurations. The shading of the lines indicates potential magnitude, from dark (high) to light (low). $\boldsymbol{y}$ is the normalized wafer thickness (electrode at zero), and $\boldsymbol{x}$ is the normalized distance along the electrode width. Adapted from [140, p.61, fig. 2.19].

4.2.1 Drift of Electrons and Holes

Charge transport under an applied electric field is dominated by *drift*, the field-directed motion of electrons and holes. In a semiconductor, acceleration by the field is balanced by scattering off lattice phonons and crystal defects, and generally defined by the Boltzmann transport equation. At fixed temperatures T and moderate field strength $\mathcal{E}$, the drift velocity follows [17, p. 122, eq. 4.127]:

$$\nu_{Drift} = \mu_{e/h}(\mathcal{E}, \mathcal{N}, T) \cdot \mathcal{E} \tag{4.30}$$

where $\mu_{e/h}$ is the field, doping- and temperature-dependent mobility defined by Equation 2.8 (cf. Section A.2). The drift velocity is proportional to the electric field strength $\mathcal{E}$, but becomes independent at high field strengths, where the mobility saturates (see Plot 4.5).

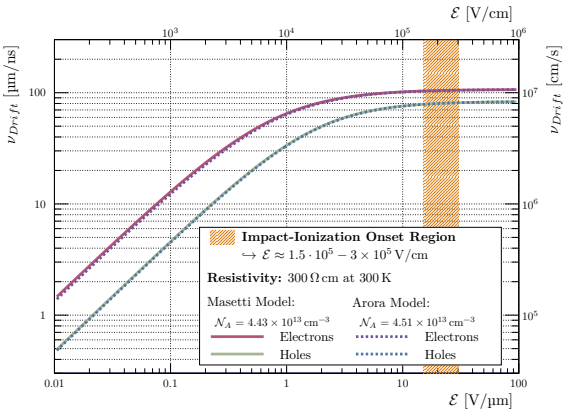

(a) Calculation of the drift velocity as a function of the electric field at 300 K ($\varrho_{substrate}$ = 300 Ω cm), based on Equation 4.30. Approximation of the impact ionization threshold taken from [141, p.711ff., sec 5.2 & fig. 6] and [142, p. 2926, sec. V].

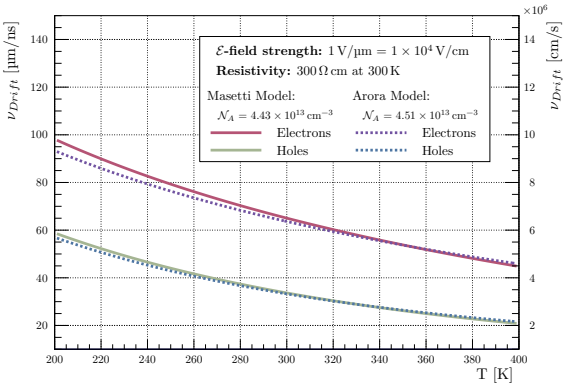

(b) Calculation of the drift velocity as a function of the temperature for a electric field strength of $\mathcal{E}$ = 1 V µm^{-1} ($\varrho_{substrate}$ = 300 Ω cm at 300 K), based on Equation 4.30.

Plot 4.5: Calculations of the drift velocity using the *Masetti* and *Arora* models for the electron and hole mobilities, respectively. See section A.2.

When charge carriers attain sufficient kinetic energy — typically for fields above 1.5×10^5 V/cm to 3.0×10^5 V/cm [141, p. 711 ff., sec 5.2 & fig. 6] and [142, p. 2926, sec. V] — they can generate additional electron-hole pairs via impact ionization (cf. Section 2.2.1). Approximating the peak electric field strength at a reverse-biased pn-junction by its depletion region boundary, Equation 2.15 in combination with Equations 2.21 and 2.22 yields:

$$\mathcal{E}_{max}(U \mid U_{bi}, \varrho_{substrate}) \approx \frac{2 \cdot (U_{bi} - U)}{w(U \mid U_{bi}, \varrho_{substrate})} \overset{\text{Si}}{\approx} 6.219\,\text{V/µm} \cdot \sqrt{\frac{(U_{bi} + |U|)}{[\text{V}]} \cdot \frac{[\Omega\,\text{cm}]}{\varrho_{substrate}}} \tag{4.31}$$

This estimation can be used to identify whether the local electric field strength exceeds the impact-ionization threshold (cf. Section 7.2.1).

4.2.2 Diffusion in Silicon

In regions of elevated carrier concentration, thermal motion drives diffusion that equalizes the concentration gradient by moving carriers from high-density to low-density areas. To describe the spread of charge carriers in silicon detectors, Fick's [143] first law of diffusion[26] is used, which relates the concentration gradient of the charge carrier density C with the diffusion current $\vec{J}_{diff}$ [17, p. 102, eq. 4.68]:

[26] Fick's first law of diffusion is not stated explicitly in the original paper [143], as it was regarded as a "common-sense" principle: a gradient in concentration naturally produces a flux (a "diffusion current") from regions of high concentration to low concentration.

$$\vec{J}_{diff} = -\mathcal{D}_{e/h}\vec{\nabla}C \tag{4.32}$$

where $\mathcal{D}_{e/h}$ denotes the electron or hole diffusion constant. Differentiation in time yields Fick's second law[27] [17, p. 102, eq. 4.69]:

$$\frac{\partial C}{\partial t} = \mathcal{D}_{e/h}\vec{\nabla}^2 C \tag{4.33}$$

which predicts the time evolution of the spatial charge distribution. The diffusion constant is linked to the carrier mobility in semiconductor $\mu_{e/h}$ (see Section 2.2.2) by the Einstein relation [144, p. 555]:

$$\mathcal{D}_{e/h}(\mathcal{N}, T) = \mu_{e/h}(\mathcal{N}, T) \cdot \frac{k_B \cdot T}{e} \tag{4.34}$$

with k_B being the Boltzmann constant, T the absolute temperature, and e the elementary charge (cf. Section A.2.3).

A general three-dimensional solution for an arbitrary initial distribution $C_0(\vec{x}')$ is obtained by Gaussian convolution [145, p. 200, eq. 51.2]:

$$C(\vec{x}, t) = \frac{1}{\sqrt{(4\pi\mathcal{D}_{e/h}t)^3}} \int C_0(\vec{x}')\, \mathrm{e}^{-\frac{|\vec{x}-\vec{x}'|^2}{4\mathcal{D}_{e/h}t}}\, \mathrm{d}^3\vec{x}' \tag{4.35}$$

exhibiting isotropic spreading with standard deviation:

$$\sigma_{diff}(\vec{x}, t) = \sqrt{2\mathcal{D}_{e/h}t} \tag{4.36}$$

For a point-charge deposition Q_0 at $\vec{x}_0$, the initial condition:

$$C_0(\vec{x}') = Q_0 \cdot \delta(\vec{x}' - \vec{x}_0) \tag{4.37}$$

yields a time-dependent Gaussian distribution centered at $\vec{x}_0$, while a uniform line deposit along the z-axis (perpendicular to the sensor surface):

$$C_0(\vec{x}') = \frac{\mathrm{d}Q_0}{\mathrm{d}z} \cdot \delta(x' - x_0)\delta(y' - y_0) \tag{4.38}$$

produces an elongated Gaussian profile upon convolution with Equation 4.35. This approach enables prediction of charge distribution for both scenarios and can be extended to more complex initial conditions.

4.2.3 Coulomb Repulsion

In localized, high-density space-charge regions — such as those generated by the photoelectric effect — the mutual Coulomb repulsion between charge carriers cannot be neglected, particularly in diffusion-dominated regimes (as shown in [146, 147]). This repulsion increases the radial expansion of the charge cloud compared to pure diffusion (see Section 4.2.2). The total charge within the spherical volume of radius r at time t is:

$$Q(r, t) = q \cdot \oint_{V_{sphere}} C(r, t)\, \mathrm{d}r \tag{4.39}$$

following [146, p. 395, eq. 12], the charge carrier concentration takes the form ($r \leq r_0(t \mid N_{e/h})$):

$$C(r, t) = \frac{\varepsilon_0 \varepsilon_{\mathrm{Si}}}{q \cdot \mu_{e/h} \cdot t} \tag{4.40}$$

where the expanding radius is given by [146, p. 396, eq. 14]:

$$r_0(t \mid N_{e/h}) = \sqrt[3]{\frac{3}{4\pi} \cdot \frac{q \cdot \mu_{e/h}}{\varepsilon_0 \varepsilon_{\mathrm{Si}}} \cdot N_{e/h} \cdot t} \tag{4.41}$$

Here, q is the elementary charge, ε_0 is the vacuum permittivity, $\varepsilon_{\mathrm{Si}}$ is the relative permittivity of silicon, $N_{e/h}$ is the number of electron-hole pairs created (see Section 2.2.1), and $\mu_{e/h}$ is the mobility of the charge carriers (see Section 2.2.2).

[27] Also, the second law of diffusion is not stated in its modern form in the original paper [143], but it can be derived by combining the first law of diffusion in Equation 4.32 with the continuity equation $\frac{\partial C}{\partial t} + \vec{\nabla} \cdot \vec{J}_{\mathrm{diff}} = 0$ (see, e.g., [17, p. 102, eq. 4.67]).

4.2.4 Charge Sharing

Charge sharing occurs when the charge generated by a traversing particle is distributed among multiple collection electrodes instead of being collected solely by the originating pixel. This redistribution can lower the SNR (**S**ignal-to-**N**oise **R**atio) in the primary pixel for a given threshold and can distort the reconstructed hit pattern. If the charge in neighboring pixels exceeds their detection threshold, those pixels are also registered as hits, forming a cluster. In energy reconstruction, summing the ToT values of all pixels in the cluster typically recovers the total deposited charge. However, in an efficiency measurement — where the readout information is binary (hit/no hit) — any fraction of the charge that ends up in neighboring pixels does not contribute to the primary pixel's signal. This effect reduces the measured efficiency and effectively raises the charge detection threshold for that pixel.

Two distinct mechanisms underlie charge sharing. First, when particles enter the material at an oblique angle or near pixel boundaries, charge carriers tend to diffuse toward neighboring collecting electrodes, which is a common behavior in Si detectors. Second, moving charge carriers can induce transient currents in neighboring electrodes in the vicinity of their weighting fields, as described by the Shockley-Ramo theorem (see Section 4.2). As a charge carrier drifts towards the collecting electrode of the primary pixel k (see Figure 4.5b), mirror charges are induced in the collecting electrodes of the neighboring pixels $k \pm 1, 2$. Owing to the symmetry of their *weighting fields*, the induced currents reverse sign as carriers enter the vicinity of the collecting electrode (see Figure 4.5a).

The impact of these transient currents depends on the integration time of the Charge Sensitive Amplifier relative to the drift time of the carriers. If the CSA integration (rise) time τ_{rise} is much longer than the carrier drift time τ_{drift}, the positive and negative contributions of the induced current in a neighboring pixel largely cancel out during integration, leading to a negligible net induced charge. Conversely, if the integration time is comparable to or shorter than the duration of the induced current, this cancellation is incomplete. In that case, a non-zero net induced charge remains in the neighboring pixels, potentially contributing to an apparent charge sharing event in the measurement.

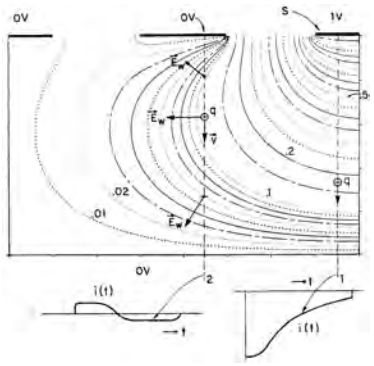

(a) Exemplary weighting field of a strip detector. Induced current shown for charge on measurement electrode (right-most) and neighbor electrode (middle), which is net zero. Taken from [91, p. 79, fig. 2.31].

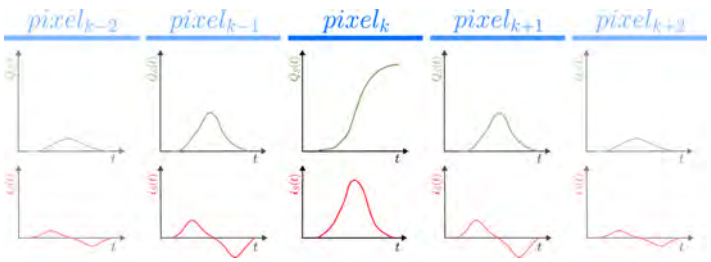

(b) Qualitative illustration of the Shockley-Ramo theorem for charge sharing. In $pixel_k$ the charge is created, which induces a current signal on the electrode. The induced charge in neighboring pixels ($k \pm 1, 2$) results in a net zero current. Illustration based on [148, p. 78].

Figure 4.5: Induced current by "charge sharing" in a silicon detector by Shockley-Ramo theorem.

4.2.5 Noise Sources

To characterize the noise affecting a pixel detector's readout electronics, one commonly relies on the ENC (**E**quivalent **N**oise **C**harge), the RMS output-voltage noise referred to the charge of a single electron. ENC is especially valuable for comparing and optimizing the performance of charge integrating devices such as a CSA. Here, the total noise can be decomposed into three dominant contributions — shot, flicker, and thermal — so that the ENC can be expressed as a sum of squares of the individual noise contributions, given by [17, p. 795, eq. 17.110]:

$$\text{ENC}^2 = \underbrace{a_{\text{shot}} \cdot \tau}_{\text{ENC}^2_{\text{shot}}} + \underbrace{a_{1/f} \cdot C_d^2}_{\text{ENC}^2_{1/f}} + \underbrace{a_{\text{thermal}} \cdot \frac{C_d^2}{\tau}}_{\text{ENC}^2_{\text{thermal}}} \tag{4.42}$$

where C_d denotes the detector capacitance, τ the shaping (filter) time, and $a_{\text{shot}}, a_{1/f}, a_{\text{thermal}}$ are the technology- and design-dependent noise coefficients that scale the respective noise mechanisms.

When considering a typical pixel detector readout chain, estimating the ENC uses a MOSFET as the input transistor (see Figure 4.6a). With the relation $i^2 = (g_m \cdot u_{in})^2$ [30, p. 11], where g_m is the transconductance and u_{in} the input voltage, the noise sources within the transistor channel can be treated as a voltage-noise source in series to the amplifier input (see Figure 4.6b). For a CSA, that input is transformed to an output voltage according to the amplifier's characteristics.

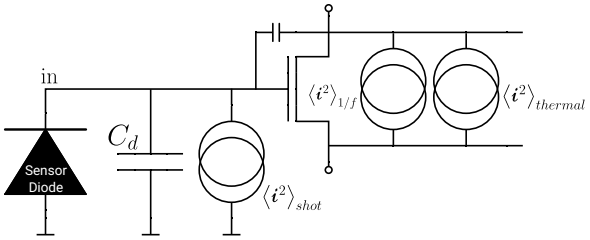

(a) The three main sources are shot noise from the detector leakage current, and thermal as well as $1/f$ noise in the transistor channel.

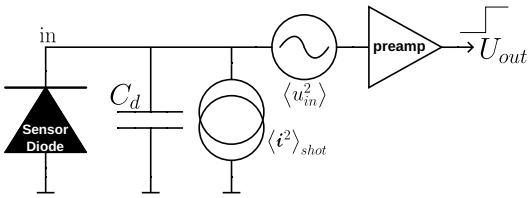

(b) Thermal and $1/f$ noise in the transistor treated as serial voltage noise to the input of the preamplifier.

Figure 4.6: Schematic depiction of the noise sources for a typical charge integrating pixel detector represented by a single MOSFET. Based on [30, p. 11, fig. 14].

Starting with *shot noise*, which stems from statistical fluctuations of charge carrier generation and recombination, it is proportional to the leakage current $\mathcal{I}_{\text{leakage}}$ in the sensor diode (see Section 2.3.3). As a type of *white noise*, it is frequency independent and grows with the integration (feedback) time τ_{fall} (see Equation 3.2) [17, p. 787, eq. 17.90][30, p. 12, eq. 20]:

$$\begin{aligned} \mathrm{d} < i_{\text{shot}}^2 >= 2q \cdot \mathcal{I}_{\text{leakage}} \cdot \mathrm{d}f \quad \longrightarrow \quad \text{ENC}_{\text{shot}} &= \sqrt{\frac{\mathcal{I}_{\text{leakage}}}{2q} \cdot \tau_{\text{fall}}} \\ &\approx 55.864\,\mathrm{e} \cdot \sqrt{\frac{\mathcal{I}_{\text{leakage}}}{[\mathrm{nA}]} \cdot \frac{\tau_{\text{fall}}}{[\mu\mathrm{s}]}} \end{aligned} \tag{4.43}$$

which explains why radiation damage — which increases $\mathcal{I}_{\text{leakage}}$ — can drive *shot noise* to dominate after high-fluence exposures.

The second mechanism is *flicker noise* ($1/f$-noise), which arises from trapping and release of charge carriers in the Si-SiO_2 interface inside a MOSFET. Exhibiting a $1/f^{\alpha}$ spectrum with $\alpha = 0.5...2 - 3$, it is in contrast to *white noise* sources frequency dependent. Its ENC term reads [17, p. 787ff][30, p. 12, eq. 20]:

$$\begin{aligned} \mathrm{d} < v_{1/f}^2 >= \frac{K_f}{C'_{ox} \cdot W \cdot L} \frac{1}{f} \mathrm{d}f \quad \longrightarrow \quad \text{ENC}_{1/f} \approx & C_d \cdot \sqrt{\frac{K_f}{C'_{ox} \cdot W \cdot L \cdot q^2}} \sqrt{\ln\left(\tau_{\text{fall}} \frac{g_m C_f}{C_0 C_d}\right)} \\ \approx & C_d \cdot \sqrt{\frac{K_f}{C'_{ox} \cdot W \cdot L \cdot q^2}} \sqrt{\ln\left(\frac{\tau_{\text{fall}}}{\tau_{\text{rise}}}\right)} \\ \approx & 51.875\,\mathrm{e} \cdot \frac{C_d}{[100\,\mathrm{fF}]} \cdot \sqrt{\frac{K_f}{[\mathrm{yJ}]} \cdot \frac{[\mathrm{fF}\,\mu\mathrm{m}^{-2}]}{C'_{ox}} \cdot \frac{[\mu\mathrm{m}^2]}{W \cdot L}} \\ & \cdot \sqrt{\ln\left(\frac{\tau_{\text{fall}}}{[\mu\mathrm{s}]} \cdot \frac{[\mathrm{ns}]}{\tau_{\text{rise}}}\right)} \end{aligned} \tag{4.44}$$

where K_f is a technology-dependent constant, W and L the input transistor's effective width and length, and $C'_{ox} = \frac{3}{2} \frac{C_{GS}}{W \cdot L}$ (with C_{GS} the gate-source capacitance) is the effective gate oxide capacitance[28].

[28] The factor $\frac{3}{2}$ is used to account for the fact that the gate-source capacitance is not equal to the oxide capacitance, but rather a fraction of it.

The third source of noise, *thermal noise* (*Johnson-Nyquist noise*), originates from the random motion of charge carriers in the input MOSFET channel. Modelling the transistor as a series voltage-noise source, its ENC contribution becomes [17, p. 790, eq. 17.95] and [30, p. 12, eq. 20]:

$$\begin{aligned} \mathrm{d} < v^2_{\text{thermal}} >= \frac{8}{3}\frac{k_B T}{g_m}\mathrm{d}f \quad \longrightarrow \quad \mathrm{ENC}_{\text{thermal}} &= \sqrt{\frac{k_B T}{q}\frac{2C_d}{3q}\frac{C_f}{C_0}} \\ &= C_d \cdot \sqrt{\frac{k_B T}{q}\frac{2}{3q}\frac{1}{g_m \tau_{\text{rise}}}} \\ &\approx 59.881\,\mathrm{e} \cdot \frac{C_d}{[100\,\mathrm{fF}]} \cdot \sqrt{\frac{T}{[\mathrm{K}]}\frac{[\mu\mathrm{S}]}{g_m}\frac{[\mathrm{ns}]}{\tau_{\text{rise}}}} \end{aligned} \tag{4.45}$$

where k_B is the Boltzmann constant, T the absolute temperature, and τ_{rise} the rise time (Equation 3.2).

Practical optimization therefore requires balancing these three terms by carefully selecting the detector capacitance C_d, shaping times τ_{rise} and τ_{fall}, input-transistor transconductance, and cooling to suppress the leakage current $\mathcal{I}_{\text{leakage}}$. In a cascaded high- and low-pass filter system — typical for pixel sensors — the total ENC exhibits a minimum at an optimal filter time τ, where the decreasing *thermal noise* term and increasing *shot noise* intersect, as illustrated in Figure 4.7. The optimal shaping time that minimizes the ENC maximizes the SNR but may reduces the desired bandwidth, so τ must balance SNR against the detector's speed requirements.

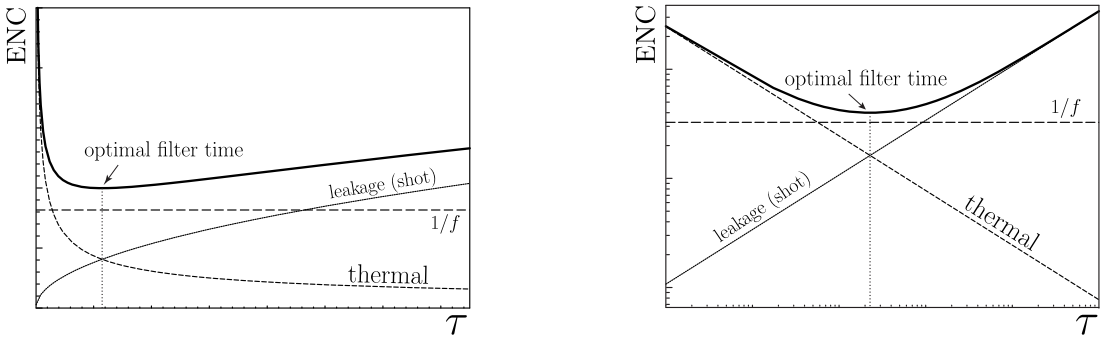

(a) Linear representation.

(b) Double logarithmic representation.

Figure 4.7: ENC as function of the filter (shaping) time τ in a typical detector-preamplifier-filter system. Adapted from [17, p. 795, fig. 17.65].

5. Measuring Efficiencies at PSI

Up to now, efficiency measurements conducted on HV-MAPS have primarily been of a phenomenological nature, focusing on the evaluation and comparison of the intrinsic performance characteristics of the sensors. Previous studies on bias settings (cf. [149]) and substrate resistivities (cf. [93]) did not systematically address charge deposition and collection as well as their connection to physics-motivated models, as this was beyond the focus of those works.

Observed variations were generally attributed to sensor-to-sensor differences or deviations in substrate resistivity, without an explicit attempt to isolate sensor-specific effects. At the same time, available simulations were limited in their ability to incorporate detector effects (cf. [7]), as these were not yet sufficiently understood and therefore inevitably not implemented. The aim of this thesis is to bridge this gap by systematically studying the influence of sensor thickness on CCE (**C**harge **C**ollection **E**fficiency), disentangling relevant detector effects, and comparing the observations to predictions from physics-motivated models.

5.1 Measurement Strategy

This measurement campaign aims to address two central questions: (i) How does the underlying charge deposition statistic (cf. Section 4.1) affect the CCE as it varies with the applied sensor bias, and to what extent can this be attributed to the depleted volume of the sensor? (ii) How does the CCE depend on the accessible detection thickness of the sensor? These two aspects are tightly coupled and therefore studied in conjunction.

For a purely depletion-driven process, the CCE is, to first order, determined solely by the depletion depth achieved for a given sensor (cf. Section 2.3.2). In such a scenario, two sensors with identical biasing and substrate resistivity are expected to yield comparable CCE, even if their total thickness differ. Any significant deviation from this assumption implies that the non-depleted volume contributes a non-negligible fraction to the overall CCE, with a possible scaling behavior linked to the available excess material.

To investigate these effects, MuPix10 sensors of varying thicknesses — ranging from 50 µm to 100 µm — are studied under bias settings from zero applied voltage[1], in equidistant steps[2], up to (approximately) their respective full depletion voltages (cf. Plot 3.1)[3]. In addition, sensors are examined in two resistivity ranges[4] : 200 Ω cm to 400 Ω cm and 10 Ω cm to 20 Ω cm.

Owing to the limited 5 bit ToT resolution of MuPix10 (cf. Section 3.5.1) and distortions introduced by its delay circuitry (cf. Section 3.5.2), ToT-based charge deposition studies are assessed to be unsuitable for this work (alternative HV-MAPS generations have been demonstrated to be more suitable; cf. [8]). Instead, the integrated *charge deposition spectrum* is evaluated. This representation, in terms of the CCE as function of the applied detection threshold, enables a systematic comparison of sensors differing in thickness, substrate resistivity, and bias voltage.

Several challenges complicate the measurement. First, the exact sensor thickness is uncertain, with nominal values specified within ±5 µm, and further production-related variations arising from the multilayer stack (see Section 3.2.1). As a result, the maximal usable active detection thickness must be estimated and validated against measurement results. Second, uncertainties in the substrate resistivity — as well as the measurement conditions (e.g., temperature) under which the vendor quotes these values — directly affect the depletion depth model used for

[1] This excludes the built-in voltage of a diode and the potential of the *n*-well, the latter being defined by the bias resistor to approximately *vdda*.
[2] This does not apply to MP10-T50-S20-1 (cf. Section 5.1.1), since the differing resistivity and the time scale of the testbeam campaign necessitate adjusted voltage steps.
[3] Bias configurations beyond −100 V can be achieved for lower resistivities, such as the "standard substrate" with 20 Ω cm.
[4] The resistivity ranges are specified by the manufacturer, ensuring that the sensors fall within this interval. This specification, however, should not be taken to imply that sensor-to-sensor variations extend across the entire range.

interpretation. Finally, detector-specific effects (cf. Chapter 4), including dispersion arising from electronic noise and non-linearities in the charge amplification, must be studied carefully and corrected for to obtain reliable results.

5.1.1 Preamble to Sensor Configuration

In this thesis, two different DAC configurations are employed (cf. Section A.5). The first configuration originates from [5] — a study that optimized the time resolution of MuPix10 — which is validated for a 100 µm thick sensor at the DESY testbeam facility [4], yielding efficiencies above 99 %. However, as will be shown in Section 5.4, this performance does not hold for all sensor thicknesses and low bias settings, particularly for ultra-thin sensors such as those with 50 µm thickness. While this does not diminish the informative value of the analysis, it complicates calibration procedures (cf. Chapter 6). It should be emphasized that this thesis presents the first in-depth analysis of a full-scale HV-MAPS with thickness below 100 µm, thus providing novel insights into the behavior of HV-MAPS at these thicknesses. In the following, this DAC configuration is referred to as *low-gain* setting.

From the corresponding testbeam studies, a modification is revealed in the design of the digital cell of MuPix10 compared to its predecessors: a change in the decoupling capacitance between the analog part (pixel) and digital domain. This adjustment is expected to have been introduced to reduce the noise coupling between analog and digital circuitry. However, it also caused a shift of the nominal working points and led to a reduction of the efficiency. Simulation studies[5] indicate that the relative voltage difference between the analog baseline (*BLPix*) and the digital baseline (*BLDig*) is the primary factor influencing the decoupling capacitance. This difference alters the gate capacitance (C_{gate}) of the input transistor, which effectively determines the decoupling capacitor (see Plot 5.1). In this context, a larger capacitance is desirable, as it allows more charge to be processed without introducing a signal bottleneck.

This observation opened a new operational regime, enabling a re-optimization of the DAC setting with a focus on large signals. This configuration is further referred to as the *high-gain* setting. A subsequent DESY testbeam campaign demonstrated that the *high-gain* setting successfully recovers the efficiency losses observed with the *low-gain* configuration (see [85, 86]). This improvement can be attributed to the higher gain and lower noise level, resulting in an increased SNR with this setting (cf. Chapter 7).

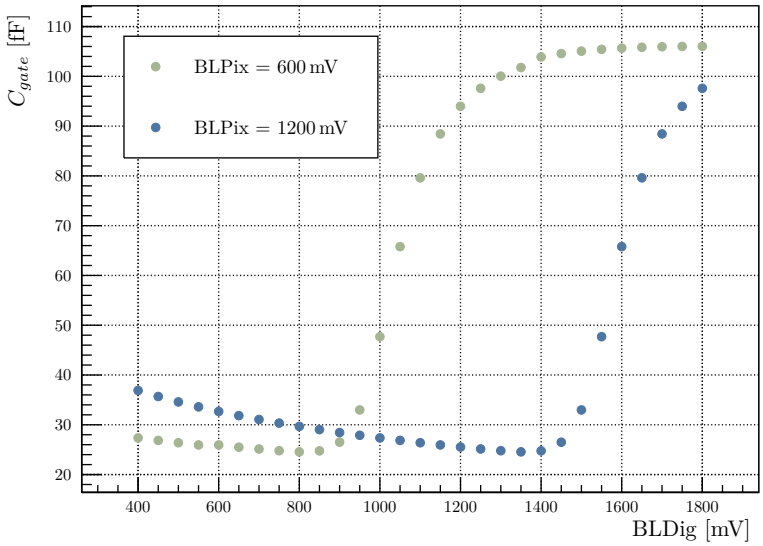

Plot 5.1: The gate capacitance (C_{gate}) of the input transistor determining the decoupling capacitor as function of the digital baseline (*BLDig*) for two levels of the analog baseline (*BLPix*) of MuPix10.

[5] This simulation was conducted by Benjamin Weinläder, whose contribution is gratefully acknowledged.

5.1.2 Sensor Nomenclature & Devices-Under-Test

The sensors employed in this thesis were handled in terms of sensor picking from a wafer, glueing to an insert PCB and wire bonded by various colleagues. This created an inconsistent naming scheme for the sensors, which sometimes are based on a wafer number and a position on the wafer, or a different internally used identifier. Hence, an unintuitive id, which is not descriptive of the sensor properties, may lead to confusion of the reader.

To avoid this confusion, a new nomenclature is introduced in Table 5.1, which is used throughout this thesis. The nomenclature is based on the following principles (separated into four parts by a hyphen):

1. Abbreviation of the sensor type (MuPix → "MP") followed by the chip's version number "10"
2. Sensor thickness identifier ("T") followed the expected thickness in [µm]
3. Sensor substrate resistivity identifier ("S") followed by the expected resistivity in [Ω cm]
4. Assignment of a unique, incrementing number to each sensor within the same thickness and resistivity category

The **D**evice-**U**nder-**T**est are produced with 200 Ω cm to 400 Ω cm ("S-300") and one sensor with 10 Ω cm to 20 Ω cm ("S-20") p-substrate resistivity wafers (see Sections 2.2.4 and 2.3.2). The former batch consist of two 50 µm thick sensor and one sensor for each of the thicknesses 60 µm, 70 µm and 100 µm. The latter batch consist of one 50 µm thick sensor. Note that the active detection thickness of the sensors is about 15 µm less than the stated total thickness (see Section 3.2.1 and fig. 3.6a) due to inactive layers for metal routing, electrical isolation, and passivation. The sensors are thinned in a DbG process by OPTIM WS with a tolerance of 5 µm on the thickness (see Section 3.2.3). Three different types of PCB cut-outs support the sensors, as shown in Figure 5.1, with Table 5.1 showing the association between each cut-out type and the sensors. These variations can affect the total material budget (PCB ∼ G10, cf. Table A.17) through their influence on scattering (see Section 1.1.5) and heat transport (cf. [150]), and thus the observed noise level.

ID	**Thickness** [µm]	**Resistivity** $\varrho_{substrate}$ [Ω cm]	**Original ID**	**PCB Cut-Out**
MP10-T50-S300-1	50	200 - 400	D1	round
MP10-T50-S300-2			W9-P12	rectangular
MP10-T50-S20-1	50	10 - 20	W18-P17	no
MP10-T60-S300-1	60	200 - 400	W1-P31	
MP10-T70-S300-1	70		T70-1-W15	
MP10-T100-S300-1	100		#100	rectangular

Table 5.1: Overview of the sensor nomenclature and DUT. The original ID is internally used to identify the sensor in the data base. The thickness of the sensors is specified with a tolerance of 5 µm by OPTIM WS. The corresponding PCB cut-outs are illustrated in Figure 5.1.

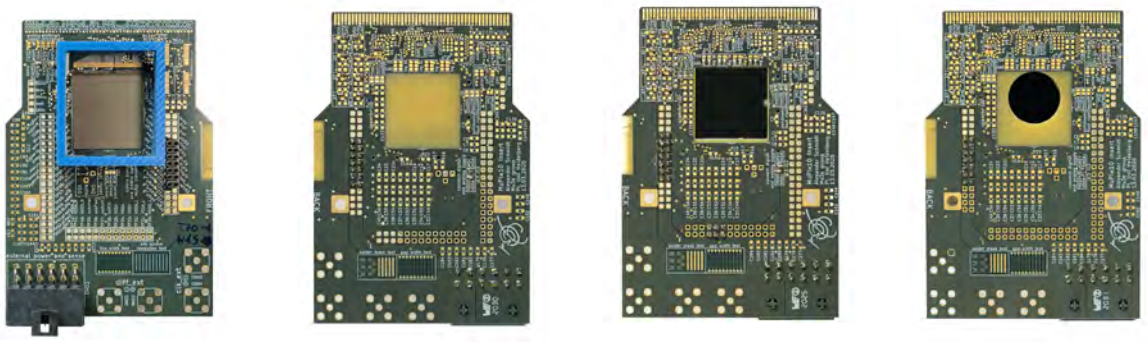

(a) Front side *(b)* No cut-out *(c)* Rectangular cut-out *(d)* Round cut-out

Figure 5.1: Photographs of MuPix10 sensors with different cut-outs configurations of the PCB.

5.2 Testbeam at the Paul-Scherrer Institute

The PSI in Switzerland operates the HIPA (**H**igh-**I**ntensity **P**roton **A**ccelerator) [151, 152], a facility specialized in the production of secondary meson and lepton beams with momenta up to a few hundred MeV c^{-1}. While the facility's original emphasis was on pion production, the current focus has shifted towards so-called (low momentum) *surface muons* for applications in particle physics experiments such as *Mu3e* (cf. Section 3.1) and muon spin spectroscopy studies [153].

Currently, the required high intensities are achieved using an intense proton beam of about 2.2 mA [151, 152] extracted from the main ring cyclotron. A planned upgrade to further increase the intensity under the HIMB (**H**igh-**I**ntensity **M**uon **B**eams) [76] initiative is scheduled for 2026 as part of the broader IMPACT (**I**sotope and **M**uon **P**roduction using **A**dvanced **C**yclotron and **T**arget technologies) project.

In the first acceleration stage, ionized hydrogen atoms attain a kinetic energy of ($\mathcal{T}$ =) 0.87 MeV [152, p. 1310, tab. 1] after passing through a Cockcroft-Walton accelerator. This is followed by a small ring cyclotron — Injector II — which boosts the protons to $\mathcal{T}$ = 72 MeV [152, p. 1310, tab. 1]. Subsequently, they are transferred to the main ring cyclotron, a 15 m diameter machine operating in continuous wave (CW) mode at a frequency of 50.6 MHz, where the protons are accelerated to their final energy of $\mathcal{T}$ = 590 MeV.

From here, secondary beams are produced by directing the high-intensity proton beam onto graphite (C) targets. For pion production (threshold $\sim$ 280 MeV [154, p. 2]), the relevant production channels arise from $pC \rightarrow (\pi^0, \pi^+, \pi^-) + X$ [154, p. 2]. Muons are subsequently obtained via the decay of short-lived charged pions $\pi \rightarrow \mu\nu$ (BR$\sim$ 99.9 % [14]). Electrons — or equivalently, positrons — may also originate from a similar charged pion decay channel but are helicity suppressed (BR$\sim 1.23 \times 10^{-4}$ [14]). Instead, they predominantly arise from neutral pion decays [155, p. 8, sec. III.D]. The π^0 decays primarily to two photons (BR$\sim$ 98.8 % [14]) or via the Dalitz decay $\pi^0 \rightarrow e^- e^+ \gamma$ with a BR$\sim$ 1.2 % [14]. These photons can interact with target material via pair-production, compton scattering or can knock out electrons (cf. Section 1.2), resulting in the generation of additional electrons. These meson and lepton beams are then transported to their corresponding experimental areas.

5.2.1 The πM1 Beamline

The HIPA beam is directed onto the production target *M* — a 2 mm thick rotating graphite[6] wheel — positioned to deflect the secondary beam 22° from the proton beam axis. The beamline layout is shown in Figure 5.2a, with a total path length of 23.12 m [158, p. 21, tab. 2.2][7]. Quadrupole magnets (*QTA*, *QTB*) focus the secondary beam, followed by a steering magnet (*SSY*) and dipole magnets (*ASM*) that bend it. Quadrupole *QSL11-14* create and correct momentum dispersion at the intermediate focus point, while *QSL15-18* focus the beam on the experimental target. Additionally, so-called "jaws" (*FS11-13*) can be used to limit the particle flux.

The beamline provides a high-momentum resolution pion beam of either polarity, with a momentum with 0.1 % [159][8] momentum accuracy and up to $\pm$1.5 % [155, p. 14, sec. V.B] acceptance (FWHM $\approx$ 2.9 % [159]). It primarily operates in the 100 MeV c^{-1} to 500 MeV c^{-1} range, with settings allowing to go as low as 10 MeV c^{-1}. Below 115 MeV c^{-1} the beam is dominated by electrons/positrons as pions decay near target *M* (see Figure 5.2b) [160, 161]. Up to around 200 MeV c^{-1}, the beam comprises electrons, muons, and pions, with pion fraction increasing at higher momenta because of the higher survival probability (cf. Table A.16, [162, p. 14, fig. 15]). Muons, produced isotropically from pion decays (cf. Section 5.2), are roughly 100 times less frequent at around 300 MeV c^{-1} [159] and contribute less to the beam. Above $\sim$280 MeV c^{-1}, protons may rarely appear in the beam composition but are negligible.

Detailed studies of the πM1 beamline can be found in [163, 157], with recent updates in [160, 161, 155]. The general beam properties are summarized in Section A.6.4 (cf. [158]).

[6] The graphite target has been rebuilt in 1985 [156] from a beryllium [157, p. 364, sec. 2] to a graphite target to handle the higher beam currents (cf. [155, p. 17, app., tab. IV]).

[7] "The difference between the path length listed here and the source [[159]] comes from more accurate survey distance [...]." [158, p. 21, tab. 2.2]

[8] " The beam flux measurements showed that the average momentum of particles passing through the channel agrees with the central set momentum to within 0.03 %." [155, p. 17, sec. VI]

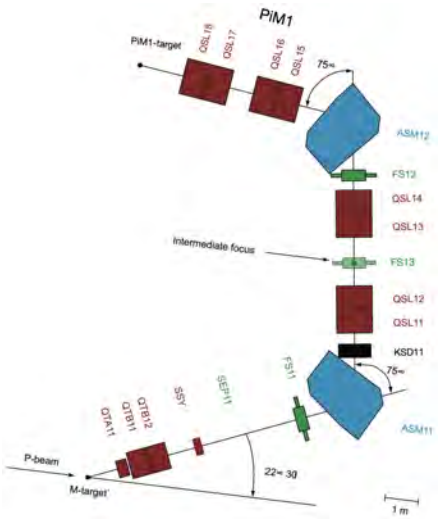

(a) Layout of the magnetic components of the πM1 beamline at PSI.

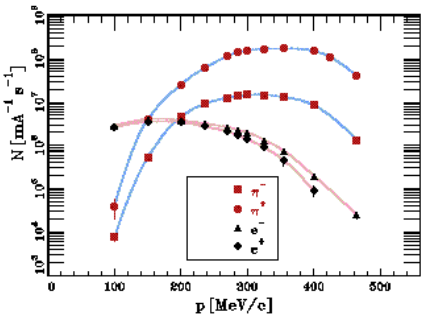

(b) The measured particle fluxes for the standard beam-line tune as a function of momentum with an uncertainty of 10 % at the peak of the yield curves. The flux of muons is 100 times smaller than the corresponding pion flux at momenta around 300 MeV/c, and falls more slowly than for the pions toward low momenta.

Figure 5.2: Overview of the πM1 beamline at PSI. Taken from [155, p. 3, fig. 2, 159].

5.2.2 The MuPix Tracking Telescope

A four-layer beam telescope (see Figure 5.3) is used for efficiency measurements, consisting of three tracking layers (layers 0, 2 & 3) and the DUT (layer 1), complemented by scintillating detectors for timing reference. The tracking layers are interchangeable and utilize the latest HV-MAPS at the time of the measurement — 100 µm thick MuPix10 sensors. Each sensor is glued and bonded to an *insert* PCB, which connects to the *MuDAQ Motherboard*. The *MuDAQ Motherboard* is an interface board (more details below), which links via an SCSI-3 connection to an HSMC-to-SCSI-3 adapter card; handling the required I/O (**I**nput/**O**utput) connections for steering and reading out the sensors. The adapter card also hosts four inputs converting discriminated signals from the scintillating detectors from TTL to LVDS.
The system is controlled by a Stratix® IV GX FPGA development board [164], operating at 500 MHz, with the discriminated signals sampled by a TDC featuring a corresponding 2 ns LSB resolution. All four inputs can be stored individually (*OR*-mode) or combined in *AND*-mode.

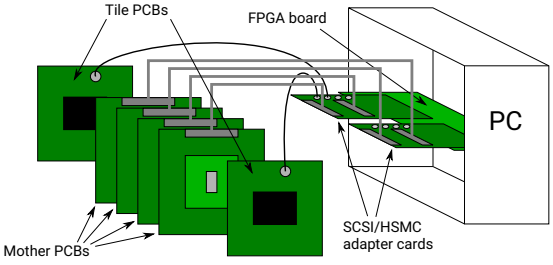

(a) Schematic of the nominal MuPix telescope setup. Taken from [149, p. 81, fig. 5.6].

(b) Photograph of the MuPix telescope setup at PSI. The telescope is mounted on a rail system to allow for easy movement.

Figure 5.3: The MuPix telescope setup.

Data-Acquisition System

The *MuDAQ* system is custom-built to characterize HV-MAPS in the (Lab) (**Lab**oratory) and at test beam facilities. Communication between sensors and the readout computer is handled by the FPGA (cf. [95]), controlled via a Qt-based GUI (cf. [93]).

Data words send from the sensors' LVDS links are received by the FPGA, 8 bit/10 bit decoded, deserialized and unpacked. The Gray-encoded timestamps (cf. Section 3.5.1) are optionally decoded — a requirement for online hit sorting[9]. The data is organized in *hit blocks*, each containing hits from one readout cycle, with one hit per EoC. Additionally, each *hit blocks* is equipped with a 48 bit timestamp running at the nominal 500 MHz, enabling offline global timestamp reconstruction. Reference timestamps (64 bit) are handled by similar *trigger blocks*.

These blocks are transferred to the host computer via PCIe using DMA (**D**irect **M**emory **A**ccess). Dedicated threads handle incoming data packages, frame construction, file writing, and online monitoring. The *frame packer* assembles hit blocks with similar timestamps into complete telescope frames. These frames are stored for offline analysis on hardware storage and forwarded to the online monitoring system, where data is processed in "real time" to provide immediate information on hit distribution, ToA, ToT, and more.
Figure 5.4 illustrates the readout chain. For more detailed information, see [95] and [93].

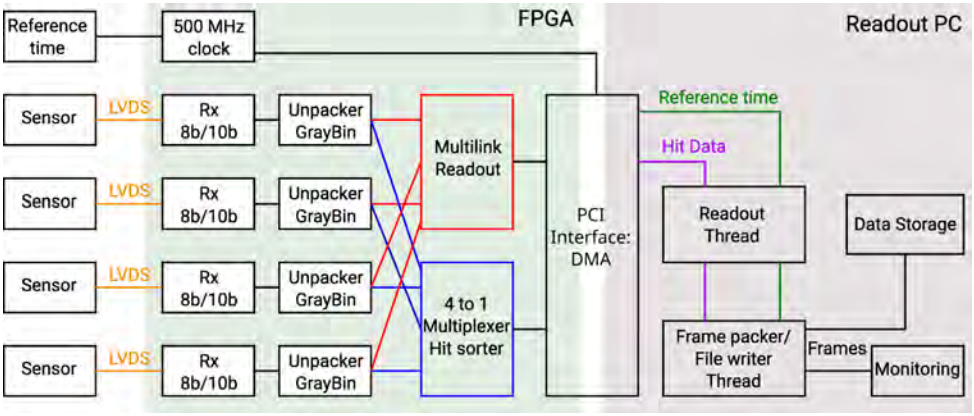

Figure 5.4: MuDAQ readout scheme. Based on [93, p. 64, fig. 6.4].

Tracking Layer Design

A sensor layer, including the *insert* PCB and *MuDAQ Motherboard*, is shown in Figure 5.5b. The *MuDAQ Motherboard* is mounted on a custom aluminum frame with two micrometer actuators for fine x- and y-axis alignment (z is along the beam). It provides the I/O interface to the FPGA and supplies high and optionally low voltages to the sensor. For 10, low voltages are supplied via a dedicated *Molex*® connector on the *insert* PCB using voltage sensing to compensate for voltage drops. Single-ended test inputs and outputs are available; *HitBus* and *Injection* signals are accessible via *LEMO*® connectors on the *MuDAQ Motherboard*, while *AmpOut* and *TestOut* are accessed through the *insert* PCB. When the DUT is in use, on-chip signals can be monitored after setup without altering telescope alignment to determine sensor power conditions and finely tune voltages (cf. Sections 3.7, 3.7.1 and 3.7.2)

[9] Link multiplexing and online hit sorting has not been implemented for the MuPix10.

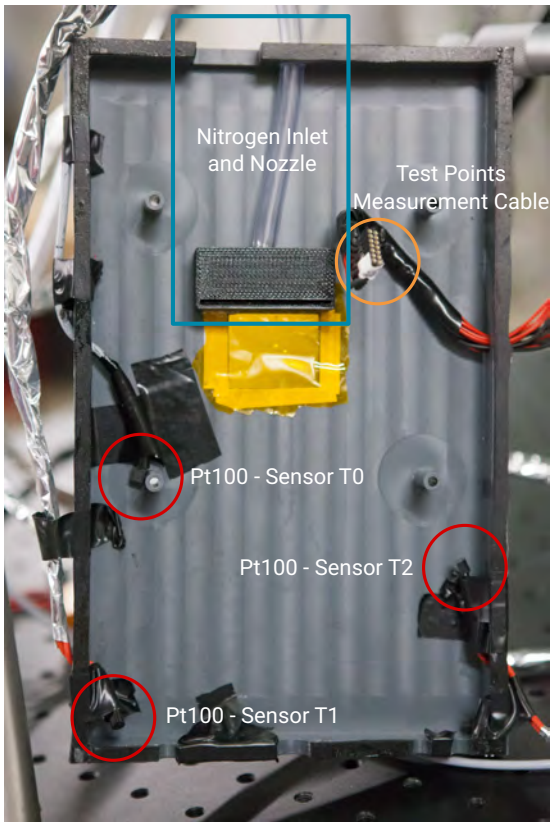

(a) Top half-shell of the cooling box. The PT100 sensors are circled in red, while the orange circle highlights the connection cable for measurement points on the DUT *insert* PCB (see Figure 5.5b). The nitrogen gas inlet and nozzle for sensor cooling are framed in blue.

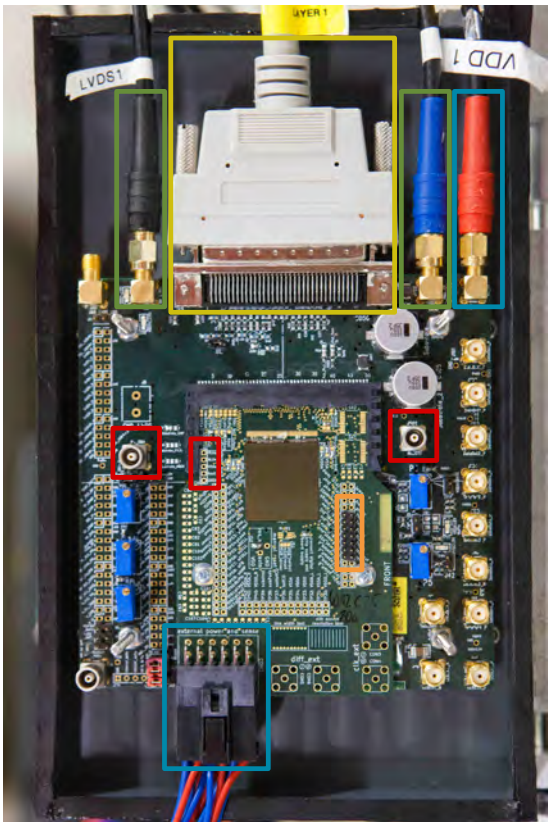

(b) Bottom half-shell of the cooling box with *MuDAQ Motherboard* and an *insert* PCB carrying a MuPix10. Features are highlighted by colored frames: orange indicates *TestOut*, red marks the connection points for *AmpOut*, *HitBus*, and *Injection*. blue shows the HV (SMA) and low voltage (*Molex*®) connections for sensor biasing, while green (for MuPix10) is exclusively used to power the *MuDAQ Motherboard*. yellow frames the SCSI-3 connection to the HSMC adapter card.

Figure 5.5: Both half-shells of the cooling box of the DUT.

5.2.3 Measurement Conditions

The beam telescope is positioned in the focal area of the πM1 beam line (cf. Section 5.2.1). Tracking layers equipped with 100 µm MuPix10 sensors, operated at a reverse bias of −100 V and under the same DAC configuration as the DUT, have demonstrated efficiencies exceeding 99 % [4]. Following the initial setup (cf. Section 5.2.2), the only modification to the telescope was the replacement of the DUT.

The spacing between sensor layers ranges from 6 cm to 8 cm. To first order, this geometry does not correspond to a weak mode in tracking; however, it detoriates resolution due to multiple Coulomb scattering (cf. Section 1.1.5), which in turn broadens the association window of DUT hits to particle tracks (cf. Section 5.3). For all measurements, the beam was configured to 350 MeV c^{-1} with a positive polarity — a selection for positively charged particles. It is adjusted once at the beginning of the testbeam campaign to cover the full sensor active area and set to a desired particle rate, remaining unchanged thereafter to ensure consistent conditions. As discussed in Section 5.2.1, the beam is expected to mainly consist of pions, with minor contributions from muons and electrons/positrons, which must be accounted in the analysis (see Section 5.1). Even though the beam composition varies, the measured charge deposition spectrum is not expected to exhibit observable differences among the particle species, due to the limited separation power for such low material thickness in silicon and particle momenta at or above the MIP regime (see Plot 5.2).

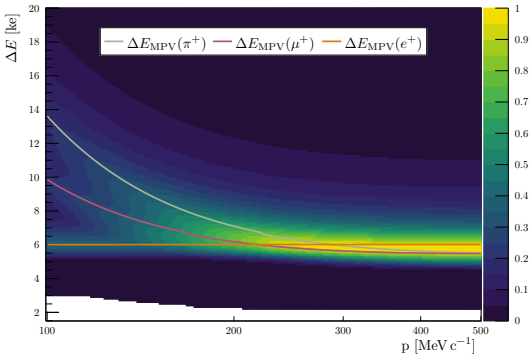

(a) Normalized Landau distributions for a 100 µm (85 µm **si**licon) sensor with MuPix10 for equal occurrence of e^+, μ^+ & π^+ as a function of the particle momentum.

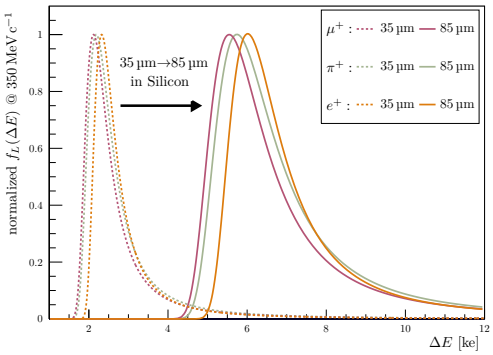

(b) Normalized Landau distributions in 100 µm (85 µm **si**licon) and 50 µm (35 µm **si**licon) thick MuPix10 sensors for a 350 MeV c^{-1} beam of e^+, μ^+ & π^+.

Plot 5.2: Normalized Landau distributions calculated with Equation 4.14, assuming equal occurrence of beam particles in πM1. Corresponding data are presented in tables A.16 and A.17.

Sensor Cooling & Temperature Stability

Although MuPix10 sensors typically require no active cooling, thinned devices (< 100 µm) may undergo thermal runaway of the leakage current near full depletion voltage (cf. Section 3.2.3). To ensure stable operation, the DUT is mounted inside a cooling box (see Figure 5.5), where gaseous nitrogen is directed from the sensor top (highest pixel row address) along its periphery, thereby preventing bond damage and removing heat from the dominant peripheral region without affecting the central area. The nitrogen is not pre-cooled, since its flow already stabilizes the thermal environment and removes heat from the sensor.

Direct on-chip temperature measurements were not performed during the testbeam. Instead, three Pt100 sensors inside the cooling box monitored the ambient temperature, logged via a SCS2000 [165] with a Pt100 slot card. Communication is handled through the MSCB (**M**idas **S**low **C**ontrol **B**us) [166], integrated into the *MuDAQ* (cf. Section 5.2.2). As shown in Plot 5.3, stable environmental conditions are achieved, with minor fluctuations. This, however, indicates the stability of the cooling environment rather than the absolute stability of the sensor's own temperature.

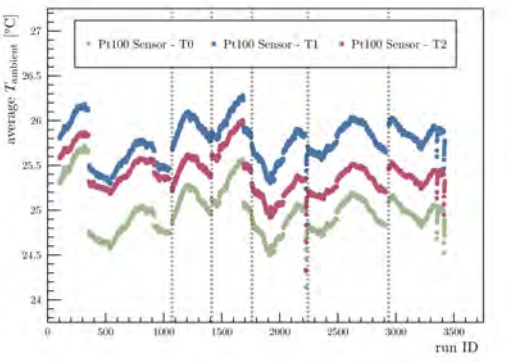

(a) Average ambient temperature as function of the run ID. The dashed vertical lines indicate a change of the DUT.

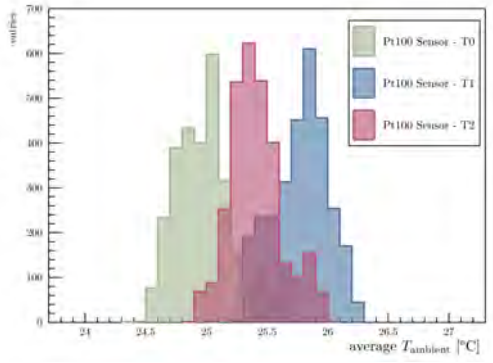

(b) Distributions of the averaged ambient temperature. The dispersion and deviations between sensors is within the accuracy expected of a Pt100.

Plot 5.3: Measured ambient temperature inside the cooling box (see Figure 5.5) with three different Pt100 sensors. The temperature is averaged per run ID.

Powering

The MuPix10 requires three distinct low-voltages (LV) and a reverse-bias high voltage (HV) for the sensor diode. The same powering scheme is applied to all sensors: *vdda* and *vddd*, as well as *gnda* and *gndd*, are electrically shorted on the *insert* PCB (cf. Section 5.2.2), while *vssa* is generated on-chip (cf. Section 3.7.1). Consequently, a single LV per sensor is sufficient for operation, supplied by a multi-channel DC power unit. In this work, the R&S® HMP4040 [167] is used, which provides low-ripple outputs and supports remote sensing to compensate voltage drops along the power distribution path (though not directly at on-chip level).

The supply voltage levels are individually adjusted to meet the on-chip requirements imposed by the applied DAC configuration settings (Section A.5.1). An overview of both the applied and internally measured voltage levels for the different configurations used throughout this thesis (cf. Section 5.1.1) is provided in Table A.12.

The reverse-bias voltage is supplied by two custom-designed HV source units[10] developed for the *Mu3e* experiment: one dedicated to the DUT and one serving the three tracking layers. Each unit provides four output channels, delivering the same output voltage while allowing independent monitoring of both voltage and current. Communication is implemented via MSCB [166], which is integrated into the *MuDAQ* (cf. Section 5.2.2) and executed in a dedicated thread for logging and control purposes.

[10] Two different versions are employed throughout the measurements presented in this thesis. The first, an older model, provides output voltages up to −120 V and is utilized for all measurements within this range, whereas the second is capable of reaching voltages up to −150 V and is exclusively employed for measurements on MP10-T50-S20-1 requiring voltages beyond −120 V (cf. Section 5.1.2).

5.3 From Data to Efficiency

To determine the CCE for all DUTs and configurations, the modular, open-source testbeam analysis framework `Corryvreckan`[11] [168, 169] is employed. This platform provides a unified base for data processing and analysis, which reduces the risk of systematic errors from closed or proprietary code.

Corryvreckan performs all analysis steps on an event-based, time-ordered data structure. Since the data are collected asynchronously (cf. Section 3.6.2) and no FPGA-based online sorting was available, the raw data are stored in an unsorted time sequence. The framework operates in a clocked mode, utilizing its `Metronome` module to sort data by assigning them to events of specified duration and global time. A duration of 100 µs is chosen as a compromise between minimizing the edge effects of overlapping events and ensuring a sufficient number of hits per time window for processing. To avoid potential edge effects, hits occurring within 420 ns of a time window boundary are discarded from the subsequent analysis.
The full analysis chain is applied to each run and consists of the following steps:

1. `EventLoaderMuPixTelescope`: Unpack raw data, creates hit information, and assigns hits to events
2. `Clustering4D`: Group hits into cluster objects
3. `Tracking4D`: Identifies track candidates and reconstructs tracks
4. `DUTAssociation`: Associates clusters with tracks
5. `AnalysisDUT`: Analyzes DUT performance on track-associated data
6. `AnalysisEfficiency`: Evaluates the overall efficiency on track-associated data

At each stage, relevant selection cuts are applied to obtain a "clean" analysis data set. The analysis data for corresponding run IDs — for DUTs of identical configuration and detection threshold — are merged and processed to produce the final results. The key steps are detailed below.

5.3.1 Clustering

Clusters form as particles traverse the sensor and deposit charge across adjacent pixels (cf. Section 4.2.4). At pixel edges, charge is typically shared between two pixels, producing up to two hits (depending if charge exceeds detection threshold). At pixel corners, charge may spread to up to three neighboring pixels, depending on the particle's incident angle, sensor thickness and the amount of deposited charge (see Figure 5.6).

Occasionally, "moderately" energetic δ-electrons (> 100 keV, cf. Section 1.1.3) or slow, heavy charged particles can deposit charge across multiple pixels (> 4 pixel), creating elongated or large clusters distinct from typical topologies[12].

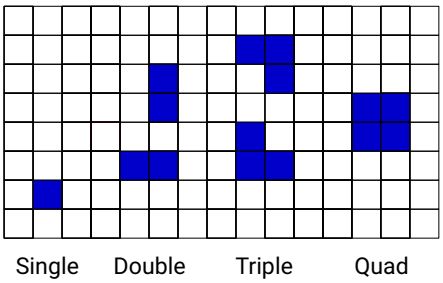

Figure 5.6: Typically cluster types topologies. Taken from [80, p. 95, fig. 5.24].

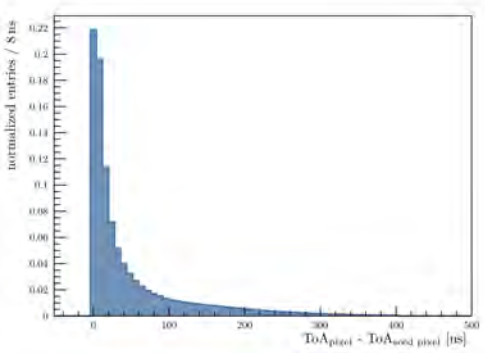

Plot 5.4: Exemplary cluster pixel ToA-latency distribution respective to the *seed pixel* of a 100 µm MuPix10.

[11] Modifications in the dedicated fork concern (i) the event loader for HV-MAPS, adapted for ToA and ToT determinations of the hit object and supplemented with developer-specific histograms, and (ii) other modules, involving histogram scaling and the inclusion of additional histograms.
[12] These events are expected to produce a distinct time evolution signature within the sensor's time resolution capabilities.

The clustering algorithm searches for directly neighboring hits within an event, applying an absolute timing cut — ranging from positive to negative differences — on the relative latency between the ToA timestamps of hits. This cut ensures that only hits within a specified time window (400 ns in this analysis, see Plot 5.4) are clustered together. Too-narrow timing cuts can split genuine clusters, increasing the risk of misidentifying particle tracks (double counting of "real" events), raising the fake track rate. Conversely, too-wide cuts can merge unrelated hits — a negligible effect at low beam rates (< 200 kHz for this testbeam campaign), aside from some spatial resolution degradation. Additionally, since the 2-threshold mode is employed for determining ToA (cf. Section 3.5), varying detection thresholds on the DUT do not influence the chosen time cut, as the overall latency distribution remains narrower (cf. Section A.1.3).

Clusters are built from a *seed pixel* — either the one with the largest charge deposition (highest ToT value) or the earliest hit (lowest ToA value) — and any secondary hits emerging from charge sharing. Secondary hits contribute to the calculation of both the cluster's center position and total deposited charge (sum of individual pixel ToT values). Here, the geometric weighting is used for the center position, and the earliest hit defines the *seed pixel*, as pixel-to-pixel variations in ToT preclude reliable charge-based identification before calibration (cf. [8]).

At high detection efficiencies (> 99 %), cluster size generally decreases with rising detection thresholds as lower charge contribution hits are excluded. Near the efficiency drop-off (< 99 %), the mean cluster size and its variance can increase because only larger charge deposition events are detected, outliers become more pronounced, and the likelihood of charge sharing rises.

5.3.2 Tracking

In this testbeam campaign, tracking is performed on three layers — excluding the DUT to avoid bias. The relatively high material budget — compared to the beam momentum of 350 MeV c^{-1} — causes significant multiple scattering, which in combination with the sparse number of tracking layers degrades the achievable spatial resolution (cf. Sections 1.1.5 and 5.2.3).

Two tracking methods were considered: a simple linear fit (offset and slope in x and y) and a GBL (**G**eneral **B**roken **L**ine) fit [170] that accounts for scattering on each layer. GBL was tested but found unsuitable, as the geometry (layer spacing, Section 5.2.3), together with the low beam momentum and non-uniform material budget (notably due to PCB cut-outs, Section 5.1.2), causes the fit to be dominated by scattering, which is overestimated in this configuration. Due to time constraints and integration effort, a solely scattering-based method was not pursued. Since the GBL (**G**eneral **B**roken **L**ine) fit offered no advantage in this scenario, the linear tracking method was chosen for its simplicity.

As both tracking methods yield only two NDF (**N**umber of **D**egrees of **F**reedom), the corresponding χ^2-distribution peaks at approximately zero. Because scattering is inadequately modeled, the expected χ^2-statistic deviates from the standard form, introducing non-centrality (cf. Section A.3.7), which complicates the selection of an appropriate χ^2-cut.

To mitigate this, a dedicated study of track χ^2 versus the DUT efficiency was performed[13] with a 100 µm DUT known to be highly efficient (> 99 %, see [4]). Efficiency remained flat below a χ^2-cut threshold (no correlation), then dropped sharply beyond, indicating the presence of "fake" tracks. This allowed defining an adequate χ^2-cut that preserves both efficiency and overall track statistics.

Alignment & Resolution

In principle, an alignment of the setup is only required when a DUT is changed, as the relative position of the layers remains fixed. For each alignment, a dedicated data set is used[14], which is excluded from the analysis to avoid bias. The iterative alignment procedure begins with a rough alignment using the `PreAlignment` module, followed by a precise spatial and rotational alignment of the tracking layers with the `AlignmentTrackChi2` module, which centers the spatial (biased) residuals around zero relative to the track and minimizes the corresponding RMS (see Plot 5.5). It concludes with a similar module (`AlignmentDUTResidual`) applied to the DUT, using the DUT's cluster position for alignment with respect to a track.

Environmental factors such as ambient temperature variations and mechanical instabilities (e.g. interconnects and actuators) can cause relative spatial (and rotational) misalignments (cf. Plots 5.5a and 5.5b). This makes a

[13] The run used for the χ^2-cut study is excluded from the main analysis. This study is repeated once per configuration to verify that the cut value is not set too high for other configurations.

[14] In this scenario, tracking can be conducted using all four layers without introducing a bias.

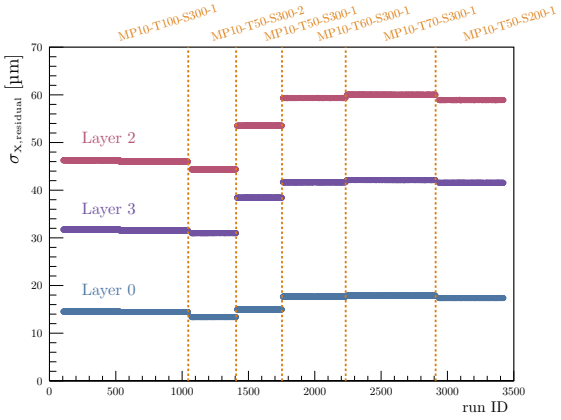

(a) Standard deviation (biased) of the residual distributions in X-plane of the tracking layers as a function of run ID.

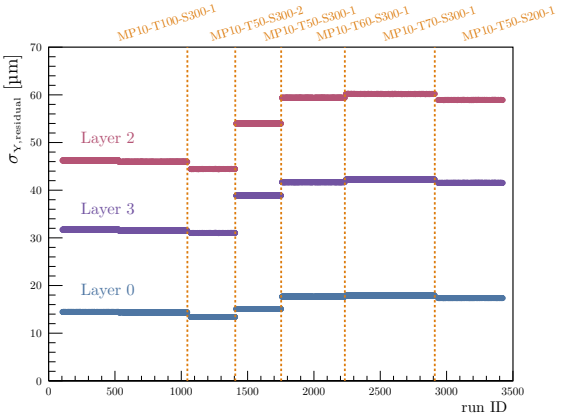

(b) Standard deviation (biased) of the residual distributions in Y-plane of the tracking layers as a function of run ID.

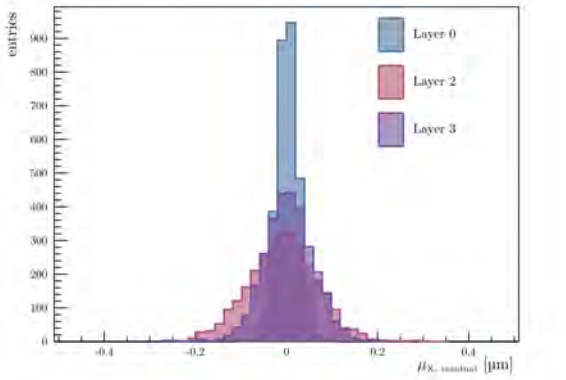

(c) Distribution of mean values of the residual distributions in X-plane of each run ID for all tracking layers.

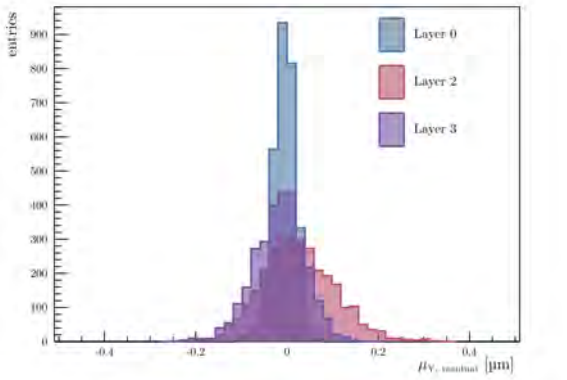

(d) Distribution of mean values of the residual distributions in Y-plane of each run ID for all tracking layers.

Plot 5.5: Overview of tracking layer residuals over all run IDs.

single alignment insufficient for the entire data-taking period. Therefore, a spatial offset correction in x and y (without rotational corrections) is applied for each run across all tracking layers to reduce the effect (see Plots 5.5c and 5.5d).

Additionally, a simple latency offset alignment of the tracking layers relative to the reference plane is performed by correcting the mode of the timing residual distribution of each layer[15]. This timing misalignment may occur due to sensor-to-sensor variations and reset signal delays[16].
For both secondary alignment steps — spatial and timing — performed on each run, the DUT is excluded to avoid introducing bias.

Beam Profile & Dispersion

The πM1 beam profile, typically focused to a small spot of several millimeters, is adjusted to cover the entire active area of the DUT to study the overall sensor performance. Although a perfectly uniform coverage could not be achieved, the beam configuration is sufficient for the intended studies, with the beam spot positioned in the upper right corner of the sensor. Due to timing constraints during a tight testbeam schedule, this configuration was not altered.

Transition regions at overlapping boundaries of the PCB and sensor are omitted from the analysis (see Plot 5.6a).

[15] No specialized position-dependent timing corrections or time-walk corrections (cf. Section 3.5.1) have been applied (cf. [5]).
[16] In the *MuDAQ*, reference clocks and reset signals are synchronized to the 500 MHz clock of the FPGA, which potentially introduces a phase offset in multiples ($n = 1, 2,$ or 3) of 8 ns at the start of a run.

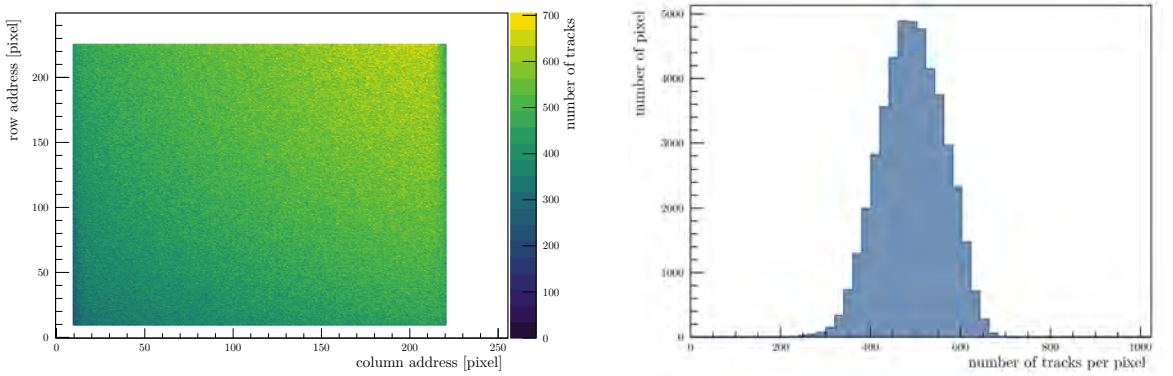

(a) Track map projected on the DUT plane.

(b) Track distribution within RoI.

Plot 5.6: Exemplary track map and distribution for the 100 µm DUT (MP10-T100-S300-1) plane.

These regions are excluded because scattering effects tend to accumulate across layers, complicating position-dependent corrections.

Track Statistic per Run

It is essential to account for the varying statistics across the sensor induced by the non-uniform beam profile in the analysis. The primary focus is on regions with higher statistics, with diminishing emphasis as one moves away from these areas. Given the limited per-pixel statistic per run data set (see Plot 5.6b), multiple runs of identical configuration are combined to enhance the statistical significance. This becomes more pronounced in the subsequent calibration procedure, which redistributes the track statistic according to the response of individual pixels.

5.3.3 Efficiency

To determine the hit efficiency, each track is tested for association with a cluster on the DUT. A cluster is considered associated if its centroid lies within a defined spatial "association window", represented by an ellipse around the predicted track position on the DUT (see Figure 5.7), and additionally satisfies an absolute timing window around the track time.

Let N be the total number of tracks (number of "independent trials") and m the number of tracks associated with a DUT cluster (number of "successes"). The probability of success per trial is the efficiency ϵ, corresponding to the binomial process:

$$\mathrm{PDF}_{\mathrm{binomial}}(m \mid N, \epsilon) = \frac{N!}{m!(N-m)!} \cdot \epsilon^m \cdot (1-\epsilon)^{N-m} \tag{5.1}$$

The log-likelihood function[17] of the unknown efficiency parameter ϵ, gives rise to estimator[18] of the efficiency $\hat{\epsilon}$ [171, p. 1, eq. 2 & 3][19]:

$$\ln(L(\epsilon)) = m \cdot \ln(\epsilon) + (N-m) \cdot \ln(1-\epsilon) \quad \xrightarrow{\frac{\partial \ln(L(\epsilon))}{\partial \epsilon} = 0} \quad \hat{\epsilon} = \frac{m}{N} \tag{5.2}$$

The efficiency (and associated statistics) defined by ϵ are assigned according to the track position[20] pointing on the DUT pixel matrix[21]. For a more detailed discussion on efficiency handling, refer to Section A.3.7.

[17] A PDF $f(x \mid \lambda)$ and its likelihood function $L(x \mid \lambda)$ share the same algebraic form; the PDF treats λ as fixed and views x as variable, whereas the likelihood treats λ as the parameter to be estimated as x is given. cf. [111, p.20]

[18] The likelihood is maximized for the estimator $\hat{\epsilon}$.

[19] The term independent of ϵ, namely $\ln\left(\frac{N!}{m!(N-m)!}\right)$, is omitted since it does not affect the parameter estimation.

[20] No cluster hit position on the DUT is used for efficiency assignment to avoid bias; only the track position is available for inefficient events without associated clusters.

[21] This procedure is performed per run, and results are aggregated into a two-dimensional efficiency object (e.g. `ROOT::TEfficiency` [172, 173]) mapped over the local coordinates of the DUT pixel matrix.

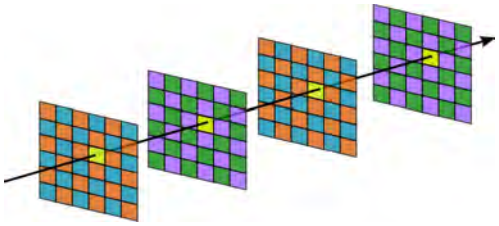

(a) Particle traversing the four layer-telescope. A straight line approximates the 2 dimensional hit information (+ layer distance) in the 3 dimensional space. Taken from [80, p. 93, fig. 5.21].

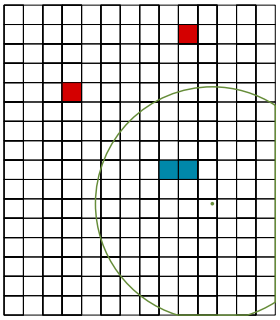

(b) Matching radius (association window, green) on the DUT plane. Potentially all cluster with center position (blue) within the ellipse are considered for association. Adapted from [80, p. 95, fig. 5.23].

Figure 5.7: Overview of tracking and matching on the DUT plane.

Combining & Handling Efficiency Data

The total hit efficiency of different data sets — statistics of individual pixels or multiple runs — is combined as[22]:

$$\epsilon_{hit} = \frac{\text{\#tracks w/ associated cluster}}{\text{\#tracks w/ associated cluster} + \text{\#tracks w/o associated cluster}} = \frac{\sum_i m_i}{\sum_i N_i} \tag{5.3}$$

Although this improves statistical significance, it does not account for potential biases arising from the limited tracking resolution, which introduces inaccuracies between the reconstructed track and the associated DUT cluster position. Additional effects such as spatially dependent pixel gain, baseline variations, and smearing caused by noise or fluctuations in the effective detection threshold may further influence the results.

Since statistics are assigned according to the track position on the DUT pixel matrix, efficiency can be evaluated across different Regions of Interest (RoIs). Incorporating the detection threshold together with a calibration linking energy to threshold level (cf. Chapter 6) allows for a more accurate characterization of the efficiency. The CCE curve is then derived by combining efficiency statistics within each RoI over the range of detection thresholds, providing a clearer picture of detector performance across different energy ranges and sensor configurations.

Region of Interest

The MuPix10 can be divided into nine distinct inner pixel regions — neglecting even-odd column address effects — and four outer regions, as illustrated in Figure 5.8. On one hand, the division is determined by readout in column space (cf. Section 3.2) and on the other hand by the signal line routing scheme (cf. Section 3.4). The four corner pixels — each representing a unique case — are not directly comparable to other regions and are therefore omitted from all analysis steps.

For efficiency studies using testbeam data, the mechanical overlaps of sensor layers and transition regions with additional scattering material influence tracking (see Section 5.3.2). To mitigate these edge effects, the outermost five pixels of the sensor are excluded from the analysis. Additionally, pixels that do not provide ToT information (column address > 231, cf. Section 3.2), including an additional safety margin of five pixels for layer overlap, are also excluded. The upper pixel rows (row address $\gtrsim$ 230) are partially covered with additional PCB material to provide mechanical stability for sensors with cut-out, applicable to all tracking layers and some DUTs (cf. Section 5.1.2). The excluded regions are likewise omitted from the analysis. The remaining active area thus comprises a pixel matrix of 210×215 pixel, spanning column addresses 10 to 220 and row addresses 10 to 225, as illustrated in the track map distribution Plot 5.6a.

At later stages of the analysis, smaller subregions of the sensor are analyzed to account for spatial variations in efficiency and calibration. For calibration purposes, several small RoIs of 20×20 pixel (see Table 5.2) are selected (cf. Chapter 6), providing a balance between sufficient statistics and calibration time.

[22] No weighting of data sets is performed.

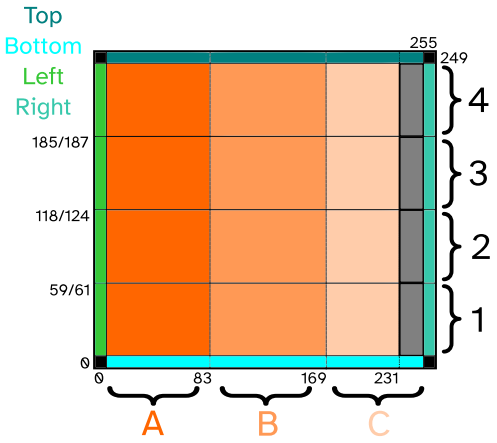

Figure 5.8: Spatial segmentation of the MuPix10 pixel matrix. Edge pixels appear in green and blue shades, corner pixels in black. Matrices A-C (orange shaded) are each divided into four routing segments. Columns in Matrix C with addresses > 231 are shown in grey. Efficiency analysis uses only orange regions; detector response includes all except corner pixels.

row \ column	10-29	100-119	200-219
10–29	A1	B1	C1
70–89	A2	B2	C2
130–149	A3	B3	C3
190–209	A4	B4	C4

Table 5.2: Definition of RoIs for the MuPix10. Segment naming scheme follows a combination of matrix (A, B, C) and routing segment (1, 2, 3, 4) (cf. Figure 5.8). Each RoI covers a pixel area of 20×20 pixel.

5.4 Testbeam Campaign Results

In the course of this testbeam campaign, various threshold scans were performed under different high-voltage biasing conditions (U_{HV}) for each DUT sensor. Within each threshold scan, emphasis was placed on the lower threshold regime — corresponding to effective threshold levels closer to the baseline — where the hit efficiency curve exhibits the most pronounced features changes related to the charge deposition characteristics under study. Due to time constraints during the testbeam, the lowest threshold regime was scanned in fine steps of 1 LSB, followed by intermediate steps of 2 LSB as the efficiency dropped significantly, and finally by coarse steps of 5 LSB to capture the tail of the efficiency curve. The same threshold step pattern was applied to all scans and sensors to ensure comparability of the results.

For all sensors of the same resistivity category (200 Ω cm to 400 Ω cm), the applied reverse bias voltage U_{HV} was varied in an identical manner to allow for direct comparison of the analysis results between different sensors. In retrospect, more detailed bias steps in the lower regime (e.g. below −20 V) would have been beneficial to better apprehend the evolution of the depletion zone, where changes in detector capacitance, signal amplification, and charge collection efficiency are most pronounced. The chosen bias steps thus represent a compromise between the available beam time and the need to cover a wide range of bias voltages to observe the overall sensor behavior.
An overview of all measured bias configurations for each sensor is provided in Table 5.3.

Sensor ID	Reverse bias voltage U_{HV}	
MP10-T100-S300-1	0 V to −20 V (5 V steps)	−20 V to −100 V (10 V steps)
MP10-T70-S300-1		−20 V to −70 V (10 V steps)
MP10-T60-S300-1		−20 V to −40 V (10 V steps)
MP10-T50-S300-1		—
MP10-T50-S300-2		—
MP10-T50-S20-1	0 V to −100 V(25 V steps)	−120 V to −130 V (10 V steps)

Table 5.3: Overview of all measured bias configurations for each DUT.

5.4.1 Impact of the Reverse Bias on the Efficiency Curve

The shape of an efficiency curve — that is, its progression as a function of the applied detection threshold U_{Th} — can be influenced by various factors, causing significant deviations from the underlying (idealized) integral of the energy deposition distribution (see Chapter 4). Factors such as electronic noise and threshold dispersion broaden the efficiency curve, while fluctuations and saturation effects in the gain stage of the pixel electronics (see Section 3.3.1) introduce non-linearities. These effectively compress the upper tail of the energy distribution towards lower values, causing the efficiency curve to appear more Gaussian-like and increasingly symmetric as a larger fraction of the charge signals are processed in a non-linear regime.

These effects also depend on the applied reverse bias voltage U_{HV}, which not only affects the depletion depth directly and hence supposedly the charge collection, but also the shaping of the analog signal pulse. The variation of the detector capacitance with the bias modifies the operating point of the in-pixel CSA, thereby altering the effective signal response. In addition, spatial dependent effects introduced by the sensor powering scheme and by the routing of the analog signal lines (see Section 7.2.2) — introducing capacitive coupling between neighboring lines affecting the signal pulse shape — can lead to non-uniform efficiency across the pixel matrix.

Together with the absence of a scientific meaningful threshold scale, these aspects complicate a direct theoretical description of the efficiency curves using an analytic straggling function. To obtain an initial estimation, a simple empirical model based on a modified error function is employed. This function introduces a skew by using a hyperbolic tangent term to account for the non-Gaussian behavior and a tail towards higher threshold values in the data. Thus an approximation of the integral of the landau distribution convoluted with the normal distribution is given by [174, p. 1873, eq. 2 & 3][23]:

[23] In comparison to the original formulation in [174, p. 1873, eq. 2 & 3], the saturation value for the efficiency has been fixed to one.

$$\epsilon_{hit}(U_{\text{Th}} \mid , M_{U_{\text{Th}}}, w, \mathit{s}) = \frac{1}{2} \cdot \left\{ 1 - \text{erf}\left(\frac{U_{\text{Th}} - M_{U_{\text{Th}}}}{\sqrt{2} \cdot w} \cdot \left[1 + 0.6 \cdot \tanh\left(-\mathit{s} \cdot \frac{U_{\text{Th}} - M_{U_{\text{Th}}}}{\sqrt{2} \cdot w} \right) \right] \right) \right\} \tag{5.4}$$

where $M_{U_{\text{Th}}}$ denotes the 50 % (median) threshold crossing of the efficiency curve, w represents the width of the normal distribution, and s is a skew factor of the hyperbolic tangent term. Plot 5.7 presents an overview of the hit efficiency measured as function of the (uncalibrated) detection threshold U_{Th} for all bias configurations and all DUTs. Here, the hit efficiency of the fiducial pixel matrix (cf. Section 5.3.3) — as illustrated in the track map of Plot 5.6a — is evaluated and the solid lines correspond to fits of Equation 5.4 to the data points.

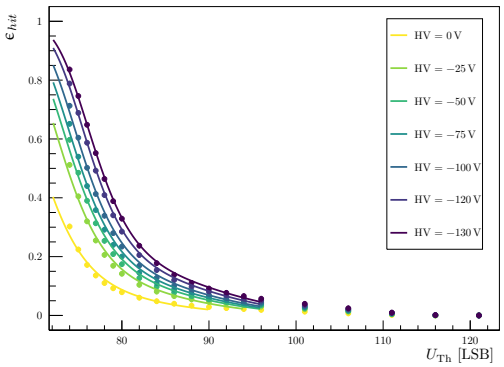

(a) MP10-T50-S20-1: 50 µm, 10 − 20 Ω cm sensor.

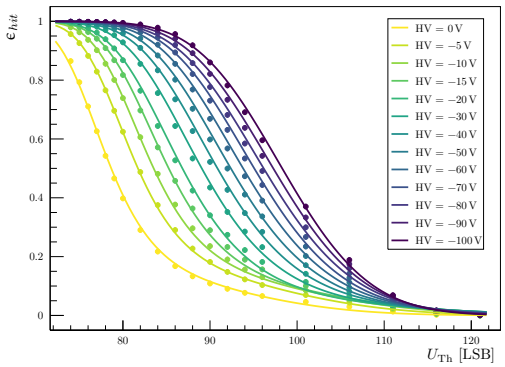

(b) MP10-T100-S300-1: 100 µm, 200 − 400 Ω cm sensor.

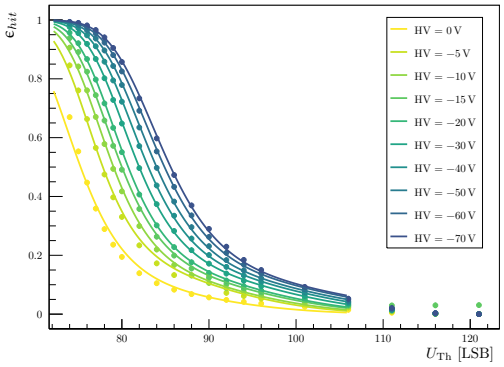

(c) MP10-T70-S300-1: 70 µm, 200 − 400 Ω cm sensor.

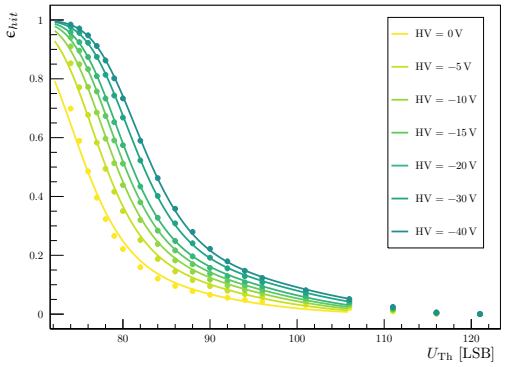

(d) MP10-T60-S300-1: 60 µm, 200 − 400 Ω cm sensor.

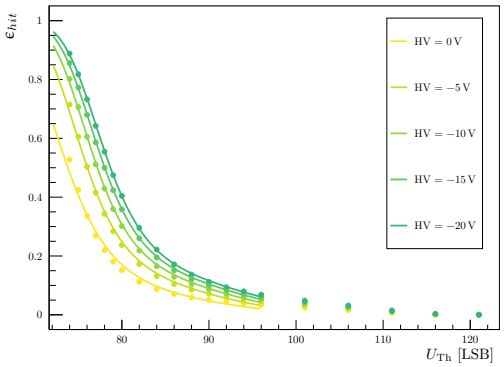

(e) MP10-T50-S300-1: 50 µm, 200 − 400 Ω cm sensor.

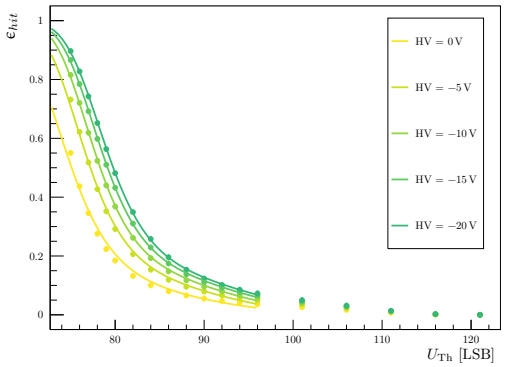

(f) MP10-T50-S300-2: 50 µm, 200 − 400 Ω cm sensor.

Plot 5.7: Efficiency curves as function of the applied (uncalibrated) detection threshold U_{Th}. Errors bars are too small to be visible. Solid lines correspond to fits of Equation 5.4 to the data points.

Influence of the Reverse Bias on the Median Efficiency Threshold

The median threshold, extracted by fitting Equation 5.4 to the data, serves as a measure to highlight the shift of the efficiency curve with applied reverse bias voltage and the corresponding sensor thickness. It serves as a useful metric to indicate the overall trend within a dataset and provides a first impression of potential issues that may arise when comparing different sensors.

Plot 5.8a illustrates the general trend of $M_{U_{\mathrm{Th}}}$ increasing approximately in proportion to $\sqrt{U_{\mathrm{HV}}}$, as expected from the depletion depth of a simple diode structure (see Section 2.3.2). This increase neither provides absolute information (even within the dataset of a single sensor) nor allows for a direct comparison between different sensors. Instead, it reveals key challenges that must be addressed when studying such devices.

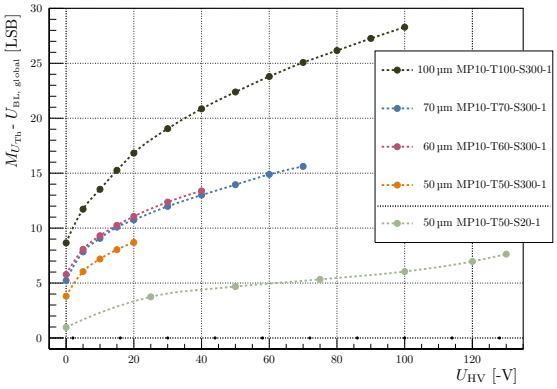

(a) All DUTs of both resistivities.

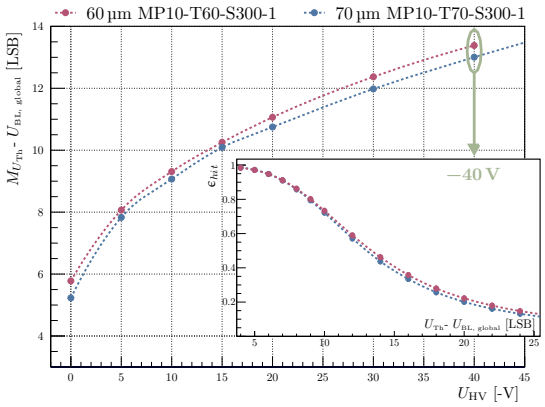

(b) 60 µm versus 70 µm.

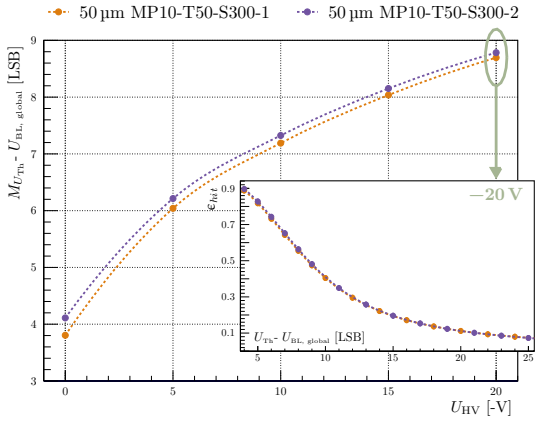

(c) Both 50 µm, 200 Ω cm to 400 Ω cm sensors.

Plot 5.8: Comparison of the median threshold ($M_{U_{\mathrm{Th}}}$, extracted with Equation 5.4) corrected for the baseline $U_{\mathrm{BL,\,global}}$ of each sensor as a function of U_{HV} for all DUTs.

For instance, Plot 5.8b compares two sensors (60 µm and 70 µm) differing in total thickness by approximately 10 µm. A corresponding difference in the deposited and thus collected charge could be expected. Assuming no charge collection from outside of the depletion region, the absence of such a difference would be consistent; however, it cannot explain the difference observed at the same bias voltages for the other thickness under investigation. While deviations of up to 5 µm in total sensor thickness could reduce the expected difference based on nominal values, this alone does not account for the significant variation in the operational bias voltage range between the two sensors. Although the observed maximum operational voltages (about −40 V for the 60 µm sensor and about −70 V for the 70 µm sensor) could be consistent with a wide range of substrate resistivity (200 Ω cm to 400 Ω cm), one would in that case expect a pronounced dispersion of this value among sensors of the same nominal thickness. Such variations were not observed; instead, the spread was only a few volts, consistent with the expected manufacturing tolerances of sensors produced from the same ingot or wafer batch. Although the statistics are limited, two sensors with identical thickness and resistivity, as shown in Plot 5.8c, exhibit no significant difference in their median threshold behavior

at first glance. This observation supports the necessity for proper calibration to enable meaningful comparisons, as no accurate comparison can be made without knowing the actual differences in the individual detector electronic responses.

Two notable features appear in the relative median threshold with respect to the global baseline level of the 10 Ω cm to 20 Ω cm sensor. At 0 V bias, the median threshold is so close to the baseline level, implying that a significant fraction of the charge distribution may fall below the baseline. Consequently, the sensor's effective "energy baseline" is shifted toward lower values. If the applied baseline does not correspond to the zero offset of the charge distribution, comparisons on the uncalibrated threshold scale become unreliable. At bias voltages exceeding −100 V, the median values start to deviate from the expected $\sqrt{U_{\mathrm{HV}}}$ trend. This deviation may be caused either by increased noise elevating the median threshold or by the onset of impact ionization in this regime (see Chapter 7, cf. Section 4.2.1).

Spatial Non-Uniformity of the Efficiency

Understanding spatial non-uniformity in the sensor's hit efficiency is crucial for accurately interpreting the analyzed data. Either the effects can be measured and corrected for or subdividing the sensor area into RoIs can be employed to minimize their impact on the overall results and be combined again after extraction of the relevant parameters.

Plot 5.9a illustrates how the hit efficiency at a defined detection threshold depends on the pixel row address of the sensor. This effect, previously observed in [80, p. 104 ff.], results from the capacitive coupling between neighboring signal lines (see Section 3.4), whose row position dependent value introduces a systematic variation as a shaping element of the analog signal pulse. The magnitude and shape of this effect can vary significantly depending on the chosen baseline levels (see Section 5.1.1), as well as between different sensors and powering schemes. Notably, efficiency rises again towards higher pixel row addresses, indicating this effect is unlikely caused by powering issues such as voltage drops. Such issues would typically cause efficiency to decrease monotonically with increasing distance from the bond pads. Overall, the averaged influence within the chosen RoIs of a matrix (see Section 5.3.3), separated by routing segments, does not differ significantly across the measured detection threshold range for a given bias configuration, as exemplary shown in (Plot 5.9b).

The observed efficiency drop along the pixel column addresses (see Plot 5.9d) is presumed to be related primarily to the sensor's powering scheme. On the PCB, elongated power bars run along the full sensor width in parallel to the sensor's bond pads, providing connections for all low-power domains of the chip, including analog and digital sectors. Power is delivered from the right side, flowing from higher pixel column addresses toward lower addresses, while on the opposite side the voltage level is sensed to compensate for voltage drops along the power distribution network on the PCB. Additionally, power distribution within the chip divides into two halves, supported by two voltage regulators for the *vssa* domain (see Section 3.7.1), to adequately supply the CSA. This partitioned scheme, especially combined with higher current flows in *low-gain* settings (cf. Table A.12), creates a non-uniformity along the sensors pixel columns, as a voltage gradient is established from the power input side to the sensing side.

The effect is evident in varying efficiency curves for the three pixel matrices, as shown in Plot 5.9c. Matrix C's efficiency curve differs notably compared to matrices A and B; however, all curves saturate toward a common behavior at high threshold values, which likely corresponds to the saturation limit of the analog pixel amplifier stage. This saturation imposes an upper bound on the efficiency measurement, overshadowing sensor differences in this regime.

5.4.2 Conclusion

Overall the primary results extracted from the testbeam campaign illustrate the complexity of the system under study and reveal the different challenges that must be addressed in order to determine the underlying physical processes. The data, as it currently stands, does not permit direct comparison between sensors exceeding the pure qualitative performance driven level. Even sensors of the same nominal thickness and resistivity, exhibiting similar behaviors, cannot be assumed to be directly comparable without applying a common calibration to ensure consistent detector response. Furthermore, it is not known to what extent the observed effects that smear the data can be attributed to specific causes, nor at what scale these effects are comparable across different bias configurations or sensors.

A comprehensive understanding of the various factors influencing the measurements is required, alongside reliable analytical and calibration tools to disentangle these instrument-related effects from the physical phenomena of interest. This underlines the necessity for proper calibrations, including conversion to an absolute energy scale, to facilitate inter- and intra-sensor comparisons and extraction of physically meaningful parameters. While empirical models can be employed to describe detector effects post hoc, they cannot fully capture all the aspects that contribute

to data smearing. Consequently, hardware-based solutions implemented prior to measurement — such as threshold trimming to achieve uniform pixel response[24] — as well as a more precise tracking system to reduce systematic effects would have been beneficial.

As calibration tools were not developed yet at the time of the testbeam, and given that not all detector effects can be fully compensated, determining detector response under varying conditions remains necessary to ensure reliable physical interpretations. The forthcoming chapter will provide insight into the calibration procedure developed to address these challenges.

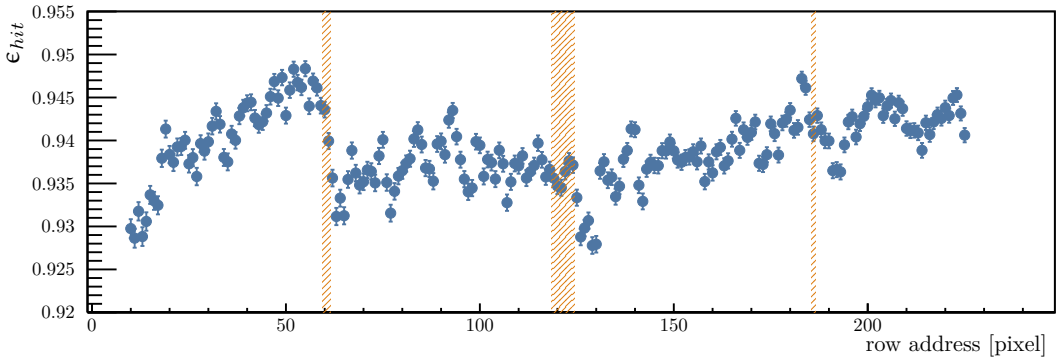

(a) Projection of the efficiency onto the pixel row address (U_{Th} = 78 LSB).

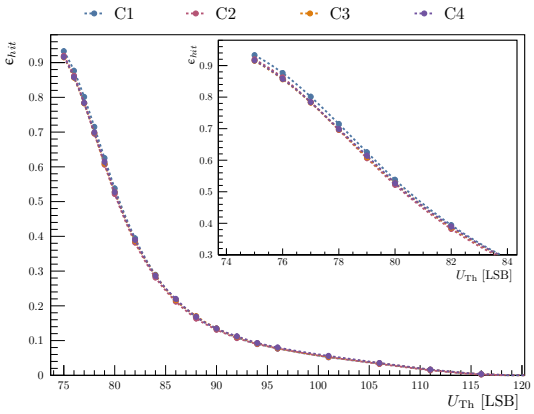

(b) Comparison of the efficiency for all four RoI quadrants.

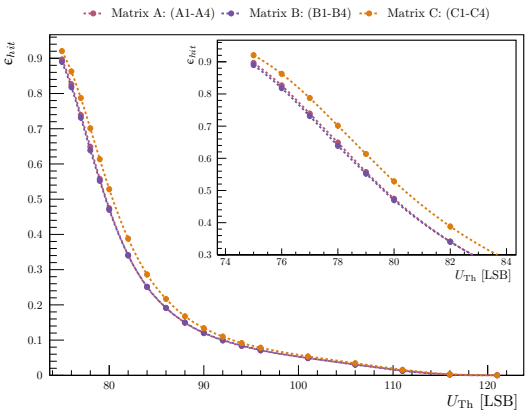

(c) Comparison of the efficiency for all three pixel matrices.

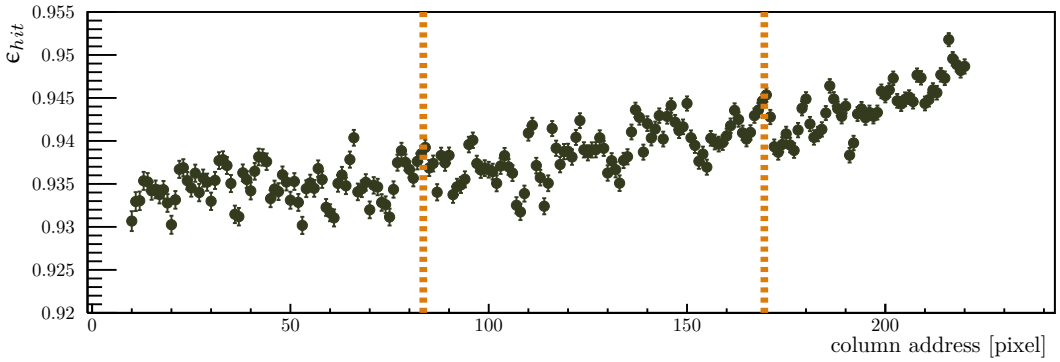

(d) Projection of the efficiency onto the pixel column address of the pixel sensor (U_{Th} = 78 LSB).

Plot 5.9: Exemplary spatial non-uniformity of the efficiency for MP10-T100-S300-1 at −20 V in with RoI.

[24] A threshold trimming can be used to achieve a more uniform response at fixed operation threshold, but would not account for variations of gain at other thresholds across a pixel matrix.

6. Energy Calibration

The energy calibration of the MuPix10 addresses three main objectives. First, it converts the detection threshold scale, typically expressed in detector-level units such as LSB or mV, into a physical energy scale in either electronvolt ([eV]) or electrons ([e]), enabling direct comparison with other detectors and theoretical models. Second, it characterizes the detector's response to known input energies, such as charge injection and Fe-55 x-rays. This includes identifying and correcting pixel-to-pixel variations in the gain leading to observed non-linearities and effective saturation due to the limited dynamic range of the in-pixel CSA, which significantly impact the energy scaling. Additionally, it involves understanding charge collection effects and spatial variations across the sensor. Third, it assesses the sensor's noise level under varying conditions such as high-voltage bias configurations and power-dependent sensor settings. The following sections provide a detailed overview of the calibration methods employed to achieve these goals.

6.1 Calibration Strategy

Accurate transformation from the detector threshold scale to a meaningful physical energy scale requires several assumptions.

The simplest approach uses a single calibration point from an ideal monochromatic external source, typically an X-ray source such as Fe-55 or fluorescence measurements [1]. This method assumes a uniform zero-point crossing (i.e. baseline) across all pixels and a perfectly linear response throughout the entire energy range of interest based on the monochromatic source. However, this approach has two significant limitations: baseline dispersion (threshold spread) is expected — especially without prior threshold trimming — and the CSA's limited dynamic range, which leads to saturation at high input charges.

To address this, the energy scaling is partitioned into linear and saturation domains. At least two calibration points are needed in the linear range (more points reduce statistical bias) to estimate gain and pixel dispersion. The calibration of the saturation domain relies on the selected model and available data, with the transition between domains being a significant source of uncertainty. A finely resolved scan of the sensor's energy response helps to describe the model accurately.

Fluorescence measurements using an X-ray machine on different materials are commonly used but limited by available spectral lines and **si**licon's narrow absorption range (see Section 1.2), which is dominated by the photoelectric effect. Extending calibration beyond this region requires modeling both photoelectric and Compton scattering effects, which complicates the process.

Due to the unavailability of a suitable X-ray machine for the MuPix setup, the sensor's inherent charge injection feature is used for alternative monochromatic calibration. Each pixel hosts a dedicated in-pixel capacitance, stimulated externally via a controlled voltage, effectively "simulating" energy depositions in form of charge injection to the pixel diode's n-well. Charge injection provides an ideal calibration by mainly bypassing charge collection processes — charge is directly injected into the n-well of the pixel —, thus isolating the amplifier's intrinsic response, free from charge sharing (cf. Section 4.2.4) or multiplication effects (cf. Section 4.2.1). The capacitance of each pixel is experimentally determined by matching its linear-domain response to a known reference (Fe-55), which provides a distinct energy peak well within the linear response region. By varying the injection voltage, a wide energy input range can be scanned, characterizing the sensor's linearity and saturation behavior.

Limitations in the sensor's operational configuration during the testbeam campaign (*low-gain* settings, see Section 5.1.1) require using a *high-gain* setting to determine injection capacitance, as the Fe-55 peak is not observable

[1] A third method is using compton scattering [175], which requires measuring the scattering angle.

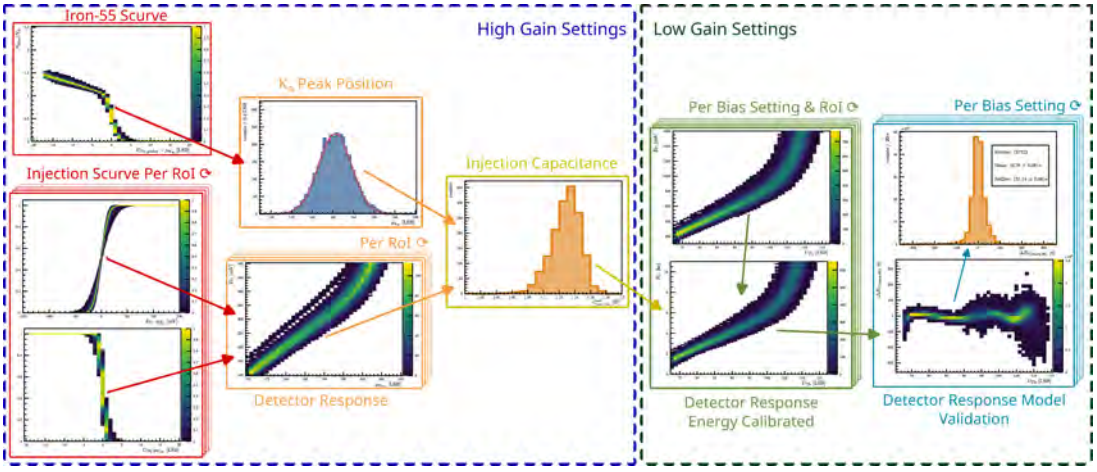

Figure 6.1: The calibration flow: The injection capacitances (yellow) are derived from the $K_{\bar{\alpha}}$-peak position and the linear response (orange), obtained through Fe-55 and *Injection* S-curve measurements in the *high-gain* settings. Applied to *Injection* measurements in the *low-gain* settings (green), a model is fitted to the energy-calibrated detector response (blue).

in the *low-gain* settings. Therefore, the *high-gain* setting is used to determine the injection capacitance, which in turn is used to convert the injection measurements into an energy scale for the *low-gain* settings.

As the *Injection* method underpins energy calibration, dividing calibration procedure into RoIs (see Section 5.3.3) is essential for multiple reasons. Increasing the number of pixels injected simultaneously raises the total capacitance to be charged at the injection node, which can reduce the effective injection voltage due to current-source limitations, risking oscillation effects as many pixels switch simultaneously, and saturating the readout bandwidth at high injection rates. Furthermore, injecting in pixel regions of overlapping routing segments can lead to noticeable cross-talk effects (see Section 3.4.1), distorting the measurement results at high injection voltages. As a broad range of injection voltages, detection thresholds and bias configurations have to be covered, a fast and reliable measurement procedure is crucial. Thus, each RoI is calibrated by executing the calibration procedure individually.

The full calibration chain is illustrated in Figure 6.1 and is based on S-curve measurements (see Section 6.1.2) using both Fe-55 and charge injection methods, discussed in more detail in the following sections.

At the *high-gain* settings, *Injection* and Fe-55 measurements are performed at the same bias voltage (−20 V)[2], corresponding to the thinnest sensor's maximum operational voltage. This minimizes systematic effects from varying depletion depths and detector capacitances that influence charge collection and analog signal shaping in the CSA.

The Fe-55 monochromatic peak detection threshold is mapped to an equivalent injection voltage (U) in the linear injection region, allowing pixel-wise calculation of *Injection* capacitance (C) using $Q = C \cdot U$, as the input charge Q of the photo-electric effect is known (cf. Section 1.2) and can be converted to electrons using the pair creation energy in silicon (Equation 2.6, see Section 2.2.1). "While additional monochromatic calibration points would improve accuracy, limited availability of radioactive sources constrains this study.

Finally, the full response range is scanned at each bias voltage (see Section 5.4) and RoI in *low-gain* mode. Injection voltages are converted to a physical energy scale using the determined capacitance, yielding a calibrated energy response modeled to correct non-linearities and saturation effects on a per pixel basis. This calibration converts detection threshold settings from the testbeam into a physical energy scale, enabling direct comparisons across sensors and configurations.

6.1.1 Modeling Monochromatic Charge Deposition

In an "ideal" case, a measurement of a monochromatic energy deposition E_0 would consistently yield the same exact signal, describable by a Dirac delta function $\delta(E - E_0)$ (see Figure 6.2a). However, in "real-world" conditions,

[2] This does not hold for MP10-T50-S20-1 (10 Ω cm to 20 Ω cm), as the corresponding detector capacitance is comparatively low. Therefore, the measurement is chosen to be conducted at −100 V, the last bias configuration point before charge multiplication presumably sets in.

detector resolution, electronic noise and fluctuations in the charge generation introduce fluctuations of the measured signal, smearing the response distribution. This behavior can be represented by a normal distribution with variance σ_E^2 and mean value E_0 (see Figure 6.2b), expressed as:

$$\mathrm{PDF}_{\mathrm{normal}}(E \mid E_0, \sigma_E) = \frac{1}{\sqrt{2\pi\sigma_E^2}} \cdot \mathrm{e}^{-\frac{(E-E_0)^2}{2\sigma_E^2}} \tag{6.1}$$

This assumption holds as long as all charge deposited is collected on a single collection electrode, typically fulfilled in case of charge injection (see Figure 6.2b).

If an external monochromatic signal source — such as a radioactive source or an X-ray tube — is used, the charge deposition can occur at pixel boundaries, leading to charge sharing between neighboring pixels (cf. Section 4.2.4), redistributing a fraction of the deposited charge. In the idealized limit without further detector effects (see Figure 6.2c), the main distribution can still be represented by a Dirac delta at E_0, while a certain fraction $\Gamma_{\mathrm{c.s.}}$ of events appears below E_0, forming a plateau between 0 and E_0. This plateau can be approximated by a step function centered at E_0 with magnitude $\Gamma_{\mathrm{c.s.}}$ describing the fraction of shared charge relative to the total deposited charge.

In a real detector, localized energy depositions — for instance, from photoelectric absorption — can be modeled by extending Equation 6.1 with a function describing this charge-sharing contribution, effectively smoothing the step function (see Figure 6.2d). Analogous to how the delta function evolves into a normal distribution, the integrated step function evolves into the (complementary) CDF of the normal distribution:

$$\begin{aligned} \mathrm{CDF\_C}_{\mathrm{normal}}(E \mid E_0, \sigma_E) &= \frac{1}{2}\left[1 - \mathrm{erf}\left(\frac{E-E_0}{\sqrt{2}\cdot\sigma_E}\right)\right] \\ \mathrm{CDF}_{\mathrm{normal}}(E \mid E_0, \sigma_E) &= \frac{1}{2}\left[1 + \mathrm{erf}\left(\frac{E-E_0}{\sqrt{2}\cdot\sigma_E}\right)\right] \end{aligned} \tag{6.2}$$

By scaling this with the charge-sharing factor $\Gamma_{\mathrm{c.s.}}$ and combining it with the normal PDF, one obtains the normalized monochromatic charge deposition spectrum including charge sharing (see [176, p. 13ff]):

$$\mathcal{S}(E \mid E_0, \sigma_E, \Gamma_{\mathrm{c.s.}}) = \mathrm{PDF}_{\mathrm{normal}}(E \mid E_0, \sigma_E) + \Gamma_{\mathrm{c.s.}} \cdot \mathrm{CDF\_C}_{\mathrm{normal}}(E \mid E_0, \sigma_E) \tag{6.3}$$

This formulation is flexible and can be adapted to various monochromatic charge-deposition scenarios.

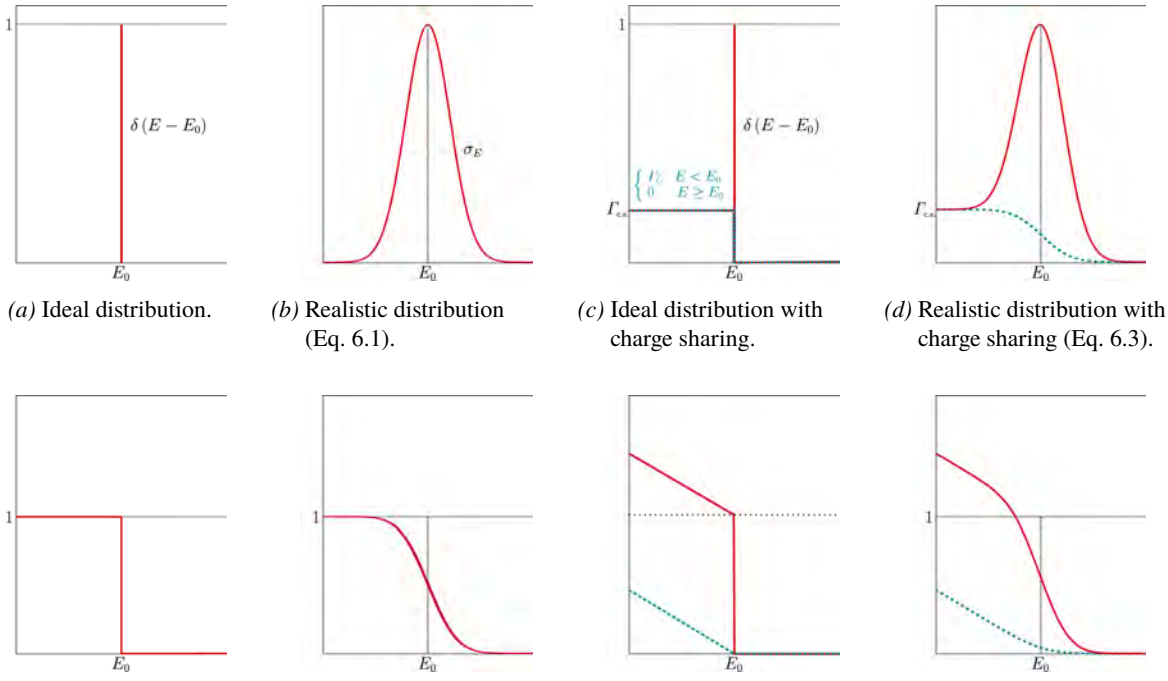

(a) Ideal distribution. *(b)* Realistic distribution (Eq. 6.1). *(c)* Ideal distribution with charge sharing. *(d)* Realistic distribution with charge sharing (Eq. 6.3).

(e) Ideal S-curve. *(f)* Realistic S-curve (Eq. 6.2) *(g)* Ideal S-curve with charge sharing. *(h)* Realistic S-curve with charge sharing (Eq. 6.4).

Figure 6.2: Different representations of a mono-energetic charge deposition.

In the context of this thesis, the charge distribution is not determined directly, but rather the response to a detection threshold in form of registered hits (a so-called S-curve measurement, see Figure 6.2h) — the integral form of Equation 6.3 is relevant. As the integral of a normal PDF yields its (complementary) CDF (see Equation 6.2), only the integral of the (complementary) CDF needs to be determined (cf. Section A.4.1) under appropriate boundary conditions. For a monochromatic charge deposition including charge sharing (see Figure 6.2d), the analytical integral takes the form (cf. [177, p. 151ff]):

$$\begin{aligned}\mathcal{IS}(E \mid E_0, \sigma_E, \Gamma_{\text{c.s.}}) &= \int_E^{\infty} \mathcal{S}(E' \mid E_0, \sigma_E, \Gamma_{\text{c.s.}})\,\mathrm{d}E' \\ &= [1 + \Gamma_{\text{c.s.}} \cdot (E_0 - E)] \cdot \text{CDF\_C}_{\text{normal}}(E \mid E_0, \sigma_E) + \Gamma_{\text{c.s.}} \cdot \sigma_E^2 \cdot \text{PDF}_{\text{normal}}(E \mid E_0, \sigma_E)\end{aligned} \tag{6.4}$$

This analytical model forms the basis for describing the S-curve response of an X-ray emitter within the photoelectric absorption dominated regime, like Fe-55, but it can be generalized to any other monochromatic input. In case of charge injection, where no charge sharing occurs (i.e.,$\Gamma_{\text{c.s.}} = 0$), the function simplifies to the (complementary) CDF of the normal distribution (see Figure 6.2f).

6.1.2 S-curve Measurement Methodology

In principle, the S-curve measurement is a counting experiment, integrating the number of registered hits for each pixel over a defined measurement time while sweeping the energy threshold. The key aspects are measurement stability, reproducibility, and speed, as a large number of configurations must be measured for each DUT. To achieve speed optimization, most functionalities of the standard *MuDAQ* readout procedure are bypassed, and data is directly accumulated on FPGA level. A dedicated memory region stores cumulative counts for each pixel and threshold setting, enabling faster access and minimizing overhead during measurements.

A dedicated FPGA register spanning up to 256×256 pixel and a depth of 16 bit (i.e. up to 65536 counts) is utilized for this[3]. If this upper limit for a pixel is reached, the hit integration for that pixel is halted to prevent overflow and bit lapsing. The concept is to integrate all hits per pixel during a defined measurement period and extract the final accumulated result for each threshold setting.

Time-dependent information like ToA or ToT, which could be used for clustering, is intentionally omitted to maximize speed and reduce data volume. This allows higher throughput from the sensor, which the software side of the DAQ might not otherwise handle. Any effects from these simplifications must be included in the corresponding S-curve fit model.

To minimize data corruption from sensor instabilities and 8 bit/10 bit encoded data transmission errors, the data stream is continuously monitored during the measurement. From the transmission, the expected frequency lock and bit error rate are checked to ensure data integrity. If a check fails, spurious or misassigned data could distort results and would have to be filtered out in post-processing. The verification is performed after each sensor configuration step and throughout each measurement point.

When errors occur, a stabilization procedure is automatically initiated to restore stable measurement conditions. Instabilities can originate from misconfigurations (rare) or low detection thresholds combined with high electronic noise. Noise may induce oscillations via rapid state switching, disrupting the internal clock tree and producing erroneous readings. Similar effects can arise when the timestamp counter resets, leading to a brief drop in power consumption that can destabilize the sensor. Generally, this effect damps quickly but may persist in the presence of "noisy" pixels.
The procedure to restore the stability of the sensor consists of:

1. Setting the detection threshold to its maximum (beyond the dynamic operation range of any signal detection, e.g. 0xFF) to suppress noise-induced hits.
2. Toggling the PLL by disabling and then re-enabling it via the DAC *EnablePLL*.
3. Restoring the previous detection threshold value.

This recovery routine is a standard procedure for HV-MAPS to re-establish stable links. If it fails after several attempts (e.g. repeated up to five times), data integrity cannot be guaranteed, and the corresponding measurement

[3] This register size is chosen to accommodate the full pixel matrix of multiple sensor generations of different pixel matrix sizes.

point is skipped — both to prevent dataset corruption and to preselect reliable measurement points for further analysis.

The measurement procedure still offers potential for time optimization, as each configuration step currently requires approximately (2.13 ± 0.02) s (due to sensor and software limitations), while the readout and processing of each measurement point takes about (5.79 ± 0.08) s (limited by FPGA register readout) [4]. For measurements with longer individual durations (e.g., several minutes, Fe-55), such overheads are negligible. However, for shorter measurement times (e.g., 1 s, *Injection*), their impact becomes significant.

6.1.3 Calibration Setup

The calibration setup, illustrated in Figure 6.3, is intended to support both Fe-55 and charge injection-based characterization of the MuPix10 sensors. Although the exact conditions of the testbeam campaign (see Section 5.2.3) cannot be fully replicated, the setup addresses two main aspects to ensure comparability of the results.

First, the environmental conditions — humidity and temperature — are kept as stable and consistent as possible throughout the calibration period. The laboratory environment is climate-controlled with respect to temperature and dehumidification, maintaining an ambient temperature of approximately (22 ± 4) °C and a relative humidity between 30 % to 40 %[5]. A cooling system using gaseous nitrogen, as employed during the testbeam campaign, was not feasible due to the absence of a continuous nitrogen supply. Instead, a forced-air cooling solution using two standard fans providing constant airflow across the sensor surface was implemented (see Figure 6.3b). Since the cooling primarily serves to suppress potential self-heating effects from sensor leakage current, and a stable operating temperature is ensured, this approach is considered sufficient. Changes in sensor configuration settings, which alter power consumption, have a more noticeable impact on the noise level of the sensor (see Section 7.3).

The second aspect concerns the minimization of light interference during measurements. Although the MuPix10 is not a highly light-sensitive sensor, stray light can still induce bulk currents that potentially increase leakage and thus noise. To mitigate this, the entire setup is enclosed with light-absorbing fabric, laboratory lights are switched off during measurements, and blinds are closed.

The setup also includes a movable gripper arm to hold the Fe-55 source at adjustable heights above the sensor, allowing fine control of the source-to-sensor distance to optimize count rates and sensor coverage.

All measurements used throughout this thesis for the comparison of calibrated efficiency data from RoIs of matrix C (if not stated otherwise) were conducted within the same presented setup. Additional measurements involvingFe-55 irradiation at varying bias configurations, as well as those calibration measurements for MP10-T100-S300-1 concerning RoIs from matrices A and B, were conducted on an identically designed setup. This was done for two reasons: (i) to increase total measurement throughput and broaden coverage by running multiple setups in parallel, and (ii) to cross-check the results among setups for potential systematic variations.

(a) Side view: Fe-55 source placed above the sensor.

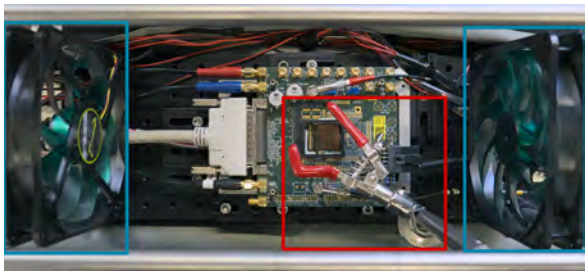

(b) Top view: The Fe-55 source holder is shown in a red frame, while the fans providing constant airflow to cool the sensor during operation are highlighted in blue.

Figure 6.3: Calibration setup for the Fe-55 & injection-based characterization of MuPix10.

[4] The time values (mean) and associated uncertainties (standard deviation) are derived from 1,174,136 measurement steps recorded.

[5] These values are based on frequent daily monitoring using multiple Pt100 sensors and hygrometers throughout the entire calibration period. The observed fluctuations reflect typical daily and seasonal variations recorded over several months during this period.

6.2 Conversion of Detector Thresholds to Electron Equivalent

Converting between physical quantities requires a well-defined relationship. In silicon, the relation between deposited energy and generated charge carriers is given by the pair creation energy (see Section 2.2.1). However, the relation between generated charge carriers and detector threshold units is not intrinsically accessible and depends mainly on the detector's gain characteristics.

HV-MAPS provide two ways to access energy-related information: through ToT measurements, a representation of the deposited charge as related to the signal pulse width, or via relative hit rate measurements at defined detection thresholds. This work emphasizes the latter approach by utilizing S-curve measurements for energy calibration, yielding binary information on whether deposited energy exceeds the threshold or not.

To assign a meaningful energy value to a detection threshold, S-curve measurements are performed using preferably monochromatic radiation sources, notably Fe-55[6]. Since a single source offers limited calibration points, a full detector response calibration is achieved by combining Fe-55 with charge injection measurements (see Section 6.1). The energy calibration point from Fe-55 measurements is essential for determining the injection capacitance, required to convert injected voltages to physical energy units.
The choice of Fe-55 as calibration source meets these experimental requirements:

- Provides a well-defined calibration point from a near-monochromatic energy spectrum in the photoelectric regime.
- Deposited energy lies within the detector's linear gain region for accurate calibration.
- Sufficient illumination of the entire pixel matrix.
- High intensity for short measurement times and suppression of (noise-induced) background events.

Note that the S-curve model describing photons undergoing the photoelectric effect must account for the effect of fractional charge collection, as the interaction will occur at pixel boundaries or within non-depleted regions (see Figure 6.4). Although the relative significance of charge sharing decreases with deeper depletion, HV-MAPS are often operated underdepleted, where partial bulk volume depletion leads to diffusion-dominated charge collection and partial charge capture. All such effects are integrated into the S-curve model, detailed in the following sections.

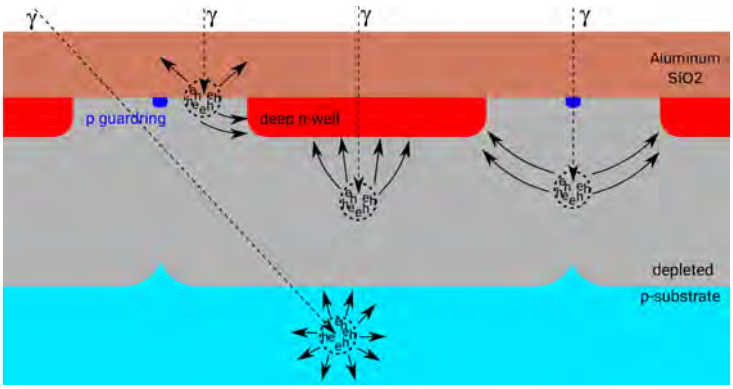

Figure 6.4: Different scenarios of a photon undergoing the photoelectric effect and depositing energy within a pixel.

6.2.1 The Energy Spectrum of Fe-55

Fe-55 is a radioactive isotope of iron that decays via electron capture to Mn-55 with a half-life of 2.756 14 yr [178] (see Figure 6.5). This decay creates a vacancy in one of its electron shells, leaving the atom in an excited state. The vacancy is filled by an electron from a higher energy level, with the energy difference emitted either as an Auger electron — an electron emitted from another shell of the same atom — or as a photon.

[6] Fe-55 is not truly monochromatic, exhibiting two distinct energy peaks, necessitating a model describing both the energy deposition spectrum and its S-curve response function.

Auger electron emission dominates with about 60 % probability, but its low kinetic energy ($\mathcal{O}(6\,\mathrm{keV})$) limits its range, rendering it insignificant for detection by MuPix10. Instead, spectral X-ray photon lines can be measured. The most common are the $K_{\alpha,1}$ and $K_{\alpha,2}$ transitions (L-shell to K-shell) and the K_β transition (M-shell to K-shell) (see Figure 1.2).

The $K_{\alpha,1}$ transition, with about 16 % probability, emits photons at roughly 5.90 keV and cannot be distinguished from the $K_{\alpha,2}$ at about 5.89 keV (8 % probability). These two are thus combined as an intensity-averaged monochromatic energy peak ($K_{\bar{\alpha}}$) for following considerations. The K_β transition occurs less frequently (3 % probability) and emits photons around 6.49 keV, potentially distinguishable with a fine energy resolution.

Other transitions to shells higher than K-shell produce significantly lower energy emissions that can be neglected for this application. A detailed list of transitions, energies, and probabilities is provided in Section A.4.1, extracted from JANIS 4 [179] based on databases such as JENDL/DDF-2015 [180], JEFF-3.3 [181], and ENDF/B-VIII.0 [182].

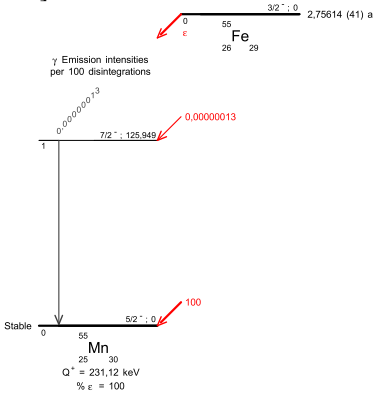

Figure 6.5: Fe-55 decay mode is 100 % via electron capture to Mn-55 [178].

	value	comment
$E_{\mathrm{K}_{\bar{\alpha}}}$	∼5.895 keV	intensity weighted average
	∼ 1615 e	conversion based on Eq. 2.6 & Tab. 2.1
$\lambda_{a,\mathrm{K}_{\bar{\alpha}}}$	∼28.927 µm	extracted from [37]
E_{K_β}	6.490 keV	—
	∼1778 e	conversion based on Eq. 2.6 & Tab. 2.1
$\lambda_{a,\mathrm{K}_{\bar{\beta}}}$	∼38.138 µm	extracted from [37]
$f_{\beta/\bar{\alpha}}$	∼11.817 %	relative intensity of K_β transition

Table 6.1: Key properties of the Fe-55. Energy and intensity values taken from JEFF-3.3 [182], whereas the corresponding absorption lengths are extracted from [37] (cf. Plot 1.3).

The measurable Fe-55 spectrum in HV-MAPS is thus approximated by two monochromatic peaks, the intensity-averaged $K_{\bar{\alpha}}$ peak and the K_β peak, scaled according to their relative intensities (summarized in Table 6.1). In addition, the location of the photon interaction within the pixel has to be considered, as the initial charge cloud expands due to Coulomb repulsion ($\mathcal{O}(4\,\mu\mathrm{m})$) [183], contributing to charge sharing between pixels. For large pixel pitches and/or deep depletion volumes this effect becomes negligible, as it only affects a small fraction of all events.

A simple model [176][7] incorporating both peaks and charge sharing effects can be constructed by combining two instances of the single energy deposition model with charge sharing as introduced in Section 6.1.1. This model is adaptable to any similar double-peak X-ray spectrum dominated by the photoelectric effect.

Applied to HV-MAPS, the model requires a reinterpretation and allows for certain modification of model parameters:

1. Lower energy resolution and coarse threshold binning obscure separation of the $K_{\bar{\alpha}}$ and K_β peaks, necessitating fixing the intensity ratio parameter $f_{\beta/\bar{\alpha}}$.

2. Not only charge sharing at the pixel boundaries but also diffusion from non-depleted regions contribute to partial charge collection, leading to a redefinition of the charge sharing parameter $\Gamma_{\mathrm{c.s.}}$ to $\Gamma_{\mathrm{f.c.}} = \Gamma_{\mathrm{c.s.}} + \Gamma_{\mathrm{diffusion}}$.[8]

3. Background, arising from cosmic ray events, is omitted due to their low detection rate[9] compared to the high intensity of the Fe-55 source ($\mathcal{O}(100\,\mathrm{Hz\,pixel}^{-1})$).

It is expected that the fraction arising from diffusion ($\Gamma_{\mathrm{diffusion}}$) vanishes for fully depleted sensors of any thickness, rendering $\Gamma_{\mathrm{c.s.}}$ the sole contributor to partial charge collection in such scenarios.
All information combined, leads to the expression for the Fe-55 energy spectrum including fractional charge collection:

[7] The original model is initially developed for pixel sensors of the Medipix family [68] used in X-ray fluorescence measurements.
[8] Both parameters ($\Gamma_{\mathrm{c.s.}}$ and $\Gamma_{\mathrm{diffusion}}$) are expected to decrease with increasing depletion depth, as they are relative to the core distribution and their relative geometric volumes decrease.
[9] Approximately $70\,\mathrm{m}^{-2}\,\mathrm{s}^{-1}\,\mathrm{sr}^{-1}$ for muons above 1 GeV at sea level [184, p. 522] yield a rate of about 2.8 µHz/pixel or 0.18 Hz/sensor for MuPix10 integrating over the upper hemisphere (2π sr).

$$\left(\frac{\mathrm{d}N}{\mathrm{d}E}\right)_{Fe55} \approx N_\gamma \cdot \left[\mathcal{S}_{K_{\bar{\alpha}}}(E \mid E_{\mathrm{K}_{\bar{\alpha}}}, \sigma_{\mathrm{K}_{\bar{\alpha},\beta}}, \Gamma_{\mathrm{f.c.}}) + f_{\beta/\bar{\alpha}} \cdot \mathcal{S}_{K_\beta}(E \mid E_{\mathrm{K}_\beta}, \sigma_{\mathrm{K}_{\bar{\alpha},\beta}}, \Gamma_{\mathrm{f.c.}})\right] \tag{6.5}$$

where $\mathcal{S}(x)$ is defined by Equation 6.3, N_γ is the relative number of photons with the full energy deposited being detected within the pixel, and both peaks share the same standard deviation ($\sigma_{\mathrm{K}_{\bar{\alpha},\beta}}$) and $\Gamma_{\mathrm{f.c.}}$ due to their minimal energy difference.

6.2.2 Dual-Peak S-curve Model Including Fractional Charge Collection

From the energy spectrum defined in Equation 6.5, the corresponding S-curve model is derived by integrating over all energies above the detection threshold U_{Th}. This approach assumes each photon interaction is independent, and the detection probability at a given threshold depends solely on whether the deposited energy exceeds that threshold (no charge collection inefficiencies apart from fractional charge collection are considered). Thus, the S-curve model for Fe-55 is expressed as:

$$N_{Fe55}(U_{\mathrm{Th}} \mid N_\gamma, E_{\mathrm{K}_{\bar{\alpha}}}, \sigma_{\mathrm{K}_{\bar{\alpha},\beta}}, E_{\mathrm{K}_\beta}, \Gamma_{\mathrm{f.c.}}, f_{\beta/\bar{\alpha}}) = \int_{U_{\mathrm{Th}}}^{\infty} \left(\frac{\mathrm{d}N}{\mathrm{d}E}\right)_{Fe55} \mathrm{d}E \tag{6.6}$$

Here, N_{Fe55} is the number of detected events associated with a photoelectric event from Fe-55, including contributions from the $K_{\bar{\alpha}}$ and K_β peaks and partially collected charge events due to charge sharing or diffusion ($\Gamma_{\mathrm{f.c.}}$). Events arising from fake hits (noise) are not included in this model and must be accounted for separately during data processing.

Since the underlying spectrum is a linear combination of two monochromatic peaks, the integral can be separated into two integrals as given in Equation 6.4. Because direct energy information is not accessible from the sensor data, the model parameters are reparametrized in terms of threshold values rather than energy values. The energy peaks $E_{\mathrm{K}_{\bar{\alpha}}}$ and E_{K_β} are replaced by the counterparts $\mu_{\mathrm{K}_{\bar{\alpha}}}$ and μ_{K_β}, representing the thresholds at which half of the respective peak events are detected (the means of their normal distributions). Similarly, $\sigma_{\mathrm{K}_{\bar{\alpha},\beta}}$ now refers to threshold smearing rather than energy resolution, incorporating detector resolution and noise. For fitting stability and simplification, μ_{K_β} is not treated as an independent parameter but defined relative to $\mu_{\mathrm{K}_{\bar{\alpha}}}$ by the energy difference $\Delta\mu_{\mathrm{K}_{\bar{\alpha},\beta}}$, such that $\mu_{\mathrm{K}_\beta} = \mu_{\mathrm{K}_{\bar{\alpha}}} + \Delta\mu_{\mathrm{K}_{\bar{\alpha},\beta}}$. Due to sensor energy resolution limitations and coarse threshold binning, the two peaks cannot be distinctly separated. Consequently, this necessitates reparametrization and requires using a fixed value for $f_{\beta/\bar{\alpha}}$, derived from literature (cf. Table 6.1).
An analytical form of the integral (cf. [177, p. 151ff]) yields the final S-curve model for Fe-55:

$$\begin{aligned} N_{Fe55}(U_{\mathrm{Th}} \mid N_\gamma, \mu_{\mathrm{K}_{\bar{\alpha}}}, \Delta\mu_{\mathrm{K}_{\bar{\alpha},\beta}}, \sigma_{\mathrm{K}_{\bar{\alpha},\beta}}, \Gamma_{\mathrm{f.c.}}, f_{\beta/\bar{\alpha}}) = & N_\gamma \Big[\mathcal{IS}(U_{\mathrm{Th}} \mid \mu_{\mathrm{K}_{\bar{\alpha}}}, \sigma_{\mathrm{K}_{\bar{\alpha},\beta}}, \Gamma_{\mathrm{f.c.}}) \\ & + f_{\beta/\bar{\alpha}} \cdot \mathcal{IS}(U_{\mathrm{Th}} \mid \underbrace{\mu_{\mathrm{K}_{\bar{\alpha}}} + \Delta\mu_{\mathrm{K}_{\bar{\alpha},\beta}}}_{\mu_{\mathrm{K}_\beta}}, \sigma_{\mathrm{K}_{\bar{\alpha},\beta}}, \Gamma_{\mathrm{f.c.}})\Big] \end{aligned} \tag{6.7}$$

An overview of all model parameters is listed in Table 6.2.

Fit Parameter	Description
$\mu_{\mathrm{K}_{\bar{\alpha}}}$ [LSB]	Threshold corresponding to the energy of the $K_{\bar{\alpha}}$ peak
$\Delta\mu_{\mathrm{K}_{\bar{\alpha},\beta}}$ [LSB]	Threshold offset between the K_β and $K_{\bar{\alpha}}$ peaks
N_γ	Number of photons associated with the $K_{\bar{\alpha}}$- and K_β-peaks
$\Gamma_{\mathrm{f.c.}}$	Fraction of events with partial charge collection relative to the $K_{\bar{\alpha}}$- and K_β- distributions
$\sigma_{\mathrm{K}_{\bar{\alpha},\beta}}$ [LSB]	Smearing of the energy distribution including the detector resolution and noise
$f_{\beta/\bar{\alpha}}$ (fixed)	Relative occurrence of the K_β peak in comparison to the $K_{\bar{\alpha}}$ peak

Table 6.2: Parameters of the S-curve fit model for the Fe-55 energy spectrum.

Fit Stability & Limitations

For the model to be applicable, certain conditions must be met. The source's measurable energy range must lie within the detector's linear response region to ensure linearity between deposited energy and measured threshold. Otherwise, two complications arise: (i) the tail of larger energy depositions compresses towards lower thresholds, distorting the shape of the S-curve, and (ii) measured fluctuations decrease, distorting parameters $\sigma_{\mathrm{K}_{\bar{\alpha}},\beta}$ and $\Delta\mu_{\mathrm{K}_{\bar{\alpha}},\beta}$. If only $\mu_{\mathrm{K}_{\bar{\alpha}}}$ is of interest, the fit may still be accurate in its representation, but no reliable GoF (**G**oodness-**o**f-**F**it) (cf. Section A.3.7) can be obtained as the S-curve tail deviates significantly from the model.

Another limitation not accounted for is charge multiplication via impact ionization (see Section 4.2.1), which occurs under high electric fields and sufficient bias voltage — not inherent to the HV-MAPS concept but possible in low resistivity substrates in combination with high reverse bias voltages. This non-linear multiplication distorts energy-threshold linearity, extending the energy tail effectively to higher threshold values.

When conditions are met and a good GoF is achieved, a visual inspection of the fitted data shows it aligns well with the model, confirming its validity. For example, Figure 6.6a illustrates a superposition of all unprocessed hit counts detected (N_{hit}) as a function of the threshold U_{Th}, revealing pixel-to-pixel baseline variations, photon intensity differences due to source placement, and a noise-induced exponential rise at low thresholds. After fitting, these variations are accounted for by scaling with N_γ and shifting by $\mu_{\mathrm{K}_{\bar{\alpha}}}$, as shown in Figure 6.6b, effectively overlaying the different data sets to check for consistency. The low-threshold noise region, visible here, must be excluded from the fit range, as demonstrated in Figure 6.6c.

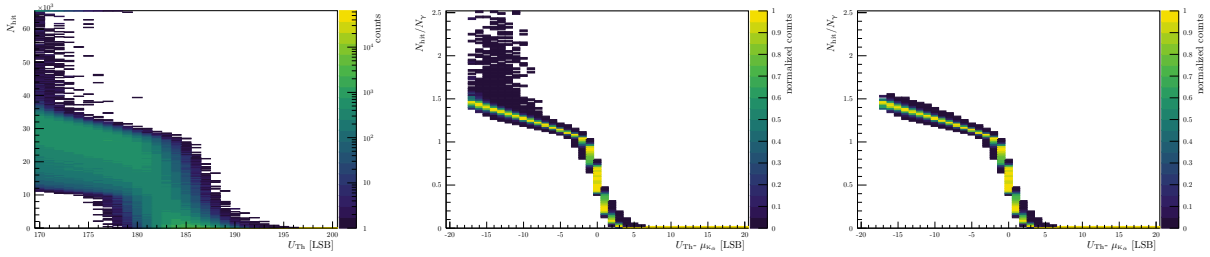

(a) N_{hit} versus U_{Th}: raw data set.

(b) ($N_{\mathrm{hit}}/N_\gamma$) versus ($U_{\mathrm{Th}}$-$\mu_{\mathrm{K}_{\bar{\alpha}}}$): scaled and shifted fitted data set.

(c) ($N_{\mathrm{hit}}/N_\gamma$) versus ($U_{\mathrm{Th}}$-$\mu_{\mathrm{K}_{\bar{\alpha}}}$): scaled and shifted fitted data set in valid fit range.

Figure 6.6: Representation of the superposition of Fe-55 threshold scan data.

Data Processing Procedure

Although initial preprocessing occurs during data taking (see Section 6.1.2), additional steps are necessary to prepare data for fitting with the Fe-55 S-curve model.

A key requirement is a monotonically decreasing data set with increasing threshold levels with respect to the baseline. This condition may not always be met due to misconfigurations or measurement instabilities affecting individual pixels. To restore monotonicity, an iterative filtering procedure removes outlier points violating this condition via a three-sigma ($\sigma_{N_{\mathrm{hit}}}$) criterion compared with neighboring threshold levels.

Each data point is assigned a poissonian uncertainty of $\sigma_{N_{\mathrm{hit}}} = \sqrt{N_{\mathrm{hit}}}$, used in weighted least-squares fitting[10] (see Section A.3.7).

Next, data coverage in the valid fit range is verified. The position of the $\mu_{\mathrm{K}_{\bar{\alpha}}}$ is estimated by a piecewise derivative and peak-finding algorithm identifying the highest slope point[11]. Pixels lacking a detected peak or insufficient data above $N_{\mathrm{hit}} > 0$ (minimum required points: fit parameters + 3) are excluded from further analysis. This typically affects only a small fraction of pixels with an effectively lower baseline, leading to a shifted S-curve outside the measured threshold range.

Reasonable initial estimates and boundary conditions for fit parameters are critical for stable, fast convergence. A proper estimate of $\mu_{\mathrm{K}_{\bar{\alpha}}}$ is essential, as it serves as reference for estimating the other parameters, particularly the

[10] Maximum LLh methods are not employed for technical simplicity; fits are performed on a `TH1` object in the `ROOT` framework [172, 173], which does not allow simple exclusion of removed outlier bins (bins with zero entries are not ignored).

[11] This method uses linear interpolation (no splining) and Gaussian kernel smoothing to reduce derivative fluctuations; details in [9].

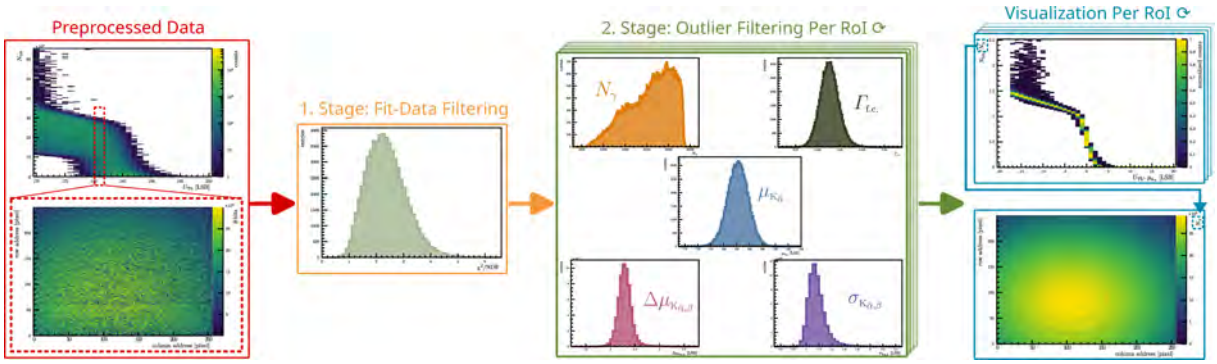

Figure 6.7: Data processing flow for Fe-55 S-curve measurements. The raw preprocessed data (red) is fitted and filtered in multiple stages: first, the data undergoes a χ^2/NDF fit quality check (orange), then split in RoIs and filtered for outliers on each fit parameter (green). In the final step the data set is visually inspected for potential misfits or systematic deviations from the model (blue).

scaling factor N_γ and the fractional charge collection parameter $\Gamma_{\text{f.c.}}$. Since noise can dominate at low thresholds, the lower fit boundary is set at the slope onset between the lowest threshold and $\mu_{\text{K}_{\bar{\alpha}}}$. The upper fit boundary is flexible; data points with zero hits (and thus $\sigma_{N_{\text{hit}}} = 0$) are ignored automatically during fitting.

After fitting, results undergo two filtering stages: a χ^2/NDF cut excludes poor fit results, followed by an outlier filtering on each fit parameter. For the outlier filtering, the fit results are split into five RoIs based on pixel positions (four edge pixels and the central region, excluding corner pixels, cf. Section 5.3.3). Edge pixels often exhibit a distinct behavior, notably in $\Gamma_{\text{f.c.}}$, due to charge collection from outside of the pixel matrix. Each fit parameter is outlier-filtered per RoI to reject unreliable fit results, primarily caused by an insufficient coverage of data points above $\mu_{\text{K}_{\bar{\alpha}}}$. Here, $\Gamma_{\text{f.c.}}$ cannot be properly constrained, leading to undefined or unphysical values for most fit parameters.

Finally, fits are visually inspected beyond the numerical GoF measure to identify potential misfits or systematic deviations from the model. Therefore, superimposed, scaled (by N_γ), and shifted (by $\mu_{\text{K}_{\bar{\alpha}}}$) data sets are examined for consistency, as shown in Figure 6.6b. Additionally, mapping the extracted source intensity N_γ across the pixel matrix can highlight spatial patterns or discrepancies.
The complete processing workflow[12] is illustrated in Figure 6.7.

[12] Implementation details can be taken from [9, 11].

6.3 "Simulating" Charge Depositions with Injection

Injecting a defined amount of charge directly into the sensor's readout chain offers several advantages, primarily because it bypasses inefficiencies in the charge collection process and isolates the response of the readout electronics. With controlled parameters such as the *Injection* magnitude and repetition rate, the *Injection* system becomes a versatile tool for systematically determining a "pseudo" efficiency of the detector response relative to a known input signal.

6.3.1 Implementation and Evaluation of the Injection Circuit in MuPix10

The injection feature in HV-MAPS is realized via an in-pixel capacitor (C), which is charged to a defined voltage (U) and deposits its charge (Q) directly into the n-well of the pixel diode upon release, as given by:

$$Q = C \cdot U \quad \rightarrow \quad Q_{\text{deposit}}[\text{e}] \approx 6.242 \cdot \frac{C_{\text{injection}}}{[\text{fF}]} \cdot \frac{U_{\text{injection}}}{[\text{mV}]} \tag{6.8}$$

Typically, the injection capacitance is designed to be approximately 1 fF, enabling to simulate charge depositions up to approximately 10 ke (for an injection voltage of 1600 mV).

Pixel injection selection is controlled via two types of enables: one for the row address and one for the column address of the pixel matrix, whereby all combinations of enabled addresses contribute to the injection matrix. Due to the "double column" structure of MuPix10, the column enable controls an even-odd pair of columns, so at least two pixels are always enabled for injection (see Figure 6.8). All injection capacitances are to first order in parallel, increasing the total capacitance to be charged with the number of enabled pixels.

The injection is controlled either from an on-chip circuitry — available only on certain HV-MAPS generations — or externally via the *MuDAQ Motherboard* (see Figure 6.9). The latter approach is used throughout this work to ensure consistent injection conditions for all DUT and be independent of on-chip variations.

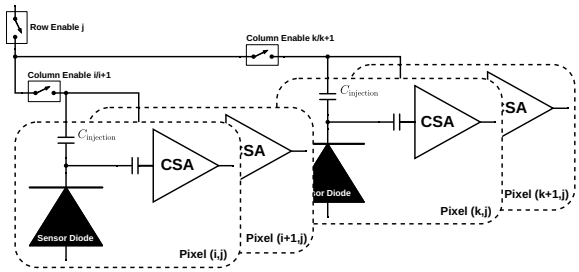

Figure 6.8: Pixel charge injection scheme in MuPix10 with row/column pixel address enable and *MuDAQ Motherboard*-controlled pulsing (see Figure 6.9).

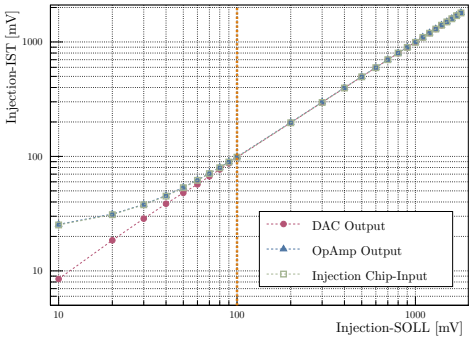

Plot 6.1: Set injection value (SOLL) versus measured injection value (IST) at 3 different points of the injection circuitry: DAC (red), OpAmp (blue) & CMOS switch (green), see Fig. 6.9.

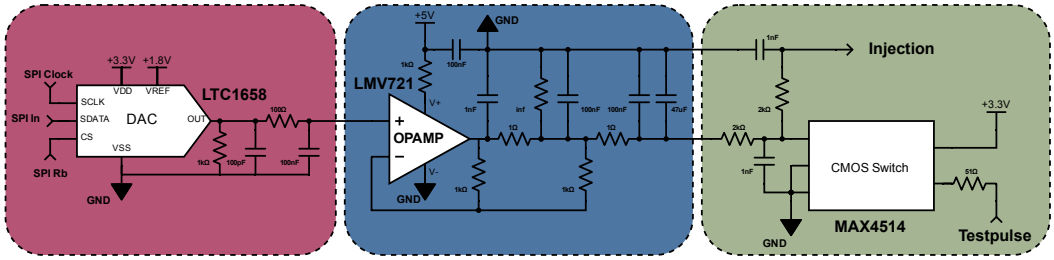

Figure 6.9: Injection circuitry on *MuDAQ Motherboard*: voltage set by 14 bit DAC (red), driven by OpAmp (blue), pulsing via CMOS analog switch (green) controlled from FPGA.

Parameter	Range	Comment
Injection Voltage [mV]	100-1600	Lower limit by OpAmp, upper limit by sensor
Injection Duration [μs]	10	Setting dependent, should exceed analog signal pulse length
Injection Frequency [Hz]	10000	Injection matrix size & duration dependent
Injection matrix [pixel×pixel]	20x20	Ranging from 1x2 to 24x24

Table 6.3: Injection parameters of the MuPix10 chip.

The injection voltage $U_{\text{injection}}$ is set by a 14 bit DAC subdividing an 1.8 V range. The OpAmp supplies the power required to charge multiple pixel capacitances, while a CMOS analog switch controls the pulsing (Figure 6.8).

Measured injection values (IST) show linearity at the DAC level, while being limited by the OpAmp performance on the lower end, see Plot 6.1. Therefore, injection voltages are limited to a 100 mV to 1600 mV range, where the upper limit is defined by the approximate voltage level of the *n*-well to avoid damage to the sensor.

As more pixels are enabled for injection, the required charge increases proportionally due to parallel capacitances; this impacts the charging and discharging behavior, causing non-ideal voltages at the pixel side (cf. Section A.4.2). If the injection voltage drops towards the injection capacitance, but is treated as an effectively ideal voltage $U^{\text{ideal}}_{\text{injection}}$, $C_{\text{injection}}$ will appear increased to compensate for the reduced voltage. This is determined experimentally by comparing the sensor's response against an absolute calibration source (e.g. Fe-55, see Section 6.2). In the following, $C^{\text{eff.}}_{\text{injection}}$ is used throughout to denote this "effective" injection capacitance, assuming an ideal voltage source:

$$C^{\text{eff.}}_{\text{injection}} = \frac{Q_{\text{input}}}{U^{\text{ideal}}_{\text{injection}}} \xrightarrow{\text{Si},Eq.\ 2.6} C^{\text{eff.}}_{\text{injection}}\,[\text{fF}] \approx 0.044\,\text{e/eV} \cdot \frac{Q_{\text{input}}}{[\text{eV}]} \cdot \frac{[\text{mV}]}{U^{\text{ideal}}_{\text{injection}}} \tag{6.9}$$

However, injecting into arbitrarily large pixel matrices is limited, as the (dis-)charging starts to dominate the signal response, affecting both pulse shape and amplitude (cf. Section A.4.2). For studying the energy-threshold response of individual pixels, amplitude accuracy is prioritized over pulse shape, necessitating a compromise between matrix size and injection accuracy. An overview of the injection parameters for MuPix10 is summarized in Table 6.3.

Injecting into RoIs of 20 × 20 pixel balance injection accuracy and matrix size. These RoIs are separated by routing domains (see Section 3.4) and sub-matrix affiliation to minimize cross talk affecting the measurements and enabling subsequent comparability of spatial variations across the sensor. For each RoI, identical injection settings in terms of repetition rate, duration, and matrix size — for both *low-gain* and *high-gain* sensor settings — are applied to study the pixel response under varying injection amplitude to minimize systematic effects. An injection frequency of 10 kHz over 1 s (fixed $N_{\text{inj}} = 10,000$ injections) per threshold or injection point provides an optimal compromise between measurement duration and statistical uncertainty.

Scans cover the detection threshold and injection voltage in fine steps (1 LSB or 5-20 mV) to capture the response curves adequately, while total measurement time remains within several hours for each RoI and bias setting (cf. Section 6.1.2). This allows to form a S-curve in both threshold and injection voltage domains by comparing the number of detected hits N_{hit} against the number of injections N_{inj} for each setting.

6.3.2 Charge Injection S-curve Model & Data Handling

Injection simulates a monochromatic charge deposition fed directly into a pixel's readout chain, with the signal distorted by noise, detector resolution, and gain limitations. The corresponding S-curve response can be modeled using a normal (complementary) CDF, as shown Equation 6.2.

The S-curve can be represented in two ways: as a function of the detection threshold U_{Th} for a fixed injected charge E_{C} (threshold S-curve), or as a function of the injected charge E_{C} for a fixed detection threshold U_{Th} (injection S-curve). Both representations yield equivalent extractable means (μ), but provide differing insights into detector performance via the standard deviation (σ):

$$\varepsilon_{\text{pseudo}}(x \mid \mu, \sigma) = \begin{cases} \text{CDF\_C}_{\text{normal}}(U_{\text{Th}} \mid \mu_{U_{\text{Th}}}, \sigma_{U_{\text{Th}}}) & \text{,if Threshold S-curve} \\ \text{CDF}_{\text{normal}}(E_{\text{C}} \mid \mu_{E_{\text{C}}}, \sigma_{E_{\text{C}}}) & \text{,if Injection S-curve} \end{cases} \tag{6.10}$$

Data normalization to the pseudo efficiency $\varepsilon_{\text{pseudo}}$ is achieved by dividing the number of detected hits N_{hit} by the number of injections N_{inj}.

For the threshold S-curve, the probability of detecting hits increases as the detection threshold U_{Th} approaches the baseline. Analogously, for an injection S-curve, the hit detection probability increases with rising injected charge E_{C}. A visual representations of both S-curve types is illustrated by Plot 6.2.

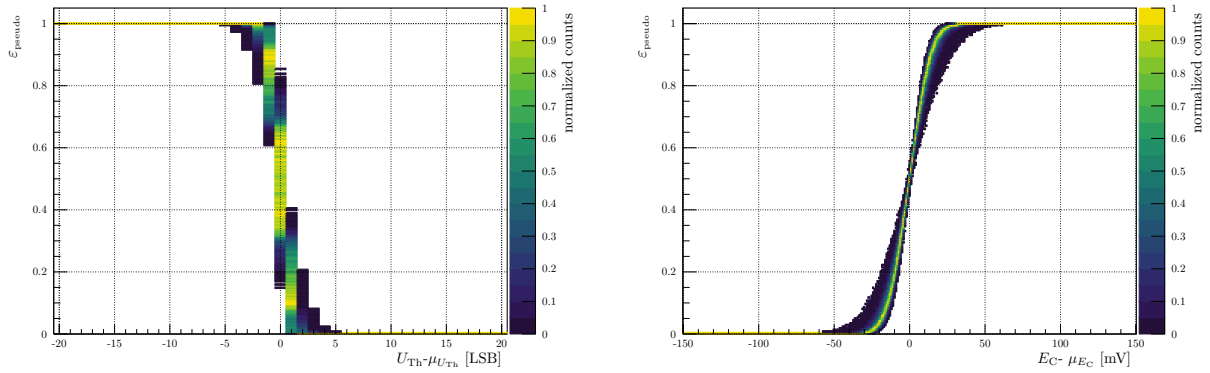

(a) Threshold S-curve.

(b) Injection S-curve.

Plot 6.2: Examples of superimposed S-curve data sets, shifted by the fitted mean.

Data Processing & Fit Procedure

Raw data is preprocessed to form a pseudo efficiency for each threshold or injection point. In the first stage, all data points exceeding the total number of injections (N_{inj}) are rejected, as these are attributed to fake hits caused by noise. Since fake and real hits cannot be distinguished, this initial filtering step is necessary. In the second stage, monotonically rising (injection S-curve) or falling (threshold S-curve) data points are ensured by removing any outliers that deviate beyond a three-sigma criterion[13] compared to neighboring data points (cf. Section 6.2.2).

Furthermore, the S-curve data is expected to cross the 50 % efficiency level to ensure sufficient coverage. A special case can occur at high detection threshold near the saturation threshold (see Section 6.4.1). The pseudo efficiency may plateau below unity as fluctuations in the baseline level rather than the magnitude of the injected charge dominate whether the detection threshold is exceeded. Such S-curve data are not considered in the models and are therefore deemed invalid and discarded. At low thresholds and high injection amplitudes, long analog signals can saturate the readout chain, blocking detection of subsequent injections at high repetition rates. This leads to a significant drop in effective efficiency at these thresholds, but does not impact the extraction of mean and standard deviation of the S-curve, as these regions are excluded from the fit range.

Start values and boundaries for the fit parameters are estimated using the 50 % crossing point and the respective $\pm 1\sigma$ crossing point ($\sim$ 0.16 % and $\sim$0.84 %). Additionally, a $\pm 5\sigma$ range around the mean is defined to limit the fit range to the relevant region of the S-curve. This avoids containing excessive amount of data points at unity or zero efficiency, which adds degrees of freedom without being informative for the fit quality[14]. Here, it is ensured that at least three NDF are present in the defined fit range. Fitting is performed using binomial bin statistics with a maximum LLh method[15] (cf. Section A.3.7), and cross checked by a χ^2-test[16].

The extracted fit parameters (mean and standard deviation) are then filtered based on GoF measures and also for outliers in the fit parameters themselves. For the mean, SNR cuts are applied to exclude unstable fits. Lastly, a visual inspection of the superposition of data and detector response is performed to ensure the fit quality. The full data processing flow is summarized in Figure 6.10.

[13] The associated error on the data points is determined assuming binomial statistics handled by the `ROOT::TEfficiency` object [172, 173].
[14] If many data points have zero or unity efficiency, the χ^2/NDF may be underestimated since these perfectly fitted points only increase the NDF.
[15] Fitting is performed using the `ROOT::TBinomialEfficiencyFitter` class from the `ROOT` framework [172, 173].
[16] A weighted least-squares method evaluates the fit results on data points represented by a `ROOT::TGraphAsymmErrors` [172, 173].

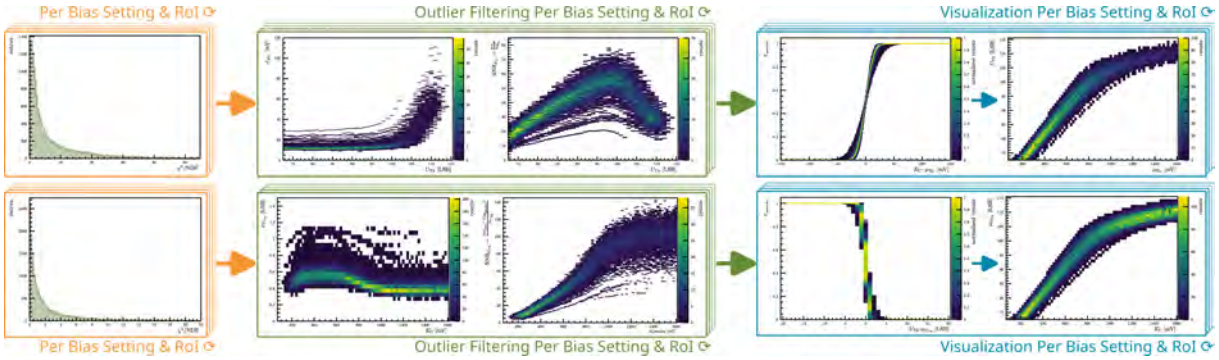

Figure 6.10: Data processing flow for *Injection* S-curve measurements. Fit results are first filtered by GoF (orange), then by outliers in σ and SNR ($\approx \mu/\sigma$) (green), and finally verified by visual inspection of superposed mean-shifted data and fitted results (blue).

Model Limitations & Informative Significance

The normal PDF modeling of charge injection may be adequate but exhibits certain limitations introduced by detector-related effects. As for the Fe-55 S-curve model (cf. Section 6.2.2), linearity of the threshold-energy relation is normally required to perfectly describe the S-curve with a normal (complementary) CDF. However, as amplification starts to saturate, this linearity generally no longer holds, leading to deviations from the expected shape. Locally, linearity may still be assumed, but global deviations arise. This particularly affects the standard deviation of the S-curve. In the linear regime, standard deviation can be seen as a measure of the detector's noise level. In the saturation regime, the standard deviation is no longer well-defined as the S-curve shape is distorted.

For a threshold S-curve, saturation leads to a compression of the S-curve (smaller $\sigma_{U_{\mathrm{Th}}}$), which may saturate at the binning resolution of a threshold ($1/\sqrt{12}$). For an injection S-curve, saturation leads to stretching of the S-curve (larger $\sigma_{E_{\mathrm{C}}}$), reflecting an increasing deterioration of the energy resolution with increasing detection threshold. In both cases, the GoF is not suitable as the sole measure to judge fit quality in the saturation regime, being either over- (threshold S-curve) or underestimated (injection S-curve). Visual inspection of the (mean-shifted) superposition of data (see Plot 6.2) and the fit results leading to the detector response is performed to assess whether an appropriate mean value has been extracted.

Especially threshold S-curves are heavily affected by the gain settings of a sensor and limited by intrinsic threshold binning resolution (see Plot 6.3). For low gain settings, the standard deviation can be overestimated because the small $\sigma_{U_{\mathrm{Th}}}$ leads to a steeply falling S-curve that cannot be adequately resolved by discrete threshold steps. For this reason, primarily the mean value is extracted from threshold S-curve to form the threshold-energy relation (cf. Section 6.4.1). Injection S-curves are preferred to approximate energy resolution and noise contribution, as they are not affected by the coarse threshold binning.

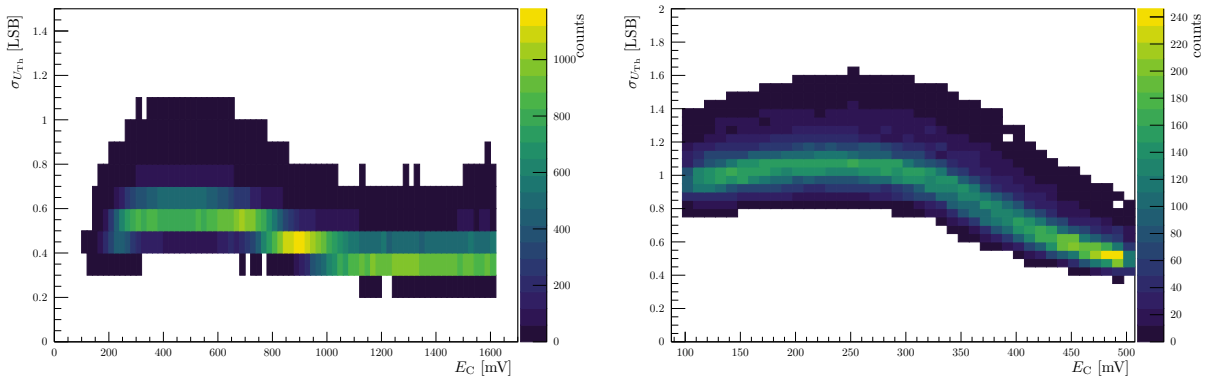

(a) At *low-gain* settings.

(b) At *high-gain* settings.

Plot 6.3: Exemplary gradients of $\sigma_{U_{\mathrm{Th}}}$ as function of E_{C} for MP10-T100-S300-1 at −20 V.

6.4 Method for Energy-Dependent Detection Threshold Scaling

After establishing precise charge injection methods to relate the detection threshold to a defined input charge (see Section 6.3) and converting detector-level units to energy equivalence using monochromatic depositions (see Section 6.2), the resulting calibrations are combined to derive an energy-dependent detection threshold scaling.

To accomplish this, a model describing the full detector response from amplification to discrimination is required. In practice, the interaction between transistor-level components is so complex that only detailed transient simulations could yield a realistic description, which would be impractical for this application. An empirical model is therefore employed to represent the detector response. It captures key characteristics such as gain, dispersion, and saturation to describe observed non-linearities and enable interpretation of physically meaningful detector quantities.

The following sections present this empirical model, applicable not only to HV-MAPS but to any sensor with a comparable front-end architecture.

6.4.1 Detector Response Characteristics

The model function representing the detector response must accurately represent the measured data, while remaining invertible for precise transformation between signal output (detector-level units) and charge input. Plot 6.4 depicts the response curve of a single pixel with fine granularity in the detector response and large coverage of the input charge range, thus enabling a precise study of the response characteristics. While typically only the response to a given input charge is considered, this work requires the inverse transformation to determine the input charge corresponding to a defined detection threshold. Therefore, a model supporting bidirectional conversion is advantageous, as it also enables the use of this information in simulating detector behavior based on input charge values — although such simulation is beyond the scope of this work.

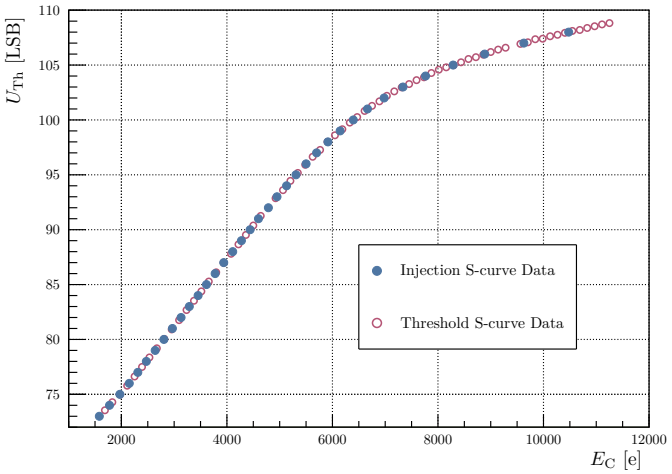

Plot 6.4: Example detector response curve extracted from threshold and *Injection* S-curve data. The data points extracted from threshold (red) and *Injection* (blue) S-curve data illustrates the equivalence of both representations and can be combined to a single response curve.

The model must encompass the entire signal chain after the charge collection, including the CSA, the analog signal transmission to the periphery, and the digitization by the comparator. In principle, the dominant effects separate into analog signal behavior and digital signal discrimination.

The analog signal transmission imparts additional shaping indistinguishable from the intrinsic CSA response at the pixel level. While signal line routing and crosstalk (see Sections 3.4 and 3.4.1) may contribute to parasitic effects such as signal distortion and effective signal loss (see Sections 3.4 and 3.4.1), their precise magnitudes remain unquantified. Consequently, these effects are incorporated into the overall amplifier behavior and are not separately corrected on a per-pixel basis. The response curve's primary form is dominated by the CSA's dynamic range, while the comparator is assumed linear across the measured range, affected only by fluctuations in the relative threshold to

baseline levels. DNL (**D**ifferential **N**on-**L**inearity) effects are neglected, as the coarse voltage DAC steps controlling threshold and baseline impose greater uncertainty[17] than the DNL effects themselves.

Not all physical effects are modeled, as some exceed measurement capabilities and cannot be validated. When the detection threshold nears the baseline, noise dominates, impairing accurate measurement in this region[18]. Consequently, this region is extrapolated from the linear domain, implying that the modeled local baseline — the extrapolated baseline level of an individual pixel — falls below the global baseline — baseline level applied to the sensor. As threshold and baseline are always defined relative to each other, knowing the absolute baseline level of an individual pixel — which may fall below the global baseline — is solely required for interpreting the physical meaning of the model parameters.

The linear gain domain can be approximated by a linear function valid up to an a priori unknown output voltage limit. Saturation onset is expected near the same output voltage across pixels and gain configurations[19], occurring due to the limited voltage range of the amplifier's output node — inherent to its design — thus capping the achievable pulse height. The required input charge to reach saturation varies with each pixel's individual gain, governed by small (feedback) currents that lack individual pixel-based tuning capabilities. As the output voltage approaches saturation, the change in gain decreases continuously, eventually reaching zero at the saturation point; this behavior can be approximated by an exponential function of the $(1 - \mathrm{e}^{-x})$-form, which reflects the asymptotic nature of saturation.

Hence, the saturation domain is the most complex to model. It has to incorporate a defined maximum response value representing the upper boundary of the amplifier's dynamic range. Additionally, a shaping component influencing saturation behavior — primarily determining the curvature of the response curve— along with a pedestal level marking the response onset[20], should also be incorporated into the model.

Considering the necessity to fit multiple pixels, each requiring estimated start values and valid ranges, a simple, flexible, and robust function is essential.

6.4.2 Empirical Detector Response Model

The detector response is modeled as a piecewise function composed of a linear domain and a saturation domain, which are continuously connected at a transition point separating the two. The linear part is defined as:

$$f_{\text{linear}}(E_{\text{C}}) = \mathcal{G}_{\mathrm{d}U/\mathrm{d}E} \cdot E_{\text{C}} + U_{\text{BL, local}} \quad \Leftrightarrow \quad \frac{U_{\text{Th}} - U_{\text{BL, local}}}{\mathcal{G}_{\mathrm{d}U/\mathrm{d}E}} = f_{\text{linear}}^{-1}(U_{\text{Th}}) \tag{6.11}$$

where $U_{\text{BL, local}}$ is the extrapolated local baseline level (not to be confused with the global $U_{\text{BL, global}}$) and $\mathcal{G}_{\mathrm{d}U/\mathrm{d}E}$ is the effective gain — the signal amplitude (in LSB) corresponding to the charge input — of an individual pixel. The inverse gain, $(\mathcal{G}_{\mathrm{d}U/\mathrm{d}E})^{-1} = \mathcal{R}_{\mathrm{d}E/\mathrm{d}U}$, represents the detector's ability to resolve small changes in energy and corresponds to the resolution of a threshold bin.

The linear model applies up to the transition point, defined by either the energy value $E_{\text{C, TRS}}$ or the detection threshold $U_{\text{Th, TRS}}$, related by:

$$E_{\text{C, TRS}} = \frac{U_{\text{Th, TRS}} - U_{\text{BL, local}}}{\mathcal{G}_{\mathrm{d}U/\mathrm{d}E}} \tag{6.12}$$

This transition point marks the onset of saturation effects and depends on the pixel's gain and local baseline. Since conversion from arbitrary threshold levels to energy units is preferred, $E_{\text{C, TRS}}$ is always defined via $U_{\text{Th, TRS}}$ for bidirectional conversion as given above.

The saturation domain is modeled based on a function satisfying $\lim_{x\to\infty} g(x) = 1$. By scaling the function with a maximum value, the output range is fully covered within the desired limits. The exponential function approach discussed in Section 6.4.1, complicates the parameter estimation and thus is estimated to reduce complexity. From *Padé-Approximation* [187], it is known that exponential functions can be approximated by ratios of polynomials (rational functions, denoted by $[m/n]$). The lowest degree rational function approximating an exponential

[17] A threshold LSB step corresponds to approximately 7 mV, yielding a binning resolution of $7\,\text{mV}/\sqrt{12} \approx 2\,\text{mV}$. Observed deviations of about 1 mV from expected values lie within the specified accuracy of the multimeter [185, 186].

[18] Additionally, the low-charge input region cannot be examined by injection measurements due to the non-linearity of the injection voltage below 100 mV, which originates from the OpAmp (cf. Section 6.3).

[19] Not accounting for minor variations caused by manufacturing process variations.

[20] The pedestal should accommodate both relative and absolute threshold levels, shifting the model across data representations.

function is the first-degree rational function ($[1/1]$), i.e., the ratio of two linear functions[21]. Incorporating these elements produces the following saturation gain model:

$$g_{\text{saturation}}(E_{\text{C}}) = \alpha_{\text{saturation}} \cdot \frac{E_{\text{C}} - \beta_{\text{pedestal}}}{E_{\text{C}} - \delta_{\text{shape}}} \quad \Leftrightarrow \quad \frac{\alpha_{\text{saturation}} \cdot \beta_{\text{pedestal}} - \delta_{\text{shape}} \cdot U_{\text{Th}}}{\alpha_{\text{saturation}} - U_{\text{Th}}} = g^{-1}_{\text{saturation}}(U_{\text{Th}}) \tag{6.13}$$

where $\alpha_{\text{saturation}}$ is the effective saturation point — a threshold level generally not exceeded by the signal amplitude[22]. The parameters β_{pedestal} and δ_{shape} define the onset (pedestal) and shaping (curvature) of the saturation model[23]. Here, β_{pedestal} corresponds to the energy point, where the output signal is zero, and δ_{shape} determines the relative[24] saturation rate. Since both fall below below the applicable range ($<E_{\text{C, TRS}}$), they serve primarily as mathematical constructs without direct physical meaning.

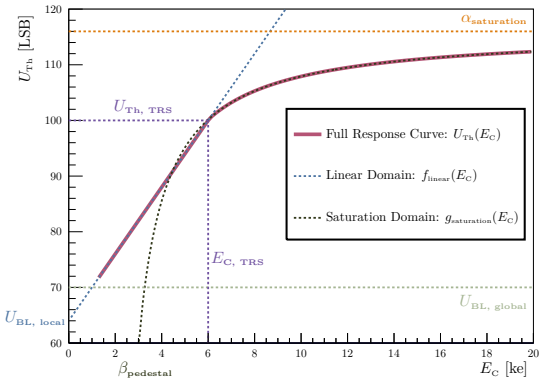

Figure 6.11: Detector response model sketch.

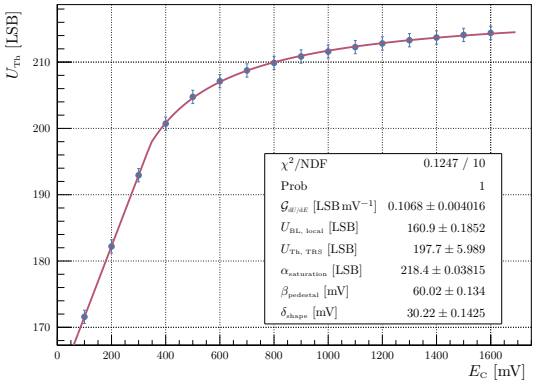

Plot 6.5: Example fit of detector response model to data.

Combining linear and saturation parts yields the full response function (see Figure 6.11):

$$U_{\text{Th}}(E_{\text{C}} \mid \mathcal{G}_{\text{dU/dE}}, U_{\text{BL, local}}, U_{\text{Th, TRS}}, \alpha_{\text{saturation}}, \beta_{\text{pedestal}}, \delta_{\text{shape}}) = \begin{cases} f_{\text{linear}}(E_{\text{C}} \mid \mathcal{G}_{\text{dU/dE}}, U_{\text{BL, local}}) & , U_{\text{Th}} \leq U_{\text{Th, TRS}} \\ g_{\text{saturation}}(E_{\text{C}} \mid \alpha_{\text{saturation}}, \beta_{\text{pedestal}}, \delta_{\text{shape}}) & , U_{\text{Th}} > U_{\text{Th, TRS}} \end{cases} \tag{6.14}$$

or:

$$E_{\text{C}}(U_{\text{Th}} \mid \mathcal{G}_{\text{dU/dE}}, U_{\text{BL, local}}, U_{\text{Th, TRS}}, \alpha_{\text{saturation}}, \beta_{\text{pedestal}}, \delta_{\text{shape}}) = \begin{cases} f^{-1}_{\text{linear}}(U_{\text{Th}} \mid \mathcal{G}_{\text{dU/dE}}, U_{\text{BL, local}}) & , U_{\text{Th}} \leq U_{\text{Th, TRS}} \\ g^{-1}_{\text{saturation}}(U_{\text{Th}} \mid \alpha_{\text{saturation}}, \beta_{\text{pedestal}}, \delta_{\text{shape}}) & , U_{\text{Th}} > U_{\text{Th, TRS}} \end{cases} \tag{6.15}$$

where $U_{\text{Th, TRS}}$ is employed as additional fit parameter, which is either directly fitted or indirectly obtained via Equation 6.12. Table 6.4 summarizes all model parameters, their units, descriptions, and valid ranges.

Data Processing & Fit Procedure

The detector response model dataset combines both threshold and S-curve measurements (cf. Plot 6.4). Each representation provides statistical errors along one axis; the error in the other axis is estimated. For the U_{Th}-axis, an uncertainty of $1/\sqrt{12}$ LSB is assigned, corresponding to the variance of a continuous uniform distribution (cf. [114, p. 151]). For the E_{C}-axis (in *Injection*-voltage units), an error of 1 mV is used, reflecting the typical deviation between defined and measured injection values (approximately one σ of the distribution, cf. Section A.4.2). The

[21] For more information on *Padé-Approximation*, see [187, p. 1ff, eq. 1.2]. Parameter reduction can be achieved by normalizing numerator and denominator gradients to unity or algebraically reorganizing coefficients to simplify the approximant without altering its properties.
[22] The saturation point $\alpha_{\text{saturation}}$ may be surpassed due to fluctuations in the threshold level and is represented by its average (mean) value.
[23] $\beta_{\text{pedestal}} > \delta_{\text{shape}}$ ensures a positive saturation rate; otherwise, the function decreases monotonically or stays constant ($\beta_{\text{pedestal}} = \delta_{\text{shape}}$).
[24] The "relative" saturation rate denotes dependence on the normalization method (whether $U_{\text{BL, global}}$ is subtracted from the threshold or not).

Parameter	Unit	Condition	Description
$\mathcal{G}_{\mathrm{d}U/\mathrm{d}E}$	[LSB/mV] or [LSB/e]	$\mathcal{G}_{\mathrm{d}U/\mathrm{d}E} \in (0, \infty)$	Linear gain of the detector
$U_{\mathrm{BL,\,local}}$	[LSB]	$U_{\mathrm{BL,\,local}} \in [0, U_{\mathrm{BL,\,global}}]$	Extrapolated local pixel baseline
$U_{\mathrm{Th,\,TRS}}$	[LSB]	$U_{\mathrm{Th,\,TRS}} \in (U_{\mathrm{BL,\,local}}, 255^{\dagger}]$	Transition threshold between linear and saturation domain
$E_{\mathrm{C,\,TRS}}$	[mV] or [e]		Transition energy corresponding to $U_{\mathrm{Th,\,TRS}}$
$\alpha_{\mathrm{saturation}}$	[LSB]	$\alpha_{\mathrm{saturation}} \in (U_{\mathrm{Th,\,TRS}}, 255^{\dagger}]$	Threshold at which the amplifier saturates
$\beta_{\mathrm{pedestal}}$	[mV] or [e]	$\beta_{\mathrm{pedestal}} \in (\delta_{\mathrm{shape}}, E_{\mathrm{C,\,TRS}})$	Input charge at threshold = 0
δ_{shape}	[mV] or [e]	$\delta_{\mathrm{shape}} \in [0, \beta_{\mathrm{pedestal}})$	Saturation rate relative to $\beta_{\mathrm{pedestal}}$

Table 6.4: Overview of the fit parameters of the detector response model. †: 255 LSB (0xFF) is the maximum value of the 8 bit voltage DACs (cf. Table A.10).

corresponding electron-equivalent uncertainty is obtained from the effective injection capacitance $C^{\mathrm{eff.}}_{\mathrm{injection}}$ of each pixel using Gaussian error propagation.

Since the data were preprocessed and filtered (cf. Sections 6.2 and 6.3), no outlier rejection is needed, but suitable initial values and parameter ranges must still be defined a priori. Determining the transition point $U_{\mathrm{Th,\,TRS}}$ is essential, separates the gain domains and ensures correct data assignment[25]. Parameters in the linear domain are estimated by linear regression, while those in the saturation domain are approximated in the first instance under the constraints of Table 6.4.

The dataset is then subdivided by $U_{\mathrm{Th,\,TRS}}$ into the two domains and fitted with their respective model functions to refine parameters[26], which then serve as initial values for a global fit of the full response model. The two data representations (i.e., U_{Th} vs. E_{C} and E_{C} vs. U_{Th}) are fitted independently to validate the model's bidirectional consistency, evaluated via weighted least-squares fits accounting for uncertainties in both dimensions (cf. Section A.3.7). Deviations between fit results may originate from numerical instabilities at $U_{\mathrm{Th,\,TRS}}$ that primarily affect the shape (δ_{shape}) and pedestal ($\beta_{\mathrm{pedestal}}$) parameters; this is acceptable since both are mathematical constructs without direct physical meaning. The remaining parameters ($\mathcal{G}_{\mathrm{d}U/\mathrm{d}E}$, $U_{\mathrm{BL,\,local}}$, $\alpha_{\mathrm{saturation}}$) remain unaffected and consistent across both representations within uncertainties. Absolute deviations between parameters of both representations are used to identify systematic effects.

Finally, the parameter set with the lower reduced χ^2-value is selected as the final result for each pixel and the absolute deviations between data and model visually inspected to identify systematic discrepancies. Figure 6.12 summarizes the main data processing steps for the detector response model fitting procedure.

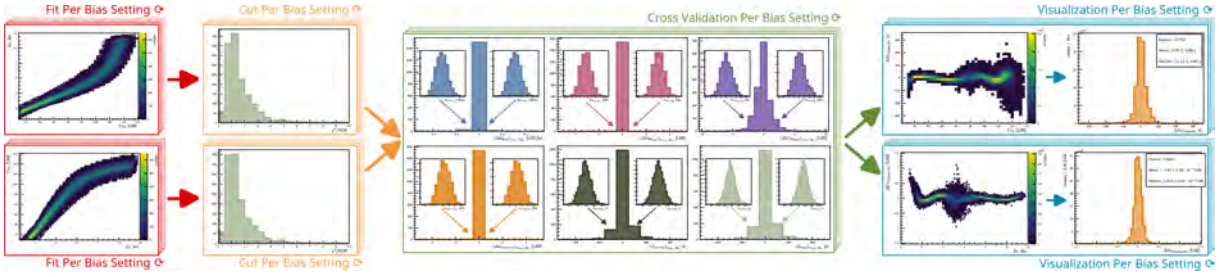

Figure 6.12: Data processing flow for the detector response. As both representation of the data should be equivalently be describable by the models, both are fitted (red) and subsequently the results are filtered based on the GoF (orange). The resulting fit parameters from both representations are compared (green) and in the last step the absolute deviation of both is visually inspected (blue). The final parameters are taken from the representation with the better GoF.

[25] $U_{\mathrm{Th,\,TRS}}$ can be estimated (i) from gain changes using piecewise derivatives, or (ii) from the sigma parameter in *Injection* S-curve fits, which rises near saturation after remaining constant in the linear region (cf. Section 7.3).

[26] For fitting subsets of both domains, at least three NDF per subset are required to ensure a reliable GoF evaluation.

7. The Detector Response of MuPix10

In the previous Chapter 6, methods to extract the energy response of the MuPix10 sensor were discussed, with the aim of calibrating the efficiency data recorded at PSI, as presented in Section 5.4. However, the methods employed cannot be used solely for data calibration. They provide deeper insight into detector performance and allow to probe sensor characteristics to be studied in greater detail as it is possible in a timely limited testbeam campaign.

This chapter discusses the results gathered from the calibration campaign, focusing on the detector response to defined input charges, as well as on the characteristics of the charge collection process itself, using Fe-55 source data. This enables comparison with general diode behavior and corresponding models, and provides insight into the assumptions made regarding the effects influencing the operation of HV-MAPS to date. Furthermore, it introduces a framework for studying the overall behavior across different sensors and operational settings, and establishes a basis for comparing and optimizing the performance of future HV-MAPS.

7.1 "Unfolding" the Non-Linearity of the Detector Energy Response

To correct for non-linearities in the energy response of a pixel detector and to calibrate its energy scale, an "unfolding" procedure is applied based on a semi-empirical model introduced in Section 6.4.2. For this procedure to work, several quantities introduced previously (cf. Chapter 6) require measurement on a per-pixel basis. In the following, the key parameters, as well as their intra- and inter-chip variations and their dependence on the applied bias voltage, are presented. Simultaneously, a step-by-step outline of the calibration process and its resulting impact is provided.

Since calibration data were taken in two gain settings (*low-gain* and *high-gain*), all quantities are compared at their respective RoIs as defined in Table 5.2 and operating points. For all DUTs except MP10-T50-S20-1, this is −20 V reverse bias voltage; MP10-T50-S20-1 was operated at −100 V. This comparison highlights the impact of the gain setting on specific parameters, enables identification of their significance for dispersion, and provides a reference for other measurements and sensors, as all parameters are calibrated to physically comparable units

Furthermore, certain assumptions on parameters are validated or excluded based on expected correlations from their physical meaning. To quantify these, the correlation between two parameters is defined by the Pearson correlation coefficient R [188, p. 26, eq. 2.28], which is the ratio of their covariance $cov(X, Y)$ to the product of their standard deviations σ_X and σ_Y:

$$R = \frac{cov(X,Y)}{\sigma_X \sigma_Y} = \frac{E[(X-\mu_X)(Y-\mu_Y)]}{E[(X-\mu_X)^2]^{1/2} E[(Y-\mu_Y)^2]^{1/2}} = \frac{\sum_i (X_i-\mu_X)(Y_i-\mu_Y)}{\sqrt{\sum_i (X_i-\mu_X)^2}\sqrt{\sum_i (Y_i-\mu_Y)^2}} \tag{7.1}$$

This formalism allows for a systematic assessment of parameter relationships, ranging from strong positive correlation ($R \approx +1$), through no correlation ($R \approx 0$), to strong negative correlation ($R \approx -1$), and supports the validation or rejection of the physical assumptions underlying the detector model.

7.1.1 Baseline Shifting and Dispersion

The baseline level for the comparators is defined globally for the entire sensor via the DAC *BLDig* and is referred to as $U_{\text{BL, global}}$ in the following. Although a common baseline is applied, local variations occur on a per-pixel basis, especially since hit detection depends not only on the baseline level but also on the respective threshold level U_{Th}. As these levels cannot be treated independently, a local baseline reference $U_{\text{BL, local}}$ is introduced, representing the effective difference between the global baseline and the idealized threshold level — also referred to as threshold or baseline dispersion. The local baseline reference $U_{\text{BL, local}}$ is derived from the extrapolation of the linear gain region to the zero-energy crossing (cf. Section 6.4.2). Thus, the effective shift between the local and global baseline

references ($U_{\text{BL, local}} - U_{\text{BL, global}}$) indicates a pixel's deviation from the global baseline, and a larger negative shift infers that the pixel's actual detection threshold in the energy domain may be higher than expected from the global baseline alone. However, this must be verified by considering the pixel's gain to accurately assess the energy level at the operational threshold (cf. Section 7.1.7).

Plot 7.1 shows the pixel-to-pixel and sensor-to-sensor dispersion in both gain settings relative to the respective global baseline reference. While sensor-to-sensor variations exhibit a similar trend in both gain settings (see Plot 7.1a), a distinct offset is observed between the two gain settings, with the *high-gain* setting generally showing a lower baseline shift compared to their *low-gain* counterparts. Although pixel-to-pixel dispersion dominates, a reduced spread is observed in the *high-gain* setting in comparison to the *low-gain* setting, as shown exemplarily in Plot 7.1b. Overall, the mean baseline shift remains relatively constant over the entire range of applied bias voltages for both gain settings, as shown in Plot 7.1c. The baseline shifts vary in the mean from approximately 20 mV to 30 mV for the *high-gain* setting to about 40 mV to 50 mV for the *low-gain* setting. Note that since $U_{\text{BL, local}}$ determines the lower limit for the actual baseline of a pixel, and because linearity is not guaranteed in the lower energy range and is not accessible via injection measurements, this limit is important.

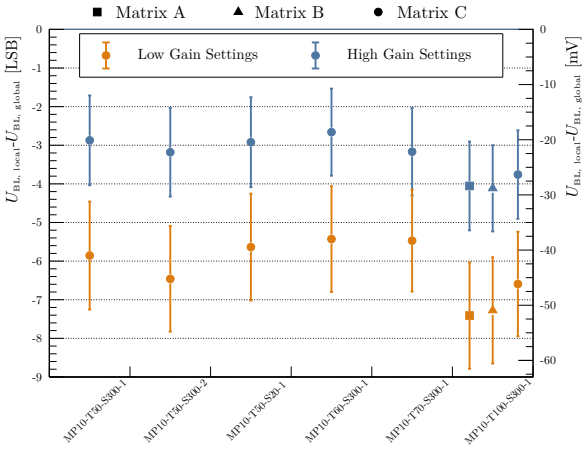

(a) Overview of mean baseline shift for all DUTs.

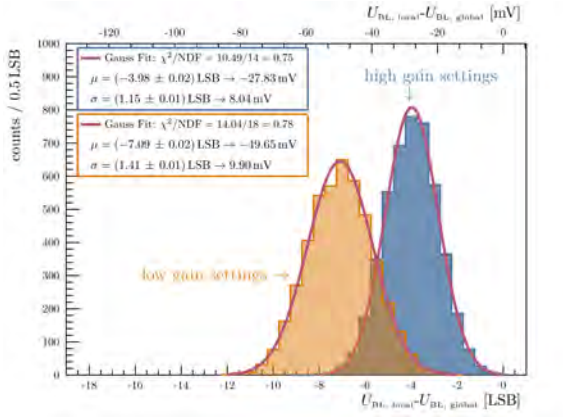

(b) Exemplary baseline shift distributions (Matrix A, B & C) of MP10-T100-S300-1.

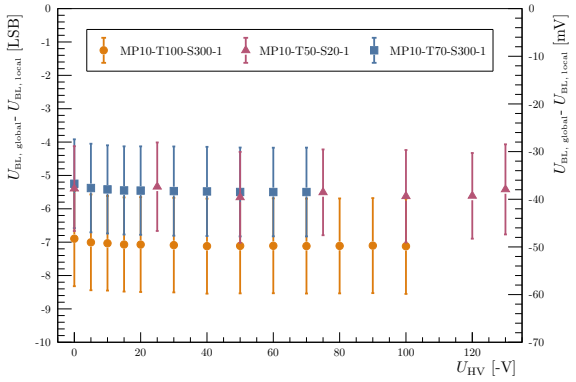

(c) Mean baseline shift as function of the reverse bias voltage in the *low-gain* setting.

Plot 7.1: Effective shift between local pixel based ($U_{\text{BL, local}}$) and global chip based ($U_{\text{BL, global}}$) baseline reference for *low-gain* (orange) and *high-gain* (blue) settings at −20 V reverse bias voltage (−100 V for MP10-T50-S20-1). The mean values are extracted from the respective baseline shift distributions, while the error bars represent the standard deviation. Conversion factor: 1 LSB = 7 mV corresponding to 1800 mV range of 8 bit DAC.

7.1.2 The Fe-55 $K_{\bar{\alpha}}$ Peak as Energy Calibration Reference

To calibrate the energy scale of each pixel, at least one well-known energy reference point is required — here, the $K_{\bar{\alpha}}$ peak position $\mu_{\mathrm{K}_{\bar{\alpha}}}$ of Fe-55 at approximately 1615 e (see Table 6.1). The measured values of $\mu_{\mathrm{K}_{\bar{\alpha}}}$ result from both the effective baseline dispersion and pixel-to-pixel gain variations.

To confirm that the local baseline reference $U_{\mathrm{BL,\,local}}$ accurately represents the effective baseline level of a pixel, its correlation with $\mu_{\mathrm{K}_{\bar{\alpha}}}$ is investigated. As shown exemplarily in Plot 7.2c, a strong correlation with a coefficient of about $R = 0.734$ is observed, though it is still smeared by pixel gain variations.

The effectiveness of the local baseline reference $U_{\mathrm{BL,\,local}}$ in reducing dispersion in the energy response, is demonstrated by comparing the spread of $\mu_{\mathrm{K}_{\bar{\alpha}}}$ when referenced to both the global baseline $U_{\mathrm{BL,\,global}}$ and the local baseline $U_{\mathrm{BL,\,local}}$. Plot 7.2b illustrates this comparison, showing that the dispersion is reduced by about a third when using $U_{\mathrm{BL,\,local}}$, as quantified by the standard deviation of the respective distributions. In the exemplary case, the sigma decreases from 1.6 LSB $\approx$ 11.3 mV with $U_{\mathrm{BL,\,global}}$ to 1.1 LSB $\approx$ 7.7 mV with $U_{\mathrm{BL,\,local}}$. A similar effect is observed for all sensors, as summarized in Plot 7.2a, confirming that $U_{\mathrm{BL,\,local}}$ effectively captures pixel-to-pixel variations in the energy response offset. However, it does not fully eliminate dispersion, as gain variations still contribute.

This demonstrates that assuming a zero crossing of the detection threshold with the global baseline $U_{\mathrm{BL,\,global}}$ and interpolating via a single energy point is insufficient for per-pixel energy scale calibration — even for the linear gain region — highlighting the necessity of more than one energy reference point.

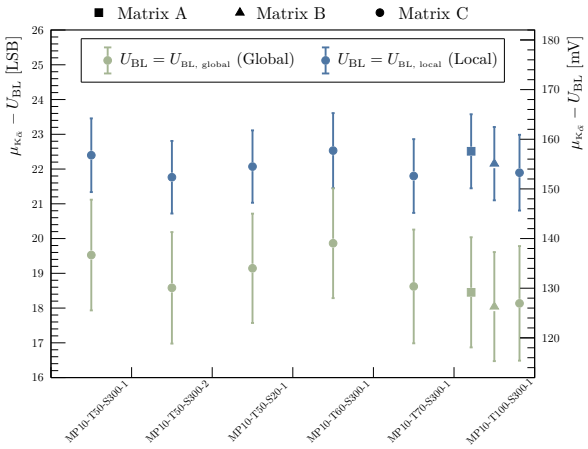

(a) Mean of the relative $\mu_{\mathrm{K}_{\bar{\alpha}}}$ to the applied baseline reference for all DUTs with error bars indicating the standard deviation.

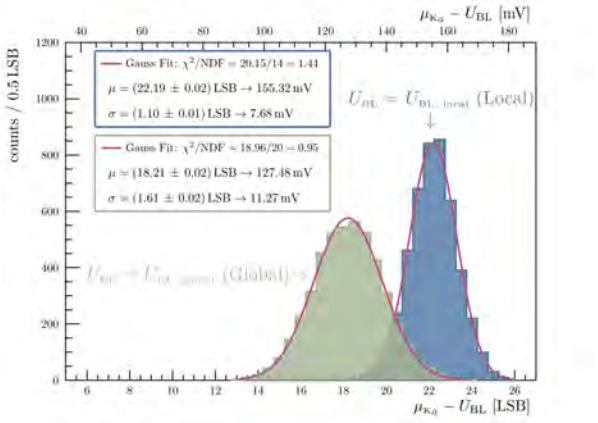

(b) Exemplary distributions of $\mu_{\mathrm{K}_{\bar{\alpha}}}$ relative the baseline references for MP10-T100-S300-1 (Matrix A, B & C).

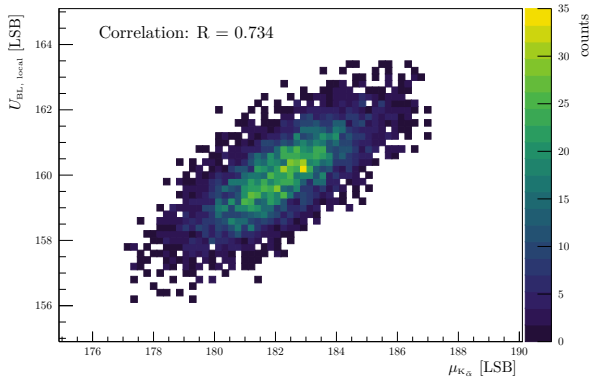

(c) Exemplary correlation between $U_{\mathrm{BL,\,local}}$ and $\mu_{\mathrm{K}_{\bar{\alpha}}}$ for MP10-T100-S300-1.

Plot 7.2: Dependency between $\mu_{\mathrm{K}_{\bar{\alpha}}}$ and the applied baseline reference ($U_{\mathrm{BL,\,global}}$ in green and $U_{\mathrm{BL,\,local}}$ in blue) in the *high-gain* settings at −20 V reverse bias voltage (−100 V for MP10-T50-S20-1). Conversion factor: 1 LSB = 7 mV corresponding to 1800 mV range of 8 bit DAC.

7.1.3 Extraction of the Injection Capacitances

Using the uncalibrated gain and local baseline parameters obtained under the *high-gain* settings, together with the $\mu_{K_{\bar{\alpha}}}$ peak position, the effective injection capacitance $C^{\text{eff.}}_{\text{injection}}$ of each pixel can be determined by evaluating the charge injection corresponding to the $K_{\bar{\alpha}}$ peak. From the linear gain function (Equation 6.11), the equivalent injected charge at $\mu_{K_{\bar{\alpha}}}$ is derived. Applying the charge-capacitance-voltage relation (Equation 6.9), then yields the effective injection capacitance.

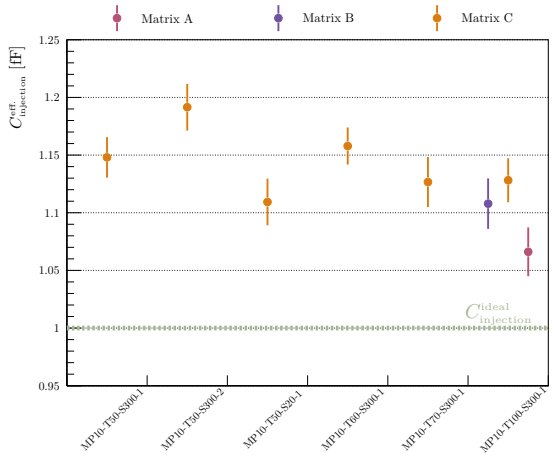

(a) Overview of the mean effective injection capacitance for each DUT. The green line indicates the intended design value of 1 fF.

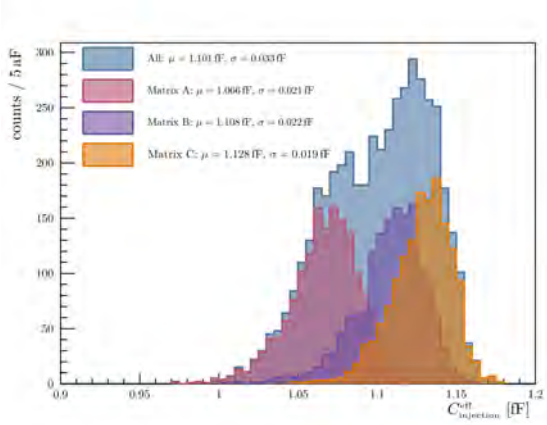

(b) Injection capacitance distributions for MP10-T100-S300-1.

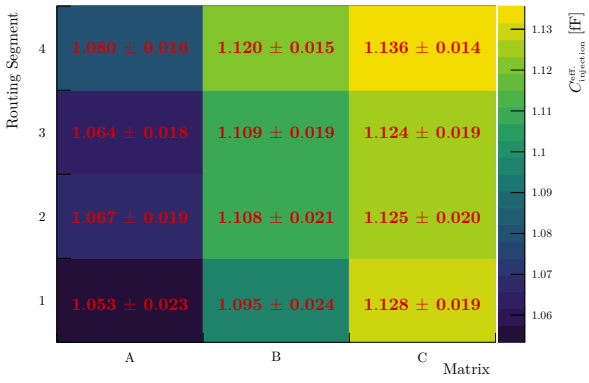

(c) Mapped injection capacitance for MP10-T100-S300-1.

Plot 7.3: Effective injection capacitance $C^{\text{eff.}}_{\text{injection}}$ for all DUTs at −20 V (−100 V for MP10-T50-S20-1) reverse bias voltage in the *high-gain* settings. The stated values indicate mean injection capacitance, while the error (bars) represent the corresponding standard deviation for each RoI.

Plot 7.3a shows that all extracted $C^{\text{eff.}}_{\text{injection}}$ exceed the nominal design value of 1 fF by approximately 10 % to 20 %. A deviation towards higher injection capacitance values can arise as parasitic capacitances add to the designed injection capacitance, while manufacturing tolerances can also lead to variations in the actual capacitance values. In practice, the applied injection voltages — sourced externally — may drop along the routing path to the sensor, introducing an effective reduction in the voltage actually reaching the pixel's injection capacitor. A more dominant expected effect is the injection voltage drop within the sensor itself. Here, the injection is routed on-chip along the column direction from lower towards higher addresses. This effect becomes more pronounced when multiple injection capacitances are addressed simultaneously, as the increased parallel capacitance load raises the current demand on the injection voltage source, which in turn leads to a voltage drop of approximately 20 mV to 40 mV — corresponding to the observed deviation in capacitance from the design value — relative to the idealized injection voltage. Measurements performed on a different setup for sensor MP10-T100-S300-1 (matrices A and B versus

matrix C) confirm this trend, as illustrated in Plot 7.3b. The distribution of injection capacitances shifts towards higher values from matrix A to matrix C. Plot 7.3c visualizes how the mean injection capacitance varies across all sub-matrices and routing segments. A clear trend of increasing injection capacitance from left to right sub-matrices — that is, from lower to higher column addresses — is observed for all RoIs. A less pronounced increase is also observed along the row direction within each sub-matrix, which is again linked to the on-chip voltage distribution network routing the injection voltage from lower to higher row addresses.

Within individual sub-matrices, pixel-to-pixel variations dominate the spread in injection capacitance, whereas differences between sensors are expected to be primarily driven by varying amounts of voltage drop within their respective injection networks. With the injection capacitances determined, additional energy calibration points can now be established through injection measurements. Consequently, all subsequent measurements can be converted directly from injection voltage to injected charge using the relation given in Equation 6.8.

7.1.4 Calibrated Gain and Resolution in the Linear Regime

The gain is a key parameter for assessing the performance of a detector, as it directly determines the achievable detector performance in terms of SNR and resolution. Using the injection capacitances obtained in Section 7.1.3, the gain $\mathcal{G}_{dU/dE}$ of each pixel is calculated by evaluating the slope of the linear region of the response curve in the charge domain. This allows for direct comparison of $\mathcal{G}_{dU/dE}$ between operational conditions as well as across sensors.

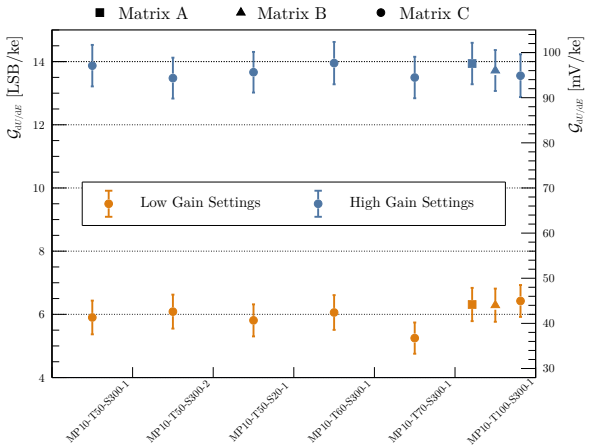

(a) Overview of the mean gain ($\mathcal{G}_{dU/dE}$) for each DUTs. Error bars indicate the standard deviation of the gain distribution.

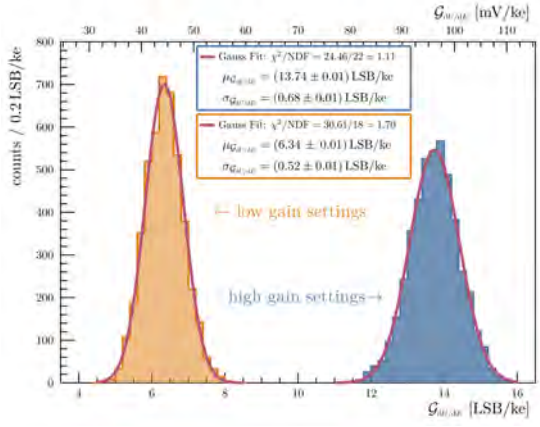

(b) Gain ($\mathcal{G}_{dU/dE}$) distributions of the *low-gain* (orange) and *high-gain* (blue) settings for MP10-T100-S300-1.

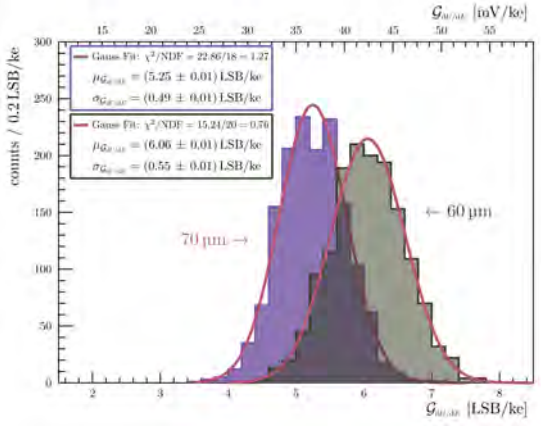

(c) Gain ($\mathcal{G}_{dU/dE}$) distributions of MP10-T70-S300-1 (70 µm) and MP10-T60-S300-1 (60 µm) at *low-gain* settings.

Plot 7.4: Calibrated gain ($\mathcal{G}_{dU/dE}$) comparison between *low-gain* (orange) and *high-gain* (blue) settings at at −20 V (−100 V for MP10-T50-S20-1) reverse bias voltage. Conversion factor: 1 LSB = 7 mV corresponding to 1800 mV range of 8 bit DAC.

Plot 7.4a summarizes the gain performance for all sensors and both gain settings. A significant improvement in gain — by more than a factor two — is observed when switching from the *low-gain* to the *high-gain* settings, as illustrated in Plot 7.4b. This improvement is consistently observed across all sensors, even when sensor-to-sensor variations are taken into account.

Under both settings, pixel-to-pixel variations dominate the gain spread, with a more pronounced exception for sensor MP10-T70-S300-1 in the *low-gain* setting. Plot 7.4c compares the gain distribution of this sensor with that of the thinner sensor MP10-T60-S300-1, revealing that the latter exhibits a generally higher gain. This difference may explain the observation in the uncalibrated efficiency curves discussed in Section 5.4.1, although this still needs to be verified by inspecting the calibrated efficiency curves (see Chapter 8).

Gain Dependence on the Bias Voltage

The gain dependence on the applied bias voltage for the *low-gain* settings is illustrated in Plot 7.5. The expected trend of increasing gain with increasing bias voltage is observed and is consistent across all sensors, including the low-resistivity sensor MP10-T50-S20-1. For bias voltages below −20 V, the gain decreases in accordance with changes in the pixel diode capacitance, as both the rise time and fall time of the CSA output signal are significantly affected (cf. Section 3.3.1). For higher bias voltages, the amplification increases only slightly because the diode capacitance changes marginally once the gradient of the depletion depth flattens out and other parasitic capacitances begin to dominate. When comparing the gain distributions at different bias voltages in Plot 7.5b, only minor shifts are observed when going from −20 V to −100 V, resulting in an increase in gain of about 2 %. Even reducing the bias voltage to 0 V decreases the gain by only about 10 % relative to −20 V, magnitudes comparable to fluctuations observed between different sensors of the same gain setting.

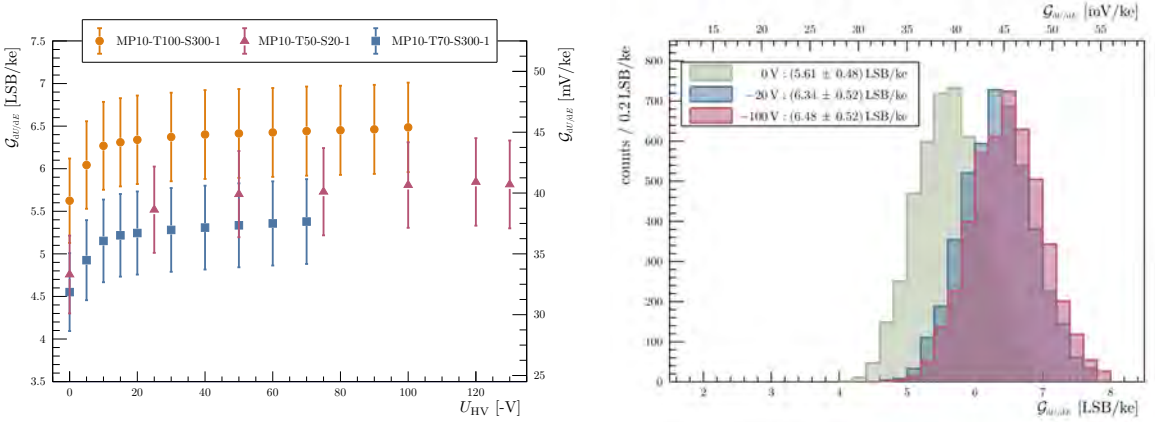

(a) Mean gain ($\mathcal{G}_{dU/dE}$) as function of the reverse bias voltage.

(b) Gain ($\mathcal{G}_{dU/dE}$) distributions of MP10-T100-S300-1 at varying bias voltages.

Plot 7.5: Gain ($\mathcal{G}_{dU/dE}$) dependence on the bias voltage for the *low-gain* settings. Mean values are extracted from the respective gain distributions, while the error (bars) represent the standard deviation. Conversion factor: 1 LSB = 7 mV corresponding to 1800 mV range of 8 bit DAC.

From Gain to Resolution

In principle, the gain directly defines the achievable detection threshold energy resolution $\mathcal{R}_{dE/dU}$, which is given by the inverse of the gain. This determines the energy step size corresponding to a single DAC step (in LSB) of the relative threshold level (cf. Section 6.4.2). As the gain increases, the energy step size exhibited by a threshold step decreases, thereby improving the achievable resolution. This allows for a finer sampling of the underlying energy deposition spectrum and reduces the relative dispersion in energy resolution.

Plot 7.6b exemplary compares the $\mathcal{R}_{dE/dU}$ between both gain settings for the sensor MP10-T100-S300-1, showing a significant improvement switching from *low-gain* to *high-gain* settings, aligned with the gain increase discussed previously. The resolution improves from about 160 e/LSB to 70 e/LSB, with a significant reduction in pixel-to-pixel spread. However, since the absolute spread decreases as gain increases, the relevant measure of dispersion

here is the relative resolution, which considers the spread normalized to the mean value. This trend is consistently observed for all sensors, as summarized in Plot 7.6a.
The resolution declines slightly with decreasing bias voltage, as illustrated in Plot 7.6c. This a direct consequence of the reduced gain at lower bias voltages discussed previously. Although a better resolution is preferable for resolving an efficiency curve, it is beneficial only if the covered energy range in the linear regime is sufficient. If the linear domain is too small, most energy depositions will fall into the non-linear or saturation regime of the detector response curve, where the resolution deteriorates significantly.

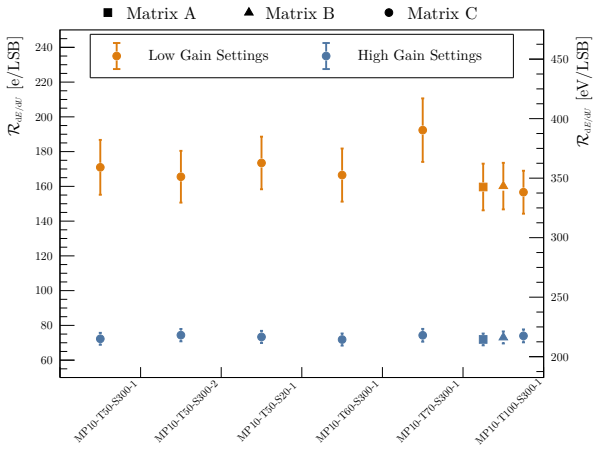

(a) Mean resolution ($\mathcal{R}_{dE/dU}$) of the *low-gain* (orange) and *high-gain* (blue) settings for all DUTs.

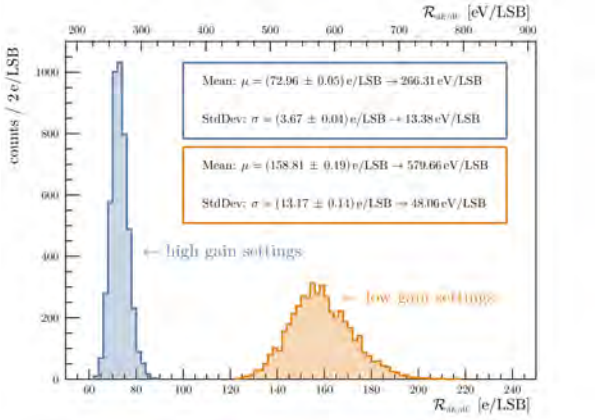

(b) Resolution ($\mathcal{R}_{dE/dU}$) distributions of the *low-gain* (orange) and *high-gain* (blue) settings for MP10-T100-S300-1.

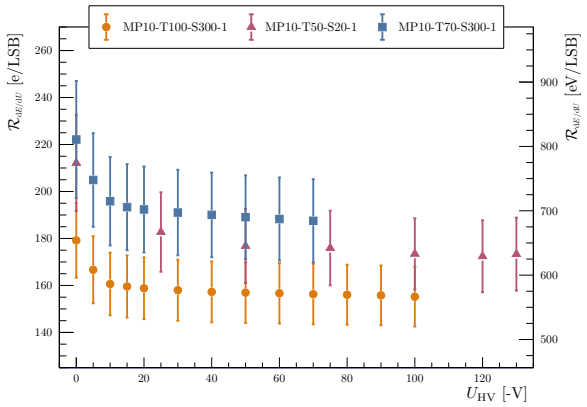

(c) Resolution ($\mathcal{R}_{dE/dU}$) as function of the reverse bias voltage at *low-gain* settings.

Plot 7.6: Resolution ($\mathcal{R}_{dE/dU}$) comparison between *low-gain* and *high-gain* settings at −20 V reverse bias voltage (−100 V for MP10-T50-S20-1). Mean values are extracted from the respective resolution distributions, while the error (bars) represent the standard deviation.

7.1.5 Leaving the Linear Gain Regime

The transition point describes the crossing from the linear gain regime into the saturation domain of the detector response curve, a regime with ever decreasing resolution of the resolvable energy as the gain gradient saturates and a limiting factor in the accuracy of energy deposition measurements. This transition can be considered in two domains: (i) the signal amplitude space, characterized by the transition threshold $U_{\text{Th, TRS}}$, and (ii) the energy space, characterized by the transition energy $E_{\text{C, TRS}}$. While the transition is assumed to occur at the same signal amplitude, the corresponding energy required to reach this amplitude varies significantly with the gain settings. Unfortunately, validating this assumption requires S-curve measurements in both gain domains — linear and saturation — which have been sufficiently performed only for the *low-gain* settings. Therefore, no results for the transition point (or the saturation level discussed in Section 7.1.6) for the *high-gain* settings are presented here. The energy range spanned

between the minimum detection threshold and the transition energy defines the most accurately observable energy window to study the energy deposition of particles within the detector.

Transition Threshold

The transition threshold $U_{\text{Th, TRS}}$ is shown in Plot 7.7 relative to the baseline references $U_{\text{BL, global}}$ and $U_{\text{BL, local}}$. In both cases, the transition threshold remains constant for bias voltages above −20 V, with a slight decrease — more pronounced when using $U_{\text{BL, local}}$ as the reference — as the pixel's diode capacitance shifts the operating point of the amplification stage at lower bias voltages. Subtracting the local baseline reference only slightly reduces the pixel-to-pixel dispersion, since the gain variations increase the spread as further the threshold is from the baseline.

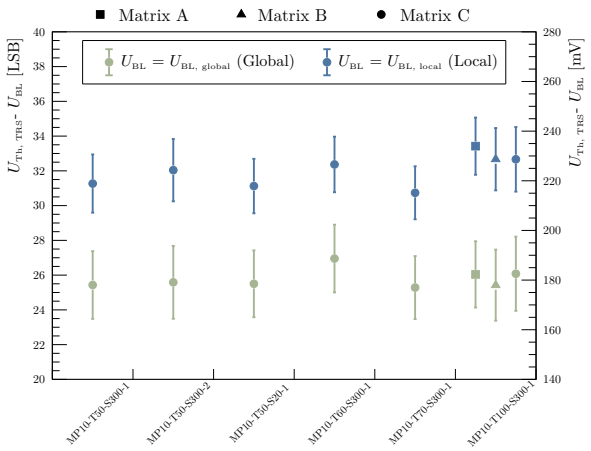

(a) Overview of the mean transition threshold for all DUT sensors.

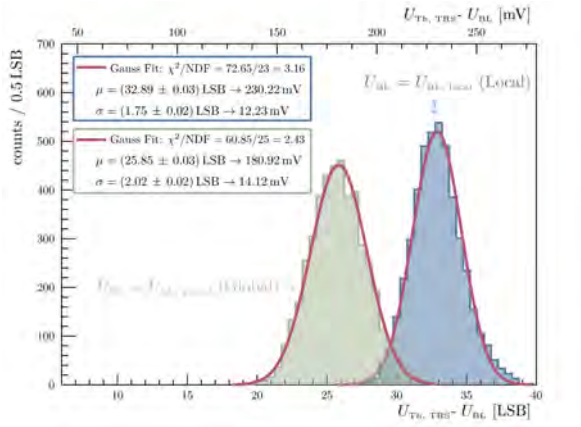

(b) Transition threshold distributions for MP10-T100-S300-1 (Matrix A, B & C).

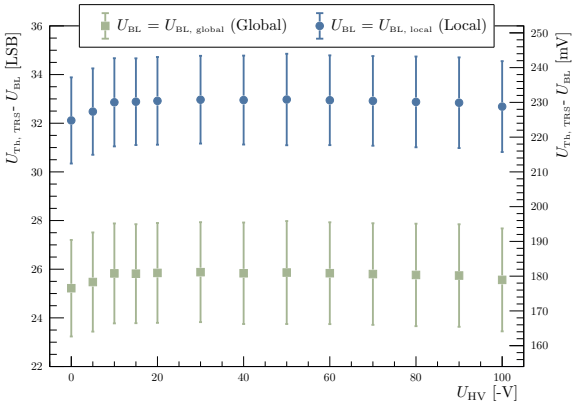

(c) Mean transition threshold versus bias voltage for MP10-T100-S300-1 (Matrix A, B & C).

Plot 7.7: Transition threshold with the baseline reference subtracted ($U_{\text{BL, global}}$ in green and $U_{\text{BL, local}}$ in blue) for the *low-gain* settings. Data points refer to the mean value of the corresponding distribution whereas the error bars indicate the standard deviation. Conversion factor: 1 LSB = 7 mV (1800 mV over 8 bit range)

The mean transition threshold lies at output signal amplitudes of approximately (180 ± 14) mV for $U_{\text{BL, global}}$ to (230 ± 12) mV for $U_{\text{BL, local}}$ in the *low-gain* settings, as illustrated in Plot 7.7b. As the actual baseline level of a pixel is not precisely known (see Section 7.1.1), it is assumed that the transition amplitude lies within the range defined by both baseline references. Plot 7.7a summarizes the sensor-to-sensor variations, which are present but negligible compared to the pixel-to-pixel spread. For reference, the transition occurs at around (60 ± 5) % of the full amplitude range of the CSA, defined by the saturation level discussed in the following Section 7.1.6.

Leaving the linear regime does not mean that higher energy depositions can no longer be measured, but rather that the resolution degrades as the detector output approaches the saturation level. The progression depends on

the specific feedback configuration of the CSA and the subsequent shaping stage, which manifests as increasing fluctuations in the S-curve data, discussed in Section 7.3.1.

Transition Energy

The transition energy $E_{\text{C, TRS}}$ corresponds to the energy level at the transition threshold $U_{\text{Th, TRS}}$, derived by evaluating the pixel's calibrated gain at that threshold relative to the local baseline reference $U_{\text{BL, local}}$ (see Equation 6.12). It is the more generally applicable quantity, as it is not influenced by unknown baseline levels and directly indicates the energy range covered by the detector's linear gain regime.

The mean transition energy of the *low-gain* settings lies between approximately 5.1 ke to 5.4 ke, with MP10-T70-S300-1 as an outlier due to its lower gain (see Section 7.1.4), at around 5.9 ke. Pixel-to-pixel variations dominate once again, with the standard deviation spanning about 400 e to 500 e for all sensors, as summarized in Plot 7.8a. The substantial spread in energy is illustrated in Plot 7.8b, where pixels in the RoI exhibit transition energies ranging roughly from 4 ke up to over 6.5 ke. As expected, the transition energy increases as the gain decreases, demonstrated by the bias voltage dependence in Plot 7.8c.

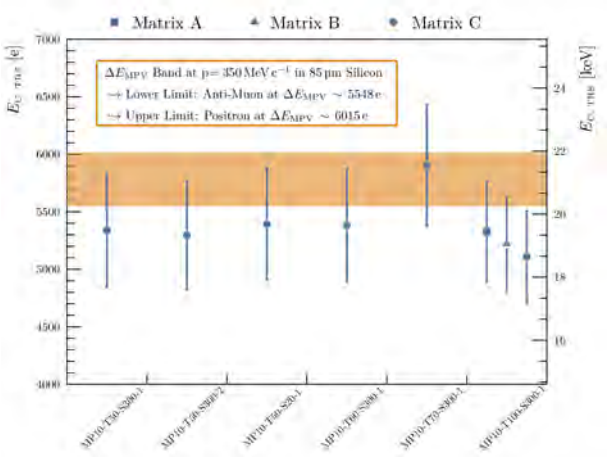

(a) Overview of the mean transition energy $E_{\text{C, TRS}}$ for all DUT sensors.

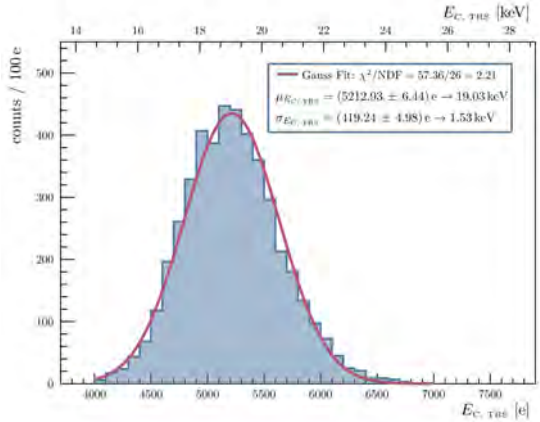

(b) Transition energy distributions for MP10-T100-S300-1 (Matrix A, B & C).

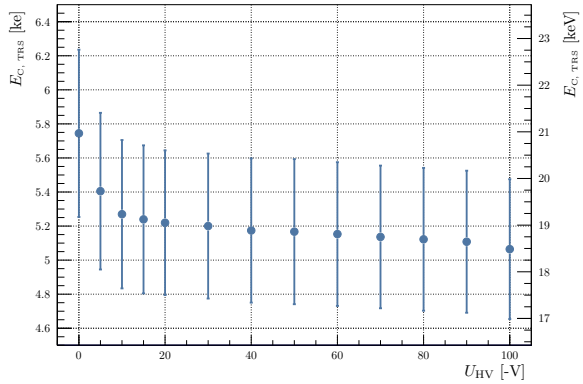

(c) Mean transition energy as function of the reverse bias voltage for MP10-T100-S300-1 (Matrix A, B & C).

Plot 7.8: Transition energy $E_{\text{C, TRS}}$ in the *low-gain* settings at −20 V (−100 V for MP10-T50-S20-1). Data points refer to the mean value of the corresponding distribution whereas the error bars indicate the standard deviation.

To classify the impact of the transition energy at the *low-gain* setting, the most probable energy deposition ΔE_{MPV} in 85 µm thick silicon under testbeam conditions is referenced (see Plot 5.2). Depending on particle type and energy, ΔE_{MPV} falls within the same order of magnitude as the transition energy, indicating that a significant fraction of energy depositions exceed the linear gain regime.

Since this case represents the upper end of a fully depleted 100 µm thick sensor, it can be deduced that even thicker sensors will exceed the linear regime more frequently. Using the *high-gain* setting would increase this issue by lowering the expected transition energy by more than a factor of two, thereby encompassing a smaller fraction of the energy depositions within the linear regime. However, the transition energy is not the sole deciding factor in selecting a gain setting, as the minimum detectable energy deposition defines the lower bound of the observable energy range (see Section 7.1.7).

7.1.6 Saturation of the Amplification Stage

The saturation threshold ($\alpha_{\text{saturation}}$) represents the asymptotic limit of the response curve, approaching but never fully reached, and defines the maximum signal output amplitude observable within the readout chain. In practice, the signal can occasionally exceed this threshold due to noise-induced fluctuations that push the output amplitude beyond the comparator threshold. Therefore, $\alpha_{\text{saturation}}$ should be interpreted as the mean maximum output amplitude of the amplification stage. As the output signal nears this level, the energy resolution, characterized by the gain gradient, deteriorates significantly because the gradient asymptotically approaches zero, resulting in no energy information being extractable. Since this degradation is continuous, it is better quantified by the σ parameter of an S-curve in this regime, as discussed in Section 7.3.2.

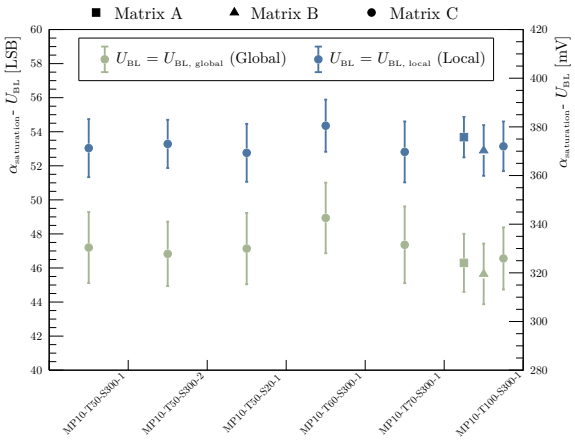

(a) Overview of the mean saturation amplitude for all DUTs.

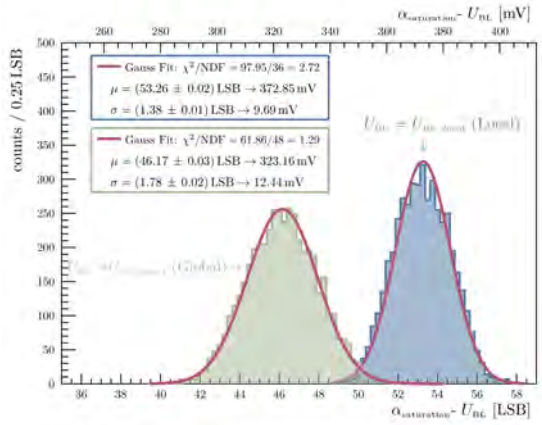

(b) Distributions of the saturation amplitude for MP10-T100-S300-1 (Matrix A, B & C).

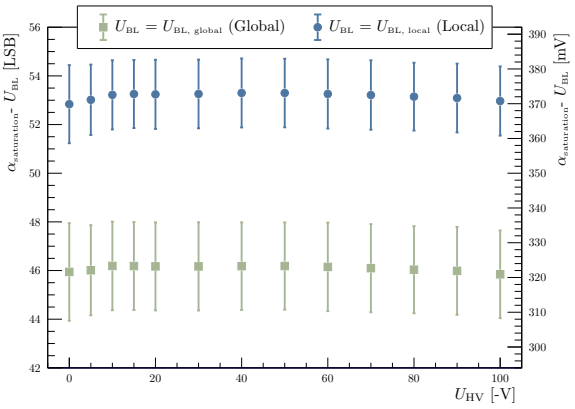

(c) Mean saturation amplitude as function of the reverse bias voltage for MP10-T100-S300-1 (Matrix A, B & C).

Plot 7.9: Saturation amplitude ($\alpha_{\text{saturation}} - U_{\text{BL}}$) relative to the baseline levels ($U_{\text{BL, global}}$ in green and $U_{\text{BL, local}}$ in blue) for the *low-gain* settings at −20 V reverse bias voltage (−100 V for MP10-T50-S20-1). Data points refer to the mean value of the corresponding distribution whereas the error bars indicate the standard deviation. Conversion factor: 1 LSB = 7 mV (1800 mV over 8 bit range)

Since $\alpha_{\text{saturation}}$ is defined as infinity in energy space, all thresholds exceeding this level are omitted, as no meaningful energy information can be extracted. This is not a severe limitation because the corresponding energy fluctuation from small changes just below $\alpha_{\text{saturation}}$ is more significant, which already limits the accuracy of energy measurements. Additionally, large energy depositions in the tail of the energy spectrum are of less interest compared to the "core" region around ΔE_{MPV}. Only when the "core" of the underlying energy deposition spectrum is pushed into the saturation regime does the accuracy of energy measurement can become significantly compromised.

Plot 7.9 summarizes the saturation amplitude[1] for all DUT sensors relative to both baseline references $U_{\text{BL, global}}$ and $U_{\text{BL, local}}$, respectively. In accordance with the transition threshold $U_{\text{Th, TRS}}$ (see Section 7.1.5), the saturation amplitude remains relatively constant for bias voltages above −20 V, with only minor pixel-to-pixel variations dominating the spread, as illustrated in Plot 7.9c. The mean saturation amplitude lies between approximately (320 ± 12) mV for $U_{\text{BL, global}}$ and (370 ± 10) mV for $U_{\text{BL, local}}$, as illustrated in Plot 7.9b. Sensor-to-sensor variations fall within the pixel dispersion exhibited by each sensor, as shown in Plot 7.9a.

7.1.7 Minimum Detection Threshold

The minimum detection threshold $U_{\text{Th, min}}$ defines the lowest energy detectable by a pixel before noise-induced fake hits cause operational instabilities. It corresponds to the lowest stable threshold setting achieved during the test beam campaign for the *low-gain* settings and during laboratory measurements for the *high-gain* settings. Note that test beam measurements reflect more realistic operational conditions, including external noise and environmental factors affecting detector stability. In the absence of threshold trimming to equalize pixel response, pixels with the lowest effective threshold and highest noise effectively define the sensor's minimum usable detection threshold and thus its overall hit efficiency (with no pixels masked).

Plot 7.10b shows that moving from the *low-gain* to the *high-gain* settings significantly lowers the minimum threshold and also reduces pixel-to-pixel dispersion, as the distance to the baseline is reduced in terms of energy, allowing for overall improved performance. This effect is observed for all sensors, as summarized in Plot 7.10a.

For bias voltages above −20 V, the minimum detection threshold remains relatively constant as the gain is no longer significantly affected (see Section 7.1.4), and it rises at lower bias voltages as the gain deteriorates, as shown in Plot 7.10c.

The observed levels of the *low-gain* setting explain the inability to detect Fe-55, as discussed in Section 5.1, since the mean minimum detection threshold generally lies above the energy deposition of the $K_{\bar{\alpha}}$ line at about 5.9 ke. Additionally, it shows that for thin sensors with low energy depositions, the minimum detection threshold can exceed the most probable energy deposition (ΔE_{MPV}). In the testbeam scenario (see Plot 5.2) for a 35 µm silicon sensor (corresponding approximately to a fully depleted 50 µm sensor), the ΔE_{MPV} is in the range 2.1 ke to 2.3 ke, resulting in substantially reduced hit detection efficiency, particularly at low bias voltages (see Section 5.4).

With the *high-gain* settings, the efficiency at low bias voltages and/or thin sensors can be significantly improved, as the minimum detection threshold is lowered into a regime where the most probable energy deposition ΔE_{MPV} lies well above this level, theoretically even for the 50 µm thin sensors of an under-depleted operation scenario.

For thicker sensors exhibiting higher energy depositions, the *low-gain* settings may still be sufficient, and might be the preferable choice when studying the deposition spectrum, as the upper end of the linear regime is extended significantly (see Section 7.1.5). Depending on the application and sensor thickness, a trade-off between minimum detection threshold and transition energy must be made when choosing the appropriate gain setting. The gain setting should be chosen based on the expected energy deposition spectrum to ensure the relevant energy range falls within the linear response regime. At the same time, it is important that a significant portion of the distribution's tail remains measurable, while keeping the detection threshold sufficiently low so that the lower part of the energy spectrum is not cut off.

[1] Note that the saturation amplitude cannot be directly compared to AmpOut measurements (cf. Section A.4.2) because the output driver stage — a source follower — modifies the signal pulse with a gain less than one.

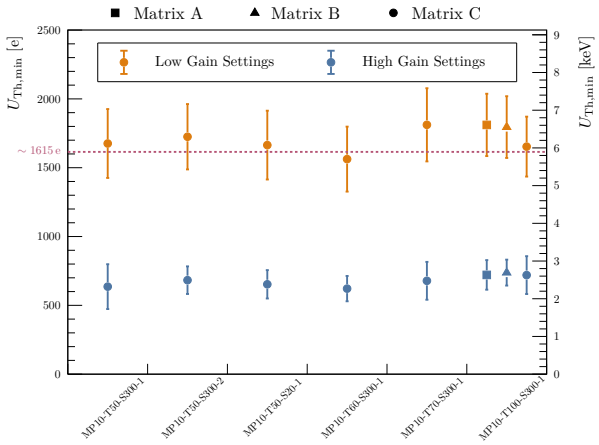

(a) Overview of the mean minimum detection threshold for all DUT sensors.

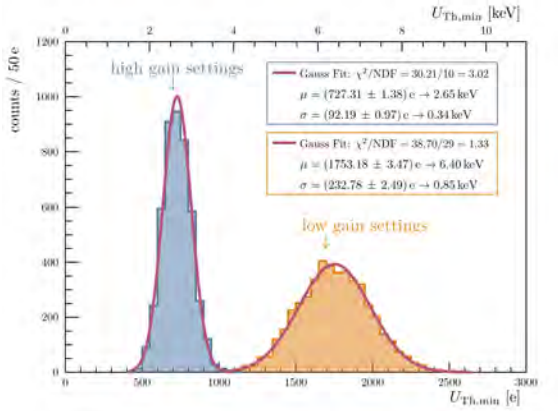

(b) Minimum threshold distribution for MP10-T100-S300-1 (Matrix A, B & C).

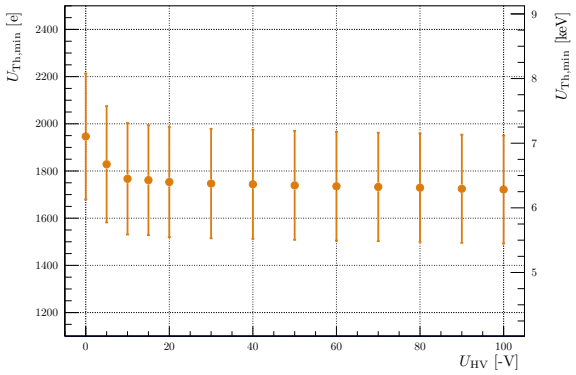

(c) Mean minimum threshold versus bias voltage for MP10-T100-S300-1 (Matrix A, B & C).

Plot 7.10: Minimum detection threshold for *low-gain* (orange) and *high-gain* (blue) settings at −20 V reverse bias voltage (−100 V for MP10-T50-S20-1). Data point markers indicate the mean value of the corresponding distribution, while the error bars represent the standard deviation.

7.2 Probing MuPix10 with Fe-55 beyond Energy Calibration

A monochromatic photon emitter with energies in the photoelectric-dominated regime (see Section 1.2) is an excellent tool for probing the charge collection properties of a silicon sensor, due to the well-defined energy deposition in the sensor bulk. In conjunction with charge injection (see Section 6.3), it enables the distinction between effects related to the sensor diode and those arising from the readout chain of the pixel, or provides an independent validation of measurements. In the following section, several studies based on Fe-55 data measured with different MuPix10 sensors are presented, demonstrating the capabilities of the Fe-55 source to probe sensor characteristics beyond simple energy calibration and according to models of general diode behavior.

7.2.1 Bias-Dependent Gain Explored Using Monochromatic Peaks

The measured peak positions of the $K_{\bar{\alpha}}$ and K_β lines of Fe-55 can be used to study the influence of the applied reverse bias voltage U_{HV} on the effective gain of the sensor readout chain. Both $\mu_{\mathrm{K}_{\bar{\alpha}}}$ and μ_{K_β} are expected to behave equally under changing bias voltages — predominantly bias-independent (see Section 7.1.1) — as they are affected by the same underlying threshold dispersion and pixel gain variations. Their dependence on U_{HV} is expected to be analogous to the gain measurements using *Injection* (see Section 7.1.4).

A significant deviation, manifesting as an excess, indicates alterations in the charge collection mechanisms of the sensor diode, such as charge multiplication effects. Conversely, uniformly distributed charge collection inefficiencies would reduce the peak positions independent of the gain, whereas local effects are more accurately reflected in the partial charge collection parameter $\Gamma_{\mathrm{c.s.}}$ of the employed S-curve model (see Section 6.2.2).

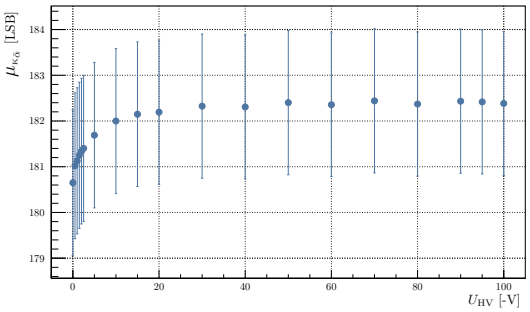

(a) Mean $\mu_{\mathrm{K}_{\bar{\alpha}}}$ as function of the applied high voltage.

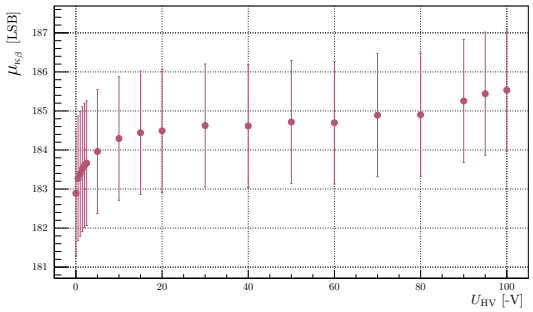

(b) Mean $\mu_{\mathrm{K}_\beta} = \mu_{\mathrm{K}_{\bar{\alpha}}} + \Delta\mu_{\mathrm{K}_{\bar{\alpha}},\beta}$ as function of the applied high voltage.

Plot 7.11: Dependency of the $K_{\bar{\alpha}}$ and K_β peak positions on the applied high voltage for MP10-T100-S300-1 (100 µm, 200 Ω cm to 400 Ω cm). Error bars indicating the corresponding sigma of the distribution. The outer pixels are excluded.

Plot 7.11 shows the dependence of $\mu_{\mathrm{K}_{\bar{\alpha}}}$ and μ_{K_β} as a function of the applied high voltage. The fit results from all pixels after outlier filtering (see Section 6.2.2) are considered, excluding the edge pixels of the pixel matrix to avoid boundary effects.

The course of $\mu_{\mathrm{K}_{\bar{\alpha}}}$ exhibits the expected behavior, remaining constant over the entire measurement range for reverse bias voltages above −20 V, as shown in Plot 7.11a, and dropping for voltages below this value due to decreasing gain. A similar trend was observed for other sensors with resistivities from 200 Ω cm to 400 Ω cm, although not shown here.

For μ_{K_β} (= $\mu_{\mathrm{K}_{\bar{\alpha}}}$ + $\Delta\mu_{\mathrm{K}_{\bar{\alpha}},\beta}$), shown in Plot 7.11b, an analogous behavior to $\mu_{\mathrm{K}_{\bar{\alpha}}}$ is observed, with error bars indicating similar pixel-to-pixel dispersion. An exception occurs for bias voltages above −80 V, where a slight increase in μ_{K_β} is seen. This effect may be caused by an increase in collected charge for the K_β photons, attributable either to multiplication of charge carriers or increased noise.

If the tail of the S-curve representing the K_β peak reaches into the saturation regime of the pixel response curve (see Plot 7.12), compression of the S-curve is expected, which suppresses fluctuations in the threshold measurement towards higher values (see Section 6.4.1). This reveals a weak mode of the applied fit model that does not account for non-linearities between deposited charge and collected charge — pulling the $\Delta\mu_{\mathrm{K}_{\bar{\alpha}},\beta}$ towards higher values — an indicator for an increased charge carrier collection occurring within the tail regime.

An increase in noise cannot be directly verified here and its origin may be linked effects concerning the pixel design itself. Typically, high electric fields occur at corners or edges of implanted structures due to the geometry of the doping profiles. For impact ionization at the boundary layer of n-well and p-substrate to be the cause, a high electric field would be necessary, which is unlikely for sensor with a resistivity of 200 Ω cm to 400 Ω cm at the applied voltages (see Section 4.2.1 and 4.31).

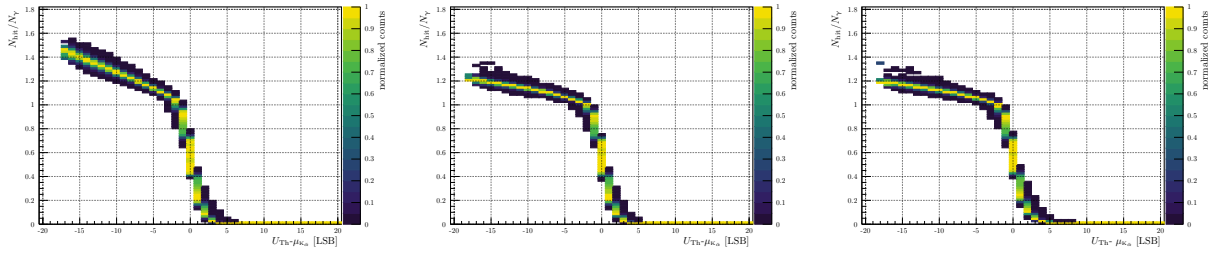

(a) −20 V reverse bias voltage. *(b)* −80 V reverse bias voltage. *(c)* −100 V reverse bias voltage.

Plot 7.12: Superposition of scaled (by N_γ) and shifted (by $\mu_{\mathrm{K}_{\bar{\alpha}}}$) Fe-55 S-curve data of MP10-T100-S300-1 (100 µm, 200 Ω cm to 400 Ω cm) at different reverse bias voltages. Outer pixels are excluded.

The only other potential high-field region is at the pixel *guard-ring* structure. The *guard-ring* is formed by a metal contact on a highly doped p^+ implant ring embedded in the p-substrate around the deep n-well, arranged equidistantly on all sides, cf. Section 3.2.1. A large doping gradient between these regions, as found in high-resistivity silicon, can lead to high electric field strengths that increase with higher applied reverse bias levels[2]. In principle, this could be investigated using sensors of varying resistivity; however, this effect is difficult to disentangle from other effects and therefore requires further study through simulation.

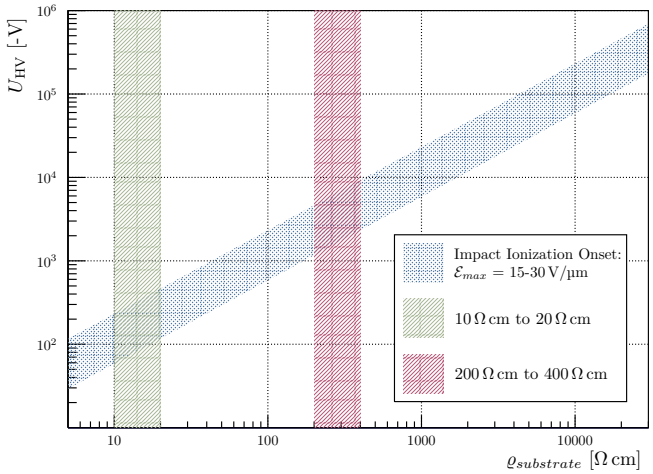

Figure 7.1: External reverse bias U_{HV} corresponding for an electric field strength threshold for impact ionization in silicon as a function of resistivity. Calculation based on Equation 4.31.

[2] A similar effect, characterized by a prolonged tail, is also observed for comparable voltage levels on TelePix sensors [189] (cf. [190, p. 68ff, sec. 11.2]), which exhibit an even higher (expected) resistivity of (370 ± 20) Ω cm. However, due to differences in pixel geometry, validation of this assumption is not currently possible and remains under investigation.

Standard Resistivity: 10 Ω cm to 20 Ω cm

The lower, or "standard", resistivity sensor MP10-T50-S20-1 exhibits similar behavior in $\mu_{K_{\bar{\alpha}}}$ and μ_{K_β} compared to the high-resistivity sensor discussed above, as shown in Plot 7.13, but displays significantly larger deviations for reverse bias voltages exceeding −100 V. Here, the curves of both $\mu_{K_{\bar{\alpha}}}$ and μ_{K_β} increase linearly towards higher detection thresholds, an effect even more pronounced for μ_{K_β}. This behavior deviates significantly from the gain dependence observed using *Injection* (see Section 7.1.4), which remains constant for voltages above −20 V.

This effect cannot be attributed to noise-induced shifts or *guard-ring* effects as speculated above, and is expected to arise from charge multiplication caused by impact ionization effects in high-field regions at the *pn*-junction boundary. An effect of the *guard-ring* connection is expected to be suppressed compared to higher resistivities due to the lower gradient between the p^+ *guard-ring* and the respectively higher doped *p*-substrate. At resistivities of 10 Ω cm to 20 Ω cm, the electric field strength at the *pn*-junction is already sufficiently high to induce impact ionization at moderate bias voltages (see Figure 7.1). This is particularly visible in the tail of the S-curve presented in Plot 7.14, which significantly stretches towards higher threshold values as the bias voltage increases.

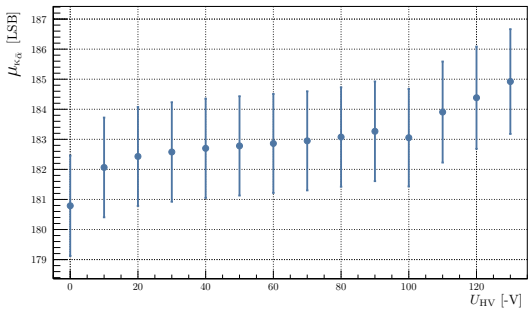

(a) Mean $\mu_{K_{\bar{\alpha}}}$ as function of the applied high voltage.

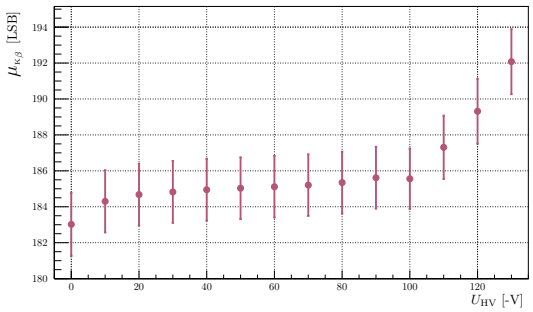

(b) Mean $\mu_{K_\beta} = \mu_{K_{\bar{\alpha}}} + \Delta\mu_{K_{\bar{\alpha},\beta}}$ as function of the applied high voltage.

Plot 7.13: Dependency of the $K_{\bar{\alpha}}$ and K_β peak positions on the applied high voltage for MP10-T50-S20-1 (50 µm, 10 Ω cm to 20 Ω cm). Error bars indicating the corresponding sigma of the distribution. The outer pixels are excluded.

Although this effect distorts the linearity assumed by the S-curve model, it presents an opportunity to use highly doped *p*-substrate sensors in thin sensor scenarios. Charge multiplication effects can compensate for lower energy deposition, enhancing the effective signal amplitude. A technique employed in LGAD (**L**ow **G**ain **A**valanche **D**etector), where an additional highly doped gain layer is implanted below the *n*-well to create high field regions for controlled charge multiplication. In this case, such an additional gain layer is unnecessary due to the already present high field at the pn-junction.

However, both low resistivities and the use of a highly doped gain layer are susceptible to radiation damage effects [191, p. 5ff][3] which cause changes in the doping profile and reduce the effective gain over time.

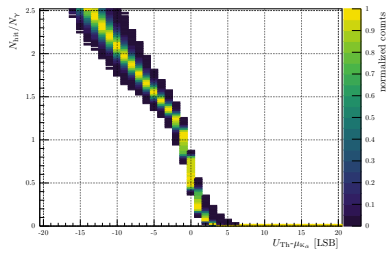

(a) −20 V reverse bias voltage.

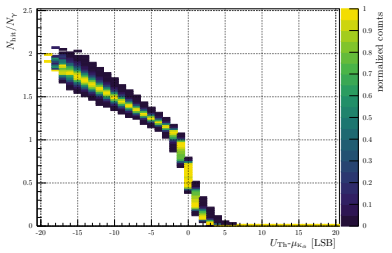

(b) −100 V reverse bias voltage.

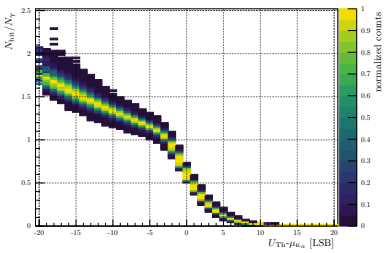

(c) −130 V reverse bias voltage.

Plot 7.14: Superposition of scaled (by N_γ) and shifted (by $\mu_{K_{\bar{\alpha}}}$) Fe-55 S-curve data of MP10-T50-S20-1 (50 µm, 10 Ω cm to 20 Ω cm) at different reverse bias voltages. Outer pixels are excluded.

[3] Annealing studies on LGADs [192] showed significant gain recovery after high-temperature annealing.

7.2.2 Investigating Gain Spatial Dependency in Signal Line Routing

In Section 5.4.1, a spatial dependency of the hit efficiency was observed. If this effect is indeed related to intrinsic sensor gain variations — influenced by the signal line routing or power distribution network — it should also be observable using monochromatic photon sources, independent of uncertainties using a tracking telescope and operational settings.

In contrast to the efficiency measurements presented in Section 5.4.1, here the mean value of $\mu_{K_{\bar{\alpha}}}$ is analyzed as a function of the pixel row and column addresses for the same sensor MP10-T100-S300-1, at the same reverse bias voltage of −20 V. Since it predominantly scales with the gain observed using *Injection* (see Section 7.1.4), variations in $\mu_{K_{\bar{\alpha}}}$ directly reflect changes in the effective gain of the pixel readout chain.

Pixel Row Dependency

To assess the spatial dependency, the data along each row address is aggregated, separating even and odd column addresses to account for the different signal routing schemes employed in MuPix10 (see Section 3.2.1). As measure the respective mean and standard deviation of the $\mu_{K_{\bar{\alpha}}}$ distributions for each row address is extracted.

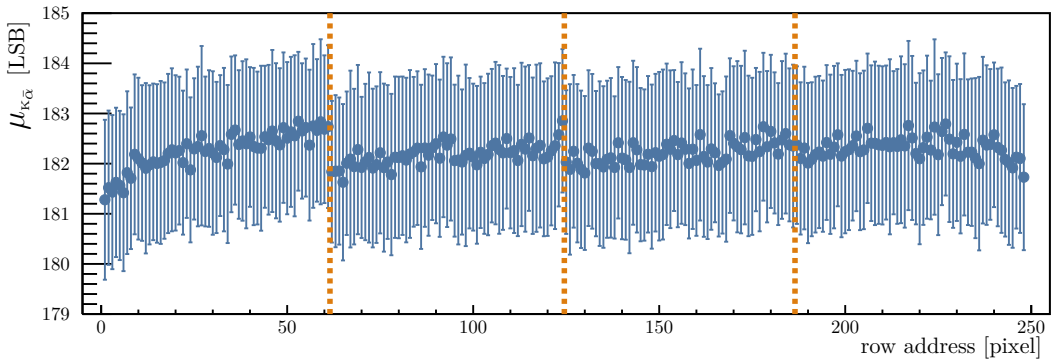

(a) Row Dependency: Even pixel column addresses

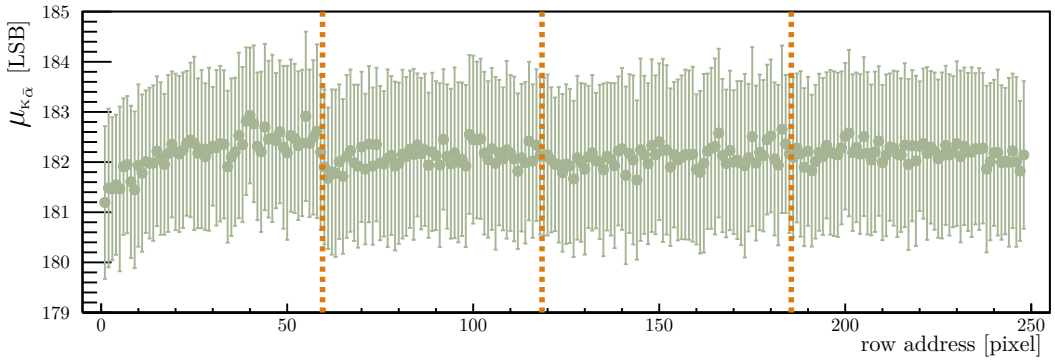

(b) Row Dependency: Odd pixel column addresses

Plot 7.15: Mean $\mu_{K_{\bar{\alpha}}}$ row dependency study of the $K_{\bar{\alpha}}$ peak position for MP10-T100-S300-1 at −20 V reverse bias voltage. The error bars indicate the corresponding sigma of the distribution. The edge pixels of the pixel matrix are omitted. The dashed orange lines indicate a signal routing metal layer transition, see Table 3.2.

Plots 7.15a and 7.15b illustrates the dependency of $\mu_{K_{\bar{\alpha}}}$ on the pixel row address for even and odd column addresses, respectively. It shows a comparable trend as observed in the hit efficiency data, not identical due to the different nature of the measurement methods, but sufficient to demonstrate the capability to analyze such dependencies using monochromatic photon sources.

For the upper three routing segments, the row-to-row fluctuations are relatively small, with a slight increase of $\mu_{K_{\bar{\alpha}}}$ observed towards higher row addresses. Only the first routing segment exhibits a more significant deviation compared to the others, showing an increasing trend of $\mu_{K_{\bar{\alpha}}}$ towards higher row addresses until the transition to

the second routing segment, where a sudden drop occurs. A similar trend is observed for odd column addresses, although the transition points differ due to the distinct routing scheme.

Overall, these measurements show that the observed influence is intrinsic to gain variations inherent in the sensor design, independent of the applied operational settings, thus validating the hypothesis presented in Section 5.4.1.

Pixel Column Dependency

The same methodology used for the row dependency is now applied to study the column dependency of $\mu_{K_{\bar{\alpha}}}$. Comparing the column dependency observed in the hit efficiency (Plot 5.9d) with the results shown in Plot 7.16 reveals a different pattern.

The suggested cause for the observed trend, discussed in Section 5.4.1, — decreasing hit efficiency towards lower column addresses, attributed to a voltage drop along the power distribution network — is not reflected in the $\mu_{K_{\bar{\alpha}}}$ distribution. Instead, the distribution appears relatively flat with a slight decrease towards higher column addresses, contrary to the hit efficiency trend. Minor fluctuations around the mean are dominated by pixel-to-pixel dispersion.

The difference in behavior between the two measurements could be due to several factors. These effects may be influenced by differing voltage drops arising from varying current consumption in different operational settings, with about a 40 % higher current consumption in the *low-gain* setting compared to the *high-gain* setting(see Table A.12). Additionally, this effect may be strongly affected by the power scheme and sensing infrastructure, including hardware components such as the *MuDAQ Motherboard*, insert PCB hosting the DUT, and low-voltage power cables, all of which are difficult to control and prone to external influences.

With this data alone, a definitive conclusion cannot be drawn regarding the origin of the column dependency observed in the hit efficiency measurements. Nevertheless, it can be concluded that this is not an intrinsic effect of the sensor design, as an intrinsic effect would be expected to appear consistently in both measurements.

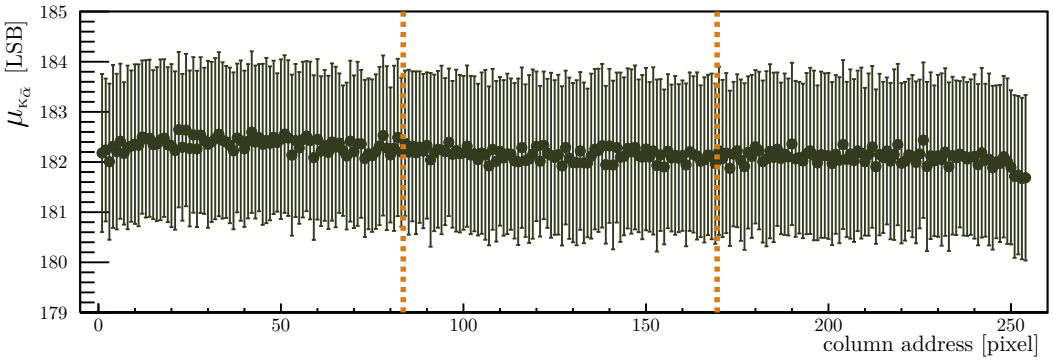

Plot 7.16: Mean $\mu_{K_{\bar{\alpha}}}$ column dependency study of the $K_{\bar{\alpha}}$ peak position for MP10-T100-S300-1 at −20 V reverse bias voltage. The error bars indicate the corresponding standard deviation of the distribution. The edge pixels of the pixel matrix are omitted. The dashed orange lines indicate the transition between sub-matrices, see Section 3.2.

7.2.3 Reconstructing the K_β-Peak

Although the K_β peak is included in the S-curve model used to describe the Fe-55 response (see Section 6.2.2), its informativeness is limited by the sensor's intrinsic energy resolution and the coarse binning of the detection threshold. The K_β peak position is extracted from the offset $\Delta\mu_{K_{\bar{\alpha},\beta}}$ relative to the $K_{\bar{\alpha}}$ peak via $\mu_{K_\beta} = \mu_{K_{\bar{\alpha}}} + \Delta\mu_{K_{\bar{\alpha},\beta}}$, making it susceptible to uncertainties in both fit parameters.

To determine whether $\Delta\mu_{K_{\bar{\alpha},\beta}}$ is more than a mere fit stabilization parameter and has genuine predictive power regarding energy deposition, its reconstructed energy response is compared to the theoretical K_β value. While this result is inherently biased — since the same data are used both for calibration and reconstruction — it serves to demonstrate the potential of this approach.

The energy reconstruction employs the linear gain model (see Equation 6.11), with gain and local baseline obtained from *Injection* measurements performed under identical operational settings and calibrated to the $\mu_{K_{\bar{\alpha}}}$ position as described in Section 7.1.

Plot 7.17a shows that the reconstructed K_β energy typically deviates from the theoretical value of 6.490 keV by about 10 eV (approximately 3 e), remaining within the fluctuations defined by the standard deviation of the μ_{K_β} distributions. The "standard" resistivity sensor is an exception, overestimating the K_β energy by approximately 65 eV (around 20 e in deposited charge). This deviation may result from charge multiplication effects (−100 V reverse bias voltage) discussed in Section 7.2.1, which cause distortions to the assumed linearity of the gain model. As the effect is relatively small, it is unclear whether the deviation arises from an overestimation of the gain or μ_{K_β}.

In summary, the K_β peak reconstruction using the S-curve model of Fe-55 combined with gain calibration from *Injection* measurements demonstrates the accuracy achievable in the *high-gain* settings to describe the detector response, while still being subject to deviations caused by noise, see Section 7.3. However, using the K_β peak as a second calibration point is not recommended due to limited resolution and increased uncertainty caused by combining multiple fit parameters. Furthermore, linearity derived from both peaks may be affected by systematic effects — such as the apparent charge multiplication discussed above — highlighting the necessity for a third calibration point within the linear regime for validation.

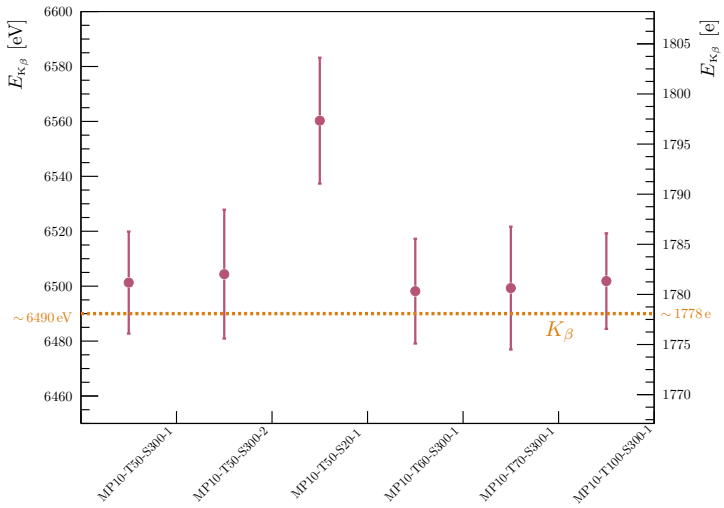

(a) Reconstructed K_β peak position for all DUTs. The data points are are the fitted mean values of the μ_{K_β} distributions and the error bars indicate the corresponding standard deviation.

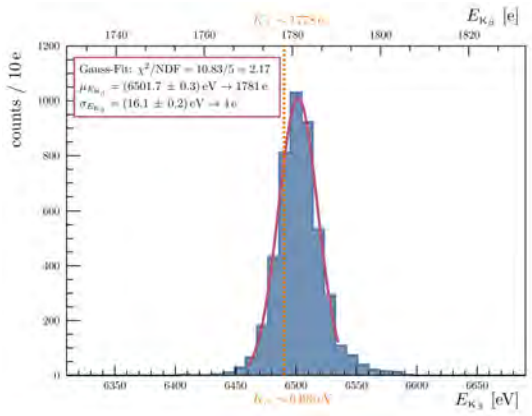

(b) MP10-T100-S300-1: 100 µm thick sensor (200 Ω cm - 400 Ω cm) at U_{HV} = −20 V.

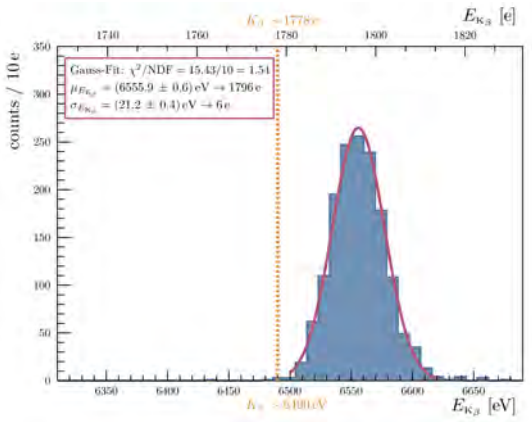

(c) MP10-T50-S20-1: 50 µm thick (10 Ω cm - 20 Ω cm) sensor at U_{HV} = −100 V.

Plot 7.17: Reconstructed K_β peak for all DUTs using the S-curve model of Fe-55 at −20 V reverse bias voltage (−100 V for MP10-T50-S20-1). The (orange) dashed line indicates the theoretical energy of the K_β peak at 6.490 keV (see Table 6.1).

7.2.4 Identification of Spatial Noise Inhomogeneities

Spatial noise inhomogeneities can be investigated either by scanning the threshold, measuring the spontaneous hit rate, or by studying the dispersion of a monochromatic source response, as performed with the *Injection* (see Section 7.3). The first approach provides a direct measurement of the "fake" rate, whereas the second allows the determination of the underlying noise level expressed as the ENC (**E**quivalent **N**oise **C**harge). Both methods, however, have inherent limitations: the noise-rate measurement is affected by threshold dispersion and may be dominated by a few highly noisy pixels that dominate the readout before full structures can be resolved, while the *Injection* method is time-intensive since only a limited number of pixels can be injected simultaneously, making the coverage of a full pixel matrix lengthy.

An alternative method to identify spatial noise inhomogeneities uses a monochromatic X-ray source such as Fe-55. The fluctuations in the measured threshold response, $\sigma_{K_{\bar{\alpha},\beta}}$, arise from the combination of the underlying noise level and charge-generation fluctuations caused by photon energy deposition (see Section 1.2.3), amplified by the respective gain of each pixel readout chain. The relationship between the Fe-55 S-curve parameter $\sigma_{K_{\bar{\alpha},\beta}}$ and noise is briefly discussed in Section 7.3.2.

Although extracting an ENC value requires validating each pixel's gain, investigating clustered effects over multiple pixels — since variations in gain tend to average out — remains feasible and can be explored in more detail as a secondary step using *Injection* measurements.

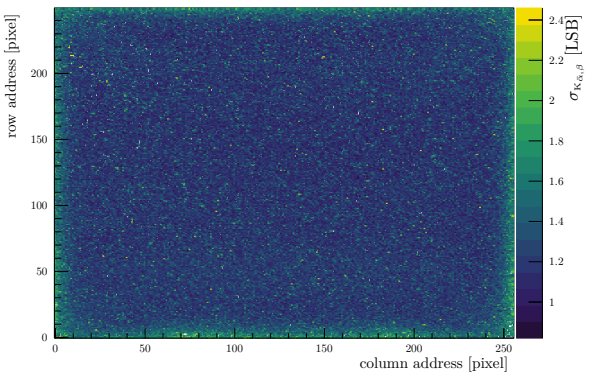

(a) Mapping of $\sigma_{K_{\bar{\alpha},\beta}}$ onto the pixel matrix at −10 V reverse bias voltage.

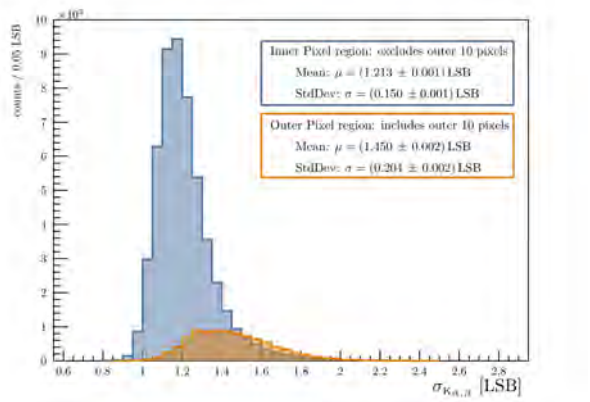

(b) Distribution of $\sigma_{K_{\bar{\alpha},\beta}}$ for inner pixel region and outer 10 pixel ring at −10 V reverse bias voltage.

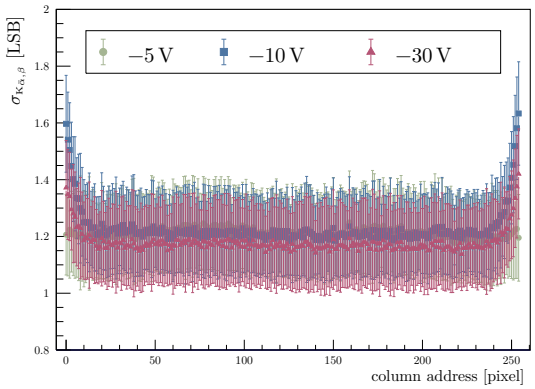

(c) Profile of $\sigma_{K_{\bar{\alpha},\beta}}$ along the pixel column address. The mean value and standard deviation of each column is plotted. The outer 10 row pixels are excluded.

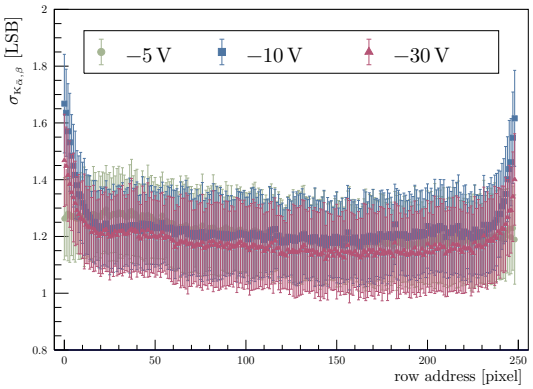

(d) Profile of $\sigma_{K_{\bar{\alpha},\beta}}$ along the pixel row address. The mean value and standard deviation of each row is plotted. The outer 10 column pixels are excluded.

Plot 7.18: Spatial noise inhomogeneities study using Fe-55 data of MP10-T60-S300-1.

If no localized noise "spots" are present, the spatial noise dependence is expected to scale primarily with the local gain variations, as observed in Section 7.2.2, fluctuating with each pixel's noise level and gain. Pixels at the matrix edge can act as outliers due to differing boundary effects, allowing charge diffusing from outside the pixel into it, which may increase the observed dispersion in $\sigma_{\mathrm{K}_{\bar{\alpha},\beta}}$.

However, as shown in Plot 7.18, a distinct pattern appears that deviates from simple gain variations. The fluctuations of $\sigma_{\mathrm{K}_{\bar{\alpha},\beta}}$ are generally uniformly distributed across the sensor (Plot 7.18b), following the local gain trend as observed in Section 7.2.2, but a clear clustering of higher $\sigma_{\mathrm{K}_{\bar{\alpha},\beta}}$ values is visible near the matrix edges beyond the outermost pixels (Plot 7.18a). The outermost approximately 10 pixel surrounding the pixel matrix exhibit higher $\sigma_{\mathrm{K}_{\bar{\alpha},\beta}}$ levels, gradually decreasing toward the inner pixels, as shown in Plots 7.18c and 7.18d. The effect is visible only for measurements taken at reverse bias voltages exceeding −5 V and decreases in magnitude at higher voltages as the overall noise level drops (see Section 7.3.3). A similar structure and behavior are consistently observed for all DUTs with resistivities between 200 Ω cm to 400 Ω cm and total thicknesses below 100 µm (excluding MP10-T100-S300-1, see Table 5.1), but are absent in the 50 µm-thick "standard" resistivity sensor MP10-T50-S20-1.

The origin of this structure is not yet fully understood and remains under investigation, but some considerations and observations can be summarized. A similar effect with higher magnitude is observed in multi-chip modules built with MuPix11, likely further enhanced by inter-chip couplings. Experiments have shown that filtering the high-voltage supply — employed on the *MuDAQ Motherboard* — or adding a series resistor in the high-voltage line significantly mitigates the effect. The effect arises independently of the voltage source used, being observed both with the custom *Mu3e* HV power supplies (see Section 5.2.3) and commercial source meters such as the *Keithley 2450* [193], albeit less pronounced, indicating that the voltage source influences but does not solely cause the effect.

Ultimately, the observed structure can be mitigated, and this analysis method has proven to be valuable for identifying potential inhomogeneities in the noise distribution of pixel sensors. For the measurements discussed in this work, no significant impact is expected, as the outermost 10 pixel are excluded.

7.2.5 Impact of Active Volume Depletion on Partial Charge Collection

As the depletion region of a silicon pixel sensor expands with increasing reverse bias voltage, the active volume for charge collection dominated by drift processes increases accordingly (see Section 2.3.1). However, the non-depleted region may still contribute to the overall charge collection, although the deposited charge is not fully collected due to the absence of an electric field.

Charge carriers generated within the depleted region are collected predominantly by drift and are expected to be fully collected, except near pixel boundaries where geometrically induced charge-sharing effects occur. In contrast, charge carriers produced in the non-depleted region primarily move by diffusion (see Section 4.2.2), resulting in partial charge collection. As the depletion region extends deeper into the sensor bulk, the hit rate attributed to partially collected charge naturally decreases, since the photon absorption interaction rate follows an exponential attenuation law (see Section 1.2). A higher abundance of generated charge carriers is expected near the entry surface — here, the top side of the sensor featuring metal layers and passivation. Therefore, with increasing reverse bias voltage causing the depletion region to grow, the occurrence of hits with partially collected charge is expected to diminish, depending on the photon absorption length in silicon (see Table 6.1).

Thus, the fraction of hits with partial charge collection is expected to vary significantly with the effective depletion volume relative to the non-depleted excess region, which is influenced by the applied reverse bias voltage, substrate resistivity, and total sensor thickness. To quantify these effects, the Fe-55 S-curve parameter $\mathit{\Gamma}_{\text{f.c.}}$ (see Section 6.2.2) is utilized, defined as the fraction of hits with partially collected charge. It incorporates both geometrically induced charge sharing and charge collection by diffusion from the non-depleted substrate. Because $\mathit{\Gamma}_{\text{f.c.}}$ is self-normalized to the distribution of hits with fully collected charge, it serves as an ideal observable for this study. However, $\mathit{\Gamma}_{\text{f.c.}}$ cannot easily be disentangled from overlapping effects and should therefore be interpreted only in relation to other measurements and trends observed when varying external parameters.

It should be noted that $\mathit{\Gamma}_{\text{f.c.}}$ scales with the pixel gain, showing a strong anti-correlation of approximately $R \approx -0.748$ with the calibrated gain $\mathcal{G}_{\mathrm{d}U/\mathrm{d}E}$, as illustrated in Plot 7.19. In other words, pixels with higher gain exhibit a lower fraction of hits attributed to partially collected charge. Since the measurement is performed at −20 V, a point where the gain dependence on the reverse bias voltage goes into saturation (see Section 7.1.4), it cannot be concluded whether the observed correlation originates from local variations in the reverse bias voltage or is inherently linked to the gain itself. To confirm the magnitude of this effect, additional measurements at varying high-voltage settings under the *high-gain* configuration are required; however, these are beyond the scope of this study.

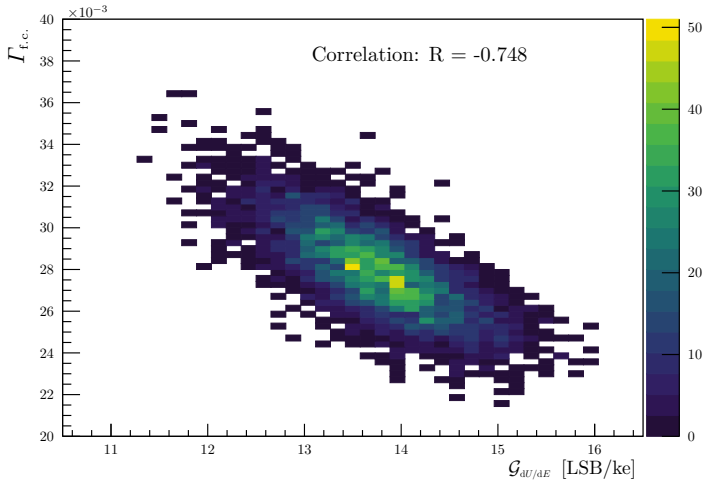

Plot 7.19: Correlation between gain $\mathcal{G}_{dU/dE}$ and $\Gamma_{\text{f.c.}}$ at −20 V for MP10-T100-S300-1 (*high-gain* settings).

Dependency on the Pixel Domain

An initial factor influencing the rate of hits at lower threshold values contributing to $\Gamma_{\text{f.c.}}$ is the pixel domain within the pixel matrix. The outermost pixels — i.e., edge and corner pixels — represent a distinctly different scenario compared to the inner pixels, as at least one side of these pixels is not bordered by another pixel.

Charge deposited in the vicinity of these edges can diffuse into the edge pixels, thereby adding to the fraction of hits attributed to partially collected charge. Since the pixel geometry is identical in both pitch directions, this effect is expected to scale primarily with the volume of the non-depleted substrate adjacent to each pixel side (see Section 3.2.1). Consequently, the pixel matrix is divided into five domains: inner pixels, top row (pixel row 249), bottom row (pixel row 0), left column (pixel column 0), and right column (pixel column 255), excluding corner pixels due to limited statistics (cf Figure 5.8).
Plot 7.20a shows the mean value of $\Gamma_{\text{f.c.}}$ as a function of the applied reverse bias voltage for the different pixel domains. As expected, all five domains exhibit a clear decreasing trend of $\Gamma_{\text{f.c.}}$ with increasing reverse bias voltage, as the depletion region extends deeper into the sensor bulk. Notably, the inner pixel domain shows a significantly lower mean value of $\Gamma_{\text{f.c.}}$ compared to all edge pixel domains, as illustrated in Plots 7.20b and 7.20c. In simplified terms, the overall shape of these curves follows a similar trend but with an offset relative to the inner pixel domain.

At voltages below −20 V, the outer pixel domains largely overlap within their statistical fluctuations (see Plot 7.20b), whereas their differences become more pronounced at higher voltages (see Plot 7.20c). The left and right pixel columns, located approximately 78.5 µm from the chip *guard-ring*, exhibit the highest values of $\Gamma_{\text{f.c.}}$ as they are adjacent to the largest volume of non-depleted substrate. They are followed by the top row, located around 48.5 µm from the chip *guard-ring*, implying the smaller adjacent non-depleted volume compared to the side columns. The bottom row, positioned only 37.7 µm from the periphery (not the chip *guard-ring*), shows the most pronounced decrease in $\Gamma_{\text{f.c.}}$ with increasing voltage, approaching the values observed for the inner pixel domain. If both the bottom pixel row and the periphery are not fully confined by the *guard-ring* structures in terms of depletion, the depleted volume may extend beyond the pixel boundaries. In this case, charge generated between the bottom row pixels and the periphery can be collected by either of them, reducing the effective volume contributing to partial charge collection.

Since $\Gamma_{\text{f.c.}}$ clearly depends on the pixel domain — an effect observed in all DUT sensors (not shown) — all subsequent studies are conducted using only the inner pixel domain to avoid potential bias in the interpretation of the results.

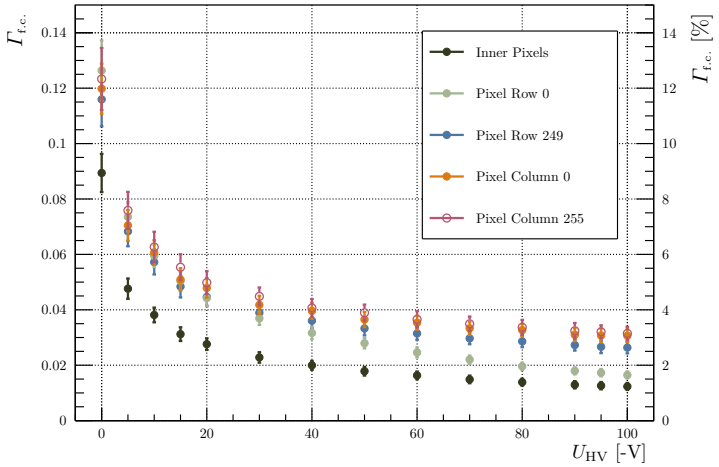

(a) $\Gamma_{\text{f.c.}}$ as function of the applied reverse bias voltage. The mean value of the respective distribution is plotted, with the error bars indicating the corresponding standard deviation.

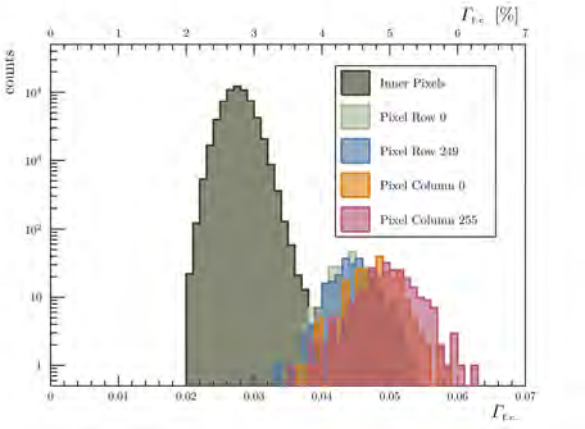

(b) $\Gamma_{\text{f.c.}}$ distributions at −20 V reverse bias voltage split by pixel domains.

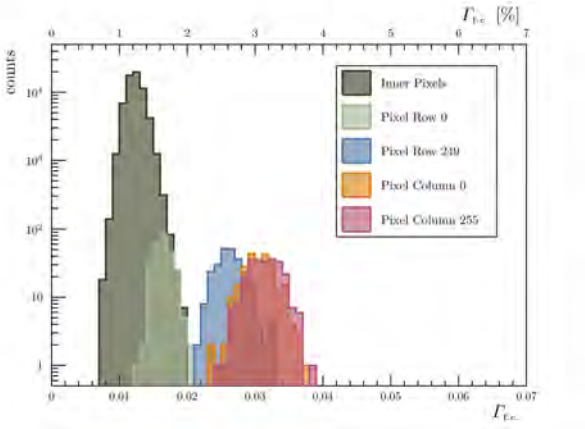

(c) $\Gamma_{\text{f.c.}}$ distributions at −100 V reverse bias voltage split by pixel domains.

Plot 7.20: Fractional charge collection ($\Gamma_{\text{f.c.}}$) as function of the applied reverse bias voltage for MP10-T100-S300-1 (100 µm). The data is split into five pixel domains, the inner pixels, and the edge pixel domains. Corner pixels are excluded due to low statistics.

Dependency of the Sensor Thickness

As it can be deduced that excess material — namely, the substrate that remains non-depleted — determines the fraction of hits with partial charge collection, it is instructive to study how differences in sensor thickness at varying depletion depths affect $\Gamma_{\text{f.c.}}$.

Plot 7.21a shows the dependency of $\Gamma_{\text{f.c.}}$ on the applied reverse bias voltage for different sensor thicknesses ranging from 50 µm to 100 µm. It becomes evident that the thicker sensor exhibits larger values of $\Gamma_{\text{f.c.}}$, when compared at the same reverse bias voltage. Examining the distributions of $\Gamma_{\text{f.c.}}$ at −20 V in Plot 7.21b, reveals that differences in sensor thickness translate directly into a systematic shift of the distributions toward higher $\Gamma_{\text{f.c.}}$ values with increasing thickness. Here, the depletion depth of the 50 µm sensor extends almost to the backside of the sensor, resulting in the lowest values of $\Gamma_{\text{f.c.}}$. The overlap of the distribution tails is primarily influenced by the respective gain conditions of each sensor, which explains why the 70 µm thick sensor (MP10-T70-S300-1) typically aligns more closely with the 100 µm thick sensor (MP10-T100-S300-1) than with the 60 µm thick sensor (MP10-T60-S300-1) (see Section 7.1.4)

These observations indicate that the contribution of the non-depleted substrate to the charge collection cannot be neglected for sensors within this thickness range. The effect is, however, expected to be less pronounced for thicker

sensors with higher-resistivity substrates, where the depletion depth extends further into the bulk at comparable voltage levels.

To quantify this effect more precisely, a gain correction could be applied to $\Gamma_{\text{f.c.}}$ to decouple gain variations from the genuine impact of partial charge collection. Although this analysis is tedious and thus not pursued within this thesis, it is noted as a potential direction for future research.

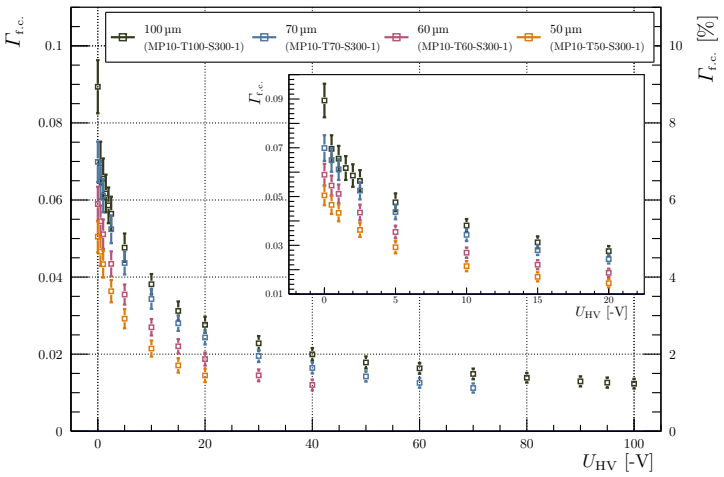

(a) Mean value of the charge sharing as function of the applied high voltage for different sensor thicknesses. Error bars indicating the corresponding sigma of the distribution.

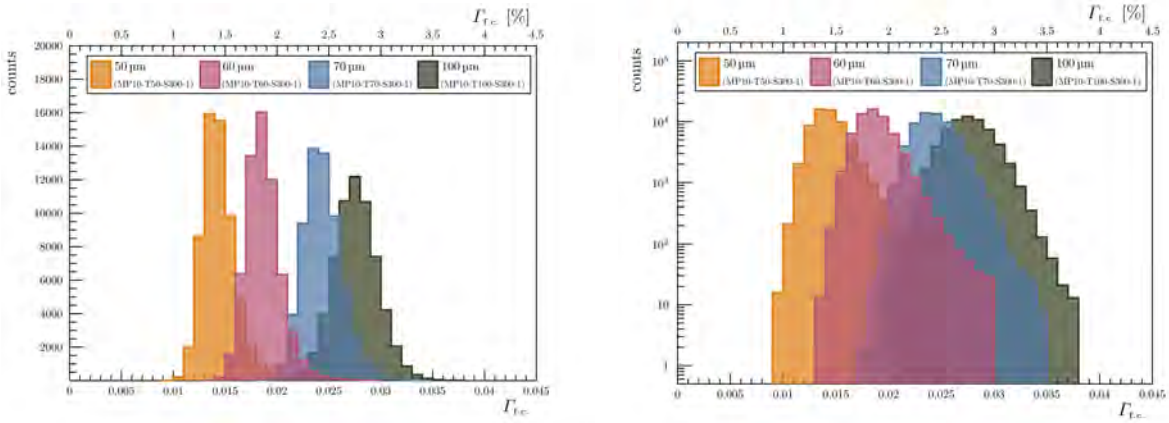

(b) Charge sharing distributions (linear: left, logarithmic: right) at −20 V reverse bias voltage split by sensor thickness.

Plot 7.21: Charge sharing study as function of the applied high voltage and sensor thickness.

Dependency of the Substrate Resistivity

The final factor directly influencing the depletion depth is the resistivity of the sensor substrate (see Section 2.3.1). In this study, all three 50 µm sensors — covering both resistivity ranges (10 Ω cm to 20 Ω cm and 200 Ω cm to 400 Ω cm) — are compared to assess the impact of substrate resistivity on $\Gamma_{\text{f.c.}}$.

The results, summarized in Plot 7.22, show the dependence of $\Gamma_{\text{f.c.}}$ on the applied reverse bias voltage for these sensors (see Plot 7.22a). Two key trends become immediately evident: (i) both 50 µm sensors with higher resistivity exhibit consistent results across the full voltage range (within the limits of gain variations), demonstrating the reproducibility of sensors fabricated with identical specifications; and (ii) the "standard" resistivity sensor exhibits significantly higher $\Gamma_{\text{f.c.}}$ values at lower voltages, as expected, since its depletion depth is substantially smaller at equivalent bias levels, resulting in a larger fraction of non-depleted substrate contributing to partial charge collection.

This observation is clearly reflected in the distributions of $\Gamma_{\text{f.c.}}$ at −20 V in Plot 7.22b, where the "standard" resistivity sensor shows a distinct shift toward higher $\Gamma_{\text{f.c.}}$ compared to the higher-resistivity sensors, accompanied

by a broader distribution that cannot be fully explained by gain variations alone. Only for voltages exceeding −80 V does the "standard" resistivity sensor approach $\Gamma_{\text{f.c.}}$ magnitudes obtained below −5 V for the higher resistivity sensors, consistent with a resistivity difference exceeding one order of magnitude (approximately by a factor of 20).

For voltages exceeding −100 V, a kink in the $\Gamma_{\text{f.c.}}$ trend is observed towards lower values agreeing with the observed onset of impact ionization processes discussed in Section 7.2.1. Combining these information, it can be concluded that this sensor was most likely fabricated on a substrate with a resistivity closer to 10 Ω cm than 20 Ω cm.

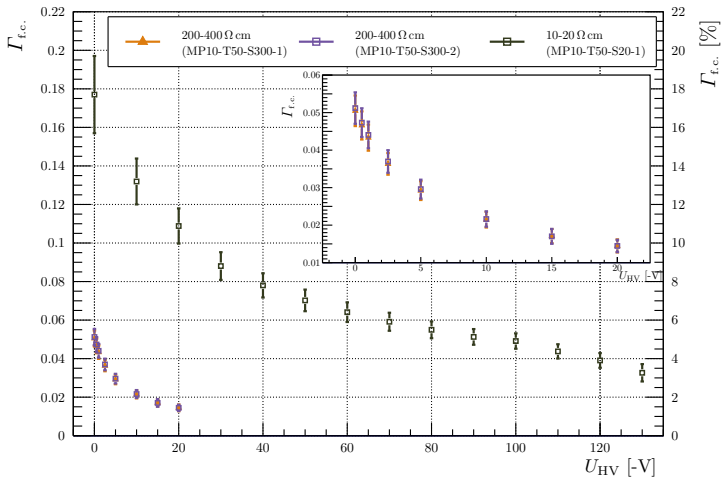

(a) Mean value of the charge sharing as function of the applied high voltage for different sensor resistivities of 50 µm MuPix10. Error bars indicating the corresponding sigma of the distribution.

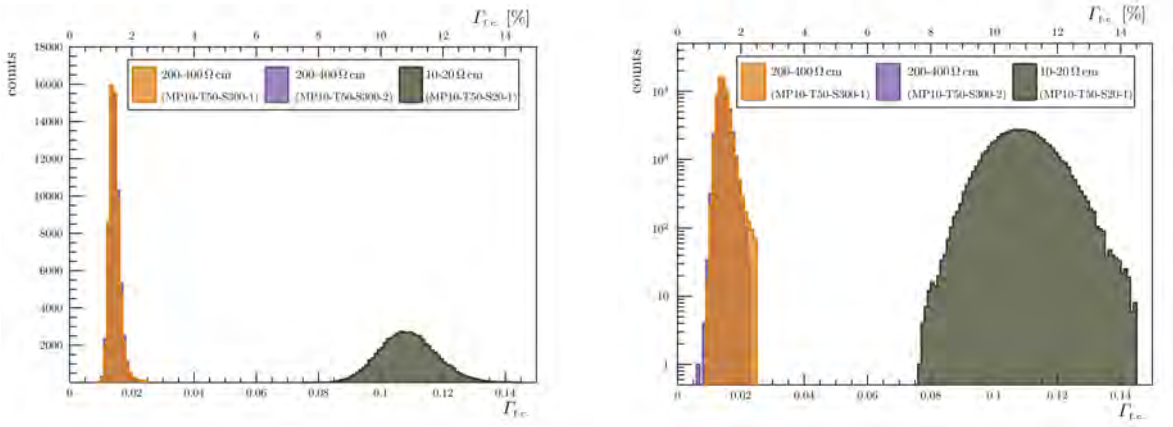

(b) Charge sharing distributions (linear: left, logarithmic: right) at −20 V reverse bias voltage split by sensor resistivities of 50 µm MuPix10.

Plot 7.22: Charge sharing study as function of the applied high voltage and sensor resistivity of 50 µm MuPix10.

7.2.6 Resistivity Reconstruction via Photon Absorption

The resistivity ranges of the DUT sensors used in this thesis (see Section 5.1.2) represent an important parameter when estimating the depletion depth (see Section 2.3.1) and all interpretations of measurements derived from it, motivating an experimental approach to more precisely constrain the actual substrate resistivity. So far, only indirect indications — such as impact ionization effects (see Section 7.2.1) or the partial charge collection behavior (see Section 7.2.5) — have been available.

A potential alternative method to estimate the substrate resistivity is to study the photon absorption rate from a monochromatic Fe-55 source as a function of the effective absorption depth, which is controlled by the depletion depth at a given reverse-bias voltage. For a stationary Fe-55 source positioned above the sensor, the detected photon rate directly reflects the charge-collection depth. By measuring this rate as a function of the applied bias voltage, utilizing an effective depletion depth model, the aim is to extract the substrate resistivity.

Methodology

Accurate resistivity reconstruction requires separating the total charge-collection depth into the depletion depth and an additional effective depth representing charge diffusion in the non-depleted region. The influence of the non-depleted volume in such a measurement introduces a large uncertainty in assessing the resistivity, as investigated in [194, p. 2ff, sec. 3 & 4]. The paper attempts to extract the theoretical depletion depth based on the measured hit rate using the photoelectric cross section of the 59.5 keV emission from an Americium-241 source. Although the reconstructed depth falls within the expected resistivity range, the data must be scaled to account for hits attributed to the non-depleted region, resulting in values at the lower end of the nominal resistivity range[4].

From the Fe-55 S-curve analysis, the number of detected photons is extracted via the normalization parameter N_γ (see Section 6.2.2), assumed to represent photon events from the depleted region, while partially collected charge events from the non-depleted region are represented by the $\Gamma_{\text{f.c.}}$ parameter. Since the photon absorption scales with the charge-collection depth, the derivative — the absorption rate defined by N_γ over the measurement time — can be expressed as a function of an effective depletion depth $d_{\text{effective}}$ (see Equation 7.3 below):

$$\left(\frac{\mathrm{d}N_\gamma}{\mathrm{d}t}\right) = \left(\frac{\mathrm{d}N_\gamma}{\mathrm{d}t}\right)_{\text{max}} \cdot \left[1 - \exp\left(-\frac{d_{\text{effective}}}{\lambda_{a,\text{K}\bar{\alpha}}}\right)\right] \tag{7.2}$$

where $\left(\frac{\mathrm{d}N_\gamma}{\mathrm{d}t}\right)_{\text{max}}$ is the maximum observable rate of a sensor completely absorbing all observable incident photons, and $\lambda_{a,\text{K}\bar{\alpha}}$ is the absorption length of $K_{\bar{\alpha}}$ photons in silicon (see Table 6.1). As it is assumed that the relative ratio between the absorption of $K_{\bar{\alpha}}$ and K_β photons remains constant, and N_γ scales both individually according to the relative abundance (see Section 6.2.2), only the absorption of $K_{\bar{\alpha}}$ photons is considered here to simplify the model. The initial photon rate and absorption length of the upper, non-active layers (cf. Section 3.2.1) are not required, as only the relative change in absorption with increasing depletion depth is of interest.

The effective collection depth follows the simple *pn*-junction depletion model introduced in Section 2.3.1, extended by an additional effective depth $d_{n\text{-well}} \approx 6\,\mu\text{m}$ to account for the deep *n*-well of the diode, which is assumed to contribute to the charge collection too:

$$d_{\text{effective}}(U \mid U_{\text{offset}}, d_{n\text{-well}}, \mathcal{N}_{eff})\,[\mu\text{m}] \approx 1.138 \cdot 10^{-3} \cdot \sqrt{\frac{[1 \times 10^{13}\,\text{cm}^{-3}]}{\mathcal{N}_{eff}} \frac{(U_{\text{offset}} + |U|)}{[\text{V}]}} + \frac{d_{n\text{-well}}}{[\mu\text{m}]} \tag{7.3}$$

Here, $U_{\text{offset}} = U_{bi} + U_{n\text{-well}}$ is the offset voltage accounting for the initial depletion at zero bias voltage, where U_{bi} is the built-in voltage $U_{n\text{-well}}$ is the potential of the *n*-well defined by *vdda* ($\approx 1.8\,\text{V}$). The effective doping concentration $\mathcal{N}_{eff} \approx \mathcal{N}_A$ is expressed in $1 \times 10^{13}\,\text{cm}^{-3}$ to simplify the numerical factor, consistent with the expected range for the DUT sensors (see Section 2.2.4).

Lateral depletion is not included in this model, which is only valid if the initial depletion at zero bias — i.e., under U_{offset} — extends up to the pixel *guard-ring*. This assumption does not hold for low-resistivity sensors (10 Ω cm to 20 Ω cm) and is therefore applied only to those with higher resistivity.

[4] In [194], the substrate resistivity for the AstroPix2 and AstroPix3 sensors is reported to range from 100 Ω cm to 400 Ω cm ((300 ± 100) Ω cm). Since AstroPix2 was fabricated in the same MPW run as TelePix [189], all sensors were manufactured on wafers from the same batch, characterized by a resistivity of (370 ± 20) Ω cm.

Spatial Dependency of the Photon Absorption Rate

As the Fe-55 source is positioned at a close distance above the sensor surface, the photon absorption rate is not uniform across the sensor area. This leads to a spatial dependence of the observed event rate due to varying effective path lengths through the sensor bulk under different incident angles.

To account for these effects, several approaches can be applied: (i) a detailed geometrical model including the source position, sensor surface coverage, and source-opening geometry; (ii) restricting the analysis to the central sensor region directly below the source, where spatial dependencies are minimal; or (iii) modeling the event-rate profile across the pixel matrix at a given bias voltage and extracting the event rate at the center position directly beneath the source using a fit function.

For the third method, the photon absorption profile on the sensor surface can be approximated by a two-dimensional normal distribution centered at the projection of the source position above the sensor. As the source holder features a finite opening diameter and may not be perfectly parallel to the sensor surface, asymmetries in the absorption profile can occur. These are modeled by allowing different standard deviations in both directions ($\sigma_x \neq \sigma_y$) and introducing a correlation coefficient $\rho_{x,y}$ between the axes[5]. The resulting model follows the bivariate normal distribution (binormal PDF [114, p. 20ff]), renormalized to peak at unity and scaled by the maximal observable photon rate $\left(\frac{\mathrm{d}N_\gamma}{\mathrm{d}t}\right)_{\text{center}}$ at the body-center:

$$\left(\frac{\mathrm{d}N_\gamma}{\mathrm{d}t}\right) = \left(\frac{\mathrm{d}N_\gamma}{\mathrm{d}t}\right)_{\text{center}} \cdot \mathrm{e}^{-\frac{1}{2\left(1-\rho_{x,y}^2\right)}\left[\left(\frac{x-\mu_x}{\sigma_x}\right)^2+\left(\frac{y-\mu_y}{\sigma_y}\right)^2-2\rho_{x,y}\cdot\frac{(x-\mu_x)(y-\mu_y)}{\sigma_x\sigma_y}\right]} \tag{7.4}$$

Using this model, the spatial dependence of the photon absorption rate can be fitted for each applied bias voltage, yielding a maximal photon rate at the center position and generally a weak correlation of $\rho_{x,y} < 0.1$, as shown in Plot 7.23a. This low correlation indicates minimal linear dependence between the axes, consistent with a plane-parallel alignment of the source opening relative to the sensor surface. Note, that the extracted maximal photon rates can exhibit rather small statistical uncertainties, a potential systematic influencing the following fit results to extract the resistivity. Additionally, the high-voltage supply may slightly deviate from the nominal setting; an uncertainty of 100 mV is assigned to the applied bias voltage in the fit, accounting for the voltage level actually reaching the bias grid of the sensor.

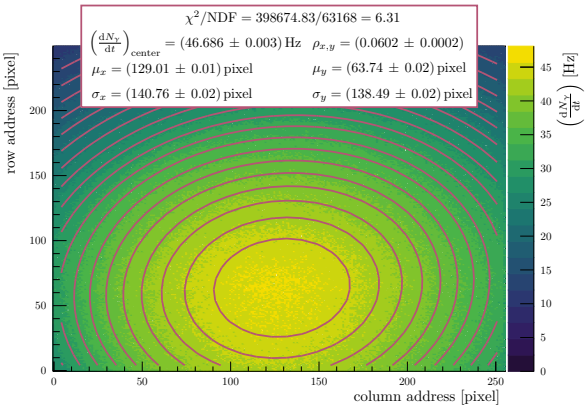

(a) Example of a rate map of absorbed Fe-55 photons for MP10-T100-S300-1 at −5 V reverse bias voltage. The red lines indicate the fitted binormal function (see Equation 7.4) and its projections onto the x- and y-axis.

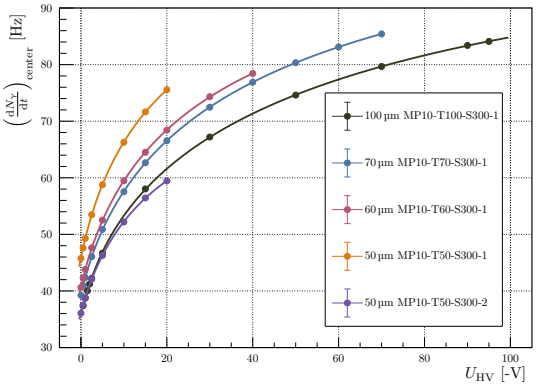

(b) Fitted photon absorption rate for all 200 Ω cm to 400 Ω cm DUT sensors as function of the applied reverse bias voltage. The solid lines indicate the fit result based on Equation 7.2 and Equation 7.3. Both U_{offset} and $d_{n\text{-well}}$ are free fit parameters in the presented fit, results are listed in Table 7.1.

Plot 7.23: Spatial dependency of the photon absorption rate and resistivity reconstruction results for 200 Ω cm to 400 Ω cm DUT sensors.

[5] For $\rho_{x,y} = 0$, the "binormal" distribution simplifies to the product of two independent normal distributions.

Model Results and Assumption Implications

The resistivity reconstruction results are summarized in Table 7.1. The effective depletion depth model from Equation 7.3 is fitted to the high-voltage dependency of the central photon absorption rates (see Plot 7.23b) for each high-resistivity DUT sensor. Four scenarios are considered, varying the treatment of the offset voltage U_{offset} and the effective n-well depth $d_{n\text{-well}}$ — either as fixed or free parameters.

In all cases, reasonable starting parameters and lower boundaries — like 0 V for U_{offset} and 0 µm for $d_{n\text{-well}}$ — were used, while leaving upper limits free to observe model behavior. A major difficulty arises from the strong correlation between U_{offset} and $d_{n\text{-well}}$; as one parameter increases, the other typically decreases, resulting in large uncertainties in the accuracy of the reconstructed effective doping concentration $\mathcal{N}_{eff}$. When both parameters are treated free and no external constraints (e.g., independent built-in voltage measurements) are available, fits for thinner sensors often yield unreasonable fit results. All their data points lie within the steepest gradient region of the model function for both depletion depth and photon absorption rate. As a result, small changes in these parameters cause large variations in the fit. Extending the voltage range could mitigate this, as leverage increases significantly when including regions of lower slope, but this is not feasible for these sensors. A similar sensitivity arises when the fitted voltage range is restricted for thicker sensors.

Applying empirical limits significantly improves stability: the built-in voltage typically ranges from 0.4 V to 0.8 V (see Section 2.3.1), here assumed to be around 0.7 V depending on the actual doping concentration, while the n-well bias voltage is capped by *vdda*, which amounts in total to around 2.5 V for U_{offset}. The n-well depth can also be constrained to approximately 6 µm, consistent with values expected for "standard" resistivity sensors, although it may deviate for higher-resistivity substrates due to altered implantation profiles. With at least one parameter constrained, values for both 50 µm sensors stabilize to overlapping ranges in all scenarios, indicating reproducible fabrication.

However, a consistent trend is observed: thinner sensors yield lower effective doping concentrations $\mathcal{N}_{eff}$, corresponding to higher reconstructed resistivities. This effect appears for all combinations of fixed and free parameters, suggesting that the assumption that hits from the non-depleted region are fully excluded when considering only the photon rate N_γ does not hold completely. Furthermore, this effect scales with the amount of excess material — defined by the total sensor thickness and applied voltage — indicating that a voltage-dependent correction factor is still necessary for accurate resistivity extraction. If this is the sole impact, the reconstructed resistivity for the thinnest sensors would be most accurate, as their depletion depth approaches the total sensor thickness at lower voltages, minimizing contributions from the non-depleted region. However, since these sensors yield reasonable values only when parameter assumptions are applied, no definitive statement on absolute resistivity can be made.

A potential solution is to acquire a fixed point — for example, by operating sensors beyond full depletion, where the photon rate saturates. One thickness alone is insufficient to disentangle all parameters reliably, but a combined fit across multiple thicknesses could provide the necessary constraints. As the current sensor cannot be operated above full depletion voltages, this hypothesis cannot be tested, and thus no conclusive statement on the absolute substrate resistivity can be made here.

In summary, while empirical constraints improve fit stability, reliable resistivity determination remains challenging without precise knowledge of key parameters and is sensitive to assumptions made regarding the depletion model. This difficulty increases as contributions from the non-depleted region become more significant, which must be considered when studying the charge deposition of charged particles traversing the entire sensor depth, leaving uniformly distributed energy deposits.

	MP10-T100-S300-1	MP10-T70-S300-1	MP10-T60-S300-1	MP10-T50-S300-1	MP10-T50-S300-2
Thickness [µm]	100	70	60	50	50
χ^2/NDF	15.747/8 ≈ 1.968	1.890/9 ≈ 0.210	2.712/6 ≈ 0.452	0.536/4 ≈ 0.134	1.210/4 ≈ 0.303
	23.712/9 ≈ 2.635	3.875/10 ≈ 0.388	5.817/7 ≈ 0.831	1.201/5 ≈ 0.240	3.066/5 ≈ 0.613
	17.758/9 ≈ 1.973	6.997/10 ≈ 0.700	6.334/7 ≈ 0.905	0.954/5 ≈ 0.191	2.669/5 ≈ 0.534
	90.637/10 ≈ 9.064	25.494/11 ≈ 2.318	7.513/8 ≈ 0.939	6.034/6 ≈ 1.006	6.998/6 ≈ 1.166
$\left(\frac{dN}{df}\right)_{max}$ [Hz]	105.050 ± 0.751	107.275 ± 0.652	101.963 ± 2.635	103.234 ± 5.118	77.841 ± 2.023
	103.796 ± 0.209	108.130 ± 0.347	105.442 ± 0.884	109.611 ± 3.026	85.352 ± 2.221
	104.382 ± 0.171	108.757 ± 0.273	105.865 ± 0.702	108.254 ± 2.344	84.473 ± 1.800
	105.118 ± 0.158	109.438 ± 0.232	106.317 ± 0.588	104.732 ± 1.364	81.963 ± 1.027
U_{offset} [V]	1.781 ± 0.343	2.895 ± 0.278	3.512 ± 0.805	3.553 ± 0.965	4.545 ± 0.803
			2.5 (fixed)		
	2.125 ± 0.045	2.286 ± 0.051	2.436 ± 0.059	2.691 ± 0.080	2.680 ± 0.083
			2.5 (fixed)		
$d_{n\text{-well}}$ [µm]	6.462 ± 0.458	5.050 ± 0.435	3.783 ± 1.833	3.562 ± 2.971	0.151 ± 8.529
	5.518 ± 0.062	5.650 ± 0.079	5.853 ± 0.118	6.457 ± 0.169	6.437 ± 0.181
			6.0 (fixed)		
			6.0 (fixed)		
$\mathcal{N}_{eff}$ [1e13 cm^{-3}]	7.741 ± 0.463	5.612 ± 0.279	3.764 ± 0.773	2.554 ± 0.942	1.833 ± 0.388
	6.954 ± 0.095	6.005 ± 0.122	4.871 ± 0.227	3.880 ± 0.529	3.684 ± 0.482
	7.321 ± 0.068	6.290 ± 0.085	5.006 ± 0.164	3.573 ± 0.362	3.430 ± 0.345
	7.647 ± 0.062	6.522 ± 0.070	5.120 ± 0.134	3.033 ± 0.183	2.951 ± 0.172
$\mathcal{N}_{eff} \longrightarrow \varrho_{substrate}$ [Ω cm] at 300 K					
Static	161.258 ± 9.680	222.434 ± 11.086	331.642 ± 71.107	488.763 ± 208.658	681.016 ± 150.916
	179.508 ± 2.453	207.877 ± 4.225	256.272 ± 11.969	321.727 ± 44.695	338.844 ± 45.105
	170.51 ± 1.584	198.458 ± 2.682	249.361 ± 8.178	349.371 ± 35.764	363.936 ± 36.980
	163.241 ± 1.324	191.399 ± 2.055	243.809 ± 6.385	411.573 ± 24.924	423.01 ± 24.739
Arora	174.933 ± 10.494	241.251 ± 12.017	359.63 ± 77.081	529.95 ± 226.186	738.36 ± 163.593
	194.717 ± 2.659	225.47 ± 4.580	277.933 ± 12.975	348.888 ± 48.451	367.443 ± 48.895
	184.962 ± 1.717	215.259 ± 2.908	270.441 ± 8.865	378.854 ± 38.769	394.644 ± 40.087
	177.082 ± 1.435	207.607 ± 2.227	264.422 ± 6.922	446.283 ± 27.018	458.68 ± 26.818
Masetti	171.927 ± 10.296	236.992 ± 11.789	353.119 ± 75.606	520.17 ± 221.825	724.551 ± 160.429
	191.338 ± 2.609	221.51 ± 4.493	272.976 ± 12.728	342.577 ± 47.524	360.777 ± 47.959
	181.767 ± 1.685	211.493 ± 2.853	265.626 ± 8.697	371.969 ± 38.026	387.456 ± 39.319
	174.036 ± 1.408	203.985 ± 2.185	259.722 ± 6.790	438.105 ± 26.499	450.264 ± 26.302

Table 7.1: Fit results for the resistivity reconstruction using the Fe-55 photon absorption rate as function of the applied bias voltage for different sensors using Equation 7.2 and Equation 7.3. Four different fit scenarios are shown: all parameters free (black), U_{offset} fixed to 2.5 V (blue), $d_{n\text{-well}}$ fixed to 6 µm (red) and both parameters fixed (green). All values are rounded to the third decimal position. Resistivity values are derived by Equation 2.13 from $\mathcal{N}_{eff}$ using three different mobility models (Static, Arora, Masetti) as described in Sections A.2 and 2.2.4. Simplified error calculation for the resistivity employed: $e_{\text{resistivity}} = \frac{|f(\mathcal{N}_{eff}+e_{\mathcal{N}_{eff}})-f(\mathcal{N}_{eff}-e_{\mathcal{N}_{eff}})|}{2}$ with $f(x)$ depends on the employed mobility model.

7.3 Equivalent Noise Charge in MuPix10

Reproducing the exact noise level during the PSI testbeam campaign (see Section 5.2.3) with laboratory measurements is challenging due to differing environmental conditions (temperature, humidity, electromagnetic interference, etc.). Nevertheless, it is essential to characterize the noise to estimate its order of magnitude and assess how diode capacitance — expressed through changes in bias voltage — as well as sensor-to-sensor variations, affect the noise performance. This analysis provides insight into how observations in the efficiency measurements (see Section 5.4) may be influenced and whether the underlying charge deposition determination is significantly affected by noise contributions or dominated by other factors.

To enable intra- and inter-sensor comparisons, as well as comparisons across different gain settings, the noise must be determined in a standardized manner. The **E**quivalent **N**oise **C**harge serves as a figure of merit to describe the noise performance of a detector system, facilitating comparison with the calibrated charge deposition measurements and other detector technologies. It is defined as the ratio of the output noise voltage to the output voltage generated by a unit charge deposition in the sensor [17, p. 794]:

$$\text{ENC} = \frac{\text{noise output voltage [V]}}{\text{output voltage of a signal of 1 e [V/e]}} \tag{7.5}$$

The ENC is typically expressed in units of electrons [e] and, for better comparability with deposited energy, also in electron-volts [eV] within this thesis. Genuine signal hits must be distinguishable from "fake" hits caused by noise fluctuations, becoming more challenging as the deposited signal charge approaches the noise level. It reflects the achievable performance of the readout electronics, directly relating to the minimum detectable signal charge, and thus influences resolution and detection efficiency.

Note that the ENC is determined on a per pixel level, but its practical impact on sensor performance is given by the combined effects of noise magnitude, its amplification by the gain and threshold dispersion across the entire sensor (cf. subsection 7.1.7). In the presence of non-uniform detection thresholds — since no threshold trimming is applied — few pixels that exhibit elevated noise at a comparatively low thresholds can dominate the sensor's overall performance by constraining operation to higher global threshold settings.

Directly probing a single electron or measuring the signal directly is not feasible; instead, the ENC is extracted indirectly through S-curve measurements, as discussed in the following section.

7.3.1 Extraction of Noise from S-curves

In principle, the ENC can be extracted from either threshold or injection S-curves (see Section 6.3), but intrinsically both methods represent different approaches to probing the sensor's response.

In the injection S-curve case, the detector system is fixed while the input signal is varied. The ENC determined utilizing this method is also known as input-referred noise, as the input signal is swept across the response curve. Here, the noise is directly measured — assuming no contribution from the injection source itself — as the dispersion of the response at each injected charge level, independent of the linear gain of a pixel. Both the measured output amplitude — the mean of the S-curve — as well as the sigma parameter (σ_{E_C}) scale with the same linearity crossing the zero-energy point, allowing a direct determination of the noise and the **S**ignal-to-**N**oise **R**atio.

In contrast, threshold S-curves keep the input signal fixed while varying the detection threshold. Here, the noise is measured as the dispersion of the response at each threshold level, amplified by the local gain of the sensor at the respective threshold point. Therefore, a gain correction is required to extract the underlying ENC from the measured sigma parameter ($\sigma_{U_{\text{Th}}}$). It is important to note that a simple scaling of the global baseline to obtain the pixel gain is insufficient, as discussed in Section 7.1.1. Underestimating the gain leads to an overestimation of the noise (or an underestimation of the signal amplitude), thereby effectively reducing the resulting SNR.

To convert the sigma parameter values into meaningful ENC values, two procedures are available: (i) for injection S-curves, a direct conversion to electrons is performed via the injection capacitance $C^{\text{eff.}}_{\text{injection}}$ (see Equation 6.8); (ii) while for threshold S-curves, the amplification component ($\mathcal{G}_{\mathrm{d}U/\mathrm{d}E}$, here uncalibrated) has to be incorporated to account for the gain dependency of the measured sigma.

Both methods are summarized in the following equation:

$$\sigma_{noise} = \begin{cases} C^{\text{eff.}}_{\text{injection}} \cdot \sigma_{E_C} & \text{,for injection S-curves} \\ \dfrac{C^{\text{eff.}}_{\text{injection}}}{\underbrace{\mathcal{G}_{dU/dE}}_{\text{calibrated gain}}} \cdot \sigma_{U_{\text{Th}}} & \text{,for threshold S-curves} \end{cases} \tag{7.6}$$

The injection method is preferred, as it is simpler and is not limited to on-chip voltage DAC resolution, allowing finer control of measurement steps. Nevertheless, both methods should yield equivalent ENC values, as discussed in the following.

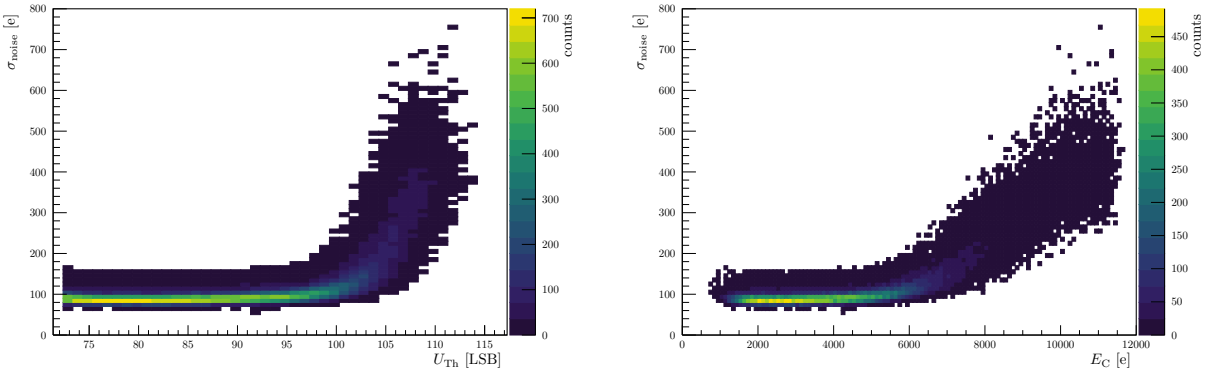

(a) Noise (σ_{noise}) from injection σ_{E_C} versus the applied threshold level U_{Th}.

(b) Noise (σ_{noise}) from injection σ_{E_C} versus the injected charge level E_C.

Plot 7.24: Injection "noise" sigma curve of MP10-T100-S300-1 at −20 V reverse bias voltage at *low-gain* settings.

7.3.2 "Noise" Dependency of the Measurement Domain

Extracting the ENC by a simple conversion method is tempting, but the measured value can significantly depend on where on the response curve the noise is evaluated. The determined noise level is strongly affected by the gain domain in which the measurement is performed — for both injection and threshold S-curves — as the measured sigma parameter values are either compressed (threshold) or stretched (injection) by the local gain gradient in the saturation domain of the sensor response curve (see subsection 6.4.1). Although the effect could be corrected for, the accuracy of the correction would dictate the overall precision of the ENC determination. Plot 7.24 illustrates this: the noise parameter σ_{noise} extracted from injection S-curves is shown as function of the applied detection threshold level U_{Th} and injected charge level E_C, respectively.

Considering the dependency along the detection threshold U_{Th} (see Plot 7.24a), the noise is flat in the linear region and increases rapidly once the saturation domain is entered. A small step in threshold corresponds here to a large fluctuation in the input charge due to the flattened response curve in this region. This behavior can be described by a function transitioning from a constant noise floor to an exponential increase with growth rate r_{growth} beyond the transition point $U_{\text{Th, TRS}}$:

$$\sigma_{noise} = \underbrace{\text{ENC}}_{\text{noise floor}} + e^{r_{\text{growth}} \cdot [U_{\text{Th}} - U_{\text{Th, TRS}}]} \tag{7.7}$$

The dependency along the injected charge E_C (see Plot 7.24b) exhibits the same behavior in the linear gain domain, but increases instead linearly in the saturation domain. This is of importance, as the efficiency curves measured in the testbeam campaign can extend well into the saturation domain, limiting the precision of the determination of the charge deposition since energy fluctuations in the amplification process start to dominate.

For the threshold S-curves an opposing effect is observed (not shown here, see Plot 6.3): the noise sigma is constant in the linear region and decreases in the saturation domain, saturating towards the intrinsic resolution limit set by the threshold binning.

Therefore, for better comparison and simplification of the problem, only noise below the transition $U_{\text{Th, TRS}}$ point is considered in the following for the determination of the ENC as it lies in the linear gain domain of the sensor. All individual noise measurement points for each pixel below their respective transition points are considered and averaged to determine the final ENC value:

$$\text{ENC} = \sum_{i}^{N} \frac{\sigma_{noise,i}}{N} \quad \text{for } \sigma_{noise,i} \text{ with } U_{\text{Th}} \leq U_{\text{Th, TRS}} \tag{7.8}$$

In the following all ENC values are based on this method, reflecting the underlying noise of a pixel instead of non-linearities and resolution limitations of the sensor.

Equivalence of ENC Determination

The ENC values determined on the gain independent injection sigma and the gain corrected threshold sigma should be equivalent within uncertainties. To validate this hypothesis, a correlation of all measured ENC values determined for each pixel under every bias voltage and gain setting is shown in Plot 7.25a. A strong correlation with a correlation coefficient of approximately $R \approx 0.9986$ is observed, with rare outliers primarily associated with higher noise values determined in the gain-corrected threshold method. The absolute difference between both methods is about 2 e with a standard deviation below 1 e (see Plot 7.25b). The shift favors smaller threshold ENC values, but remains within the accuracy of the ENC determination obtained with the averaging method described in Equation 7.8, and is therefore considered insignificant. This study confirms the equivalence of both methods and supports using either method for ENC determination, with the injection method being preferred for its simplicity and higher precision in the measurement process.

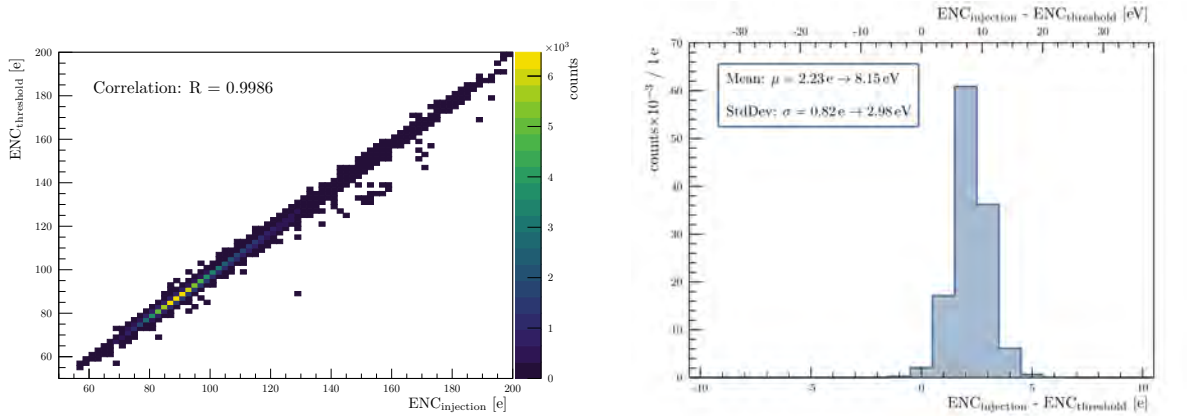

(a) Correlation of ENC determined on the standard deviation of injection and threshold S-curves for all sensors, bias configurations and gain settings.

(b) Difference of ENC determined on the standard deviation of injection and threshold S-curves for all sensors, bias configurations and gain settings.

Plot 7.25: Comparison of ENC determination from injection and threshold S-curves for all DUT sensors at different bias voltages and gain settings.

Fe-55 as a Noise Indicator and Analysis of Gain Independence

In contrast to charge injection, X-rays generating charge carriers via the photoelectric effect are bound to fluctuations in the charge-generation process (see Section 1.2.3). Thus, the smearing of the Fe-55 S-curves incorporates both the intrinsic noise seen by the readout chain as well as fluctuations in the charge generation process. Furthermore, the description of an Fe-55 S-curve (see Section 6.2.2) is less constraint than that of an injection or threshold S-curve, leading to larger uncertainties in the extracted sigma parameter $\sigma_{\text{K}\bar{\alpha},\beta}$.

In Plot 7.26a, the sigma parameter of Fe-55 S-curves ($\sigma_{\text{K}\bar{\alpha},\beta}$) is correlated with the mean noise sigma extracted from threshold S-curves ($\sigma_{U_{\text{Th}}}$). A strong correlation with an approximate correlation coefficient of $R \approx 0.895$ is observed, confirming that both methods probe the same underlying noise performance of the readout chain, and both are amplified by the local gain of the sensor at the respective measurement point. The deviation of the difference ($\sigma_{U_{\text{Th}}} - \sigma_{\text{K}\bar{\alpha},\beta}$) has its mean at about (-0.032 ± 0.063) LSB (the error indicated the standard deviation), as the

Fe-55 S-curves sigma is generally larger than the threshold S-curve sigma. Rare outlier points are attributed to an overestimation of the Fe-55 sigma caused by imperfect Fe-55 S-curve fitting, as discussed in Section 6.2.2. From this it is deduced that the influence of the injection source itself does not contribute to the noise as significantly as the fluctuations in the charge-generation process by the Fe-55 X-rays, and the parameter $\sigma_{\mathrm{K}_{\tilde{\alpha},\beta}}$ can be used to study the spatial dependencies of the noise performance across the sensor.

The gain independence of the extracted noise values is further examined to assess the robustness of the ENC determination method. To validate that the extracted ENC values of an injection S-curve is essentially gain independent, the calibrated gain is correlated with the corresponding ENC of each pixel. A weak anti-correlation with $R \approx -0.212$ is observed as shown (see Plot 7.26b), indicating that the extraction method is largely gain independent as expected. This was probed for different RoIs on the sensor, yielding similar results.

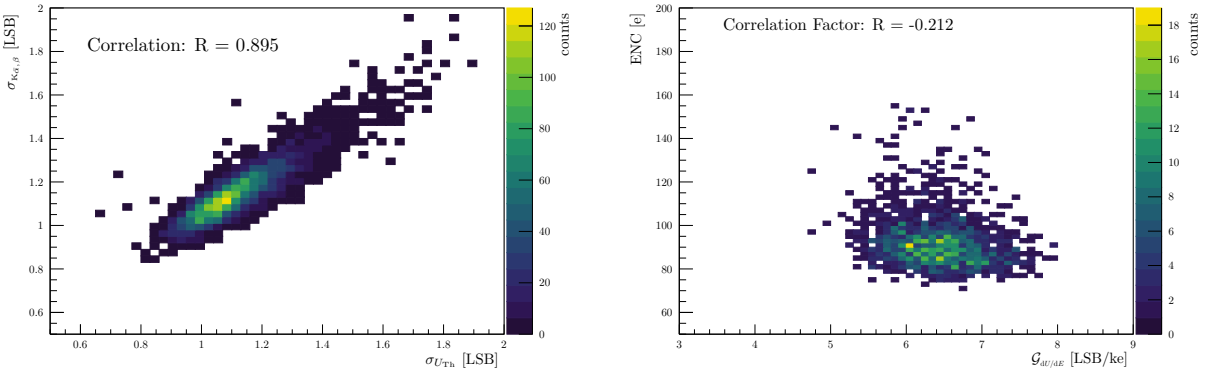

(a) Correlation of mean threshold S-curve noise sigma $\sigma_{U_{\mathrm{Th}}}$ and Fe-55 S-curve sigma $\sigma_{\mathrm{K}_{\tilde{\alpha},\beta}}$ (*high-gain* settings).

(b) Correlation between $\mathcal{G}_{\mathrm{d}U/\mathrm{d}E}$ and ENC determined from injection S-curves for sub-matrix C (*low-gain* settings).

Plot 7.26: Correlation studies between threshold S-curve and Fe-55 S-curve sigma and ENC and gain for MP10-T100-S300-1 at −20 V reverse bias voltage.

7.3.3 A Holistic View of ENC Distribution

The noise level can vary significantly from pixel-to-pixel caused by process variations in the bulk substrate as well as the implementation of shallow, doped wells and their embedded electronics. Whereas defects in the silicon and local hot spots result in an increased generation of thermally excited leakage currents, changes in the shaping characteristics across the pixel matrix influence the observed frequency spectrum of the noise for each pixel. The resulting variation of measured ENC contributions from each pixel exhibits a predominantly normal distributed shape with a "thin" tail towards higher noise levels (see Plot 7.27b). A change in operational settings also does not effect the overall shape of the distribution significantly, but shifts the distribution corresponding to the mean change in noise level. The various noise sources and their dependencies are discussed in more detail in Section 4.2.5.

In this section, the mean and standard deviation (used as error bars) of the ENC distributions are presented to provide an overview of the noise performance under different operating conditions, accompanied by exemplary distributions for illustration. Most examples focus on measurements performed on MP10-T100-S300-1, the sensor for which all routing segments and sub-matrices were characterized, covering the largest bias range within the studied RoIs (see Table 5.2).

Reverse Bias Dependency

To first-order approximation, the ENC is expected to depend linearly on the detector capacitance, facilitated by the diode capacitance of a pixel C_d, as described by [17, p. 798, eq. 17.114]:

$$\mathrm{ENC} = A\,[\mathrm{e}] + B\,[\mathrm{e}] \cdot \frac{C_d}{[\mathrm{fF}]} \tag{7.9}$$

where A and B depend on the specific shaping time, temperature, and technology node. This is a simplified version of the more general noise equation, which splits into the different noise contributions presented in Equation 4.42.

From this, a $C_d \sim 1/\sqrt{U_{\text{HV}}}$ dependence (see Equation 3.1) on the ENC is expected. While this exact dependence is not conclusively observed, an effect resembling it can be seen, as shown in Plot 7.27. It shows the mean ENC of three different DUT sensors plotted against the applied reverse bias voltage at *low-gain* settings. The increase in noise for bias voltages below approximately −20 V is attributed to changes in the diode capacitance, and this noise tends to decrease at higher voltages, where the change in diode capacitance becomes less significant and other capacitances — such as inter-pixel coupling capacitance (see Section 3.2.2) and parasitic capacitances — become more relevant in defining the total detector capacitance. This is also reflected in the distribution of the ENC at different bias voltages, as shown in Plot 7.27b. At 0 V reverse bias voltage, the mean ENC is approximately 20 % higher compared to −20 V. Increasing the bias voltage further to −100 V results in only a minor reduction of the mean ENC, on the order of a few electrons.

From Plot 7.27a, it is apparent that the diode capacitance plays a significant role only in the regime of large gradients in the capacitance-voltage characteristic, i.e., at lower bias voltages. For higher-resistivity substrates (200 Ω cm to 400 Ω cm) as well as the standard substrate (20 Ω cm), similar ENC levels are observed despite significant differences in diode capacitance at comparable reverse bias voltages. This indicates that other capacitance contributions are more relevant in the shaping times, and only slight deviations due to sensor-to-sensor variations are observed at higher bias voltages.

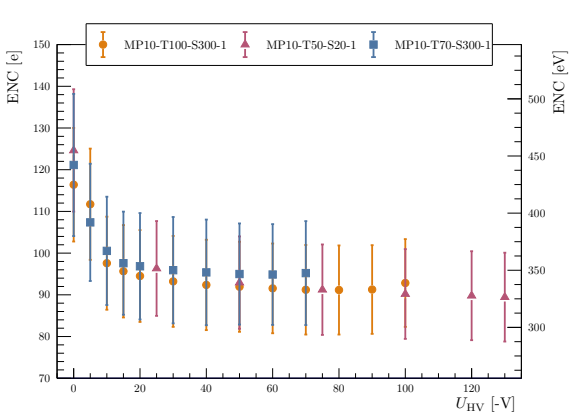

(a) Mean ENC as function of the applied reverse bias voltage. The error bars indicate the standard deviation within each sensor's RoIs.

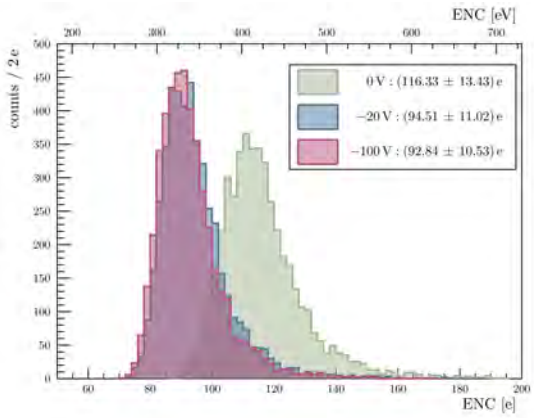

(b) ENC distributions of pixels in RoIs of matrix C of MP10-T100-S300-1 at different reverse bias voltages.

Plot 7.27: ENC measurements comparison between different reverse bias voltages of all DUT sensors at *low-gain* settings.

Sensor-to-Sensor Variations and Gain Setting Dependency

When leaving the bias sensitive regime, the sensor-to-sensor variation observed in the mean ENC across all sensors within a given gain setting amount to only a few electrons, negligible compared with the intra-chip pixel-to-pixel dispersion (see Plot 7.27). Also, switching to a different gain setting does not significantly affect the noise level; it only causes a minor shift in the noise distribution. This shift corresponds to a lowering of the mean ENC from about 90 e to 99 e at the *low-gain* setting to noise levels ranging from 76 e to 83 e when transitioning to the *high-gain* setting (see Plot 7.28b), both within the standard deviations of approximately 10 e exhibited by the two distributions. Although the mean noise level increases by about 10 %, the noise alone still allows relatively low detection thresholds (see Section 7.1.7). Outlier pixels with high noise are more critical, as they can dominate the overall sensor performance. Applying a threshold trimming can mitigate this by increasing the local threshold for those pixels.

The difference in gain is not expected to be the dominant factor influencing the noise level, but cannot be completely ruled out as the different noise source contributions cannot be separated from each other (see Section 4.2.5). Foremost, a thermal difference is expected to be the main driver, as a significant increase in power consumption accompanies a change in gain setting. A rise of the current flow of about 40 % from *high-gain* to *low-gain* settings (see Table A.12) necessitates a higher sensor bias to account for voltage drops towards and across the sensor. The primary DACs, controlling the current sources in the analog pixel cell, decrease for the *high-gain* setting (see

Table A.9), while the current sources for the comparators in the periphery increase. The overall higher power consumption can heat the sensor, leading to increased thermal noise (see Equation 4.45). An equivalent behavior is observed for all sensors, see Plot 7.28a, even when the pixel-to-pixel dispersion is more pronounced than sensor-to-sensor variations.

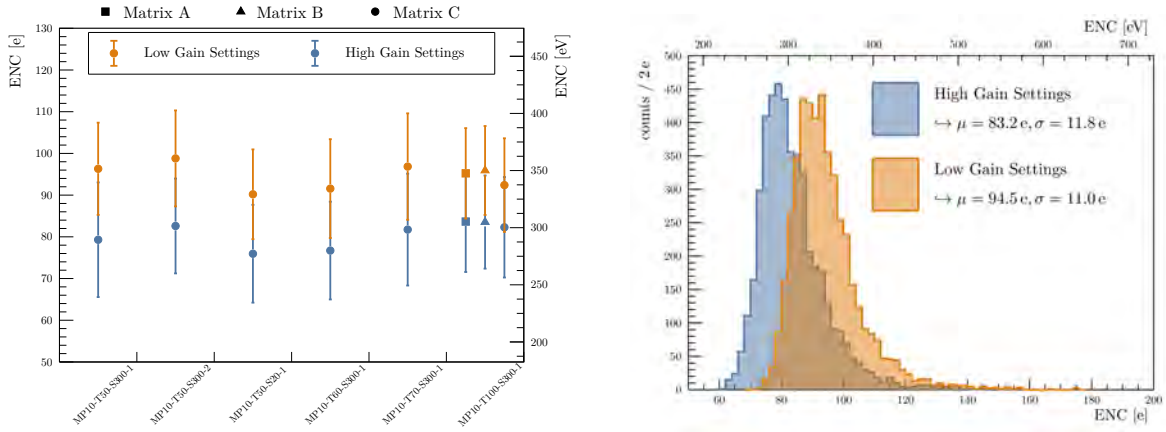

(a) Mean ENC of all DUT sensors. The error bars indicate the standard deviation within each sensor's RoIs.

(b) ENC distributions of pixels in RoIs of matrix C of MP10-T100-S300-1.

Plot 7.28: ENC measurements comparison between *low-gain* and *high-gain* settings of all DUT sensors at −20 V reverse bias voltage (−100 V for MP10-T50-S20-1).

Spatial Dependency of the Noise

Within the pixel matrix itself, only limited spatial variations are expected arising from localized differences in the shaping characteristics across the matrix. An increased power consumption would affect all pixels equally if current sources within the in-pixel analog circuits are the cause for an increased temperature (within pixel-to-pixel variations). The more relevant heat sources on the MuPix10 are located in the periphery, where the fast switching logic of the FSM and output links is situated, as well as the *vssa* regulators (see Section 3.7.1). If the heat conduction is sufficiently significant, a temperature gradient distributed radially from the heat sources towards higher pixel row addresses is expected, as observed in thermal imaging of the sensor under different operational conditions reported in [150, p.34ff, sec. 3.2.4, fig. 3.8].

To validate that these heat sources effect the noise, the ENC data of MP10-T100-S300-1 is divided into the different sub-matrices A, B & C (see Plots 7.29a and 7.29b) and routing segments 1 to 4 (see Plots 7.29c and 7.29d) of the sensor (see Sections 3.2 and 3.4). The results are summarized in Plot 7.29, presented in both gain settings next to each other for comparison.

Although the absolute deviations between RoIs are small compared to the deviations from pixel-to-pixel, expected tendencies in the spatial distribution of the noise are observed. A difference of less than 3 e is observed between the cumulative mean ENC of the different sub-matrices, whereas a larger shift of about 10 e is obtained for the different routing segments. Foremost the higher noise level in the lowest routing segment (1) of each submatrix is visible, which can be attributed to the higher heat dissipation coming from the periphery (see Plots 7.29e and 7.29f). Towards higher routing segments (2-4), further away from the periphery, a decrease in the mean noise level of about 10 % to 15 % is observed — depending on the RoIs considered — indicating a temperature gradient across the pixel matrix. Differences in local shaping times across the pixel matrix can also contribute to this effect, reflected by slight variations in the gain observed across the sensor (see Section 7.1.4).

Note, that the observed distributions can vary depending on the sensor thickness, affecting the heat transportation within the silicon bulk, as well as the mounting method on the carrier PCB. The PCB material below the active area, present in some of the studied sensors (see Section 5.1.2), can act as a heat sink. This can alter the heat dissipation characteristics, leading to different spatial noise distributions compared to sensors that have a cutout in this region. As the overall mean noise level seems not to be significantly affected by these effects (see Plot 7.28a), the spatial distributions are not further studied here.

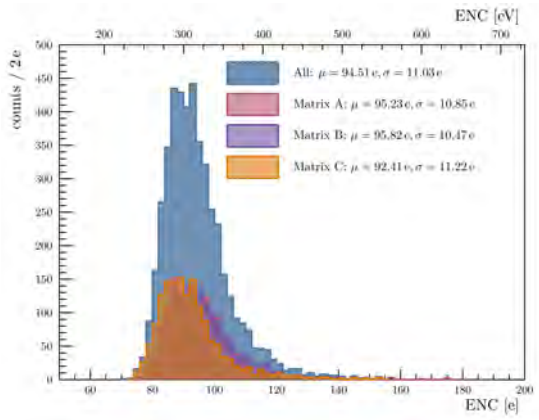

(a) ENC distributions of pixels in RoIs of matrix A, B, and C, as well as the combined region, at *low-gain* settings.

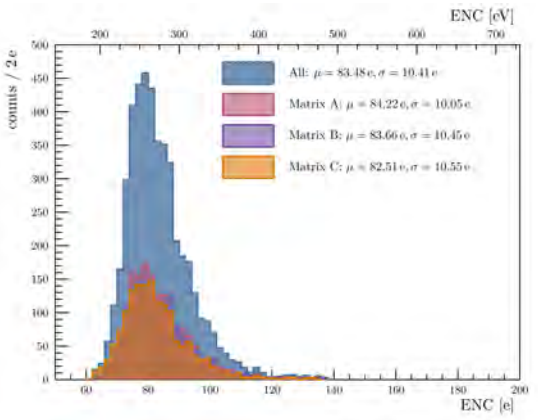

(b) ENC distributions of pixels in RoIs of matrix A, B, and C, as well as the combined region, at *high-gain* settings.

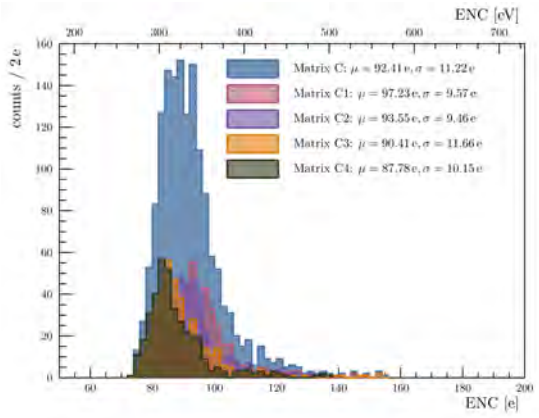

(c) ENC distributions of pixels in RoIs of routing segments 1-4 of matrix C, as well as the combined region, at *low-gain* settings.

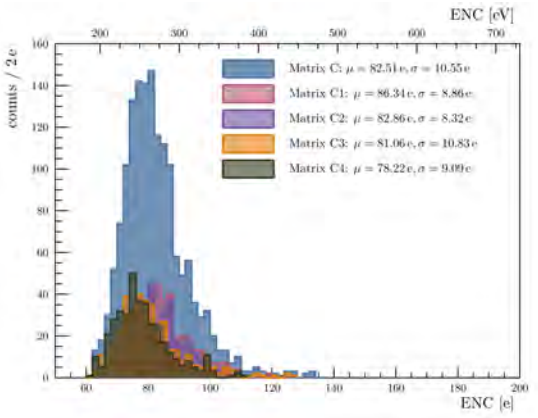

(d) ENC distributions of pixels in RoIs of routing segments 1-4 of matrix C, as well as the combined region, at *high-gain* settings.

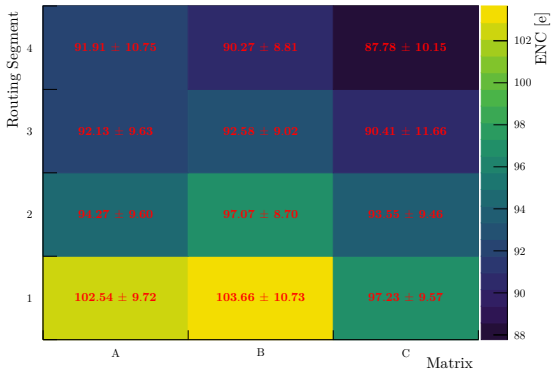

(e) Mean ENC of all RoIs mapped onto the sensor at *low-gain* settings.

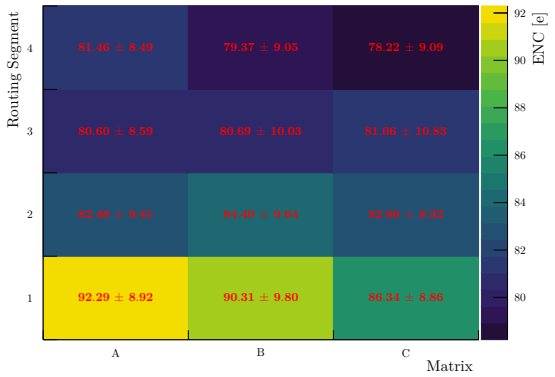

(f) Mean ENC of all RoIs mapped onto the sensor at *high-gain* settings.

Plot 7.29: Spatial ENC dependencies for MP10-T100-S300-1 at −20 V reverse bias voltage. Left side the *low-gain*, right side the *high-gain* are shown. Errors indicate the standard deviation within each RoI.

7.4 Conclusions

This chapter presented a detailed outline of the measurement results conducted for the energy calibration of the MuPix10 sensor. Charge *Injection* was used to probe the sensor's readout chain energy response, complemented by well-known energy points obtained from studying monochromatic X-ray absorption using an Fe-55 source. Both are obtained from S-curve measurements and combined to extract key parameters of the detector response — such as gain, noise, and threshold dispersion — all provided in universally comparable units to facilitate comparison with other HV-MAPS sensors. For all key parameters, consistent results were obtained within a gain setting, with inter-chip variations primarily dominated by process variations observed in pixel-to-pixel differences. Only for reverse bias voltages below −20 V are deviations observed, which are attributed to changes in gain and noise performance, likely caused by the increasing diode capacitance as the depletion zone shrinks.

The calibrated detector response model allows precise conversion from detection threshold to input charge, enabling an accurate energy calibration of hit efficiency measurements presented in Chapter 8. However, this precision depends on the reproducibility of the actual operational settings of each DUT sensor during the PSI testbeam campaign (see Section 5.4) in the laboratory. Measured noise levels and high-voltage dependencies allow an assessment of whether the observed smearing of the hit efficiency curves is intrinsic to the sensor or influenced by external factors, such as the underlying charge deposition statistics or inaccuracies in the beam telescope resolution. A comparison with the obtained data from calibrated hit efficiency curves will be discussed in the upcoming Chapter 8.

Beyond calibration, the combination of *Injection* and Fe-55 measurements showed to provide a comprehensive framework for studying the characteristics of the detector response of HV-MAPS. While *Injection* S-curves provide a fine-grained analysis of the sensor response, limited to pixel subsets ($\sim$ 400 pixel), the Fe-55 methodology can cover the entire pixel matrix to reveal spatial inhomogeneities in gain, noise, and charge collection (see Sections 7.2.2 and 7.2.4).

Laboratory evaluation of the sensor's gain, threshold, and noise can thus be used to facilitate optimization procedures in operational settings, allowing for improved testbeam campaign planning by focusing on promising configurations and sensor effects. As the Fe-55 S-curves have proven to be a robust method for determining the $K_{\bar{\alpha}}$ peak position of individual pixels, their application can be extended to threshold trimming procedures. This aims to achieve uniform sensor operation by reducing threshold dispersion, as preliminary work has shown promising results [195]. Improvements to this method, especially for handling outlier pixels in the response at the extremes of threshold dispersion, can be achieved by better constraining the initial parameters and their boundary conditions. For example, by incorporating additional information about the photon absorption profile of the Fe-55 source (cf. Section 7.2.6) or by utilizing interpolated data from neighboring pixels.

Photon absorption measurements with the Fe-55 source also highlighted challenges in validating assumptions using simple diode models, as charge collection beyond the depletion zone affects measurement results. An effect, expected to be more pronounced with charged particles, where charge deposition is spread along the track path length. Although the contribution of the non-depleted region stemming from diffusion, cannot be quantified with the current dataset, further studies involving hit clustering (cf. Section 5.3.1) and varying X-ray irradiation profiles could provide deeper insights into charge collection mechanisms in HV-MAPS. Clustering would allow to isolate diffusion-dependent charge collection effects by removing geometrically induced charge sharing components, while varying the X-ray irradiation from front-side to backside could elucidate the impact of deposition profiles on charge collection, especially at lower bias voltages.

In summary, the combined use of *Injection* and Fe-55 measurements offers a powerful toolkit for characterizing and optimizing the detector response of HV-MAPS, paving the way to study the charge deposition and collection mechanisms in greater detail as targeted in the following Chapter 8.

8. Charge Deposition and Collection in HV-MAPS

This chapter incorporates all previous discussions and measurements, culminating in the quantification of effective charge collection in HV-MAPS across various depletion scenarios. The hit efficiency data presented in Section 5.4 is calibrated according to the procedures outlined in Chapter 6, with the detector response to defined energy inputs measured and discussed in Chapter 7.

Using the calibrated hit efficiency data, the objective is to extract the underlying charge deposition spectrum of the incident particles and to analyze the charge collection behavior of the MuPix10 sensor under varying bias voltages and sensor thicknesses. This aims to directly facilitate determining the influence of the non-depleted region of the sensor on charge collection, a contribution that appears to be non-negligible, as discussed in Section 7.2.6.

In the following sections, the methodology and results of the investigation are presented in detail. Initially, the employed charge deposition models are scrutinized, and their parametrizations are investigated using both simulated and independent experimental data for validation. Subsequently, the charge collection behavior is analyzed using the testbeam data set across various sensor thicknesses and bias voltages, resulting in the characterization of the effective charge collection depth as a quantitative measure of the sensor's performance.

8.1 Validation of the Charge Deposition Models

The energy loss distributions of charged particles, introduced in Section 4.1, constitute the fundamental basis for describing charge deposition in silicon sensors. Although common "analytical" functions such as the Landau-Vavilov distributions or the Moyal approximation are frequently employed to characterize the energy loss spectra, it is experimentally established that the spectral shape deviates from these idealized models as the sensor thickness decreases (see Section 4.1.4).

From this, it can be concluded that the measured spectrum may deviate significantly from the simplified theoretical expectation of energy loss distributions, particularly for thin sensors or, as in this case, effectively thinner sensors due to operation in an under-depleted state. Furthermore, the actual measured quantity in a silicon sensor is the collected charge, which may not directly correspond to the energy loss due to various sensor-intrinsic effects. Even assuming that the energy loss spectrum also represents the charge deposition spectrum (i.e., all energy loss converts into electron-hole pairs), the charge collection spectrum may still differ due to charge collection inefficiencies or charge multiplication effects, leading to nonlinear transformations between deposited energy and collected charge. Additionally, the energy-response correction applied during calibration introduces further uncertainties in the measurements. Moreover, since the extracted data represent an average response over at least the entire pixel area, they are affected by apparent "charge loss" in pixel-edge regions due to charge-sharing effects, which reduce the charge collected in the pixel of interest.

Charge collection inefficiencies are expected to shift the measured spectra towards lower values. However, no definitive prediction exists regarding changes in the spectral shape. If the charge collection inefficiency averages out linearly, assuming uniform sensor properties and electric fields, the overall shape may remain similar but with a reduced most probable value and a modified scale parameter corresponding to a reduced effective thickness. In contrast, in the presence of an uncorrected charge multiplication process, the spectral shape is expected to change depending on the deposited charge, as a nonlinear amplification alters the relationship between deposited and collected charge.

Nevertheless, the approach adopted here is based on physically motivated models while allowing increased flexibility in parameter fitting. This grants a more agnostic leverage over the actual measured spectra, enabling better matching to observed spectral shapes and facilitating the evaluation of deviations from theoretical expectations without being strictly constrained by the original assumptions of the underlying physical processes.

To validate the charge deposition models employed here, two complementary approaches are undertaken in the following sections. First, a comparative analysis using simulated data is performed to assess the performance of the various models. Subsequently, experimental data extracted from calibrated ToT measurements [8] are used to further validate the model parametrizations against real-world observations.

8.1.1 Parametrization of the Charge Deposition Models

To describe the charge deposition spectra, three charge deposition models serve as the basis: (i) the classical Landau distribution (see Section 4.1.1), (ii) the generalized Vavilov distribution (see Section 4.1.3), and (iii) the Moyal distribution approximation (see Section 4.1.2). All three distributions are defined by two parameters: the mode of the distribution, given by ΔE_{MPV}, and a scaling parameter determining the distribution width, given by $\xi(\Delta x, \beta)$[1].

To account for noise and other broadening mechanisms affecting the measured spectra, these distributions are convolved with a normal distribution according to Equations 4.25 and 4.26. This convolution introduces an additional parameter, the standard deviation σ_{RSS}, which encapsulates the combined effects of detector resolution and other broadening mechanisms (cf. Section 4.1.4). No dependency of σ_{RSS} on the deposited energy for a given spectrum is assumed here for simplicity, to avoid introducing additional complexity to the model. This assumption may necessitate considering a reduced fit range on the upper energy limit because detector resolution can vary significantly with energy depositions (see Section 7.3.1). Generally, σ_{RSS} broadens the distribution, shifts the most probable value toward higher energies, and reduces the skewness, making the distribution more symmetric, as illustrated in Plot 8.1a.

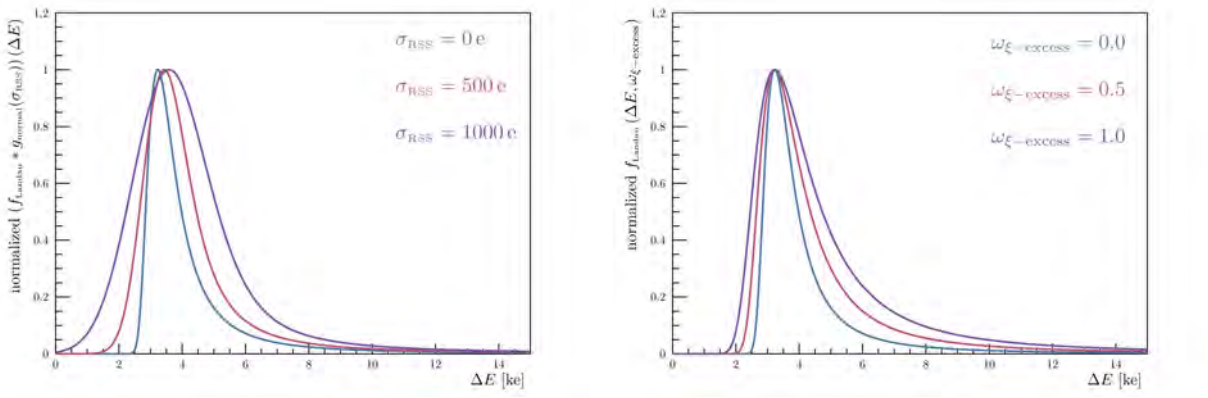

(a) Influence of differing σ_{RSS} on the energy loss distribution.

(b) Influence of differing $\omega_{\xi-\text{excess}}$ on the energy loss distribution.

Plot 8.1: Comparison of the influence of σ_{RSS} and $\omega_{\xi-\text{excess}}$ (convolution with a normal PDF g_{normal}) on the theoretical Landau distribution f_{Landau} for energy loss of a π^+ with p = 350 MeV c^{-1} traversing 50 µm silicon. Calculations based on Equations 1.9, 4.9 and 4.25 combined with the data from Tables A.16, A.17 and 2.1.

An agnostic approach is taken toward the specific charge deposition model since no precise analytical description exists for thin absorbers, and the effects of charge collection inefficiencies as well as non-depleted regions would complicate such a description further. To ensure flexibility in the shape while maintaining alignment with physical expectations, two different parametrizations of the charge deposition models are employed, each comprising three parameters: the MPV (**M**ost **P**robable **V**alue), the scaling parameter of the underlying distribution, and the Gaussian width σ_{RSS} of the convolution.

The first parametrization is based on deposited energy space, treating all three fit parameters as free and independent of physical assumptions. It is indicated by "free", naturally excluding σ_{RSS}, which remains unchanged in both parametrizations. From this representation, the most probable charge deposition is directly extracted, denoted as $\Delta E_{\text{MPV, free}}$, while the scale parameter ξ_{free} is not constrained by theoretical expectations to the MPV.

[1] Note that since the Moyal distribution is less heavy-tailed than the Landau and Vavilov distributions (for sufficiently small values of κ), its scale parameter does not have the same physical meaning and is typically larger to achieve a comparable width.

The second parametrization is more physically motivated, incorporating the incident particle at a given energy (see Table A.16) and the material properties of silicon (see Tables A.17 and 2.1), to relate the most probable value and scaling parameter to an effective sensor thickness $\Delta x_{\text{effective}}$. Using Equation 4.9 with these inputs leaves only one free parameter, the traversed thickness $\Delta x_{\text{effective}}$, to describe the most probable value:

$$\Delta E_{\text{MPV, free}} \quad \longrightarrow \quad \Delta E_{\text{MPV, theo.}}\left(\Delta x_{\text{effective}}\right) \tag{8.1}$$

Note that for all particles and energies considered throughout this thesis, only the non-high-energy form of Equation 4.9 is employed — the expression for $\beta\gamma \gtrsim 100$ is excluded, as it applies only to electrons/positrons (in this thesis), to improve comparability across particle types. Furthermore, density correction effects are incorporated according to Equation 1.10.

The same applies to the scale parameter, though deviations from theoretical expectations are anticipated. To accommodate potential discrepancies — arising from calibration inaccuracies or asymmetries causing to alter the shape for thin sensors (see Section 4.1.4) — the theoretical scale parameter of Equation 1.9 is modified by an additional scaling factor $\omega_{\xi-\text{excess}}$, such that:

$$\xi_{\text{free}} \quad \longrightarrow \quad \xi = \xi_{\text{theo.}}\left(\Delta x_{\text{effective}}\right) \cdot \left(1 + \omega_{\xi-\text{excess}}\right) \tag{8.2}$$

If the physical model accurately describes the measured spectra and no broadening effects beyond those accounted for by σ_{RSS} are present, $\omega_{\xi-\text{excess}}$ would be expected to be zero. However, a positive excess is expected to account for shape corrections due to broadening effects not captured by convolution with a normal distribution, which diminishes towards zero for thicker sensors where the theoretical model is more accurate. The influence of $\omega_{\xi-\text{excess}}$ on the energy loss distribution is illustrated in Plot 8.1b. While the most probable value remains unchanged, the scale parameter affects the width and skewness, with larger values leading to broader, more skewed distributions.

As both $\omega_{\xi-\text{excess}}$ and σ_{RSS} influence the distribution's width, a strong correlation between these parameters is expected and must be considered when interpreting fit results. Since both adjust the distribution shape to accommodate calibration uncertainties or systematic effects, disentangling their individual contributions can be challenging.

In what follows, these two parametrizations are referred to as *energy parametrization* and *effective thickness parametrization*, respectively. A comparison of their fit parameters is summarized in Table 8.1.

Three key questions arise to be addressed in the following sections: (i) Which model provides the most accurate and realistic description of the charge deposition spectrum? (ii) To what extent does the *effective thickness parametrization* represent the physical properties of the sensor and charge deposition process? (iii) How equivalent are the two parametrizations regarding the physical interpretation and implications of their parameters?

Parameter	**Energy Parametrization**	**Effective Thickness Parametrization**
Most Probable Value (MPV) ΔE_{MPV}	$\Delta E_{\text{MPV, free}}$ in [e]	$\Delta x_{\text{effective}}$ in [µm]
Scale Parameter $\xi(\Delta x, \beta)$	ξ_{free} in [e]	$\omega_{\xi-\text{excess}}$ in $[\xi(\Delta x, \beta)]$
Standard deviation	σ_{RSS} in [e]	σ_{RSS} in [e]

Table 8.1: Parameter comparison of the *energy* and *effective thickness* parametrization of the charge deposition models.

8.1.2 Comparative Analysis of Models Using Simulated Data

To identify the charge deposition model that most accurately characterizes the charge deposition process in silicon sensors, a comparative analysis using simulated data is performed. This study also evaluates the informativeness of the effective thickness parametrization introduced in section 8.1.1.

To isolate the charge deposition process, the simulation models pure charge deposition in silicon, excluding charge collection effects and noise contributions. Consequently, only the simulated spectrum itself — not the integral spectrum as in hit efficiency data — is investigated here.

The simulation conditions mirror the experimental setup discussed later in Section 8.1.3, involving a 4 GeV electron beam incident perpendicularly on a pure silicon sensor. The simulation[2] is performed using the `Allpix`[2]

[2] This simulation was performed by Ruben Kolb, whose contribution is gratefully acknowledged.

framework [59], which interfaces with `Geant4` [196]. It is carried out in increments of 5 µm silicon thickness, spanning from 5 µm to 750 µm, with 200 000 impinging electrons simulated at each thickness step.
`Geant4` employs a simplified atomic physics model to simulate energy loss of charged particles traversing matter [197, p. 76ff, sec. 7.3.1]. Energy loss in thin absorbers arises mainly from two processes: (i) ionization, and (ii) excitation of atomic electrons. For excitation, only two energy levels are considered: one approximately corresponding to the K-shell energy of an atom, and the other scaled to fulfill Equation 1.6. The contribution of atomic excitation is a coarse approximation of the shell excitation discussed in Section 4.1.4, which is expected to broaden the energy loss distribution, particularly for thin absorbers.

Both ionization and excitation contributions to total energy loss are scaled by factors r and $(1-r)$, respectively, with $r = 0.55$ fixed from experimental data [197, p. 77-78]. Additionally, bremsstrahlung photon emission by electrons is included via the PAI (**P**hoto-**A**bsorption **I**onization model) model [197, p. 81ff, sec. 7.6]. Although its effect is negligible for higher thicknesses, it becomes increasingly relevant for absorbers below 50 µm, adding energy loss fluctuations in the lower energy region of the spectrum and broadening the overall distribution [198, p. 10, sec. 4.10.2 & fig. 15].

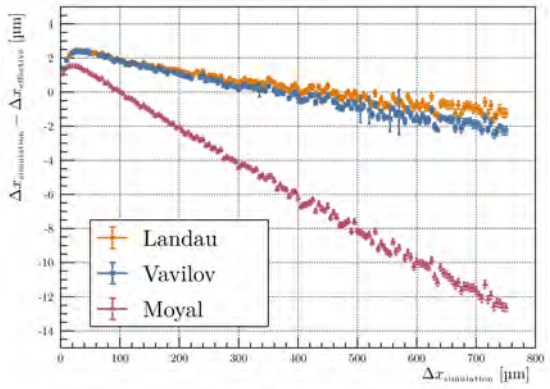

(a) Deviation of fitted effective thickness from simulated thickness.

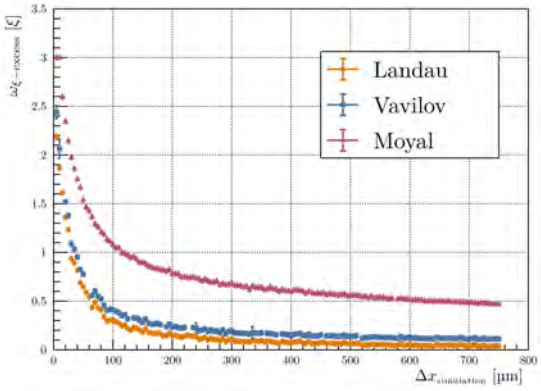

(b) Excess of scale parameter $\omega_{\xi-\text{excess}}$ over simulated thickness.

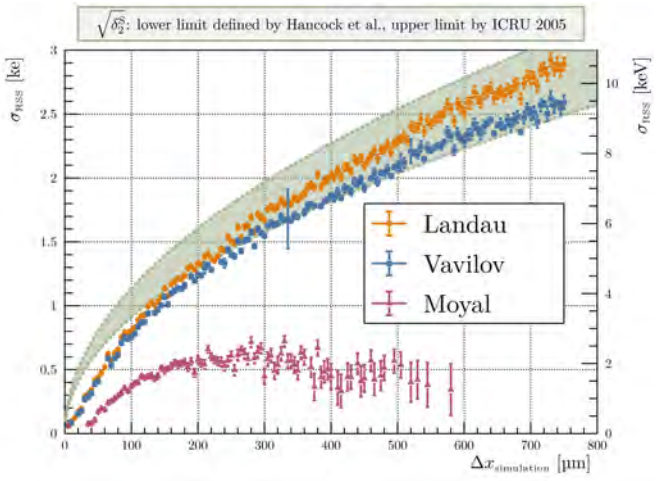

(c) Broadening parameter σ_{RSS} over simulated thickness. The green shaded area represents the expected range of $\sqrt{\delta_2^S}$ based on Equation 4.24, with the lower limit given by Equation A.23 (*Hancock et al.* [199, p. 16 ff., eq. 3]) and the upper limit by Equation A.25 (ICRU 2005 data, see Table A.14). All fit results with $\sigma_{\text{RSS}} - e_{\sigma_{\text{RSS}}}$ below zero are omitted for better visibility.

Plot 8.2: Fit results of the effective thickness parametrization on simulated data for a 4 GeV electron beam traversing **si**licon of varying thickness.

The simulated data analysis follows the fitting procedure detailed in Section 8.1.1, applying the Landau, Vavilov[3] and Moyal distributions using the *effective thickness parametrization*.

Since the Moyal distribution has a notably suppressed tail relative to the Landau and Vavilov models, fits are restricted to the interval $[-3\xi, +8\xi]$ around the mode, where ξ corresponds to the distribution's approximated FWHM based on Equation 4.13, ensuring fair model comparison. The simulation input parameter — the silicon thickness $\Delta x_{\text{simulation}}$ — is used as the starting value for the $\Delta x_{\text{effective}}$ in the fit.

Fit results summarized in Plot 8.2 indicate good agreement of the Landau and Vavilov distributions with simulated data across the entire thickness range, with only minor deviations. The Moyal distribution exhibits increasing discrepancies as thickness increases.

The extracted $\Delta x_{\text{effective}}$ closely matches $\Delta x_{\text{simulation}}$ for Landau and Vavilov fits, differing by no more than about 2 µm across the full simulated thickness range, as detailed in Plot 8.2a. The Moyal fit shows smaller deviations for thin sensors but overestimates thickness by up to 13 µm at 750 µm.

The parameter $\omega_{\xi-\text{excess}}$ exhibits a similar decreasing trend with increasing thickness across all models, as shown in Plot 8.2b. For Landau and Vavilov, $\omega_{\xi-\text{excess}}$ decreases sharply from approximately 2.5 ξ and approaches zero with increasing thickness, as expected when the theoretical prediction becomes more accurate as discussed in Section 8.1.1. Whereas the Moyal distribution retains a higher $\omega_{\xi-\text{excess}}$ even for thicker sensors, reflecting its inadequate modeling of the energy loss tail, which is compensated by an increased scale parameter.

Regarding the broadening parameter σ_{RSS} (see Plot 8.2c), the Landau and Vavilov distributions follow a similar trend ($\sigma_{\text{RSS}} \sim \sqrt{\Delta x}$) as predicted by Equation 4.24, though with steeper decreases for thin sensors (< 200 µm). This shows that the impact of shell-electron excitation (cf. Section 4.1.4) on the energy-loss distribution is not fully captured by $\sqrt{\delta_2^S}$, which overestimates the broadening, particularly for thin absorbers. The Moyal distribution fails to reproduce shell excitation broadening at any thickness, remaining consistently below theoretical expectations, further indicating its inadequacy for precise spectral description.

In summary, the Moyal distribution does not accurately model the charge deposition spectrum in idealized simulations and is excluded from further analysis. However, if a rough approximation is sufficient and computational efficiency is prioritized, it may still be considered. The Landau and Vavilov distributions perform comparably well, but due to the higher computational cost of the Vavilov distribution and the fact that all scenarios throughout this work exhibit a $\kappa \ll 0.01$ (where the Vavilov distribution converges to the Landau distribution), the Landau distribution is selected as the exclusive charge deposition model for subsequent analysis.

Having established that the Landau model can accurately represent charge deposition in an idealized simulation and that the *effective thickness parametrization* yields physically meaningful parameters, the next step is to validate the equivalence of both parametrizations using experimental data.

8.1.3 Experimental Validation of Charge Deposition Models Using Calibrated ToT Data

The data used to validate the charge deposition model parametrization are calibrated ToT spectra from measurements with a TelePix sensor [189] of (370 ± 20) Ω cm substrate resistivity. The TelePix offers the advantage of finer ToT granularity (10 bit compared to 5 bit for MuPix10, cf. Section 3.5.1) and is not limited on the upper end by a cut-off in the ToT spectrum (cf. Section 3.5.2).

The measurements were performed at the DESY test beam facility [200] using a 4 GeV electron beam impinging perpendicularly on the sensor surfaces of 50 µm and 100 µm thicknesses. The sensors were operated at bias voltages of −15 V and −130 V, corresponding to the maximum operating voltages for their respective thicknesses. Note that TelePix sensors exhibit earlier backside touching after thinning (see Section 3.2.3) than MuPix10 sensors produced on a different wafer batch with 200 Ω cm to 400 Ω cm, indicating higher resistivity for the TelePix sensors[4].

The data originate from [8] but employs an enhanced calibration scheme based on the empirical response function $a \cdot \ln(\text{ToT}) + b$, derived from *Injection* measurements with input charges[5] up to 10 ke, which provides a good approximation for lower charge depositions. Although the energy response of the ToT may be nonlinear at low charge deposits, it does not saturate at higher energy deposits like the signal amplitude does (cf. Section 6.4.1), thereby extending the measurable energy range.

[3] Here, the Vavilov parameter κ is fixed to its minimum value (0.001) since the simulation yields $\kappa < 1 \times 10^{-5}$, below the lower limit for the Vavilov implementation in ROOT [172, 173] (cf. Section A.3.4).

[4] The assumption that the substrate resistivity of the MuPix10 falls below (370 ± 20) Ω cm is supported by analogous observations with MuPix11, produced from the same wafer batch and thus having the same substrate resistivity as TelePix.

[5] For charges significantly exceeding 10 ke, empirical calibration functions as described in [194, p. 5] or [201, p. 5, eq. 2 & p. 13, eq. 4] may be employed.

The reconstructed deposited charge spectrum sums the ToT values of pixel hits in a cluster, mitigating charge sharing effects, which are more significant in TelePix due to its asymmetric pixel pitch (25 µm × 165 µm) [189]. To suppress noise and crosstalk, only clusters associated with tracks from a reference tracking telescope are considered, ensuring high purity. This is combined with an operational threshold for the TelePix sensor, which achieves hit efficiency exceeding 99 %. Thus, the deposited charge is hereafter referred to as the "associated cluster charge".

The calibrated charge deposition spectra along with corresponding fits of both Landau model parametrizations are presented in Plot 8.3. Both parametrizations provide comparable fits to the measured spectra, with minor differences in extracted parameters when compared within the same representation, as summarized in Table 8.2.

Parameter	50 µm	100 µm	
	−15 V	−15 V	−130 V
$\Delta E_{\text{MPV, free}}$	(1948 ± 1) e	(2902 ± 1) e	(5992 ± 4) e
$\Delta x_{\text{effective}}$	(29.68 ± 0.02) µm	(43.06 ± 0.03) µm	(84.76 ± 0.06) µm
$\hookrightarrow \Delta E_{\text{MPV, theo.}}$	≈ 1948 e	≈ 2904 e	≈ 5996 e
$\Delta x_{\text{simulation}}{}^{\dagger}$	30 µm	45 µm	85 µm
ξ_{free}	(305 ± 2) e	(338 ± 2) e	(708 ± 5) e
$\omega_{\xi-\text{excess}}$	(1.11 ± 0.01) ξ	(0.59 ± 0.01) ξ	(0.72 ± 0.01) ξ
$\hookrightarrow \xi_{\text{theo.}}$	(306 ± 2) e	(335 ± 2) e	(711 ± 4) e
$\omega_{\xi-\text{excess}}$	(0.93 ± 0.01) ξ	(0.69 ± 0.01) ξ	(0.34 ± 0.01) ξ
σ_{RSS}	(260 ± 5) e	(471 ± 3) e	(847 ± 9) e
σ_{RSS}	(262 ± 4) e	(472 ± 3) e	(850 ± 8) e
σ_{RSS}	(289 ± 4) e	(416 ± 5) e	(754 ± 9) e

Table 8.2: Fit results comparison of the *energy* (red) and *effective thickness* (blue) parametrization of the charge deposition models for calibrated ToT data from the TelePix sensor for different thicknesses and bias voltages for 4 GeV electrons traversing silicon. All values given in electron units are rounded to the nearest integer. Fit results from Section 8.1.2 (green) are chosen on the fit values corresponding to $\Delta x_{\text{simulation}}$ as the closest match† to $\Delta x_{\text{effective}}$ extracted from the experimental data for comparison.

At −15 V, the 50 µm sensor operates near full depletion, yielding an effective thickness close to 30 µm, consistent with the physical thickness minus non-active layers. For the 100 µm sensor at this voltage, an effective thickness of approximately 43 µm is observed, indicating an additional 13 µm of non-depleted silicon contributing to charge deposition. Since the spectral shape remains consistent with the model, it is reasonable to assume that the non-depleted region does not significantly alter the charge deposition spectrum beyond modifications accounted for by the *effective thickness parametrization*.

Increasing the bias to −130 V for the 100 µm sensor — near its breakdown voltage — yields an effective thickness around 85 µm, consistent with the expectation of a fully depleted sensor.

An $\omega_{\xi-\text{excess}}$ between approximately 0.6 ξ to 1.1 ξ is observed across scenarios, deviating from the simulation results in Section 8.1.2, where $\omega_{\xi-\text{excess}}$ approaches zero for thicker sensors. Notably, $\omega_{\xi-\text{excess}}$ for −130 V exceeds that at −15 V in the 100 µm sensor, counter to simulation trends where excess decreases with thickness. This discrepancy likely originates from calibration uncertainties at higher charges, as the calibration curve's reliability extends only up to about 10 ke, with a significant fraction of the charge spectrum exceeding this.

Although the $\omega_{\xi-\text{excess}}$ (for the lower bias settings) and σ_{RSS} fall within the magnitude expected from the simulation results in Section 8.1.2, the exact values differ, as the data presented here are prone to noise and other broadening mechanisms not considered in the idealized simulation.

In conclusion, both Landau model parametrizations fit calibrated ToT spectra comparably well, yielding physically reasonable parameters only roughly consistent with simulation-based expectations. Under-depleted sensor operation can be sufficiently described by an effective thickness, suggesting the non-depleted region has limited impact on the spectral shape. However, comprehensive validation including charge collection inefficiencies and possible charge multiplication effects requires further study, as pursued in the following Section 8.2.

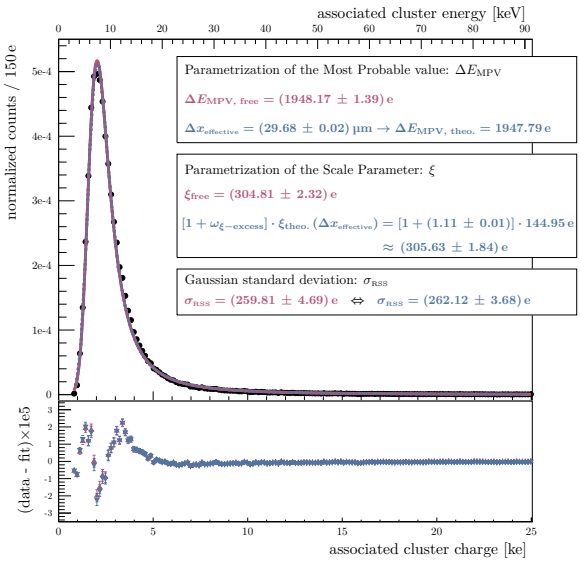

(a) 50 µm at −15 V

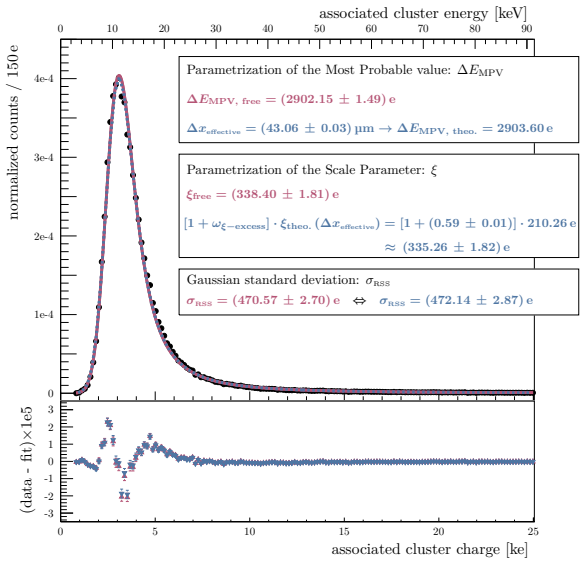

(b) 100 µm at −15 V

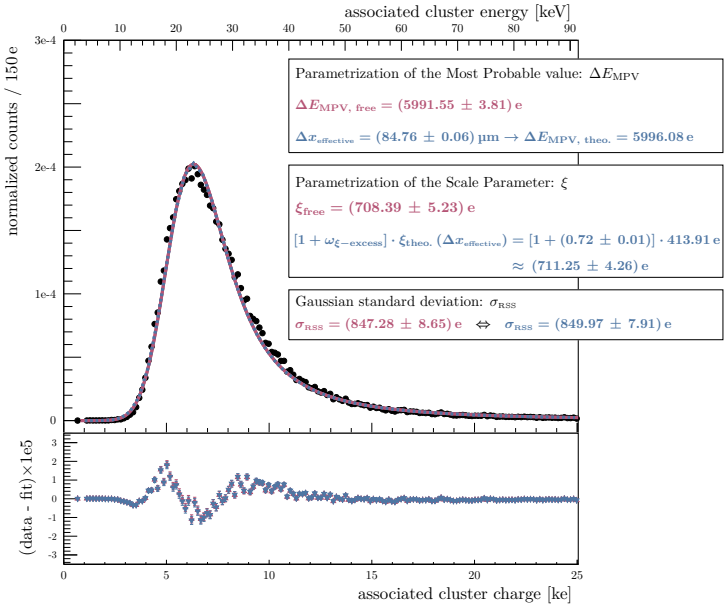

(c) 100 µm at −130 V

Plot 8.3: Fitted charge deposition spectra of calibrated ToT data from TelePix sensor for different thicknesses and bias voltages using both parametrizations of the Landau distribution. The fit results are summarized in Table 8.2 for better visibility.

8.2 Charge Collection Spectrum from Calibrated Hit Efficiency

The energy-calibrated form of the hit efficiency data discussed in Section 5.4 is used to analyze the charge collection spectrum of the MuPix10 DUT sensors (cf. Section 5.1.2). Only data from the RoIs of matrix C — as specified in Table 5.2 — is considered (unless stated otherwise), as calibration data for matrices A and B is only available for MP10-T100-S300-1 (100 µm sensor).

For each pixel, the threshold value is individually converted from the detector level threshold U_{Th} to the equivalent energy threshold $\Delta E_{\text{threshold}}$ using Equation 6.15 (see Section 6.4.2), with calibration parameters determined in Chapter 6 for each bias voltage setting. Note, due to strict outlier rejection in the calibration procedure, not all pixels within a RoI have sufficient data after filtering and are excluded from further analysis.

The transition from the detector level threshold space to the energy threshold space, necessitates a re-binning of the hit efficiency data. This is achieved by aggregating all tracks associated with pixels within the considered RoI, and grouping them into bins based on their corresponding energy threshold $\Delta E_{\text{threshold}}$. The binning is chosen to ensure a sufficient statistic in each bin (50 000 tracks/bin), thereby minimizing statistical fluctuations in the calculated hit efficiency values. The starting point is based on observations of the minimum detection threshold (see Section 7.1.7), and extends to higher thresholds in incremental steps[6]. Here, the minimum threshold[7]is set to 1.5 ke (except for MP10-T70-S300-1 and MP10-T100-S300-1 Matrix A & B, which use 1.7 ke). It is then increased in steps of 100 e up to 3 ke, 200 e up to 6 ke, and finally 400 e up to 10 ke

The upcoming measurements do not represent a simple spectrum, as in Section 8.1, but rather the integral of the spectrum above a certain threshold. Therefore, the convolution of the Landau distribution with a normal distribution is integrated according to Equation 4.3 (cf. Chapter 4). This yields the following expression for the hit efficiency ϵ_{hit} as a function of the detection threshold $\Delta E_{\text{threshold}}$:

$$\begin{aligned}\epsilon_{hit}\left(\Delta E_{\text{threshold}} \mid \Delta E_{\text{MPV}}, \xi, \sigma_{\text{RSS}}\right) &= \int_{\Delta E_{\text{threshold}}}^{\infty} \left(\text{PDF}_{\text{Landau}}\left(\Delta E_{\text{MPV}}, \xi\right) * \text{PDF}_{\text{normal}}\left(\sigma_{\text{RSS}}\right)\right)\left(\Delta E'\right) \mathrm{d}\Delta E' \\ &= \left(\text{CDF\_C}_{\text{Landau}}\left(\Delta E_{\text{MPV}}, \xi\right) * \text{PDF}_{\text{normal}}\left(\sigma_{\text{RSS}}\right)\right)\left(\Delta E_{\text{threshold}}\right) \end{aligned} \tag{8.3}$$

The model parameters follow the parametrization in Section 8.1.1, with the index "free" omitted for readability (distinctions from theoretical values are made as needed).

Data above a threshold of 10 ke are excluded because the detector response saturates rapidly, and the statistics in these bins decrease with increasing threshold, resulting in large uncertainties in the efficiency values. The transition from the linear to the saturation gain regime occurs at approximately 6 ke for reverse bias voltages exceeding −20 V (cf. Section 7.1.5). However, a significant fraction of the charge deposition spectra of thicker sensors at higher bias voltages extends above 6 ke into the saturation regime. To provide a consistent baseline for all sensors and bias voltages, the upper fit boundary is set to 8 ke. This ensures sufficient coverage for the thicker sensors, while the thinner sensors are not significantly affected, as their charge deposition spectra are predominantly below this value.

The confluence of the calibrated hit efficiency data — combined data of matrix C — is illustrated for all DUT sensors in Plot 8.4, showing efficiency curves versus $\Delta E_{\text{threshold}}$ for all bias voltage configurations.

The fit model closely matches the calibrated data, but for thicker sensors at higher reverse bias voltages, the extrapolated curve falls below the data points above 8 ke. This is expected, as the charge deposition spectrum extends further into the saturation regime, increasing smearing effects linearly from the transition energy onward (cf. Plot 7.24). The assumption of a constant σ_{RSS} becomes then invalid, and higher hit efficiency values are observed at these thresholds due to the increased broadening of the charge collection spectrum.

At low reverse bias voltages, insufficient depletion volume amplifies the impact of charge sharing at the pixel edges, causing deviations from the model. A superposition of several Landau distributions with varying most probable values is expected, making the spectrum more symmetric if these contributions vary smoothly. This effect cannot be captured by the current model, and as tracking resolution (cf. Section 5.3.2) does not allow in-pixel precision, it cannot be disentangled here. Additionally, the influence of track-to-pixel association errors — where statistics are assigned based on track pointing rather than actual cluster position — further smears the charge collection spectrum.

[6] Note that, as asymmetric binning is employed, bin sizes vary in the transition between step sizes.

[7] As the minimum detection threshold is observed to increase at lower reverse bias voltages (cf. Section 7.1.7), the respective minimum threshold for 0 V is elevated by 200 e, and for the next closest bias configuration by 100 e.

Furthermore, varying particle momenta and types may contribute to these effects (see Section 5.2.1), as neither the exact particle composition and momentum distribution in the testbeam is known. The beam is expected to be dominated by pions, but contributions from muons and positrons are possible.

Differences in the noise levels across bias voltages and RoIs (Section 7.3) are not incorporated in the fit model, as a constant σ_{RSS} is assumed for each fit. To assess deviation observed in the different RoIs, the data are split by routing segment (see Table 5.2), as done during calibration (cf. Chapter 6), and fit results are handled as discussed in the following Section 8.2.1.

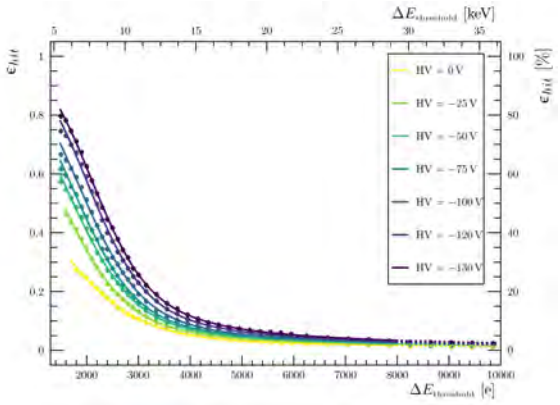

(a) MP10-T50-S20-1: 50 µm, 10 − 20 Ω cm sensor.

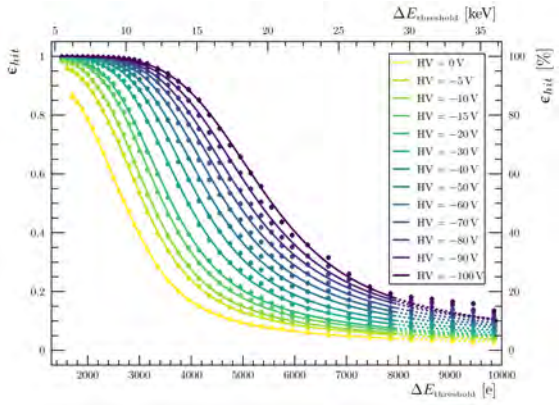

(b) MP10-T100-S300-1: 100 µm, 200 − 400 Ω cm sensor.

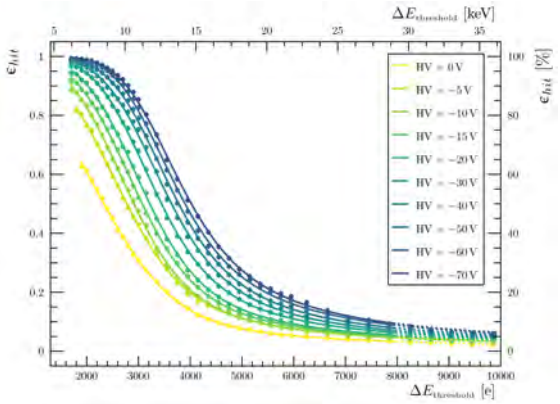

(c) MP10-T70-S300-1: 70 µm, 200 − 400 Ω cm sensor.

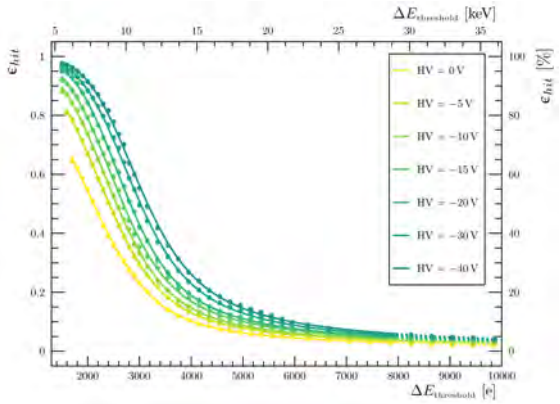

(d) MP10-T60-S300-1: 60 µm, 200 − 400 Ω cm sensor.

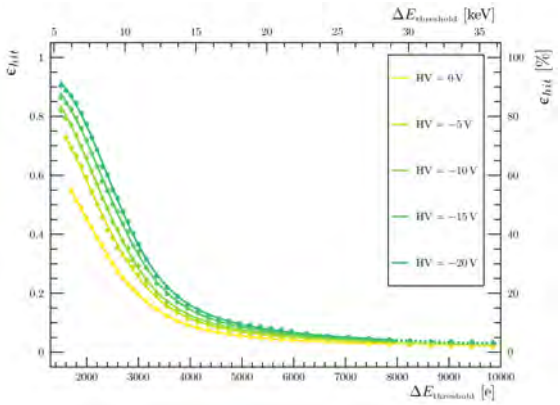

(e) MP10-T50-S300-1: 50 µm, 200 − 400 Ω cm sensor.

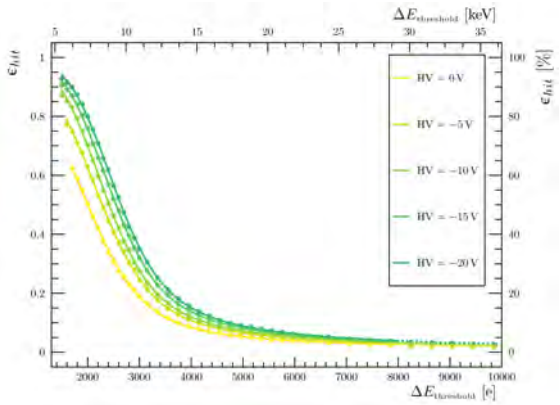

(f) MP10-T50-S300-2: 50 µm, 200 − 400 Ω cm sensor.

Plot 8.4: The hit efficiency curves as a function of the calibrated threshold $\Delta E_{\text{threshold}}$. Data from all routing segments of matrix C are combined (data from matrix A & B of MP10-T100-S300-1 are not considered here for better comparability). The errors bars are too small to be visible. The solid lines correspond to fits of the Equation 8.3 to the data points. The dashed lines indicates the extrapolation of the respective fit function.

8.2.1 Extraction Methodology of the Charge Deposition Parameters

Since the threshold calibration simply shifts statistics between bins based on the response function derived from S-curve measurements (cf. Chapter 6), and no systematic uncertainties are accounted for, only statistical uncertainties on the hit efficiency data points are considered in the fit. The systematic error on the data points is currently unquantified. Due to the calibration's focus on closely reproducing the testbeam setup — neglecting potential systematic deviations between testbeam and laboratory conditions — the propagation of these uncertainties is not straightforward. Attempting to propagate them could introduce additional bias, potentially overestimating the errors, and is therefore omitted here. Thus, only statistical uncertainties are used, leading to an underestimation of the actual uncertainties. As a result, the confidence in the fit parameter uncertainties is undermined. Additionally, deviations between the model and data may emerge, as described previously in Section 8.2, which also contribute to the **G**oodness-**o**f-**F**it values of the fits.

These fits use a LLh (**L**og-**L**ikeli**h**ood) method that handles efficiency statistic directly, as discussed in Section A.3.7. Only fits with a $\chi^2_{\text{LLh}}/\text{NDF} < 100$ are considered valid. The high χ^2_{LLh} values arise from fits on the hit efficiency data of thick sensors, where a high reverse bias voltage was applied. There a significant fraction of the data falls into the saturation regime, which is deemed to exhibit worse GoF as this region is not modeled accurately. The fit validity is ensured by introducing half the respective bin width as an additional uncertainty on the threshold value $\Delta E_{\text{threshold}}$, which is then propagated to the efficiency value as described in Section A.3.7. This approach yields more reasonable GoF values. The resulting GoF is used solely to reject bad fits and as a reassessment. It is not to weighted into the fit results itself.

Since the data is fitted using two different fit parametrizations, both results are compared at each step to ensure consistency. Therefore, the fit parameters of the effective thickness parametrization are converted into the energy parametrization according to theoretical predictions (cf. Section 8.1.1). The parameter σ_{RSS} remains unchanged as no conversion is required for this quantity. For all valid fits, both parametrizations agree to within 10 e, confirming their equivalence.

The dominant factor observed in deviations of the resulting fit parameters is the use of individual routing segments in the analysis, which provides better control over systematic effects compared to combining all data beforehand. Unless otherwise stated, the results are first extracted for each routing segment individually and then combined into a final result by averaging, as described in the following.

Influence of Different Momenta and Particles Types

Since particle type and momentum influence only the *effective thickness parametrization*, which serves as input for theoretical predictions of charge deposition parameters (cf. Section 8.1.1), the assumption made here will directly affect the fit results. Although, deviations due to varying momentum and particle type are expected to be small, they are deemed to increase with higher charge deposition (i.e., thicker active sensor thickness), as shown in Plot 8.5.

Since the interactions of different particle types do not occur simultaneously, the resulting charge deposition spectrum is a weighted superposition of the individual spectra, not a convolution [111, p. 292ff, sec, 3.3.16]. Thus, the spectrum is no longer simply described by Equation 8.3. It is expected that the MPV position is mainly determined by the dominant particle type, while the shape of the spectrum can be further distorted, deviating from a Landau distribution. The beam is expected to be dominated by pions (Section 5.2.1), the influence of different particle types on the extracted charge deposition parameters is discussed only qualitatively, and all further assumptions are based on pions.

The particle momentum used in the testbeam campaign is defined with a mean of $\mu_p = 350\,\text{MeV}\,\text{c}^{-1}$ and a standard deviation of $\sigma_p \approx 4.31\,\text{MeV}\,\text{c}^{-1}$, assumed from a normal PDF (see Equation 6.1), based on the beam acceptance for the πM1 beamline (see Section 5.2.1). Using theoretical predictions for each particle type (cf. Section 8.1.1), a weighted average of the parameters is calculated as follows:

$$\langle par \rangle = \frac{\sum_{i=1}^{4} \sum_j w_i\left(p_j\right) \cdot par_i\left(p_j\right)}{\sum_{i=1}^{4} \sum_j w_i\left(p_j\right)} \quad \text{with} \quad w_i\left(p_j\right) = \text{PDF}_{\text{normal}}\left(p_j \mid \mu_p, \sigma_p\right) \tag{8.4}$$

Here, $\langle par \rangle$ represents the weighted average of each model fit parameter. The index i runs over the four routing segments, and j runs over discrete momentum values sampled from the assumed normal distribution centered at μ_p with standard deviation σ_p, considering $\pm 5 \cdot \sigma_p$ in step sizes of $0.5 \cdot \sigma_p$. If only one routing segment is considered, the index i is omitted, and the average is based solely on the momentum distribution. The corresponding (population) standard deviation of the weighted average is used as the error estimate, as it provides a better representation of the uncertainty due to the unknown momentum distribution (largest contribution still arises from the routing segments).

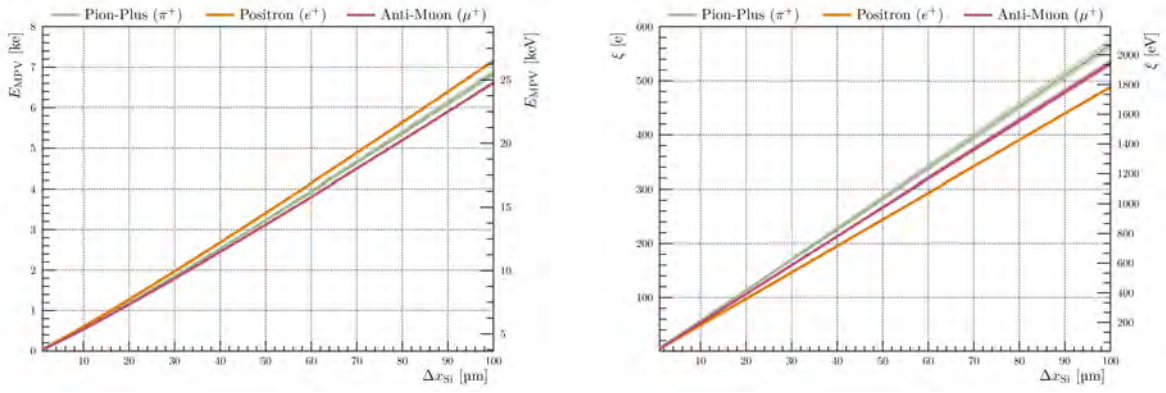

(a) Most probable value ΔE_{MPV} as a function of the traversed silicon thickness.

(b) $\xi(\Delta x, \beta)$ as a function of the traversed silicon thickness.

Plot 8.5: Calculations of ΔE_{MPV} and $\xi(\Delta x, \beta)$ (scale of landau distribution) as a function of the traversed silicon thickness for different particle types at p = 350 MeV c^{-1} (solid lines) and varying momentum (shaded bands, $\pm 5\sigma$ around p). The calculations are based on Equations 1.9 and 4.9 with data from Tables A.16 to A.18.

For the *energy parametrization*, where theoretical predictions are independent of particle type and momentum, the values from the *effective thickness parametrization* are converted into the *energy parametrization*. These converted values are then used as starting parameters for fitting in the *energy parametrization*, with boundaries set to ± 50 % around these values. In the same manner as described by Equation 8.4 — an attempt to reduce potential bias arising from the choice of starting values provided to the fit — the fit results are then combined by averaging over the routing segments, with the standard deviation used as the error estimate.

A more refined approach would be to subdivide the data further at the individual pixel level. However, the current testbeam data set lacks sufficient statistics (cf. Section 5.3.2) for such an analysis, and thus this is reserved for future studies.

8.2.2 Broadening of the Charge Deposition Spectrum

For thin absorbers, the excitation of shell electrons in the ionisation process becomes significant, leading to an additional broadening of the energy loss spectrum beyond intrinsic Landau fluctuations, as discussed in Section 4.1.4. However, no analytical description of this broadening currently exists, and previous attempts tend to overestimate the effect, particularly for thin sensors (Section 8.1.2).

In the performed measurements, the spectrum broadening is mandated by the calibrated shape of the hit efficiency curve, which is characterized by two parameters: the Landau scale parameter $\xi(\Delta x, \beta)$ and the Gaussian broadening σ_{RSS}. While σ_{RSS} incorporates all broadening effects describable by a normal distribution — such as electronic noise and contributions from shell electron excitation — the Landau scale parameter $\xi(\Delta x, \beta)$ captures deviations in the asymmetry of the Landau distribution itself, evaluated relative to the expectation for an incident particle of known kinematics.

Since the present approach averages over the full pixel cross section, charge losses due to charge sharing at pixel edges are inherently included in the observed broadening and cannot be compensated for (Section 4.2.4). As a result, the measured spectrum represents a superposition of several Landau distributions with varying most probable values, making the overall spectrum more symmetric and thereby contributing to the parameter σ_{RSS}. Additionally, the non-linear response of the readout electronics across the full charge range introduces further deviations at high charge depositions as the spectrum approaches saturation (Section 7.1.5).

The combined influence of both broadening parameters, based on fitted data, is illustrated in Plot 8.6. In this scenario, σ_{RSS} is the dominant broadening effect, as it is significantly larger than the theoretical prediction from Equation 4.24 for a 60 µm thick silicon sensor, while the Landau scale parameter $\xi(\Delta x, \beta)$ primarily affects the distribution's tail. Since no analytical theoretical prediction for σ_{RSS} is available, its value must be treated empirically showing the necessity of a proper simulation including all relevant effects. Because it shifts the position of the MPV to lower values with increasing σ_{RSS}, it must be considered when interpreting the extracted ΔE_{MPV} from the fitted data.

The subsequent discussion evaluates both the Gaussian broadening σ_{RSS} and the Landau scale parameter $\xi(\Delta x, \beta)$ in comparison with theoretical predictions. As both parameters depend on the shape of the calibrated hit efficiency curve, deviations may also arise from systematic effects in the calibration procedure (Chapter 6) differing from actual testbeam conditions.

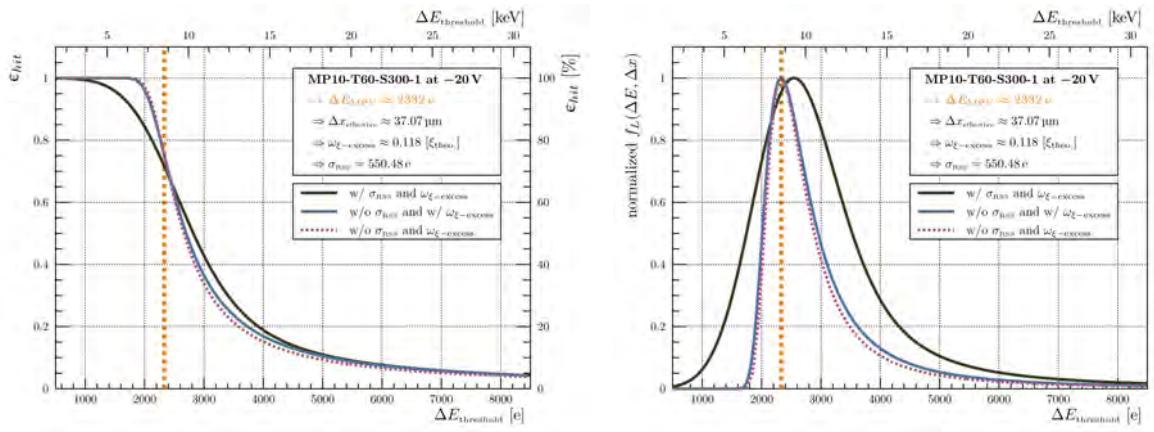

(a) Idealized form of the hit efficiency curves for differing scenarios of broadening effects.

(b) Idealized form of the normalized charge collection spectra for differing scenarios of broadening effects.

Plot 8.6: Exemplary comparison of the influence of the broadening parameters σ_{RSS} and $\xi(\Delta x, \beta)$ on the hit efficiency curves and the corresponding normalized charge collection spectra. The data is taken from the measurement of MP10-T60-S300-1 at 20 V reverse bias voltage. Idealized forms of both is plotted assuming a pion (π^+) with p = 350 MeV c^{-1} using calculations according to Equations 1.9 and 4.9 with data from Tables A.16 to A.18.

Gaussian Broadening Impact

The employed model is intended to capture Gaussian broadening originating from two primary sources, the shell electron excitations and electronic noise contributions. Because the data represent an average over the full pixel area, charge-sharing losses near pixel boundaries add another effective broadening component.

In the MuPix10 sensor, the collection electrode ($59 \times 59\,\mu\text{m}^2$) covers a large fraction of the total pixel ($80 \times 80\,\mu\text{m}^2$, cf.Section 3.2.1), minimizing charge sharing for particles traversing the pixel center. However, charge depositions of particles passing near pixel edges are expected to experience significant losses in their collected charge spectrum, whose extent is governed by the lateral depletion of the sensor. Its impact is expected to reduce with higher reverse bias voltage and is more pronounced in low-ohmic substrates (10 Ω cm to 20 Ω cm) than in high-ohmic ones (200 Ω cm to 400 Ω cm). Consequently, stronger broadening is expected at low bias voltages due to reduced lateral depletion, leading to more charge-sharing and a downward shift in the ΔE_{MPV} from increased charge loss.

This trend is confirmed by the data in Plot 8.7, where σ_{RSS} is plotted against reverse bias voltage and effective charge collection depth $\Delta x_{\text{effective}}$. At low bias voltages — corresponding to smaller $\Delta x_{\text{effective}}$ — significantly larger σ_{RSS} values are observed, even exceeding predictions from Equation 4.24, which itself tends to overestimate broadening effect in thin absorbers (Section 8.1.2).

In most sensors, σ_{RSS} decreases with increasing reverse bias voltage. The only exception is observed for sensor MP10-T100-S300-1, where σ_{RSS} increases noticeably again at bias voltages exceeding −70 V. This rise may result from a substantial part of the charge spectrum entering the saturation regime of the sensor's gain response (Section 7.1.5). As this effect cannot be corrected during calibration — leading to a more symmetric apparent distribution — the fitting procedure compensates by increasing σ_{RSS}, which is not modeled as energy-dependent.

To improve the informative value of σ_{RSS}, two approaches can be considered for future studies. In the lower bias regime, a significantly improved tracking resolution would allow the analysis to be restricted to the pixel center region, minimizing charge sharing effects, or would enable studying the effect as a function of the in-pixel impact position. In the higher bias regime, only a widened dynamic range of the readout electronics would allow capturing the full charge deposition spectrum without saturation effects, necessitating either a lower gain setting for these

measurements or a different CSA design. A better solution, if the resolution of the employed sensors permits, would be to perform such measurements based on calibrated ToT spectra.

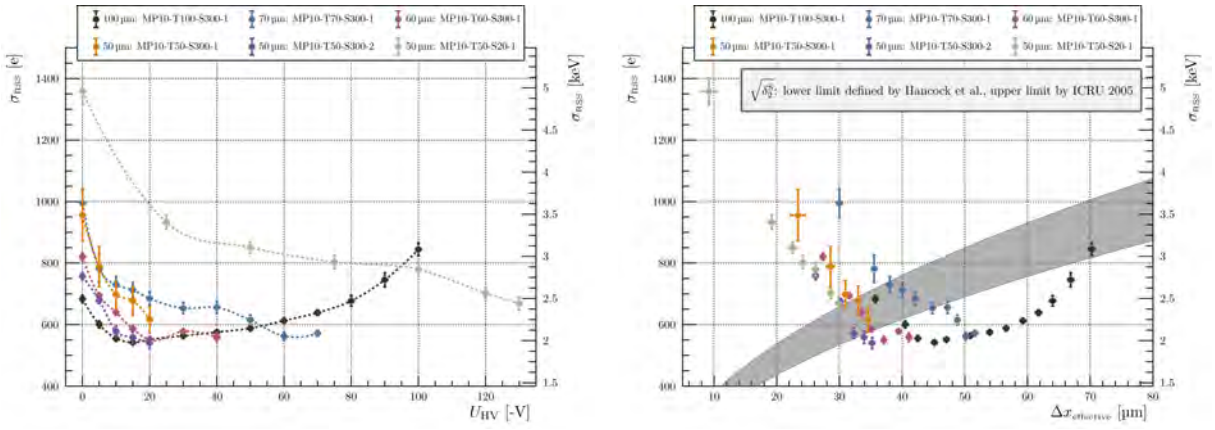

(a) σ_{RSS} as a function of the applied reverse bias voltage.

(b) σ_{RSS} as a function of the effective charge collection depth $\Delta x_{\mathrm{effective}}$.

Plot 8.7: The Gaussian broadening parameter σ_{RSS} extracted from the calibrated hit efficiency data as a function of the applied reverse bias voltage and the effective charge collection depth $\Delta x_{\mathrm{effective}}$. Assumed is a pion beam with a momentum of 350 MeV c^{-1}. The gray shaded area in Plot 8.7b represents the corresponding expected range of $\sqrt{\delta_2^S}$ based on Equation 4.24, with the lower limit given by Equation A.23 (*Hancock et al.* [199, p. 16 ff., eq. 3]) and the upper limit by Equation A.25 (ICRU 2005 data, see Table A.14).

Landau Scale Broadening

In general, no excess for the scale parameter $\xi(\Delta x, \beta)$ relative to theory is expected. However, observation with thin silicon absorbers, as discussed in Section 4.1.4, report a deviation of the energy loss spectra shape not fully captured by the Landau distribution convoluted by a normal distribution consistent with calculated shell electron excitation effects. Since the *energy parametrization* employed here takes the scale parameter as a free fit parameter, deviations from theoretical predictions can be evaluated as done by the *effective thickness parametrization* in Section 8.1.1.

An excess in the Landau scale parameter $\xi(\Delta x, \beta)$ relative to theory does not shift the ΔE_{MPV} but governs the shape of the high-energy tail of the charge deposition spectrum (Plot 8.6b). Because the fitted $\xi(\Delta x, \beta)$ and σ_{RSS} are not defined interdependently in the fitting process — although, from shell excitation theory, $\sigma_{\mathrm{RSS}} \propto \sqrt{\xi}$ — any deviations may also reflect systematic calibration errors rather than intrinsic physical effects (Chapter 6).

Plot 8.8a shows that $\xi(\Delta x, \beta)$ increases approximately with $\sqrt{U_{\mathrm{HV}}}$, consistent with a larger effective charge collection depth $\Delta x_{\mathrm{effective}}$ as depletion depth grows. Deviations occur for sensor MP10-T100-S300-1 at bias voltages above −80 V, where saturation effects, together with an increased σ_{RSS}, cause the fit to yield a reduced $\xi(\Delta x, \beta)$, as the distribution shape becomes more symmetric. Conversely, in sensor MP10-T50-S20-1, the $\xi(\Delta x, \beta)$ increases more rapidly above −100 V, consistent with enhanced charge collection caused by impact ionization, which leads to a more skewed distribution as higher charge values become more probable. This observation is consistent with independent Fe-55 measurements performed under *high-gain* settings (Section 7.2.1).

When plotted against $\Delta x_{\mathrm{effective}}$, assuming incidence pion (Plot 8.8b), most sensors show a 20 % excess in $\xi(\Delta x, \beta)$ compared to theory (Equation 1.9). This value may seem rather large but corresponds to an excess of less than 60 e for $\Delta x_{\mathrm{effective}}$ below 50 µm. Between 20 µm and 45 µm, the $\xi(\Delta x, \beta)$ scales linearly with $\Delta x_{\mathrm{effective}}$, as expected, whereas notable deviations occur outside this range. For small $\Delta x_{\mathrm{effective}}$, likely from MP10-T50-S20-1 at low bias, charge sharing distorts the spectrum such that it no becomes only broader but also stretched out as the many differing Landau distributions superimpose, increasing σ_{RSS} and indirectly affecting $\xi(\Delta x, \beta)$. For large $\Delta x_{\mathrm{effective}}$, attributed to MP10-T70-S300-1 and MP10-T100-S300-1 at high bias, gain saturation reappears as a likely source of distortion.

Note that these values are derived under the assumption of incident pions only. Taking other particle types into account would result in a greater excess relative to theory, as lighter particles correspond to higher β values at the same momentum, leading to a reduced theoretical $\xi(\Delta x, \beta) \propto 1/\beta^2$ (cf. Plot 8.5b).

In conclusion, a deeper investigation into systematic uncertainties affecting the calibrated hit efficiency data is necessary before attributing all the observed excess in $\xi(\Delta x, \beta)$ either to genuine physical broadening in thin absorbers or to artifacts from calibration and readout non-linearities.

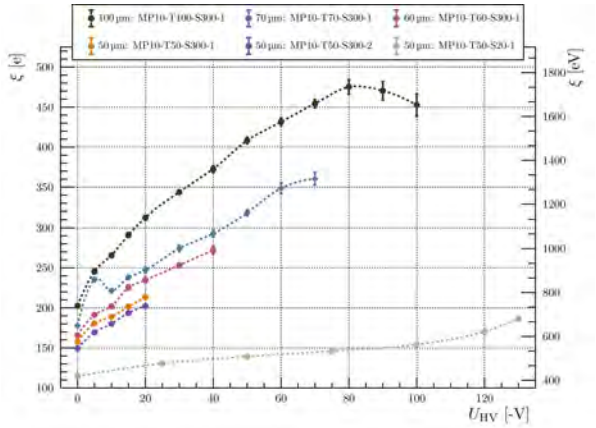

(a) $\xi(\Delta x, \beta)$ as a function of the applied reverse bias voltage.

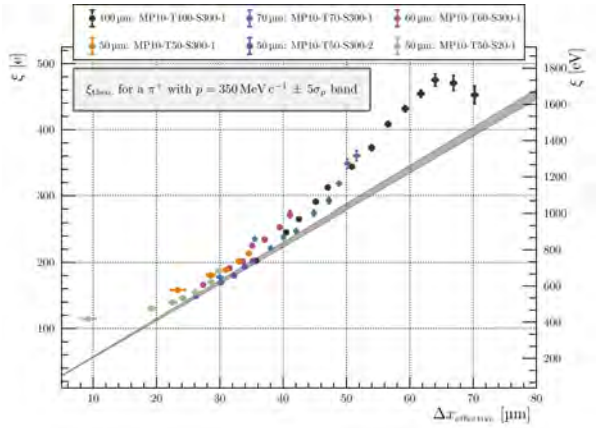

(b) $\xi(\Delta x, \beta)$ as a function of the effective charge collection depth $\Delta x_{\text{effective}}$. The gray shaded area represents the expected range of $\xi(\Delta x, \beta)$ based on Equation 1.9, with a momentum range of $\pm 5\sigma_p$ around p.

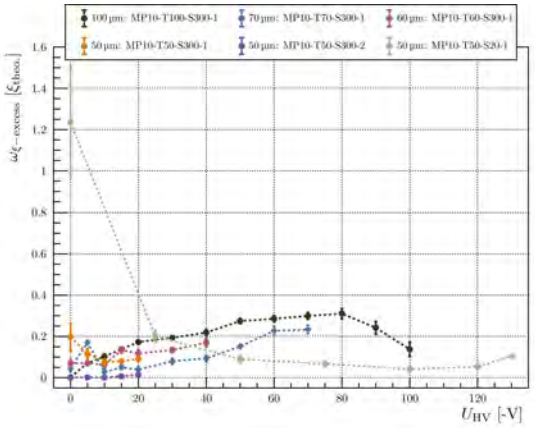

(c) Excess broadening of $\xi(\Delta x, \beta)$ ($\omega_{\xi-\text{excess}}$) relative to theoretical predictions as a function of the effective charge collection depth $\Delta x_{\text{effective}}$.

Plot 8.8: The Landau scale parameter $\xi(\Delta x, \beta)$ and its excess ($\omega_{\xi-\text{excess}}$) to theoretical predictions extracted from calibrated hit-efficiency data, as a function of reverse-bias voltage and effective charge-collection depth $\Delta x_{\text{effective}}$, for a pion beam with p = 350 MeV c^{-1}.

8.2.3 Most Probable Charge Deposition Value

The shape of the charge deposition distribution is essential for assessing the hit efficiency, because the low-energy tail — particularly influenced by σ_{RSS} — determines the probability of exceeding a given threshold. However, ΔE_{MPV} remains the primary parameter governing the overall performance. It is the most robust measure of the charge deposition spectrum (cf. Section 8.1.1). Thus, the subsequent discussion concentrates on the ΔE_{MPV} values derived from the calibrated hit efficiency data. To interpret these values both in relative terms and with respect to theoretical expectations, they are compared with the predicted charge deposition range derived from the simple parallel-plate capacitor diode model, which provides the expected thickness used in the theoretical ΔE_{MPV} calculations (cf. Equation 4.9).

The measured charge collection can be expressed as a function of the effective charge collection depth, $\Delta x_{\text{effective}}$, assuming an idealized one-dimensional dependence. This depth consists of two contributions, the active (depletion-driven) depth Δx_{active} and the non-depleted (excess) depth Δx_{excess}:

$$\Delta x_{\text{effective}} = \Delta x_{\text{active}} + \underbrace{\eta \cdot (d_{\text{total}} - \Delta x_{\text{active}})}_{\Delta x_{\text{excess}}} \tag{8.5}$$

Here, d_{total} is the total sensor thickness and η the charge-collection efficiency in the non-depleted region.

The active depletion depth Δx_{active} is estimated using the simple diode model, following the methods discussed in Section 7.2.6. Since no explicit reconstruction of the substrate resistivity is performed here, the estimation relies on the nominal resistivity range values provided by the manufacturer (cf. Section 5.1.2) and applies Equation 2.22 (using the static mobility approximation) to estimate the depletion depth as:

$$\Delta x_{\text{active}} = w(U_{\text{HV}} \mid U_{\text{offset}}, \varrho_{substrate})_{\text{depletion}} + d_{n\text{-well}} \tag{8.6}$$

The built-in voltage U_{bi} (assumed to be in the range 0.4 V to 0.8 V, cf. Section 2.3.1) is extended by the n-well potential such that $U_{\text{offset}} = U_{bi} + U_{n\text{-well}}$, which is assumed to reach up to 1.9 V. The n-well depth $d_{n\text{-well}}$ is approximated as (6 ± 1) µm (cf. Section 7.2.6).

For simplicity, only incident pions with a momentum of 350 MeV c^{-1} — the dominant particle type in the beam (Section 5.2.1) — and a momentum spread of $\pm 5 \cdot \left(\sigma_p \approx 4.31\,\text{MeV}\,\text{c}^{-1}\right)$ around this mean are considered here. Although momentum variations and the presence of other particle types are accounted for, these effects are not the dominant sources of uncertainty. The main uncertainty in estimating the depletion depth arises from the substrate resistivity.

In the subsequent discussion, the extracted ΔE_{MPV} values are first examined based on observed deviations between different RoIs, followed by comparisons between sensors with varying thicknesses and resistivities.

Routing Segment Dependency

Different routing segments along the pixel row address space showed variations in gain and noise performance (cf. Sections 5.4, 7.2.6 and 7.3.3). These effects may influence the extracted ΔE_{MPV} values, so the calibration procedure (Chapter 6) is performed for each routing segment individually. The fitting is also carried out at this level to ensure consistency. This allows a comparison of the ΔE_{MPV} values between segments to identify potential systematic effects not fully compensated during calibration. This is done relative to the mean value over all routing segments $\langle \Delta E_{\text{MPV}} \rangle$, both determined as discussed in Section 8.2.1.

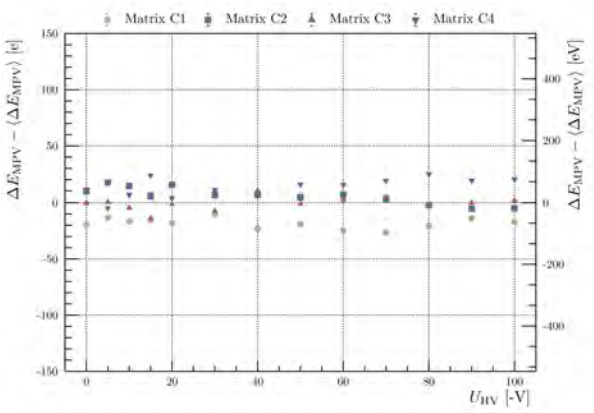

(a) Relative ΔE_{MPV} variations as function of the applied reverse bias voltage for MP10-T100-S300-1.

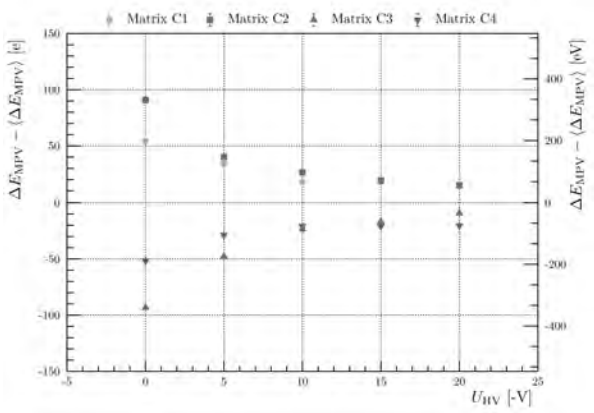

(b) Relative ΔE_{MPV} variations as function of the applied reverse bias voltage for MP10-T50-S300-1.

Plot 8.9: Exemplary differences between extracted ΔE_{MPV} value of each routing segment of matrix C to the combined mean value over all routing segments $\langle \Delta E_{\text{MPV}} \rangle$ as a function of the applied reverse bias voltage.

For most DUT sensors, deviations between routing segments remain within about 30 e across the entire range of applied reverse bias voltages, as demonstrated by MP10-T100-S300-1 (matrix C) in Plot 8.9a. These small deviations align with the expected calibration accuracy, given that the detector response is idealized (without considering differential nonlinearity effects, cf. Section 6.4.2), and reflect binning effects in the calibrated hit efficiency curves. They constitute the dominant known sources of uncertainty in the extracted ΔE_{MPV} values.

For MP10-T50-S300-1, larger deviations up to 100 e are observed at low bias voltages (< -20 V) but diminish at higher voltages (see Plot 8.9b). The voltage-dependent pattern suggests a mismatch between laboratory and testbeam calibration conditions. Gain measurements performed in the laboratory show no significant segment variations at low voltage, whereas uncalibrated testbeam data reveal a pronounced drop in hit efficiency from sub-matrix C1 to C4 at low threshold settings. This behavior may result from imperfect reproducibility of gain settings or from non-uniform high-voltage distribution across the sensor area.

Because no single routing segment can serve as a reliable reference, the observed deviations are treated as systematic uncertainties and included in the final ΔE_{MPV} uncertainty estimate for this sensor.

Sub-Matrix Dependency

In addition to routing-segment variations, different sub-matrices (A, B, & C) showed slight differences in gain and noise performance (cf. Sections 5.4, 7.2.6 and 7.3.3). However, such comparisons are possible only for MP10-T100-S300-1, as calibration measurements for other sensors were limited to matrix C due to time constraints. Moreover, the calibration for sub-matrices A and B were performed on a separate but nominally identical setup, possibly introducing additional systematic differences. This allows a qualitative assessment of potential systematic effects on the extracted ΔE_{MPV} values, since a different setup was used during the testbeam operation.

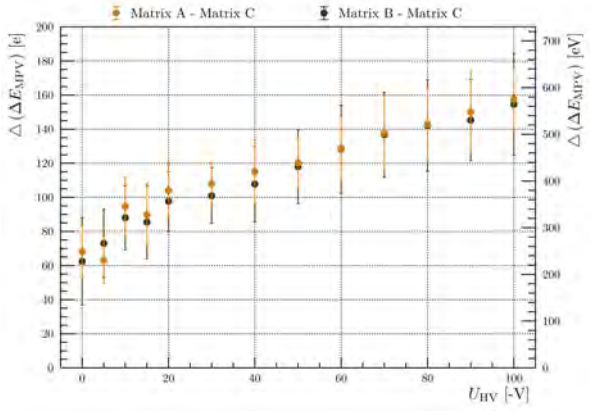

(a) Difference of ΔE_{MPV} as a function of the applied reverse bias voltage.

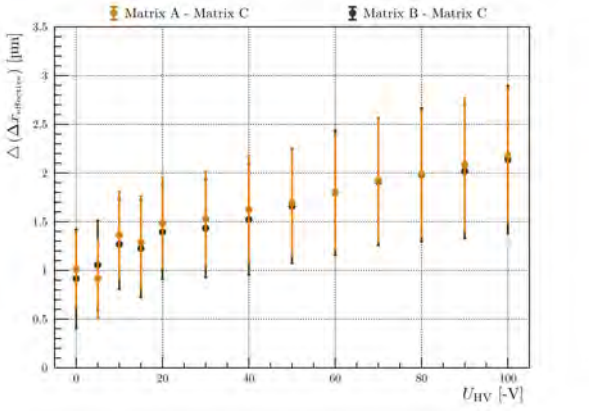

(b) Difference of $\Delta x_{\text{effective}}$ as a function of the applied reverse bias voltage.

Plot 8.10: Difference of ΔE_{MPV} and $\Delta x_{\text{effective}}$ extracted from matrix A & B to matrix C for MP10-T100-S300-1 as a function of the applied reverse bias voltage. For the extraction a pion beam with a momentum of 350 MeV c^{-1} is assumed. The Y-axis error are propagated according to Gaussian error propagation.

As shown in Plot 8.10, the deviations between matrices A and B relative to matrix C start around 60 e at low bias and increase up to 160 e at higher voltages. The same trend appears in the effective charge collection depth $\Delta x_{\text{effective}}$, increasing from 1 µm to about 2 µm, a rather small difference compared to the uncertainties thinning a sensor (cf. Section 3.2.3). The consistently higher charge collection in matrices A and B suggests a systematic offset originating either from calibration differences between setups (cf. Section 7.1.4) or from subtle mismatches between laboratory and beamline conditions. As these deviations are modest compared to the total collected charge, they are again treated as systematic effects but not included in the quantitative uncertainty propagated to other sensors (which were only calibrated for matrix C).

Charge-Collection Dependency on Sensor Thickness

The expected form of the ΔE_{MPV} dependence on bias voltage is more complex than linear intuition suggests. In simplified terms, ΔE_{MPV} can be approximated by a proportionality of the form $a_1 \cdot \Delta x + b_1 \cdot \Delta x \cdot \ln(\Delta x)$ (cf. Equation 4.9), while for a simple diode model $\Delta x \propto c_1 \cdot \sqrt{U_{\text{HV}}} + \delta x$. Here δx accounts for contributions from the non-depleted region, the voltage offset and the n-well depth (cf. Equation 8.6), which, if neglected, would lead

to $\Delta E_{\text{MPV}} \propto a_2 \cdot \sqrt{U_{\text{HV}}} + b_2 \cdot \sqrt{U_{\text{HV}}} \cdot \ln(U_{\text{HV}})$.[8] The square-root term dominates at low voltages, while the logarithmic term becomes more significant at higher bias.

This inherent non-linearity is further complicated in thicker sensors, where the non-depleted region represents a larger fraction of the total substrate.

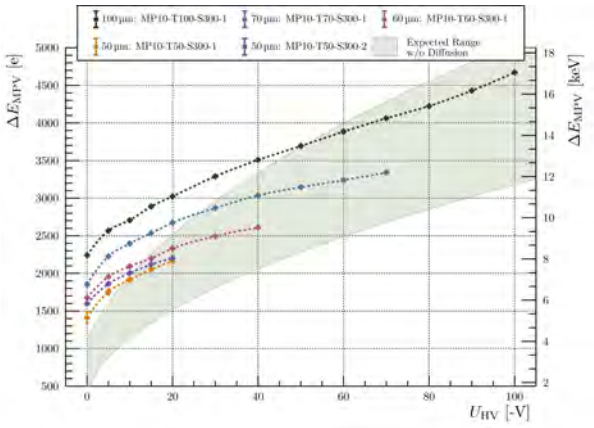

(a) ΔE_{MPV} as a function of the applied reverse bias voltage for DUT sensors with a substrate resitivity of 200 Ω cm to 400 Ω cm. The green shaded area represents the idealized expected range of ΔE_{MPV} values in the absence of charge collection contributions from the non-depleted region.

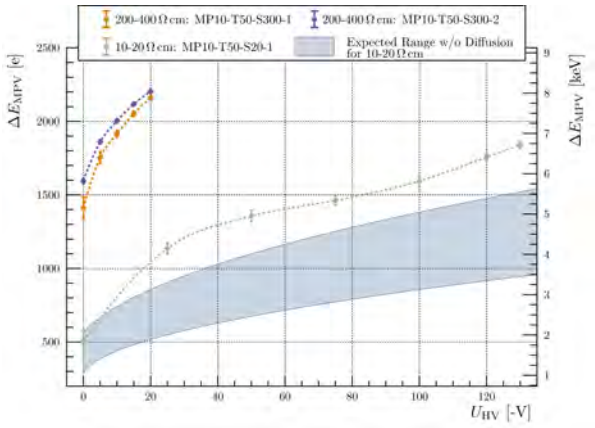

(b) ΔE_{MPV} as a function of the applied reverse bias voltage for all 50 µm thick DUT sensors of both resistivity ranges. The blue shaded area represents the idealized expected range of ΔE_{MPV} values in the absence of charge collection contributions from the non-depleted region for the 10 Ω cm to 20 Ω cm sensor.

Plot 8.11: Extracted ΔE_{MPV} values as a function of the applied reverse bias voltage for sensors of varying thicknesses and resistivities compared to the idealized expected range based on theoretical predictions. The shaded areas represent the expected range of ΔE_{MPV} values based on Equation 4.9 in combination with Equation 8.6 for an incident pion (π^+) beam with a momentum of 350 MeV c^{-1} and $\pm 5\sigma_p$ around.

As summarized in Plot 8.11, the ΔE_{MPV} increases with bias voltage across all sensors, consistent with a growing depletion depth and effective collection volume. However, the absolute values and growth rates differ significantly by thickness and resistivity.

For the higher-ohmic sensors (200 Ω cm to 400 Ω cm, see Plot 8.11a), ΔE_{MPV} rises smoothly with bias, eventually approaching the idealized theoretical range as the respective sensor starts to reach full depletion. The expected hierarchy between thicker sensors (e.g., MP10-T60-S300-1 vs. MP10-T70-S300-1) becomes apparent post-calibration, illustrating the importance of accurate gain calibration before cross-comparison, not clear from uncalibrated data (cf. Section 5.4). It is evident that the depletion depth alone cannot explain the observed ΔE_{MPV} values, as they consistently exceed the expected trend, with the sensor of greater total thickness showing higher ΔE_{MPV} at every voltage step.

Among the 50 µm thick high-ohmic sensors, a larger-than-expected deviation persists between MP10-T50-S300-1 and MP10-T50-S300-2. For MP10-T50-S300-1, a larger discrepancy between calibrated RoIs of matrix C have been observed, as discussed previously, which is not handled by the calibration. However, this difference diminishes as full depletion is approached but does not vanish completely, showing the limitation of this methodology when systematic effects are not fully compensated.

At voltages below −20 V, charge-sharing effects increasingly influence the extracted ΔE_{MPV}, causing an underestimation of the true deposited charge. An improved track reconstruction allowing impact-position selection within the pixel could mitigate these effects or would allow to divide the analysis into different in-pixel regions to study the effect more systematically.

For MP10-T100-S300-1, a slight increase in ΔE_{MPV} deviating from the proportionality to $\sqrt{U_{\text{HV}}}$ is observed beyond −70 V. This behavior corresponds to the observed saturation of the gain response, which distorts the hit-efficiency data the calibration cannot compensate (cf. Section 8.2.2). Thereby the extracted ΔE_{MPV} is biased.

[8] Note that the square root dependence of U_{HV} is extracted from the logarithm term, according to the power rule of logarithms: $\ln(x^n) = n \cdot \ln(x)$.

This limitation highlights the need for either variable gain settings matched to expected signal sizes or enhanced modeling of detector saturation in future analyses.

Notably, the low-ohmic 50 µm sensor (MP10-T50-S20-1) also shows significantly higher ΔE_{MPV} values than predicted when neglecting contributions from the non-depleted region, even at modest reverse biases (Plot 8.11b). The apparent agreement of the 0 V data point with the theoretical range is assumed to be coincidental. The distribution here is heavily distorted by charge sharing due to minimal lateral depletion, as also reflected in the previously discussed σ_{RSS} and $\xi(\Delta x, \beta)$ values (Section 8.2.2). At higher bias voltages, all measured ΔE_{MPV} values exceed the idealized range, confirming considerable charge collection from the non-depleted volume.

Beyond −75 V, the ΔE_{MPV} approaches values similar to those of the high-ohmic 50 µm sensors at low bias voltages. At higher reverse biases, it then rises more steeply, consistent with enhanced charge multiplication through impact ionization, as discussed previously (Sections 7.2.1 and 7.2.5). This demonstrates the potential of low-ohmic substrates for improved charge collection in thin sensors, provided that sufficiently high voltages and the corresponding charge multiplication can be achieved.

In the following Section 8.2.4, the effective charge-collection depth $\Delta x_{\text{effective}}$ is evaluated to provide a more physical interpretation of these observations, reducing the complex dependence on sensor thickness and particle incidence to an intuitive representation of effective collection thickness.

8.2.4 Evaluation of the Effective Charge Collection Depth

To interpret the extracted ΔE_{MPV} values in a more physical manner, the effective charge collection depth $\Delta x_{\text{effective}}$ is evaluated using the theoretical ΔE_{MPV} calculations from Equation 4.9. The data are fitted using the *effective thickness parametrization* described in Section 8.1.1, taking into account the incident particle type, momentum, and material properties of silicon listed in Table A.17. This reparametrization provides a more intuitive interpretation of the results and allows a clearer evaluation of charge collection from the non-depleted region. The total sensor thickness is known, but an uncertainty of 5 µm from the thinning process must also be considered (cf. Section 5.1.2)[9]. It should be noted that the usable substrate thickness for charge collection is reduced by approximately 15 µm to 18 µm compared to the nominal thickness due to the presence of metal, isolation, and passivation layers (cf. Section 3.2.1). Additionally, the roughness of the backside surface resulting from the thinning process may influence the charge collection (cf. Section 3.2.3).

The following discussion first examines the influence of assumed momentum and particle type on the extracted $\Delta x_{\text{effective}}$ values before comparing results for sensors with different thicknesses and resistivities.

Influence of Momentum Dispersion and the Dominant Particle Type

Three particle types are considered as possible incident particles: positrons (e^+), muons (μ^+), and pions (π^+). Since the exact beam composition was not determined during the testbeam campaign, the influence of each particle type is studied separately, assuming a momentum of 350 MeV c^{-1} with a spread of a spread of $\pm 5\sigma_p$ around the mean momentum (cf. Sections 5.2.1 and 8.2.1).

To assess the influence of the momentum relative to the fitting uncertainties, the fit is evaluated for each assumed momentum within the $\pm 5\sigma_p$ range (in steps of $0.5\sigma_p$) for all applied reverse bias voltages and particle types, allowing the variation in the extracted $\Delta x_{\text{effective}}$ to be studied. These values are then compared to the mean $\langle \Delta x_{\text{effective}} \rangle$ in each routing segment and for each particle type to quantify the relative momentum dependence.

The influence of the momentum on $\Delta x_{\text{effective}}$ results in absolute deviations below 1 µm for pions, and even smaller values for muons and positrons (see Plot 8.12a). This confirms that the input assumptions yield only a minor effect on the particle kinematics at these energies. At these energies, pions reach approximately (93 ± 1) % of the speed of light, while muons reach about (96.0 ± 0.6) % and positrons nearly (99.999 90 ± 0.000 01) %. For pions, the momentum-induced deviations are comparable to those observed between routing segments, whereas for muons and positrons they are negligible.

However, the assumed incident particle type significantly affects the absolute $\Delta x_{\text{effective}}$ values (Plot 8.12b). Positrons, with their higher β value at the same momentum, yield lower theoretical ΔE_{MPV} values for a given thickness, and this deviation increases with the charge collected at higher reverse bias (cf. Plot 8.5a). Muons yield higher $\Delta x_{\text{effective}}$ values than pions, as their ΔE_{MPV} curve is closer to the global minimum in this momentum range[10]

[9] Test measurements on sensors from thinned wafers show deviations of 1 µm to 2 µm from the nominal thickness, which are within the measurement tolerance.

[10] Only for momenta above 400 MeV c^{-1} would muons and pions yield similar ΔE_{MPV} values for a given thickness.

(cf. Plot 5.2a). At most, absolute deviations between particle types remain below 4 µm relative to the pion, yet this can correspond to 5 % to 10 % of the extracted $\Delta x_{\text{effective}}$ values, depending on the sensor thickness. This highlights the need to reduce this uncertainty either by determining the beam composition to isolate the contributions of different particle types or by increasing the beam momentum[11] so that all particle types converge to similar ΔE_{MPV} values for a given thickness.

For the remainder of this section, only results assuming incident pions are discussed, as they dominate the beam (cf. Section 5.2.1). However, the contribution of other particle types must be treated as a systematic uncertainty when interpreting $\Delta x_{\text{effective}}$ as an absolute measure.

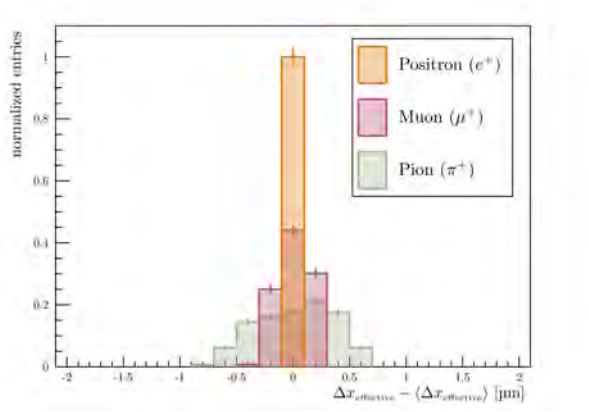

(a) Distribution of extracted $\Delta x_{\text{effective}}$ of each fit performed assuming different momenta ($\pm 5\sigma_p$ around 350 MeV c^{-1}) relative to the respective mean value $\langle \Delta x_{\text{effective}} \rangle$ in a routing segment. Shown for all applied reverse bias voltages and performed separately for each particle type.

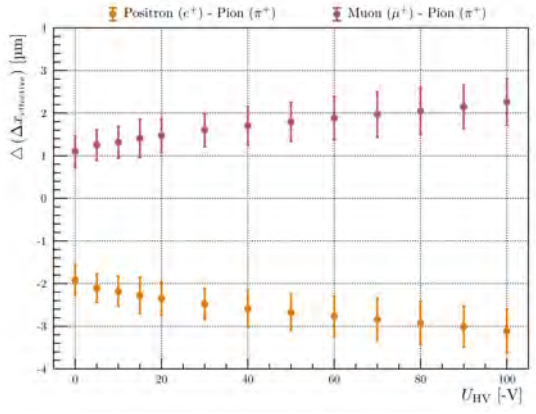

(b) Difference of extracted $\Delta x_{\text{effective}}$ assuming positrons (e^+) and muons (μ^+) relative to pions (π^+) as a function of the applied reverse bias voltage. The Y-axis error are propagated according to Gaussian error propagation.

Plot 8.12: Influence of the assumed momentum p and particle type on the extracted effective charge collection depth $\Delta x_{\text{effective}}$. Data extracted from calibrated hit efficiency data of MP10-T100-S300-1 matrix C.

Effective Charge Collection Depth in Sensors of Varying Thickness

The extracted $\Delta x_{\text{effective}}$ values for sensors of varying thicknesses and resistivities are summarized in Plot 8.13. For all sensors, $\Delta x_{\text{effective}}$ increases with applied reverse bias, consistent with an expected growth of the depletion zone.

Although the shape of the $\Delta x_{\text{effective}}$ curves resembles the expected depletion depth growth, the curves do not directly correspond to the actual depletion depth as given by the simple diode model. A distinct offset appears between sensors of different total thickness, and this offset changes with bias voltage — unexpected for sensors with the same substrate resistivity if diffusion effects would be negligible.

In Plot 8.13a, the $\Delta x_{\text{effective}}$ values for the higher-ohmic sensors (200 Ω cm to 400 Ω cm) are shown. The $\Delta x_{\text{effective}}$ value for maximum operation voltages for the 60 µm (MP10-T60-S300-1) and 70 µm (MP10-T70-S300-1) sensors lie close to the expected line assuming a substrate resistivity of $0.75 \times (370 \pm 20)$ Ω cm. This empirical factor arises from comparing the maximum operation voltage of 50 µm MuPix10 (−20 V) to TelePix and MuPix11 (−15 V), for which more precise substrate resistivity data ((370 ± 20) Ω cm) is provided by the manufacturer. However, since only one thickness reference point is available and voltages vary, this factor is a rough estimate, reflected in the extracted values for 50 µm sensors, which exceed this idealized line at −20 V.

If all sensors had identical substrate resistivity and operated under full depletion, their data points would align along the same line, which is not observed. The parallel-plate capacitor model used here represents a simplification and may not be valid at low depletion voltages, where charge-sharing effects can substantially distort the behavior. Thus, comparison to a proper simulation would be needed for further conclusions.

[11] At higher momenta, protons can constitute a non-negligible fraction of the beam composition in πM1, complicating the approach (cf. Section 5.2.1).

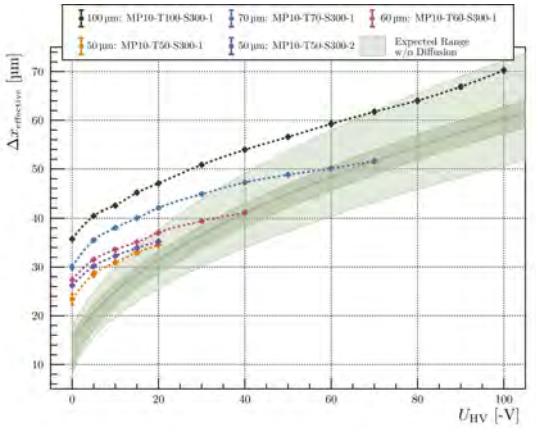

(a) $\Delta x_{\text{effective}}$ as a function of the applied reverse bias voltage for high-ohmic DUT sensors. The green shaded area represents the expected range of $\Delta x_{\text{effective}}$ values in the absence of charge collection contributions from the non-depleted region. The smaller darker shaded green area yields a resistivity range of about $0.75\times(370\pm20)\,\Omega\,\text{cm}$, while the dark green line is the idealized line assuming a resistivity of $0.75\times370\,\Omega\,\text{cm}$.

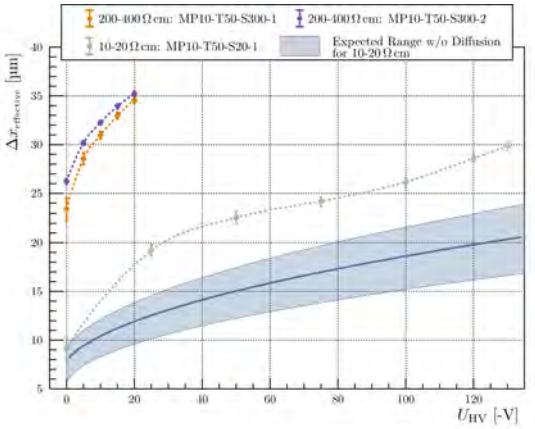

(b) $\Delta x_{\text{effective}}$ as a function of the applied reverse bias voltage for low-ohmic 50 µm thick DUT sensors. The blue shaded area represents the expected range of $\Delta x_{\text{effective}}$ values in the absence of charge collection contributions from the non-depleted region for the 10 Ω cm to 20 Ω cm sensor. The dark blue line is the idealized line assuming a resistivity of 15 Ω cm.

Plot 8.13: Effective charge collection depth $\Delta x_{\text{effective}}$ as a function of the applied reverse bias voltage for sensors of varying thicknesses and resistivities compared to the idealized expected range based on theoretical predictions for an incident pion (π^+) beam with a momentum of 350 MeV c^{-1} and $\pm5\sigma_p$ around in an active thickness described by Equation 8.6. Idealized line in both plots assume a U_{offset} of 2.5 V and a $d_{n\text{-well}}$ of 6 µm.

The 100 µm sensor (MP10-T100-S300-1) does not reach full depletion, which would require significantly higher voltage levels than allowed by the breakdown voltage of the MuPix10 sensor. At high voltages, an equivalent rise in $\Delta x_{\text{effective}}$ is observed, similar to the ΔE_{MPV} behavior discussed in Section 8.2.3, again attributed to saturation effects in the sensor response, which distort the calibrated hit efficiency data and affect the extracted $\Delta x_{\text{effective}}$.

For the low-ohmic 50 µm sensor (MP10-T50-S20-1), shown in Plot 8.13b, $\Delta x_{\text{effective}}$ values deviate significantly from expectations excluding non-depleted contributions, even at 0 V. At this voltage, charge sharing dominates, yet the extracted $\Delta x_{\text{effective}}$ value still lies at the upper end of the range expected for the given resistivities. This is inconsistent with observations of impact ionization (cf. Sections 7.2.1 and 7.2.5), which imply a lower resistivity. This shows that contributions from the non-depleted region can be beneficial to overall charge collection, potentially overcoming inefficiencies at pixel edges if detection thresholds are set low enough.

In summary, while the $\Delta x_{\text{effective}}$ curves resemble the expected depletion depth growth, their form does not directly reflect the actual depletion depth. The distinct offset between sensors of different thicknesses changes with bias voltage, which is not expected for identical resistivity without charge collection contribution from the non-depleted region. Thus, for such thin sensors, diffusion is a significant factor in the charge-collection process and cannot be neglected, as it can even be beneficial in low-bias regimes.

To quantify these contributions more precisely, a better understanding of depletion depth formation in thin sensors is HV-MAPS with the aid of tcad simulations. Measurements at voltages beyond full depletion, where a kink in the $\Delta x_{\text{effective}}$ curve appears as the value saturates, would provide stronger leverage on the absolute values and help to better constrain the substrate resistivity. Combining this with higher momenta and improved tracking resolution to minimize charge sharing effects would further enhance extraction accuracy.

Currently, the range of unknown factors and the available dataset do not allow for more precise conclusions regarding the actual depletion depth formation or quantification of the contributions from diffusion and impact ionization to charge collection.

8.3 Conclusions

The measurements presented in this chapter demonstrate three key points. First, the convolution of a Landau distribution with a normal distribution is a valid approach to model the charge deposition spectrum of HV-MAPS, even under the influence of charge sharing effects. Second, the use of a calibrated hit efficiency is a valid method for extracting the charge collection behavior of HV-MAPS. Third, the effective charge-collection depth $\Delta x_{\text{effective}}$, as a measure, has the potential to serve as a characteristic parameter for describing the charge-collection behavior of HV-MAPS. Simple modeling approaches for the charge deposition spectrum and charge collection efficiency achieve reasonable agreement between measured hit efficiency and modeled behavior.

However, clear limitations are observed at low bias voltages, where charge sharing becomes significant, and at high voltages, where gain response saturation occurs. Both effects can be mitigated in future measurements with improved methodologies and setups. To validate that charge sharing corresponds to a superposition of multiple Landau distributions (convoluted with a normal distribution), further measurements with higher spatial resolution and improved statistics are required. Sub-pixel resolution would allow the study of charge collection behavior at different positions within a pixel, as the effective charge deposition length is expected to vary with lateral depletion of the sensor

These limitations can be circumvented exemplary by performing such measurements at DESY with a high-momentum (> 1 GeV/c) electron beam and a high-resolution beam telescope [200]. At such high momenta, tracking resolution is greatly improved due to reduced multiple Coulomb scattering (cf. Section 1.1.5), and theoretical uncertainties in $\xi(\Delta x, \beta)$ and ΔE_{MPV} become negligible. With well-defined theoretical parameters, the extraction of $\Delta x_{\text{effective}}$ becomes more reliable, and the focus can shift to deviations from the model itself, such as charge sharing, charge collection inefficiencies, diffusion, or other sensor effects.

First, a better understanding of the processes involved must be established, ideally under optimal conditions to minimize the influence of charge-sharing and saturation effects. Once validated, measurements at differing conditions can be performed to study the impact of charge collection inefficiencies and diffusion, improving the accuracy of modeling HV-MAPS.

Equally important is assessing the reproducibility of results with different sensors of the same thickness and resistivity to validate the universality of extracted parameters. The impact of the calibration procedure on gain reproducibility at the pixel level also needs further study, as it can introduce systematic uncertainties in the extracted charge collection spectra.

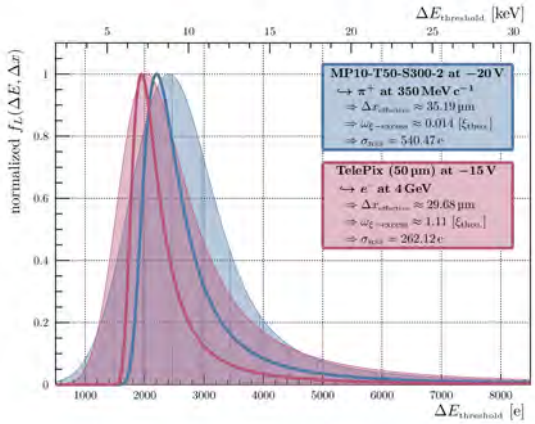

(a) "Idealized" charge collection spectra for 50 µm thick MuPix10 (blue) at −20 V and TelePix (red) at −15 V.

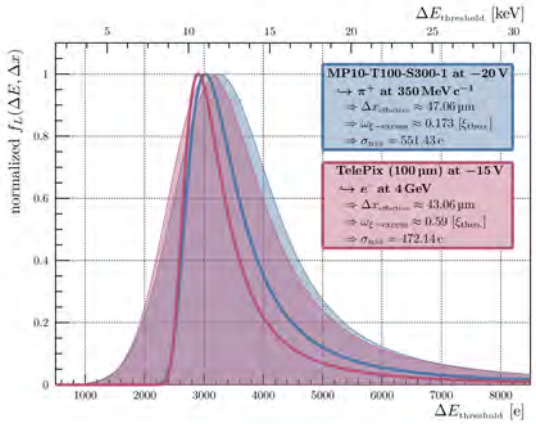

(b) "Idealized" charge collection spectra for 100 µm thick MuPix10 (blue) at −20 V and TelePix (red) at −15 V.

Plot 8.14: Comparison of "idealized" charge collection spectra extracted from calibrated ToT measurements of TelePix sensors (red) and hit efficiency measurements of MuPix10 sensors (blue) at comparable reverse bias voltages. The shaded spectra represent the convolution of the Landau distribution with a normal distribution based on the extracted fit parameters of measured data, while the bold line spectra represent the "pure" Landau distribution without smearing effects.

At last, a comparison of charge collection spectra extracted from calibrated ToT measurements and hit efficiency data is necessary to validate the consistency of both methodologies. Unfortunately, no data exist for the same sensors measured with both methods under identical conditions. However, a qualitative comparison of similar reverse bias voltages (relative to resistivity) between MuPix10 and TelePix sensors of the same thicknesses shows promising agreement in the extracted charge collection spectra (cf. Section 8.1.3). The "idealized" spectra (based on the convolution of the Landau distribution with a normal distribution) are shown for 50 µm and 100 µm sensors of TelePix and MuPix10, with operation voltages representing the maximum for each sensor type for 50 µm thickness. Although these measurements were conducted with different sensors, particle types, momenta, and methodologies, the overall shape of the distributions agrees well for the 100 µm sensors. For the 50 µm sensors, a larger deviation is observed, with MuPix10 showing a more symmetric distribution and a higher $\Delta x_{\text{effective}}$ value. This difference in symmetry may arise because uncollected charge is lost in hit efficiency measurements, while ToT measurements can partially compensate for charge sharing by summing charge from all pixels in a cluster, which is not as significant in thicker sensors.

A systematic offset of about 4 µm to 5 µm in $\Delta x_{\text{effective}}$ is observed between the TelePix and MuPix10 sensors for both thicknesses. This may result from differences in applied voltage and substrate resistivity, which deviate from the factor of 0.75 used in Section 8.2.4. However, the accuracy of $\Delta x_{\text{effective}}$ parametrization is limited by calibration differences, setup variations, and particle choice, introducing deviations of a few micrometers. This makes it challenging to draw definitive conclusions from the observed offset. However, what becomes evident is the relative offset between the two thickness measurements for each sensor type, revealing a 12 µm to 13 µm excess in $\Delta x_{\text{effective}}$ for the 100 µm sensors compared to the 50 µm sensors. This excess is consistent across both sensor types, indicating that $\Delta x_{\text{effective}}$ effectively reflects the relative differences in charge collection behavior arising from sensor thickness.

Epilogue

Conclusion

This thesis has provided a comprehensive overview of the theory and practical implementation for measuring the charge deposition spectrum of charged particles in silicon sensors, particularly for ultra-thin HV-MAPS sensors (see Chapters 1 and 4). A novel methodology has been developed to extract the charge deposition spectrum from calibrated hit detection efficiency data, obtained by scanning hit efficiency as a function of applied detection threshold in a testbeam environment (see Chapters 5 and 8). For this purpose, a calibration procedure to determine the detector response of HV-MAPS sensors has been established (see Chapters 6 and 7), based on S-curve measurements using the internal charge injection circuitry to simulate deposited charges and an Fe-55 source for absolute energy calibration.

The calibration campaign conducted in this thesis demonstrates that the extracted data are not only useful for calibration but also provide valuable insights into the noise performance (see Section 7.3) as well as the charge-collection and amplification behavior of the pixel sensor (see Sections 7.1 and 7.2). Indications of impact ionization in low-resistivity substrate sensors at high bias voltages have been observed (see Section 7.2.1), and deviations from expectations can be investigated by comparing data from *Injection* to Fe-55 measurements. Photon absorption measurements using Fe-55 imply that, even with careful handling, the distortion of simple models by contributions from diffusion cannot be neglected (see Section 7.2.6), which is consistent with findings from the simulations presented in [194].

These findings are confirmed by charge deposition spectrum measurements using calibrated hit efficiency data (see Chapter 8). A significant contribution from the non-depleted region to the overall charge collection spectrum is observed, with the most probable value increasing with detector thickness at the same reverse bias voltage. However, the dataset does not provide sufficient spatial resolution in the tracking to disentangle charge-sharing effects from diffusion contributions (see Section 8.2). It is also sensitive to theoretical assumptions in the charge deposition model, making the quantification of diffusion effects challenging. Noise contributions at the levels measured in Section 7.3 do not limit the determination of the charge collection spectrum, as smearing from charge sharing and intrinsic energy deposition fluctuations dominate the resolution (see Section 8.2.2).

In the future, improved methodologies could make noise performance relevant again, especially for sensors thinner than 50 µm or when utilizing a reference system with sub-pixel resolution.

To enhance the accuracy and precision of future measurements, the following steps are recommended:

1. Use a single particle type beam, or identification of particle types for each event, to reduce uncertainties from mixed particle compositions.
2. Employ higher momentum beams to minimize multiple Coulomb scattering (cf. Section 1.1.5), improving spatial association between the telescope and the DUT (see Section 5.3.2).
3. Use a more precise tracking telescope, enabling in-pixel resolution for detailed charge sharing studies.
4. Calibrate the sensor prior to data collection to ensure reproducible gain and threshold settings across the pixel matrix.
5. Determine the detector response on-site during beamtime to improve reproducibility and adapt to changing conditions.

Currently, no reliable on-chip calibration procedure exists for equalizing the response of all pixels, and using *Injection* is slow (cf. [6]) and subject to varying injection capacitances. A more promising approach is to use Fe-55 or X-ray fluorescence lines to calibrate the pixel response to a fixed threshold and gain setting. First attempts have been made in this direction (cf. [195]), based on the Fe-55 S-curve model and the procedure introduced in Section 6.2.2, but a fully automated calibration procedure has not yet been established. Calibrating the gain of each pixel individually is not possible with current sensors, which would require a tunable feedback circuit on a per pixel basis. Until then, the detector response of each pixel must be measured to achieve a precise energy deposition spectrum.

Measuring the detector response as performed in this thesis is too slow for beamtime application (cf. Section 6.1.2). By shifting the procedure to the FPGA, including sensor configuration and faster data readout, the measurement time per *Injection* point could be reduced from $\mathcal{O}(9\,\mathrm{s})$ to $\mathcal{O}(1\,\mathrm{s})$. Further reduction of the number of injected voltage points and the use of adaptive threshold scan ranges could speed up the process. This is assumed to reduce the total measurement time for a full response curve of a selected RoI from $\mathcal{O}(10\,\mathrm{h})$ to $\mathcal{O}(15\,\mathrm{min})$. While not fast enough for a full sensor, this would allow on-site calibration of a small sensor area during beamtime. On-site measurement would also validate reproducibility in the laboratory, making a post-beamtime remeasurement for other pixel RoI more reliable.

To further improve understanding of detector effects on the measured charge deposition spectrum, additional studies are necessary:

1. Compare different gain settings to validate spectral equivalence across dynamic ranges.
2. Compare to the ToT methodology on the same sensor and dataset to assess calibration and energy resolution differences.
3. Validate the calibration methodology using more monochromatic energy sources to evaluate the predictive power of the detector response curve.
4. Unfold the noise contribution from the measured spectrum for each pixel to extract the intrinsic energy resolution of the sensor.

Measuring in finer energy increments (i.e., finer threshold steps) and increasing statistics would further enhance parameter precision. However, this requires either a higher gain (cf. Section 7.1.4), which potentially reduces the linear dynamic range (see Section 7.1.5), or finer threshold steps (more bits for the voltage DACs). The latter can introduce additional uncertainties due to DNL effects, which must be calibrated or incorporated into the analysis. For the ToT methodology, finer granularity is already provided by TelePix chips [189] compared to MuPix sensors. However, an even finer binning of the ToT is not beneficial, as it is currently limited by the stability of the feedback loop and the noise performance. Achieving such finer granularity would require a higher clock speed for switching the timestamp counters, resulting in significantly increased power consumption.

In summary, the methodology to extract the charge deposition spectrum from calibrated hit detection efficiency data is effective, but sensitive to tracking resolution. With sufficiently precise tracking, it also allows the study of charge collection effects in low-efficiency regions of the pixel. An on-chip calibration and improved beam conditions can significantly enhance future measurement accuracy. However, the measurement time required for each threshold step remains a limiting factor, especially in scenarios with low particle rates. In this regard, the ToT methodology remains the more practical approach for studying the energy deposition spectrum in pixel sensors, as only a single detection threshold dataset is needed to extract the full spectrum, and charge sharing effects can be mitigated by summing the ToT of neighboring pixels. Nevertheless, in low-efficiency scenarios, the shape of the ToT spectrum is not only cut off by the threshold but also distorted by missing hits, making precise extraction of the most probable value challenging.

Outlook

The next step is to compare the results from this thesis with simulations. This requires a 3D simulation of the electric field inside the sensor, using tcad tools. Such simulations are sensitive to assumptions about the sensor's doping profile and pixel diode geometry, especially the *n*-well structure within the *p*-substrate. With empirical start values, initial comparisons may already yield valuable insights into the charge collection behavior, which can then be refined to match experimental data. The resulting electric field map can be used with `Allpix`^{2} [59], a framework based on `Geant4` [196] for simulating silicon pixel detectors, including charge transport and signal digitization. Basic simulations of charge deposition in silicon of varying thicknesses, as discussed in Section 8.1.2, have already provided useful insights, and more detailed simulations including detector effects represent the next logical step. Modeling the electronics for digitization in `Allpix`^{2} is still ongoing, with initial work presented in [7, 202], but is not yet mature enough to deliver fully accurate results. With a validated simulation framework, further studies can be conducted to deepen the understanding of charge collection in HV-MAPS, particularly in under-depleted operation.

Another important step is to validate the equivalence of the results obtained with the calibrated hit detection efficiency methodology to established methods such as calibrated ToT spectrum measurements. Since MuPix sensors do not provide sufficiently fine granularity for ToT measurements, other sensors like TelePix [189] are better suited for this purpose. A calibration procedure for ToT measurements is already established and thoroughly tested [8] (cf. Section 8.1.3), and the hit detection efficiency methodology can be easily adapted to this sensor. A direct comparison of both methods on the same sensor and dataset is therefore feasible. These measurements should ideally be performed at DESY using an EUDET [73] or ALPIDE-based [72] reference tracking telescope, which offer excellent tracking resolution for in-pixel studies.

With sufficient in-pixel resolution, data can be divided into pixel center and edge regions to study the influence of charge sharing on the measured spectrum, or binned into finer spatial regions within the pixel for more detailed analysis. By scanning different high voltages, a three-dimensional evolution of charge collection behavior can be studied, similar to TCT measurements but with charged particles instead of laser pulses.

Given the indications of impact ionization in low-ohmic sensors at high bias voltages observed in this thesis (cf. Section 7.2.1), remeasuring the charge deposition spectrum at *high-gain* settings for high bias voltages would be valuable. This could be a first step toward developing efficient sensors for even thinner devices, where charge multiplication is used to boost the signal.

In general, a more precise model for the depletion of the pixel diode — beyond the simple plate capacitor approximation — would improve the accuracy of predictions for depletion depth. A better understanding of pixel capacitance and its voltage dependence would enhance models for detector response and calibration, and provide further insight into the substrate resistivity, as already begun in [203]. Capacitance-voltage measurements on dedicated MuPix10 sensors of different thicknesses and resistivities could lead to improved predictions for pixel diode depletion behavior, or even allow direct extraction of the depletion depth from such measurements.

A. Appendix

A.1 Supplementary Data and Information

A.1.1 CSDA range of electrons in silicon

The mean free path length of an electron with in a material can be approximated by the CSDA (**C**ontinuous **S**lowing **D**own **A**pproximation) range, which is the average distance an electron travels in a medium before losing all its kinetic energy and can be extracted from the NIST (**N**ational **I**nstitute of **S**tandards and **T**echnology) *ESTAR* database [31]. Plot A.1 shows the CSDA range of electrons in various materials as a function of kinetic energy. The data is converted to [µm] with data from Table A.17.

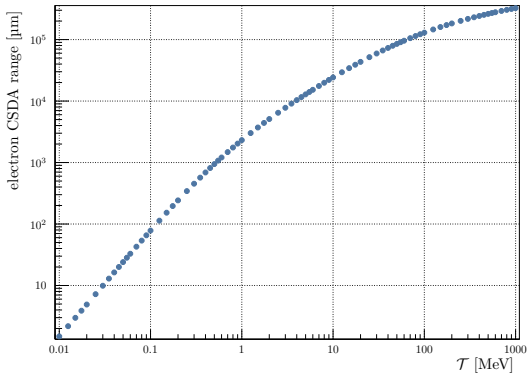

(a) The CSDA range of electrons in **si**licon as a function of kinetic energy $\mathcal{T}$.

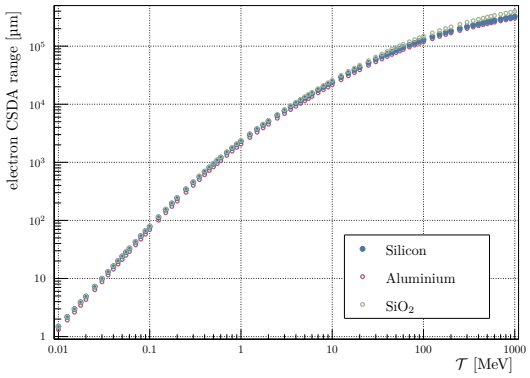

(b) The CSDA range of electrons in **si**licon, **al**uminium and SiO_2 as a function of kinetic energy $\mathcal{T}$.

Plot A.1: The CSDA range of electrons in various materials as a function of kinetic energy $\mathcal{T}$. The data is taken from the NIST *ESTAR* database [31].

A.1.2 Kinematic Variables and Identities

In particle physics, several kinematic variables are commonly used to describe the motion and energy of particles. Here are some of the key variables along with their definitions and relationships, assuming natural units where the speed of light $c = 1$. For the energy (E), momentum (p), kinetic energy ($\mathcal{T}$), relative velocity (β), and Lorentz factor (γ) of a particle with mass (M), the following relationships hold:

$$E = \mathcal{T} + M = \sqrt{p^2 + M^2} \quad \rightarrow \quad \mathcal{T} = E - M = \sqrt{p^2 + M^2} - M \quad \rightarrow \quad p = \sqrt{E^2 - M^2} = \sqrt{\mathcal{T}^2 + 2\mathcal{T}M}$$

$$\beta = \sqrt{1 - \frac{1}{\gamma^2}} = \frac{p}{E} \quad \rightarrow \quad \gamma = \frac{1}{\sqrt{1 - \beta^2}} = \sqrt{1 + (\beta\gamma)^2} = \frac{E}{M} \quad \rightarrow \quad \beta\gamma = \frac{p}{M}$$

A.1.3 Time Resolution and Efficiency

Plot A.2 shows the uncorrected time resolution and latency for each run ID fo all DUTs and configurations. The time resolution and latency are extracted from the standard deviation and mean of the respective distribution of each run, whereas the ToA timestamp of the DUT is subtracted from the combined track timestamp of the tracking layers. With increasing run ID the detection threshold is increased stepwise within a data subset of a specific HV setting, while the HV is decreased stepwise between different data subsets of a specific DUT. Each DUT subset is indicated by the vertical dashed lines in Plot A.2. It can be observed that while the time resolution seems to improve at first glance, the relative latency increases with higher run IDs in a data subset. This can be attributed to the two threshold mode, where the higher threshold of the two comparators defines the detection threshold, while the lower threshold is used for ToA timestamp definition. With increasing detection threshold small signal amplitudes are cut from the distribution, decreasing the influence from time walk and increasing the relative latency at the same time.

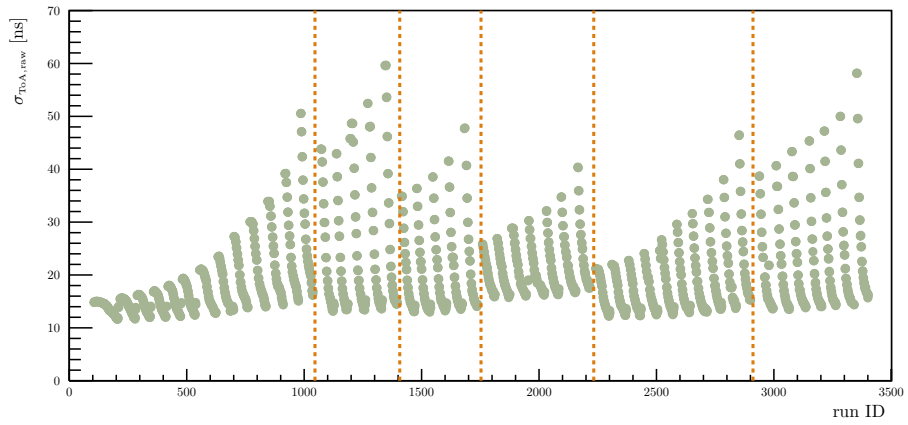

(a) Uncorrected time resolution of DUTs as function of the run ID.

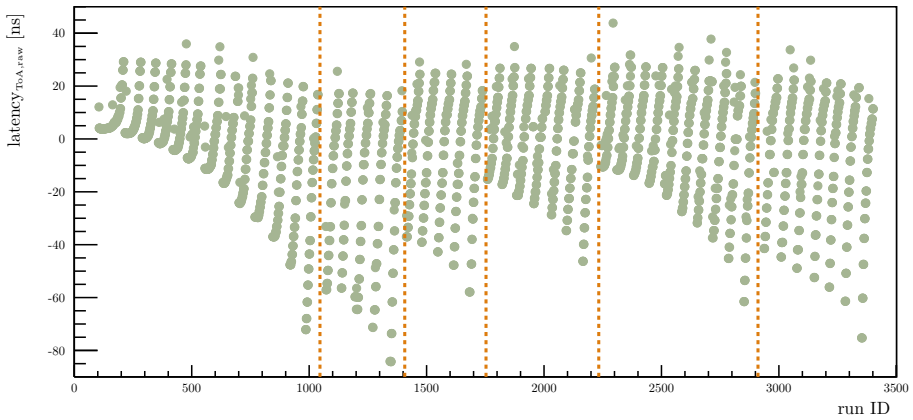

(b) Latency of DUTs with respect to the tracking layers as function of the run ID.

Plot A.2: The time resolution and latency as a function of the run ID for all DUTs and configurations. The vertical dashed lines indicate the change of a DUT. Within such a subset the applied HV decreases with increasing run ID and for each HV setting again the applied threshold decreases with increasing run ID.

Plot A.3 illustrates the correlation of uncorrected time resolution, latency and efficiency for all DUTs and configurations. A clear trend between time resolution and latency can be observed in Plot A.3c, where a better time resolution corresponds to a relative earlier latency. This is expected as small signal are detected later in time arising from time walk effects and are being cut when applying a higher detection threshold. Furthermore, Plot A.3a and Plot A.3b illustrate the space of time resolution and latency with respect to the efficiency. It clearly exhibits the effect of the two threshold mode that independent of the initial time resolution or latency all configurations saturate to the same values when approaching low efficiencies, as large charge deposition detectable by the comparators end up in the saturation domain of the CSA.

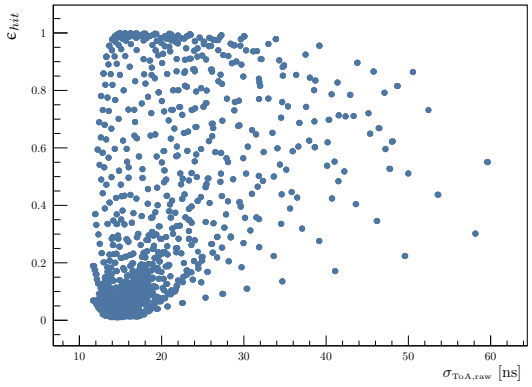

(a) Correlation of uncorrected time resolution and efficiency for all DUTs and configurations.

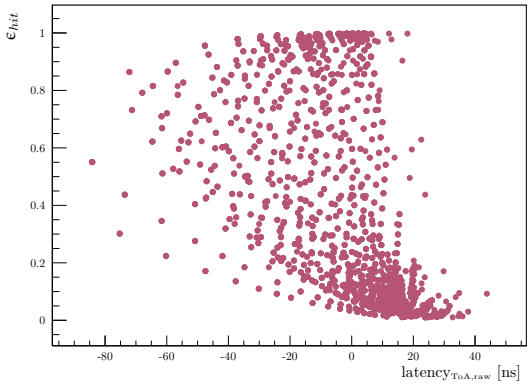

(b) Correlation of latency and efficiency for all DUTs and configurations.

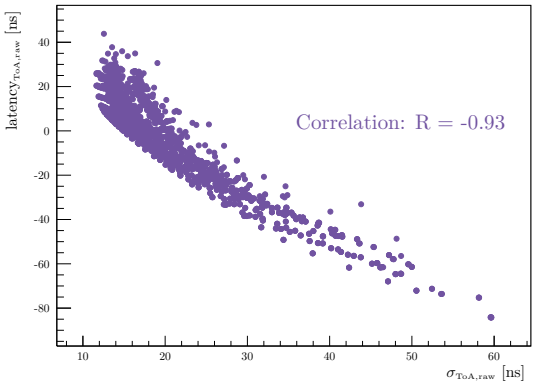

(c) Correlation of uncorrected time resolution and latency for all DUTs and configurations.

Plot A.3: Correlation of time resolution, latency and efficiency for all DUTs and configurations.

A.2 Mobility Models for Silicon

The mobility of charge carriers in silicon is influenced by various factor as the doping concentration, temperature and electric field strength. Several empirical models have been developed to describe the mobility of electrons and holes in doped silicon. Two commonly used models are the Arora Model [204] and the Masetti Model [205], introduced in the following sections. The course of the mobility as a function of resistivity and temperature employing these models is shown in Plot A.4.

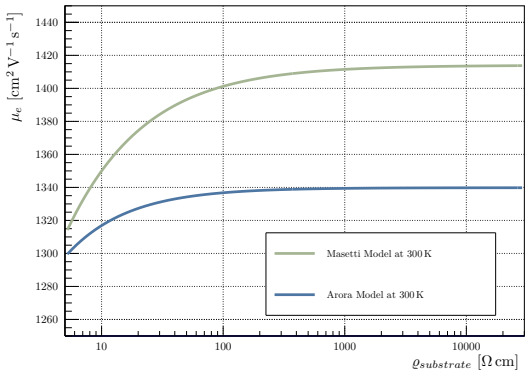

(a) Electron mobility as a function of resistivity in silicon.

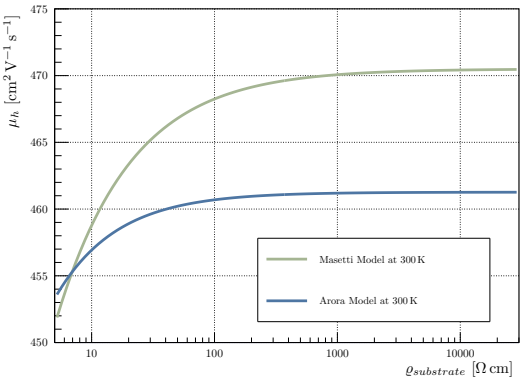

(b) Hole mobility as a function of resistivity in silicon.

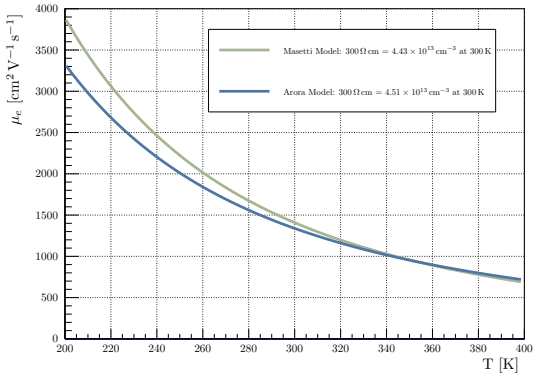

(c) Electron mobility as a function of temperature in silicon.

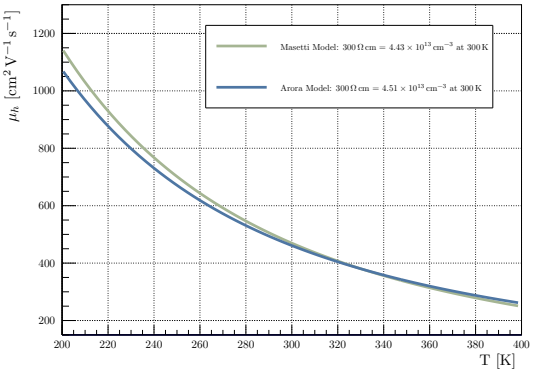

(d) Hole mobility as a function of temperature in silicon.

Plot A.4: Mobility of electrons and holes in silicon as a function of resistivity and temperature. The values are calculated based on the Arora- and Masetti-Models for the charge carrier mobilities (cf. Sections A.2.1 and A.2.2).

A.2.1 Arora Model

The mobility of electrons/holes in doped silicon given by the Arora Model Equation A.1 [204, p. 293-294, eq. 8 & 13][1]:

$$\mu_{e/h}(T,\mathcal{N}) = \mu_{min,e/h} \cdot T_n^{-0.57} + \frac{\mu_{0,e/h} \cdot T^{\mathcal{b}_{e/h}}}{1 + [\mathcal{N}/(\mathcal{N}_{ref,e/h} \cdot T_n^{2.4})]^a} \quad , \quad a = 0.88 \cdot T_n^{-0.146} \tag{A.1}$$

where T_n is given by Equation 2.10 and $\mathcal{N}$ is the total doping concentration of the silicon. The parameters for the model are given in Table A.1.

Parameter	e: **Electron**	h: **Hole**
$\mu_{min,i}$ [cm^2 V^{-1} s^{-1}]	88.0	54.3
$\mu_{0,i}$ [cm^2 V^{-1} s^{-1}]	$7.4 \cdot 10^8$	$1.36 \cdot 10^8$
$\mathcal{b}_i$	-2.33	-2.23
$\mathcal{N}_{ref,i}$ [cm^{-3}]	$1.26 \cdot 10^{17}$	$2.35 \cdot 10^{17}$

Table A.1: Arora mobility model parameters for electron and holes in silicon. Taken from [204].

A.2.2 Masetti Model

The mobility of electrons/holes in doped silicon given by the Masetti Model Equation A.2 [205, p. 765-767, eq. 1 & 4][2]:

$$\begin{aligned}
\mu_e(T,\mathcal{N}) &= \mu_{0,e} + \frac{\mu_{max,e} \cdot T_n^{-2.5} - \mu_{0,e}}{1 + \left(\frac{\mathcal{N}}{\mathcal{N}_{r,e}}\right)^{0.711}} - \frac{\mu_{1,e}}{1 + \left(\frac{\mathcal{N}}{\mathcal{N}_{s,e}}\right)^{1.98}} \\
\mu_h(T,\mathcal{N}) &= \mu_{0,h} \cdot \mathrm{e}^{-\frac{\mathcal{N}_{ref,h}}{\mathcal{N}}} + \frac{\mu_{max,h} \cdot T_n^{-2.2}}{1 + \left(\frac{\mathcal{N}}{\mathcal{N}_{r,h}}\right)^{0.719}} - \frac{\mu_{1,h}}{1 + \left(\frac{\mathcal{N}}{\mathcal{N}_{s,h}}\right)^{2.0}}
\end{aligned} \tag{A.2}$$

where T_n is given by Equation 2.10 and $\mathcal{N}$ is the total doping concentration of the silicon. The parameters for the model are given in Table A.2.

Parameter	e: **Electron**	h: **Hole**
$\mu_{0,i}$ [cm^2 V^{-1} s^{-1}]	68.5	44.9
$\mu_{max,i}$ [cm^2 V^{-1} s^{-1}]	1414.0	470.5
$\mu_{1,i}$ [cm^2 V^{-1} s^{-1}]	56.1	29.0
$\mathcal{N}_{ref,i}$ [cm^{-3}]	-	$9.23 \cdot 10^{16}$
$\mathcal{N}_{r,i}$ [cm^{-3}]	$9.2 \cdot 10^{16}$	$2.23 \cdot 10^{17}$
$\mathcal{N}_{s,i}$ [cm^{-3}]	$3.41 \cdot 10^{20}$	$3.41 \cdot 10^{20}$

Table A.2: Masetti mobility model parameters for phosphorus (electron) and boron (hole) doped silicon [205, p. 766, tab. 1]. Values taken from [59] since the values in the original paper are not readable for boron.

[1] The presented form of the formula shown is taken from the Allpix^2 manual [59] which provides better readability.

[2] The presented form is altered to improve readability in comparison to the original paper. The values for boron are taken from [59] since the values in the original paper are not readable.

A.2.3 Diffusion coefficient

The diffusion coefficient of the respective charge carrier $\mathcal{D}_{e/h}$, as stated in Equation 4.34, can be calculated from the mobility using the Einstein relation, which incorporates the temperature dependency as well doping concentration if either the Arora or Masetti mobility models are used (cf. Sections A.2.1 and A.2.2). Employing the Einstein relation in combination with these models yield the course of the diffusion coefficient in silicon as a function of resistivity and temperature shown in Plot A.5.

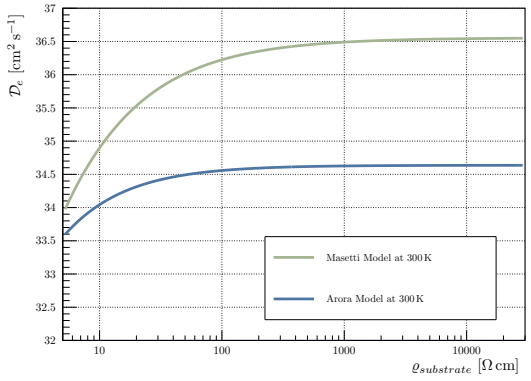

(a) Diffusion coefficient of electrons as a function of resistivity in silicon.

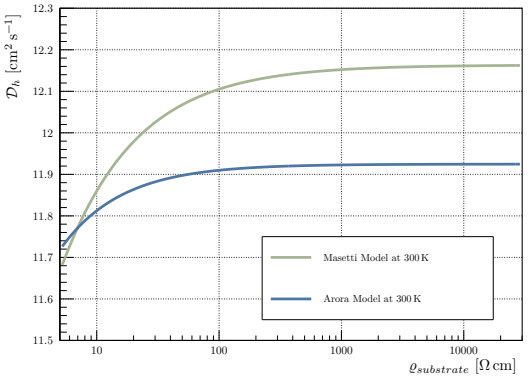

(b) Diffusion coefficient of holes as a function of resistivity in silicon.

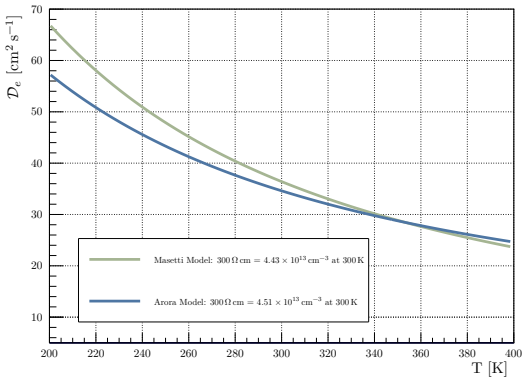

(c) Diffusion coefficient of electrons as a function of temperature in silicon.

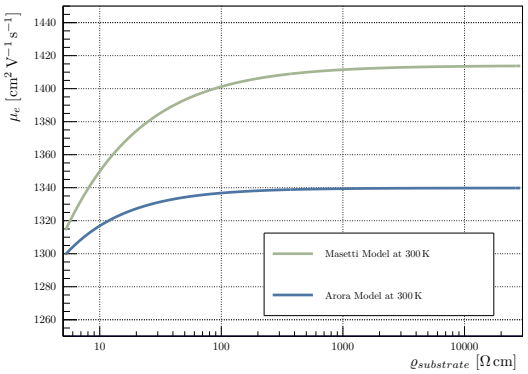

(d) Diffusion coefficient of holes as a function of temperature in silicon.

Plot A.5: Diffusion coefficients of electrons and holes in silicon as a function of resistivity and temperature. The values are calculated based on the Arora- and Masetti-Models for the charge carrier mobilities (cf. Sections A.2.1 and A.2.2).

A.3 Usage and Properties of Distributions

A.3.1 Deriving the Kinetic Equation

The kinetic equation presented by Landau [102, p. 417, eq. 1] (cf. Equation 4.8) can be derived from Equation 4.6 as shown in the following. In the first step the derivative of Equation 4.6 is taken with respect to Δx, yields:

$$\frac{\partial f(\Delta E \mid \Delta x)}{\partial \Delta x} = \sum_{n=0}^{\infty} \frac{\partial \text{PDF}_{\text{poisson}}(n \mid \mathcal{M}_0(\Delta x))}{\partial \Delta x} \cdot f^{(n)}(\Delta E) \tag{A.3}$$

Since $f^{(n)}(\Delta E)$ is independent of Δx, and the *rate*-factor of the Poisson distribution $\mathcal{M}_0$ indirectly, the chain rule can be applied to the Poisson distribution:

$$\begin{aligned}
\frac{\partial \text{PDF}_{\text{poisson}}(n \mid \mathcal{M}_0(\Delta x))}{\partial \Delta x} &= \frac{\partial \mathcal{M}_0(\Delta x)}{\partial \Delta x} \cdot \frac{\partial \text{PDF}_{\text{poisson}}(n \mid \mathcal{M}_0)}{\partial \mathcal{M}_0} \\
&= \mathcal{M}_0' \cdot \frac{\partial \text{PDF}_{\text{poisson}}(n \mid \mathcal{M}_0)}{\partial \mathcal{M}_0} \\
&= \mathcal{M}_0' \cdot \left[n \cdot \frac{\mathcal{M}_0^{(n-1)}}{n!} \cdot \mathrm{e}^{-\mathcal{M}_0} + (-1) \cdot \frac{\mathcal{M}_0^{n}}{n!} \cdot \mathrm{e}^{-\mathcal{M}_0} \right] \\
&= \mathcal{M}_0' \cdot \left(\frac{n}{\mathcal{M}_0} - 1 \right) \cdot \text{PDF}_{\text{poisson}}(n \mid \mathcal{M}_0)
\end{aligned} \tag{A.4}$$

Inserting this into Equation A.3 yields:

$$\begin{aligned}
\frac{\partial f(\Delta E \mid \Delta x)}{\partial \Delta x} =& \mathcal{M}_0' \cdot \sum_{n=0}^{\infty} \left(\frac{n}{\mathcal{M}_0} - 1 \right) \text{PDF}_{\text{poisson}}(n \mid \mathcal{M}_0) \cdot f^{(n)}(\Delta E) \\
=& \frac{\mathcal{M}_0'}{\mathcal{M}_0} \cdot \sum_{n=0}^{\infty} n \cdot \text{PDF}_{\text{poisson}}(n \mid \mathcal{M}_0) \cdot f^{(n)}(\Delta E) \\
& - \mathcal{M}_0' \cdot \sum_{n=0}^{\infty} \text{PDF}_{\text{poisson}}(n \mid \mathcal{M}_0) \cdot f^{(n)}(\Delta E)
\end{aligned} \tag{A.5}$$

The first term of Equation A.5 can be simplified using the identity of the Poisson distribution, which states that the expected value of a Poisson distribution is equal to its rate parameter $\mathcal{M}_0$:

$$\begin{aligned}
n \cdot \text{PDF}_{\text{poisson}}(n \mid \mathcal{M}_0) &= n \cdot \frac{\mathcal{M}_0^n}{n!} \cdot e^{-\mathcal{M}_0} \\
&= \mathcal{M}_0 \cdot \frac{\mathcal{M}_0^{n-1}}{(n-1)!} \cdot e^{-\mathcal{M}_0} \\
&= \mathcal{M}_0 \cdot \text{PDF}_{\text{poisson}}(n-1 \mid \mathcal{M}_0)
\end{aligned} \tag{A.6}$$

This allows to rewrite the first term of Equation A.5 as:

$$\begin{aligned}
\sum_{n=0}^{\infty} n \cdot \text{PDF}_{\text{poisson}}(n \mid \mathcal{M}_0) \cdot f^{(n)}(\Delta E) &= \mathcal{M}_0 \cdot \sum_{m=0}^{\infty} \text{PDF}_{\text{poisson}}(m \mid \mathcal{M}_0) \cdot f^{(m+1)}(\Delta E) \\
&= \mathcal{M}_0 \cdot \sum_{m=0}^{\infty} \text{PDF}_{\text{poisson}}(m \mid \mathcal{M}_0) \cdot (f^{(m)} * f^{(1)})(\Delta E) \\
&= \mathcal{M}_0 \cdot (f(\Delta x) * f^{(1)})(\Delta E)
\end{aligned} \tag{A.7}$$

If this is inserted into Equation A.5, the kinetic equation simplifies to:

$$\frac{\partial f(\Delta E \mid \Delta x)}{\partial \Delta x} = \mathcal{M}_0' \cdot \Big[(f(\Delta x) * f^{(1)})(\Delta E) - f(\Delta E \mid \Delta x) \Big] \tag{A.8}$$

Using now the relations of Equation 4.4 and Equation 4.5, the kinetic equation can be rewritten as:

$$\begin{aligned}\frac{\partial f(\Delta E \mid \Delta x)}{\partial \Delta x} =& \mathcal{M}_0' \cdot \left[\int_0^{\Delta E_{max}} f(\Delta E - E \mid \Delta x) \cdot f^{(1)}(E)\, \mathrm{d}E - \frac{1}{\mathcal{M}_0'} \int_0^{\Delta E_{max}} \omega(E) \cdot f(\Delta E \mid \Delta x)\, \mathrm{d}E \right] \\ =& \mathcal{M}_0' \cdot \int_0^{\Delta E_{max}} f(\Delta E - E \mid \Delta x) \cdot \frac{\omega(E)}{\mathcal{M}_0'}\, \mathrm{d}E - \int_0^{\Delta E_{max}} \omega(E) \cdot f(\Delta E \mid \Delta x)\, \mathrm{d}E \\ =& \int_0^{\Delta E_{max}} \omega(E) \cdot \left[f(\Delta E - E \mid \Delta x) - f(\Delta E \mid \Delta x) \right] \mathrm{d}E \end{aligned} \tag{A.9}$$

This is the kinetic equation of Equation 4.8, quod erat demonstrandum.

A.3.2 Extended Information on the Landau Distribution

"The full family of Landau distributions is obtained by extending the original distribution to a location-scale family of stable distributions with parameters $\alpha = 1$ and $\beta = 1$ [206], with characteristic function [207]" [208]:

$$\varphi(t \mid \mu, c) = \mathrm{e}^{i \cdot t \cdot \mu - \frac{2i \cdot c \cdot t}{\pi} \ln |t| - c \cdot |t|} \tag{A.10}$$

with $t = u$, $\mu \epsilon (-\infty, \infty)$ being the location parameter and $c \epsilon (0, \infty)$ the scale parameter. By performing the inverse Fourier transform, one obtains the generalized real expression for the PDF of the Landau distribution [208]:

$$\phi(x \mid \mu, c) = \frac{1}{\pi c} \int_0^{\infty} \mathrm{e}^{-u} \cos\left(u \left[\frac{x - \mu}{c} \right] + \frac{2t}{\pi} \ln\left(\frac{u}{c} \right) \right) \mathrm{d}u \tag{A.11}$$

This form seems to be used by `Mathematica`[3] [209] and differs from the version used by the `ROOT` framework [172, 173]. With the approach setting $c = \frac{\pi}{2}$ and $\mu = 0$, Equation A.11 can be reduced to the real form of the Landau distribution given by Equation 4.11. Its (generalized) complex counterpart (see [102, p. 420, eq. 13]) as stated in the documentation of ROOT::Math::landau_pdf [210] (see also the erratum [211]) in the "MathMore"-Package of the `ROOT` framework [172, 173] is:

$$\phi(\lambda_L) = \frac{1}{2\pi i} \int_{a - i\infty}^{a + i\infty} \mathrm{e}^{\lambda_L \cdot s + s \cdot \ln(s)}\, \mathrm{d}s \tag{A.12}$$

where a is an arbitrary positive real number and s is the complex integration variable used in the inverse Laplace transform.
Take note that this form of the Landau distributions peaks at $\lambda_{L,mode}(\xi = 1) = -0.222782...$[4] [210, p. 101] (cf. Section 4.1.1) in contrast to its original quoted value of $\lambda_L = -0.05$ [102, p. 420]. This allows the parameterization used for the Landau distribution in `ROOT` to be written as:

$$\begin{aligned}\lambda_L = \frac{x - \mu}{\xi} &= \frac{x - (x_{mode} - \xi \cdot \lambda_{L,mode}(\xi = 1))}{\xi} = \frac{x - x_{mode}}{\xi} + \lambda_{L,mode}(\xi = 1) \\ &= \frac{x - x_{mode}}{\xi} - 0.222782... \end{aligned} \tag{A.13}$$

where for $x = \Delta E$, x_{mode} is ΔE_{MPV} and ξ is the $\xi(\Delta x, \beta)$ of the Landau distribution.
The Landau distribution is a special case of the *stable* distributions with the following properties [111, 292.ff]:

- It is closed under convolution, meaning that the sum of two independent Landau-distributed random variables is also Landau-distributed.
- The landau distribution has no moments of any order, which means that neither the mean nor the variance is defined.
- For $\xi = 1$, the half maximum coordinates are at $\lambda_{L,1} = -1.5865$ and $\lambda_{L,2} = 2.4319$

[3] The definite form used in `Mathematica` (LandauDistribution) is not directly stated in the documentation and is approximated by comparing the internal function with Equation A.11.
[4] Value used for calculation within the context of this thesis is $\lambda_L = -0.22278298125640$, which is stated in the [112, p. 124].

As a consequence of the last point, the FWHM of the Landau distribution is often quoted with a factor about 4.0 to 4.02 times $\xi(\Delta x, \beta)$. The most accurate approximation commonly used is $W_L = 4.018 \cdot \xi(\Delta x, \beta)$ [17, p.42], whereas other sources relate the factor with the FWHM of a Gaussian distribution in the form $W_L = (2 \cdot \sqrt{2 \cdot \ln(2)}/0.586) \cdot \xi \approx 4.0184 \cdot \xi(\Delta x, \beta)$ [212, p. 1, eq. 3b, 213, p. 77], which fits the listed values $\lambda_{L,1}$ and $\lambda_{L,2}$.

The upper (ROOT::Math::landau_cdf_c) and lower (ROOT::Math::landau_cdf) tails of the Landau PDF as well as their respective inverse functions (ROOT::Math::landau_quantile_c, ROOT::Math::landau_quantile) — the quantile functions — are provided in the "MathMore"-Package of ROOT and can be reparametrized in the same way as the Equation 4.14:

$$\begin{aligned} \text{CDF}_{Landau}(\Delta E \mid \Delta E_{\text{MPV}}, \xi(\Delta x, \beta)) &= \int_{-\infty}^{\Delta E} \text{PDF}_{Landau}(\Delta E' \mid \Delta E_{\text{MPV}}, \xi(\Delta x, \beta))\, \mathrm{d}\Delta E' \\ \text{CDF\_C}_{Landau}(\Delta E \mid \Delta E_{\text{MPV}}, \xi(\Delta x, \beta)) &= \int_{\Delta E}^{\infty} \text{PDF}_{Landau}(\Delta E' \mid \Delta E_{\text{MPV}}, \xi(\Delta x, \beta))\, \mathrm{d}\Delta E' \end{aligned} \tag{A.14}$$

A.3.3 Extended Information on the Moyal Distribution

Introduced as distributions of the energy loss by ionization of fast charged particles in a thin absorber, the distribution named after Moyal is an approximation of the Landau distribution [113, p. 271, eq. 5.8]:

$$\text{PDF}_{\text{Moyal}}(\lambda_M) = \frac{1}{\sqrt{2\pi}} \cdot \mathrm{e}^{-\frac{1}{2}\left[\lambda_M + \mathrm{e}^{-\lambda_M}\right]} \tag{A.15}$$

which peaks if $\lambda_M = 0$ (mode) is fulfilled. In contrast to the Landau Distribution, the Moyal distribution is provides a closed form for the CDF and is defined as [114, p. 93]:

$$\text{CDF}_{\text{Moyal}}(\lambda_M) = \int_{-\infty}^{\lambda_M} \text{PDF}_{\text{Moyal}}(\lambda'_M)\, \mathrm{d}\lambda'_M = 1 - \text{P}_{\text{lower}}\left(\frac{1}{2}, \frac{\mathrm{e}^{-\lambda_M}}{2}\right) \tag{A.16}$$

with $\text{P}_{\text{lower}}(a, x)$ representing the regularized lower incomplete gamma function. The lower $[\gamma(a, x)]$ and upper $[\Gamma(a, x)]$ incomplete gamma functions are defined as [114, p. 159]:

$$\gamma(a, x) = \int_0^x t^{a-1} e^{-t} \mathrm{d}t \quad \text{and} \quad \Gamma(a, x) = \int_x^\infty t^{a-1} e^{-t} \mathrm{d}t \tag{A.17}$$

Using the identity $\Gamma(a) = \gamma(a, x) + \Gamma(a, x)$ (and $\Gamma(1/2) = \sqrt{\pi}$ [114, p. 180]) results in the regularized lower $[\text{P}_{\text{lower}}(a, x)]$ and upper $[\text{Q}_{\text{upper}}(a, x)]$ incomplete gamma functions:

$$\text{P}_{\text{lower}}(a, x) = \frac{\gamma(a, x)}{\Gamma(a)} \quad \text{and} \quad \text{Q}_{\text{upper}}(a, x) = \frac{\Gamma(a, x)}{\Gamma(a)} \tag{A.18}$$

Finally, the closed form of the (complementary) CDF of the Moyal distribution can be expressed in terms of the regularized upper incomplete gamma function as follows:

$$\text{CDF\_C}_{\text{Moyal}}(\lambda_M) = \int_{\lambda_M}^{\infty} \text{PDF}_{\text{Moyal}}(\lambda'_M)\, \mathrm{d}\lambda'_M = 1 - \text{Q}_{\text{upper}}\left(\frac{1}{2}, \frac{\mathrm{e}^{-\lambda_M}}{2}\right) \tag{A.19}$$

C++ code for the regularized forms of the incomplete gamma functions can be found in the "MathMore"-Package of the ROOT framework [172, 173] by using the functions `ROOT::Math::inc_gamma` and `ROOT::Math::inc_gamma_c`.

[214] introduced a modified version of the Moyal function, based on the original formulation but incorporating additional parameters to better fit experimental data [214, p. 559, eq. 11]:

$$\phi(\lambda_L) = a_1 \cdot \mathrm{e}^{-a_2 \cdot \left[\lambda_L + a_5 \cdot \lambda_L^2\right] - a_3 \cdot \mathrm{e}^{-a_4 \cdot \left[\lambda_L + a_6 \cdot \lambda_L^2\right]}} \tag{A.20}$$

where λ_L is defined by Equation 4.12 and the parameters $a_1, ..., a_6$ are determined by fitting the function to experimental data. In [215], corresponding values for different regimes of κ are determined to fit the Vavilov distribution. The general properties of the Moyal distribution are presented in Table A.3. Further details on generalizations of the Moyal distribution are available in [216] and [217].

Parameter	Value
FWHM	$W_M \approx 2.28447 \cdot \xi_M - (-1.30634 \cdot \xi_M) \approx 3.59081 \cdot \xi_M$
mean†	$\Delta E_{\text{MPV}} + \xi_M \cdot (\gamma_{\text{EM}} + \log(2)) \approx \Delta E_{\text{MPV}} + 1.270363 \cdot \xi_M$
median	$\Delta E_{\text{MPV}} - \xi_M \cdot \log\left(2 \cdot \left[\text{erfc}^{-1}(\frac{1}{2})\right]^2\right) \approx \Delta E_{\text{MPV}} + 0.787598 \cdot \xi_M$
variance	$\frac{\pi^2 \xi_M^2}{2}$
skewness‡	$\frac{28\sqrt{2} \cdot \zeta(3)}{\pi^3} \approx 1.53514$
Kurtosis	4

Table A.3: Properties of the Moyal distribution adapted from [114, p. 92-93] for the form of Equation 4.15. †: γ_{EM} is the Euler-Mascheroni constant. ‡ : $\zeta(n)$ is the Riemann zeta function (see [114, p. 59]) (see `std::riemann_zeta`).

A.3.4 Extended Information on the Vavilov Distribution

The Vavilov distribution is implemented in the `ROOT` framework [172, 173] as a set of C++ classes (detailed information in [115, 215]).

The *base class*, `ROOT::Math::Vavilov`, provides core functionalities for the Vavilov distribution, including the PDF, (complementary) CDF, quantile functions, and calculations of moments as shown in Table A.4. Respective changes are overridden by the derived classes, which `ROOT` offers two variants of the Vavilov distribution, differing in accuracy and performance:

- `ROOT::Math::VavilovFast`: a fast approximation, valid for $0.01 \lesssim \kappa \lesssim 12$.
- `ROOT::Math::VavilovAccurate`: an accurate implementation, valid for $0.001 \lesssim \kappa$.

If the supplied κ falls outside of the valid range, the classes emit an error message indicating an out-of-range value, and override the input with the closes boundary value. Neglecting the incorrect κ value and fixing it, ΔE_{MPV} values exceeding the valid range still return a valid result, but no distinct statement can be made about the accuracy of the result. For κ values below the supported range, the Landau distribution is recommended, while for larger values, the Gaussian distribution may be more appropriate.

Unlike the Landau distribution (cf. Section A.3.2), the relevant Vavilov classes accept only a single (λ_L) input parameter as input during evaluation; the parameters κ and β^2 must be set at object construction. Modifying these parameters requires recalculation and incurs significant computational overhead; therefore, it should be avoided for optimal performance. For this reason, the C++ classes should be used rather than the `ROOT` functions in the "MathMore"-Package for Probability Density Functions, Cumulative Distribution Functions, and Quantile Functions.
The remaining parameterization used by `ROOT` takes the form:

$$\lambda_L = \frac{\lambda_V}{\kappa} - \ln(\kappa) \tag{A.21}$$

This can be defined equivalent to the parameterization of the Landau distribution (see Equation A.13):

$$\lambda_L = \frac{x - x_{mode}}{\xi} + \delta_{Mode} \tag{A.22}$$

Here, the shift parameter δ_{Mode} is defined by the function `ROOT::Math::Vavilov::Mode()`,and depends on the parameters κ and β^2 set at object construction.
If λ_L is reparameterized, ensure that the PDF is properly normalized by dividing the result of the respective classe's PDF by $\xi(\Delta x, \beta)$.
Note that the supported calculation range for λ_L is limited to $\lambda_{\text{min}} < \lambda_L < \lambda_{\text{max}}$, accessible via the `ROOT::Math::Vavilov::GetLambdaMin()` and `ROOT::Math::Vavilov::GetLambdaMax()` functions. If λ_L falls outside this interval, the PDF and the (complementary) CDF will return zero or one, as appropriate.
For `ROOT::Math::VavilovAccurate`, this truncation is negligible for most practical use cases; but with `ROOT::Math::VavilovFast`, pay careful attention to this range limitation, especially if it is used for fitting purposes.

Parameter	Value
mean	$\gamma_{\text{EM}} - 1 - \ln(\kappa) - \beta^2/2$
variance	$\sigma^2 = \left(2 - \beta^2\right) \cdot (2 \cdot \kappa)^{-1}$
skewness	$\gamma_1 = \left(\frac{1}{2} - \frac{\beta^2}{3}\right) \cdot \left(\kappa^2 \cdot \sigma^3\right)^{-1}$
Kurtosis	$\gamma_2 = \left(\frac{1}{3} - \frac{\beta^2}{4}\right) \cdot \left(\kappa^3 \cdot \sigma^4\right)^{-1}$

Table A.4: Properties of the Vavilov distribution. Calculations of moments based [215, p. 216 ff., eq. 10 & 14] (cf. `ROOT::Math::Vavilov`).

A.3.5 Extended Information on Straggling functions

The correction introduced in Section 4.1.4, as given by Equation 4.24, may be only a rough approximation, as pointed out by Bichsel [101, p. 696]. Bichsel's calculations are based on simplified assumptions for f_k, using the relative occurrence of shell electrons and their respective binding energies (cf. [101, p. 697, tab. X]), which are, to first order, consistent with the values presented in Table A.13. However, a cross-check of these binding energies applied to Equation 1.6, yields approximate values for I that significantly deviate from those given in Table A.17. Readers interested in the relationship between f_k, I_k and Equation 1.6 (I) may refer to [24, 25, 26].
To calculate the expression for δ_2^{S} in Equation 4.24, *Hancock et al.* assumed [199, p. 16 ff., eq. 3]:

$$\delta_2^{\text{S}} = \frac{8}{3} \cdot \xi \cdot \text{F}(\beta) \quad \text{with} \quad \text{F}(\beta) = \sum_k I_k \cdot \underbrace{\left(\frac{Z_k}{Z}\right)}_{=f_k} \cdot \ln\left(\frac{2m_e c^2 \beta^2}{I_k}\right)$$
$$= \left[2.319 + 0.670 \cdot \ln(\beta)\right] \cdot 10^{-3}\,\text{MeV} \tag{A.23}$$

Here, the ratio of the number of electrons Z_k in the k-th shell to the total number of electrons Z approximates the oscillator strength f_k. Furthermore, it is assumed that for all shell electrons, $I_k < 2m_e c^2 \beta^2$ holds.
Unfortunately, no source exactly specifies how Equation 4.24 is calculated in their estimates. Assuming the validity of the δ_2^{S} expression, the following expression can be derived:

$$\delta_2^{\text{S}} = \frac{8}{3} \cdot \xi \cdot \sum_k I_k \cdot f_k \cdot \ln\left(\frac{2m_e c^2 \beta^2}{I_k}\right) = \frac{8}{3} \cdot \xi \cdot \sum_k I_k \cdot f_k \cdot \left[\underbrace{\ln\left(\frac{2m_e c^2}{I_k}\right)}_{\text{constant for } I_k < 2m_e c^2 \beta^2} + 2 \cdot \ln(\beta)\right]$$
$$\overset{\text{Si}}{=} \frac{8}{3} \cdot \xi \cdot \left[3.62042 + 1.10861 \cdot \ln(\beta)\right] \cdot 10^{-3}\,\text{MeV} \tag{A.24}$$
$$\overset{\text{Si}}{=} \frac{8}{3} \cdot 17.825\,\text{eV}\,\mu\text{m}^{-1} \cdot \frac{\Delta x}{\beta^2} \cdot \left[3620.42 + 1108.61 \cdot \ln(\beta)\right] \cdot \text{eV} \tag{A.25}$$

Here, the values for I_k and f_k are taken from Table A.14, for which $\sum_k f_k = 1$ and Equation 1.6 holds (the logarithmic summation amounts to about 169.526 , consistent with the value of I for **si**licon in Table A.17). Although the constants in Equation A.24 are of the same order as those in Equation A.23, a meaningful comparison cannot be made without a detailed derivation of the logarithmic term and its corresponding values.

A different approach from the convolution method presented in Equation 4.25 was proposed by *Findlay and Dusautoy* [218]. They approximated the influence of the correction term ([125]) as a sum of nine Gaussians [218, p. 531ff]:

$$\phi(\lambda_L) = \sum_{i=1}^{9} \frac{c_i \cdot \gamma_i}{\sqrt{\gamma_i^2 + b^2}} \text{e}^{-\frac{(\lambda_L - \lambda_i)^2}{\gamma_i^2 + b^2}} \quad \text{with} \quad b^2 = 2 \times 10^{-5}\,\text{MeV} \cdot Z^{\frac{4}{3}} \cdot \frac{\langle \Delta E \rangle}{\xi^2} \tag{A.26}$$

where λ_L is the Landau variable, $\xi(\Delta x, \beta)$ is defined by Equation 1.9, $\langle \Delta E \rangle$ is the mean energy loss, and c_i, λ_i, γ_i are constants defined in Table A.5.
The FWHM of the distribution is given by [218, p. 533]:

$$W = 4.022 + 0.3600 \cdot \text{H}(b) + 0.4320 \cdot \text{H}(b)^2 - 0.04088 \cdot \text{H}(b)^3 + 0.01677 \cdot \text{H}(b)^4 \quad \text{with} \quad \text{H}(b) = \ln\left(b^2 + 1\right) \tag{A.27}$$

and the peak (mode) of the distribution is at [218, p. 533]:

$$\lambda_{mode} = -0.2570 + 0.3318 \cdot \mathrm{H}(b) + 0.02510 \cdot \mathrm{H}(b)^2 - 0.001750 \cdot \mathrm{H}(b)^3 \tag{A.28}$$

Note that Equation A.26 does not fulfill the normalization condition in Equation 4.7; instead, the integral of the distribution amounts to 0.9916 [218, p. 533].

	1	2	3	4	5	6	7	8	9
c_i	0.0368	0.0843	0.0882	0.0647	0.0359	0.0164	0.0064	0.0021	0.0006
λ_i	-1.48	-0.738	0.170	1.33	2.95	5.39	9.40	16.8	30.8
γ_i	0.737	0.947	1.23	1.68	2.40	3.68	6.18	12.3	39.7

Table A.5: Parameters of the convolution method by *Findlay and Dusautoy* (Equation A.26). Taken from [218, p. 531, tab. 1].

A.3.6 Numerical Convolution

The numerical convolution algorithm is based on the fit tutorial `langaus.C` from the `ROOT` framework [172, 173]. The code has been adapted for general use with a PDF or (complementary) CDF (`Distribution::PCDF`), and is combined with a Gaussian (`ROOT::Math::normal_pdf`). The implementation is integrated into the `PCDF` framework [9].

```
double Distribution::NuNormalConv(const double *x,
                                  const double *parFunction,
                                  const double *sigma,
                                  const Const::PDtype &type) const
{
    if (!x || !parFunction || !sigma)
    {
        LOG(WARNING) << "PCDF::Distribution: [NuNormalConv]"
                     << " x, parFunction or sigma is nullptr";
        return 0.;
    }

    double sigma_pdf = sigma[0]; // sigma of convoluted normal distribution

    // Variables
    const double num_conv_steps = 1024.; // number of steps for convolution integral
    const double num_sigmas_conv = 5.;   // number of sigmas for normal distribution

    // Range of convolution integral
    double nSigma = num_sigmas_conv * sigma_pdf;
    double xlow = x[0] - nSigma; // lower limit
    double xupp = x[0] + nSigma; // upper limit

    double step = (2. * nSigma) / num_conv_steps; // step size

    double sum = 0.0; // sum of convolution integral

    // Convolution integral of Landau and Gaussian by sum
    for (double i = 1.0; i <= (num_conv_steps / 2); ++i)
    {
        // lower half
        double xxFac = step * (i - .5);
        double xx = xlow + xxFac; // x value of convolution integral

        // cumulative or probability density function
        double pcdf = this->PCDF(&xx, parFunction, type);
        sum += pcdf * ROOT::Math::normal_pdf(x[0], sigma_pdf, xx);

        // upper half
        xx = xupp - xxFac;
        pcdf = this->PCDF(&xx, parFunction, type);
        sum += pcdf * ROOT::Math::normal_pdf(x[0], sigma_pdf, xx);
    }

    if (std::fabs(sum) > 0.)
    {
        return (step * sum);
    }

    return 0.;
}
```

A.3.7 Quantifying Fit Models

This work employs several statistical methods to evaluate the GoF of models. A common approach is to minimize[5] the chi-squared (χ^2) statistic. When a model is applied repeatedly to independent data sets, χ^2-statistic is expected to follow a chi-squared distribution with k being the NDF [114, p. 36]:

$$\mathrm{PDF}_{\chi^2}(x \mid k) = \frac{\left(\frac{x}{2}\right)^{\frac{k}{2}-1} \cdot \mathrm{e}^{-\frac{x}{2}}}{2 \cdot \Gamma\left(\frac{k}{2}\right)} \tag{A.29}$$

where $\Gamma(x)$ denotes the gamma function (see Section A.3.3). This distribution has a mode at $max(k-2, 0)$, mean k, and variance $2k$ [114, p. 36 ff.]. Since k can vary between data sets, the reduced chi-squared[6] is often compared in comparison, which is given by the ratio χ^2/NDF.

If the fit model is only an approximation to the data-generating process, the χ^2-distribution may deviate from its central form. In such cases, the non-central chi-squared distribution (cf. [114, p. 110 ff.]) provides a better description, e.g. in the presence of unaccounted non-linearities.
The weighted least-squares method (neglecting correlations) defines the χ^2 as [219, p. 438]:

$$\chi^2 = \sum_i w_i \cdot (O_i - E_i)^2 \begin{cases} w_i = \frac{1}{\sigma_i^2} & \text{variance-weighted} \\ w_i = \frac{1}{E_i} & \text{Pearson's chi-squared} \\ w_i = \frac{1}{O_i} & \text{Neyman's chi-squared} \end{cases} \tag{A.30}$$

with O_i the observed value, E_i the expected value, and σ_i^2 being the variance of the i-th bin.

This definition is straightforward for binned data (histograms). For unbinned data objects with uncertainties in both coordinates (e.g. `ROOT::TGraphErrors`, `ROOT::TGraphAsymmErrors`), the "effective variance method" incorporates the x-error [172, 173] (see `ROOT::TGraph`):

$$\chi^2_{\mathrm{w/}e_x}(\lambda) = \sum_i \frac{\left[y_i - \mathcal{P}(x_i \mid \lambda)\right]^2}{e_{y,i}^2 + \left[\frac{1}{2} \cdot (e_{x,i}^{\mathrm{low}} + e_{x,i}^{\mathrm{up}}) \cdot \mathcal{P}'(x_i \mid \lambda)\right]^2} \tag{A.31}$$

where $\mathcal{P}(x_i \mid \lambda)$ is the model function, $\mathcal{P}'(x_i \mid \lambda)$ its derivative, $e_{y,i}$ denotes the asymmetric y-error taken according to the sign of the residual (lower if $y_i > \mathcal{P}(x_i \mid \lambda)$, otherwise upper), and $e_{x,i}^{\mathrm{low}}/e_{x,i}^{\mathrm{up}}$ are the lower/upper x-errors, respectively. If the fit option "`EX0`" is set, x-errors are ignored.

As an alternative, **M**aximum **L**ikelihood **E**stimation maximizes the likelihood (or, equivalently, minimizes the negative LLh (**L**og-**L**ikeli**h**ood)) of observing the data given a model. This method is particularly robust for low-statistics histograms, though care is required: empty bins in `ROOT` are not excluded automatically[7].

In the special case of efficiency fits (`ROOT::TEfficiency`), the `ROOT::TBinomialEfficiencyFitter` is commonly used, which automatically handles bins with zero trials (no statistic). The efficiency ($\epsilon_i(x_i \mid \lambda)$) of the i-th bin is modeled as $\mathcal{P}(x_i \mid \lambda)$, giving the joint likelihood (see Section 5.3.3) [220, p. 71, eq. 5.1]:

$$L(\lambda) = \prod_i \mathrm{PDF}_{\mathrm{binomial}}(m_i \mid N_i, \mathcal{P}(x_i \mid \lambda)) \tag{A.32}$$

where m_i successes are observed from N_i trials in the i-th bin.
Taking the logarithm yields (using the logarithm product rule):

$$\begin{aligned} \ln L(\lambda) &= \sum_i \ln\left(\mathrm{PDF}_{\mathrm{binomial}}(m_i \mid N_i, \mathcal{P}(x_i \mid \lambda))\right) \\ &= \sum_i \left[m_i \cdot \ln\left(\mathcal{P}(x_i \mid \lambda)\right) + (N_i - m_i) \cdot \ln\left(1 - \mathcal{P}(x_i \mid \lambda)\right)\right] \end{aligned} \tag{A.33}$$

[5] The minimizer `Minuit2` employing the `Migrad` algorithm (see `ROOT::Math::Minimizer`) is used throughout this thesis.
[6] It should be noted that the χ^2/NDF ratio alone can be misleading; thus, both the absolute value of χ^2 and the NDF should be reported for proper interpretation.
[7] To ignore empty bins, they must be excluded from the fit range or handled directly in the fit function (`ROOT::TF1`).

The likelihood-ratio test provides a GoF measure [171, p. 438]:

$$\begin{aligned}
\chi^2_{\text{LLh}} &= -2 \cdot \ln\left(\frac{L(\epsilon)}{L(\hat{\epsilon})}\right) \\
&= -2 \sum_i \left[\ln L(\epsilon_i) - \ln L(\hat{\epsilon}_i)\right] \\
&= -2 \sum_i \left[m_i \cdot \ln\left(\frac{\mathcal{P}(x_i \mid \lambda)}{\hat{\epsilon}_i}\right) + (N_i - m_i) \cdot \ln\left(\frac{1 - \mathcal{P}(x_i \mid \lambda)}{1 - \hat{\epsilon}_i}\right)\right] \\
&= -2 \sum_i \left[m_i \cdot \ln\left(\frac{N_i \cdot \mathcal{P}(x_i \mid \lambda)}{m_i}\right) + (N_i - m_i) \cdot \ln\left(\frac{N_i \cdot (1 - \mathcal{P}(x_i \mid \lambda))}{N_i - m_i}\right)\right]
\end{aligned} \tag{A.34}$$

which is compared to a χ^2-test (based on Equation A.31) on the same data set, represented as `ROOT::TGraphAsymmErrors`[8] obtained via `ROOT::TGraphAsymmErrors::BayesDivide`.

All fits in this work[9] are performed using the `ROOT` framework. Fit results are obtained from the `ROOT::TFitResult` object, returned by `ROOT` function `Fit` — inherent of each `ROOT` data object — when the fit option "`S`" is set.

[8] Take note that for a `ROOT::TGraphAsymmErrors` derived from `ROOT::TEfficiency`, the x-errors are defined by the corresponding bin width.

[9] Ignoring the testbeam analysis using `Corryvreckan` [168, 169].

A.4 Extended Information on Calibration

A.4.1 Extended Information on Fe-55 Model Calculation

Fe-55 Data Base Values

Shell Transition	E [eV]	ΔE [eV]	Intensity [%]	ΔIntensity [%]
L_α	640.0	0.0	0.419949	0.140388
K_α	5887.65	0.03	8.23713	0.613531
	5898.75	0.03	16.2789	1.19843
K_β	6490.00	0.0	3.28515	0.24929

Table A.6: JEFF-3.3 [181] data values of the most relevant Fe-55 energy lines (Auger-electron is excluded) extracted with JANIS 4 [179].

Shell Transition	E [eV]	ΔE [eV]	Intensity [%]	ΔIntensity [%]
L_α	640.0	0.0	0.66	0.1
K_α	5888.00	0.00	8.46	0.09
	5899.00	0.00	16.59	0.17
K_β	6490.00	0.00	3.4	0.04

Table A.7: JENDL/DDF-2015 [180] data values of the most relevant Fe-55 energy lines (Auger-electron is excluded) extracted with JANIS 4 [179].

Shell Transition	E [eV]	ΔE [eV]	Intensity [%]	ΔIntensity [%]
L_α	557.6039	55.88445	0.5349321	0.05308855
	640.4896	79.77364	0.1013559	0.01258908
	655.7200	86.88943	0.003599678	4.756329E-4
	678.8113	48.73113	0.1111887	0.008004016
K_α	5847.930	58.47930	8.345271	0.8570937
	5858.680	58.58680	16.36352	1.680601
K_β	6448.810	64.48810	0.9944567	0.1021348
	6450.120	64.50121	1.957168	0.2010093
	6499.050	64.99050	3.505678E-4	3.600476E-5
	6499.180	64.99180	5.130036E-4	5.268759E-5

Table A.8: ENDF/B-VIII.0 [182] data values of the most relevant Fe-55 energy lines (Auger-electron is excluded) extracted with JANIS 4 [179].

Derivation of the Integral of the Normal (complementary) CDF

To achieve the analytical form of Equation 6.7 from integrating Equation 6.5 following relations for the error function have to be considered:

$$\text{erfc}(x) = 1 - \text{erf}(x) \tag{A.35}$$
$$\text{erf}(-x) = -\text{erf}(x) \tag{A.36}$$
$$\lim_{x\to\infty} \text{erf}(x) = 1 \tag{A.37}$$
$$\lim_{x\to\infty} x \cdot \text{erfc}(x) = 0 \tag{A.38}$$
$$\frac{\mathrm{d}}{\mathrm{d}x}\text{erf}(x) = \frac{2}{\sqrt{\pi}}\mathrm{e}^{x^2} \tag{A.39}$$
$$\int \text{erf}(x)\mathrm{d}x = x \cdot \text{erf}(x) + \frac{\mathrm{e}^{-x^2}}{\sqrt{\pi}}\big(+C\big) \tag{A.40}$$

While the integration of the normal PDF ends in that of the normal (complementary) CDF (an error function), the integration of the complementary error function can be derived as follows. The first approach lies in the substitution of the inner function of the error function:

$$\begin{aligned}
\int \text{erfc}\left(\frac{x-\mu}{\sqrt{2}\sigma}\right)\mathrm{d}x &\overset{u=\frac{x-\mu}{\sqrt{2}\sigma}}{=} \sqrt{2}\sigma\int \text{erfc}(u)\mathrm{d}u \\
&\overset{A.35}{=} \sqrt{2}\sigma\left(\int 1\mathrm{d}u - \int \text{erf}(u)\mathrm{d}u\right) \\
&\overset{A.40}{=} \sqrt{2}\sigma\left(u - u\cdot\text{erf}(u) - \frac{\mathrm{e}^{-\mathrm{u}^2}}{\sqrt{\pi}}\right) \\
&\overset{A.35}{=} \sqrt{2}\sigma\left(u\cdot\text{erfc}(u) - \frac{\mathrm{e}^{-\mathrm{u}^2}}{\sqrt{\pi}}\right) \\
&\overset{u=\frac{x-\mu}{\sqrt{2}\sigma}}{=} \sqrt{2}\sigma\left(\frac{x-\mu}{\sqrt{2}\sigma}\text{erfc}\left(\frac{x-\mu}{\sqrt{2}\sigma}\right) - \frac{\mathrm{e}^{-\frac{(\mathrm{x}-\mu)^2}{2\sigma^2}}}{\sqrt{\pi}}\right) \\
&= (x-\mu)\cdot\text{erfc}\left(\frac{x-\mu}{\sqrt{2}\sigma}\right) - \sqrt{\frac{2}{\pi}}\sigma\mathrm{e}^{-\frac{(\mathrm{x}-\mu)^2}{2\sigma^2}}
\end{aligned} \tag{A.41}$$

Applying now the analytical form for the reparameterized complementary error function allows to derive the integral of the normal (complementary) CDF, which is referred to as "Super (complementary) CDF". Equation A.41 can be rearranged with Equation A.35 to fit the form of Equation 6.2. With consideration of Equation 6.1 and the relations of Equation A.37 and Equation A.38 the following analytical form can be derived:

$$\begin{aligned}
\int_x^\infty \frac{1}{2}\text{erfc}\left(\frac{x'-\mu}{\sqrt{2}\sigma}\right)\mathrm{d}x' =& (x'-\mu)\cdot\text{CDF_C}_{\text{normal}}(x' \mid \mu,\sigma) - \sigma^2\cdot\text{PDF}_{\text{normal}}(x' \mid \mu,\sigma)\Big|_x^\infty \\
=& \underbrace{\lim_{x'\to\infty}(x'-\mu)\cdot\text{CDF_C}_{\text{normal}}(x' \mid \mu,\sigma) - \sigma^2\cdot\text{PDF}_{\text{normal}}(x' \mid \mu,\sigma)}_{=0} \\
&+ (\mu-x)\cdot\text{CDF_C}_{\text{normal}}(x \mid \mu,\sigma) + \sigma^2\cdot\text{PDF}_{\text{normal}}(x \mid \mu,\sigma) \\
=& (\mu-x)\cdot\text{CDF_C}_{\text{normal}}(x \mid \mu,\sigma) + \sigma^2\cdot\text{PDF}_{\text{normal}}(x \mid \mu,\sigma)
\end{aligned} \tag{A.42}$$

A.4.2 Extended Information on Injection Studies

To evaluate the performance and limitations of the injection circuitry in the MuPix10 sensor, a series of dedicated injection studies were conducted. The analysis investigates the accuracy of the injection process itself and examines how different configuration parameters affect the analog pulse characteristics of the MuPix10. For this purpose, the same pixel (1,0) was consistently used across all measurements to ensure comparability. Two instruments, a digital multimeter (*Keithley 2001* [221]) and an oscilloscope (*Tektronix DPO7254C* [222]), were employed for all measurements.

Injection Voltage Level Accuracy

The accuracy of the injection voltage level is assessed between the input setting (SOLL) and the actual measured voltage output (IST). The measurement can be performed in two modes, the fixed voltage level mode and the pulsed mode, whereas the latter is more representative of the actual injection conditions during operation. The results of both measurement modes are presented in Plot A.6. To be observed is that in both modes, the injection voltage level deviates from the target voltage in the order of a few millivolts, with a slightly larger deviation in the pulsed mode, which can arise from the larger uncertainty in assessing the voltage level during the pulse. A significant deviation is observed at low injection voltages below approximately 100 mV, attributed to an offset arising form the OpAmp.

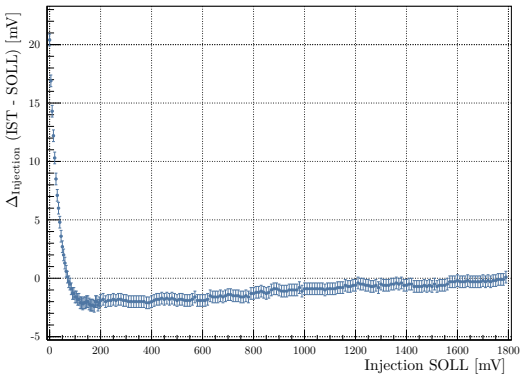

(a) Injection voltage SOLL versus IST in fixed voltage level mode.

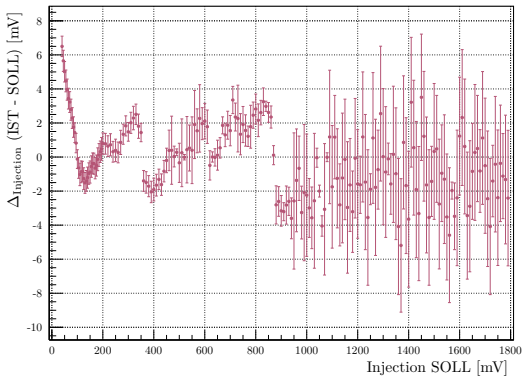

(b) Injection voltage SOLL versus IST in pulsed mode.

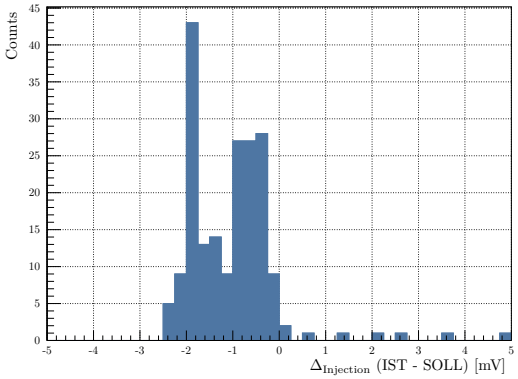

(c) Absolute deviation of the injection voltage from the target voltage in fixed voltage level mode.

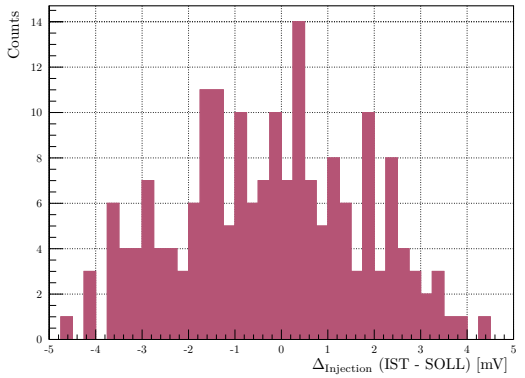

(d) Absolute deviation of the injection voltage from the target voltage in pulsed mode.

Plot A.6: Measurement of injection voltage accuracy by applying a fixed injection target (SOLL) voltage and measuring the actual (IST) voltage.

Injection Duration: Discharging and Charging

The injection pulse is generated by applying a voltage level to the pixel's injection capacitance, being released on command via the CMOS analog switch, dropping the voltage back to zero, and subsequently recharging it to the target voltage after a defined injection duration. The injection duration, is measured as the time interval between the 90 % falling edge and the 10 % rising edge of the injection pulse. The actual linearity of the injection duration with respect to the target duration is presented in Plots A.7a and A.7b, showing slight deviation on the $\mathcal{O}(200\,\mathrm{ns})$ level, which may arise from the measurement method and the limitations of the measurement methods of the oscilloscope. In addition, the charging — time period between 10 % to 90 % of signal rise — and discharging times — time period between 90 % to 10 % of signal fall — of the injection pulse are investigated as a function of the injection voltage, see Plots A.7c and A.7d. In both cases, the times increase steeply between 100 mV and about 200 mV, subsequently starting to saturate. Whereas the charging behavior must be taken into account when selecting a injection frequency, the discharging behavior can directly impact the rising signal edge of the analog pulse shape.

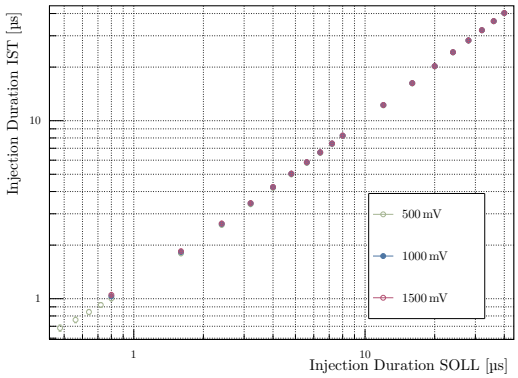

(a) Injection duration SOLL versus IST.

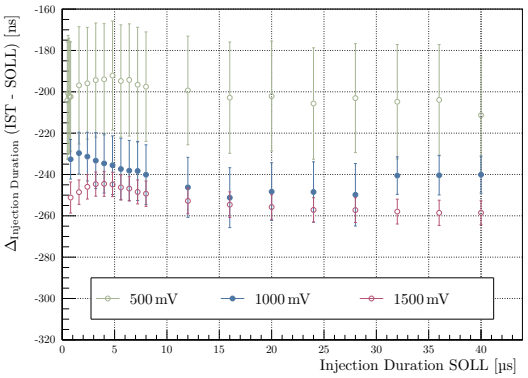

(b) Absolute deviation of the injection duration from the target duration.

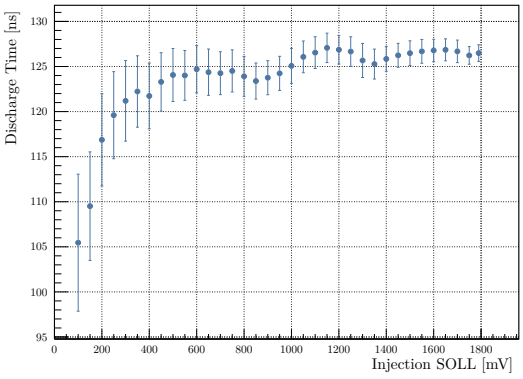

(c) Discharging time as function of the injection voltage.

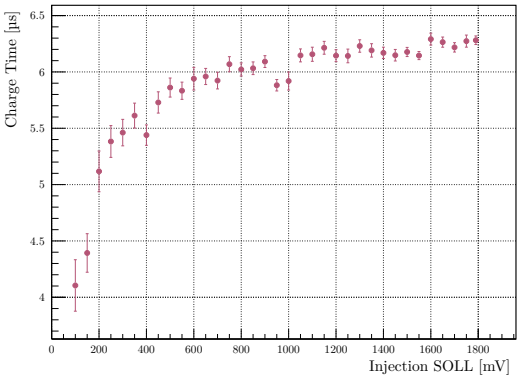

(d) Charging time as function of the injection voltage.

Plot A.7: The injection pulse duration, discharging and charging time as a function of the injection voltage.

Injection Duration influence on Analog Pulse Shape

The analog signal pulse of the MuPix10 can be accessed via the AmpOut test point, allowing for a direct study of the pulse shape characteristics under varying injection configurations. The pulse shape is characterized by four main parameters: amplitude, FWHM, rise and fall. The latter two are defined as the ratios of the amplitude of the rise and fall time, respectively, both measured between 10 % and 90 % of the target voltage.

This study should explore how the injection duration influences the analog pulse shape parameters, using a moderate injection voltage of 0.5 V avoiding extreme long pulses, while injecting a frequency of 1 kHz. Plot A.8 presents the results of this study, showing that the injection duration has a significant impact on all pulse shape parameters, if chosen too low. For injection duration values significantly shorter < 100 ns, which is still within the falling edge of the injection pulse, the injection pulse cannot fully discharge the injection capacitance, leading to a reduced amplitude and distorted pulse shape. Afterwards the injection duration enters the domain (up to about 14 µs) of the analog pulse shaping time, affecting in the lower regime the amplitude and rise and in the higher regime the FWHM and fall time. If the injection duration is chosen to short the charging of the injection capacitance during the analog pulse shaping time, withdraws charge from the system leading to a reduced amplitude and shortening the effective pulse length. Above all these effects saturate, and the pulse shape parameters reach constant values for injection durations above approximately 4 µs. Giving a safety margin, an injection duration of 10 µs is chosen for all further injection studies.

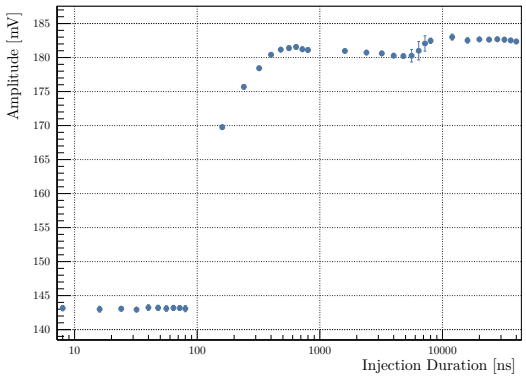

(a) AmpOut amplitude as function of the injection duration.

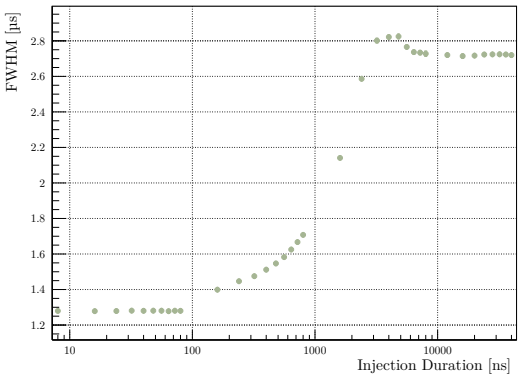

(b) AmpOut FWHM as function of the injection duration.

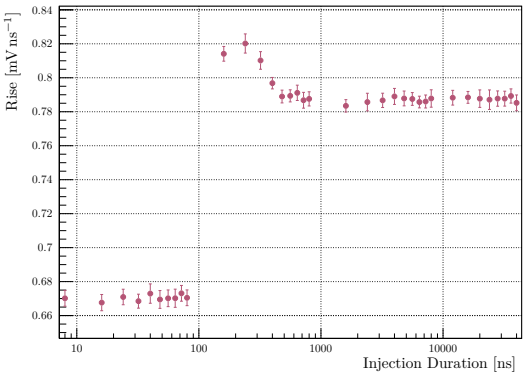

(c) AmpOut rise as function of the injection duration.

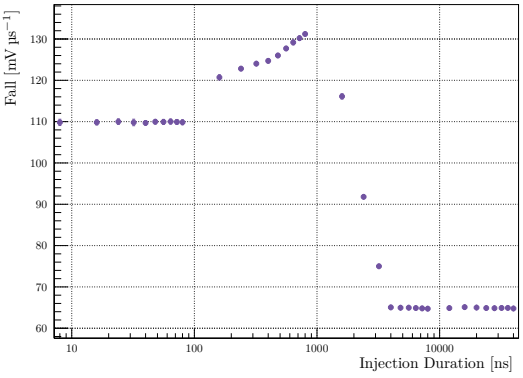

(d) AmpOut fall function of the injection duration.

Plot A.8: The AmpOut pulse shape parameters as a function of the injection duration.

Injection Frequency influence on Analog Pulse Shape

From the previous study, an injection duration of 10 µs is chosen to ensure undistorted pulse shapes. Now the influence of the injection frequency on the analog pulse shape is investigated by enforcing an extreme long signal pulse via a high injection voltage of 1.6 V.

Plot A.9 presents the results of this study, showing the influence of the injection frequency on all pulse shape parameters. Whereas, amplitude and rise are not being significantly affected, the fall starts to steeply decrease, effectively increasing the FWHM for injection frequencies above approximately 10 kHz. Here, the analog pulses can get so long that a subsequent injection starts with the falling edge, whereby new charge injected into the system prolongs the pulse. The problem is severe, as a subsequent injection pulse will be failed to be recognized by the readout, leading to a loss of efficiency. For this reason, a maximum injection frequency of 10 kHz is chosen for all injection studies, maximizing the statistical significance while avoiding inefficiencies.

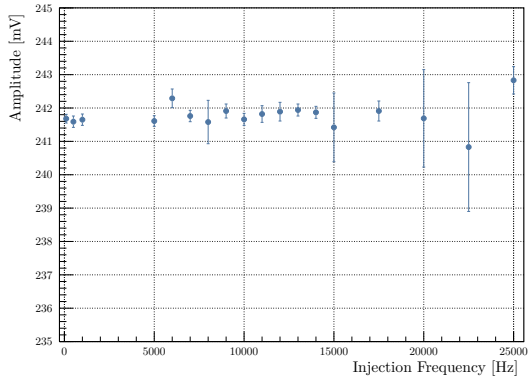

(a) AmpOut amplitude as function of the injection frequency.

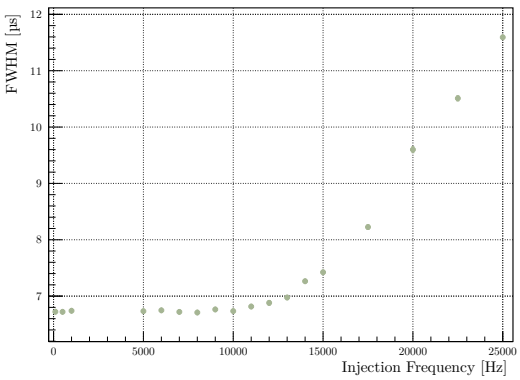

(b) AmpOut FWHM as function of the injection frequency.

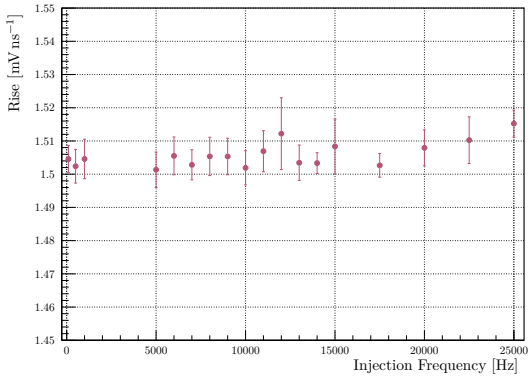

(c) AmpOut rise as function of the injection frequency.

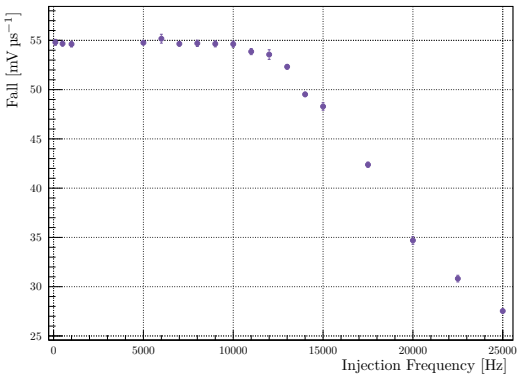

(d) AmpOut fall as function of the injection frequency.

Plot A.9: The AmpOut pulse shape parameters as a function of the injection frequency.

Injection Pixel Matrix Size influence on Analog Pulse Shape

The final study investigates the influence of the injection pixel matrix size on the analog pulse shape, again using a long signal pulse generated by a high injection voltage of 1.6 V and a long injection duration of 10 µs, applied at a moderate injection frequency of 1 kHz to avoid being affected by bandwidth limitations.

Plot A.10 presents the results of this study, showing the influence of the injection pixel matrix size on all pulse shape parameters. Whereas significant influence is only observable for matrix sizes exceeding 1000 pixel for the amplitude, fall and FWHM, the rise time starts to be affected already for small matrix sizes above about 10 pixel. This can be associated to an increasing discharge time of the effectively increasing injection capacitance, as all pixel injection capacitances are charged to first order in parallel. For timing studies, where the rise time is of importance, small injection matrix sizes should be chosen to avoid distorted pulse shapes. In the case, where only the amplitude is of interest, larger injection matrix sizes may be chosen without significant impact, which has to be validated by dedicated study applied to various injection voltages to reconstruct the effect on the full response curve.

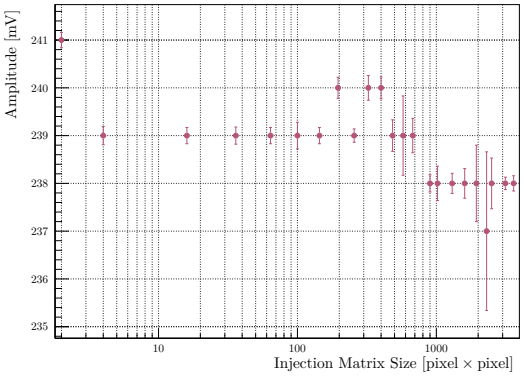

(a) AmpOut amplitude as function of the injection pixel matrix size.

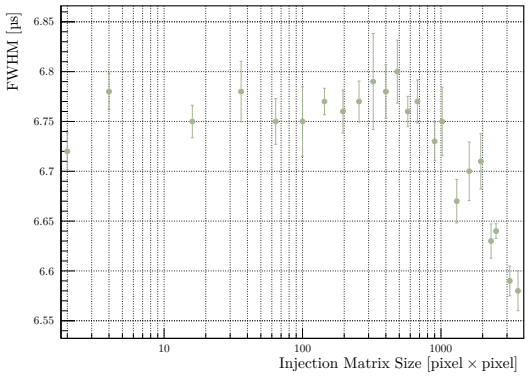

(b) AmpOut FWHM as function of the injection pixel matrix size.

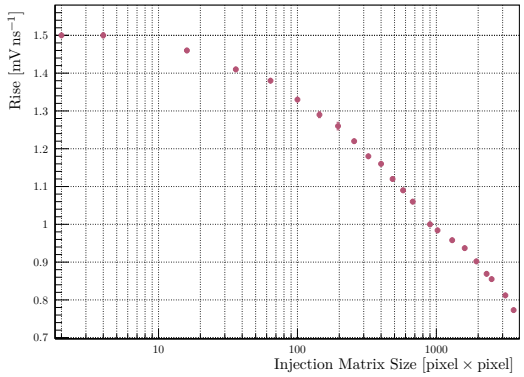

(c) AmpOut rise as function of the injection pixel matrix size.

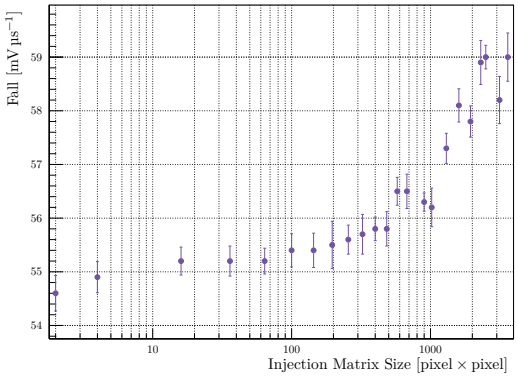

(d) AmpOut fall as function of the injection pixel matrix size.

Plot A.10: The AmpOut pulse shape parameters as a function of the injection pixel matrix size.

Injection Pixel Matrix Size influence on the Detector Response

In addition to analyzing the analog pulse shape, the effect of the injection pixel matrix size on the overall detector response is investigated. The response of the same pixel is measured for varying injection matrix sizes, ranging from 4×4 up to a 30×30 pixel matrix, with each step increasing the matrix by two columns and two rows.

Plot A.11 summarizes the results, illustrating how the injection matrix size influences all six response model parameters. Only deviations exceeding the binning resolution threshold ($1/\sqrt{12}$) and the fit uncertainty are considered significant. The influence remains negligible for all parameters up to matrix sizes of approximately 20×20 pixels,

while parameters in the saturation domain become more affected beyond this point. Consequently, a maximum injection matrix size of 20×20 pixels is adopted for all subsequent studies to ensure sufficient charge injection without a significant impact on the detector response.

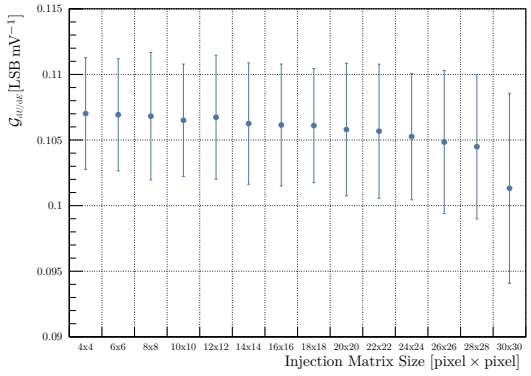

(a) Gain ($\mathcal{G}_{dU/dE}$) versus injection pixel matrix size.

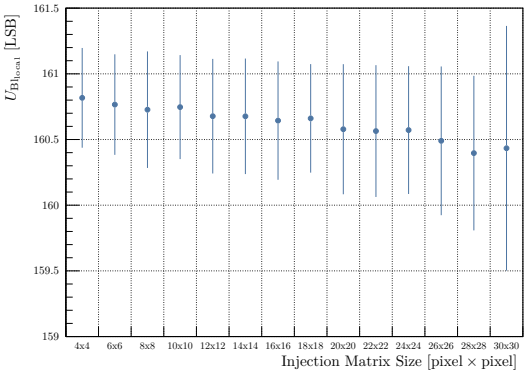

(b) Local baseline ($U_{\mathrm{BL,\,local}}$) versus injection pixel matrix size.

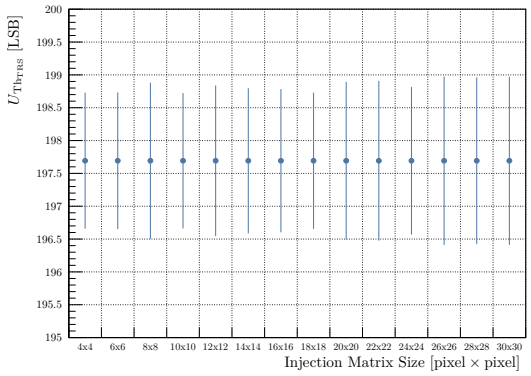

(c) Transition threshold ($U_{\mathrm{Th,\,TRS}}$) versus injection pixel matrix size.

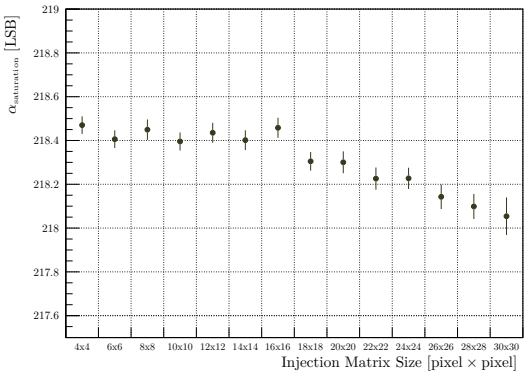

(d) Saturation threshold ($\alpha_{\mathrm{saturation}}$) versus injection pixel matrix size.

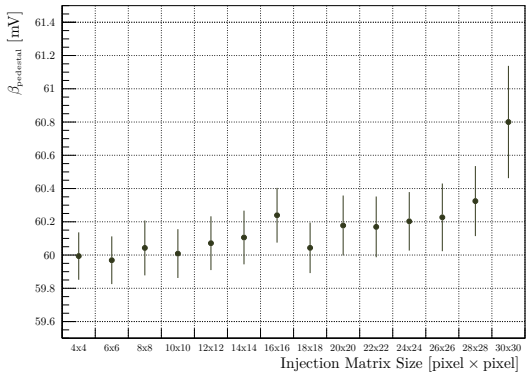

(e) Pedestal ($\beta_{\mathrm{pedestal}}$) versus injection pixel matrix size.

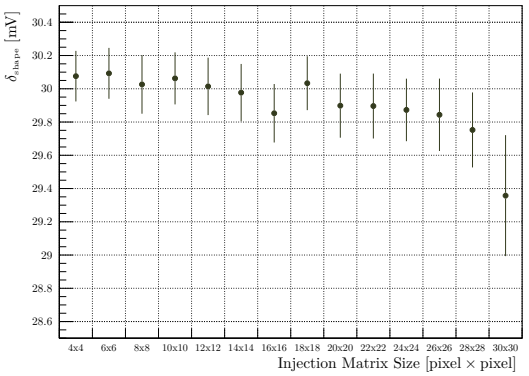

(f) Shape parameter (δ_{shape}) versus injection pixel matrix size.

Plot A.11: The response parameter of the same pixel in MuPix10 as a function of the injection pixel matrix size. Parameters associated with the linear domain are colored in light blue, the parameters associated with the saturation domain are colored in dark green, see Equation 6.14.

A.5 Sensor Configuration

A.5.1 DAC Settings

Bias Voltage	DAC	Function	DAC Value	
			high-gain	*low-gain*
VNPix	6 bit	Main current source for the CSA	0xa	0x12
VCascPix	(fixed)	CSA cascode voltage	-	-
VPLoadPix	6 bit	Defines feedback capacitance C_f and amplifier load	0x2	0xa
VNFBPix	6 bit	Defines resistive feedback R_f	0x5	0x4
VNFollPix	6 bit	Current source for feedback stabilization	0x2	0xc
VNBiasPix	6 bit	n-well bias restoration	0x0	0x0
BLPix	8 bit	Baseline for analog signal transmission	0x8e	0x70 (0x71)†
BLResPix	6 bit	Baseline restoration	0x2	0x14
VNOutPix	6 bit	Current source for signal transmission	0x5	0xa

Table A.9: The bias DACs of the analog pixel cell.†: Deviating DAC value for MP10-T50-S300-2 corresponds to same voltage level.

Bias Voltage	DAC	Function	DAC Value	
			high-gain	*low-gain*
VPComp1	6 bit	Current source for the first comparator	0xa	0x5
VPComp2	6 bit	Current source for the second comparator	0xa	0x5
BLDig	8 bit	Baseline for digital signal transmission	0xa4	0x46 (0x47)†
BLResDig	6 bit	Baseline restoration	0x2	0x5
ThLow	8 bit	Threshold level of the first comparator	variable > BLDig	
ThHigh	8 bit	Threshold level of the second comparator	variable > BLDig	
En2thres	1 bit	Enable signal for the second threshold comparator	0x1	0x1
VNDel	6 bit	Current source for the edge detector	0xa	0xa
VPDAC	6 bit	Current source for the threshold tuning	0x0	0x0
VPTimerDel	6 bit	Readout-buffer delay cell	variable	
VNTimerDel	6 bit	Power for delay cell	variable	

Table A.10: The bias DACs of the periphery pixel cell.†: Deviating DAC value for MP10-T50-S300-2 corresponds to same voltage level.

Bias Voltage	**DAC**	**Effect**
VPVCO	6 bit	Bias voltage for the VCO
VNVCO	6 bit	Bias of the charge pump for the VCO
VPPump	6 bit	Bias voltage for the charge pump
EnablePLL	1 bit	Enable signal for the phase detector of the PLL
Invert	1 bit	Invert signal for the phase detector of the PLL
timerend	4 bit	Clock divider of the readout FSM
resetckdivend	4 bit	Defines number of comma words for synchronization
slowdownend	4 bit	Defines the number of wait cycles of the priority encoder
ckdivend	6 bit	Clock divider for TS1
ckdivend2	6 bit	Clock divider for TS2
sendcounter	6 bit	Set 24 bit counter mode for FSM
maxcycend	6 bit	Defines the maximum number of read cycles for the RCU
V(P/N)Dcl	6 bit	global DCL bias
V(P/N)DelDcl	6 bit	Delay of DCL clock
V(P/N)DelDclMux	6 bit	Delay of DCL multiplexer clock
VNLVDS	6 bit	Bias voltage for the LVDS driver
VNLVDSDel	6 bit	Bias voltage of the pre-emphasis of the LVDS driver
V(P/N)DelPreEmp	6 bit	Delay of the pre-emphasis
Serializer_reset_n	1 bit	Reset signal for the serializer
Aurora_reset_n	1 bit	8 bit/10 bit encoder reset

Table A.11: The bias DACs for the PLL, FSM, DCL and LVDS driver.

A.5.2 Test Points & Powering

Sensor ID	Config	Supply		ref_vss	Analog Voltage Levels [mV]					Digital Voltages Levels [mV]		
		V [mV]	I [mA]	[hex]	*gnda*	*vssa*	*vdda*	VSSA	VDDA	*gndd*	*vddd*	VDDD
MP10-T50-S300-1	*high-gain*	2000	426.4	0xc5	119	1321	1929	1202	1810	70	1944	1874
					118	1323	1930	1205	1812	69	1945	1876
	low-gain (Lab)	2235	596.7	0xba	241	1246	2041	1005	1800	57	2197	2140
					237	1249	2046	1012	1809	57	2197	2140
	low-gain (TB)	-	-	0xb8	233	1237	2040	1004	1807	56	2180	2124
MP10-T50-S300-2	*high-gain*	2010	427.6	0xc8	132	1332	1936	1200	1804	72	1951	1879
					130	1334	1939	1204	1809	71	1952	1881
	low-gain (Lab)	2250	588.7	0xbc	256	1258	2049	1002	1793	57	2210	2153
					252	1261	2054	1009	1802	57	2210	2153
	low-gain (TB)	-	-	0xbb	246	1250	2040	1004	1794	56	2180	2124
MP10-T50-S20-1	*high-gain*	2000	441	0xc6	124	1324	1930	1200	1806	71	1943	1872
					122	1325	1932	1203	1810	70	1944	1874
	low-gain (Lab)	2235	610.9	0xb9	242	1243	2046	1001	1804	55	2198	2143
					238	1246	2051	1008	1813	55	2199	2144
	low-gain (TB)	-	-	0xb8	232	1239	2040	1007	1808	54	2170	2116
MP10-T60-S300-1	*high-gain*	1990	411.1	0xc2	113	1316	1921	1203	1808	69	1932	1863
					111	1318	1923	1207	1812	69	1933	1864
	low-gain (Lab)	2220	574	0xb3	226	1225	2034	999	1808	57	2179	2122
					223	1227	2039	1004	1816	57	2179	2122
	low-gain (TB)	-	-	0xb3	221	1223	2030	1002	1809	55	2160	2105
MP10-T70-S300-1	*high-gain*	2010	428.6	0xc3	126	1329	1937	1203	1811	72	1953	1881
					123	1331	1940	1208	1817	71	1954	1883
	low-gain (Lab)	2260	600	0xb5	252	1256	2054	1004	1802	58	2220	2162
					249	1258	2059	1009	1810	58	2220	2162
	low-gain (TB)	-	-	0xb4	244	1247	2050	1003	1806	60	2200	2140
MP10-T100-S300-1	*high-gain*	2000	448.5	0xc6	122	1322	1928	1200	1806	76	1938	1862
					120	1324	1930	1204	1810	75	1939	1864
	low-gain (Lab)	2240	614.6	0xbb	246	1245	2041	999	1795	58	2201	2143
					242	1247	2046	1005	1804	58	2200	2142
	low-gain (TB)	-	-	0xb9	235	1236	2040	1001	1805	57	2190	2133

Table A.12: Sensor biasing configurations for the *high-gain* & *low-gain* settings (Lab) (**Lab**oratory) and (TB) (**T**est **B**eam) for all DUTs. Measurement values are split for TP1 & TP2, whereas values indicate deviations in the configurations. *Values* represent the corresponding *high-gain* & *low-gain* of a supply voltage, respectively, and VALUES the supply voltage (level difference) itself.

A.6 General Properties

A.6.1 Binding & Ionization Energies of Silicon

Calculated values (†) from EADL in Table A.13 can be found in the file "G4AtomicShells_XDB_EADL.cc" of `Geant4` [196] and values from PAS are congruent to the ones in the file "G4AtomicShells.hh" of `Geant4` [196].

Shell	$\frac{e^-}{\text{Shell}}$	**Database Value** [eV]	
		XDB/EADL	PAS
$K-1s$	2	1839	1844
L_1-2s	2	149.7	154.0
$L_2-2p_{1/2}$	2	99.82	104.0
$L_3-2p_{3/2}$	4	99.42	104.0
M_1-3s	2	7.6†	13.46
$M_2-3p_{1/2}$	2	3.0†	8.151

Table A.13: Binding energies of the electron shells in silicon. Values are taken from [223, p. 1-9, tab. 1-2.] for values of XDB and from EADL [196] (based on [224]) for values (†) and from [225, p. 338, tab. A1.A] for PAS.

$Z \cdot f_k$	$I_k = \hbar \cdot \omega_k$ [eV]	E_k [eV]
1.631	3206.1	1844.1
2.094	586.4	154.04
6.588	186.8	103.71
2.041	23.52	13.46
1.646	14.91	8.1617

Table A.14: The sub-shell occupation $Z \cdot f_k$, corresponding sub-shell I value I_k and sub-shell binding energy E_k for Si with I = 169.5. Taken from ICRU (2005) [226, p. 135, tab. 6.2] (Draft version February 11, 2004) (cf. [227, p. 257, tab. 7.1]).

Ion Charge	**Ionization Energy** [eV]	**Uncertainty** [eV]
0	8.15168	0.00003
+ 1	16.34585	0.00004
+ 2	33.49300	0.00009
+ 3	45.14179	0.00007
+ 4	166.767	0.003
+ 5	205.279†	0.005
+ 6	246.57†	0.05
+ 7	303.59†	0.05
+ 8	351.28†	0.06
+ 9	401.38†	0.04
+ 10	476.273†	0.019
+ 11	523.415‡	0.007
+ 12	2437.65805‡	0.00017
+ 13	2673.177958‡	0.000017

Table A.15: NIST atomic spectra database ionization energies data for silicon [228]. †: "This level was determined by interpolation or extrapolation of known experimental values or by semi-empirical calculation; its absolute accuracy is reflected in the number of significant figures assigned to it". ‡: Theoretical value.

A.6.2 Particle Properties

	Symbol	Mass [MeV c^{-2}]	Mean Lifetime	Charge [e]	Spin
electron	e^-	0.51099895000 ± 0.00000000015	> 6.6 × 10^{28} yr	-1	$\frac{1}{2}$
positron	e^+			+1	
muon	μ^-	105.6583755 ± 0.0000023	(2.196 981 1 ± 0.000 002 2) µs	-1	$\frac{1}{2}$
antimuon	μ^+			+1	
pion-minus	π^-	139.57039 ± 0.00018	(26.033 ± 0.005) ns	-1	0
pion-plus	π^+			+1	
pion-zero	π^0	134.9768 ± 0.0005	(84.3 ± 1.3) as	0	0
photon	γ	0	stable	0	1

Table A.16: Particle properties used for calculations within this thesis. The values are taken from the Particle Data Group [14].

A.6.3 General Material Property Values

The corresponding values of I are expected to be based on the ICRU report 49 (1993) [229, tab. 1.1, 1.2, 2.8] and ICRU report (37) (1984) (based on [230]), which have been updated in the ICRU report 73 (2005) [226] that small correction to the present-day standard of ICRU report 1993.

	N_2	Al	Si	SiO_2	Kapton	Epotek	G10	Air
Z/A [mol/g]	≈ 0.4998	≈ 0.4818	≈ 0.4985	0.49930	0.51264	0.53409	0.51176	0.49919
ρ [g cm^{-3}]	0.001165	2.699	2.329	2.200	1.420	1.190	1.800	0.001205
I [eV]	82.0	166.	173.	139.2	79.6	76.7	110.4	85.7
	(82 ±2)	(166 ±2)	(173 ±3)	—	—	—	—	—
	78.5†	158.3†	169.5†	—	—	—	—	—
X_0 [cm]	32600	8.897	9.370	12.29	28.57	34.64	17.87	30390
$\hbar\omega_p$ [MeV]	0.70	32.86	31.05	30.20	24.59	22.97	27.66	0.71
a	0.15349	0.08024	0.14921	0.08408	0.15972	0.42698	0.12971	0.10914
k	3.2125	3.6345	3.2546	3.5064	3.1921	3.0000	3.0000	3.3994
$\zeta_0 = x_0$	1.7378	0.1708	0.2015	0.1500	0.1509	0.2000	0.2000	1.7418
$\zeta_1 = x_1$	4.1323	3.0127	2.8716	3.0140	2.5631	2.0000	3.0000	4.2759
$C_d = \overline{C}_d$	10.54	4.2395	4.4355	4.0560	3.3497	3.4112	3.7685	10.5961
δ_0	0.0	0.12	0.14	0.00	0.00	0.00	0.00	0.00
	[231]	[232]	[32]	[233]	[234]	[235]	[236]	[237]

Table A.17: Material properties used for calculation within this thesis. The values are taken from the Particle Data Group [231, 232, 32, 233, 234, 235, 236, 237]. Values in parenthesis taken from ICRU report 49 (1993) [229, p. 2.8], † indicated values taken from ICRU report 73 (2005) [226].

A.6.4 The πM1 Beamline Properties

The πM1 beamline at **P**aul-**S**cherrer **I**nstitute is a high-intensity, low-momentum beamline for pions, muons, and electrons. Its characteristics are summarized in Table A.18.

Parameter	**Value**
Total path length	21 m
Momentum range	100 MeV c^{-1} to 500 MeV c^{-1}
Solide angle	6 msr
Momentum acceptance (FWHM)	2.9 %
Momentum resolution	0.1 %
Dispersion at focal plane	7 cm/%
Horizontal spot size on target (FWHM)	15 mm
Vertical spot size on target (FWHM)	10 mm
Horizontal Angular Divergence on target (FWHM)	35 mrad
Vertical Angular Divergence on target (FWHM)	25 mrad

Table A.18: The characteristics of the πM1 beamline at **P**aul-**S**cherrer **I**nstitute [159].

List of Figures

List of Plots

List of Tables

Glossary

ε_0 : The vacuum permittivity in [F m^{-1}]. It is defined as $\varepsilon_0 = 8.854\,187\,812\,8 \times 10^{-12}$ F m^{-1} [14]. 21, 59, 61, IX

$\varepsilon_{\mathbf{Si}}$: The relative permittivity of silicon which is unitless. See Table 2.1. 21, 61

ε_r : The relative permittivity of a material which is unitless given by $\varepsilon_r = \frac{\varepsilon}{\varepsilon_0}$, where ε is the absolute permittivity of the material and ε_0 is the vacuum permittivity. 59

A : The mass number of a nucleus in [g mol^{-1}]. 5, X

C_d : The capacitance of the pixel diode in [fF]. See Section 3.2.2. 63, 64

C_f : Feedback capacitance of the charge sensitive amplifier is nominal 1.6 fF [90, p. 2493, tab. 2], but is adjustable via DAC *VPLoadPix*. C.f. Section 3.3.1 187

E_C : The energy of the conduction band edge of a semiconductor in [eV]. 14, 15, 22

E_F : The Fermi energy of a doped semiconductor in [eV]. 15, 16

E_V : The energy of the valence band edge of a semiconductor in [eV]. 14, 15, 22

E_f : The intrinsic Fermi energy of a semiconductor in [eV]. 15

E_g : The band gap energy of a semiconductor in [eV]. For silicon at 300 K it is about 1.12 eV. See Table 2.1. 14, 17

I : The mean excitation energy of a medium given in [eV] . 4, 5, 50, 56, 175, 190, 191, VII

IV : The current-voltage characteristic of a semiconductor. See Section 2.3.3. 23, 35

I_k : Excitation energy of the k-th atomic shell of a material in [eV]. 4, 56, 175, 190, VII

M : The particle mass in [MeV c^{-2}]. 3, 5, 49, 165, X

N_A : The Avogadro constant $6.02214076 \times 10^{23}$mol^{-1} [14]. 3, 5

N_C : The effective density of states in the conduction band of a semiconductor in [cm^{-3}]. For silicon at 300 K it is about 3.05 × 10^{19} cm^{-3} [17, p.268, eq. 8.16]. 15

N_V : The effective density of states in the valence band of a semiconductor in [cm^{-3}]. For silicon at 300 K it is about 2.55 × 10^{19} cm^{-3} [17, p.268, eq. 8.16]. 15

R_f : Feedback resistance of the charge sensitive amplifier in [MΩ to GΩ], adjustable via DAC *VNFBPix*. C.f. Section 3.3.1. 187

T : Temperature in [K]. 15, 18, 20, 60, 61, 64, IX

T_n : Unitless temperature ratio, defined in Equation 2.10 where T is the temperature in [K]. This is used to normalize the temperature for semiconductor properties. 19, 169

U_{bi} : The built-in potential of a semiconductor in [V]. 22

$W_{\mathbf{FWHM}}$: The FWHM of a energy loss distribution. 56

W_{pair} : The energy required to create an electron-hole pair in a semiconductor in [eV]. See Table 2.1. 17

X_0 : The radiation length of a material in [cm]. 8, 11, 191

Z : The atomic number of a nucleus. 5, 9, 175, 190, X

Z/A : The ratio of the atomic number Z to the mass number A of a nucleus in [mol g^{-1}]. 3, 4, 191

$\Delta E_{\mathbf{MPV}}$: The most probable energy loss of a particle in a material, which is defined by Equation 4.9 in [MeV]. 49, 50, 52–56, 111, 113, 140, 141, 172, 174, III

Δx : The thickness of a material a particle is traversing. 3, 5, 7–9, 48–52, 56, 57, III

β : The relative velocity of a particle with respect to the speed of light. It is defined as $\beta = \frac{v}{c}$, where v is the velocity of the particle and c is the speed of light in vacuum. 3, 5, 8, 50, 54, 151, 156, 165, 174, X

$\beta\gamma$: The product of the relative velocity β and the Lorentz factor γ. It is defined as $\beta\gamma = \frac{v}{c\sqrt{1-\frac{v^2}{c^2}}}$, where v is the velocity of the particle and c is the speed of light in vacuum. 4–7, 49, 50, 57, III

$\delta(\beta\gamma)$: The density correction factor, which is defined by Equation 1.10. 6, 7, 50

$\delta_2^{\mathbf{S}}$: The Shulek factor defined by Equation 4.24. 56, 57, 175

γ : The Lorentz factor $\gamma = \frac{1}{\sqrt{1-\beta^2}}$, where β is the relative velocity of a particle with respect to the speed of light. 3, 5, 7, 165, X

γ_{EM} : The Euler-Mascheroni constant. Defined to be about $\gamma_{\text{EM}} \approx 0.577215664901532860...$ [14]. 54, 174, 175

$\hbar$: The reduced Planck constant $\hbar = h/2\pi = 1.054\,571\,817 \times 10^{-34}$ J s [14]. 15

$\hbar\omega_p$: Plasma energy of a material in [eV]. 5, 50, 191

κ : The κ factor defined by Equation 4.10. 50, 51, 54, 55, 140, 143, 173, 174, III

λ_L : The Landau parameterization defined by Equation 4.12, which is dimensionless. 52, 55, 173, 175

$\mathcal{E}$: The electric field strength. 18, 21, 60

$\mathcal{F}$: The Fano factor is a measure of the statistical fluctuation of the number of electron-hole pairs created in a semiconductor by incident radiation. 17

$\mathcal{M}_0$: The mean number of collisions. 3, 7, 48, 49, 53, 57, 171

$\mathcal{N}$: The total carrier concentration of a semiconductor in [cm^{-3}]. It is defined as $\mathcal{N} = \mathcal{N}_D + \mathcal{N}_A$, where $\mathcal{N}_D$ is the donor concentration and $\mathcal{N}_A$ is the acceptor concentration. 16, 18, 19, 169

$\mathcal{N}_A$: The acceptor concentration of a semiconductor in [cm^{-3}]. 16, 19–22, X

$\mathcal{N}_D$: The donor concentration of a semiconductor in [cm^{-3}]. 16, 19, 21, 22, X

$\mathcal{T}$: The kinetic energy of a particle, which is the energy that it possesses due to its motion. It is defined as $T = \frac{1}{2}Mv^2$, where M is the mass of the particle and v is its velocity. 3, 7, 10, 17, 48, 55, 68, 165, V

$\mathcal{T}_{cut}$: Restricted kinetic energy transfer cut-off value in a single collision with the condition $\mathcal{T}_{cut} < \mathcal{T}_{max}$. 5, 6

$\mathcal{T}_{max}$: Maximal kinetic energy transfer in a single collision. 3–7, 50, 51, 53, 55, III

$\mathcal{T}_{min}$: Minimum kinetic energy transfer in a single collision. 3, 4, 7, III

ρ : Material density in g cm^{-3} 3–5, 7, 8, 191

AmpOut : The test output for the CSA of the sensor. In case of MuPix10, this feature is available for each pixel of the lowest row address of the sensor. The output requires an 1 kΩ termination on PCB level and a high termination impedance (1 MΩ) on oscilloscope level. The output is single-ended and measured with respect to the PCB ground level. 113, 183–185, V

GND : The common ground (low reference) level. 30, 45, XI

HV : The high voltage level for the pixel sensors. 30, 33, 34, 71, 73, 122, 166

LV : The low voltage level for the pixel sensors. For a MuPix10 this level generally refers to the voltage difference of VDD and GND. 73

TS1 : Time-of-Arrival timestamp of a hit word. For MuPix10 it covers a 11 bit range, where the LSB is defined by (1 + ckdivend) times a clock . Nominal (for ckdivend = 0) at 125 MHz clock frequency, the LSB is 8 ns. 188

TS2 : The ToT associated timestamp of a hit word. For MuPix10 it covers a 5 bit range, where the LSB is defined by (1 + ckdivend2) times a clock. Nominal (for ckdivend2 = 0xf) at 125 MHz clock frequency, the LSB is 128 ns. 188

VDD : The common supply (high reference) level for the pixel sensors. 30, 45, XI

gnda : The ground (low reference) level for the analog domain of the sensor. 36, 45, 73, XII

gndd : The ground (low reference) reference level of the digital domain of the sensor. 45, 73, XII

vdda : The supply (high reference) level for the analog domain of the sensor. 34, 36, 45, 46, 65, 73, 127, 129, XII

vddd : The supply (high reference) level for the digital domain of the sensor. 45, 46, 73, XII

vssa : A supply (high reference) level for the CSA in the analog of the sensor. 36, 45, 73, 83, 136, I, III, XII

$\varrho_{substrate}$: Substrate resistivity in [Ω cm]. 20, 23, 59, 60, 67, 130

$\xi(\Delta x, \beta)$: The ξ factor defined by Equation 1.9 in [MeV]. It is used to calculate the energy loss of a particle in a material. 5–7, 50, 52–56, 140, 141, 149–152, 156, 159, 172–175, IV

c : The speed of light in vacuum 299 792 458 m s^{-1} [14]. 3, 10, 165, X

e : The electron charge magnitude in [C]. It is defined as $e = 1.602\,176\,634 \times 10^{-19}$ C [14]. 21

f_k : Oscillator strength of the k-th atomic shell of a material. 4, 56, 175, 190

k_B : The Boltzmann constant defined to be $1.380\,649 \times 10^{-23}$ J K^{-1} [14]. 15, 61, 64

m_e : The mass of the electron or positron, respectively. The mass is $m_e = 0.510\,998\,950\,00(15)$ MeV c^{-2} [14]. 3, 5, 7, 10, 49

n_i : The intrinsic carrier concentration of a semiconductor in [cm^{-3}]. Value about 1.01 × 10^{10} cm^{-3} for silicon at 300 K [17, p.269, eq. 8.20]. 15

p : The momentum of a particle, which is defined as the product of its mass and velocity. It is given in [MeV c^{-1}]. 5, 8, 51, 52, 140, 149, 150, 152, 157, 165, III, V

r_e : The classical electron radius, which value is $r_e = 2.817\,940\,326\,2(13)$ fm [14]. 5

z : Charge of a particle in units of the elementary charge [e]. 5

λ_a : Photon absorption length given in [µm]. 9, 91, 127

n_e : The electron density of a material (see Equation 1.1). 3, 48

AmpOut : The *AmpOut* is a test output with its own output driver operated via the 6 bit DAC *VPFoll* (default value 0x14). It outputs the analog signal of the CSA of the HV-MAPS sensor. See Section 3.3. 36, 43, 70, 71

HitBus : The *HitBus* is a test output with its own output driver operated via the 6 bit DAC *VNHB* (default value 0x3f). It outputs the comparator signal of the HV-MAPS sensor. See Section 3.5. 40, 43, 70, 71

Injection : The *Injection* is a test pulse charging an in-pixel capacitance, which is used to mimic a known charge input to the CSA of the HV-MAPS sensor. See Sections 3.3 and 6.3. 36, 43, 70, 71, 86, 89, 95, 96, 98, 99, 101, 102, 115, 117–121, 138, 143, 161, 162, II, III, XII

LEMO® : A company of push-pull connectors founded in Switzerland and named after its founder Léon Mouttet. 70

Molex® : Molex LLC is a manufacturer of electronic, electrical, and fiber optic connectivity systems. 70, 71

Mu3e : A particle physics experiment at the **P**aul-**S**cherrer **I**nstitute in Switzerland, designed to search for charged lepton flavor violation by studying the decay of muons into three electrons. See Section 3.1. i, ix, 1, 27, 29, 30, 68, 73, 122, I

MuDAQ Motherboard : Host the indiviudal sensor insert and provides the interface to the FPGA for the *MuDAQ* system. See Section 5.2.2. 69–71, 95, 119, 122, II

MuDAQ : The data acquisition system of the MuPix telescope. It is used to control and read out the the MuPix sensors. See Section 5.2.2. 70, 72, 73, 76, 88, II, XII

TestOut : The *TestOut* is a configurable multiplexer, which among others outputs *gnda*, *gndd*, *vdda*, *vssa* & *vddd*. See Section 3.7.2. 45, 46, 70, 71

high-gain : The *high-gain* settings refer to the optimized settings used for Fe-55 & *Injection* measurements for charge calibration. See Sections A.5 and 5.1.1. 66, 85, 86, 96, 98, 103–109, 112–114, 119, 120, 122, 123, 134–137, 151, 163, 187, 189, IV, VII

low-gain : The *low-gain* settings refer to the settings used in the testbeam conducted in this thesis. See Sections A.5 and 5.1.1. 66, 83, 85, 86, 96, 98, 103, 104, 107–114, 119, 132, 134–137, 187, 189, IV, VII

MuPix : A family of **H**igh-**V**oltage **M**onolithic **A**ctive **P**ixel **S**ensor developed for the Mu3e experiment. i, iii, ix, 1, 2, 27, 29, 31–36, 38–47, 65–67, 69–74, 78, 79, 85, 89, 91, 95, 96, 103, 115, 118, 122, 126, 136, 138, 139, 143, 146, 150, 157–160, 162, 163, 181, 183, 186, I–V, VII, XI, XII

Acronyms

(Lab) Laboratory 70, 189, VII

(TB) Test **B**eam 189, VII

(complementary) CDF (complementary) Cumulative Distribution Function 48, 52, 53, 87, 88, 96, 98, 173, 174, 176, 180

***CZ C**zochralski* 13

***FZ F**loat-**Z**one* 13

`CISE` Compact P**I**xel **S**ensor **E**fficiency ix

`PCDF` Probability / **C**umulative **D**ensity/istribution **F**unction ix, 176

`PiCa` Pixel **Ca**libration ix

`SILICA` Silicon p**I**xe**L** phys**I**cs cal**c**ul**a**tor ix

AC Alternating **C**urrent 26

AFM Atomic **F**orce **M**icroscopy 35

Al aluminium 3, 9, 31, 33, 57, 165, 191

Am-241 Americium-241 127

ASIC Application-**S**pecific **I**ntegrated **C**ircuit 25

Bethe-Bloch Bethe-Bloch formula 5, 6, 50, III

BR Branching **R**atio 29, 68

C.L. Confidence **L**evel 29

CCD Charge-**C**oupled **D**evice 25

CCE Charge **C**ollection **E**fficiency 48, 65, 74, 78

CDF Cumulative Distribution Function 48, 173

CERN Conseil Européen pour la Recherche Nucléaire [European Organization for Nuclear Research] 26

cLFV charged **L**epton **F**lavor **V**iolation 29, I

CMOS Complementary **M**etal-**O**xide-**S**emiconductor 25, 26, 32, 36, 95, 96, 182

CSA Charge Sensitive Amplifier 32, 36, 37, 45, 47, 62, 63, 80, 83, 85, 86, 99, 108, 110, 111, 151, 167, 187, X, XI

CSDA Continuous **S**lowing **D**own **A**pproximation viii, 7, 165, V

DAC **D**igital-to-**A**nalog **C**onverter 36, 40, 42–46, 66, 71, 73, 88, 95, 96, 102–105, 107, 108, 132, 135, 162, 187, 188, III, VII, IX, XI

DAQ **D**ata-**A**cquisition **S**ystem 70, 88

DbG **D**icing **b**efore **G**rinding 35, 67

DC **D**irect **C**urrent 26, 73

DCL **D**ifferential **C**urreent Mode **L**ogic 188, VII

DEPFET **De**pleted **P**-channel **F**ield-**E**ffect **T**ransistor 25

DESY Deutsches Elektronen-Synchrotron [German Electron Synchrotron] ix, 26, 66, 159, 163

DMA **D**irect **M**emory **A**ccess 70

DMAPS **D**epleted **M**onolithic **A**ctive **P**ixel **S**ensor v, 25–27, I

DNL **D**ifferential **N**on-**L**inearity 100, 162

DUT **D**evice-**U**nder-**T**est 67, 69–78, 80–82, 88, 95, 103–107, 109–114, 119, 120, 122, 123, 127–129, 133, 135, 136, 138, 146, 153, 155, 158, 161, 166, 167, 189, II–V, VII

EADL **E**valuated **A**tomic **D**ata **L**ibrary 190

ELSA ELectron Stretcher Aanlage [Electron Stretcher Facility] (University of Bonn) 26

ENC **E**quivalent **N**oise **C**harge 62–64, 121, 131–137, I, IV

ENDF/B-VIII.0 **E**valuated **N**uclear **D**ata **F**ile, B-VIII.0 91, 179, VII

EoC **E**nd **o**f **C**olumn 44, 70

Fe-55 Iron-55 i, iii, viii, ix, 17, 41, 85, 86, 88–94, 96, 98, 103, 105, 113, 115–117, 119–122, 127, 128, 130, 133, 134, 138, 151, 161, 162, 179, II, IV, VII, XII

FPGA **F**ield-**P**rogrammable **G**ate **A**rray 70, 74, 76, 88, 89, 95, 162, XII

FSM **F**inite **S**tate **M**achine 32, 33, 41, 43, 44, 136, 188, VII

FWHM **F**ull **W**idth at **H**alf **M**aximum 52, 53, 55–57, 68, 143, 173–175, 183–185, IX

GBL **G**eneral **B**roken **L**ine 75

GoF **G**oodness-**o**f-**F**it 93, 94, 97, 98, 102, 148, 177, 178

GUI **G**raphical **U**ser **I**nterface 70

HDI **H**igh-**D**ensity **I**nterconnect 30, 31, I

HIMB **H**igh-**I**ntensity **M**uon **B**eams 68

HIPA **H**igh-**I**ntensity **P**roton **A**ccelerator 68

HSMC **H**igh-**S**peed **M**ezzanine **C**ard 69, 71

HV-CMOS **H**igh-**V**oltage **C**omplementary **M**etal-**O**xide-**S**emiconductor 26, 32

HV-MAPS **H**igh-**V**oltage **M**onolithic **A**ctive **P**ixel **S**ensor i, iii, ix, 1, 2, 26, 27, 29, 30, 32, 35, 36, 41, 65, 66, 69, 70, 88, 90, 91, 93, 95, 99, 103, 138, 139, 158, 159, 161, 163, I, III, XI, XII

I/O **I**nput/**O**utput 69, 70

ICRU **I**nternational **C**ommission on **R**adiological **U**nits Measurements 190, 191

IMPACT **I**sotope and **M**uon **P**roduction using **A**dvanced **C**yclotron and **T**arget technologies 68

JANIS 4 The NEA **J**ava-based **N**uclear **I**nformation **S**ystem, version 4 91, 179

JEFF-3.3 The **J**oint **E**valuated **F**ission and **F**usion Nuclear Data Library V3.3 91, 179, VII

JENDL/DDF-2015 **J**apanese **E**valuated **N**uclear **D**ata **L**ibrary / **D**ecay **D**ata **F**ile 2015 91, 179, VII

LGAD **L**ow **G**ain **A**valanche **D**etector 117

LLh **L**og-**L**ikeli**h**ood 93, 97, 148, 177

LSB **L**east **S**ignificant **B**it 40, 69, 85, XI

LVDS **L**ow **V**oltage **D**ifferential **S**ignaling 32, 43, 44, 69, 70, 188, VII

MAPS **M**onolithic **A**ctive **P**ixel **S**ensor 25, 26, I

MIP **M**inimum **I**onizing **P**article 5, 71

MLE **M**aximum **L**ikelihood **E**stimation 177

Mn-55 Manganese-55 90, 91, II

MOSFET **M**etal-**O**xide-**S**emiconductor **F**ield-**E**ffect **T**ransistor 63, 64, I

MPV **M**ost **P**robable **V**alue 140, 148, 149

MPW **M**ulti-**P**roject **W**afer 127

MSCB **M**idas **S**low **C**ontrol **B**us 72, 73

NDF **N**umber of **D**egrees of **F**reedom 75, 97, 102, 177

NIST **N**ational **I**nstitute of **S**tandards and **T**echnology 9, 165, 190, VII

NMOS **N**-channel **M**etal-**O**xide-**S**emiconductor 36

OpAmp **Op**erational **Amp**lifier 95, 96, 100, 181

OPTIM WS OPTIM **W**afer **S**ervice 35, 67

PAI **P**hoto-**A**bsorption **I**onization model 142

PAS **P**hotoelectron and **A**uger **S**pectroscopy 190

PCB **P**rinted **C**ircuit **B**oard 33, 67, 69–71, 73, 75, 76, 78, 83, 119, 136, I, X

PCIe **P**eripheral **C**omponent **I**nterconnect **E**xpress 70

PDF Probability Density Function 47–50, 52, 77, 87, 88, 98, 128, 140, 148, 172–174, 176, 180

PI **p**olyimide 31

PLL **P**hase-**L**ocked **L**oop 44, 88, 188, VII

PMOS **P**-channel **M**etal-**O**xide-**S**emiconductor 36

PSI **P**aul-**S**cherrer **I**nstitute ix, 29, 68, 69, 103, 131, 138, 192, I, VII, XII, XXXIII

RAM **R**andom **A**ccess **M**emory 43

RCU **R**eadout **C**ontrol **U**nit 188

RHIC **R**elativistic **H**eavy **I**on **C**ollider 26

RMS **R**oot **M**ean **S**quare 8, 62, 75

RoI Region of Interest 77–79, 83, 84, 86, 89, 94, 96, 103, 106, 107, 111, 134–137, 146, 147, 153, 155, 162, III, VII

RSS **R**oot **S**um **S**quare 56

SCSI **S**mall **C**omputer **S**ystem **I**nterface 69, 71

Si **si**licon viii, 3–7, 9, 13–22, 24, 25, 27, 47–52, 54–58, 60–63, 72, 85, 90, 96, 111, 113, 140, 142, 144, 149, 156, 165, 168–170, 175, 190, 191, I, III–V, VII

Si_3N_4 **si**licon **n**itride 9, 33

SiO_2 **si**licon **d**ioxide 9, 33, 63, 165, 191

SLAC Standford Linear Accelerator Center 26

SMA **S**ub**M**iniature version **A** 71

SNR **S**ignal-to-**N**oise **R**atio 62, 64, 66, 97, 98, 107, 131

SOI-MAPS **S**ilicon-**O**n-**I**nsulator **M**onolithic **A**ctive **P**ixel **S**ensor 25

SPI **S**erial **P**eripheral **I**nterface 43

SRH **S**hockley-**R**ead-**H**all 19

tcad **T**echnology **C**omputer-**A**ided **D**esign 158, 163

TCT **T**ransient **C**urrent **T**echnique 163

TDC **T**ime-**D**igital **C**onverter 69

TEM **T**ransmission **E**lectron **M**icroscopy 35, I

ToA **T**ime-**o**f-**A**rrival 40, 41, 70, 74, 75, 88, 166, III

ToT **T**ime-**o**ver-**T**hreshold 32, 39–42, 48, 62, 65, 70, 74, 75, 78, 88, 90, 140, 143–145, 151, 159, 160, 162, 163, III–V, VII, XI

TTL **T**ransistor-**T**ransistor **L**ogic 69

VCO **V**oltage-**C**ontrolled **O**scillator 188

XDB **X**-ray **D**ata **B**ooklet 190

Bibliography

[1] Sebastian Preuß. "Electron-Irradiation and Performance Test of the MuPix8 Silicon Pixel Sensor for the Mu3e Experiment". Bachelor thesis. Heidelberg, Germany: Heidelberg University, 2020. URL: https://www.physi.uni-heidelberg.de/Publications/Bachelorarbeit_Sebastian_Preuss.pdf (cit. on p. ix).

[2] Lukas Mandok. "Analoge Charakterisierung und Optimierung des HV-MAPS Prototypen ATLASPix3". Bachelor thesis. Heidelberg, Germany: Heidelberg University, 2020. URL: https://www.physi.uni-heidelberg.de/Publications/Bachelorabeit-LukasMandok.pdf (cit. on p. ix).

[3] Dohun Kim. "Analoge Charakterisierung und Optimierung des HV-MAPS Prototypen ATLASPixTiming Study and Optimization of ATLASPix3 a full-scale HV-MAPS Prototype". Master thesis. Heidelberg, Germany: Heidelberg University, 2020. URL: https://www.physi.uni-heidelberg.de/Publications/Masterarbeit_Dohun_Kim_01_11_2020.pdf (cit. on p. ix).

[4] Jakob Stricker. "Testing of a Method for the Sensor Thickness Determination and a Cluster Size Study for the MuPix10". Bachelor thesis. Heidelberg, Germany: Heidelberg University, 2021. URL: https://www.physi.uni-heidelberg.de/Publications/Bachelor_Thesis_Stricker.pdf (cit. on pp. ix, 66, 71, 75).

[5] Florian Frauen. "Characterisation of the time resolution of the MuPix10 pixel sensor". Bachelor thesis. Heidelberg, Germany: Heidelberg University, 2021. URL: https://www.physi.uni-heidelberg.de/Publications/Bachelorarbeit_Florian_Frauen_final.pdf (cit. on pp. ix, 66, 76).

[6] Marius Wilm Menzel. "Calibration of the MuPix10 Pixel Sensor for the Mu3e Experiment". Bachelor thesis. Heidelberg, Germany: Heidelberg University, 2020. URL: https://www.physi.uni-heidelberg.de/Publications/Bachelor_Menzel.pdf (cit. on pp. ix, 162).

[7] Stephan Lachnit. "Pulse Shape Characterization and Allpix Squared Simulation of the MuPix10". Bachelor thesis. Heidelberg, Germany: Heidelberg University, 2021. URL: https://www.physi.uni-heidelberg.de/Publications/BachelorLachnit.pdf (cit. on pp. ix, 65, 163).

[8] Ruben Kolb. "Disentangling the Diffusive Part of the Drift-Dominated Signal Generation in a High-Ohmic Run2021v2 HV-MAPS Prototype". Master thesis. Heidelberg, Germany: Heidelberg University, 2023. URL: https://www.physi.uni-heidelberg.de/Publications/Master_Kolb_Ruben.pdf (cit. on pp. ix, 65, 75, 140, 143, 163).

[9] David Maximilian Immig. ***P**robability / **C**umulative **D**ensity/istribution **F**unction (PCDF)*. Version v0.11.00. This framework is in development and therefore set private, contact the author for access. July 7, 2025. URL: https://github.com/daimmig/PCDF (cit. on pp. ix, 93, 94, 176).

[10] David Maximilian Immig. ***S**ilicon p**I**xe**L** phys**I**cs cal**C**ul**A**tor (SILICA)*. Version v0.12.02. This framework is in development and therefore set private, contact the author for access. July 7, 2025. URL: https://github.com/daimmig/Silica (cit. on p. ix).

[11] David Maximilian Immig. *Scurve*. Version v0.10.03. This framework is in development and therefore set private, contact the author for access. July 7, 2025. URL: https://github.com/daimmig/Scurve (cit. on pp. ix, 94).

[12] David Maximilian Immig. ***Pi**xel **Ca**libration (PiCa)*. Version v0.03.00. This framework is in development and therefore set private, contact the author for access. July 7, 2025. URL: https://github.com/daimmig/PiCa (cit. on p. ix).

[13] David Maximilian Immig. ***C**ompact **PI**xel **S**ensor **E**fficiency (CISE)*. Version v0.03.01. This framework is in development and therefore set private, contact the author for access. July 7, 2025. URL: https://github.com/daimmig/CISE (cit. on p. ix).

[14] S. Navas et al. "Review of particle physics". In: *Phys. Rev. D* 110.3 (2024), p. 030001. DOI: 10.1103/PhysRevD.110.030001 (cit. on pp. 3, 5–8, 49, 57, 68, 191, IX–XI).

[15] Christian Wolfgang Fabjan and Herwig Schopper, eds. *Particle Physics Reference Library. Volume 2: Detectors for Particles and Radiation*. Springer, 2020. ISBN: 978-3-030-35317-9, 978-3-030-35320-9, 978-3-030-35318-6. DOI: 10.1007/978-3-030-35318-6 (cit. on pp. 3, 48, 49, 57).

[16] Siméon Denis Poisson. *Recherches sur la probabilité des jugements en matière criminelle et en matière civile*. Préambule. Paris: Bachelier, 1837. URL: https://gallica.bnf.fr/ark:/12148/bpt6k110193z (visited on 06/19/2025) (cit. on p. 3).

[17] Hermann Kolanoski and Norbert Wermes. *Particle Detectors*. Oxford University Press, June 2020. ISBN: 978-0-19-885836-2 (cit. on pp. 3–5, 7–11, 13–17, 21–27, 49, 51–53, 60–64, 131, 134, 173, IX, XI).

[18] U Fano. "Penetration of Protons, Alpha Particles, and Mesons". In: *Annual Review of Nuclear and Particle Science* 13.Volume 13, (1963), pp. 1–66. ISSN: 1545-4134. DOI: https://doi.org/10.1146/annurev.ns.13.120163.000245 (cit. on p. 4).

[19] C. Tschalär and Hans Bichsel. "Mean Excitation Potential of Light Compounds". In: *Phys. Rev.* 175 (2 Nov. 1968), pp. 476–478. DOI: 10.1103/PhysRev.175.476 (cit. on p. 4).

[20] Bruno Benedetto Rossi. *High-energy particles*. Prentice-Hall physics series. New York, NY: Prentice-Hall, 1952. URL: https://cds.cern.ch/record/99081 (cit. on p. 5).

[21] H. Bethe. "Zur Theorie des Durchgangs schneller Korpuskularstrahlen durch Materie". In: *Annalen der Physik* 397.3 (1930), pp. 325–400. DOI: https://doi.org/10.1002/andp.19303970303. eprint: https://onlinelibrary.wiley.com/doi/pdf/10.1002/andp.19303970303 (cit. on p. 5).

[22] M. Stanley Livingston and H. A. Bethe. "Nuclear Physics C. Nuclear Dynamics, Experimental". In: *Rev. Mod. Phys.* 9 (3 1937), pp. 245–390. DOI: 10.1103/RevModPhys.9.245 (cit. on p. 5).

[23] U Fano. "Penetration of Protons, Alpha Particles, and Mesons". In: *Annual Review of Nuclear and Particle Science* 13.Volume 13, (1963), pp. 1–66. ISSN: 1545-4134. DOI: https://doi.org/10.1146/annurev.ns.13.120163.000245 (cit. on p. 5).

[24] R. M. Sternheimer. "Range Straggling of Charged Particles in Be, C, Al, Cu, Pb, and Air". In: *Phys. Rev.* 117 (2 Jan. 1960), pp. 485–488. DOI: 10.1103/PhysRev.117.485 (cit. on pp. 5, 175).

[25] R. M. Sternheimer and R. F. Peierls. "General Expression for the Density Effect for the Ionization Loss of Charged Particles". In: *Phys. Rev. B* 3 (11 June 1971), pp. 3681–3692. DOI: 10.1103/PhysRevB.3.3681 (cit. on pp. 5, 175).

[26] R. M. Sternheimer. "Density Effect for the Ionization Loss of Charged Particles". In: *Phys. Rev.* 145 (1 Apr. 1966), pp. 247–250. DOI: 10.1103/PhysRev.145.247 (cit. on pp. 5, 175).

[27] Stephen M. Seltzer and Martin J. Berger. "Evaluation of the collision stopping power of elements and compounds for electrons and positrons". In: *The International Journal of Applied Radiation and Isotopes* 33.11 (1982), pp. 1189–1218. ISSN: 0020-708X. DOI: https://doi.org/10.1016/0020-708X(82)90244-7 (cit. on p. 6).

[28] Stephen M. Seltzer and Martin J. Berger. "Improved procedure for calculating the collision stopping power of elements and compounds for electrons and positrons". In: *The International Journal of Applied Radiation and Isotopes* 35.7 (1984), pp. 665–676. ISSN: 0020-708X. DOI: https://doi.org/10.1016/0020-708X(84)90113-3 (cit. on p. 6).

[29] Hans Bichsel. "A method to improve tracking and particle identification in TPCs and silicon detectors". In: *Nuclear Instruments and Methods in Physics Research Section A: Accelerators, Spectrometers, Detectors and Associated Equipment* 562.1 (2006), pp. 154–197. ISSN: 0168-9002. DOI: https://doi.org/10.1016/j.nima.2006.03.009 (cit. on pp. 7, 57).

[30] Norbert Wermes. "Pixel Vertex Detectors". In: *Proceedings of the 34th SLAC Summer Institute on Particle Physics (SSI 2006)*. Lecture presented at the SLAC Summer Institute: https://www.slac.stanford.edu/econf/C060717/lec_notes/Wermes072006v2.pdf. SLAC, Stanford, California, USA: SLAC ECONF, 2006. URL: https://www.slac.stanford.edu/econf/C060717/papers/L008.PDF (cit. on pp. 7, 63, 64).

[31] M. J. Berger et al. *Stopping-Power & Range Tables for Electrons, Protons, and Helium Ions*. NIST Standard Reference Database 124, Last update: July 2017, ESTAR: http://physics.nist.gov/PhysRefData/Star/Text/ESTAR.html. URL: https://dx.doi.org/10.18434/T4NC7P (visited on 07/13/2025) (cit. on pp. 7, 165).

[32] *Atomic and nuclear properties of silicon (Si)*. See also Table of muon dE/dx and Range: https://pdg.lbl.gov/2024/AtomicNuclearProperties/MUE/muE_silicon_Si.pdf. URL: https://pdg.lbl.gov/2024/AtomicNuclearProperties/HTML/silicon_Si.html (visited on 04/15/2025) (cit. on pp. 8, 191).

[33] K Nakamura and (Particle Data Group). "Review of Particle Physics". In: *Journal of Physics G: Nuclear and Particle Physics* 37.7A (2010), p. 075021. DOI: 10.1088/0954-3899/37/7A/075021 (cit. on p. 8).

[34] H. A. Bethe. "Molière's Theory of Multiple Scattering". In: *Phys. Rev.* 89 (6 Mar. 1953), pp. 1256–1266. DOI: 10.1103/PhysRev.89.1256 (cit. on p. 8).

[35] Virgil L. Highland. "Some practical remarks on multiple scattering". In: *Nuclear Instruments and Methods* 129.2 (1975), pp. 497–499. ISSN: 0029-554X. DOI: https://doi.org/10.1016/0029-554X(75)90743-0 (cit. on p. 8).

[36] Gerald R. Lynch and Orin I. Dahl. "Approximations to multiple Coulomb scattering". In: *Nuclear Instruments and Methods in Physics Research Section B: Beam Interactions with Materials and Atoms* 58.1 (1991), pp. 6–10. ISSN: 0168-583X. DOI: https://doi.org/10.1016/0168-583X(91)95671-Y (cit. on p. 8).

[37] B.L. Henke, E.M. Gullikson, and J.C. Davis. "X-Ray Interactions: Photoabsorption, Scattering, Transmission, and Reflection at E = 50-30,000 eV, Z = 1-92". In: *Atomic Data and Nuclear Data Tables* 54.2 (1993). Attenuation length data taken from: https://henke.lbl.gov/optical_constants/atten2.html, pp. 181–342. ISSN: 0092-640X. DOI: https://doi.org/10.1006/adnd.1993.1013 (cit. on pp. 9, 91).

[38] C. T. Chantler et al. *X-Ray Form Factor, Attenuation, and Scattering Tables (version 2.1)*. NIST Standard Reference Database 66. Data can be taken from: https://physics.nist.gov/PhysRefData/FFast/html/form.html. 2005. DOI: 10.18434/T4HS32 (cit. on p. 9).

[39] Y.P. Varshni. "Temperature dependence of the energy gap in semiconductors". In: *Physica* 34.1 (1967), pp. 149–154. ISSN: 0031-8914. DOI: https://doi.org/10.1016/0031-8914(67)90062-6 (cit. on p. 15).

[40] D.D.L. Chung and Dang Q. Duong. "New method of measuring the permittivity of silicon wafer, with relevance to permittivity-based quality sensing". In: *Materials Chemistry and Physics* 299 (2023), p. 127516. ISSN: 0254-0584. DOI: https://doi.org/10.1016/j.matchemphys.2023.127516 (cit. on p. 17).

[41] Stojan Ristić, Aneta Prijić, and Zoran Prijić. "Dependence of static dielectric constant of silicon on resistivity at room temperature". In: *Serbian Journal of Electrical Engineering* 1.2 (2004), pp. 237–247. URL: https://doiserbia.nb.rs/Article.aspx?ID=1451-48690402237R (visited on 06/26/2025) (cit. on p. 17).

[42] W. Bludau, A. Onton, and W. Heinke. "Temperature dependence of the band gap of silicon". In: *Journal of Applied Physics* 45.4 (Apr. 1974), pp. 1846–1848. ISSN: 0021-8979. DOI: 10.1063/1.1663501. eprint: https://pubs.aip.org/aip/jap/article-pdf/45/4/1846/18367322/1846_1_online.pdf (cit. on p. 17).

[43] I.V. Kotov, H. Neal, and P. O'Connor. "Pair creation energy and Fano factor of silicon measured at 185 K using 55 F e X-rays". en. In: *Nuclear Instruments and Methods in Physics Research Section A: Accelerators, Spectrometers, Detectors and Associated Equipment* 901 (Sept. 2018), pp. 126–132. ISSN: 01689002. DOI: 10.1016/j.nima.2018.06.022. (Visited on 06/17/2025) (cit. on p. 17).

[44] B.G. Lowe and R.A. Sareen. "A measurement of the electron–hole pair creation energy and the Fano factor in silicon for 5.9keV X-rays and their temperature dependence in the range 80–270K". In: *Nuclear Instruments and Methods in Physics Research Section A: Accelerators, Spectrometers, Detectors and Associated Equipment* 576.2 (2007), pp. 367–370. ISSN: 0168-9002. DOI: https://doi.org/10.1016/j.nima.2007.03.020 (cit. on p. 17).

[45] W. C. Dunlap and R. L. Watters. "Direct Measurement of the Dielectric Constants of Silicon and Germanium". In: *Phys. Rev.* 92 (6 Dec. 1953), pp. 1396–1397. DOI: 10.1103/PhysRev.92.1396 (cit. on p. 17).

[46] Karlheinz Seeger. "Microwave dielectric constants of silicon, gallium arsenide, and quartz". In: *Journal of Applied Physics* 63.11 (June 1988), pp. 5439–5443. ISSN: 0021-8979. DOI: 10.1063/1.341153. eprint: https://pubs.aip.org/aip/jap/article-pdf/63/11/5439/18617631/5439_1_online.pdf (cit. on p. 17).

[47] R. C. Alig, S. Bloom, and C. W. Struck. "Scattering by ionization and phonon emission in semiconductors". In: *Phys. Rev. B* 22 (12 Dec. 1980), pp. 5565–5582. DOI: 10.1103/PhysRevB.22.5565 (cit. on p. 17).

[48] R. C. Alig and S. Bloom. "Electron-Hole-Pair Creation Energies in Semiconductors". In: *Phys. Rev. Lett.* 35 (22 Dec. 1975), pp. 1522–1525. DOI: 10.1103/PhysRevLett.35.1522 (cit. on p. 17).

[49] U. Fano. "Ionization Yield of Radiations. II. The Fluctuations of the Number of Ions". In: *Phys. Rev.* 72 (1 July 1947), pp. 26–29. DOI: 10.1103/PhysRev.72.26 (cit. on p. 17).

[50] C. Jacoboni et al. "A review of some charge transport properties of silicon". In: *Solid-State Electronics* 20.2 (1977), pp. 77–89. ISSN: 0038-1101. DOI: https://doi.org/10.1016/0038-1101(77)90054-5 (cit. on pp. 18, 19).

[51] D.M. Caughey and R.E. Thomas. "Carrier mobilities in silicon empirically related to doping and field". In: *Proceedings of the IEEE* 55.12 (1967), pp. 2192–2193. DOI: 10.1109/PROC.1967.6123 (cit. on p. 18).

[52] S.M. Sze and Kwok K. Ng. *Physics of Semiconductor Devices*. John Wiley & Sons, Ltd, 2006. ISBN: 9780471143239. DOI: 10.1002/0470068329 (cit. on p. 18).

[53] W. Shockley and W. T. Read. "Statistics of the Recombinations of Holes and Electrons". In: *Phys. Rev.* 87 (5 1952), pp. 835–842. DOI: 10.1103/PhysRev.87.835 (cit. on p. 19).

[54] R. N. Hall. "Electron-Hole Recombination in Germanium". In: *Phys. Rev.* 87 (2 1952), pp. 387–387. DOI: 10.1103/PhysRev.87.387 (cit. on p. 19).

[55] J.G. Fossum and D.S. Lee. "A physical model for the dependence of carrier lifetime on doping density in nondegenerate silicon". In: *Solid-State Electronics* 25.8 (1982), pp. 741–747. ISSN: 0038-1101. DOI: https://doi.org/10.1016/0038-1101(82)90203-9 (cit. on p. 19).

[56] A. Schenk. "A model for the field and temperature dependence of Shockley-Read-Hall lifetimes in silicon". In: *Solid-State Electronics* 35.11 (1992), pp. 1585–1596. ISSN: 0038-1101. DOI: https://doi.org/10.1016/0038-1101(92)90184-E (cit. on p. 19).

[57] *Sentaurus™ Device User Guide*. Version V-2024.03. Copyright © 2024 Synopsys, Inc. Synopsys, Inc. Mar. 2024 (cit. on p. 19).

[58] M.S. Tyagi, J.F. Nijs, and R.J. Van Overstraeten. "Effect of surface recombination on the transient decay of excess carriers produced by short wavelength laser pulses". In: *Solid-State Electronics* 25.5 (1982), pp. 411–415. ISSN: 0038-1101. DOI: https://doi.org/10.1016/0038-1101(82)90126-5 (cit. on p. 19).

[59] Simon Spannagel, Koen Wolters, and Paul Schütze. *Allpix Squared - Generic Pixel Detector Simulation Framework*. Version 2.2.0. Feb. 2022. DOI: 10.5281/zenodo.6387859 (cit. on pp. 19, 142, 163, 169).

[60] J.G. Fossum et al. "Carrier recombination and lifetime in highly doped silicon". In: *Solid-State Electronics* 26.6 (1983), pp. 569–576. ISSN: 0038-1101. DOI: https://doi.org/10.1016/0038-1101(83)90173-9 (cit. on p. 19).

[61] J. Dziewior and W. Schmid. "Auger coefficients for highly doped and highly excited silicon". In: *Applied Physics Letters* 31.5 (Sept. 1977), pp. 346–348. DOI: 10.1063/1.89694. eprint: https://pubs.aip.org/aip/apl/article-pdf/31/5/346/18435350/346_1_online.pdf (cit. on p. 19).

[62] Mark J. Kerr and Andres Cuevas. "General parameterization of Auger recombination in crystalline silicon". In: *Journal of Applied Physics* 91.4 (Feb. 2002), pp. 2473–2480. ISSN: 0021-8979. DOI: 10.1063/1.1432476. eprint: https://pubs.aip.org/aip/jap/article-pdf/91/4/2473/19278569/2473_1_online.pdf (cit. on p. 19).

[63] *Resistivity Measurements of Semiconductor Materials Using the 4200A-SCS Parameter Analyzer and a Four-Point Collinear Probe*. Tech. rep. Application Note, Document 070816 1KW-60640-0. Tektronix, 2020. URL: https://www.tek.com/de/documents/application-note/resistivity-measurements-semiconductor-materials-using-4200a-scs-parameter (cit. on p. 20).

[64] W. Shockley. "The theory of p-n junctions in semiconductors and p-n junction transistors". In: *The Bell System Technical Journal* 28.3 (1949), pp. 435–489. DOI: 10.1002/j.1538-7305.1949.tb03645.x (cit. on p. 23).

[65] Daniele Ielmini et al. "A recombination- and trap-assisted tunneling model for stress-induced leakage current". In: *Solid-State Electronics* 45.8 (2001), pp. 1361–1369. ISSN: 0038-1101. DOI: https://doi.org/10.1016/S0038-1101(01)00173-3 (cit. on p. 23).

[66] Gerhard Lutz. *Semiconductor Radiation Detectors: Device Physics*. New York: Springer, 1999. ISBN: 978-3-540-64859-8 (cit. on p. 23).

[67] A Chilingarov. "Temperature dependence of the current generated in Si bulk". In: *Journal of Instrumentation* 8.10 (Oct. 2013), P10003. DOI: 10.1088/1748-0221/8/10/P10003 (cit. on p. 24).

[68] R. Ballabriga, M. Campbell, and X. Llopart. "An introduction to the Medipix family ASICs". In: *Radiation Measurements* 136 (2020), p. 106271. ISSN: 1350-4487. DOI: https://doi.org/10.1016/j.radmeas.2020.106271 (cit. on pp. 25, 91).

[69] T. Poikela et al. "The VeloPix ASIC". In: *Journal of Instrumentation* 12.01 (Jan. 2017), p. C01070. DOI: 10.1088/1748-0221/12/01/C01070 (cit. on p. 25).

[70] G. Alimonti et al. "RD53 pixel readout integrated circuits for ATLAS and CMS HL-LHC upgrades". In: *Journal of Instrumentation* 20.03 (Mar. 2025), P03024. DOI: 10.1088/1748-0221/20/03/P03024 (cit. on p. 25).

[71] Giacomo Contin et al. "The STAR MAPS-based PiXeL detector". In: *Nuclear Instruments and Methods in Physics Research Section A: Accelerators, Spectrometers, Detectors and Associated Equipment* 907 (2018). Advances in Instrumentation and Experimental Methods (Special Issue in Honour of Kai Siegbahn), pp. 60–80. ISSN: 0168-9002. DOI: https://doi.org/10.1016/j.nima.2018.03.003 (cit. on p. 26).

[72] M. Mager. "ALPIDE, the Monolithic Active Pixel Sensor for the ALICE ITS upgrade". In: *Nuclear Instruments and Methods in Physics Research Section A: Accelerators, Spectrometers, Detectors and Associated Equipment* 824 (2016). Frontier Detectors for Frontier Physics: Proceedings of the 13th Pisa Meeting on Advanced Detectors, pp. 434–438. ISSN: 0168-9002. DOI: https://doi.org/10.1016/j.nima.2015.09.057 (cit. on pp. 26, 163).

[73] C. Hu-Guo et al. "First reticule size MAPS with digital output and integrated zero suppression for the EUDET-JRA1 beam telescope". In: *Nuclear Instruments and Methods in Physics Research Section A: Accelerators, Spectrometers, Detectors and Associated Equipment* 623.1 (2010). 1st International Conference on Technology and Instrumentation in Particle Physics, pp. 480–482. ISSN: 0168-9002. DOI: https://doi.org/10.1016/j.nima.2010.03.043 (cit. on pp. 26, 163).

[74] Hermann Kolanoski and Norbert Wermes. *Teilchendetektoren. Grundlagen und Anwendungen*. Springer, 2016. ISBN: 978-3-662-45349-0, 978-3-662-45350-6. DOI: 10.1007/978-3-662-45350-6 (cit. on p. 26).

[75] Ivan Perić. "A novel monolithic pixelated particle detector implemented in high-voltage CMOS technology". In: *Nuclear Instruments and Methods in Physics Research Section A: Accelerators, Spectrometers, Detectors and Associated Equipment* 582.3 (2007). VERTEX 2006, pp. 876–885. ISSN: 0168-9002. DOI: https://doi.org/10.1016/j.nima.2007.07.115 (cit. on pp. 26, 32).

[76] M. Aiba et al. *Science Case for the new High-Intensity Muon Beams HIMB at PSI*. 2021. arXiv: 2111.05788 [hep-ex]. URL: https://arxiv.org/abs/2111.05788 (cit. on pp. 29, 68).

[77] R.H. Bernstein and Peter S. Cooper. "Charged lepton flavor violation: An experimenter's guide". In: *Physics Reports* 532.2 (2013). Charged Lepton Flavor Violation: An Experimenter's Guide, pp. 27–64. ISSN: 0370-1573. DOI: https://doi.org/10.1016/j.physrep.2013.07.002 (cit. on p. 29).

[78] K. Arndt et al. "Technical design of the phase I Mu3e experiment". In: *Nuclear Instruments and Methods in Physics Research Section A: Accelerators, Spectrometers, Detectors and Associated Equipment* 1014 (2021), p. 165679. ISSN: 0168-9002. DOI: https://doi.org/10.1016/j.nima.2021.165679 (cit. on pp. 29–31).

[79] U. Bellgardt et al. "Search for the decay $\mu^+ \to e^+e^+e^-$". In: *Nuclear Physics B* 299.1 (1988), pp. 1–6. ISSN: 0550-3213. DOI: https://doi.org/10.1016/0550-3213(88)90462-2 (cit. on p. 29).

[80] Heiko Christian Augustin. *Development of a novel slow control interface and suppression of signal line crosstalk enabling HV-MAPS as sensor technology for Mu3e*. eng. Dissertation. 2021. DOI: 10.11588/heidok.00030885 (cit. on pp. 31, 32, 36, 38, 39, 41, 43, 74, 78, 83).

[81] Ann-Kathrin Perrevoort. "Characterisation of High Voltage Monolithic Active Pixel Sensors for the Mu3e Experiment". Master thesis. Heidelberg, Germany: Heidelberg University, 2012. URL: https://www.physi.uni-heidelberg.de/Publications/MasterPerrevoort.pdf (cit. on p. 32).

[82] A. Cerdeira and M. Estrada. "Analytical expressions for the calculation of pixel detector capacitances". In: *IEEE Transactions on Nuclear Science* 44.1 (1997), pp. 63–66. DOI: 10.1109/23.554825 (cit. on p. 34).

[83] Optim Wafer Services. *Optim Wafer Services*. Accessed: 2025-07-07. 2025. URL: https://www.optimwaferservices.com/ (cit. on p. 35).

[84] Keithley Instruments, Tektronix. *Keithley 2611B Source Measure Unit*. Series 2600B System SourceMeter Instrument Reference Manual, 2600BS-901-01 Rev. F. Aug. 2021. URL: https://download.tek.com/manual/2600BS-901-01F_2600B_Reference_Aug2021.pdf (cit. on p. 35).

[85] David Maximilian Immig. *MuPix10: An Unexpected Journey*. Presentation for the seminar of the HighRR Graduate school, University Heidelberg. Mar. 2021. URL: https://indico.cern.ch/event/1134245/ (cit. on pp. 35, 66).

[86] Heiko Augustin et al. "MuPix: An HV–MAPS for the Mu3e Experiment". In: *Proceedings of the 31st International Workshop on Vertex Detectors (VERTEX2022)*. 2022. DOI: 10.7566/JPSCP.42.011020. eprint: https://journals.jps.jp/doi/pdf/10.7566/JPSCP.42.011020 (cit. on pp. 35, 66).

[87] Masao Okihara et al. *Lapis SOI Pixel Process*. 2015. arXiv: 1511.05224 [physics.ins-det]. URL: https://arxiv.org/abs/1511.05224 (cit. on p. 35).

[88] David-Leon Pohl. "3D-Silicon and Passive CMOS Sensors for Pixel Detectors in High Radiation Environments". PhD thesis. Rheinische Friedrich-Wilhelms-Universität Bonn, Oct. 2020. URL: https://hdl.handle.net/20.500.11811/8743 (cit. on p. 35).

[89] Anna Lelia Maria Fuchs. "Development of a Quality Control Procedure for MuPix11 Pixel Sensors for the Mu3e Vertex Detector". Bachelor thesis. Heidelberg, Germany: Heidelberg University, 2023. URL: https://www.physi.uni-heidelberg.de/Publications/Bachelor_Thesis_Fuchs_Lelia.pdf (cit. on p. 35).

[90] Ivan Perić et al. "High-Voltage CMOS Active Pixel Sensor". In: *IEEE Journal of Solid-State Circuits* 56.8 (2021), pp. 2488–2502. DOI: 10.1109/JSSC.2021.3061760 (cit. on pp. 36, 37, IX).

[91] Helmuth Spieler. *Semiconductor Detector Systems*. Vol. v.12. Semiconductor Science and Technology. Oxford: Oxford University Press, 2005. ISBN: 978-0-19-852784-8 (cit. on pp. 37, 62).

[92] Heiko Augustin et al. "MuPix10: First Results from the Final Design". In: *Proceedings of the 29th International Workshop on Vertex Detectors (VERTEX2020)*. DOI: 10.7566/JPSCP.34.010012. eprint: https://journals.jps.jp/doi/pdf/10.7566/JPSCP.34.010012 (cit. on pp. 38, 39, 42, 45).

[93] Lennart Huth. "A High Rate Testbeam Data Acquisition System and Characterization of High Voltage Monolithic Active Pixel Sensors". eng. Dissertation. Heidelberg University, Faculty of Physics and Astronomy, Institute of Physics, 2018. DOI: 10.11588/heidok.00025785 (cit. on pp. 38, 65, 70).

[94] Jan Patrick Hammerich. "Analog Characterization and Time Resolution of a Large Scale HV-MAPS Prototype". MA thesis. Heidelberg, Germany: Heidelberg University, 2018. URL: https://www.physi.uni-heidelberg.de/Publications/MasterHammerich.pdf (cit. on pp. 40, 41).

[95] Sebastian Dittmeier. "Fast data acquisition for silicon tracking detectors at high rates". eng. Dissertation. Heidelberg University, Faculty of Physics and Astronomy, Institute of Physics, 2018. DOI: 10.11588/heidok.00025791 (cit. on pp. 44, 70).

[96] David Maximilian Immig. "Characterization of ATLASPix1, an HV-CMOS Demonstrator for the Phase-II Upgrade of the ATLAS Inner Tracker". Master thesis. Heidelberg, Germany: Heidelberg University, 2019. URL: https://www.physi.uni-heidelberg.de/Publications/MasterThesisImmig.pdf (cit. on p. 44).

[97] David Maximilian Immig. "Charakterisierung des VCO, der PLL und der Pulsform des MuPix7 in Abhängigkeit der Umgebungstemperatur". Bachelor thesis. Heidelberg, Germany: Heidelberg University, 2016. URL: https://www.physi.uni-heidelberg.de/Publications/BachelorImmig.pdf (cit. on p. 44).

[98] B. Sellers and F.A. Hanser. "Difference between average and most probable energy losses for the valivov distribution". In: *Nuclear Instruments and Methods* 104.1 (1972), pp. 233–235. ISSN: 0029-554X. DOI: https://doi.org/10.1016/0029-554X(72)90327-8 (cit. on p. 47).

[99] P. Mertens. "Experiments on the difference between most probable and mean energy loss for foil transmitted protons". In: *Nuclear Instruments and Methods in Physics Research Section B: Beam Interactions with Materials and Atoms* 13.1 (1986), pp. 91–94. ISSN: 0168-583X. DOI: https://doi.org/10.1016/0168-583X(86)90480-5 (cit. on p. 47).

[100] P. A. Bromiley. *Products and Convolutions of Gaussian Probability Density Functions*. Tech. rep. Internal Report. Last updated 11/9/2013. Imaging Science and Biomedical Engineering Division, Medical School, University of Manchester, 2013. URL: https://citeseerx.ist.psu.edu/document?repid=rep1&type=pdf&doi=ebf0adc76e49a9619c042792b26e0c599e1aef5c (cit. on p. 48).

[101] Hans Bichsel. "Straggling in thin silicon detectors". In: *Rev. Mod. Phys.* 60 (3 1988), pp. 663–699. DOI: 10.1103/RevModPhys.60.663 (cit. on pp. 49, 50, 56, 57, 175).

[102] Lev Davidovich Landau. "56 - ON THE ENERGY LOSS OF FAST PARTICLES BY IONISATION". In: *Collected Papers of L.D. Landau*. Ed. by D. TER HAAR. Translation from original journal: J. Phys. (USSR) from 1944. Pergamon, 1965, pp. 417–424. ISBN: 978-0-08-010586-4. DOI: https://doi.org/10.1016/B978-0-08-010586-4.50061-4 (cit. on pp. 49, 52, 53, 171, 172).

[103] F. Rohrlich and B. C. Carlson. "Positron-Electron Differences in Energy Loss and Multiple Scattering". In: *Phys. Rev.* 93 (1 Jan. 1954), pp. 38–44. DOI: 10.1103/PhysRev.93.38 (cit. on pp. 49, 50, 54).

[104] D. P. Heddle and Leonard C. Maximon. "Differences in straggling for positrons and electrons". In: *Phys. Rev. C* 40 (4 Oct. 1989), pp. 1632–1640. DOI: 10.1103/PhysRevC.40.1632 (cit. on pp. 49, 54, 55).

[105] D. P. Heddle and Leonard C. Maximon. "Erratum: Differences in straggling for positrons and electrons". In: *Phys. Rev. C* 41 (3 Mar. 1990), pp. 1320–1320. DOI: 10.1103/PhysRevC.41.1320.2 (cit. on pp. 49, 54, 55).

[106] H. D. Maccabee, M. R. Raju, and C. A. Tobias. "Fluctuations of Energy Loss by Heavy Charged Particles in Thin Absorbers". In: *Phys. Rev.* 165 (2 Jan. 1968), pp. 469–474. DOI: 10.1103/PhysRev.165.469 (cit. on p. 50).

[107] Richard Talman. "On the statistics of particle identification using ionization". In: *Nuclear Instruments and Methods* 159.1 (1979), pp. 189–211. ISSN: 0029-554X. DOI: https://doi.org/10.1016/0029-554X(79)90348-3 (cit. on p. 50).

[108] J.F. Bak et al. "Large departures from Landau distributions for high-energy particles traversing thin Si and Ge targets". In: *Nuclear Physics B* 288 (1987), pp. 681–716. ISSN: 0550-3213. DOI: https://doi.org/10.1016/0550-3213(87)90234-3 (cit. on pp. 50, 51).

[109] P. V. Vavilov. "Ionization losses of high-energy heavy particles". In: *Sov. Phys. JETP* 5 (1957). English translation (Russian original - ZhETF, Vol. 32, No. 4, p. 920, October 1957), pp. 749–751. URL: http://jetp.ras.ru/cgi-bin/dn/e_005_04_0749.pdf (cit. on pp. 51, 53).

[110] Eugene Bulyak and Nikolay Shul'ga. *Landau distribution of ionization losses: history, importance, extensions*. 2022. arXiv: 2209.06387 [physics.plasm-ph]. URL: https://arxiv.org/abs/2209.06387 (cit. on p. 51).

[111] R. Frühwirth and R. K. Bock. *Data analysis techniques for high-energy physics experiments*. Ed. by H. Grote, D. Notz, and M. Regler. Vol. 11. Cambridge University Press, 2000. ISBN: 978-0-521-63548-6, 978-1-139-14219-9 (cit. on pp. 52, 77, 148, 172).

[112] K.S. Kölbig and B. Schorr. "Asymptotic expansions for the Landau density and distribution functions". In: *Computer Physics Communications* 32.2 (1984), pp. 121–131. ISSN: 0010-4655. DOI: https://doi.org/10.1016/0010-4655(84)90065-1 (cit. on pp. 52, 172).

[113] J. E. Moyal. "XXX. Theory of ionization fluctuations". en. In: *The London, Edinburgh, and Dublin Philosophical Magazine and Journal of Science* (Apr. 2009). Publisher: Taylor & Francis Group. DOI: 10.1080/14786440308521076. (Visited on 03/28/2023) (cit. on pp. 53, 173).

[114] Christian Walck. *Hand-book on statistical distributions for experimentalists*. Dec. 1996. URL: https://staff.fysik.su.se/~walck/suf9601.pdf (cit. on pp. 53, 101, 128, 173, 174, 177).

[115] B. Schorr. "Programs for the Landau and the Vavilov distributions and the corresponding random numbers". In: *Computer Physics Communications* 7.4 (1974), pp. 215–224. ISSN: 0010-4655. DOI: https://doi.org/10.1016/0010-4655(74)90091-5 (cit. on pp. 53, 174).

[116] H. Esbensen et al. "Random and channeled energy loss in thin germanium and silicon crystals for positive and negative 2-15-GeV/c pions, kaons, and protons". In: *Phys. Rev. B* 18 (3 Aug. 1978), pp. 1039–1054. DOI: 10.1103/PhysRevB.18.1039 (cit. on p. 55).

[117] P. Gehrmann, K. Lenkeit, and R. Stolle. "Measurements of Proton Channeling Energy Losses in Silicon in the Intermediate Energy Region". In: *physica status solidi (b)* 131.2 (1985), pp. 519–526. DOI: https://doi.org/10.1002/pssb.2221310213. eprint: https://onlinelibrary.wiley.com/doi/pdf/10.1002/pssb.2221310213 (cit. on p. 55).

[118] B. R. Appleton, C. Erginsoy, and W. M. Gibson. "Channeling Effects in the Energy Loss of 3-11-MeV Protons in Silicon and Germanium Single Crystals". In: *Phys. Rev.* 161 (2 Sept. 1967), pp. 330–349. DOI: 10.1103/PhysRev.161.330 (cit. on p. 55).

[119] S. V. Trofymenko and I. V. Kyryllin. "Ionization loss spectra of high-energy protons in an oriented crystal at various incidence angles with respect to a crystalline plane". In: *European Physical Journal C* 84 (Nov. 2024). Received 01 August 2024, Accepted 05 November 2024, Published 22 November 2024. DOI: 10.1140/epjc/s10052-024-13579-8 (cit. on p. 55).

[120] Trofymenko, S. V. and Kyryllin, I. V. "On the ionization loss spectra of high-energy channeled negatively charged particles". In: *Eur. Phys. J. C* 80.7 (2020), p. 689. DOI: 10.1140/epjc/s10052-020-8127-z (cit. on p. 55).

[121] Michael Nastasi and James W. Mayer. *Ion Implantation and Synthesis of Materials*. 1st ed. Springer-Verlag Berlin Heidelberg, 2006. ISBN: 978-3-540-45298-0. DOI: 10.1007/978-3-540-45298-0 (cit. on p. 55).

[122] Peter Sigmund. *Particle Penetration and Radiation Effects. Volume 2: Penetration of Atomic and Molecular Ions*. 1st ed. Springer Series in Solid-State Sciences. Springer Cham, 2014. ISBN: 978-3-319-05563-3. DOI: 10.1007/978-3-319-05564-0 (cit. on p. 55).

[123] P. White, G. Millington, and Ernest Rutherford. "The velocity distribution of β-particles after passing through thin foils". In: *Proceedings of the Royal Society of London. Series A, Containing Papers of a Mathematical and Physical Character* 120.786 (1928), pp. 701–726. DOI: 10.1098/rspa.1928.0176. eprint: https://royalsocietypublishing.org/doi/pdf/10.1098/rspa.1928.0176 (cit. on p. 56).

[124] W. Paul and H. Reich. "Energieverlust schneller Elektronen in Be, C, H_2O, Fe und Pb". In: *Zeitschrift für Physik* 127 (1950). Received 16 December 1949; Issue date August 1950, pp. 429–442. DOI: 10.1007/BF01329840 (cit. on p. 56).

[125] O. Blunck and S. Leisegang. "Zum Energieverlust schneller Elektronen in dünnen Schichten". In: *Zeitschrift für Physik* 128 (1950). Received 18 September 1950; Issue date August 1950, pp. 500–505. DOI: 10.1007/BF01330032 (cit. on pp. 56, 175).

[126] O. Blunck and K. Westphal. "Zum Energieverlust energiereicher Elektronen in dünnen Schichten". In: *Zeitschrift für Physik* 130 (1951). Received 21 August 1951; Issue date October 1951, pp. 641–649. DOI: 10.1007/BF01329538 (cit. on p. 56).

[127] P. Shulek et al. "FLUCTUATIONS OF IONIZATION LOSSES". In: *Yad. Fiz.* 4 (1966), pp. 564–566 (cit. on p. 56).

[128] *Soviet journal of nuclear physics* (1965–1992). und. ISSN: 0038-5506 (cit. on p. 56).

[129] J. Ph. Perez, J. Sevely, and B. Jouffrey. "Straggling of fast electrons in aluminum foils observed in high-voltage electron microscopy (0.3-1.2 MV)". In: *Phys. Rev. A* 16 (3 Sept. 1977), pp. 1061–1069. DOI: 10.1103/PhysRevA.16.1061 (cit. on p. 57).

[130] S. Hancock et al. "Energy loss and energy straggling of protons and pions in the momentum range 0.7 to 115 GeV/c". In: *Phys. Rev. A* 28 (2 Aug. 1983), pp. 615–620. DOI: 10.1103/PhysRevA.28.615 (cit. on p. 56).

[131] S Meroli, D Passeri, and L Servoli. "Energy loss measurement for charged particles in very thin silicon layers". In: *Journal of Instrumentation* 6.06 (June 2011), P06013. DOI: 10.1088/1748-0221/6/06/P06013 (cit. on p. 56).

[132] Hans Bichsel. "Straggling of Heavy Charged Particles: Comparison of Born Hydrogenic-Wave-Function Approximation with Free-Electron Approximation". In: *Phys. Rev. B* 1 (7 Apr. 1970), pp. 2854–2862. DOI: 10.1103/PhysRevB.1.2854 (cit. on p. 56).

[133] Hans Bichsel. "Energy loss and ionization of fast charged particles in a 20 μm silicon detector". In: *Nuclear Instruments and Methods in Physics Research Section A: Accelerators, Spectrometers, Detectors and Associated Equipment* 235.1 (1985), pp. 174–179. ISSN: 0168-9002. DOI: https://doi.org/10.1016/0168-9002(85)90258-X (cit. on pp. 56, 57).

[134] Hans Bichsel and Roberta P. Saxon. "Comparison of calculational methods for straggling in thin absorbers". In: *Phys. Rev. A* 11 (4 Apr. 1975), pp. 1286–1296. DOI: 10.1103/PhysRevA.11.1286 (cit. on p. 56).

[135] W. Shockley. "Currents to Conductors Induced by a Moving Point Charge". In: *Journal of Applied Physics* 9.10 (Oct. 1938), pp. 635–636. ISSN: 0021-8979. DOI: 10.1063/1.1710367. eprint: https://pubs.aip.org/aip/jap/article-pdf/9/10/635/18304047/635_1_online.pdf (cit. on p. 58).

[136] S. Ramo. "Currents Induced by Electron Motion". In: *Proceedings of the IRE* 27.9 (1939), pp. 584–585. DOI: 10.1109/JRPROC.1939.228757 (cit. on p. 58).

[137] W. Riegler. "An application of extensions of the Ramo–Shockley theorem to signals in silicon sensors". In: *Nuclear Instruments and Methods in Physics Research Section A: Accelerators, Spectrometers, Detectors and Associated Equipment* 940 (2019), pp. 453–461. ISSN: 0168-9002. DOI: https://doi.org/10.1016/j.nima.2019.06.056 (cit. on p. 59).

[138] J. Schwandt and R. Klanner. "On the weighting field of irradiated silicon detectors". In: *Nuclear Instruments and Methods in Physics Research Section A: Accelerators, Spectrometers, Detectors and Associated Equipment* 942 (2019), p. 162418. ISSN: 0168-9002. DOI: https://doi.org/10.1016/j.nima.2019.162418 (cit. on p. 59).

[139] W. Riegler. "Extended theorems for signal induction in particle detectors VCI 2004". In: *Nuclear Instruments and Methods in Physics Research Section A: Accelerators, Spectrometers, Detectors and Associated Equipment* 535.1 (2004). Proceedings of the 10th International Vienna Conference on Instrumentation, pp. 287–293. ISSN: 0168-9002. DOI: https://doi.org/10.1016/j.nima.2004.07.129 (cit. on p. 59).

[140] Leonardo Rossi et al. *Pixel Detectors. From Fundamentals to Applications*. Particle Acceleration and Detection. Springer, 2006. ISBN: 978-3-540-28332-4, 978-3-642-06652-8, 978-3-540-28333-1. DOI: 10.1007/3-540-28333-1 (cit. on p. 59).

[141] W. Maes, K. De Meyer, and R. Van Overstraeten. "Impact ionization in silicon: A review and update". In: *Solid-State Electronics* 33.6 (1990), pp. 705–718. ISSN: 0038-1101. DOI: https://doi.org/10.1016/0038-1101(90)90183-F (cit. on p. 60).

[142] Esteban Currás Rivera and Michael Moll. "Study of Impact Ionization Coefficients in Silicon With Low Gain Avalanche Diodes". In: *IEEE Transactions on Electron Devices* 70.6 (2023), pp. 2919–2926. DOI: 10.1109/TED.2023.3267058 (cit. on p. 60).

[143] Adolf Fick. "Ueber Diffusion". In: *Annalen der Physik* 170.1 (1855), pp. 59–86. ISSN: 1521-3889. DOI: 10.1002/andp.18551700105. (Visited on 05/19/2025) (cit. on pp. 60, 61).

[144] A. Einstein. "Über die von der molekularkinetischen Theorie der Wärme geforderte Bewegung von in ruhenden Flüssigkeiten suspendierten Teilchen". In: *Annalen der Physik* 322.8 (1905), pp. 549–560. DOI: https://doi.org/10.1002/andp.19053220806. eprint: https://onlinelibrary.wiley.com/doi/pdf/10.1002/andp.19053220806 (cit. on p. 61).

[145] "Fluid Mechanics (Second Edition)". In: ed. by L. D. Landau and E. M. Lifshitz. Pergamon, Jan. 1987, p. iv. ISBN: 978-0-08-033933-7. DOI: 10.1016/B978-0-08-033933-7.50004-0. (Visited on 06/15/2025) (cit. on p. 61).

[146] Emilio Gatti et al. "Dynamics of electrons in drift detectors". In: *Nuclear Instruments and Methods in Physics Research Section A: Accelerators, Spectrometers, Detectors and Associated Equipment* 253.3 (1987), pp. 393–399. ISSN: 0168-9002. DOI: https://doi.org/10.1016/0168-9002(87)90522-5 (cit. on p. 61).

[147] Klaus Jürgen Engel, Roger Steadman, and Christoph Herrmann. "Pulse Temporal Splitting in Photon Counting X-Ray Detectors". In: *IEEE Transactions on Nuclear Science* 59.4 (2012), pp. 1480–1490. DOI: 10.1109/TNS.2012.2203610 (cit. on p. 61).

[148] Norbert Wermes. *Signal Formation and Signal Processing in Detectors: Lectures at the University of Freiburg, March 9-14, 2020, Lecture 1*. Lecture notes. Available at https://www.grk2044.uni-freiburg.de/dateien/dateien/wermes-freiburg-lecture-1.pdf. 2020 (cit. on p. 62).

[149] Adrian Herkert. "Characterization of a Monolithic Pixel Sensor Prototype in HV-CMOS Technology for the High-Luminosity LHC". eng. Dissertation. Heidelberg University, Faculty of Physics and Astronomy, Institute of Physics, 2020. DOI: 10.11588/heidok.00027893 (cit. on pp. 65, 69).

[150] Paul Wolf. "On-chip temperature measurements and studies of temperature effects on the pulse shaping of the MuPix11". Bachelor thesis. Heidelberg, Germany: Heidelberg University, 2023. URL: https://www.physi.uni-heidelberg.de/Publications/BSch_Thesis_Paul_updated-3.pdf (cit. on pp. 67, 136).

[151] W. Wagner et al. "PSI status 2008—Developments at the 590MeV proton accelerator facility". In: *Nuclear Instruments and Methods in Physics Research Section A: Accelerators, Spectrometers, Detectors and Associated Equipment* 600.1 (2009), pp. 5–7. ISSN: 0168-9002. DOI: https://doi.org/10.1016/j.nima.2008.11.018 (cit. on p. 68).

[152] Mike Seidel et al. "Production of a 1.3 MW Proton Beam at PSI". In: *Conf. Proc. C* 100523 (2010). Ed. by Akira Noda et al., TUYRA03. URL: https://accelconf.web.cern.ch/IPAC10/papers/tuyra03.pdf (cit. on p. 68).

[153] R. Khasanov et al. "High pressure research using muons at the Paul Scherrer Institute". In: *High Pressure Research* 36.2 (2016), pp. 140–166. DOI: 10.1080/08957959.2016.1173690 (cit. on p. 68).

[154] F. Berg et al. "Target studies for surface muon production". In: *Phys. Rev. Accel. Beams* 19 (2 Feb. 2016), p. 024701. DOI: 10.1103/PhysRevAccelBeams.19.024701 (cit. on p. 68).

[155] E. Cline et al. "Characterization of muon and electron beams in the Paul Scherrer Institute PiM1 channel for the MUSE experiment". In: *Phys. Rev. C* 105 (5 May 2022), p. 055201. DOI: 10.1103/PhysRevC.105.055201 (cit. on pp. 68, 69).

[156] G. Heidenreich. "Carbon and Beryllium Targets at PSI". In: *AIP Conference Proceedings* 642.1 (Dec. 2002), pp. 122–124. ISSN: 0094-243X. DOI: 10.1063/1.1522602. eprint: https://pubs.aip.org/aip/acp/article-pdf/642/1/122/12020635/122_1_online.pdf (cit. on p. 68).

[157] J.P. Albanese et al. "The SIN high resolution pion channel and spectrometer". In: *Nuclear Instruments and Methods* 158 (1979), pp. 363–370. ISSN: 0029-554X. DOI: https://doi.org/10.1016/S0029-554X(79)93570-5 (cit. on p. 68).

[158] Ethan Cline. *Understanding the Paul Scherrer Institute's PiM1 beamline for MUSE*. 2019. DOI: https://doi.org/doi:10.7282/t3-py63-f028 (cit. on p. 68).

[159] K. Deiters. *πM1 Beam Line*. Particle flux measurement in Fig. 3: https://aea.web.psi.ch/beam2lines/pim1c.html. URL: https://aea.web.psi.ch/beam2lines/beam_pim1.html (visited on 05/10/2025) (cit. on pp. 68, 69, 192).

[160] W. Hajdas et al. "High Energy Electron Radiation Exposure Facility at PSI". In: *Journal of Applied Mathematics and Physics* 2 (2014), pp. 910–917. DOI: http://dx.doi.org/10.4236/jamp.2014.29103 (cit. on p. 68).

[161] M. Tulej et al. "Detection efficiency of microchannel plates for e− and π− in the momentum range from 17.5 to 345 MeV/c". In: *Review of Scientific Instruments* 86.8 (Aug. 2015), p. 083310. ISSN: 0034-6748. DOI: 10.1063/1.4928063. eprint: https://pubs.aip.org/aip/rsi/article-pdf/doi/10.1063/1.4928063/14052646/083310_1_online.pdf (cit. on p. 68).

[162] A. Bravar et al. *Development of the Scintillating Fiber Timing Detector for the Mu3e Experiment*. 2022. arXiv: 2208.09906 [physics.ins-det]. URL: https://arxiv.org/abs/2208.09906 (cit. on p. 68).

[163] R. Balsiger et al. "Technical aspects of the SIN pion channel and spectrometer". In: *Nuclear Instruments and Methods* 157.2 (1978), pp. 247–255. ISSN: 0029-554X. DOI: https://doi.org/10.1016/0029-554X(78)90298-7 (cit. on p. 68).

[164] *Stratix® IV GX FPGA Development Kit, 530 Edition User Guide*. Accessed: 2025-07-09. Intel Corporation. Nov. 4, 2010. URL: https://www.intel.com/content/www/us/en/content-details/654684/stratix-iv-gx-fpga-development-kit-530-edition-user-guide.html (cit. on p. 69).

[165] *SCS2000/3000 System Units and Slot Card Datasheets*. Documentation and datasheets for the LTP Electronics SCS2000/3000 system units and slot cards, accessed July 2025. Paul Scherrer Institut (PSI). 2023. URL: https://www.psi.ch/de/ltp-electronics/www-documents (cit. on p. 72).

[166] R. Schmidt and S. Ritt. *Midas Slow Control Bus (MSCB)*. Accessed July 2025, Repository: https://bitbucket.org/tmidas/mscb/src/master/. Paul Scherrer Institut (PSI). 2025. URL: https://elog.psi.ch/mscb/ (cit. on pp. 72, 73).

[167] *R&S® HMP4040 Programmable Power Supply*. Product page accessed July 2025. Rohde & Schwarz GmbH & Co. KG. 2025. URL: https://scdn.rohde-schwarz.com/ur/pws/dl_downloads/dl_common_library/dl_brochures_and_datasheets/pdf_1/HMP_dat_en_5215-4981-32_v0201.pdf (cit. on p. 73).

[168] D. Dannheim et al. "Corryvreckan: a modular 4D track reconstruction and analysis software for test beam data". In: *Journal of Instrumentation* 16.03 (Mar. 2021), P03008. DOI: 10.1088/1748-0221/16/03/P03008 (cit. on pp. 74, 178).

[169] Morag Williams et al. *Corryvreckan - A Modular 4D Track Reconstruction and Analysis Software for Test Beam Data*. Version 2.0.0. Dec. 2020. DOI: 10.5281/zenodo.4384186 (cit. on pp. 74, 178).

[170] Claus Kleinwort. "General broken lines as advanced track fitting method". In: *Nuclear Instruments and Methods in Physics Research Section A: Accelerators, Spectrometers, Detectors and Associated Equipment* 673 (2012), pp. 107–110. ISSN: 0168-9002. DOI: https://doi.org/10.1016/j.nima.2012.01.024 (cit. on p. 75).

[171] Glen Cowan. *Error analysis for efficiency*. RHUL Physics. Accessed August 24, 2025. 2008. URL: https://www.pp.rhul.ac.uk/~cowan/stat/notes/efferr.pdf (cit. on pp. 77, 178).

[172] R. Brun and F. Rademakers. "ROOT: An object oriented data analysis framework". In: *Nucl. Instrum. Meth. A* 389 (1997). Ed. by M. Werlen and D. Perret-Gallix, pp. 81–86. DOI: 10.1016/S0168-9002(97)00048-X (cit. on pp. 77, 93, 97, 143, 172–174, 176, 177).

[173] Rene Brun et al. *root-project/root: v6.32/04*. Version v6-32-04. Aug. 2024. DOI: 10.5281/zenodo.848818 (cit. on pp. 77, 93, 97, 143, 172–174, 176, 177).

[174] Y. Unno et al. "Beamtest of nonirradiated and irradiated ATLAS SCT microstrip modules at KEK". In: *IEEE Transactions on Nuclear Science* 49.4 (2002), pp. 1868–1875. DOI: 10.1109/TNS.2002.801505 (cit. on p. 80).

[175] Patrick McCormack et al. *New Method for Silicon Sensor Charge Calibration Using Compton Scattering*. 2020. arXiv: 2008.11860 [physics.ins-det]. URL: https://arxiv.org/abs/2008.11860 (cit. on p. 85).

[176] R. P. M. van der Boog. "Energy calibration procedure of a pixel detector". en. foaf:name, 2013. URL: https://hbo-kennisbank.nl/details/sharekit_hh:oai:surfsharekit.nl:907ed951-3f7b-439a-bd1e-9a85a5a447b8 (visited on 06/17/2025) (cit. on pp. 87, 91).

[177] E. J. Schioppa. *The color of X-rays: Spectral X-ray computed tomography using energy sensitive pixel detectors*. en. 's-HertogenboschBoxpress, 2014. ISBN: 978-90-8891-983-1. URL: https://www.dare.uva.nl/search?field1=meta;value1=schioppa;join=and;field2=meta;smode=advanced;docsPerPage=1;startDoc=1 (visited on 06/22/2025) (cit. on pp. 88, 92).

[178] Xavier Mougeot et al. "Evaluations of the decay data of 55Fe, 55Co, 103mRh, 103Pd, 129mSn and 166Ho from the Decay Data Evaluation Project (DDEP)—2024". In: *Metrologia* 62.2 (Feb. 2025). For Figure see: https://www.

bipm.org/documents/d/guest/fe-55_report, p. 029001. DOI: 10.1088/1681-7575/adb275 (cit. on pp. 90, 91).

[179] N. Soppera, M. Bossant, and E. Dupont. "JANIS 4: An Improved Version of the NEA Java-based Nuclear Data Information System". In: *Nuclear Data Sheets* 120 (2014), pp. 294–296. ISSN: 0090-3752. DOI: https://doi.org/10.1016/j.nds.2014.07.071 (cit. on pp. 91, 179).

[180] J. Katakura and F. Minato. *JENDL Decay Data File JENDL/DDF-2015*. en. 2016. DOI: 10.11484/jaea-data-code-2015-030. (Visited on 06/23/2025) (cit. on pp. 91, 179).

[181] A. J. M. Plompen et al. "The joint evaluated fission and fusion nuclear data library, JEFF-3.3". In: *The European Physical Journal A* 56.7 (July 2020), p. 181. ISSN: 1434-601X. DOI: 10.1140/epja/s10050-020-00141-9 (cit. on pp. 91, 179).

[182] D.A. Brown et al. "ENDF/B-VIII.0: The 8 th Major Release of the Nuclear Reaction Data Library with CIELO-project Cross Sections, New Standards and Thermal Scattering Data". en. In: *Nuclear Data Sheets* 148 (Feb. 2018), pp. 1–142. ISSN: 00903752. DOI: 10.1016/j.nds.2018.02.001. (Visited on 06/23/2025) (cit. on pp. 91, 179).

[183] Kouichi Hagino et al. "Measurement of Charge Cloud Size in X-Ray SOI Pixel Sensors". In: *IEEE Transactions on Nuclear Science* 66.7 (2019), pp. 1897–1905. DOI: 10.1109/TNS.2019.2920281 (cit. on p. 91).

[184] R. L. Workman et al. "Review of Particle Physics". In: *PTEP* 2022 (2022), p. 083C01. DOI: 10.1093/ptep/ptac097 (cit. on p. 91).

[185] *Fluke 175, 177, 179 True-rms Multimeters User Manual*. Fluke 175 used, Accessed: 2025-08-31. Fluke Corporation. URL: https://media.fluke.com/4d153033-ae82-4c9e-8226-b10800c13c70_original%20file.pdf (cit. on p. 100).

[186] *Fluke 3000 FC Series Wireless Multimeter User Manual*. Accessed: 2025-08-31. Fluke Corporation. URL: https://media.fluke.com/437e18a0-de4d-4090-ab8a-b0df016de4fd_original%20file.pdf (cit. on p. 100).

[187] George A. Baker and Peter R. Graves-Morris. *Padé Approximants: Basic Theory*. Vol. 13. Encyclopedia of Mathematics and its Applications. Reading, Mass.: Addison-Wesley, 1981. ISBN: 978-0-201-13512-1 (cit. on pp. 100, 101).

[188] F. James. *Statistical Methods in Experimental Physics*. 2nd. World Scientific Publishing Co. Pte- Ltd., 2006. ISBN: 978-981-270-527-3, 981-270-527-9 (cit. on p. 103).

[189] Heiko Augustin et al. "TelePix - A fast region of interest trigger and timing layer for the EUDET Telescopes". In: *Nuclear Instruments and Methods in Physics Research Section A: Accelerators, Spectrometers, Detectors and Associated Equipment* 1048 (2023), p. 167947. ISSN: 0168-9002. DOI: https://doi.org/10.1016/j.nima.2022.167947 (cit. on pp. 116, 127, 143, 144, 162, 163).

[190] Benedict Maisano. "Validation of an NMOS Comparator Design in High Voltage Monolithic Active Pixel Sensors for LHCb Upgrade II Mighty-Tracker Performances". Master thesis. Heidelberg, Germany: Heidelberg University, 2025 (cit. on p. 116).

[191] G. Kramberger et al. "Radiation effects in Low Gain Avalanche Detectors after hadron irradiations". In: *Journal of Instrumentation* 10.07 (July 2015), P07006. DOI: 10.1088/1748-0221/10/07/P07006 (cit. on p. 117).

[192] I. Mandić et al. "Gain recovery in heavily Irradiated Low Gain Avalanche Detectors by high temperature annealing". In: *Nuclear Instruments and Methods in Physics Research Section A: Accelerators, Spectrometers, Detectors and Associated Equipment* 1055 (2023), p. 168553. ISSN: 0168-9002. DOI: https://doi.org/10.1016/j.nima.2023.168553 (cit. on p. 117).

[193] Inc. Tektronix. *2450 SourceMeter® SMU Instrument Datasheet*. 1KW-60904-2, Rev. 121724. 2024. URL: https://download.tek.com/datasheet/1KW-60904-2_2450_Datasheet_121724.pdf (cit. on p. 122).

[194] Yusuke Suda et al. "Performance evaluation of the high-voltage CMOS active pixel sensor AstroPix for gamma-ray space telescopes". In: *Nuclear Instruments and Methods in Physics Research Section A: Accelerators, Spectrometers, Detectors and Associated Equipment* 1068 (2024), p. 169762. ISSN: 0168-9002. DOI: https://doi.org/10.1016/j.nima.2024.169762 (cit. on pp. 127, 143, 161).

[195] Moritz Amadeus Lill. "Charakterisierung eines HV-MAPS für das P2-Experiment". Bachelor thesis. Mainz, Germany: Johannes Gutenberg-Universität Mainz, 2025 (cit. on pp. 138, 162).

[196] J. Allison et al. "Recent developments in Geant4". In: *Nuclear Instruments and Methods in Physics Research Section A: Accelerators, Spectrometers, Detectors and Associated Equipment* 835 (2016), pp. 186–225. ISSN: 0168-9002. DOI: https://doi.org/10.1016/j.nima.2016.06.125 (cit. on pp. 142, 163, 190).

[197] Geant4 Collaboration. *Geant4 Physics Reference Manual, Version 11.2*. Rev8.0: December 8th, 2023. CERN. 2023. URL: https://geant4-userdoc.web.cern.ch/UsersGuides/PhysicsReferenceManual/html/index.html (cit. on p. 142).

[198] Håkan Wennlöf et al. "Simulating monolithic active pixel sensors: A technology-independent approach using generic doping profiles". In: *Nuclear Instruments and Methods in Physics Research Section A: Accelerators, Spectrometers, Detectors and Associated Equipment* 1073 (2025), p. 170227. ISSN: 0168-9002. DOI: https://doi.org/10.1016/j.nima.2025.170227 (cit. on p. 142).

[199] S. Hancock et al. "Energy-loss distributions for single particles and several particles in a thin silicon absorber". In: *Nuclear Instruments and Methods in Physics Research Section B: Beam Interactions with Materials and Atoms* 1.1 (1984), pp. 16–22. ISSN: 0168-583X. DOI: https://doi.org/10.1016/0168-583X(84)90472-5 (cit. on pp. 142, 151, 175).

[200] R. Diener et al. "The DESY II test beam facility". In: *Nuclear Instruments and Methods in Physics Research Section A: Accelerators, Spectrometers, Detectors and Associated Equipment* 922 (2019), pp. 265–286. ISSN: 0168-9002. DOI: https://doi.org/10.1016/j.nima.2018.11.133 (cit. on pp. 143, 159).

[201] Florian Michael Pitters et al. *Time and Energy Calibration of Timepix3 Assemblies with Thin Silicon Sensors*. 2018. URL: https://cds.cern.ch/record/2649493 (cit. on p. 143).

[202] Jens Cravan Cisneros. "Hit Rate Study of an Amplifier Model in a Combined Allpix2 and LTspice Simulation". Bachelor thesis. Heidelberg, Germany: Heidelberg University, 2025. URL: https://www.physi.uni-heidelberg.de/Publications/FinalThesisCravanCisneros.pdf (cit. on p. 163).

[203] Ian David Linnett. "First Sensor Capacitance Measurements of High-Voltage Monolithic Active Pixel Sensors for the LHCb Upgrade II Mighty Tracker". Bachelor thesis. Heidelberg, Germany: Heidelberg University, 2025. URL: https://www.physi.uni-heidelberg.de/Publications/BAIan.pdf (cit. on p. 163).

[204] N.D. Arora, J.R. Hauser, and D.J. Roulston. "Electron and hole mobilities in silicon as a function of concentration and temperature". In: *IEEE Transactions on Electron Devices* 29.2 (1982), pp. 292–295. DOI: 10.1109/T-ED.1982.20698 (cit. on pp. 168, 169).

[205] G. Masetti, M. Severi, and S. Solmi. "Modeling of carrier mobility against carrier concentration in arsenic-, phosphorus-, and boron-doped silicon". In: *IEEE Transactions on Electron Devices* 30.7 (1983), pp. 764–769. DOI: 10.1109/T-ED.1983.21207 (cit. on pp. 168, 169).

[206] *Random Number Generation and Monte Carlo Methods*. en. Statistics and Computing. New York: Springer-Verlag, 2003. ISBN: 978-0-387-00178-4. DOI: 10.1007/b97336. (Visited on 06/27/2025) (cit. on p. 172).

[207] V. M. Zolotarev. *One-dimensional stable distributions*. eng. Provindence, R.I. : American Mathematical Society, 1986. ISBN: 978-0-8218-4519-6. URL: http://archive.org/details/onedimensionalst00zolo_0 (visited on 06/27/2025) (cit. on p. 172).

[208] *Landau distribution*. en. Page Version ID: 1291978611. May 2025. URL: https://en.wikipedia.org/w/index.php?title=Landau_distribution&oldid=1291978611#cite_note-5 (visited on 06/27/2025) (cit. on p. 172).

[209] Wolfram Research, Inc. *Mathematica, Version 13.0*. https://www.wolfram.com/mathematica/. Wolfram Research, Inc. Champaign, Illinois, 2021 (cit. on p. 172).

[210] K.S. Kölbig and B. Schorr. "A program package for the Landau distribution". In: *Computer Physics Communications* 31.1 (1984), pp. 97–111. ISSN: 0010-4655. DOI: https://doi.org/10.1016/0010-4655(84)90085-7 (cit. on p. 172).

[211] K.S. Kölbig and B. Schorr. "Erratum to: "A program package for the Landau distribution" [Comput. Phys. Commun. 31 (1984) 97–111]". In: *Computer Physics Communications* 178.12 (2008), p. 972. ISSN: 0010-4655. DOI: https://doi.org/10.1016/j.cpc.2008.03.002 (cit. on p. 172).

[212] T Davidek and R. Leitner. "Parametrization of the Muon Response in the Tile Calorimeter". In: (Apr. 1997). URL: https://cds.cern.ch/record/683578?ln=de (cit. on p. 173).

[213] Prof. Bernhard Ketzer. *Modern Particle Detectors*. Contribution to SFB School 2016, MITP, Mainz. Accessed: 2025-07-30. 2016. URL: https://indico.mitp.uni-mainz.de/event/81/contributions/2488/ (cit. on p. 173).

[214] V.C. Ermilova, L.P. Kotenko, and G.I. Merzon. "Fluctuations and the most probable values of relativistic charged particle energy loss in thin gas layers". In: *Nuclear Instruments and Methods* 145.3 (1977), pp. 555–563. ISSN: 0029-554X. DOI: https://doi.org/10.1016/0029-554X(77)90586-9 (cit. on p. 173).

[215] Alberto Rotondi and Paolo Montagna. "Fast calculation of Vavilov distribution". In: *Nuclear Instruments and Methods in Physics Research Section B: Beam Interactions with Materials and Atoms* 47.3 (1990), pp. 215–223. ISSN: 0168-583X. DOI: https://doi.org/10.1016/0168-583X(90)90749-K (cit. on pp. 173–175).

[216] Gauss Cordeiro et al. "The beta Moyal: a useful skew distribution". In: *International Journal of Research and Reviews in Applied Sciences* 10 (Feb. 2012). See: https://www.researchgate.net/publication/229432075_The_beta_Moyal_a_useful_skew_distribution, pp. 171–192 (cit. on p. 173).

[217] M. M. Nassar and M. Ibrahem. "A New Generalization of the Moyal Distribution". In: *Journal of Statistics Applications & Probability* 9.2 (2020). See: https://www.naturalspublishing.com/files/published/763gr68q1npt59.pdf, pp. 361–378. DOI: 10.18576/jsap/090215 (cit. on p. 173).

[218] D.J.S. Findlay and A.R. Dusautoy. "Improvements to the Blunck-Leisegang energy loss straggling distribution". In: *Nuclear Instruments and Methods* 174.3 (1980), pp. 531–533. ISSN: 0029-554X. DOI: https://doi.org/10.1016/0029-554X(80)91106-4 (cit. on pp. 175, 176).

[219] Steve Baker and Robert D. Cousins. "Clarification of the use of CHI-square and likelihood functions in fits to histograms". In: *Nuclear Instruments and Methods in Physics Research* 221.2 (1984), pp. 437–442. ISSN: 0167-5087. DOI: https://doi.org/10.1016/0167-5087(84)90016-4 (cit. on p. 177).

[220] Roger J. Barlow. *Statistics: A Guide to the Use of Statistical Methods in the Physical Sciences*. Manchester Physics Series. Chichester, England: John Wiley & Sons, 1989. ISBN: 0471922951 (cit. on p. 177).

[221] Inc. Keithley Instruments. *Model 2001 Multimeter Operator's Manual*. Accessed: 2025-09-09. Cleveland, Ohio, USA, 2010. URL: https://download.tek.com/manual/2001-900-01(K-Aug2010)(Operator).pdf (cit. on p. 181).

[222] Tektronix. *Digital Phosphor Oscilloscopes - DPO7000 Series Datasheet*. Used version DPO7254C, Accessed: 2025-09-09. Tektronix Inc. URL: https://download.tek.com/datasheet/DPO7000C-Oscilloscope-Datasheet-48W2654321.pdf (cit. on p. 181).

[223] A. C. Thompson et al. *X-Ray Data Booklet*. Third. Berkeley, CA: Center for X-Ray Optics and Advanced Light Source, Lawrence Berkeley National Laboratory, 2009. URL: https://cxro.lbl.gov/PDF/X-Ray-Data-Booklet.pdf (cit. on p. 190).

[224] T. Kibédi et al. "Evaluation of theoretical conversion coefficients using BrIcc". In: *Nuclear Instruments and Methods in Physics Research Section A: Accelerators, Spectrometers, Detectors and Associated Equipment* 589.2 (2008), pp. 202–229. ISSN: 0168-9002. DOI: https://doi.org/10.1016/j.nima.2008.02.051 (cit. on p. 190).

[225] Thomas A. Carlson. *Photoelectron and Auger Spectroscopy*. en. Boston, MA: Springer US, 1975. ISBN: 978-1-4757-0120-3 978-1-4757-0118-0. DOI: 10.1007/978-1-4757-0118-0. (Visited on 06/22/2025) (cit. on p. 190).

[226] R. Bimbot et al. "Stopping of Ions Heavier than Helium". In: *Journal of the ICRU* 5 (June 2005). See: https://www.researchgate.net/publication/286266914_Stopping_of_Ions_Heavier_than_Helium, pp. i–253. DOI: 10.1093/jicru/ndi001 (cit. on pp. 190, 191).

[227] Peter Sigmund. *Particle Penetration and Radiation Effects: General Aspects and Stopping of Swift Point Charges*. 1st ed. Vol. 151. Springer Series in Solid-State Sciences. Springer Berlin, Heidelberg, 2006. ISBN: 978-3-540-31713-5. DOI: 10.1007/3-540-31718-X (cit. on p. 190).

[228] A. Kramida et al. NIST Atomic Spectra Database (ver. 5.12), [Online]. Available: https://physics.nist.gov/asd [2025, July 30]. National Institute of Standards and Technology, Gaithersburg, MD. Silicon data taken directly from: https://physics.nist.gov/cgi-bin/ASD/ie.pl?spectra=Si&submit=Retrieve+Data&units=1&format=0&order=0&at_num_out=on&sp_name_out=on&ion_charge_out=on&el_name_out=on&seq_out=on&shells_out=on&level_out=on&ion_conf_out=on&e_out=0&unc_out=on&biblio=on. 2024 (cit. on p. 190).

[229] "Stopping powers and ranges for protons and alpha particles". In: (1994). Report Number: ICRU-1993-49 (cit. on p. 191).

[230] M. J. Berger and S. M. Seltzer. *Stopping Powers and Ranges of Electrons and Positrons (2nd Ed.)* Tech. rep. NBSIR 82-2550A. Washington, DC: U.S. Department of Commerce, National Bureau of Standards, 1982. URL: https://nvlpubs.nist.gov/nistpubs/Legacy/IR/nbsir82-2550A.pdf (cit. on p. 191).

[231] *Atomic and nuclear properties of nitrogen gas (N2)*. See also Table of muon dE/dx and Range: https://pdg.lbl.gov/2024/AtomicNuclearProperties/MUE/muE_nitrogen_gas.pdf. URL: https://pdg.lbl.gov/2024/AtomicNuclearProperties/HTML/nitrogen_gas.html (visited on 04/15/2025) (cit. on p. 191).

[232] *Atomic and nuclear properties of aluminum (Al)*. See also Table of muon dE/dx and Range: https://pdg.lbl.gov/2024/AtomicNuclearProperties/MUE/muE_aluminum_Al.pdf. URL: https://pdg.lbl.gov/2024/AtomicNuclearProperties/HTML/aluminum_Al.html (visited on 04/15/2025) (cit. on p. 191).

[233] *Atomic and nuclear properties of silicon dioxide (fused quartz) (SiO2)*. See also Table of muon dE/dx and Range: https://pdg.lbl.gov/2024/AtomicNuclearProperties/MUE/muE_silicon_dioxide_fused_quartz.pdf. URL: https://pdg.lbl.gov/2024/AtomicNuclearProperties/HTML/silicon_dioxide_fused_quartz.html (visited on 04/15/2025) (cit. on p. 191).

[234] *Atomic and nuclear properties of polyimide film [(C22H10N2O5)n]*. See also Table of muon dE/dx and Range: https://pdg.lbl.gov/2024/AtomicNuclearProperties/MUE/muE_polyimide_film.pdf. URL: https://pdg.lbl.gov/2024/AtomicNuclearProperties/HTML/polyimide_film.html (visited on 04/15/2025) (cit. on p. 191).

[235] *Atomic and nuclear properties of Epotek-301-1*. See also Table of muon dE/dx and Range: https://pdg.lbl.gov/2024/AtomicNuclearProperties/MUE/muE_Epotek-301-1.pdf. URL: https://pdg.lbl.gov/2024/AtomicNuclearProperties/HTML/Epotek-301-1.html (visited on 04/15/2025) (cit. on p. 191).

[236] *Atomic and nuclear properties of G10*. See also Table of muon dE/dx and Range: https://pdg.lbl.gov/2024/AtomicNuclearProperties/MUE/muE_G10.pdf. URL: https://pdg.lbl.gov/2024/AtomicNuclearProperties/HTML/G10.html (visited on 04/15/2025) (cit. on p. 191).

[237] *Atomic and nuclear properties of air (dry, 1 atm)*. See also Table of muon dE/dx and Range: https://pdg.lbl.gov/2024/AtomicNuclearProperties/MUE/muE_air_dry_1_atm.pdf. URL: https://pdg.lbl.gov/2024/AtomicNuclearProperties/HTML/air_dry_1_atm.html (visited on 04/15/2025) (cit. on p. 191).

Publications

Articles

[1] Heiko Augustin et al. "TelePix - A fast region of interest trigger and timing layer for the EUDET Telescopes". In: *Nuclear Instruments and Methods in Physics Research Section A: Accelerators, Spectrometers, Detectors and Associated Equipment* 1048 (2023), p. 167947. ISSN: 0168-9002. DOI: https://doi.org/10.1016/j.nima.2022.167947.

[2] L. Huth et al. "TelePix2: Full scale fast region of interest trigger and timing for the EUDET-style telescopes at the DESY II test beam facility". In: *Nuclear Instruments and Methods in Physics Research Section A: Accelerators, Spectrometers, Detectors and Associated Equipment* 1080 (2025), p. 170720. ISSN: 0168-9002. DOI: https://doi.org/10.1016/j.nima.2025.170720.

[3] H. Augustin et al. "Upgrading the beam telescopes at the DESY II Test Beam Facility". In: *Nuclear Instruments and Methods in Physics Research Section A: Accelerators, Spectrometers, Detectors and Associated Equipment* 1040 (2022), p. 167183. ISSN: 0168-9002. DOI: https://doi.org/10.1016/j.nima.2022.167183.

[4] K. Arndt et al. "Technical design of the phase I Mu3e experiment". In: *Nuclear Instruments and Methods in Physics Research Section A: Accelerators, Spectrometers, Detectors and Associated Equipment* 1014 (2021), p. 165679. ISSN: 0168-9002. DOI: https://doi.org/10.1016/j.nima.2021.165679.

[5] H. Augustin et al. "Performance of the large scale HV-CMOS pixel sensor MuPix8". In: *Journal of Instrumentation* 14.10 (Oct. 2019), p. C10011. DOI: 10.1088/1748-0221/14/10/C10011.

[6] M. Kiehn et al. "Performance of the ATLASPix1 pixel sensor prototype in ams aH18 CMOS technology for the ATLAS ITk upgrade". In: *Journal of Instrumentation* 14.08 (Aug. 2019), p. C08013. DOI: 10.1088/1748-0221/14/08/C08013.

[7] Heiko Augustin et al. "Efficiency and timing performance of the MuPix7 high-voltage monolithic active pixel sensor". In: *Nuclear Instruments and Methods in Physics Research Section A: Accelerators, Spectrometers, Detectors and Associated Equipment* 902 (2018), pp. 158–163. ISSN: 0168-9002. DOI: https://doi.org/10.1016/j.nima.2018.06.049.

[8] H. Augustin et al. "Irradiation study of a fully monolithic HV-CMOS pixel sensor design in AMS 180 nm". In: *Nuclear Instruments and Methods in Physics Research Section A: Accelerators, Spectrometers, Detectors and Associated Equipment* 905 (2018), pp. 53–60. ISSN: 0168-9002. DOI: https://doi.org/10.1016/j.nima.2018.07.044.

[9] H. Augustin et al. "MuPix7—A fast monolithic HV-CMOS pixel chip for Mu3e". In: *Journal of Instrumentation* 11.11 (2016), Art.–Nr.: C11029. ISSN: 1748-0221. DOI: 10.1088/1748-0221/11/11/C11029.

Proceedings

[1] Heiko Augustin et al. "MuPix10: First Results from the Final Design". In: *Proceedings of the 29th International Workshop on Vertex Detectors (VERTEX2020)*. DOI: 10.7566/JPSCP.34.010012. eprint: https://journals.jps.jp/doi/pdf/10.7566/JPSCP.34.010012.

[2] Andre Schoening et al. "MuPix & ATLASpix: Architectures and Results". In: *Proceedings of The 28th International Workshop on Vertex Detectors — PoS(Vertex2019)*. Vol. 373. 2020, p. 024. DOI: 10.22323/1.373.0024.

[3] Heiko Christian Augustin et al. “MuPix8 - A large-area HV-MAPS chip”. In: *Proceedings of The 26th International Workshop on Vertex Detectors — PoS(Vertex 2017)*. Vol. 309. 2018, p. 057. DOI: 10.22323/1.309.0057.

[4] Dirk Wiedner et al. “Readout Electronics for the First Large HV-MAPS Chip for Mu3e”. In: *Proceedings of Topical Workshop on Electronics for Particle Physics — PoS(TWEPP-17)*. Vol. 313. 2018, p. 099. DOI: 10.22323/1.313.0099.

[5] Thomas Rudzki et al. “The Mu3e experiment: Toward the construction of an HV-MAPS vertex detector”. In: *International Workshop on Future Linear Colliders (LCWS2021)*. 2021. DOI: 10.48550/arXiv.2106.03534. arXiv: 2106.03534 [physics.ins-det].

[6] Heiko Augustin et al. “MuPix: An HV–MAPS for the Mu3e Experiment”. In: *Proceedings of the 31st International Workshop on Vertex Detectors (VERTEX2022)*. 2022. DOI: 10.7566/JPSCP.42.011020. eprint: https://journals.jps.jp/doi/pdf/10.7566/JPSCP.42.011020.

[7] Thomas Theodor Rudzki et al. “An ultra-light helium cooled pixel detector for the Mu3e experiment”. In: vol. 18. 10. IOP Publishing, Oct. 2023, p. C10022. DOI: 10.1088/1748-0221/18/10/C10022.

[8] H. Augustin et al. “Timing characterisation of TelePix2”. In: *Journal of Instrumentation* 20.06 (June 2025), p. C06071. DOI: 10.1088/1748-0221/20/06/C06071.

Danksagung

Zum Abschluss dieser Dissertation möchte ich die letzten Zeilen nutzen, um all jenen zu danken, ohne deren Unterstützung die Entstehung dieser Arbeit nicht möglich gewesen wäre.

Angefangen bei meinem Doktorvater Prof. Dr. André Schöning, der mir die Möglichkeit gab, diese Arbeit durchzuführen und mein Wissen sowie meine Fähigkeiten seit meinem Beginn in dieser Arbeitsgruppe als Bachelorstudent kontinuierlich zu erweitern. Mein Dank gilt zudem Prof. Dr. Ulrich Uwer, der sich bereit erklärt hat, als Zweitgutachter meiner Dissertation zu fungieren.

Darüber hinaus danke ich all jenen, deren Engagement die Messungen und Analysen in dieser Arbeit erst ermöglichte. Einen großen Dank geht an Ralf Achenbach, der sich immer bereit erklären ließ, auch unter Zeitdruck Sensoren zu bonden, ohne den viele spontane Messungen nicht möglich gewesen wären. Ebenso danke ich den Mitgliedern der Werkstatt des Physikalischen Instituts für ihre vorbildliche Arbeit, die die Fertigung zahlreicher Messaufbauten und Vorrichtungen ermöglicht hat. Der Testbeam Crew am PSI, Annie Meneses González, Dohun Kim und Luigi Vigani, danke ich herzlich für die Unterstützung bei der Durchführung der Teststrahlmessungen ohne die diese Arbeit nicht möglich gewesen wäre. Darüber hinaus danke ich Dohun Kim, Benjamin Weinläder und Ruben Kolb für die Durchführung von Messungen und Simulationen, die in meine Dissertation eingegangen sind.

Danke an allen Kolleginnen und Kollegen aus den Mu3e-, ATLAS- und HV-MAPS-Arbeitsgruppen für ihre Begleitung über all diese Jahre. Einen Dank an Maarten DeKieviet und alle, die mich an den unzähligen Wochenenden am Institut begleitet und mir in dieser Zeit eine angenehme Atmosphäre geschaffen haben. Ohne akribische Korrekturleser wäre diese Arbeit nicht in dieser Form möglich gewesen und wäre für die Leserinnen und Leser stellenweise wohl sehr verwirrend geblieben. Daher gilt ein besonderer Dank meine Korrekturleser: Ruben Kolb, Benjamin Weinläder, Lucas Dittmann und Heiko Augustin.

In Zeiten der Corona-Pandemie und Homeoffice war es nicht immer einfach, motiviert zu bleiben, doch viele virtuelle Treffen mit Freunden und Kollegen haben mir dabei geholfen. Herzlichen Dank an Heiko Augustin, Sebastian Dittmeier, Jan Hammerich, Adrian Herkert, Katharina (Alter-) Huth, Lennart Huth, Dohun Kim, Jens Kroeger, Lars Noehte, Ann-Kathrin Perrevoort und Benjamin Weinläder.

Ein großes Danke geht an Adrian Herkert, Heiko Augustin, Jan Hammerich, Lennart Huth, Lukas Mandok, Ruben Kolb, Sebastian Dittmeier, Dohun Kim, Lucas Dittmann, Benjamin Weinläder und Christof Sauer. Sie haben mich all die Jahre begleitet, mit zahlreichen Diskussionen, Anregungen und Hilfestellungen bei der Durchführung dieser Arbeit sowie vielen schönen gemeinsamen Momenten innerhalb und außerhalb des Arbeitsumfelds.

Ein so langes Studium wäre ohne den Beistand meiner Eltern nicht möglich gewesen. Insbesondere in den letzten Monaten der Schreibphase waren sie mit offenem Ohr und tatkräftiger Unterstützung eine unverzichtbare Stütze, die mir die Kraft gaben, diese Arbeit zu vollenden. Von ganzem Herzen danke ich Euch beiden!